Transactions of the ASME® Journal of Heat Transfer

Published Bimonthly by The American Society of Mechanical Engineers

VOLUME 124 • NUMBER 5 • OCTOBER 2002

TECHNICAL PAPERS

(Contents continued on inside back cover)

Transactions of the ASME, Journal of Heat Transfer (ISSN 0022-1481) is published bi-monthly (Feb., Apr., June, Aug., Oct., Dec.) by The American Society of Mechanical Engineers, Three Park Avenue, New York, NY 10016. Periodicals postage paid at New York, NY and additional mailing offices. POSTMASTER: Send address changes to Transactions of the ASME, Journal of Heat Transfer, c/o THE AMERICAN SOCIETY OF MECHANICAL ENGINEERS, 22 Law Drive, Box 2300, Fairfield, NJ 07007-2300. **CHANGES OF ADDRESS** must be received at Society headquarters seven weeks before they are to be effective. Please send old label and new address. **STATEMENT from By-Laws.** The Society shall not be responsible for statements or opinions advanced in papers or ... printed in its publications (B7.1, Para. 3), **COPYRIGHT © 2002** by The American Society of Mechanical Engineers. For authorization to photocopy material for internal or personal use under those circumstances not falling within the fair use provisions of the Copyright Act, contact the Copyright Clearance Center (CCC), 222 Rosewood Drive, Danvers, MA 01923, tel: 978-750-8400, *www.copyright.com*. Request for special permission or bulk copying should be addressed to Reprints/Permission Department. **INDEXED** by Applied Mechanics Reviews and Engineering Information, Inc. Canadian Goods & Services Tax Registration #126148048.

(**Contents continued**)

Journal of Heat Transfer **Volume 124, Number 5** **OCTOBER 2002**

Heat Transfer Enhancement

Heat and Mass Transfer

Heat Transfer in Manufacturing

Microscale Heat Transfer

TECHNICAL NOTES

ANNOUNCEMENTS

Optimum Design of Spacecraft Radiators With Longitudinal Rectangular and Triangular Fins

Rizos N. Krikkis
Institute of Chemical Engineering and High
Temperature Chemical Processes,
P.O. Box 1414,
Stadiou St., Platani, 26 500 Patras,
Greece

Panagiotis Razelos
Mem. ASME
Professor Emeritus,
College of Staten Island,
CUNY, NY

In the present study the optimum dimensions of longitudinal rectangular and triangular radiating fins with mutual irradiation are determined. The basic assumptions are one-dimensional heat conduction and gray diffuse surface radiation. The governing equations are formulated by means of dimensionless variables and solved numerically in order to carry out the required minimization procedure. The optimum fin dimensions, thickness and height, are presented in generalized dimensionless form and correlations are provided in order to assist the spacecraft thermal systems designer. The results are analyzed and expressed in explicit correlations. Several diagrams, are also included, that give insight to the operational characteristics of the heat rejection mechanism. Moreover, special attention is given to the error analysis of the numerical methods used, since the accuracy and the reliability of the algorithms employed for the solution of the integro-differential equation is important for the calculation of the heat dissipation at the fin base and its subsequent optimization. [DOI: 10.1115/1.1497359]

Keywords: *Finned Surfaces, Heat Transfer, Radiation*

Introduction

Radiating extended surfaces are widely used to reject heat from a spacecraft, which became very important with the advent, in the middle of the last century, of space exploration. Substantial effort has been made to understand the fundamental energy exchange mechanisms involved in order to design radiating equipment. Bartas and Sellers [1], obtained the efficiency of rectangular radiating fins. Kern and Kraus [2], expressed the heat dissipation and the temperature distribution from a radiating fin in terms of the complete and incomplete beta functions. Liu [3,4], Wilkins [5], Chung and Nguyen [6], and Kern and Kraus [2], employed different methods to obtain the optimum dimensions of longitudinal radiating fins. Chung and Zhang [7,8], also determined the optimum dimensions of fins and fin arrays taking into consideration fin to fin and fin to base interactions. Chung et al. [9], proposed a new design for space radiators and determined its optimum dimensions in a fuzzy environment. Krishnaprakas [10,11], obtained the optimum dimensions for fin arrays and presented the results with correlations. Sunil Kumar et al. [12], optimized a space radiator with variable base temperature. Ramesh et al. [13], optimized a two-dimensional tubular space radiator and gave correlations for the optimum dimensions. Schnurr et al. [14], determined and compared the optimum dimensions of circular and straight fin arrays of various profiles. The reader will find additional references in the recent review article on this subject by Aziz and Kraus [15] and in the new book by Kraus et al. [32].

In the present work we determine the optimum dimensions of constant thickness and triangular longitudinal radiating fins that includes radiant heat exchange between fins. All the surfaces involved are considered gray and diffuse with constant thermal properties. Sparrow et al. [18] examined fins of rectangular profile, while Karlekar and Chao [19], rectangular and trapezoidal profiles. Employing the results of the above references to determine the optimum fin dimensions, one should use diagrams, which apparently will introduce inaccuracies (see Aziz and Kraus [15]). In contrast, the present study proposes a method where the optimum dimensions are obtained directly from explicit relations without the need of interpolations from graphs or tables.

Statement of the Problem

Consider a uniform density longitudinal fin in a tubular radiator assembly depicted schematically in Figs. 1(*a*) and 1(*b*). The fin is made of material with thermal conductivity k, profile $Y=Y(X)$ base thickness $2w$, height L, and length H. The fin base is maintained at constant temperature T_b. Assuming one-dimensional heat conduction $(L/w \gg 1)$, no heat sources or sinks in the fin, radiation from all surfaces according to the Stefan-Boltzmann law, length of the fin H much larger than L or w, $(H/L, H/w \gg 1)$, the steady-state temperature and radiosity must satisfy the following equations:

$$\frac{d}{dX}\left(kA\frac{dT}{dX}\right)=P\frac{dS}{dX}Q_r \tag{1}$$

$$Q_r(X)=J(X)-\int_{X'=0}^{L}J(X')dF_{dX-dX'} \tag{2}$$

$$J(X)=\epsilon\sigma T^4(X)+(1-\epsilon)\int_{X'=0}^{L}J(X')dF_{dX-dX'} \tag{3}$$

where Q_r is the net radiative flux, and J is the radiosity. The boundary conditions are

$$T(0)=T_b, \quad -k\frac{dT}{dX}\bigg|_{X=L}=\epsilon\sigma T^4(L) \tag{4}$$

In Eq. (1), $A=2Y(X)H$ is the area perpendicular to the heat flow and $P=2H$ is the participating perimeter in the radiative energy exchange. The area factor $P\,dS/dX$ is equal to

$$P\,dS/dX=2H[1+(dY/dX)^2]^{1/2} \tag{5}$$

Given the volume of the fin

$$V=HA_p=H\int_0^L 2Y(X)dX \tag{6}$$

we seek the fin semi-thickness w and height L that will maximize the fin heat dissipation

---

Contributed by the Heat Transfer Division for publication in the JOURNAL OF HEAT TRANSFER. Manuscript received by the Heat Transfer Division December 20, 2001; revision received May 23, 2002. Associate Editor: B. T. F. Chung.

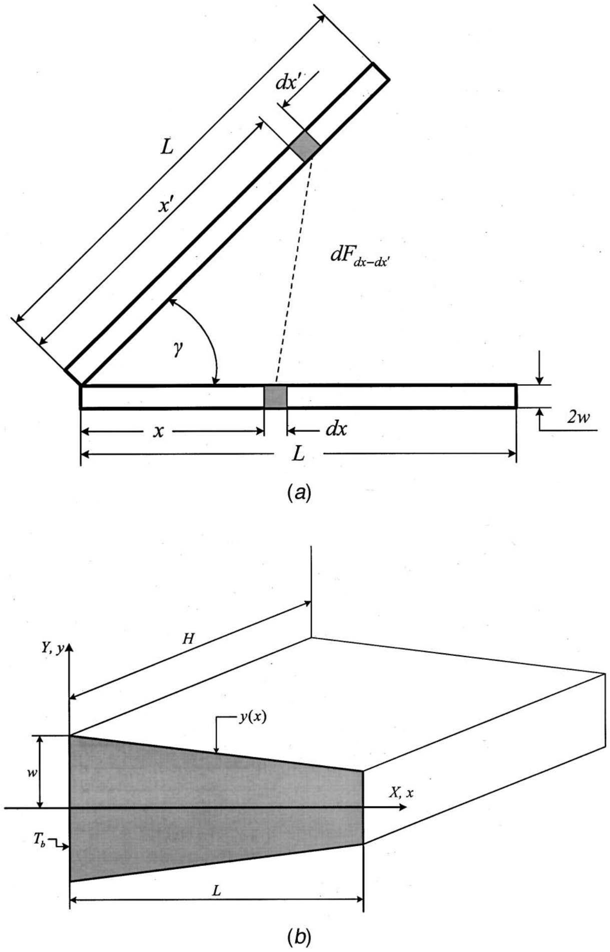

(a)

(b)

Fig. 1 (a) Schematic tubular space radiator; and (b) longitudinal fin geometry

$$q_f = -kA\left.\frac{dT}{dX}\right|_{X=0} \tag{7}$$

Note that according to the earlier stated assumptions regarding the length of the fin, we can take $H=1$ m without loss of generality and all quantities will be per unit length. All the above equations are nondimensionalized with the aid of the following dimensionless variables:

$$x = X/L, \quad y = Y/w, \quad \Theta = T/T_b \tag{8}$$

and

$$j = J/(h_r T_b), \quad q_r = Q_r/(h_r T_b) \tag{9}$$

Furthermore, the dimensionless parameters that describe the problem is the radiation-conduction coefficient,

$$u^2 = \frac{h_r L^2}{kw} = \frac{L^2}{w^2}\mathrm{Bi} \tag{10}$$

and the radiation Biot number $\mathrm{Bi} = h_r w/k$ where $h_r = \sigma T_b^3$ denotes the black radiation heat transfer coefficient. With the aid of Eq. (8) the perimetry factor, Eq. (5), may be written as:

$$P\frac{dS}{dX} = 2\left[1 + \frac{w^2}{L^2}\left(\frac{dy}{dx}\right)^2\right]^{1/2} \tag{11}$$

Using now the earlier defined Biot number and the radiation-conduction coefficient yields:

$$P\frac{dS}{dX} = 2\left[1 + \frac{\mathrm{Bi}}{u^2}\left(\frac{dy}{dx}\right)^2\right]^{1/2} \tag{12}$$

On the basis of the previously stated assumption regarding the one dimensional heat conduction into the fin, the order of magnitude of the radiation-conduction coefficient is one and $\mathrm{Bi}^{1/2} \ll 1$, Razelos and Georgiou [17]. Taking this into consideration Eq. (12) reduces to $P\, dS/dX \approx 2$. Substituting Eqs. (8) and (9) into Eqs. (1) to (3), we obtain the following expressions:

$$\Theta''(x) = [u^2 q_r(x) - y'\Theta']/y, \quad 0 \leqslant x \leqslant 1 \tag{13}$$

$$q_r(x) = \frac{\epsilon}{1-\epsilon}[\Theta^4(x) - j(x)] \tag{14}$$

$$j(x) - \int_{x'=0}^{1} K(x,x')j(x')dx' = \epsilon\Theta^4(x) \tag{15}$$

where in Eqs. (13) and (17) Θ'' and Θ' represent the second and the first derivatives with respect to x. The corresponding boundary conditions are

$$\Theta(0) = 1 \tag{16}$$

$$\Theta'(1) + \epsilon u \mathrm{Bi}^{1/2}\Theta^4(1) = \Theta'(1) + \epsilon B_L \Theta^4(1) = 0 \tag{17}$$

where B_L is a dimensionless parameter:

$$B_L = h_r L/k = L\mathrm{Bi}/w = u\mathrm{Bi}^{1/2} \tag{18}$$

Using the same arguments as before, Eq. (17) reduces to $\Theta'(1) \approx 0$. It is worth noticing that the problem was also solved using both boundary conditions $\Theta'(1) = 0$ or Eq. (17) where the same results were obtained and therefore the optimum environment is independent of the value of B_L since $B_L \ll 1$. This is because $\epsilon \leqslant 1$, u is of $O(1)$, $\Theta^4(1) < 1$ and $\mathrm{Bi}^{1/2} \ll 1$. The kernel function in Eq. (15) takes the form

$$K(x,x') = \frac{(1-\epsilon)xx' \sin^2(\gamma + \gamma_f)}{2[x^2 - 2xx' \cos(\gamma + \gamma_f) + x'^2]^{3/2}} \tag{19}$$

where γ is the opening angle between the fins. In the above equations the physical quantities, thermal parameters and the fin dimensions, have been combined to form a number of nondimensional variables that describe the problem. The equation that describes the profile of the fin is

$$y = 1 + (\lambda - 1)x \tag{20}$$

where $\lambda = 1$ corresponds to the rectangular profile and $\lambda = 0.01$ to the triangular. It can be seen from Eqs. (13–15) that the dimensionless temperature is

$$\Theta = \Theta(x; u, \gamma, \epsilon) \tag{21}$$

The heat dissipated by the fin, after introducing dimensionless variables becomes

$$Q = \frac{q_f}{2kT_b} = -\frac{w}{L}\Theta'(0; u, \gamma, \epsilon) = -\frac{\mathrm{Bi}^{1/2}\Theta'(0; u, \gamma, \epsilon)}{u}$$
$$= \mathrm{Bi}^{1/2} D(u, \gamma, \epsilon) \tag{22}$$

where $D = -\Theta'(0; u, \gamma, \epsilon)/u$. It has been pointed out by Razelos and Georgiou [17] that the condition that will economically justify the use of fins is: "the ratio of heat dissipated by the fin to be much larger in comparison with the heat that would have been dissipated from the surface $2wH$, in the absence of the fin." This ratio is the removal number and it is equal to

$$N_r = \frac{q_f}{q_b} = \frac{2kT_b Q}{(2w)\epsilon\sigma T_b^4} = \frac{D}{\mathrm{Bi}^{1/2}} \tag{23}$$

Optimization

In terms of the dimensionless variables introduced, the optimization statement given earlier becomes: *Given the profile of the fin and the desired heat dissipation determine the dimensions of the fin that minimize its volume* (Razelos and Imre [20], Razelos and Krikkis [16]). There is also the equivalent problem stated as: *For a given fin volume we seek the dimensions that will maximize the heat dissipation*. Following Razelos and Krikkis [16], a dimensionless volume is introduced as

$$U=\frac{h_r^2 V}{2C_V k^2}=u\mathrm{Bi}^{3/2} \tag{24}$$

The fin volume in terms of dimensionless variables is calculated from Eq. (6) as

$$V=2Lw\int_0^1 y(x)dx=2C_V Lw=C_V V_c \tag{25}$$

From Eqs. (22) and (24) we may observe that the dimensionless heat dissipation and volume can be expressed as functions of u and Bi

$$Q=Q(u,\mathrm{Bi};\gamma,\epsilon) \tag{26}$$

$$U=U(u,\mathrm{Bi}) \tag{27}$$

We now recast the optimization problem in terms of Q and U as: *Given U, determine the parameters u and* Bi, *that will maximize Q*. For a specified volume, after taking the differential of Eq. (27) and remembering that the parameters ϵ and γ are specified by the problem, we obtain

$$dU=\left(\frac{\partial U}{\partial \mathrm{Bi}}\right)d\mathrm{Bi}+\left(\frac{\partial U}{\partial u}\right)du=0 \tag{28}$$

The stationary value of Q for a given U can be expressed as

$$dQ=\left(\frac{\partial Q}{\partial \mathrm{Bi}}\right)d\mathrm{Bi}+\left(\frac{\partial Q}{\partial u}\right)du=0 \tag{29}$$

which after inserting the constrain Eq. (28) is written as:

$$\left(\frac{\partial Q}{\partial \mathrm{Bi}}\right)\left(\frac{\partial U}{\partial u}\right)-\left(\frac{\partial Q}{\partial u}\right)\left(\frac{\partial U}{\partial \mathrm{Bi}}\right)=0 \tag{30}$$

Introducing now the expressions for Q and U [Eqs. (22) and (24)] into the above relationship yields:

$$3u\frac{dD}{du}-D=0 \tag{31}$$

Therefore, the optimum value u_{opt} is the root of Eq. (31), and since in this case there is not analytical expression available, it is numerically calculated. It must be emphasized here that in Eq. (31) the dimensionless volume U or heat dissipation Q do not appear in Eq. (31) and the optimum values of u and D are independent of the particular values of Q or U whichever is being given. They depend only on the fin's profile. Thus the problem defined by Eqs. (13–15) with the corresponding boundary conditions Eqs. (16–17), are solved numerically and the optimization is performed using the univariate minimization routine DUVMIF from the IMSL library, IMSL [21], with a requested absolute accuracy of 10^{-4} in the calculated optima. In practical applications the designers are interested in the actual optimum fin dimensions w_{opt} and L_{opt} instead of those of u_{opt} or $\mathrm{Bi}_{\mathrm{opt}}$. This is accomplished, by introducing the values of u_{opt} and L_{opt} into Eqs. (10) and (22) to define certain dimensionless profile coefficients first proposed by Razelos [22]. Two sets of these coefficients are given. One when the optimization process is based on specified heat dissipation q_f, and the second when the fin volume V is given.

Table 1 Coefficients for the rectangular profile, Eqs. (39) and (40)

	c_0	c_1	c_2	c_3
a_u	1.74114	-4.50904	10.91660	-5.88675
b_u	1.67029	0.30729	-1.02869	0.67358
a_D	0.49070	-0.28698	1.07081	-0.69941
b_D	2.26446	-3.31047	3.98299	-1.86400

Heat Dissipation Given

$$w^*=\frac{h_r k w_{\mathrm{opt}}}{(q_f/T_b)^2}=\frac{1}{4D_{\mathrm{opt}}^2} \tag{32}$$

$$L^*=\frac{h_r L_{\mathrm{opt}}}{(q_f/T_b)}=\frac{u_{\mathrm{opt}}}{2D_{\mathrm{opt}}} \tag{33}$$

$$V^*=\frac{h_r^2 k V_{\mathrm{opt}}}{(q_f/T_b)^3}=2C_V w^* L^*=\frac{C_V u_{\mathrm{opt}}}{4D_{\mathrm{opt}}^3} \tag{34}$$

$$N_r^*=N_r Q=D_{\mathrm{opt}}^2 \tag{35}$$

Fin Volume Given

$$w_V^*=\left(\frac{k}{h_r V_{\mathrm{opt}}^2}\right)^{1/3} w_{\mathrm{opt}}=\frac{w^*}{(V^*)^{2/3}}=(2C_V u_{\mathrm{opt}})^{-2/3} \tag{36}$$

$$L_V^*=\left(\frac{h_r}{kV_{\mathrm{opt}}}\right)^{1/3} L_{\mathrm{opt}}=\frac{L^*}{(V^*)^{1/3}}=\left(\frac{u_{\mathrm{opt}}^2}{2C_V}\right)^{1/3} \tag{37}$$

$$Q^*=\frac{q_f}{T_b(h_r^2 k V_{\mathrm{opt}})^{1/3}}=(V^*)^{-1/3}=\frac{D_{\mathrm{opt}}}{(0.25C_V u_{\mathrm{opt}})^{1/3}} \tag{38}$$

$$N_{rV}^*=N_r U_{\mathrm{opt}}^{1/3}=(C_V u_{\mathrm{opt}})^{1/3} D_{\mathrm{opt}} \tag{39}$$

The important characteristic of this formulation is that the above expressions are independent of the actual value of q_f or V whichever is specified. For specified opening angle γ and emissivity ϵ they depend on the fin's profile. Therefore the dimensionless coefficients, Eqs. (32–39), can be correlated as functions of γ and ϵ. From the above eight expressions, only the parameters u_{opt} and D_{opt} need to be calculated, since they all depend on u_{opt} and D_{opt}. The correlations used for both the rectangular ($\lambda=1$) and the triangular ($\lambda=0.01$) profiles are the following:

$$(\epsilon u_{\mathrm{opt}}^2)=(u_{\mathrm{opt}}^2)_{sf}+a_u\exp(-b_u\gamma) \tag{40}$$

$$\epsilon^{-1/2}D_{\mathrm{opt}}=(D_{\mathrm{opt}})_{sf}-a_D\exp(-b_D\gamma) \tag{41}$$

where the opening angle is in radians, and the correlation coefficients are polynomials of the emissivity for both profiles

$$z=\sum_i c_i\epsilon^i,\quad 0.50\leqslant\epsilon\leqslant 0.90,\quad z=a_u,b_u,a_D,b_D \tag{42}$$

The polynomial coefficients c_i in Eq. (42) can be found in Table 1 for the rectangular profile and in Table 2 for the triangular profile.

Table 2 Coefficients for the triangular profile, Eqs. (39) and (40)

	c_0	c_1	c_2	c_3
a_u	0.19652	2.29083	-0.36976	-
b_u	2.53536	-3.73719	5.00721	-2.26317
a_D	0.31289	0.51408	-0.23599	-
b_D	1.79085	-0.90984	0.30884	-

Table 3 Single fin values for Eqs. (39) and (40)

Profile	$(u^2_{\mathrm{opt}})_{\mathrm{sf}}$	$(D_{\mathrm{opt}})_{\mathrm{sf}}$
Rectangular ($\lambda=1$)	0.8464	0.5201
Triangular ($\lambda=0.01$)	0.7773	0.4657

In correlations (40) and (41) the corresponding values of the single fin configuration (without fin to fin radiant interaction) are used (Razelos and Kakatsios [23]). These values are shown in Table 3.

It is worth mentioning the procedure that Karlekar and Chao [19] followed for the maximization of the heat dissipation of an assembly when the volume is specified. The authors defined the dimensionless heat dissipation for the assembly as:

$$\xi=\frac{q_T}{[(h_rT_b)^2kT_bV_T]^{1/3}} \tag{43}$$

where $q_T=Nq_f$ is the total heat rejection, $V_T=NV$ is the total volume and N is the number of fins in the assembly. Substituting in the above relation we obtain:

$$\xi=\frac{Nq_f}{T_b(h_r^2kNV)^{1/3}}=N^{2/3}\left[\frac{q_f}{T_b(h_r^2kV)^{1/3}}\right]=N^{2/3}Q^*=(N^2/V^*)^{1/3} \tag{44}$$

It is evident from Eq. (44) that maximizing ξ is equivalent to minimize V^* for a constant N as it is done in [19]. Moreover, the present analysis in the paragraph entitled "OPTIMIZATION" is applicable to this problem provided that the Biot number is now defined by

$$\mathrm{Bi}=\left(\frac{U_T}{Nu}\right)^{2/3} \tag{45}$$

Consequently the problem of maximizing the heat dissipation of a fin assembly when its volume is given is equivalent to the minimization of the assembly volume when the desired heat dissipation is given. The above statement will be used in the following examples for comparison purposes.

Numerical Solution

The integro-differential equation, (13–15), was solved numerically using an iterative procedure (Modest [24]). First a temperature distribution is calculated and then inserted into the FIE Eq. (15), which is solved for the radiosity and the procedure is repeated solving the ODE (13) for an updated temperature distribution. Convergence is considered successful when the infinite norm of the temperature derivative is less than 10^{-6}. In order to accelerate the convergence, the solution starts with the higher opening angle first (i.e., $\gamma=150$ deg). The starting temperature employed is the one corresponding to the single fin configuration, Razelos and Kakatsios [23], which is quite close to the exact one since at these high opening angles the mutual irradiation is less significant. The second order, two-point BVP is transformed into a first order IVP with the following relations,

$$\Theta_1=\Theta, \quad \Theta_2=\Theta' \tag{46}$$

which is then solved using a multi-shooting technique, Ascher et al. [25], Keller [26], and a newton method for the iterations on the unknown initial condition. The algorithm used is a variable step embedded Runge-Kutta algorithm of order 5(4), Papakostas et al. [27], Tsitouras and Papageorgiou [28]. A procedure utilizing such a pair advances the integration from x_n to $x_{n+1}=x_n+\Delta x_n$, computing at each step two approximations of the solution of orders 5 and 4 respectively. From the embedded form it can be obtained an estimate E_{n+1} of the local truncation error in the formula of order 4, which may be used to adjust the step size Δx_n. The step size control algorithm

$$\Delta x_{n+1}=0.9\Delta x_n\left(\frac{\mathrm{TOL}}{\|E_{n+1}\|_\infty}\right)^{1/5} \tag{47}$$

is in common use and this formula is used whether or not the tolerance TOL (requested accuracy which is supplied by the user) is exceeded $\|E_{n+1}\|_\infty$. Thus in one case a rejected step is being recomputed and in the other case the next step is being predicted. In practice the propagated solution of the problem is the one provided by the 5th order formula (local extrapolation), as proposed by Shampine [29]. Since the function evaluations in Eq. (13) are not expensive a value of 10^{-8} was used for TOL as a compromise between accuracy and computer time.

The FIE Eq. (15) was solved using both Simpson's and Gauss-Legendre quadrature formulas (to ensure consistency) with an automatic error control algorithm, Atkinson [30,31]. Both methods gave identical results (the diagrams presented are calculated using Gauss–Legendre integration formulas). The Nyström method is used for the discretization of the integral equation and an iterative two-grid algorithm is used for the solution of the linear system when it becomes large. The procedure begins by solving for a discretization parameter $m=m_0$ (and l_{m_0} linear equations), with an initial guess $j^{(0)}_{m_0}=0$ for the radiosity. Then the discretization parameter m is increased until an approximate solution with sufficient accuracy is obtained. Given a tolerance $\delta>0$, an approximate solution for the radiosity j_δ is computed which satisfies the criterion

$$\|j-j_\delta\|_\infty<\delta \tag{48}$$

where j is the exact solution. $\delta=10^{-6}$ was used for the computations which resulted in a variation of the discretization parameter m between 32 and 128. It is worth noticing that the corresponding discretization parameter used by Karlekar and Chao [19] was $m=16$, while, no discretization information were given by Sparrow et al. [18]. The kernel function Eq. (19), at the point $(x,x')=(0,0)$ becomes indefinite. To overcome this difficulty the exact value of the radiosity is employed, Sparrow et al. [18], Karlekar and Chao [19],

$$j(0)=\frac{\epsilon}{1-(1-\epsilon)\{[1-\sin(\gamma-120\ \mathrm{deg})]/2\}} \tag{49}$$

It should be noted here that the fin heat dissipation is computed directly from the solution of the ordinary differential equation, Eq. (46), using Eqs. (22) and (49). In this way the calculated solution is very accurate since Eq. (49) is exact and the truncation error in the temperature derivative is of fifth order. The discrete temperature distribution $\Theta(\xi_i)$, $0\leqslant\xi_i\leqslant1$, obtained from the ODE solver and the corresponding discrete radiosity distribution $j(\xi_n)$, $0\leqslant\xi_n\leqslant1$, are used for the construction of a temperature and a radiosity interpolating piecewise polynomials of the form:

$$\Theta_1(x)=\sum_{j=1}^{k}c_{ij}\frac{(x-\xi_i)^{j-1}}{(j-1)!}, \quad \xi_i\leqslant x\leqslant\xi_{i+1} \tag{50}$$

and

$$j(x)=\sum_{j=1}^{k}c_{nj}\frac{(x-\xi_n)^{j-1}}{(j-1)!}, \quad \xi_n\leqslant x\leqslant\xi_{n+1} \tag{51}$$

where the breakpoint sequences ξ_i and ξ_n are provided by the ODE and the FIE solvers respectively. For the interpolants constructed above $k=8$, was used (degree $k-1$) so that the right hand side of Eq. (13) has continuous derivatives. In this way full advantage is taken of the accuracy characteristics of the ODE solver since an optimum Runge-Kutta algorithm of order 5 must agree with the Taylor expansion of the same order and minimize as

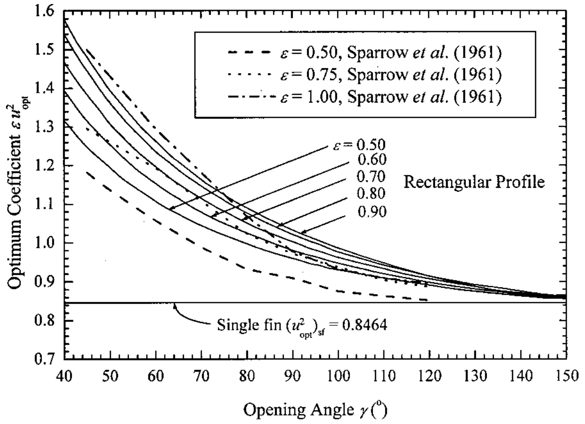

Fig. 2 Optimum parameter ϵu^2_{opt} as a function of the opening angle for various emissivities and rectangular profile

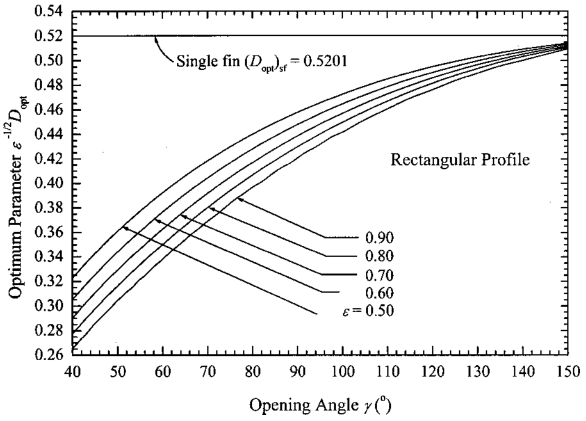

Fig. 3 $\epsilon^{-1/2} D_{opt}$ versus the opening angle for various emissivities and rectangular profile

many as possible error coefficients of higher orders. It is therefore evident that the derivative continuation is essential for an accurate and reliable solution (temperature distribution). Furthermore there is no need to integrate over the fin surface the radiosity and the irradiation, reducing in this way the accuracy of the numerical scheme, as it is obvious that an accurate and reliable calculation of the fin heat dissipation is very important for the minimization process. In the solution the equivalence relation, Eq. (30), is taken into consideration, that is for a given value of U an optimum (maximum) value of Q is calculated which is equivalent to calculate an optimum (minimum) U from the given value of Q. Calculations were carried out using values of the dimensionless volume in the range $U = 10^{-5} \div 10^{-3}$ obtaining the same optimum. These calculations were obtained to verify and numerically that the results obtained earlier who have shown that the optimum values of u and D are independent of the values of U or Q whichever was specified for the optimization process.

Results and Discussion

Figure 2 shows the optimum parameter ϵu^2_{opt} as a function of the opening angle for various emissivities between 0.50 and 0.90 for the rectangular profile. As the opening angle $\gamma \rightarrow 180$ deg the optimum radiation conduction coefficient becomes independent of the emissivity. For this limiting value the view factor in Eq. (3) also vanishes and the radiosity equals $\epsilon \Theta^4$. Thus in the governing Equation (13), as it is expected, there are no terms involving radiation interaction and the problem reduces to a single fin configuration. This is a well-studied case, Wilkins [5], Razelos and Kakatsios [23] (Table 1) and the optimum radiation-conduction parameter is $(u^2_{opt})_{sf} = 0.8464$. This trend is a confirmation of the consistency of the numerical solution achieved. For comparison purposes the corresponding results of Sparrow et al. [18] are indicated in Fig. 2. The data have been obtained from copies of their original figures and this circumstance explains the occasional scatter in their points, which appears in our figure since no smoothing has been applied on the data. The agreement is better at high opening angles, while there are deviations at smaller angles. Since the mathematical formulation of the problem is the same the differences can only be attributed to the numerical methods employed. Figure 3 shows the optimum function $\epsilon^{-1/2} D_{opt}$ versus the opening angle for various emissivities between 0.50 and 0.90 for the rectangular profile. Again as $\gamma \rightarrow 180$ deg D_{opt} becomes independent of the emissivity and tends to the single fin configuration value, which is $(D_{opt})_{sf} = 0.5201$. Figures 4 and 5 show the corresponding results for the triangular profile. For the purpose of illustration and comparison the use of Eqs. (32) to (38) is demonstrated by two examples.

Example 1. Determine the optimum dimensions of the tubular radiator of Fig. 1, operating in free space at 0 K, where the base temperature is $T_b = 500\,\mathrm{K}$. The emissivity is 0.75 and the fin thermal conductivity is $k = 173\,\mathrm{W/(mK)}$. The radiator is designed to dissipate $q_T = 2400\,\mathrm{W}$ per unit tube length with $N = 6$ fins of rectangular profile.

Solution. First we calculate the opening angle $\gamma = 360$ deg/6 = 60 deg. Then q_f and h_r are calculated as follows: $q_f = q_T/N$

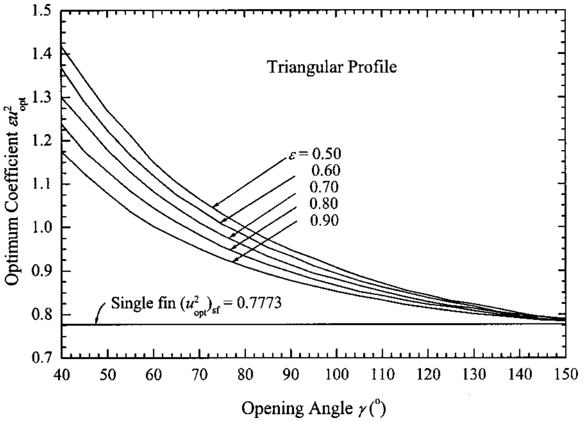

Fig. 4 Optimum parameter ϵu^2_{opt} as a function of the opening angle for various emissivities and triangular profile

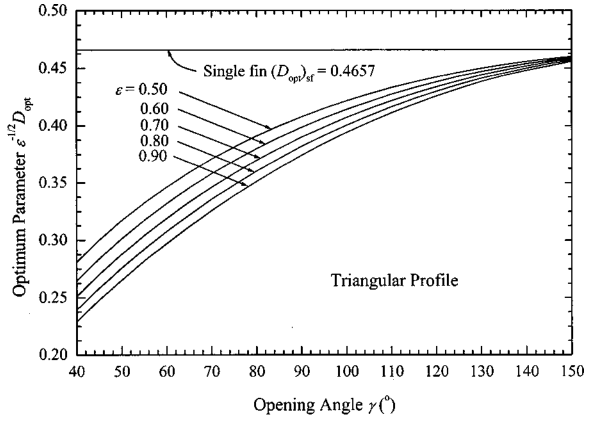

Fig. 5 $\epsilon^{-1/2} D_{opt}$ versus the opening angle for various emissivities and triangular profile

Table 4 Results and comparisons for example 1

Reference	w_{opt} [mm]	L_{opt} [mm]	V_{opt} [mm^3/m]
Present study	1.26	217.0	546
Sparrow *et al.* [18]	1.42	235.0	667
Karlekar and Chao [19]	1.43	234.5	671
Schnurr *et al.* [14]	1.30	217.4	565

Table 5 Results and comparisons for example 2

Reference	w_{opt} [mm]	L_{opt} [mm]	V_{opt} [mm^3/m]
	$\epsilon = 0.90$		
Present study	1.30	194.4	253
Karlekar and Chao [19]	1.38	197	272
Schnurr *et al.* [14]	1.475	184.1	272
	$\epsilon = 0.50$		
Present study	1.30	258.8	336
Karlekar and Chao [19]	1.374	258.9	356

$=2400/6=400$ W/m and $h_r=\sigma T_b^3=5.67\times 10^{-8}(500)^3=7.09$ W/(m^{2}K). From Eq. (42) and Table 1 we obtain the correlation coefficients as $a_u=2.018$, $b_u=1.6062$ and $a_D=0.5668$, $b_D=1.2818$. From Eqs. (40) and (41) we obtain $u_{\mathrm{opt}}=1.276$ and $D_{\mathrm{opt}}=0.322$. From Figs. 2 and 3 we obtain respectively $u_{\mathrm{opt}}=1.269$ and $D_{\mathrm{opt}}=0.308$ which differ by 0.55 percent and 4.5 percent respectively from the correlations. Then the dimensionless semi thickness w^* and height L^* are calculated as $w^*=0.25/D_{\mathrm{opt}}^2=2.4112$ and $L^*=0.5u_{\mathrm{opt}}/D_{\mathrm{opt}}=1.9217$. Now the optimum fin dimensions w_{opt} and L_{opt} can be obtained from Eqs. (32) and (33) respectively: $w_{\mathrm{opt}}=1.26$ mm and $L_{\mathrm{opt}}=217$ mm. The optimum fin volume is calculated as $V_{\mathrm{opt}}=2w_{\mathrm{opt}}L_{\mathrm{opt}}=546$ mm^3/m. From the fin height now the value of parameter B_L is obtained as: $B_L=h_rL/k=8.89\times 10^{-3}$ which provides justification for the use of $\Theta'(1)=0$ instead of the boundary condition Eq. (17). The results are summarized in Table 4 together with the corresponding results obtained by the methodologies of references [18], [19] and [14], where an outside tube radius $r_i=0.015$ m was assumed.

Example 2. Determine the optimum fin dimensions of a radiator consisting of a tube fitted with uniformly spaced triangular fins which is designed to dissipate $q_T=2000$ W/m when operating with a base temperature of 500 K. Furthermore, $k=173$ W/(m K), $\epsilon=0.90$, and $\gamma=72$ deg ($N=5$ fins). Repeat the calculations when $\epsilon=0.50$ and $\gamma=51.43$ deg ($N=7$ fins).

Solution. Using the same methodology as in the previous example we obtain $q_f=2000/5=400$ W/m, $u_{\mathrm{opt}}=1.0834$ and $D_{\mathrm{opt}}=0.31437$. Then the dimensionless semi thickness w^* and height L^* are calculated as $w^*=2.5296$ and $L^*=1.7231$. Now the optimum fin dimensions w_{opt} and L_{opt} can be obtained from Eqs. (32) and (33) respectively $w_{\mathrm{opt}}=1.3$ mm and $L_{\mathrm{opt}}=194.4$ mm. The optimum fin volume is calculated as $V_{\mathrm{opt}}=2w_{\mathrm{opt}}L_{\mathrm{opt}}C_V=253$ mm^3/m. For the second case where $\epsilon=0.50$ and $\gamma=51.43$ deg ($N=7$ fins) the corresponding results are summarized in Table 5 together with the corresponding results obtained by the methodology of Karlekar and Chao [19] and Schnurr et al. [14], where an outside tube radius $r_i=0.01$ m was assumed.

Conclusions

In the present study the problem of designing the optimum fin for the tubular space radiator is solved. The governing equations are formulated by means of dimensionless variables. The optimization is carried out for two cases, that is: First, when the heat dissipation is being given and the fin volume must be minimized, and second when the fin volume is being given and the total heat dissipation must be maximized. It has been shown here that the two problems are equivalent, as in the works of Razelos and Imre [20], Razelos and Kakatsios [23], Razelos and Krikkis [16]. The first important conclusion is that using the simplifying assumptions of the length of arc idealization and/or the insulated tip *the optimum fin dimensions and the profile coefficients* defined in Eqs. (32–39) *depend only on the opening angle* γ*, the emissivity* ϵ *and the profile of the fin and not on the specific values of* Q *or* U.

The second important conclusion, for the problem treated by Karlekar and Chao [19], is that *the maximization of the heat dissipation of a fin assembly when its volume is given is equivalent to the minimization of the assembly volume when the desired heat dissipation is given*. Furthermore we suggest a fast and accurate procedure suitable for all practical engineering purposes. The present procedure can be easily adapted for computer calculations, although there is a direct calculation from diagrams.

Nomenclature

A = surface area [m^2/m]
A_p = fin profile area [m^2]
Bi = (h_rw/k) radiation Biot number
B_L = dimensionless parameter, Eq. (18)
C_V = [1/2(1+λ)] ratio of fin volume to the volume of constant thickness fin
$dF_{dx-dx'}$ = view factor
D = function defined by Eq. (22)
h_r = (σT_b^3) black radiation heat transfer coefficient [W/(m^{2}K)]
H = fin length [m]
j = dimensionless radiosity
J = radiosity [W/m^2]
k = fin thermal conductivity [W/(mK)]
K = kernel in integral equation, Eq. (19)
L = fin height [m]
N = number of fins in the assembly
N_r = removal number
O = order of magnitude
P = perimetry [m/m]
q_f = fin heat loss per unit length [W/m]
q_r = dimensionless radiative heat flux
Q = dimensionless fin heat dissipation
Q_r = radiative heat flux [W/m^2]
S = arc length [m]
T = temperature [K]
x = (X/L) dimensionless distance along fin
X = distance along fin [m]
y = (Y/w) dimensionless fin semi-thickness, Eq. (20)
Y = fin semi-thickness [m]
u = radiation-conduction coefficient, Eq. (10)
U = dimensionless fin volume
V = fin volume [m^3/m]
V_c = $(2Lw)$ rectangular fin volume [m^3/m]
w = base semi-thickness [m]

Greek Symbols

γ = opening angle [deg]
γ_f = $[2\tan^{-1}(w/L)]$ triangular profile semi angle [deg]
ϵ = emissivity
Θ = (T/T_b) dimensionless temperature
λ = tip to base fin semi-thickness ratio
ξ = dimensionless assembly heat dissipation used by Karlekar and Chao [19]
σ = Stefan-Boltzmann constant

Subscripts—Superscripts

$(')$ = derivative with respect to x
b = fin base
D = reference to function D, Eq. (22)
f = fin
opt = optimum

r = radiative transfer
sf = single fin configuration (without mutual irradiation)
T = total (assembly)
u = reference to conduction-radiation parameter u

Abbreviations

BVP = Boundary Value Problem
FIE = Fredholm Integral Equation
IVP = Initial Value Problem
LAI = Length of Arc Idealization
ODE = Ordinary Differential Equation

References

[1] Bartas, J. G., and Sellers, W. H., 1960, ''Radiation Fin Effectiveness,'' ASME J. Heat Transfer, **82**, pp. 73–75.
[2] Kern, D. Q., and Kraus, A. D., 1972, *Extended Surface Heat Transfer*, McGraw-Hill, New York.
[3] Liu, C. Y., 1960, ''On Minimum Weight Rectangular Radiating Fins,'' J. Aerosp. Sci., **27**, p. 871.
[4] Liu, C. Y., 1961, ''On Optimum Rectangular Cooling Fins,'' Q. Appl. Math., **19**, p. 72.
[5] Wilkins, J. E., Jr., 1960, ''Minimizing the Mass of Thin Radiating Fins,'' J. Aerosp. Sci., **27**, pp. 145.
[6] Chung, B. T. F., and Nguyen, L. D., 1986, ''Optimization of Design Parameters for Radiating Longitudinal Fins of Various Geometries,'' 24th AIAA Aerospace Sciences Meeting, Reno, NV, Paper AIAA-86-0150.
[7] Chung, B. T. F., and Zhang, B. X., 1991, ''Minimum Mass Longitudinal Fins with Radiation Interaction at the Base,'' J. Franklin Inst. **328**(1), pp. 143–161.
[8] Chung, B. T. F., and Zhang, B. X., 1991, ''Optimization of Radiating Fin Array Including Mutual Irradiations Between Radiator Elements,'' ASME J. Heat Transfer, **113**, pp. 814–822.
[9] Chung, B. T. F., Zhang, B. X., and Lee, E. T., 1996, ''A Multi-Objective Optimization of Radiative Fin Array Systems in a Fuzzy Environment,'' ASME J. Heat Transfer, **118**, pp. 642–649.
[10] Krishnaprakas, C. K., 1996, ''Optimum Design of Radiating Rectangular Plate Fin Array Extending From a Plane Wall,'' ASME J. Heat Transfer, **118**, pp. 490–493.
[11] Krishnaprakas, C. K., 1997, ''Optimum Design of Radiating Longitudinal Fin Array Extending From a Cylindrical Surface,'' ASME J. Heat Transfer, **119**, pp. 857–860.
[12] Sunil, Kumar S., Venketesh, Nayak, and Venkateshan, S. P., 1992, ''Optimum Finned Space Radiators,'' Int. J. Heat Fluid Flow, **14**(2), pp. 191–200.
[13] Ramesh, N., and Venkateshan, S. P., 1997, ''Optimum Finned Tubular Space Radiator,'' Heat Transfer Eng., **18**(4), pp. 69–87.
[14] Schnurr, E. M., Shapiro, A. B., and Townsend, M. A., 1976, ''Optimization of Radiating Fin Arrays With Respect to Weight,'' ASME J. Heat Transfer, **98**, pp. 643–648.
[15] Aziz, A., and Kraus, A. D., 1996, ''Optimum Design of Radiating and Convective-Radiating Fins,'' Heat Transfer Eng., **17**(3), pp. 44–78.
[16] Razelos, P., and Krikkis, R. N., 2001, ''Optimum Design of Longitudinal Rectangular Fins with Base to Fin Radiant Interaction,'' Heat Transfer Eng., **22**(3), pp. 3–17.
[17] Razelos, P., and Georgiou, E., 1992, ''Two-Dimensional Effects and Design Criteria for Convective Extended Surfaces,'' Heat Transfer Eng., **13**(3), pp. 38–48.
[18] Sparrow, E. M., Eckert, E. R. G., and Irvine, T. F., Jr., 1961, ''The Effectiveness of Radiating Fins with Mutual Irradiation,'' J. Aerosp. Sci., **28**, pp. 763–778.
[19] Karlekar, B. V., and Chao, B. T., 1963, ''Mass Minimization of Radiating Trapezoidal Fins with Negligible Base Cylinder Interaction,'' Int. J. Heat Mass Transf., **6**, pp. 33–48.
[20] Razelos, P., and Imre, K., 1980, ''The Optimum Dimensions of Circular Fins with Variable Thermal Parameters,'' ASME J. Heat Transfer, **102**, pp. 420–425.
[21] IMSL, Inc., 1991, *IMSL Library Reference Manual*, Houston, TX.
[22] Razelos, P., 1979, ''The Optimization of Convective Fins with Internal Heat Generation,'' Nucl. Eng. Des., **52**(2), pp. 289–299.
[23] Razelos, P., and Kakatsios, X. K., 2000, ''Optimum Dimensions of Convective-Radiating Fins: Part I—Longitudinal Fins,'' Appl. Therm. Eng., **20**(13), pp. 1161–1192.
[24] Modest, M. F., 1993, *Radiative Heat Transfer*, McGraw-Hill, New York.
[25] Ascher, U. M., Mattheij, R. M. M., and Russel, R. D., 1995, *Numerical Solution of Boundary Value Problems for Ordinary Differential Equations*, 2nd ed., SIAM, Philadelphia, PA.
[26] Keller, H. B., 1992, *Numerical Methods for Two-Point Boundary-Value Problems*, Dover, New York.
[27] Papakostas, S. N., Tsitouras, Ch., and Papageorgiou, G., 1993, ''A General Family of Explicit Runge-Kutta Pairs of Order 6 and 5,'' National Technical University of Athens, Report NA-1/93.
[28] Tsitouras, Ch., and Papageorgiou, G., 1990, ''Runge-Kutta Interpolants Based on Values from Two Successive Integration Steps,'' Computing, **43**, pp. 255–266.
[29] Shampine, L. F., 1973, ''Local Extrapolation in the Solution of Ordinary Differential Equations,'' Math. Comput., **27**, pp. 91–97.
[30] Atkinson, K. E., 1976, *ACM TOMS*, Vol. 2, pp. 196–199.
[31] Atkinson, K. E., 1997, *The Numerical Solution of Integral Equations of the Second Kind*, Cambridge University Press, New York.
[32] Kraus, A. D., Aziz, A., and Welty, J., 2001, *Extended Surface Heat Transfer*, John Wiley, New York.

Nonstaggered APPLE Algorithm for Incompressible Viscous Flow in Curvilinear Coordinates

S. L. Lee
e-mail: sllee@pme.nthu.edu.tw

Y. F. Chen

Department of Power Mechanical Engineering,
National Tsing-Hua University,
Hsinchu 30043, Taiwan

The NAPPLE algorithm for incompressible viscous flow on Cartesian grid system is extended to nonorthogonal curvilinear grid system in this paper. A pressure-linked equation is obtained by substituting the discretized momentum equations into the discretized continuity equation. Instead of employing a velocity interpolation such as pressure-weighted interpolation method (PWIM), a particular approximation is adopted to circumvent the checkerboard error such that the solution does not depend on the under-relaxation factor. This is a distinctive feature of the present method. Furthermore, the pressure is directly solved from the pressure-linked equation without recourse to a pressure-correction equation. In the use of the NAPPLE algorithm, solving the pressure-linked equation is as simple as solving a heat conduction equation. Through two well-documented examples, performance of the NAPPLE algorithm is validated for both buoyancy-driven and pressure-driven flows. [DOI: 10.1115/1.1484109]

Keywords: Computational, Finite Difference, Flow, Heat Transfer, Numerical Methods

Introduction

Many important industrial flow processes have boundaries of irregular shape. Heat exchangers, airfoils, turbomachines, cooling objects, and combustors are some of the examples. For these flow configurations, the Navier-Stokes equation might be efficiently solved on a Cartesian grid system with an adequate numerical scheme [1] in case the boundary layer thickness is sufficiently large. However, very fine grids are generally needed when the boundary layer is thin. Under this situation, use of a body-fitted curvilinear grid system would be more practical.

In an early study, Rhie and Chow [2] derived a pressure-correction equation for nonstaggered curvilinear nonorthogonal grids. The cross derivative terms due to grid skewness were dropped to retain the structure of the five-point approximation. To ensure a strong pressure-velocity coupling, a pressure-weighted interpolation method (PWIM) was proposed. This precluded the checkerboard error for the pressure and allowed the SIMPLE algorithm be performed on nonstaggered grid systems. The PWIM was extended to three-dimensional problems [3,4] and unsteady situation [5]. However, the solution provided by PWIM depends on the under-relaxation factor as pointed out by Patankar [6]. Furthermore, the PWIM could produce physically impossible velocity when the pressure gradient has a rapid variation as remarked by Miller and Schmidt [7].

Shyy and coworkers [8,9] were one of the early groups to apply computational fluid dynamics on nonorthogonal grids. Staggered grid systems were used. Like in the standard SIMPLE algorithm on Cartesian grid system, Shyy et al. [8] proposed a pressure-correction equation that took the mass residual of the starred velocity (velocity from previous iteration) as the only nonhomogeneous term. This was done in hopes that the mass residual would approach zero to achieve zero pressure correction after a number of iterations. Unfortunately, the mass residual never disappeared in their studies [8,9]. This led to a nonzero pressure correction and thus a changing pressure that never converged. In addition, their numerical results were found to depend on the under-relaxation factor. Such numerical difficulties were encountered also in a similar formulation proposed by Peric [10] for nonstaggered curvilinear nonorthogonal grid systems.

More recently, Lee and Tzong [11] developed the APPLE (Artificial Pressure for Pressure-Linked Equation) and NAPPLE (APPLE on Nonstaggered grids) algorithms for Cartesian grid systems. In both algorithms, the pressure-linked equation is solved directly without recourse to a pressure-correction equation. The pressure-linked equation used in the APPLE algorithm is an *algebraic combination* of the discretized continuity equation and the discretized momentum equations. Thus, the solution satisfying the pressure-linked equation and the discretized momentum equations is also the *exact solution* of the discretized continuity equation and the discretized momentum equations. This is evidenced from the fact that the APPLE algorithm is able to produce velocity having mass-free residual. In the NAPPLE algorithm, however, an approximation is imposed on the pressure-linked equation to circumvent the checkerboard error. Due to the truncation error arising from this approximation, the pressure-linked equation is no longer an exact combination of the discretized continuity equation and the discretized momentum equations. As a result, there is a certain level of mass residual after the solution *perfectly* converges. Nevertheless, the mass residual *steadily* approaches zero while the grid mesh is decreasing as demonstrated by Lee and Tzong [11].

For curvilinear grids, both velocity components (u and v) are needed at the same point when the discretized momentum equations are substituted into the discretized continuity equation to form a pressure-linked equation (or pressure-correct equation). This implies the need of a velocity interpolation procedure if a staggered grid system is employed. Thus, the resulting pressure-linked equation for staggered grid systems is not an exact combination of the discretized equations due to the interpolation errors. Under such a situation, no zero mass residual is guaranteed. This might account for the great numerical difficulties encountered by Shyy and coworkers [8,9]. For nonstaggered grids, a particular treatment such as PWIM proposed by Rhie and Chow [2] and the interpolation procedure used by Peric [10] is needed for the success of pressure-velocity coupling as mentioned earlier. Unfortunately, these treatments are unavoidable to introduce numerical errors to the pressure-linked equation such that mass-free residual

---

Contributed by the Heat Transfer Division for publication in the JOURNAL OF HEAT TRANSFER. Manuscript received by the Heat Transfer Division September 1, 2000; revision received April 1, 2002. Associate Editor: D. A. Kaminski.

is not guaranteed either. The nonzero mass residual continuously produces pressure correction ($p' \neq 0$) and thus gives rise to endless iterations.

Logically, the mass residual will not vanish for both staggered and nonstaggered curvilinear grids due to the need of velocity interpolation. Obviously, the principal merit of the APPLE algorithm that guarantees zero mass residual on staggered Cartesian grids will be lost when extended to curvilinear grid systems. In the present study, the NAPPLE algorithm for Cartesian grids [11] is extended to curvilinear grids. Its performances will be examined through two well-documented examples.

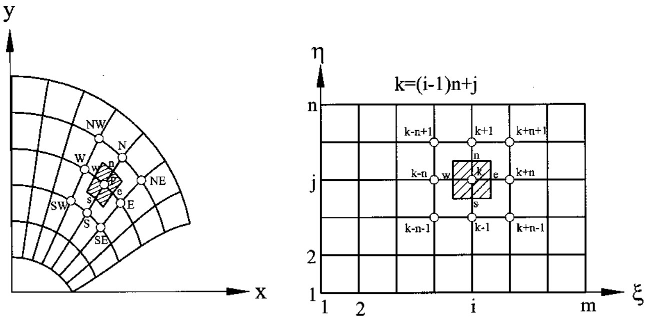

(*a*) (*b*)

Fig. 1 A schematic coordinate transformation from (*a*) the physical plane (x,y) to (*b*) the computational plane (ξ,η)

The NAPPLE Algorithm

The dimensionless conservation equations for heat convection in a two-dimensional incompressible viscous flow can be written as

$$\frac{\partial u}{\partial x}+\frac{\partial v}{\partial y}=0 \tag{1}$$

$$\mathrm{Re}_c\left(\frac{\partial u}{\partial t}+u\frac{\partial u}{\partial x}+v\frac{\partial u}{\partial y}\right)=-\frac{\partial p^*}{\partial x}+\frac{\partial^2 u}{\partial x^2}+\frac{\partial^2 u}{\partial y^2} \tag{2}$$

$$\mathrm{Re}_c\left(\frac{\partial v}{\partial t}+u\frac{\partial v}{\partial x}+v\frac{\partial v}{\partial y}\right)=-\frac{\partial p^*}{\partial y}+\frac{\partial^2 u}{\partial x^2}+\frac{\partial^2 u}{\partial y^2}+\frac{\mathrm{Gr}}{\mathrm{Re}_c}(\theta-\theta_{\mathrm{ref}}) \tag{3}$$

$$\mathrm{Pr}\,\mathrm{Re}_c\left(\frac{\partial \theta}{\partial t}+u\frac{\partial \theta}{\partial x}+v\frac{\partial \theta}{\partial y}\right)=\frac{\partial^2 \theta}{\partial x^2}+\frac{\partial^2 \theta}{\partial y^2} \tag{4}$$

where the gravity acceleration is assigned in the $-y$ direction. The variables in equations (1)–(4) have been non-dimensionalized with the characteristic length L, characteristic velocity U_c, and characteristic temperature difference ΔT. The Grashof number, the characteristic Reynolds number, and the dimensionless pressures are defined, respectively, by

$$\mathrm{Gr}=\frac{g\beta\Delta T L^3}{v^2},\quad \mathrm{Re}_c=\frac{U_c L}{v},\quad p=\frac{P-P_{\mathrm{ref}}}{\rho U_c^2},\quad p^*=p\,\mathrm{Re}_c \tag{5}$$

where P_{ref} is a reference pressure. After introducing a coordinate transformation from (x,y) to (ξ,η) as illustrated in Fig. 1, Eqs. (1)–(4) become

$$\frac{\partial U}{\partial \xi}+\frac{\partial V}{\partial \eta}=0 \tag{6}$$

$$\begin{aligned}\mathrm{Re}_c J\frac{\partial u}{\partial t}&+\mathrm{Re}_c U\frac{\partial u}{\partial \xi}+\mathrm{Re}_c V\frac{\partial u}{\partial \eta}\\&=-\left(y_\eta\frac{\partial p^*}{\partial \xi}-y_\xi\frac{\partial p^*}{\partial \eta}\right)+\frac{\partial}{\partial \xi}\left(\frac{\alpha}{J}\frac{\partial u}{\partial \xi}\right)+\frac{\partial}{\partial \eta}\left(\frac{\gamma}{J}\frac{\partial u}{\partial \eta}\right)\\&\quad-\frac{\partial}{\partial \xi}\left(\frac{\beta}{J}\frac{\partial u}{\partial \eta}\right)-\frac{\partial}{\partial \eta}\left(\frac{\beta}{J}\frac{\partial u}{\partial \xi}\right)\end{aligned} \tag{7}$$

$$\begin{aligned}\mathrm{Re}_c J\frac{\partial v}{\partial t}&+\mathrm{Re}_c U\frac{\partial v}{\partial \xi}+\mathrm{Re}_c V\frac{\partial v}{\partial \eta}\\&=-\left(-x_\eta\frac{\partial p^*}{\partial \xi}+x_\xi\frac{\partial p^*}{\partial \eta}\right)+\frac{\partial}{\partial \xi}\left(\frac{\alpha}{J}\frac{\partial v}{\partial \xi}\right)+\frac{\partial}{\partial \eta}\left(\frac{\gamma}{J}\frac{\partial v}{\partial \eta}\right)\\&\quad-\frac{\partial}{\partial \xi}\left(\frac{\beta}{J}\frac{\partial v}{\partial \eta}\right)-\frac{\partial}{\partial \eta}\left(\frac{\beta}{J}\frac{\partial v}{\partial \xi}\right)+J\frac{\mathrm{Gr}}{\mathrm{Re}_c}(\theta-\theta_{\mathrm{ref}})\end{aligned} \tag{8}$$

$$\begin{aligned}\mathrm{Pr}\,\mathrm{Re}_c J\frac{\partial \theta}{\partial t}&+\mathrm{Pr}\,\mathrm{Re}_c U\frac{\partial \theta}{\partial \xi}+\mathrm{Pr}\,\mathrm{Re}_c V\frac{\partial \theta}{\partial \eta}\\&=\frac{\partial}{\partial \xi}\left(\frac{\alpha}{J}\frac{\partial \theta}{\partial \xi}\right)+\frac{\partial}{\partial \eta}\left(\frac{\gamma}{J}\frac{\partial \theta}{\partial \eta}\right)-\frac{\partial}{\partial \xi}\left(\frac{\beta}{J}\frac{\partial \theta}{\partial \eta}\right)-\frac{\partial}{\partial \eta}\left(\frac{\beta}{J}\frac{\partial \theta}{\partial \xi}\right)\end{aligned} \tag{9}$$

where

$$U=y_\eta u-x_\eta v,\quad V=-y_\xi u+x_\xi v \tag{10a}$$

$$J=x_\xi y_\eta-x_\eta y_\xi,\quad \alpha=x_\eta^2+y_\eta^2,\quad \beta=x_\xi x_\eta+y_\xi y_\eta,\quad \gamma=x_\xi^2+y_\xi^2 \tag{10b}$$

The subscripts ξ and η appearing in the geometric quantities x_ξ, x_η, y_ξ, y_η represent partial derivatives with respect to ξ and η, respectively.

For convenience, the grid system in Fig. 1 is generated such that the grid points on the computational coordinates are expressible as

$$\begin{aligned}\xi_i&=(i-1)\Delta\xi,\quad i=1,2\ldots,m\\ \eta_j&=(j-1)\Delta\eta,\quad j=1,2\ldots,n\end{aligned} \tag{11}$$

The point $P(\xi_i,\eta_j)$ is numbered as the kth point with $k=(i-1)n+j$. Physical coordinates (x,y) and variable ϕ at point P are simply denoted by (x_k,y_k) and ϕ_k, respectively. Upon discretizing Eq. (7) at point P with a finite-difference-like method such as the weighting function scheme [12,13], one obtains an algebraic equation of the form

$$\begin{aligned}&(a_{SW})_k u_{k-n-1}+(a_W)_k u_{k-n}+(a_{NW})_k u_{k-n+1}+(a_S)_k u_{k-1}\\&\quad+(a_N)_k u_{k+1}+(a_{SE})_k u_{k+n-1}+(a_E)_k u_{k+n}\\&\quad+(a_{NE})_k u_{k+n+1}-(a_P)_k u_k\\&\quad-\left(y_\eta\frac{\partial p^*}{\partial \xi}-y_\xi\frac{\partial p^*}{\partial \eta}\right)=(a_u)_k\end{aligned} \tag{12}$$

Like the conventional notation system [11,12,14], the subscripts *SW*, *W*, *NW*, *S*, *N*, *SE*, *E*, *NE* in Eq. (12) represent quantities at the grid points adjacent to point P as demonstrated in Fig. 1. More detailed information on the discretized Eq. (12) will be discussed later. Note that the factor $(a_u)_k$ is the source term excluding the pressure gradient.

Next, recast Eq. (12) in the form

$$u_k=\hat{u}_k-\frac{1}{(a_P)_k}\left(y_\eta\frac{\partial p^*}{\partial \xi}-y_\xi\frac{\partial p^*}{\partial \eta}\right)_k \tag{13}$$

$$\hat{u}_k=\frac{1}{(a_P)_k}\left(\sum_{nb=1}^{8}(a_{nb})_k u_{nb}-(a_u)_k\right) \tag{14}$$

where the subscript nb stands for the neighbors of point P. Similarly, discretization of Eq. (8) at point P yields

$$v_k=\hat{v}_k-\frac{1}{(a_P)_k}\left(-x_\eta\frac{\partial p^*}{\partial \xi}+x_\xi\frac{\partial p^*}{\partial \eta}\right)_k \tag{15}$$

$$\hat{v}_k=\frac{1}{(a_P)_k}\left(\sum_{nb=1}^{8}(a_{nb})_k v_{nb}-(a_v)_k\right) \tag{16}$$

Substituting Eqs. (13) and (15) into Eq. (10*a*), one has

$$U_k=\hat{U}_k-\left(\frac{\alpha}{J^*}\frac{\partial p^*}{\partial \xi}\right)_k+\left(\frac{\beta}{J^*}\frac{\partial p^*}{\partial \eta}\right)_k \tag{17}$$

$$V_k=\hat{V}_k+\left(\frac{\beta}{J^*}\frac{\partial p^*}{\partial \xi}\right)_k-\left(\frac{\gamma}{J^*}\frac{\partial p^*}{\partial \eta}\right)_k \tag{18}$$

where $\hat{U}_k=y_\eta\hat{u}_k-x_\eta\hat{v}_k$, $\hat{V}_k=-y_\xi\hat{u}_k+x_\xi\hat{v}_k$, and $(J^*)_k=(a_P)_k$. Finally, substituting Eqs. (17) and (18) into the discretized continuity equation (see Eq. (6))

$$\frac{U_{k+n}-U_{k-n}}{2\Delta\xi}+\frac{V_{k+1}-V_{k-1}}{2\Delta\eta}=0 \tag{19}$$

followed by making the approximations

$$\begin{aligned}
\frac{\left(\frac{\alpha}{J^*}\frac{\partial p^*}{\partial \xi}\right)_{k+n}-\left(\frac{\alpha}{J^*}\frac{\partial p^*}{\partial \xi}\right)_{k-n}}{2\Delta\xi}&=\frac{\partial}{\partial \xi}\left(\frac{\alpha}{J^*}\frac{\partial p^*}{\partial \xi}\right)\\
\frac{\left(\frac{\gamma}{J^*}\frac{\partial p^*}{\partial \eta}\right)_{k+1}-\left(\frac{\gamma}{J^*}\frac{\partial p^*}{\partial \eta}\right)_{k-1}}{2\Delta\eta}&=\frac{\partial}{\partial \eta}\left(\frac{\gamma}{J^*}\frac{\partial p^*}{\partial \eta}\right)\\
\frac{\left(\frac{\beta}{J^*}\frac{\partial p^*}{\partial \eta}\right)_{k+n}-\left(\frac{\beta}{J^*}\frac{\partial p^*}{\partial \eta}\right)_{k-n}}{2\Delta\xi}&=\frac{\partial}{\partial \xi}\left(\frac{\beta}{J^*}\frac{\partial p^*}{\partial \eta}\right)\\
\frac{\left(\frac{\beta}{J^*}\frac{\partial p^*}{\partial \xi}\right)_{k+1}-\left(\frac{\beta}{J^*}\frac{\partial p^*}{\partial \xi}\right)_{k-1}}{2\Delta\eta}&=\frac{\partial}{\partial \eta}\left(\frac{\beta}{J^*}\frac{\partial p^*}{\partial \xi}\right)
\end{aligned} \tag{20}$$

one arrives at a pressure-linked equation for the point (x_k,y_k)

$$\frac{\partial}{\partial \xi}\left(\frac{\alpha}{J^*}\frac{\partial p^*}{\partial \xi}\right)+\frac{\partial}{\partial \eta}\left(\frac{\gamma}{J^*}\frac{\partial p^*}{\partial \eta}\right)-\frac{\partial}{\partial \xi}\left(\frac{\beta}{J^*}\frac{\partial p^*}{\partial \eta}\right)-\frac{\partial}{\partial \eta}\left(\frac{\beta}{J^*}\frac{\partial p^*}{\partial \xi}\right)=\hat{\varepsilon} \tag{21a}$$

$$\hat{\varepsilon}=\frac{\hat{U}_{k+n}-\hat{U}_{k-n}}{2\Delta\xi}+\frac{\hat{V}_{k+1}-\hat{V}_{k-1}}{2\Delta\eta} \tag{21b}$$

It is interesting to note that the coefficient $(a_P)_k$ acts as a pseudo-Jacobian for the pressure-linked equation if Eq. (21) is regarded as a heat conduction equation with heat generation. For a Cartesian grid system ($\xi=x$ and $\eta=y$), the pressure-linked Eq. (21) reduces to Eq. (23) of Lee and Tzong [11].

Solution Method

Equations (7), (8), (21), and (9) constitute a system of partial differential equations for the physical quantities u, v, p, and θ. All of these equations possess a common form, i.e.,

$$C\frac{\partial \phi}{\partial t}+A\frac{\partial \phi}{\partial \xi}+B\frac{\partial \phi}{\partial \eta}=\frac{\partial}{\partial \xi}\left(\frac{\alpha}{J}\frac{\partial \phi}{\partial \xi}\right)+\frac{\partial}{\partial \eta}\left(\frac{\gamma}{J}\frac{\partial \phi}{\partial \eta}\right)-\frac{\partial}{\partial \xi}\left(\frac{\beta}{J}\frac{\partial \phi}{\partial \eta}\right)-\frac{\partial}{\partial \eta}\left(\frac{\beta}{J}\frac{\partial \phi}{\partial \xi}\right)+S \tag{22}$$

where J represents the pseudo-Jacobian $(a_P)_k$ if $\phi=p^*$, $A=B=C=0$, and $S=-\hat{\varepsilon}$. Let a grid system with $\Delta\xi=\Delta\eta=1$ be generated for the problem. Next, applying the weighting function scheme [12,13] to Eq. (22) at point $P(x_k,y_k)$, one gets an algebraic equation of the form

$$\begin{aligned}
&(a_{SW})_k\phi_{k-n-1}+(a_W)_k\phi_{k-n}+(a_{NW})_k\phi_{k-n+1}+(a_S)_k\phi_{k-1}\\
&\quad-(a_P)_k\phi_k+(a_N)_k\phi_{k+1}+(a_{SE})_k\phi_{k+n-1}+(a_E)_k\phi_{k+n}\\
&\quad+(a_{NE})_k\phi_{k+n+1}=(a_R)_k
\end{aligned} \tag{23}$$

where

$$\begin{aligned}
&(a_W)_k=\frac{\alpha_w}{J_w}w_f(z_w),\quad (a_E)_k=\frac{\alpha_e}{J_e}w_f(-z_e),\\
&(a_S)_k=\frac{\gamma_s}{J_s}w_f(z_s),\quad (a_N)_k=\frac{\gamma_n}{J_n}w_f(-z_n),\\
&(a_{SW})_k=-2\left(\frac{\beta_{sw}}{J_{sw}}\right)\hat{w}_f(z_s)\hat{w}_f(z_w),\\
&(a_{NW})_k=2\left(\frac{\beta_{nw}}{J_{nw}}\right)\hat{w}_f(z_n)\hat{w}_f(z_w),\\
&(a_{SE})_k=2\left(\frac{\beta_{se}}{J_{se}}\right)\hat{w}_f(z_s)\hat{w}_f(z_e),\\
&(a_{NE})_k=-2\left(\frac{\beta_{ne}}{J_{ne}}\right)\hat{w}_f(z_n)\hat{w}_f(z_e),\\
&(a_P)_k=(a_W)_k+(a_S)_k+(a_N)_k+(a_E)_k+\frac{C_k}{\Delta t},\\
&(a_R)_k=-\left(S_k+\frac{C_k}{\Delta t}(\phi_0)_k\right)
\end{aligned} \tag{24}$$

Note that the implicit method has been applied to the unsteady term, i.e.,

$$\frac{\partial \phi}{\partial t}=\frac{\phi-\phi_0}{\Delta t},\quad \phi_0=\phi(\xi,\eta,t-\Delta t) \tag{25}$$

Before the momentum Eqs. (7) and (8) are solved, the pressure gradient is estimated from the guessed (or updated) pressure solution with a central difference scheme.

In Eq. (24), the weighting functions $w_f(z)$ and $\hat{w}_f(z)$, and the grid Peclet numbers z_w, z_e, z_s, z_n are defined, respectively, by

$$\begin{aligned}
w_f(z)&=\frac{z}{1-\exp(-z)}\approx[0,(1-0.1|z|)^5]+[0,z]\\
\hat{w}_f(z)&=\frac{z}{\exp(z)-\exp(-z)}\approx(2+0.3332z^2+0.0172z^4)^{-1}
\end{aligned} \tag{26}$$

and

$$z_w=\frac{A_wJ_w}{\alpha_w},\quad z_e=\frac{A_eJ_e}{\alpha_e},\quad z_s=\frac{B_sJ_s}{\gamma_s},\quad z_n=\frac{B_nJ_n}{\gamma_n}. \tag{27}$$

where $[a,b]$ stands for the greater of a and b. For simplicity, the arithmetic mean of properties at two adjacent grid points is used to approximate the mean value over the interval between them. For instance,

$$\begin{aligned}
&A_w=(A_{k-n}+A_k)/2,\quad J_w=(J_{k-n}+J_k)/2,\\
&\alpha_w=(\alpha_{k-n}+\alpha_k)/2,\quad \beta_{sw}=(\beta_{k-n-1}+\beta_k)/2
\end{aligned} \tag{28}$$

System of algebraic equations defined by Eqs. (23) and (24) can be efficiently solved with the SIS solver [15]. The convergence problem due to high grid aspect ratios encountered by Peric [10] can be remedied by using the SIS solver instead of the SIP solver [16]. This point has been well clarified by Lee [15].

It is quite straightforward to show that the weighting factors for the pressure-linked Eq. (21) reduce to

$$
\begin{gathered}
(a_W)_k=\frac{\alpha_w}{(J^*)_w},\quad (a_E)_k=\frac{\alpha_e}{(J^*)_e},\quad (a_S)_k=\frac{\gamma_s}{(J^*)_s},\\
(a_N)_k=\frac{\gamma_n}{(J^*)_n},\\
(a_{SW})_k=-0.5\frac{\beta_{sw}}{(J^*)_{sw}},\quad (a_{NW})_k=0.5\frac{\beta_{nw}}{(J^*)_{nw}},\\
(a_{SE})_k=0.5\frac{\beta_{se}}{(J^*)_{se}},\quad (a_{NE})_k=-0.5\frac{\beta_{ne}}{(J^*)_{ne}},\\
(a_P)_k=(a_W)_k+(a_S)_k+(a_N)_k+(a_E)_k,\quad (a_R)_k=-(\hat{\varepsilon})_k
\end{gathered}
\tag{29}
$$

Suppose the velocity (u,v) on the boundary $\xi=0$ is known such that the contravariant velocity U_{k-n} with $n+1\leqslant k\leqslant 2n$ can be determined from Eq. (10*a*). This gives rise to

$$\hat{U}_{k-n}=U_{k-n}\quad \text{and}\quad (J^*)_{k-n}=(a_P)_{k-n}=\infty \tag{30}$$

from Eq. (17), and thus

$$(a_W)_k=\frac{\alpha_w}{(J^*)_w}=0 \tag{31}$$

As a result, no pressure boundary condition is needed on a boundary where the velocity is known. This is one of the major differences between the pressure-linked Eq. (21) and the conventional pressure Poisson equation. Although both equations are of the Poisson type, the former comes directly from the continuity equation, while the latter is essentially a divergence of the momentum equation. Their numerical characteristics thus are quite different as remarked by Lee and Tzong [11].

It is very important to note that, to obtain a pressure solution without checkerboard error, the present study employs the approximation (20) instead of using a velocity interpolation procedure such as the PWIM [2] and a similar method [10]. This precludes the possibility of resulting a spurious velocity arising from improper velocity interpolation. In addition, unlike in conventional numerical methods [2,8–10], the solution based on the present method does not depend on the under-relaxation factor. This is the most important feature of the present method. Due to the truncation error arising from this approximation, however, the discretized pressure-linked Eqs. (23) and (29) is no longer an exact combination of the discretized continuity Eq. (19) and the discretized momentum equations as mentioned earlier. A certain level of mass residual thus could remain after the solution perfectly converges. Nevertheless, the mass residual is expected to disappear when the grid size approaches zero.

Performances of the NAPPLE Algorithm

Two well-known examples are employed in this section to examine the performances of the NAPPLE algorithm. Example 1, a natural convection in the annulus between two horizontal cylinders, is conducted to study the performance of the NAPPLE algorithm in the presence of buoyancy term. In example 2, the problem of fluid flow through an axisymmetric constricted tube is used to investigate the performance of the NAPPLE algorithm when the flow is driven by a pressure difference. It is important to note that the coefficient matrix formed with Eq. (23) is no longer diagonally dominant for steady-state problems due to the grid skewness ($\beta\neq 0$). This might lead to a numerical difficulty in achieving a convergent solution as reported by Shyy et al. [8] and Peric [10]. In the present study, both examples 1 and 2 are treated as unsteady problems with made-up initial conditions, although they are actually at steady-state. Such a treatment could produce a strictly diagonally dominant coefficient matrix for the discretized momentum equations, and thus gains a good numerical stability. Nevertheless, the fictitious time step Δt could be assigned infinity to reach the steady-state solution directly (see Eq. (24)) in case the Reynolds number and the Rayleigh number are not large. The results will be compared with that based on the stream-vorticity formulation as well as the available numerical solutions and experimental data from previous investigations.

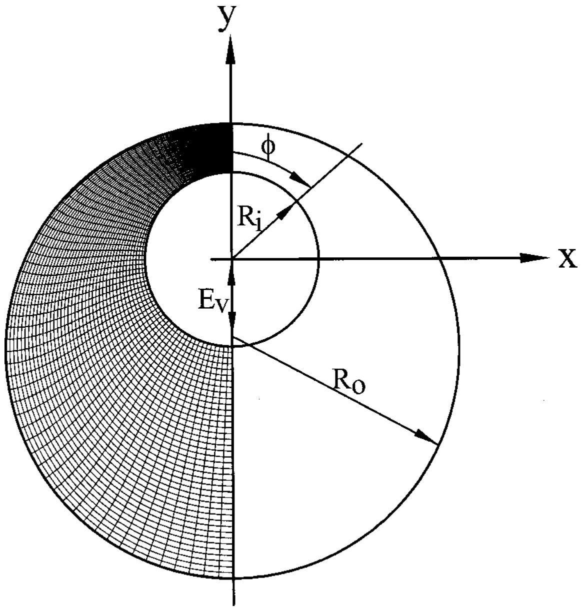

Fig. 2 Geometry description and a grid system for example 1

Example 1 Natural Convection in the Annulus Between Two Horizontal Cylinders. Consider two horizontal cylinders of radius R_i and R_0. Center of the inner cylinder lies above that of the outer cylinder by a distance E_v as shown in Fig. 2. The surfaces of both cylinders are maintained at their own uniform temperatures (T_i and T_o) such that a natural convection prevails in the annulus between them. Let the characteristic velocity be assigned as $U_c=\alpha_t/L$. This leads to $\mathrm{Re}_c=1/\mathrm{Pr}$ and thus $\mathrm{Gr}/\mathrm{Re}_c=\mathrm{Ra}$. The characteristic length L, the eccentricity e_v, and the dimensionless temperature θ are defined by

$$L=R_o-R_i,\quad e_v=E_v/L,\quad \theta=\frac{T-T_o}{\Delta T}=\frac{T-T_o}{T_i-T_o} \tag{32}$$

The associated boundary conditions are

$$
\begin{gathered}
u=0,\quad \partial v/\partial x=0,\quad \partial\theta/\partial x=0\quad \text{on the y-axis}\\
u=0,\quad v=0,\quad \theta=1\quad \text{on the inner cylinder}\\
u=0,\quad v=0,\quad \theta=0\quad \text{on the outer cylinder}
\end{gathered}
\tag{33}
$$

In the present study, steady-state solutions are obtained for the three cases having the parameters $(e_v,\mathrm{Ra})=(0.652,4.80\times 10^4)$, $(0,4.70\times 10^4)$, $(-0.623,4.93\times 10^4)$, while $R_o/R_i=2.6$ and $\mathrm{Pr}=0.706$. The numerical procedure is similar to that for the Cartesian grid system [11]. Once the temperature solution is available, the equivalent thermal conductivity along the boundaries is evaluated from

$$(k_{eq})_i=\frac{R_i}{L}\ln\left(\frac{R_o}{R_i}\right)\left(-\frac{\partial\theta}{\partial n}\right),\quad (k_{eq})_o=\frac{R_o}{L}\ln\left(\frac{R_o}{R_i}\right)\left(-\frac{\partial\theta}{\partial n}\right) \tag{34a}$$

$$\frac{\partial\theta}{\partial n}=-\frac{\beta}{J}\left(\frac{\partial\theta}{\partial\xi}\right)+\frac{\gamma}{J}\left(\frac{\partial\theta}{\partial\eta}\right) \tag{34b}$$

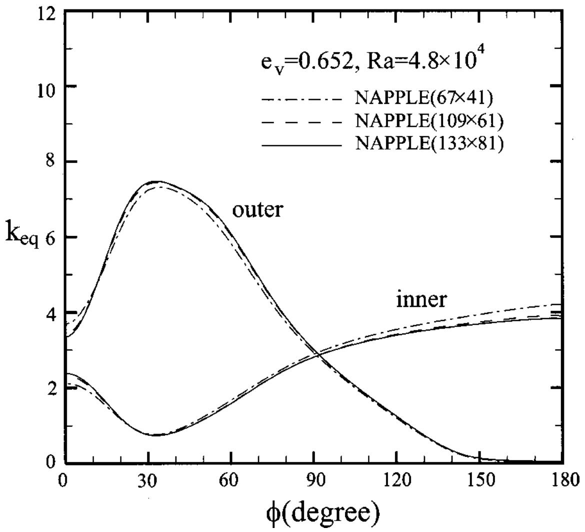

Fig. 3 Influence of grid mesh on the equivalent thermal conductivity k_{eq}

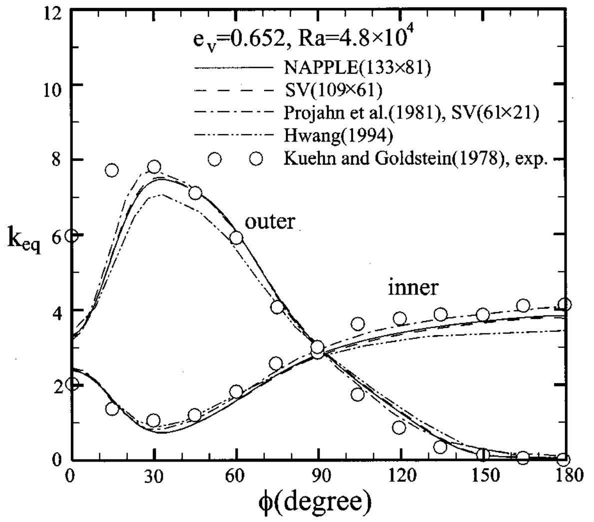

Fig. 4 Comparison of k_{eq} among the numerical predictions and the experimental result for $(e_v,\mathrm{Ra})=(0.652,4.8\times10^4)$

where n is a coordinate normal to the boundary specified by $\eta=constant$. When the boundary grid is orthogonal ($\beta=0$), the first term on the right-hand-side of Eq. (34*b*) vanishes.

For the case of $e_v=0.652$, three grid systems with 67×41, 109×61, and 133×81 grid points are employed. These grid systems are generated with the weighting function scheme proposed by Hsu and Lee [13]. The boundary values of the control functions required for orthogonal boundary grids with desired grid meshes are determined along all of the boundaries. The control functions inside the computational domain are then interpolated with

$$\frac{\partial^2 P}{\partial \xi^2}+\frac{\partial^2 P}{\partial \eta^2}=0, \quad \frac{\partial^2 Q}{\partial \xi^2}+\frac{\partial^2 Q}{\partial \eta^2}=0 \tag{35}$$

The resulting grid system of 67×41 points is illustrated in Fig. 2.

Based on the three grid systems 67×41, 109×61, and 133×81, influence of the grid meshes on the equivalent thermal conductivity k_{eq} is revealed in Fig. 3 for the case $(e_v,\mathrm{Ra})=(0.652,4.80\times10^4)$. From Fig. 3, the grid system of 133×81 points is found adequate for this case. In this connection, the mass residual reduces monotonously as the mesh size reduces, similar to that in the Cartesian coordinates [11]. To examine the accuracy of the NAPPLE algorithm, this same problem was solved with the stream-vorticity formulation. The weighting function scheme [12,13] was employed to discretize the partial differential equations. The grid mesh was reduced until grid independence was achieved. For convenience, results based on the stream-vorticity formulation will be referred to as "SV results" in the present study. Figure 4 shows both NAPPLE (133×81) and SV (109×61) results of k_{eq}. The available numerical and experimental results from previous investigations are plotted in Fig. 4 also for comparison. From Fig. 4, one observes an excellent agreement between the NAPPLE and SV results. This evidences the accuracy of the NAPPLE algorithm. The SV results from Projahn et al. [17] poses numerical errors from the coarse grids (61×21) as well as the central difference scheme used by them. The interpolation procedure proposed by Hwang [18] seems to under-predict the heat transfer coefficient at a great amount.

It is very interesting to note that in the region of $\phi<30$ deg on the outer cylinder there are great discrepancies between the experimentally measured [19] and the numerically predicted k_{eq}. This might be attribute to the possibility of the Benard instability occurring in the experiment. To clarify this point, the isotherms and streamlines from the present NAPPLE and SV results are depicted in Fig. 5. As observable from Fig. 5, there is a little positive (counterclockwise) circulation flow near $\phi=0$ deg. It moves the isotherms downward and thus decreases the temperature gradient on the outer cylinder. However, the Benard instability (occurs when heated from below) might have brought about three-dimensional vortices in Kuehn and Goldstein's experiment [19]. Under such a situation, strength of the little positive circulation flow could be weakened. As a result, a larger heat transfer rate was observed in the experiment.

Comparisons of the resulting equivalent thermal conductivity among the present results and that from previous investigations [17–20] are shown in Figs. 6 and 7 for the cases of $(e_v,\mathrm{Ra})=(0,4.70\times10^4)$ and $(-0.623,4.93\times10^4)$, respectively. Again, excellent performances of the NAPPLE algorithm are confirmed.

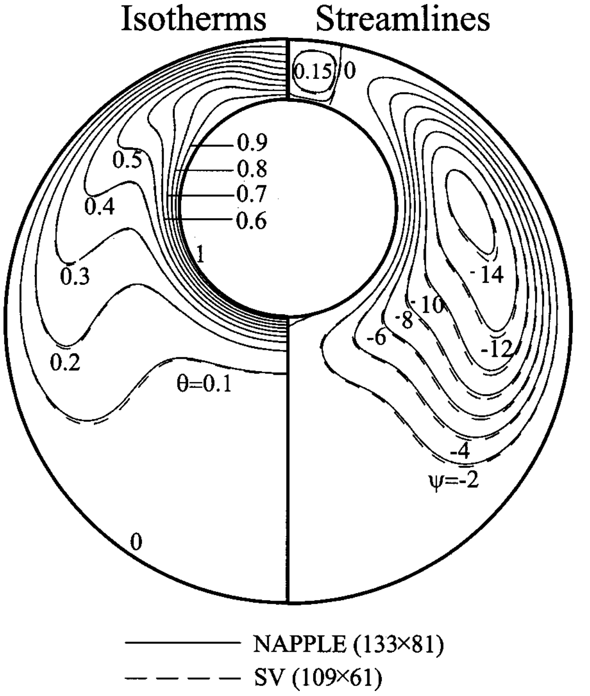

Fig. 5 Isotherms and streamlines for the case $(e_v,\mathrm{Ra})=(0.652,4.80\times10^4)$

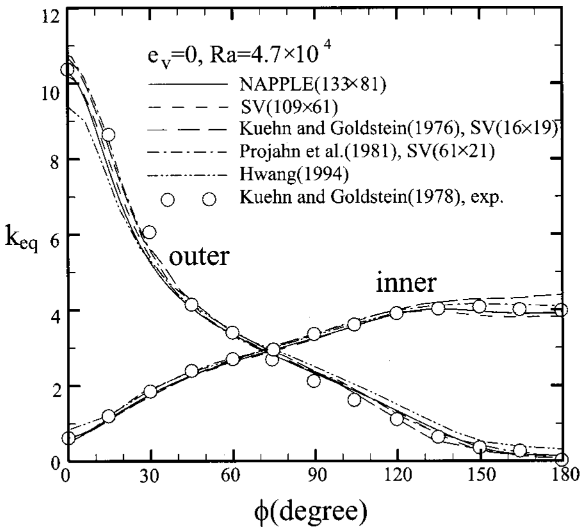

Fig. 6 Comparison of k_{eq} among the numerical predictions and the experimental result for $(e_v,\mathrm{Ra})=(0,4.70\times10^4)$

Example 2 Fluid Flow Through an Axisymmetric Constricted Tube. In their experimental study on a fluid flow through a locally constricted tube, Young and Tsai [21] employed an axisymmetric constriction with the cosine shape

$$r=r_s=\frac{1}{6}(2-\cos(\pi x/x_0)) \tag{36}$$

to simulate an arterial stenosis in the portion $-x_0\leqslant x\leqslant x_0$ as shown in Fig. 8(*a*), where the cylindrical coordinates (x,r) has been normalized with the tube diameter D_0 in the portion ($|x|>x_0$) without constriction. The pressure drop ΔP across the constriction was measured at $x=\pm l$. The length l was held at $l=8$ for all tests to insure fully developed flow in both sites. In the present study, this same flow configuration is solved with the NAPPLE algorithm.

Let the characteristic length and the characteristic velocity be assigned as $L=D_0$ and $U_c=\sqrt{\Delta P/\rho}$, respectively. After introducing a coordinate transformation from (x,r) to (ξ,η), the governing equations become

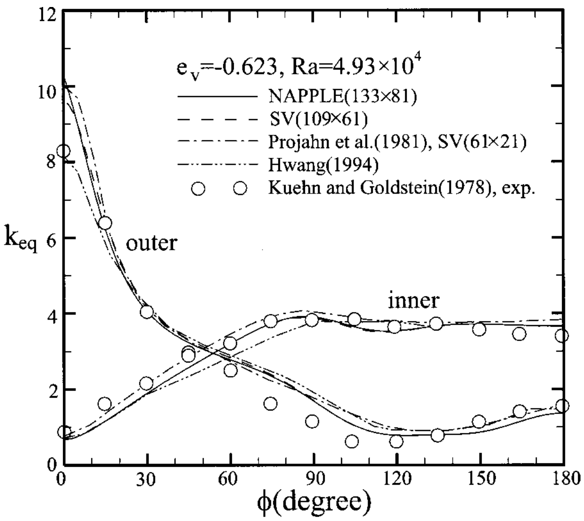

Fig. 7 Comparison of k_{eq} among the numerical predictions and the experimental result for $(e_v,\mathrm{Ra})=(-0.623,4.93\times10^4)$

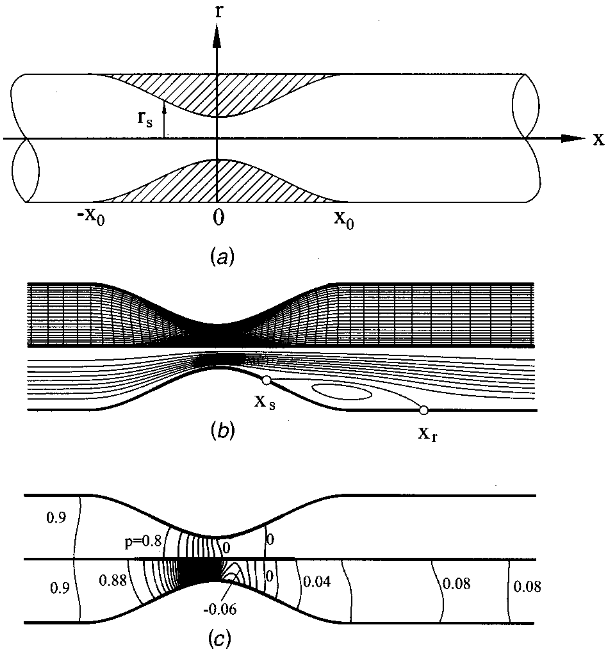

Fig. 8 (*a*) Flow configuration, (*b*) grid system and streamlines, and (*c*) isobars with increments 0.1 and 0.02 for example 2

$$\frac{\partial(rU)}{\partial\xi}+\frac{\partial(rV)}{\partial\eta}=0 \tag{37}$$

$$\begin{aligned}\mathrm{Re}_c\,J\frac{\partial u}{\partial t}+\mathrm{Re}_c\,U\frac{\partial u}{\partial\xi}+\mathrm{Re}_c\,V\frac{\partial u}{\partial\eta}\\=-\left(r_\eta\frac{\partial p^*}{\partial\xi}-r_\xi\frac{\partial p^*}{\partial\eta}\right)-\frac{1}{r}\left(-x_\eta\frac{\partial u}{\partial\xi}+x_\xi\frac{\partial u}{\partial\eta}\right)+\frac{\partial}{\partial\xi}\left(\frac{\alpha}{J}\frac{\partial u}{\partial\xi}\right)\\+\frac{\partial}{\partial\eta}\left(\frac{\gamma}{J}\frac{\partial u}{\partial\eta}\right)-\frac{\partial}{\partial\xi}\left(\frac{\beta}{J}\frac{\partial u}{\partial\eta}\right)-\frac{\partial}{\partial\eta}\left(\frac{\beta}{J}\frac{\partial u}{\partial\xi}\right)\end{aligned} \tag{38}$$

$$\begin{aligned}\mathrm{Re}_c\,J\frac{\partial v}{\partial t}+\mathrm{Re}_c\,U\frac{\partial v}{\partial\xi}+\mathrm{Re}_c\,V\frac{\partial v}{\partial\eta}\\=-\left(-x_\eta\frac{\partial p^*}{\partial\xi}+x_\xi\frac{\partial p^*}{\partial\eta}\right)-\frac{1}{r}\left(-x_\eta\frac{\partial v}{\partial\xi}+x_\xi\frac{\partial v}{\partial\eta}\right)+J\frac{v}{r^2}\\+\frac{\partial}{\partial\xi}\left(\frac{\alpha}{J}\frac{\partial v}{\partial\xi}\right)+\frac{\partial}{\partial\eta}\left(\frac{\gamma}{J}\frac{\partial v}{\partial\eta}\right)-\frac{\partial}{\partial\xi}\left(\frac{\beta}{J}\frac{\partial v}{\partial\eta}\right)-\frac{\partial}{\partial\eta}\left(\frac{\beta}{J}\frac{\partial v}{\partial\xi}\right)\end{aligned} \tag{39}$$

where (u,v) is the velocity in the cylindrical coordinates (x,r). The corresponding pressure-linked equation based on the NAPPLE algorithm is

$$\begin{aligned}\frac{\partial}{\partial\xi}\left(\frac{\alpha r}{J^*}\frac{\partial p^*}{\partial\xi}\right)+\frac{\partial}{\partial\eta}\left(\frac{\gamma r}{J^*}\frac{\partial p^*}{\partial\eta}\right)-\frac{\partial}{\partial\xi}\left(\frac{\beta r}{J^*}\frac{\partial p^*}{\partial\eta}\right)\\-\frac{\partial}{\partial\eta}\left(\frac{\beta r}{J^*}\frac{\partial p^*}{\partial\xi}\right)=\hat{\varepsilon}\end{aligned} \tag{40a}$$

$$\hat{\varepsilon}=\frac{r_{k+n}\hat{U}_{k+n}-r_{k-n}\hat{U}_{k-n}}{2\Delta\xi}+\frac{r_{k+1}\hat{V}_{k+1}-r_{k-1}\hat{V}_{k-1}}{2\Delta\eta} \tag{40b}$$

The associated boundary conditions are

$$\begin{gathered}\partial u(x,0)/\partial r=0,\quad v(x,0)=0,\quad u(x,r_s)=0,\quad v(x,r_s)=0,\\ \partial u(-l,r)/\partial x=0,\quad v(-l,r)=0,\quad p^*(-l,r)=\mathrm{Re}_c,\\ \partial u(l,r)/\partial x=0,\quad v(l,r)=0,\quad p^*(l,r)=0\end{gathered} \tag{41}$$

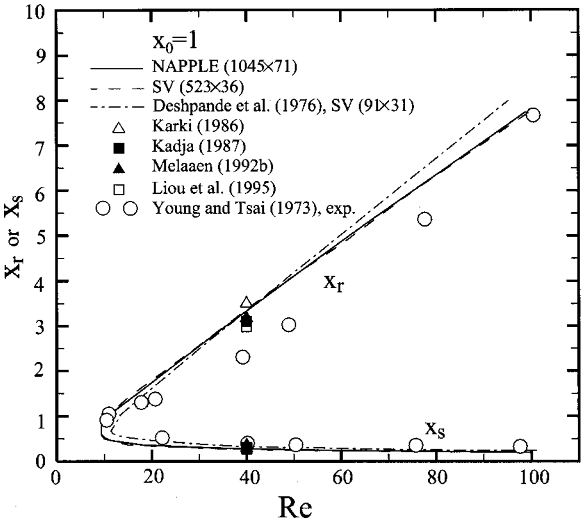

Fig. 9 Comparison of separation point x_s and reattachment point x_r among the numerical predictions and the experimental result for $x_0=1$

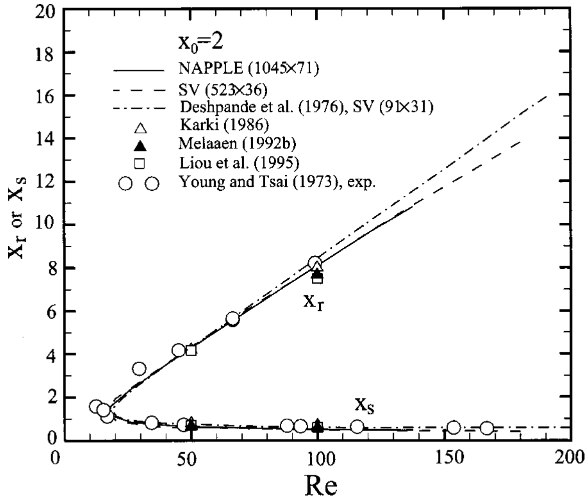

Fig. 10 Comparison of separation point x_s and reattachment point x_r among the numerical predictions and the experimental result for $x_0=2$

Note that the only parameter in the problem (37)–(41) is

$$\mathrm{Re}_c=\frac{U_cL}{\upsilon}=\frac{\sqrt{\Delta P/\rho}D_0}{\upsilon} \tag{42}$$

Once the solution (u,v,p) corresponding to a given pressure drop ΔP (or Re_c) is obtained, the Reynolds number can be evaluated from

$$\mathrm{Re}=\frac{4Q}{\pi\upsilon D_0}=8\ \mathrm{Re}_c\int_0^{r_s}urdr \tag{43}$$

where Q is the volume flow rate through the tube.

In this example, two models of stenoses (i.e., $x_0=1$ and $x_0=2$) are investigated. Grid systems with the desired grid size and skewness (orthogonal) along all of the boundaries are generated with the weighting function scheme (see Hsu and Lee [13], and Eq. (35)). Figure 8(*b*) reveals one of the resulting grid systems. The numerical solution based on the NAPPLE algorithm is refined by reducing the grid size until grid independence is achieved. The resulting streamlines and isobars for $x_0=1$ and $\mathrm{Re}_c=100$ are illustrated in Fig. 8(*b*) and 8(*c*), respectively. Increment of the streamlines is one tenth of the flow rate in Fig. 8(*b*), while that of the isobars is 0.1 and 0.02, respectively, in the upper and lower portion of Fig. 8(*c*). As observable from Fig. 8(*b*), the separation point x_s and the reattachment point x_r can be clearly identified.

Figure 9 shows the separation point x_s and the reattachment point x_r obtained with the NAPPLE algorithm for $x_0=1$ at various Reynolds numbers. Results based on the stream-vorticity (SV) formulation and that from previous numerical [4,22–25] and experimental [21] investigations are presented also in Fig. 9 for comparisons. The numbers $(m\times n)$ appearing in Fig. 9 denote the numbers of grid points used in each numerical investigations. As in example 1, the stream-vorticity equations were discretized with the weighting function scheme [12,13]. The SV results were grid-independent.

From Fig. 9, an excellent agreement is found to exist between the present NAPPLE and SV results. The SV results from Deshpande et al. [22] seems to possess a considerable numerical error due to a coarse grid mesh used by them. On the separation point x_s, all of the numerical predictions agree with the experimental observation from Young and Tsai [21]. For the reattachment point x_r, however, a great discrepancy between the numerical predictions and the experiment result is seen. This might be attributed to the experimental difficulties in delineating the reattachment point as remarked by Young and Tsai [21] and Deshpande et al. [22].

For the case of $x_0=2$, the separation point x_s and the reattachment point x_r based on the NAPPLE algorithm and the SV formulation are revealed in Fig. 10. The available numerical predictions from Deshpande et al. [22], Karki [23], Melaaen [4], and Liou et al. [25] as well as the experimental observation from Young and Tsai [21] are shown also in Fig. 10 for comparison. Again, an excellent agreement is found to exist between the present NAPPLE and SV results. Due to the use of a coarse grid mesh, the SV results from Deshpande et al. [22] over-predicts the reattachment point x_r when the Reynolds number is large. Otherwise, satisfactory agreements are observable among the numerical predictions and the experimental result. This validates the performance of the NAPPLE algorithm.

As a final note, it is mentioned that the coefficient matrix of the discretized pressure-linked equation in example 1 is singular because of $(a_P)_k=\infty$ along all of the boundaries. This implies the need of an artificial pressure with a pressure level to ensure the existence and uniqueness of the pressure solution for the updated velocity [11]. In example 2, the weighting factor $(a_P)_k$ has a finite value on both upstream and downstream boundaries $(x=\pm 1)$. Thus, the Dirichlet boundary conditions

$$p^*(-l,r)=\mathrm{Re}_c,\quad p^*(l,r)=0 \tag{44}$$

can be imposed there. In this case, no artificial pressure is needed when the pressure-linked equation is solved.

Conclusion

In the present study, the NAPPLE algorithm is extended to nonorthogonal curvilinear grid system for incompressible viscous flow. A pressure-linked equation is derived from the discretized governing equations. In the course of the derivation, a particular treatment is adopted for a strong pressure-velocity coupling. No velocity interpolation is needed such that the solution does not depend on the under-relaxation factor. This is the most important feature of the present method. In the present method, solving the pressure-linked equation is as simple as solving a heat conduction equation. Due to the truncation error, the pressure-linked equation is not an exact combination of the discretized continuity equation and the discretized momentum equations. Thus, there is a certain level of mass residual after the solution perfectly converges. Nevertheless, the mass residual approaches zero when the grid mesh is reduced. Through two well-documented examples, performance of the NAPPLE algorithm on non-orthogonal curvilinear grid system is validated. Due to its simplicity and accuracy, the NAPPLE algorithm is believed to have good performances for fluid flow and heat transfer problems.

Acknowledgment

The authors would like to express their appreciation to the National Science Council of Taiwan for the financial support of this work through the project NSC 89-2212-E007-032.

Nomenclature

Gr = Grashof number, $g\,\beta\Delta TL^3/v^2$
J = Jacobian (10b)
J^* = pseudo-Jacobian
k_{eq} = equivalent thermal conductivity (34)
P,p = pressure, and dimensionless pressure (5)
p^* = dimensionless pressure, $p\,\mathrm{Re}_c$
Pr = Prandtl number, ν/α_t
(r,x) = cylindrical coordinates
Ra = Rayleigh number, Pr Gr
Re = Reynolds number
Re_c = characteristic Reynolds number, U_cL/v
T = temperature
t = dimensionless time (normalized with L/U_c)
(U,V) = contravariant velocity (10a)
(u,v) = velocity in Cartesian coordinates
$(\hat{u},\hat{v})$ = pseudo-velocity in Cartesian coordinates
U_c = characteristic velocity
$w_f(z)$ = weighting function, $z/(l-\exp(-z))$
$\hat{w}_f(z)$ = weighting function, $z/(\exp(z)-\exp(-z))$
z = grid Peclet number

Greek

$\alpha,\ \beta,\ \gamma$ = geometric parameters (10b)
α_t = thermal diffusivity
ΔP = pressure difference
ΔT = characteristic temperature
$\hat{\varepsilon}$ = pseudo-dilation
θ = dimensionless temperature
v = kinematic viscosity
(ξ,η) = computational coordinates
ϕ = a function or an angle

Subscripts

ref = reference
e,s,w,n = surfaces of control volume, Fig. 1
$\xi,\ \eta$ = derivatives with respective to ξ and η
i = inner
o = outer

References

[1] Lee, S. L., and Lin, D. W., 1997, ''Transient Conjugate Heat Transfer on a Naturally Cooled Body of Arbitrary Shape,'' Int. J. Heat Mass Transf., **40**, pp. 2133–2145.

[2] Rhie, C. M., and Chow, W. L., 1983, ''Numerical Study of the Turbulent Flow Past an Airfoil With Trailing Edge Separation,'' AIAA J., **21**, pp. 1525–1532.

[3] Melaaen, M. C., 1992, ''Calculation of Fluid Flow With Staggered and Nonstaggered Curvilinear Nonorthogonal Grids—The Theory,'' Numer. Heat Transfer, Part B, **21B**, pp. 1–19.

[4] Melaaen, M. C., 1992, ''Calculation of Fluid Flow With Staggered and Nonstaggered Curvilinear Nonorthogonal Grids—A Comparison,'' Numer. Heat Transfer, Part B, **21B**, pp. 21–39.

[5] Zang, Y., Street, R. L., and Koseff, J. R., 1994, ''A Non-Staggered Grid, Fractional Step Method for Time-Dependent Incompressible Navier-Stokes Equations in Curvilinear Coordinates,'' J. Comput. Phys., **114**, pp. 18–33.

[6] Patankar, S. V., 1988, ''Recent Developments in Computational Heat Transfer,'' ASME J. Heat Transfer, **110**, pp. 1037–1045.

[7] Miller, T. F., and Schmidt, F. W., 1988, ''Use of a Pressure-Weighted Interpolation Method for the Solution of the Incompressible Navier-Stokes Equations on a Non-Staggered Grid System,'' Numer. Heat Transfer, **14**, pp. 213–233.

[8] Shyy, W., Tong, S. S., and Correa, S. M., 1985, ''Numerical Recirculating Flow Calculation Using a Body-Fitted Coordinate System,'' Numer. Heat Transfer, **8**, pp. 99–113.

[9] Braaten, M., and Shyy, W., 1986, ''A Study of Recirculating Flow Computation Using Body-Fitted Coordinates: Consistency Aspect and Mesh Skewness,'' Numer. Heat Transfer, **9**, pp. 559–574.

[10] Peric, M., 1990, ''Analysis of Pressure-Velocity Coupling on Nonorthogonal Grids,'' Numer. Heat Transfer, Part B, **17B**, pp. 63–82.

[11] Lee, S. L., and Tzong, R. Y., 1992, ''Artificial Pressure for Pressure-Linked Equation,'' Int. J. Heat Mass Transf., **35**, pp. 2705–2716.

[12] Lee, S. L., 1989, ''Weighting Function Scheme and Its Application on Multidimensional Conservation Equations,'' Int. J. Heat Mass Transf., **32**, pp. 2065–2073.

[13] Hsu, K., and Lee, S. L., 1991, ''A Numerical Technique for Two-Dimensional Grid Generation With Grid Control at All of the Boundaries,'' J. Comput. Phys., **96**, pp. 451–469.

[14] Patankar, S. V., 1980, *Numerical Heat Transfer and Fluid Flow*, Hemisphere, New York, Chap. 6.

[15] Lee, S. L., 1989, ''A Strongly Implicit Solver for Two-Dimensional Elliptical Differential Equations,'' Numer. Heat Transfer, Part B, **16B**, pp. 161–178.

[16] Stone, H. L., 1968, ''Iterative Solutions of Approximations of Multidimensional Partial Differential Equations,'' SIAM (Soc. Ind. Appl. Math.) J. Numer. Anal., **5**, pp. 530–558.

[17] Projahn, U., Rieger, H., and Beer, H., 1981, ''Numerical Analysis of Laminar Natural Convection Between Concentric and Eccentric Cylinders,'' Numer. Heat Transfer, **4**, pp. 131–146.

[18] Hwang, Y. H., 1994, ''Arbitrary Domain Velocity Analyses for the Incompressible Navier-Stokes Equations,'' J. Comput. Phys., **110**, pp. 134–149.

[19] Kuehn, T. H., and Goldstein, R. J., 1978, ''An Experimental Study of Natural Convection Heat Transfer in Concentric and Eccentric Horizontal Cylindrical Annuli,'' ASME J. Heat Transfer, **100**, pp. 635–640.

[20] Kuehn, T. H., and Goldstein, R. J., 1976, ''An Experimental and Theoretical Study of Natural Convection in the Annulus Between Horizontal Concentric Cylinders,'' J. Fluid Mech., **74**, pp. 695–719.

[21] Young, D. F., and Tsai, F. Y., 1973, ''Flow Characteristics in Models of Arterial Stenoses—I. Steady Flow,'' J. Biomech., **6**, pp. 395–410.

[22] Deshpande, M. D., Giddens, D. P., and Mabon, R. F., 1976, ''Steady Laminar Flow Through Modeled Vascular Stenoses,'' J. Biomech., **9**, pp. 165–174.

[23] Karki, K. C., 1986, ''A Calculation Procedure for Viscous Flows at All Speeds in Complex Geometries,'' Ph.D. thesis, University of Minnesota.

[24] Kadja, M., 1987, ''Computation of Recirculating Flow in Complex Domains With Algebraic Reynolds Stress Closure and Body Fitted Meshes,'' Ph.D. thesis, University of Manchester.

[25] Liou, T. M., Chen, S. H., and Chen, L. T., 1995, ''Numerical Simulation on Fluid Flow Through a Locally Constricted Tube (in Chinese),'' *Proceedings of the Third National Conference on Computational Fluid Dynamics, Taiwan*, pp. 139–148.

Film Cooling Effectiveness and Heat Transfer Coefficient Distributions Around Diffusion Shaped Holes

Y. Yu[1]
C.-H. Yen[2]
T. I.-P. Shih[3]
M. K. Chyu

Department of Mechanical Engineering,
University of Pittsburgh,
Pittsburgh, PA 15261

S. Gogineni

Innovative Scientific Solution, Inc.,
Dayton, OH 45440

Presented in this paper is an experimental study focusing on the effects of diffusion hole-geometry on overall film cooling performance. The study consists of three different but closely related hole shapes: (1) Shape A: straight circular hole with a 30 deg inclined injection, (2) Shape B: same as Shape A but with a 10 deg forward diffusion, and (3) Shape C: same as Shape B with an additional 10 deg lateral diffusion. The blowing ratios tested are 0.5 and 1.0. The density ratio is nominally equal to one. Measurements of the experiment use a transient liquid crystal technique that reveals local distributions of both film effectiveness (η) and heat transfer coefficient (h). The data obtained indicate that Shape C with a combined forward and lateral diffusion produces a significant increase in η and decrease in h as compared to Shape A, the baseline case. These improvements combined yield an about 20 percent to 30 percent reduction in heat transfer or thermal load on the film protected surface. Shape B, with forward diffusion only, shows a much less significant change in both film effectiveness and overall heat transfer reduction than Shape C. However, it has the lowest heat transfer coefficient in the vicinity of the injection hole among all the three hole-shapes studied. A flow visualization study using pulsed laser sheet-light reveals that Shape A and Shape B inherit quite similar flow structures. The coolant injected out of Shape C flows much closer to the protected wall than that of Shape A and Shape B. [DOI: 10.1115/1.1418367]

Keywords: *Convection, Cooling, Film Cooling, Heat Transfer, Turbines*

Introduction

Film cooling is one of the major schemes for protection of turbine airfoils from thermal deterioration imposed by the hot gas stream. Turbine engines with effective cooling permit a higher gas temperature at the turbine inlet, which in turn, improves the thermal efficiency and performance of the system. Since the coolant that facilitates the film cooling is extracted from the compressor, poor management of the cooling air can be otherwise detrimental to the engine overall efficiency. Therefore, the design of an effective cooling system with a minimum amount of coolant expended requires a sufficient database as well as fundamental knowledge of the transport phenomena associated with film cooling.

Heat transfer pertaining to film cooling has been actively investigated in the gas turbine community for nearly three decades. One key parameter in measuring the film cooling performance is the film effectiveness (η), which is the dimensionless form of the adiabatic wall temperature, i.e., $\eta=(T_{\mathrm{aw}}-T_m)/(T_f-T_m)$. While the values of η vary with the actual flow conditions, optimal film effectiveness for coolant injected through discrete round holes occurs when the blowing ratio (M) is about 0.5 or the momentum ratio (I) is about 0.25 [1,2]. Such an optimal blowing ratio phenomenon is closely related to the interaction between the injected coolant and the mainstream. For cases with low blowing ratios, better film protection over the hot surface is expected with an increase in the amount of the coolant injected to the mainstream. However, excessive coolant in conjunction with higher blowing ratio elevates the linear momentum of the injectant, which in turn, lifts the coolant away from the surface. This phenomenon is undesirable due to the penetration of injection into the mainstream apparently, permitting the hot gas to flow under the coolant jet close to the surface for protection.

In addition to film effectiveness, the heat transfer coefficient (h) can also be affected by the coolant-mainstream interaction. The focus of interest in the past has been placed primarily in the region sufficiently downstream from the injection hole, where the magnitude of heat transfer coefficient appears to be uninfluenced by the presence of injection. However, the situation is expected to be quite different in the vicinity of an injection hole. The interaction between the injection and the mainstream can drastically alter the flow conditions in the neighboring region, causing the magnitude of heat transfer coefficient to be either substantially higher or lower than that without injection. Eriksen and Goldstein [3] earlier indicated that the heat transfer coefficient with injection is lower than that without injection, because the injection thickens the boundary layer. However, this notion only prevails in the cases of low blowing ratios. Hay et al. [4] later reported that the ratio of heat transfer coefficient between the cases with and without injection (h/h_o) increases with the blowing ratio. The maximum ratio reaches about 1.35 with an injection of 35 deg inclined to the mainstream. The active momentum exchange between the participating streams along with excessive shear generated in the region is responsible for the increased heat transfer coefficient.

Primarily for more effective downstream cooling, film cooling in actual turbine engines often uses a coolant flow rate substantially greater than that corresponding to the optimal film effectiveness condition. As a result, an increase in the blowing ratio, possibly with an elevated heat transfer coefficient near the injection hole, can in fact, increase the overall heat load on the airfoil. In an attempt to reduce the momentum of the injected flow, while still

---

[1] MTU Aeroengine Design Inc., Rocky Hill, CT 06067.

[2] Currently at General Motor, Milford, MI 48380

[3] Currently at Department of Mechanical Engineering, Michigan State University, East Lansing, MI 48824

Contributed by the Heat Transfer Division for publication in the JOURNAL OF HEAT TRANSFER. Manuscript received by the Heat Transfer Division February 26, 2000; revision received May 25, 2001. Associate Editor: J.-C. Han.

maintaining a sufficient amount of coolant flow for proper downstream cooling, one possible approach is to alter the geometry by enlarging the flow passage near the film hole exit. Film holes of such nature are commonly known as shaped-diffusion holes, shaped holes or diffusion holes.

Film cooling pertaining to shaped holes has been little studied until recently. In one of the earliest studies, Goldstein et al. [5] reported a significant increase in film effectiveness in the near hole region as well as an improved lateral spread of the coolant. The test geometry in their study is a 10 deg expansion over a row of circular holes inclined 35 deg relative to the mainstream. More recently, Sen et al. [6] and Schmidt et al. [7] examined the performance of forward-expanded holes with compound-angle injection. Their data suggest that diffusion shaped-holes show particularly better performance with high blowing and momentum ratios. Wittig et al. [8], Gritsch et al. [9,10] examined both the film effectiveness and heat transfer coefficient of two fan-shaped holes with about 14 deg lateral expansion. Haven et al. [11] performed detailed flow visualization around three different diffusion holes and assessed their effects on the film effectiveness. Most recently, Chen et al. [12] studied the compound-angle injection through a row of conical holes. They observed that an increase in the spanwise injection angle can in fact, impose a higher level of heat load on the airfoil, as the heat transfer coefficient is higher and the film effectiveness is lower compared to the streamwise-directed holes.

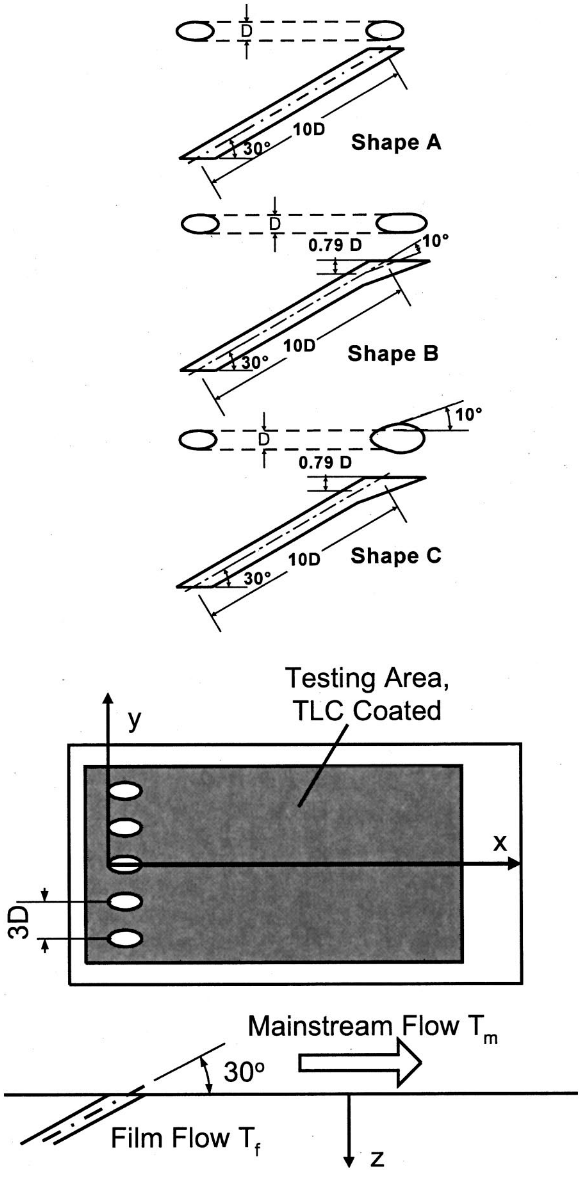

Fig. 1 Shape hole geometry and test section

The present study evaluates the performance of two different, but closely related, shaped diffusion holes, along with a direct comparison to the corresponding baseline case of standard circular holes under the same flow conditions. Figure 1 schematically illustrates the three hole configurations, labeled as Shape A, B, and C. Shape A is the baseline circular injection with a 30 deg inclined angle relative to the freestream. The hole inlet diameter (D) is about 6.4 mm (0.25 in.) and the length is 10 times the diameter. Although such a length-to-diameter ratio is significantly greater than that in the modern day turbine engines, it permits a study focused exclusively on the effects of hole-exit shape without much influence of the inlet conditions. Also shown in Fig. 1, the test section consists of five holes spaced three-dimensional in the spanwise direction. Shape B has all the same geometric parameters as Shape A except that the hole has a 10 deg forward, streamwise diffusion initiated at approximately 0.8 hole-inlet diameter below the test surface. Shape C has all the features of Shape B, but with an additional 10 deg diffusion in the lateral direction. Viewing from the top toward the test surface, Shape B has an elongated oval opening, while Shape C has a tear-drop profile. Performance characterization of each hole geometry is made by measurements of both the film effectiveness and heat transfer coefficient using a transient liquid crystal imaging technique. In addition, pulsed laser-sheet flow visualization is also performed to complement the heat transfer results.

Transient Liquid Crystal Technique for Film Cooling Measurements

The use of liquid crystal coating as a surface temperature indicator for heat transfer imaging has been quite popular, especially in the gas turbine community. When the technique is operated in a transient mode, the change of liquid crystal color provides the temporal variation of local surface temperature over the test region of interest. The local heat transfer coefficient can be inferred by assuming the one-dimensional, transient conduction model prevailing in the solid substrate underneath the test surface. The heat transfer coefficient is defined in a general sense, i.e., $h=q/(T_w-T_r)$, where T_r is the reference temperature of the system. Such a model can be represented in the following governing equation, with z being the coordinate pointing into the substrate:

$$k\frac{\partial^2 T}{\partial^2 z}=\rho C_p\frac{\partial T}{\partial t} \tag{1}$$

$$-k\left.\frac{\partial T}{\partial z}\right|_{z=0}=h(T_w-T_r) \tag{2}$$

$$T|_{z=\infty}=T_i \tag{3}$$

$$T|_{\tau=0}=T_i \tag{4}$$

The solution of the above equation leads to a relationship among the heat transfer coefficient, the thermal properties of the substrate, the initial and reference temperatures of the system, and the time-varying surface temperature.

$$\frac{T_w-T_i}{T_r-T_i}=1-\exp\left[\frac{h^2\alpha\tau}{k^2}\right]\mathrm{erfc}\left[\frac{h\sqrt{\alpha\tau}}{k}\right] \tag{5}$$

While the above approach is generally valid for resolving heat convection problems, it is, however, unsuitable for film cooling. Film cooling is known to be a three-temperature problem, as its thermal transport is governed by the temperatures of two participating streams and the surface exposed to the mixture of those streams. As a contrast to conventional two-temperature problems, the reference temperature T_r in Eq. (5) is no longer a known quantity and needs to be solved simultaneously with the heat transfer coefficient. T_r is also termed the adiabatic wall temperature, T_{aw}, and has a dimensionless appearance as the film effectiveness, as previously mentioned. The overall implication of this is that a second relation similar to Eq. (5) needs to be established.

The technique based on transient liquid crystal imaging for three-temperature, film cooling problems was first introduced by Vedula and Metzger [13]. They delineated the approach of determining η and h by using the same test setup and a transient test with natural boundary conditions. Ekkad et al. [14,15] and Chen et al. [12] used the same method for studying film cooling with compound-angle injection. Yu and Chyu [16] extended the method further for four-temperature problems involving two injection of different temperatures. The fundamental principle of Vedula and Metzger's approach is based on the notion that the turbulent convection is predominantly controlled by flow dynamics rather than thermal conditions. Hence the second relation can be obtained by performing two different, but closely related, heat transfer tests under the same flow conditions. The resulting equations for the two unknowns; i.e., h and T_{aw}, are

$$\frac{T_w-T_{i1}}{T_{\mathrm{aw}}-T_{i1}}=1-\exp\left[\frac{h^2\alpha\tau_1}{k^2}\right]\mathrm{erfc}\left[\frac{h\sqrt{\alpha\tau_1}}{k}\right], \tag{6}$$

$$\frac{T_w-T_{i2}}{T_{\mathrm{aw}}-T_{i2}}=1-\exp\left[\frac{h^2\alpha\tau_2}{k^2}\right]\mathrm{erfc}\left[\frac{h\sqrt{\alpha\tau_2}}{k}\right]. \tag{7}$$

In reality, one of the two tests, so-called the "hot test," uses a film injection close to, but slightly lower than, the heated mainstream; while the "cold test" uses an unheated or slightly heated injection. A key criterion for selecting these test temperatures is to ensure that the two equations, Eqs. (6) and (7), are well coupled, so that when combined they yield a solution for the two unknowns.

True step changes in both the mainstream and injection temperatures during an actual test are usually not possible, hence the reference temperature which appears as a boundary condition in Eq. (2) can vary with time. This fact is accounted by modifying the solution of Eqs. (6) and (7) with the use of superposition and Duhamel's theorem. Decomposing the temporal variation into a series of finite-step changes, these two equations are transformed to the following form:

$$T_w-T_i=\sum_{i=1}^{N} U(\tau-\tau_i)\Delta T_r, \tag{8}$$

where

$$U(\tau-\tau_i)=1-\exp\left[\frac{h^2\alpha(\tau-\tau_i)}{k^2}\right]\mathrm{erfc}\left(\frac{h\sqrt{\alpha(\tau-\tau_i)}}{k}\right). \tag{9}$$

Since ΔT_r is related directly to the variations of the mainstream temperature, T_m, and injection temperature, T_c, by the definition of film effectiveness η,

$$\Delta T_r=(1-\eta)\Delta T_m+\eta\Delta T_c. \tag{10}$$

Substituting Eq. (10) into Eq. (8), the unknowns for the present system become the film effectiveness, η, and the heat transfer coefficient, h.

In view of the geometrical complexity, the heat transfer characteristic in the close vicinity of an injection hole is understandably multi-dimensional in reality. Any amount of heat diffused deviated from the direction normal to the substrate surface (z-axis, Fig. 1) is considered to be an error in the present transient measurement. While an attempt to systematically investigate such an issue has been reported recently [17], the error in the present system may not be as significant as it is generally perceived. The film effectiveness is determined predominantly by the "cold test," where temperatures of the injectant and the Plexiglas substrate are very close throughout the test. Hence the effect of lateral heat transfer in the substrate is expected to be insignificant. The "hot test," on the other hand, has a strong influence on the outcome of the heat transfer coefficient. The injectant and the mainstream air during this test are heated to nearly the same level, about 40~50 C higher than the initial temperature of the substrate. Except for the region immediate adjacent to the injection hole and sufficiently below the surface, the temperature gradients along the lateral directions (perpendicular to the z-axis, see Fig. 1) are expected to be far lower than that along the z-direction in the substrate. Therefore, the one-dimensional model is mostly valid throughout the entire test section, provided that the test duration is not overly long.

Experimental Apparatus and Procedures

The test section consists of a Plexiglas rectangular duct, with 102 mm (4 in.) across the span and 51 mm (2 in.) in height. For each shape, five coolant injection holes with a 30 deg inclination are located near the upstream portion of the test surface. The test surface is coated with a thin layer of thermochromic liquid crystal (TLC) about 0.1 to 0.3 mm thick. An airbrush is used to spray the coating. The temperature calibrated for the particular TLC used in the present study is 38.4°C, 39.8°C and 43.5°C for red, green and blue, respectively. Primarily because of its distinct intensity strength, the green color displayed by TLC is used as the surface temperature tracer during a transient measurement.

Figure 2 shows a schematic of the overall test setup. A laboratory compressor supplies both the mainstream and film flows. Flow rates of the compressed air are measured by standard ASME orifices. After metering each stream is routed through a tubular in-line heater controlled by an auto-transformer, and its temperatures can be accurately set to a desired level. Downstream of the heater, the two flows are initially diverted away from the test section by a three-way ball valve until the actual test starts.

A transient test is initiated by switching both ball valves simultaneously to introduce the main flow and film injection into the test section. The switching of these valves is made only when the flow rates and temperatures of both streams have reached steady state. Initiation of the test also triggers an automated data acquisition system for recording thermocouple readings at flow inlets as well as exits. Simultaneously, a CCD camera starts to record the video images of the TLC coated on the test surface. The video provides the follow-on data reduction procedure with the lap time of TLC changing from colorless to green at every pixel of the viewing domain. The post-run data reduction procedure uses custom developed software run in a personal computer [18]. The test cases include two blowing ratios ($M=0.5$ and 1.0) for Reynolds numbers (based on hole inlet-diameter) from $\mathrm{Re}_D=2300$ to 4300. The corresponding Reynolds number based on the hydraulic diameter of the housed channel is Re=25,000 and 46,000, respec-

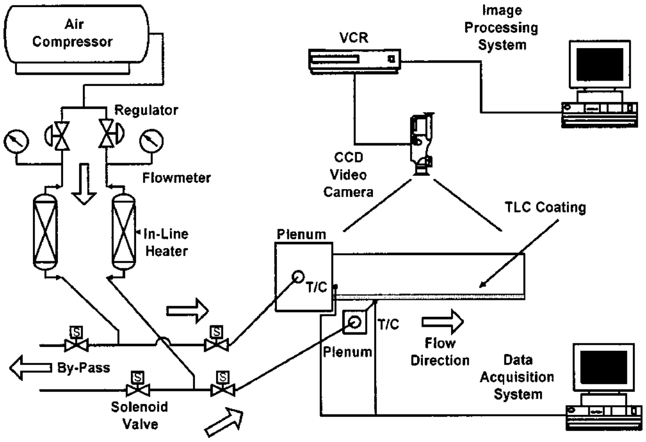

Fig. 2 Test apparatus

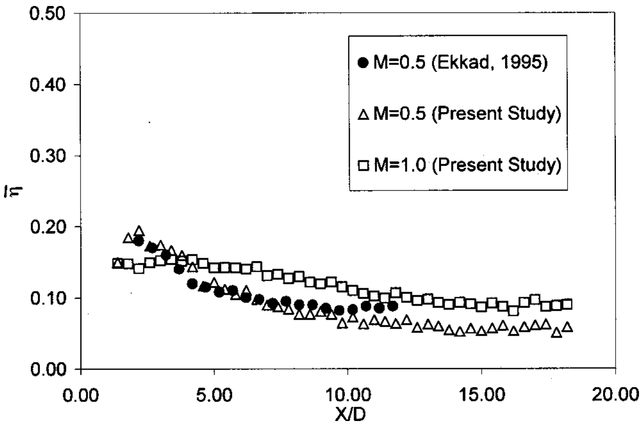

Fig. 3 Spanwise-average film effectiveness

tively. The density ratio in the present study is nominally equal to one, though the actual value during a transient test varies between 0.95 and 1.1. Hence the existing blowing ratio is essentially the flow velocity ratio between the injection and the mainstream. For purpose of validation and comparison, the case with no film injection ($M=0$) was also performed. Under such a non-injecting condition, the boundary layer at the location of injection exhibits fully turbulent characteristics, with a thickness about 8 mm and 6

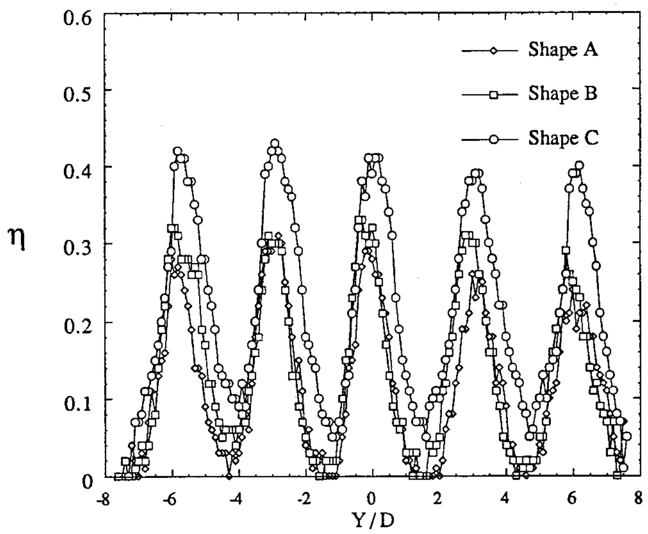

Fig. 4 Spanwise distribution of film effectiveness for non-shaped circular holes at $X/D=3.0$, $M=0.5$, and $\mathrm{Re}_D=4300$

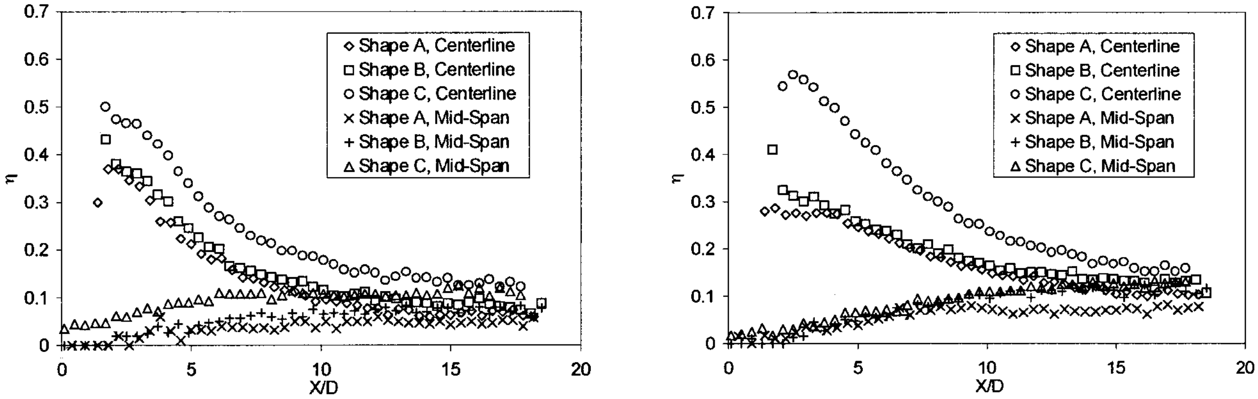

(*a*) **M=0.5**

(*b*) **M=1.0**

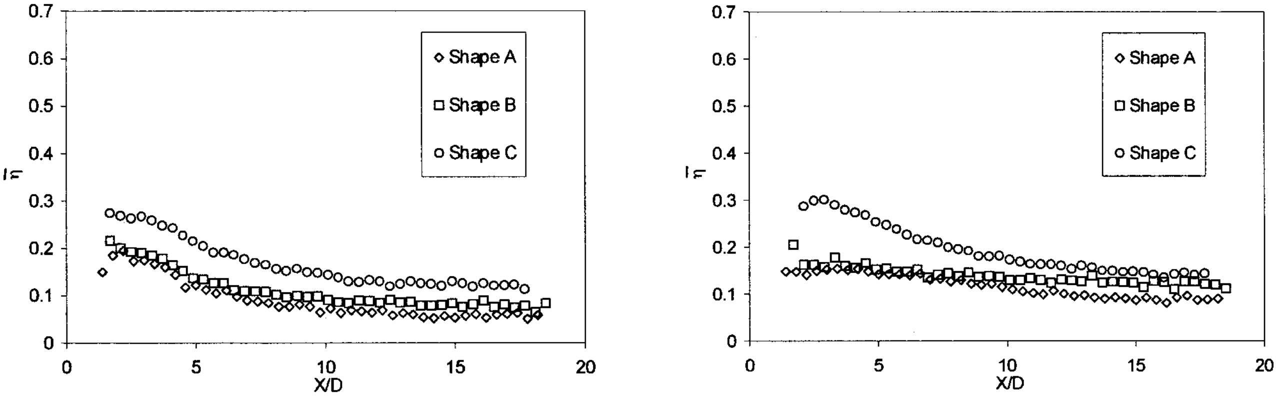

(*c*) **Spanwise Average, M=0.5**

(*d*) **Spanwise Average, M=1.0**

Fig. 5 Streamwise distribution of film effectiveness: (*a*) $M=0.5$; (*b*) $M=1.0$; (*c*) spanwise average, $M=0.5$; and (*d*) spanwise average, $M=1.0$.

mm for Re=25,000 and 46,000, respectively. The turbulence intensity in the mainstream measured by a hot-wire anemometer is about 1.2 percent.

Results and Discussion

Most of the results presented below are in the form of film effectiveness (η) and heat transfer coefficient (h). The uncertainty analysis with a 95 percent confidence level in the measured parameters is based on the method of Kline and McClintock [19]. Both η and h measured in the present liquid-crystal-based system depend strongly on the temperatures of the test surface, inlet, and exit. The uncertainties of these temperature readings are about ±0.2 C, which correspond to 0.5 percent, 0.3 percent, and 0.7 percent at these key locations, respectively. In addition, the uncertainty of both η and h is also affected by the errors in the temperature-color calibration of liquid crystal, the lap-time for the liquid crystal reaching the designated color, and the thermal diffusivity of the substrate. The errors in these three parameters are estimated at 0.5 percent, 0.4 percent, and 1 percent, respectively. Another major error contributing to the uncertainty is the error in measuring the flow rate or Reynolds number in the air supply system, which is about 4 percent. Combining all these errors leads to the overall 7 percent uncertainty for both η and h.

Film Effectiveness. Although the present TLC imaging technique is capable of revealing detailed distributions and contour data over the entire viewing domain, most local data are presented along two key streamwise paths for direct comparison. One of the paths is along the centerline of the test section and directly behind an injection hole, and the other is along the mid-span of two adjacent injection holes. These line data are good representatives of the transport features over the entire measurement domain, as the overall distributions in both η and h are very symmetric across the span of the test section. Figure 3 illustrates a sample comparison of the present film-effectiveness data with the similar results published recently by Ekkad et al. [14]. Although their film holes are spaced relatively wider (4D) and hole inclined angle is different (35 deg), the comparison is very favorable. To demonstrate the level of data symmetry in the present experiments, Fig. 4 shows the spanwise variation of local film effectiveness at $X/D=3.0$ for all three hole configurations, $M=0.5$ and $\mathrm{Re}_D=4300$. At this near-hole location, there is little evidence of coolant spread laterally.

Figure 5 shows the effect of hole shaping on the streamwise distribution of film effectiveness. The origin of X, the streamwise coordinate, locates at the leading edge of an injection hole. Since the influence of Reynolds number is rather insignificant overall, only the case with Re=2350 is presented here. Shape C, which has both forward and lateral expansion, consistently results in the highest film effectiveness among the three hole shapes studied. As shown in Figs. 5(*c*) and (*d*), its spanwise-averaged η is approximately 50 percent higher than the baseline case, Shape A. The enhancement appears to be more significant with $M=1.0$ than with $M=0.5$, particularly in the near-hole region, say $X/D<8$. The aforementioned averaged characteristics are consistent with the local data along the centerline, directly behind an injection hole. As seen in Figs. 5(*a*) and (*b*), the magnitude of local η along the centerline for Shape C is approximately 30 percent and 50 percent higher than the corresponding values of Shape A, for $M=0.5$ and 1.0, respectively.

As a typical feature of discrete-hole film cooling, local values of η along the mid-span are much lower than those along the centerline in the region sufficiently close to the injection hole. The coolant just ejected out of the film cooling holes provides virtually no coverage in the region between neighboring holes and then spreads out laterally toward downstream. Hence η along the two streamwise paths displays completely opposite trends and converges eventually to the same level at a location sufficiently downstream. Overall, Shape C shows a better lateral coverage than the other cases, especially when the Reynolds number is relatively low. As an intermediate case, Shape B, which features a forward expansion only, exhibits a notable but unsubstantial improvement in film effectiveness as compared to the baseline case, Shape A. This implies that, at least for simple, non-compound-angle injection, lateral expansion may be a more effective mechanism than the forward expansion in terms of shaping the injection holes.

Shape A

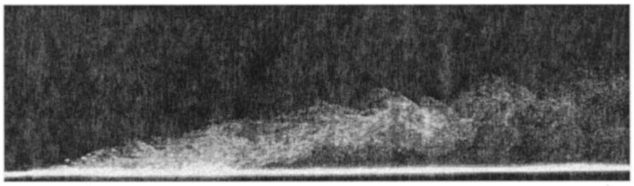

Shape B

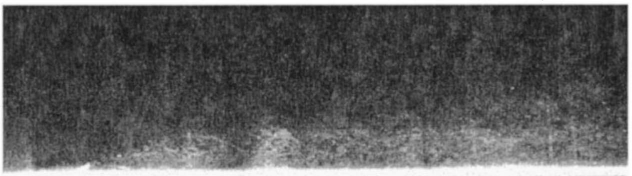

Shape C

Fig. 6 Laser-sheet flow visualization

The quantitative measure of film effectiveness is closely related to its inherent jet flow behavior for each hole geometry. Figure 6 shows flow visualization photos (turn 90 deg in photo) using a laser sheet illumination along the centerline for $M=1.0$ and $\mathrm{Re}_D=2350$. To facilitate the visualization experiment, the injected flow is seeded with 1 μm alumina particles, which form the white traces in the photos. Image recording uses a Kodak ES1.0 camera which has a CCD imager with 1000 by 1000 pixels. It is evident that the flow injected from Shape C remains the closest to the wall among all the three cases studied. This is an indication that proper hole-shaping reduces the jet momentum for penetration to the freestream as well as increases the coolant concentration near the wall. In addition, the scales of flow structure appear to be the smallest for Shape C, implying more effective flow diffusion and mixing. On the other hand, the jets from both Shape A and Shape B exhibit strong lift-off, hence relatively poor wall coverage as well as film effectiveness is expected. In fact, these two cases display quite comparable flow features. As a result, their magnitudes of film effectiveness are also very similar. Similar life-off effect with non-shaped, circular hole was reported earlier by Ligrani et al. [1,2].

Heat Transfer Coefficient. Figure 7 shows the streamwise distributions of the local heat transfer coefficient for various hole shapes. The particular cases shown here are $M=0.5$ and 1.0 at $\mathrm{Re}_D=2350$. Hole geometry has a pronounced influence on the

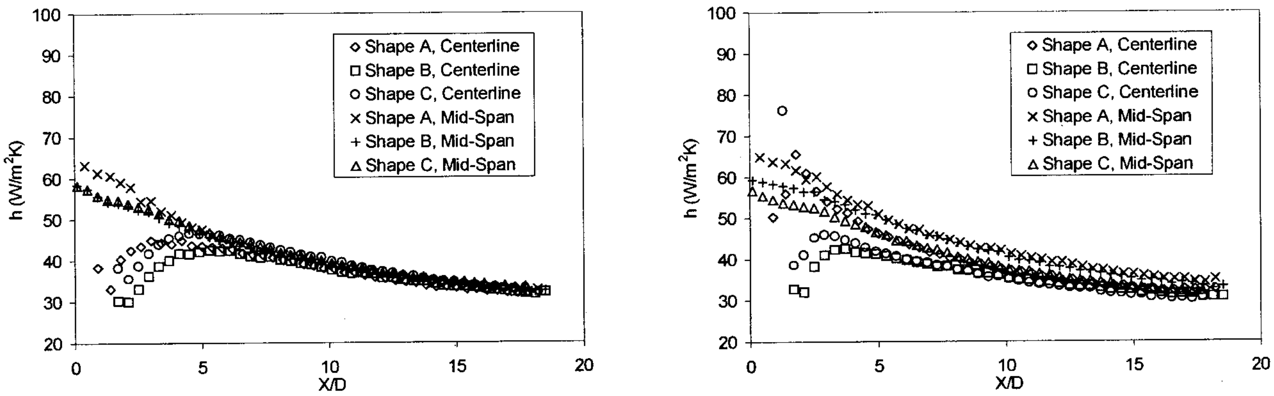

(*a*) **M=0.5** (*b*) **M=1.0**

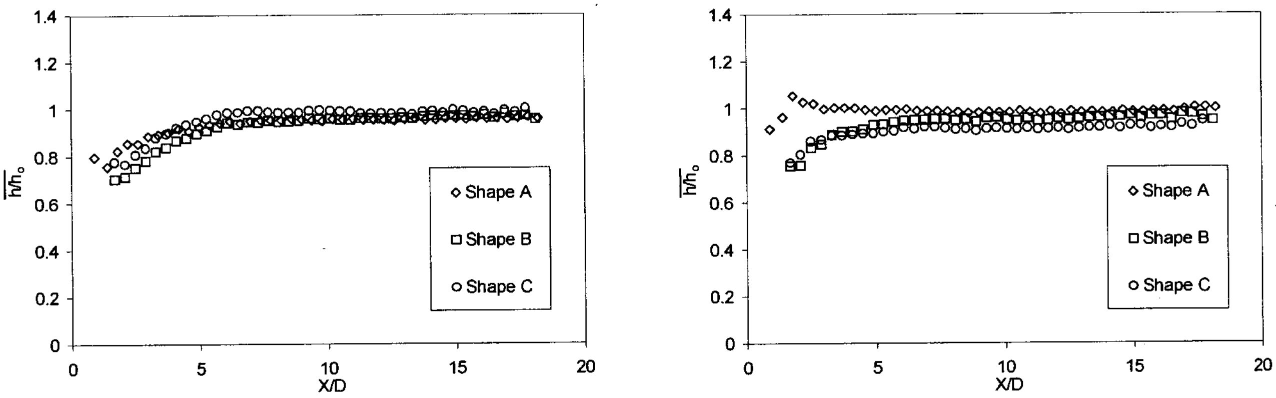

(*c*) **Spanwise Average, M=0.5** (*d*) **Spanwise Average, M=1.0**

Fig. 7 Streamwise distribution of heat transfer coefficient: (*a*) $M=0.5$; (*b*) $M=1.0$; (*c*) spanwise average, $M=0.5$; and (*d*) spanwise average, $M=1.0$.

local heat transfer coefficient, particularly in the region $X/D<6$. Regardless of the nature of hole shaping, the heat transfer coefficient in this region is always lower along the centerline than that along the mid-span. In fact, the magnitude of h along the centerline are the lowest for any given hole geometry. Although the difference in the centerline h among the three hole shapes is rather modest or even within the range of measurement uncertainty, the forward-diffusion hole, i.e., Shape B, consistently exhibits the lowest value. On the other hand, Shape A, which is the non-shaped, baseline case, exhibits the highest value. The heat transfer coefficients along the mid-span for all three cases studied are relatively comparable and, in fact, are similar to that over the test wall without injection. All the local data collapse to more or less a single curve sufficiently downstream to the injection holes.

The magnitude of heat transfer coefficient around a film-cooling hole is influenced by two competing factors. First, it decreases with a thickening boundary layer induced by injection added flow mass and linear momentum normal to the wall. Thicker boundary layer presents more heat convection resistance between the mainstream and the film-protected wall. Second, the value of heat transfer coefficient may increase with enhanced flow shear induced by interaction between the injection and the mainstream. The first effect appears to be the predominant feature near the centerline, particularly when the blowing ratio or the jet exit velocity is relatively low. The second effect with flow shear is expected to prevail along the side-edge of an injection hole, which is responsible for the high heat transfer coefficient along the mid-span. In view of the flow structure revealed in Fig. 6, Shape A induces the greatest boundary layer thickening as well as flow shear in the near-hole region. Shape C, on the other hand, represents the opposite extreme, with the thinnest boundary layer and lowest level of shear generation. Shape B is expected to be mid-level of both effects, which when combined ultimately results in the lowest heat transfer coefficient along the centerline. For the case with a higher blowing ratio, $M=1.0$, Shape A exhibits a sharp rise of heat transfer coefficient directly behind the injection hole, as shown in Fig. 7(*b*). Strong local shear generation apparently overwhelms the effect of boundary layer thickening in this region.

Figures 7(*c*) and 7(*d*) show the streamwise distribution of spanwise-average heat transfer coefficient normalized by its counterpart without injection (h_o). The value of h_o was obtained using the same experimental setup, but without injection. The test under this condition is a conventional "two-temperature-driven convection problem" and it requires only a "hot-test" to reveal the heat transfer coefficient. The results in Fig. 7(*c*) indicate that discrete-hole film cooling with $M=0.5$, in average, enables a 20 to 30 percent reduction of heat transfer coefficient compared to h_o in the near hole region. Due mainly to excessive interaction between the injection and the mainstream, the situation can be drastically different when the blowing ratio is sufficiently high. As evidenced in Fig. 7(*d*) for $M=1.0$, the h/h_o data for Shape A exceed unity around $X/D=3$ and in certain regions further downstream. This implies that, depending on the nature of flow interaction between the participating streams, implementation of film cooling can be either favorable or detrimental to the overall thermal protection from the viewpoint of heat transfer coefficient. Nevertheless, the

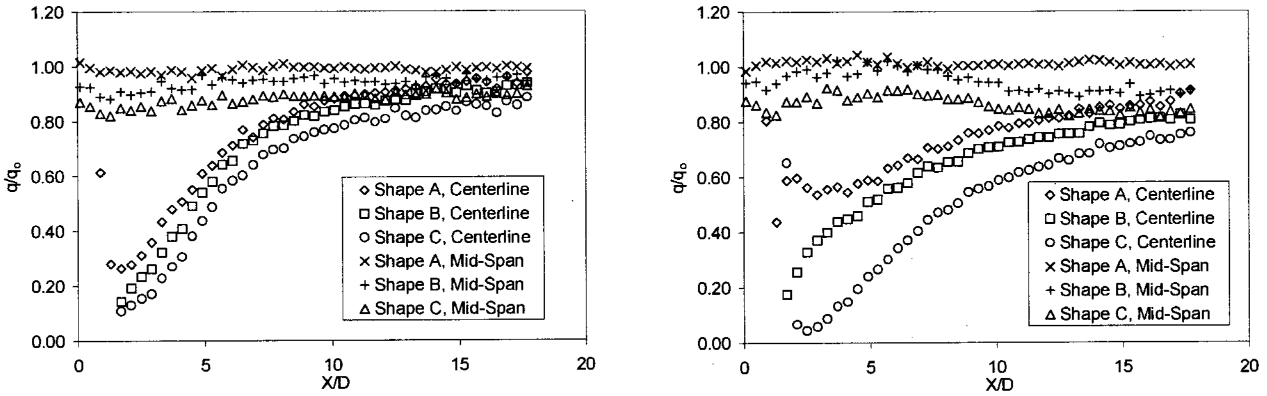

(*a*) **M=0.5** (*b*) **M=1.0**

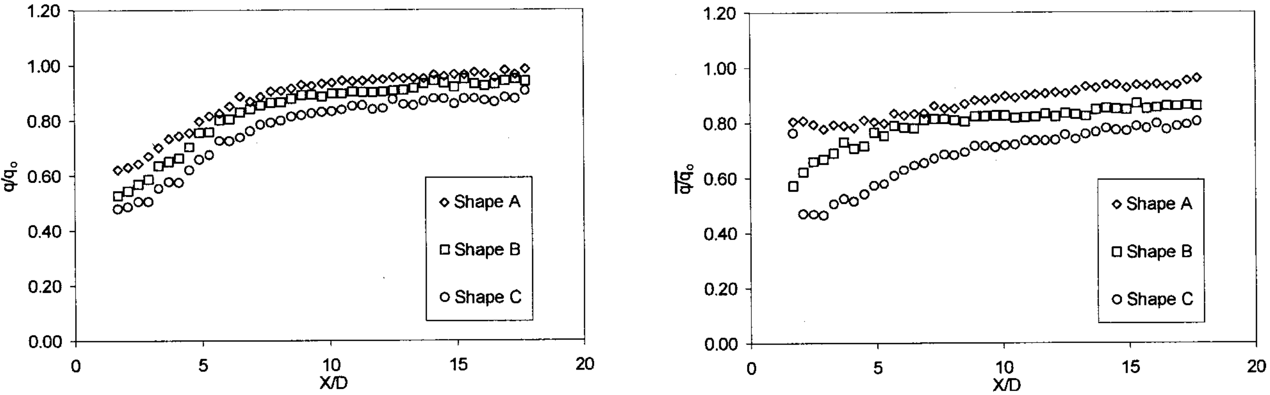

(*c*) **Spanwise Average, M=0.5** (*d*) **Spanwise Average, M=1.0**

Fig. 8 Heat flux ration: (*a*) $M=0.5$; (*b*) $M=1.0$; (*c*) spanwise average, $M=0.5$; and (*d*) spanwise average, $M=1.0$.

information revealed in Fig. 7(*d*) confirms that one of the major effects of hole shaping is the reduction of heat transfer coefficient, particularly for high-blowing-ratios.

Heat Transfer Relative to Uncooled Situation. As mentioned earlier, to estimate the wall heat transfer rate with film cooling requires the knowledge of both heat transfer coefficient (h) and reference temperature (T_r or T_{aw}), i.e.,

$$q=h(T_{\mathrm{aw}}-T_w). \tag{11}$$

T_{aw} is related to the film effectiveness (η) via the definition of $\eta=(T_{\mathrm{aw}}-T_m)/(T_c-T_m)$, as previously mentioned. According to Metzger et al. [20], Sen et al. [6] and Ekkad et al. [14,15], the ratio of heat flux on a film-protected surface to the corresponding baseline value without film cooling can be expressed by

$$q/q_o=(h/h_o)(1-\eta/\varphi), \tag{12}$$

where φ is the overall cooling effectiveness given by $\varphi=(T_w-T_m)/(T_c-T_m)$. Typical values of φ in actual engines range from 0.5 to 0.7. The present study uses $\varphi=0.6$, as the mean value of the actual range.

Figure 8 gives both the local and spanwise-averaged distributions of q/q_o along the streamwise coordinate for different blowing ratios. According to Figs. 8(*c*) and (*d*), all the three cases studied, in average, provide the surface with a certain degree of thermal protection, as the values of spanwise-averaged $\overline{q/q_o}$ are always less than one. In addition, the case with $M=1.0$ appears to be more effective overall in reducing the local heat flux than that with $M=0.5$. The only exception lies in the region of $X/D<5$, where Shape A and Shape B with $M=0.5$, in fact, have lower values of q/q_o than with $M=1.0$. This observation is consistent with the general notion that the optimal cooling performance with injection through non-shaped, discrete circular holes occurs when $M\sim0.5$.

As a result of favorably combining film effectiveness and heat transfer coefficient, Shape C with diffusion in both forward and lateral directions produces the lowest heat transfer, by a margin of 20 to 30 percent lower than Shape A. The most significant improvement lies in the region near the injection hole with a higher blowing ratio, $M=1.0$. Shape B with forward expansion only yields a relatively moderate heat transfer reduction compared to Shape A. However, it is notably less effective than Shape C.

Conclusions

The transient liquid crystal technique has been further demonstrated as an effective means of experimentally examining film cooling performance in great detail. The technique is unique in its capability of revealing both the film effectiveness and heat transfer coefficient simultaneously. The present study marks the first attempt of using the transient liquid crystal technique to systematically evaluate the effects of film hole shaping as compared to the reference case with a row of five straight circular holes oriented 30 deg relative to the mainstream direction (Shape A). Two closely related, diffusion shaped holes, one with a 10 deg forward expansion (Shape B) and the other with a 10 deg expansion in both forward and lateral directions (Shape C) are evaluated and compared. The heat transfer results are substantiated by a flow visualization study using a pulsed laser sheet with alumina seedings in the injection. Summarized below are key conclusions.

Shape C with both forward and lateral diffusion produces the most significant effect on the film cooling performance in terms of hole shaping. It gives the highest film effectiveness as well as overall heat transfer reduction among all the three hole-geometries studied. The margin of improvement for these two performance measures is about 30 to 50 percent, depending on the blowing ratio and location. While its heat transfer coefficient is not overall the lowest, the magnitude is substantially lower than that of the baseline, Shape A, and somewhat close to that of Shape B.

Shape B with forward-expansion and without lateral diffusion shows a moderate performance improvement compared to Shape A and a notably worse performance than Shape C. It inherits the lowest heat transfer coefficient in the near-hole region among all the three cases studied. This outcome appears to be a compromise of two competing effects, i.e., boundary layer thickening and injection-mainstream shear interaction. Its film effectiveness, on the other hand, resembles greatly to that around Shape A. This observation further attests to the fact that the flow features around these two shaped holes are quite similar, as evidenced in the laser-sheet flow visualization also performed in this study.

Spatial variations in both film effectiveness and heat transfer coefficient are very significant regardless of hole shaping. The range of variation across a measurement span often exceeds ten folds for both variables. As expected, the local film effectiveness always reveals the highest magnitudes along the centerline and the lowest along the mid-span for a given streamwise location downstream to the injection hole. On the contrary, the heat transfer coefficient generally has its greatest values around the side-edge of an injection hole. Such an elevated *h* is attributable to excessive flow shear generated locally, due mainly to the injection-mainstream interaction. As a result, the mid-span, which is closer to the side-edge of an injection hole, generally has the higher heat transfer coefficient than the centerline. However, Shape A with a relatively high blowing ratio reveals a sharp rise in *h* immediately behind the injection hole. Again, the strong shear generated beneath the lifted jet may be responsible for such an phenomenon [21].

Acknowledgment

Support of this work, in part, is under a DOE Advanced Gas Turbine System Research program sponsored by the South Carolina Energy Research Center.

Nomenclature

C_p = fluid specific heat
D = injection hole inlet diameter
D_h = channel hydraulic diameter
h = convective heat transfer coefficient
k = thermal conductivity of test surface
M = blowing ratio $=(\rho V)_c/(\rho V)_m$
q = wall heat flux
Re = Reynolds number based on $D_h, = V_c D_h/\mu$
Re_D = Reynolds number based on film hole inlet diameter, $= V_c D/\mu$
T = temperature
V = mean flow velocity
X = streamwise coordinate
Y = spanwise coordinate

Greek Symbol

α = test surface thermal diffusivity
β = injection angle
η = film cooling effectiveness
μ = fluid dynamic viscosity
τ = time

Subscript

aw = adiabatic wall
D = based on jet inlet diameter
D_h = based on hydraulic diameter of test channel
c = coolant at hole exit
i = initial
m = mainstream
o = without injection
r = reference
w = wall

Superscript

- = spanwise average

References

[1] Ligrani, P. M., Wigle, J. M., Ciriello, S., and Jackson, S. M., 1994, ''Film-Cooling From Holes With Compound Angle Orientations: Part 1—Results Downstream of Two Staggered Rows of Holes with 3d Spanwise Spacing,'' ASME J. Heat Transfer, **116**, pp. 341–352.
[2] Ligrani, P. M., Wigle, J. M., and Jackson, S. M., 1994, ''Film-Cooling from Holes With Compound Angle Orientations: Part 2—Results Downstream of a Single Row of Holes with 6d Spanwise Spacing,'' ASME J. Heat Transfer, **116**, pp. 341–352.
[3] Eriksen, and Goldstein, 1974, ''Heat Transfer and Film Cooling Following Injection Through Inclined Tubes,'' ASME J. Heat Transfer, **96**, pp. 239–245.
[4] Hay, N., Lampard, D., and Saluja, C. L., 1985, ''Effects of Cooling Films on the Heat Transfer Coefficient on a Flat Plate With Zero Mainstream Pressure Gradient,'' ASME J. Eng. Gas Turbines Power, **107**, pp. 104–110.
[5] Goldstein, R. J., Eckert, E. R. G., and Burggraf, F., 1974, ''Effects of Hole Geometry and Density on Three-Dimensional Film Cooling,'' Int. J. Heat Mass Transf., **17**, pp. 595–607.
[6] Sen, B., Schmidt, D. L., and Bogard, D. G., 1996, ''Film Cooling with Compound Angle Holes: Heat Transfer,'' ASME J. Turbomach., **118**, pp. 800–806.
[7] Schmidt, D. L., Sen, B., and Bogard, D. G., 1996, ''Film Cooling with Compound Angle Holes: Adiabatic Effectiveness,'' ASME J. Turbomach., **118**, pp. 807–813.
[8] Wittig, S., Schultz, Gritsch, M., and Thole, K. A., 1996, ''Transonic Film-Cooling Investigations: Effects of Hole Shapes and Orientations,'' ASME Paper 96-GT-222.
[9] Gritsch, M., Schultz, A., and Wittig, S., 1998, ''Adiabatic Wall Effectiveness Measurements of Film-Cooling Holes with Expanded Exits,'' ASME J. Turbomach., **120**, pp. 549–556.
[10] Gritsch, M., Schultz, A., and Wittig, S., 1998, ''Heat Transfer Measurements of Film-Cooling Holes with Expanded Exits,'' ASME Paper 98-GT-28.
[11] Haven, B. A., Yamagata, D. K., Kurosaka, M., Yamawaki, S., and Maya, T., 1997, ''Anti-Kidney Pair of Vortices in Shaped Holes and Their Influence on Film Cooling Effectiveness,'' ASME Paper 97-GT-45.
[12] Chen, P-H., Ai, D., and Lee, S.-H., 1998, ''Effects of Compound Angle Injection on Flat-Plate Film Cooling Through a Row of Conical Holes,'' ASME Paper 98-GT-459.
[13] Vedula, R. J., and Metzger, D. E., 1991, ''A Method for the Simultaneous Determination of Local Effectiveness and Heat Transfer Distributions in Three-Temperature Convection Situations,'' ASME Paper 91-GT-345
[14] Ekkad, S. V., Zapata, D., and Han, J. C., 1997, ''Heat Transfer Coefficients Over a Flat Surface With Air and CO_2 Injection Through Compound Angle Holes Using a Transient Liquid Crystal Image Method,'' ASME J. Turbomach., **119**, pp. 580–586.
[15] Ekkad, S. V., Zapata, D., and Han, J. C., 1997, ''Film Effectiveness over a Flat Surface With Air and CO_2 Injection Through Compound Angle Holes Using a Transient Liquid Crystal Image Method,'' ASME J. Turbomach., **119**, pp. 587–593.
[16] Yu, Y., and Chyu, M. K., 1998, ''Influence of Gap Leakage Downstream of the Injection Holes on Film Cooling Performance,'' ASME J. Turbomach., **120**, pp. 541–548.
[17] Kassab, A. J., Divo, E., and Chyu, M. K., 1999, ''A BEM-Based Inverse Algorithm to Retrieve Multi-dimensional Heat Transfer Coefficients from Transient Temperature Measurements,'' BETECH99, *Proc. 13th International Boundary Element Technology Conference*, *Computational Mechanics*, Las Vegas, June 8–10, 1999, C. S. Chen, C. A. Brebbia, and D. Pepper, eds., Billerica, MA.
[18] Chyu, M. K., and Ding, H., 1997, ''Heat Transfer in a Cooling Channel With Vortex Generators,'' ASME J. Heat Transfer, **119**, p. 206.
[19] Kline, S. J., and McClintock, F. A., 1953, ''Describing Uncertainties in Single-Sample Experiments,'' Mech. Eng. (Am. Soc. Mech. Eng.), **75**, pp. 3–8.
[20] Metzger, D. E., Carper, H. J., and Swank, L. R., 1968, ''Heat Transfer with Film Cooling Near Nontangential Injection Slots,'' J. Eng. Power, **90**, pp. 157–163.
[21] Metzger, D. E., and Larson, D. E., 1986, ''Use of Melting Point Surface Coating for Local Convective Heat Transfer Measurements in Rectangular Channel Flows with 90 Degree Turns,'' ASME J. Heat Transfer, **108**, pp. 48–54.

Energy and Exergy Balance in the Process of Spray Combustion in a Gas Turbine Combustor

S. K. Som
e-mail: sksom@mech.iitkgp.ernet.in

N. Y. Sharma[1]

Department of Mechanical Engineering
Indian Institute of Technology
Kharagpur 721 302, India

A theoretical model of exergy balance based on availability transfer and flow availability in the process of spray combustion in a gas turbine combustor has been developed to evaluate the total thermodynamic irreversibility and second law efficiency of the process at various operating conditions, for fuels with different volatilities. The velocity, temperature and concentration fields in the combustor, required for the evaluation of the flow availabilities and process irreversibilities, have been computed numerically from a two phase separated flow model of spray combustion. The total thermodynamic irreversibility in the process of spray combustion has been determined from the difference in the flow availability at inlet and outlet of the combustor. The irreversibility caused by the gas phase processes in the combustor has been obtained from the entropy transport equation, while that due to the inter-phase transport processes has been obtained as a difference of gas phase irreversibilities from the total irreversibility. A comparative picture of the variations of combustion efficiency and second law efficiency at different operating conditions for fuels with different volatilities has been made to throw light on the trade off between the effectiveness of combustion and the lost work in the process of spray combustion in a gas turbine combustor. [DOI: 10.1115/1.1484393]

Keywords: *Combustion, Energy, Exergy, Heat Transfer, Second Law, Sprays*

Introduction

The combustion of liquid fuel spray has widespread applications in gas turbines, internal combustion engines, rocket motors and industrial furnaces. The research in the area of spray combustion is going on over the last few decades and a host of articles, including the exhaustive reviews of Faeth [1,2] and Sirignano [3–5], are available in the literature. However, all the works were centered around in predicting the different aspects of combustion performance like combustion efficiency, temperature and species concentration distribution within the combustor and emission characteristics. Thus the basic motivation of the studies, already done in the field, remained to identify the operating parameters to achieve a high combustion efficiency with a low liner temperature and a relatively uniform exit temperature distribution for turbomachinery consideration.

From the viewpoint of energy economy, an efficient spray combustion process should be guided not only by the combustion efficiency of the process but also by its second law efficiency that gauges the effectiveness in preserving the quality of energy. Hence the exergy analysis of a spray combustion process to evaluate the second law efficiency provides additional thermodynamic information to determine the locations, types and magnitude of losses. A minimization of the losses by suitable choice of operating parameters leads to an optimum design of the process for an overall energy economy.

The information regarding the thermodynamic irreversibilities and exergy loss in the process of spray combustion is not available in the literature till date. While the work of Dash et al. [6] provides information regarding the thermodynamic irreversibilities in droplet evaporation, the works of Dash and Som [7], Puri [8], and Hiwase et al. [9], provide similar information in case of droplet combustion. Som and Dash [10] studied the second law analysis in the process of spray evaporation based on the exergy loss in the process. Dunbar and Lior [11] calculated the sources of combustion irreversibilities with hydrogen and methane flames and found that approximately one-third of the useful energy of the fuel is destroyed during the combustion process.

The objective of the present work is to furnish a comparative picture of the effectiveness in the quantitative conversion of energy and the effectiveness in preserving the quality (work potential) of energy in a spray combustion process in a gas turbine combustor. This is made through a comparison of combustion efficiency and second law efficiency for fuels with different volatilities at various operating conditions of the combustor. The relative role of gas phase and interphase transport processes towards the loss of exergy has also been analyzed. In the first part of the work, a basic flow and combustion modeling of a typical spray combustion process is described. In the second part, a theoretical model of exergy balance is developed to evaluate the second law efficiency with the help of the data on velocity, temperature and species concentration fields in the combustor provided by the spray combustion model in the first part of the work.

Theoretical Formulation

Physical Model. The physical problem refers to the evaporation and combustion of a continuously injected liquid fuel spray in a can type combustor (Fig. 1), typical of a gas turbine combustion process. The air supply to the combustor is split among the swirler at the entry and through two radial jets in the form of secondary and dilution air. Fuel spray is injected from an atomizer located at the hub of the swirler. The problem is assumed to be axi-symmetric.

Flow and Combustion Modeling. A numerical model of the spray combustion process within the combustor has been developed to determine the velocity, temperature and species concentration fields along with the combustion efficiency.

Numerical Computation of Spray Combustion. The computation is based on a typical two phase Eulerian-Lagrangian for-

---

[1] On leave from Dept. of Mech & IP Engg, Manipal Institute of Technology, MAHE, Manipal, India.

Contributed by the Heat Transfer Division for publication in the JOURNAL OF HEAT TRANSFER. Manuscript received by the Heat Transfer Division May 9, 2001; revision received April 11, 2002. Associate Editor: H. Lee.

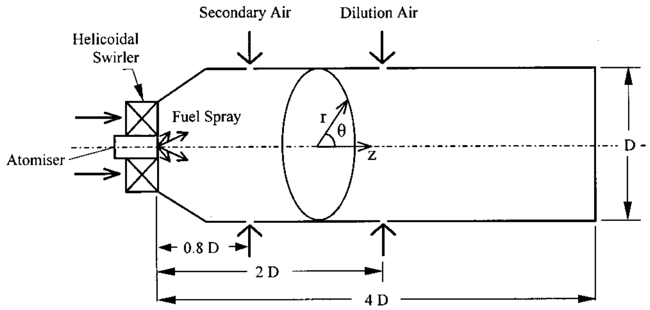

Fig. 1 Physical model

mulation of an axi-symmetric gas-droplet flow with a standard κ-ε model for the gas phase turbulence and a global reaction kinetics for the gas phase reaction of fuel vapor with oxygen. The body force and buoyancy force are neglected in the analysis, so also the virtual mass force and Besset force are not considered due to high density ratio between the phases. Droplets do not take part in radiative energy exchange, which is solved purely as a gas phase phenomenon.

The adoption of standard κ-ε model has been made despite the fact that many researchers observe some shortcomings in the ability of the κ-ε model in predicting a swirling flow field quantitatively. However, there is no conclusive information available in the literature regarding the accurate adaptability of a suitable modification of the κ-ε model for a confined swirling flow. The models like ASM and RSM are either too complex or equally poor in predicting a strong swirling flow. Moreover, it is expected that the accuracy in predicting the gross flow parameters like combustion efficiency and second law efficiency will not be much affected with the adoption of a standard κ-ε model. Therefore the standard κ-ε model has been considered for the solution in the present work.

The axi-symmetric spray model is a simplified assumption. However, it predicts a fairly accurate results in the primary zone of fuel rich region, though it fails to generate accurate quantitative results in the secondary zone due to blowing of secondary and dilution air through radial holes. The simplification of axi-symmetric model provides at least an understanding in recognizing the pertinent controlling parameters and their qualitative influences on the irreversibility rate and second law efficiency of a spray combustion process which is the prime objective of the present work. Moreover, it can be argued that, since the major part of irreversibilities occurs in the primary zone due to droplet vaporization, chemical reaction and the sharp temperature and concentration gradients, the quantitative results related to the thermodynamic aspects may not be far from the actual ones.

Gas Phase Conservation Equations. The average gas phase conservation equations are as follows:

Continuity.

$$\frac{\partial\rho}{\partial t}+\frac{\partial}{\partial x_i}(\rho U_i)=\dot{S} \tag{1}$$

Momentum.

$$\frac{\partial}{\partial t}(\rho U_i)+\frac{\partial}{\partial x_j}(\rho U_i U_j)=-\frac{\partial p'}{\partial x_i}+\frac{\partial}{\partial x_j}\left\{\mu_{\text{eff}}\left(\frac{\partial U_i}{\partial x_j}+\frac{\partial U_j}{\partial x_i}\right)\right\}+\dot{S}_{M_i}+\dot{S}U_i \tag{2}$$

where,

$$\mu_{\text{eff}}=\mu+c_\mu\rho\frac{k^2}{\varepsilon} \tag{3}$$

$$p'=p+\frac{2}{3}\rho k+\frac{2}{3}\mu_{\text{eff}}\frac{\partial U_j}{\partial x_j} \tag{4}$$

Turbulent Kinetic Energy (κ).

$$\frac{\partial}{\partial t}(\rho\kappa)+\frac{\partial}{\partial x_i}(\rho U_i\kappa)=\frac{\partial}{\partial x_i}\left(\frac{\mu_t}{\sigma_k}\frac{\partial\kappa}{\partial x_i}\right)+P-\rho\varepsilon+\dot{S}\kappa \tag{5}$$

where, turbulent kinetic energy production rate P is given by

$$P=\mu_t\left(\frac{\partial U_i}{\partial x_j}+\frac{\partial U_j}{\partial x_i}\right)\frac{\partial U_i}{\partial x_j}-\frac{2}{3}\frac{\partial U_i}{\partial x_i}\left(\rho\kappa+\mu_t\frac{\partial U_i}{\partial x_i}\right) \tag{6}$$

Turbulent Kinetic Energy Dissipation Rate (ε).

$$\frac{\partial}{\partial t}(\rho\varepsilon)+\frac{\partial}{\partial x_i}(\rho U_i\varepsilon)=\frac{\partial}{\partial x_i}\left(\frac{\mu_t}{\sigma_\varepsilon}\frac{\partial\varepsilon}{\partial x_i}\right)+c_{1\varepsilon}\frac{\varepsilon}{\kappa}P-\rho c_{2\varepsilon}\frac{\varepsilon^2}{\kappa}+\dot{S}\varepsilon \tag{7}$$

Constants for standard κ-ε model are taken as,
$c_\mu=0.09$, $c_{1\varepsilon}=1.44$, $c_{2\varepsilon}=1.92$, $\sigma_k=1.0$, and $\sigma_\varepsilon=1.3$

Energy.

$$\frac{\partial}{\partial t}(\rho c_p^g T^g)+\frac{\partial}{\partial x_i}(\rho c_p^g U_i T^g)=\frac{\partial}{\partial x_i}\left(\rho c_p^g\alpha_{\text{eff}}\frac{\partial T^g}{\partial x_i}\right)-\frac{\partial q_i^r}{\partial x_i}+\dot{S}_E+c_p^g T^g\dot{S} \tag{8}$$

The Energy source term, $\dot{S}_E$ has two components—one of which is the energy absorbed by the liquid droplets during their heating-up period calculated from the inter-phase transport and the other is the energy generated due to chemical reaction.

The energy addition due to combustion is determined in consideration of a single step, irreversible, global reaction between the fuel vapor and oxygen following a finite rate chemistry as,

$$\lambda_F F+\lambda_O O_2\rightarrow\lambda_P P$$

The reaction in the combustion chamber is either kinetic or turbulent diffusion controlled. The kinetic controlled reaction rate is determined following an Arrhenius-type equation with the corresponding kinetic parameters taken from the work of Westbrook and Dryer [12], as

$$\dot{\omega}_k=B\rho^2\frac{C_j C_{O_2}}{M_f M_{O_2}}\exp\left(-\frac{E}{RT}\right) \tag{9}$$

In a turbulent diffusion flame, the rate of combustion may be guided by the rate of inter mixing on a molecular scale of fuel and oxygen eddies. The rate of turbulent diffusion reaction is given by

$$\dot{\omega}_d=A\frac{\rho}{M_f}\frac{\varepsilon}{\kappa}\left[\min\left(C_f,\frac{C_{O_2}}{\gamma},\frac{cC_P}{1+\gamma}\right)\right] \tag{10}$$

where,

$$\gamma=\chi_o M_o/\chi_f M_f$$

The empirical constants A and c are as suggested by Magnussen et al. [13]. Thus the energy source term due to chemical reaction will be,
$\Delta H_R M_f[\min(\dot{\omega}_k,\dot{\psi}_d)]$
where, ΔH_R is the enthalpy of reaction. The radiative energy exchange within the gas phase is evaluated by neglecting the influence of the droplets, and assuming the gas phase to be gray absorbing emitting medium. The radiative transfer equation is solved following a first order moment method, (Ozisik [14]) which reduces the integro-differential equation of radiative energy transfer into a differential equation as shown below.

$$\frac{\partial q_i^r}{\partial x_i}=\kappa[4\pi I_b(T)-G] \tag{11}$$

where the irradiation G is related to q_i^r as

$$q_i^r = -\frac{1}{3\kappa}\frac{\partial G}{\partial x_i} \tag{12}$$

In the light of the assumption of a gray gas radiation model, the absorption coefficient κ is replaced by Planck's mean absorption coefficient, κ_P. The local value of κ_P is computed as

$$\kappa_{\mathrm{P}} = C_{\mathrm{H_2O}}\kappa_{\mathrm{PH_2O}}(T) + C_{\mathrm{CO_2}}\kappa_{\mathrm{PCO_2}}(T) \tag{13}$$

The values of $\kappa_P(T)$ as a function of temperature, for the radiatively participating gases CO_2 and H_2O, are taken from Sparrow and Cess [15]

Individual Species Conservation.

$$\frac{\partial}{\partial t}(\rho C_j) + \frac{\partial}{\partial x_i}(\rho U_i C_j) = \frac{\partial}{\partial x_i}\left(\rho D_{\mathrm{eff}}\frac{\partial C_j}{\partial x_i}\right) + \dot{S}_{C_j} + \dot{S}C_j \tag{14}$$

The species conservation equation is solved for fuel vapor, oxygen, carbon-di-oxide and water vapor while nitrogen concentration is obtained by difference. The conservation equation for each species contains a source term S_{C_j} given by

$$S_{C_j} = -\omega M_f \quad \text{for fuel vapor}$$

$$S_{C_j} = -\omega M_f \gamma \quad \text{for oxygen}$$

$$S_{C_j} = -\omega M_f (1+\gamma)$$

$$\text{for the product (carbon—dioxide and water vapor)}$$

where the rate of reaction ω is equal to $\min(\omega_k, \omega_d)$.

The additional source term SC_j is zero for all species except the fuel vapor. This takes care of the fuel mass evaporated from the droplets.

Generation of Droplet Phase Information. The velocity, mass and temperature history of all droplet classes along their trajectories are obtained from the respective conservation equations on a Lagrangian frame as follows.

Droplet Velocity.

$$m^d \frac{dV_i^d}{dt} = \frac{\pi}{8}\rho d^2 C_D \left|V_i^g - V_i^d\right| (V_i^g - V_i^d) \tag{15}$$

Drag coefficient C_D is computed following the standard drag law by Clift et al. [16]
The effect of gas phase turbulence on the droplet motion is simulated using a stochastic approach. The instantaneous gas phase velocity (V_i^g) is obtained by computing the fluctuating velocity component from the turbulent kinetic energy in consideration of isotropic turbulence, and using a normally distributed random number ζ, as

$$V_i^g = U_i + \varsigma\sqrt{\frac{2\kappa}{3}} \tag{16}$$

Droplet Mass.

$$\frac{dm^d}{dt} = -\rho^m \beta \pi d^2 (C_{f_s} - C_f) \tag{17}$$

where ρ^m and C_{f_s}, are the density of the gas phase and the mass fraction of fuel vapor respectively at the droplet surface. In consideration of thermodynamic equilibrium at the droplet surface, C_{f_s}, is calculated from the vapor pressure at droplet temperature as

$$C_s = \frac{1}{1 + \dfrac{M_o}{M_f}\left(\dfrac{p}{p_v} - 1\right)}$$

where p_v and p are the partial pressure of fuel vapor at droplet surface and total pressure of the local gas phase, respectively.

Droplet Temperature.

$$m^d c_p^d \frac{dT^d}{dt} = h\pi d^2 (T^g - T^d) + \frac{dm^d}{dt}\Delta H_v \tag{18}$$

where, ΔH_v is the enthalpy of vaporization of the liquid fuel at droplet temperature. Mass transfer coefficient β and heat transfer coefficient h in Eqs. (17) and (18), respectively, are evaluated from the standard correlations by Ranz and Marshall [17] and Dash et al. [6] as

$$\mathrm{Nu}(1+B) = 2 + 0.6\,\mathrm{Re}_d^{0.5} Pr^{0.33} \tag{19}$$

$$\mathrm{Sh}(1+B) = 2 + 0.6\,\mathrm{Re}_d^{0.5} Sc^{0.33} \tag{20}$$

where B is the Transfer Number. Eqs. (15), (17), and (18) are solved for V_i^d, m^d, and T^d respectively, with appropriate initial conditions.

The initial drop size distribution of liquid fuel spray is assumed to follow a realistic four-parameter Rosin-Rammler distribution function given by,

$$G'(d_i) = \frac{\exp(-bd_i^n) - \exp(-bd_{\max}^n)}{\exp(-bd_{\min i}^n) - \exp(-bd_{\max i}^n)} \tag{21}$$

where, $G'(d_i)$ is the mass fraction of the spray having diameter above d_i. The dispersion parameter n is taken as 3, as recommended by Mugele and Evans [18].

Method of Solution

The gas phase conservation equations (Eqs. (1), (2), (5), (7), (8), and (14)) were solved simultaneously by an explicit finite difference computing technique developed by Hirt and Cook [19] following the original MAC (Marker and Cell) method due to Harlow and Welch [20]. The space derivatives of the diffusion terms were discretized by the central differencing scheme, while the advection terms were discretized by a hybrid differencing scheme based on the local Peclet number (*Pe*) associated with the cell. The conservation equations for the droplets (Eqs. (15), (17) and (18)) were solved by fourth order Runge-Kutta method with appropriate initial conditions. A variable sized adaptive grid system was considered and the variations in the size of the grids were made smoothly. A numerical mesh of 89×31 grid nodes was used after several numerical experiments, which showed that further refinement in grids in either direction did not change the result (maximum change in velocity or any scalar variable in the carrier phase) by more than 2 percent. The choice of time increment Δt was made to ensure stability in the computation in accordance with the criteria of cell transit time of fluid due to convection and diffusion respectively. Often a more stringent restriction was required to have a converged solution and was fixed by trail and error in the computation.

The total air flow to the combustor was splitted among the swirler, and two radial jets according to a ratio of 5:7:8 following Cameron et al. [21]. Air flow entering the combustor through the swirler was considered to be in a plug flow mode with a typical solid body type rotation imparted by helicoidal vane-swirler. Therefore, a uniform axial velocity distribution and a linear tangential velocity distribution of air were considered at the inlet plane of the combustor. The temperature distribution of air at the inlet plane was also considered to be uniform. A zero axial gradient was prescribed at the outlet for all the variables. Standard logarithmic law of wall was considered for the near wall region. For radiation calculation, the end planes were assumed to be radiatively adiabatic and Marshak boundary condition was applied at the solid combustor wall. The fuels were considered to be *n*

Table 1 Fuel volatility characteristics

Fuels	Molecular Weight	Normal Boiling Point Temperature, T_B (K)
n hexane	86.178	342
kerosene	140.26	454
n dodecane	170.34	490

hexane (C_6H_{14}), kerosene($C_{10}H_{20}$) and *n* dodecane($C_{12}H_{26}$). The volatility characteristics of the fuels considered are as shown in Table 1.

Combustion Efficiency. In consideration of a global reaction kinetics and without any possibility of the existence of liquid fuel droplet at the exit, the combustion efficiency for a given inflow of fuel is determined from the fuel vapor concentration at the combustor exit as,

$$\eta_c = 1 - \left(\frac{2\pi \int_0^R \rho_e U_{z_e} C_{f_e} r\,dr}{\dot{m}_f} \right) \tag{22}$$

Calibration of the Numerical Model. The accuracy of the quantitative and even the qualitative trends of the predicted results relating to combustion efficiency, process irreversibilities, and second law efficiency depends mainly on the accuracy with which the velocity, temperature and species concentration fields in the process of spray combustion have been determined from the numerical computation of the present model. A comparison of the results predicted from the present model with those of earlier works in identical situations is not always possible, since the information available in those works do not give explicitly all the input parameters required to generate the output data of the present model for the purpose of comparison. However a possible comparison of the present results in case of an axisymmetric sudden expansion isothermal swirling flow, and also for a reactive swirling flow in a dump combustor has been made with the relevant empirical and computational results available in the literature.

In case of an isothermal flow, the comparison of the present results with the computational work of Chang and Chen [22] and the experimental results of Dellenback [23] under the similar situations are shown in Figs. 2(*a*)–(*d*). Figures 2(*a*) and (*c*) show a fair agreement of the predicted axial and tangential velocity profiles near the inlet region ($z=0.75$) with the computations of Chang and Chen and the empirical values of Dellenback. However it is observed from Figs. 2(*b*) and (*d*) that the present numerical results and the computations of Chang and Chen, being in agreement with each other, do not conform well with the experimental results of Dellenback for the tangential velocity distribution at far down stream from the inlet ($z=4.0$) and mainly near the axis. This was explained by Chang and Chen in the light of under-prediction of the length of central toroidal recirculation zone by the standard κ-ε model.

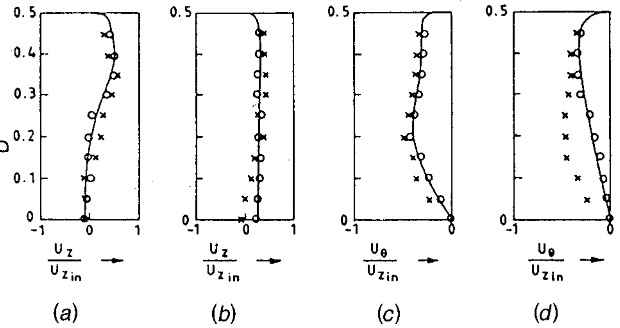

(*a*) (*b*) (*c*) (*d*)

Fig. 2 Comparisons of predicted axial and tangential velocity distributions, with Chang and Chen [22] and Dellenback [23] (—Present computation, ○ Chang and Chen, and × Dellenback) (*a*) *z*/*D*=0.75; (*b*) *z*/*D*=4.0; (*c*) *z*/*D*=0.75; and (*d*) *z*/*D*=4.0.

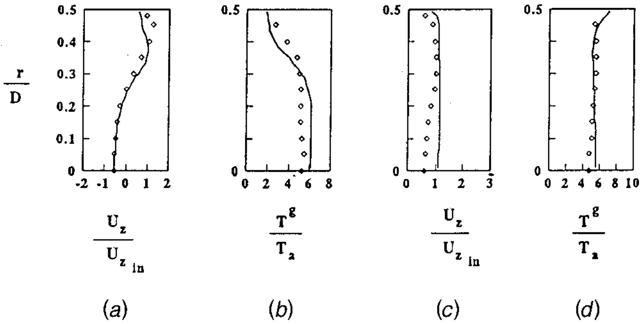

(*a*) (*b*) (*c*) (*d*)

Fig. 3 Comparisons of predicted axial velocity and temperature distributions with experimental results of Khalil et al. [24] (—present computation, ○ Khalil et al.): (*a*) *z*/*D*=0.55; (*b*) *z*/*D*=0.55; (*c*) *z*/*D*=3.6; and (*d*) *z*/*D*=3.6.

A possible comparison of axial velocity and temperature distributions predicted by the present model in case of an axisymmetric swirling flow in a dump combustor has been made with the experimental work of Khalil et al., [24] under a similar situation (Figs. 3(*a*–*d*)). Due to a lack of information on spray parameters in the reported experimental work of Khalil et al., the spray parameters considered for the comparison are chosen after several trials taken over the mean drop diameter and spray cone angle. Since the fuel used in the experiments of Khalil et al., was kerosene, the same fuel has been chosen in the present model for the purpose of comparison. It is observed that the predictions of axial velocity components agree fairly well with the experimental results at an upstream location within the combustor (Fig. 3(*a*)), while a deviation between the two results is observed mainly near the axis at a section far downstream from the inlet (Fig. 3(*c*)). This discrepancy may be attributed to the fact that the standard κ-ε model under-predicts the length of the central toroidal recirculating zone in the swirling flow field. Moreover, the assumption of an axi-symmetric model is less justified at a far downstream location because of the introduction of secondary air through radial holes. The temperature distributions predicted by the present model show a fair agreement with the empirical results both at upstream and downstream locations of the combustor (Figs. 3(*b*) and 3(*d*)). However, the predicted temperature distribution at the downstream location shows an increasing trend near the wall, unlike that obtained in the experimental results of Khalil et al. This may possibly be attributed to the fact that the assumption of stick model for the droplet evaporation results in a zone of burning near the wall in the downstream part of the combustor.

Exergy Model of Spray Combustion

The exergy analysis of the problem has been made on the basis of flow availability to the system comprising the entire combustor (Fig. 1), considering the outer wall to be adiabatic. Since the words "availability" and "exergy" are synonymous in their thermodynamic implications, both of them will be referred to in the remaining part of the text, depending upon the appropriate uses at places following the general convention. It can be written for the conservation of exergy of the system that,

$$\dot{A}_{\text{in}} = \dot{A}_e + \dot{I} \tag{23}$$

where, A_{in} and A_e are the rates of flow availability coming in and going out of the system, respectively, and i is the rate of thermodynamic irreversibility within the system.

Determination of Flow Availabilities. The flow availabilities of different species at inlet and outlet of the combustor have been evaluated with respect to an exergy reference thermodynamic state of $P_r = 101.35\ \text{kN/m}^2$, $T_r = 298.15\ \text{K}$ with mole fractions of the constituents as $x_r^{\text{O}_2} = 0.2035$, $x_r^{\text{CO}_2} = 0.0003$, and $x_r^{\text{H}_2\text{O}} = 0.0303$ as recommended by Moran and Shapiro (25).

The flow availability at the inlet, being associated with the inflow of air and fuel to the system, can be written as,

$$\dot{A}_{\text{in}} = \dot{m}_{a_{\text{in}}} a_{\text{in}}^a + \dot{m}_{f_{\text{in}}} a_{\text{in}}^f \tag{24}$$

where,

$\dot{m}_{a_{\text{in}}}$ = mass flow rate of air into the combustor
a_{in}^a = specific flow availability of air at inlet
$\dot{m}_{f_{\text{in}}}$ = mass flow rate of fuel into the combustor
a_{in}^f = specific flow availability of fuel at inlet

The specific flow availability of air is determined from the following equation:

$$a_{\text{in}}^a = (h_{\text{in}}^a - h_r) - T_r(s_{\text{in}}^a - s_r) \tag{25a}$$

where,

$$h_{\text{in}}^a - h_r = \int_{T_r}^{T_{\text{in}}^a} c_p^a(T)\,dT \tag{25b}$$

$$s_{\text{in}}^a - s_r = \int_{T_r}^{T_{\text{in}}^a} \frac{c_p^a(T)}{T}\,dT - \frac{\overline{R}}{M_a} \int_{p_r}^{p_{\text{in}}^a} \frac{dP}{P} \tag{25c}$$

The molar flow availability (comprising both chemical and thermo-mechanical components) of a generic hydrocarbon fuel C_aH_b undergoing a single step global reaction

$$C_aH_b + \left(a + \frac{b}{4}\right)\text{O}_2 \rightarrow a\text{CO}_2 + \frac{b}{2}\text{H}_2\text{O}$$

can be written, following Moran and Shapiro [25] as,

$$\overline{a}_{\text{in}}^f = \left(\overline{h}_{\text{in}}^f + \left(a + \frac{b}{4}\right) h_r^{\text{O}_2} - a\overline{h}_r^{\text{CO}_2} - \frac{b}{2}\overline{h}_r^{\text{H}_2\text{O}}\right)$$
$$- T_r\left(\overline{s}_{\text{in}}^f + \left(a + \frac{b}{4}\right)\overline{s}^{\text{O}_2} - a\overline{s}^{\text{CO}_2} - \frac{b}{2}\overline{s}^{\text{H}_2\text{O}}\right) \tag{26a}$$

where,

$$\overline{h}_{\text{in}}^f = \Delta\overline{h}_F^f + \int_{T_r}^{T_{\text{in}}^f} \overline{c}_p^f(T)\,dT \tag{26b}$$

$$\overline{h}_r^{\text{O}_2} = 0 \tag{26c}$$

$$\overline{h}_r^{\text{CO}_2} = \Delta\overline{h}_F^{\text{CO}_2} \tag{26d}$$

$$\overline{h}_r^{\text{H}_2\text{O}} = \Delta\overline{h}_F^{\text{H}_2\text{O}} \tag{26e}$$

$$\overline{s}_{\text{in}}^f = \overline{s}_r^f + \int_{T_r}^{T_{\text{in}}^f} \frac{C_p^f(T)}{T}\,dT - \frac{\overline{R}}{M_f} \int_{p_r}^{p_{\text{in}}^f} \frac{dP}{P} \tag{26f}$$

$$\overline{s}^{\text{O}_2} = \overline{s}_r^{\text{O}_2} - \overline{R}\ln(x_r^{\text{O}_2}) \tag{26g}$$

$$\overline{s}^{\text{CO}_2} = \overline{s}_r^{\text{CO}_2} - \overline{R}\ln(x_r^{\text{CO}_2}) \tag{26h}$$

$$\overline{s}^{\text{H}_2\text{O}} = \overline{s}_r^{\text{H}_2\text{O}} - \overline{R}\ln(x_r^{\text{H}_2\text{O}}) \tag{26i}$$

The specific flow availability of the fuel is calculated from the molar availability as,

$$a_{\text{in}}^f = \frac{\overline{a}_{\text{in}}^f}{M_f} \tag{27}$$

where, M_f the molecular weight of the fuel.

The flow availability at the combustor exit can be expressed as,

$$\dot{A}_e = 2\pi \int_0^R \left(\sum_j C_e^j a_e^j\right) \rho_e^g U_{z_e} r\,dr \tag{28}$$

where, C_e^j is the mass fraction of the j^{th} species and U_{ze} is the local axial gas velocity at the exit plane.

The specific flow availability of each species at a point in the exit plane (a_e^j) is calculated based on local pressure and temperature in the similar fashion as done for inlet. Both chemical and thermo-mechanical availabilities for fuel vapor, and only thermo-mechanical availability for the other species are considered

Estimation of Process Irreversibilities. The total irreversibility in a typical two phase gas-droplet flow in the combustor is composed of two parts, namely, (i) the irreversibility due to the transport processes and chemical reaction in the continuous gas phase, $\dot{I}_g$ and (ii) the irreversibility due to the inter-phase transports (transport processes between the discrete evaporating droplets and their local ambience) $\dot{I}_d$. Therefore, it can be written as,

$$\dot{I} = \dot{I}_g + \dot{I}_d = T_r(\dot{E}_g + \dot{E}_d) \tag{29}$$

where $\dot{E}_g$ is the entropy generation rate due to transport processes and chemical reaction in the gas phase and $\dot{E}_d$ is the entropy generation rates due to inter-phase transport processes of discrete evaporating droplets.

The total irreversibility $\dot{I}$ is determined from Eq. (23). To assess the relative weightage of $\dot{I}_g$ and $\dot{I}_d$ in $\dot{I}$, any one of these two ($\dot{I}_g$ and $\dot{I}_d$) has to be determined independently. The entropy generation $\dot{I}_g$ due to gas phase transport process and chemical reaction is determined from the general entropy transport equation in a continuous field of compressible Newtonian fluid. The entropy generation rate per unit volume, $\dot{e}_g$ at a point in the gas phase can be written, following Hirschfelder et al. [26] as,

$$\dot{e}_g = \frac{\Delta : \sigma}{T^g} + \frac{-J_q \nabla T^g}{(T^g)^2} + \frac{\Sigma(-J_{m_j} \nabla \mu_{c_j})}{T^g}$$
$$+ \frac{\Sigma(-\overline{s}_j J_{m_j} \nabla T^g)}{T^g} + \frac{1}{T^g}\Sigma\lambda_j \mu_{c_j}\dot{\omega} \tag{30}$$

where, σ and Δ are the stress and rate of strain tensors respectively, J_q the heat flux per unit area and J_{m_j}, μ_{c_j}, $\overline{s_j}$ are the mole flux per unit area, chemical potential and partial molal entropy of the j^h species respectively. The first term in Eq. (30) is due to fluid friction, the second term is due to conduction and radiation of heat, the third term pertains to mass transfer, the fourth term arises from the coupling between heat and mass transfer and the fifth term is due to chemical reaction

The total gas phase entropy generation is, therefore, calculated as,

$$\dot{E}_g = \int\int\int_{\forall} \dot{e}_g\, d\forall \tag{31}$$

where, $\forall$ is the volume of the domain of physical processes. Each term of the Eq. (8) is expanded in a cylindrical coordinate system to determine $\dot{e}_g$ under the present situation, with the help of gas phase velocity, temperature and concentration fields calculated from numerical computations of spray combustion.

Second Law Efficiency. The second law efficiency of the combustor can be expressed as,

$$\eta_{II}=\frac{\dot{A}_e}{\dot{A}_{\text{in}}}=1-\frac{\dot{I}}{\dot{A}_{\text{in}}} \tag{32}$$

Results and Discussion

Influences of Inlet Pressure on Combustion Efficiency and Second Law Efficiency for Fuels With Different Volatilities. It is observed from Table 2(*a*) that an increase in fuel volatility increases the combustion efficiency only at a higher pressure for any given inlet temperature and swirl number. The success for complete combustion depends on the penetration of fuel droplets, their rate of vaporization and mixing of fuel vapor with air. At low pressures, for a given temperature, all these three physical processes are relatively fast and combustion efficiency is usually very high. Therefore, the change in the rate of droplet vaporization with fuel volatility does not make any marked influence in combustion efficiency.

However, on the other hand, when the pressure in the combustion chamber is high, at a given inlet temperature, there occur (i) a reduction in droplet penetration due to increased density of ambient air, (ii) a reduction in the rate of droplet vaporization because of a reduction in mole fraction of fuel vapor at droplet surface, and (iii) a reduction in the diffusion of fuel vapor in surrounding air due to a decrease in fuel-air diffusivity. Therefore for a given fuel, an increase in combustion pressure for a fixed inlet temperature always reduces the combustion efficiency. Under this situation, the favorable effects of enhanced droplet vaporization and its mixing with ambient air, due to an increase in fuel volatility is felt sharply through a marked increase in the combustion efficiency.

While the combustion efficiency decreases, the second law efficiency increases with an increase in pressure at a given temperature. The increase in second law efficiency with pressure can be attributed to simultaneous increase in flow availability of incoming air at a high pressure and less process irreversibility due to reduced droplet vaporization. The reduction in total irreversibility ($\dot{I}$), is manifested mostly through a marked reduction in the irreversibility rate due to inter-phase transport processes $\dot{I}_d$, with an increase in pressure (Table 2(*b*)). The gas phase irreversibility ($\dot{I}_g$) increases with pressure for the higher volatile fuel (*n* hexane), while it decreases with pressure for the lower volatile fuels (kerosene and *n* dodecane).

Influences of Inlet Swirl on Combustion Efficiency and Second Law Efficiency for Fuels With Different Volatilities. It is observed from Table 2(*a*) that the combustion efficiency is uninfluenced by the inlet swirl to the flow of air at its lower pressure of 100 kPa., while it decreases with an increase in inlet swirl when the pressure is increased to 1000 kPa. The purpose of imparting swirl to incoming primary air, is to cause an on-axis recirculatory flow near the upstream region of the primary zone to enhance the rates of droplet vaporization and mixing of fuel vapor in air, along with the subsequent stabilization of flame. But on the other hand, the recirculatory flow field in the inlet region of the combustor, reduces the penetration of droplets to further downstream in the primary zone for a more effective droplet vaporization and burning. The relative role of these two counter-weighing effects depends on the range of inlet air pressure. At a lower pressure, these two counter-weighing effects nullify each other in producing any change in combustion efficiency. However, when the pressure in the combustion chamber is high, the droplet penetration is as such low. A further reduction in droplet penetration due to an increase in inlet swirl counter weighs the favorable influence on droplet vaporization and mixing of fuel vapor, and finally results in a lower combustion efficiency.

The inlet swirl causes a marginal increase in second law efficiency at a lower inlet pressure of 100 kPa., while it causes a considerable decrease in the second law efficiency at a higher inlet pressure of 1000 kPa. At any inlet pressure and swirl, the second law efficiency increases with a decrease in fuel volatility. It is most important to note that at higher inlet pressure, an increase in inlet swirl decreases both the combustion efficiency and second law efficiency for all the fuels. While the reduction in combustion efficiency is due to the lack of effective droplet penetration in the primary zone, the reduction in second law efficiency is mainly because of an increase in $\dot{I}_g$ due to enhanced gas phase transport processes at increased swirl. Therefore an increase in inlet swirl at

Table 2 Influences of inlet pressure and swirl on combustion efficiencies and process irreversibilities for fuels with different volatilities ($\dot{m}_{a_{\text{in}}}=0.1$ kg/s, $A_s=0.02$ m^2, $A_d=0.04$ m^2, $T_{\text{in}}=600$ K, Re$_{\text{in}}=52400$, $\psi=80°$, SMD$_i=52$ μm, $A/F=60$): (*a*) comparison of combustion efficiency and second law efficiency (%); and (*b*) process irreversibilities (J/s).

Inlet Air Pressure (kPa)	Inlet Swirl Number	Combustion efficiencies			Second law efficiencies		
		n hexane	kerosene	n dodecane	n hexane	kerosene	n dodecane
100	0.36	95.37	96.06	94.34	54.54	65.84	71.14
	0.76	95.40	96.92	94.81	56.11	70.64	74.44
1000	0.36	91.14	82.92	64.43	74.04	83.27	86.43
	0.76	84.21	78.47	45.90	67.12	72.27	82.73

(*a*)

Inlet Air Pressure (kPa)	Inlet Swirl Number	n hexane			kerosene			n dodecane		
		$\dot{I}_g$	$\dot{I}_d$	$\dot{I}$	$\dot{I}_g$	$\dot{I}_d$	$\dot{I}$	$\dot{I}_g$	$\dot{I}_d$	$\dot{I}$
100	0.36	20731	19746	40477	17137	12427	29564	18278	7097	25375
	0.76	21154	17930	39084	22963	2454	25417	21481	1474	22955
1000	0.36	26032	2224	28256	14633	3167	17800	8852	1788	10640
	0.76	30422	5375	35797	19342	6777	20019	11418	722	12140

(*b*)

Table 3 Influences of spray cone angle on combustion efficiencies and process irreversibilities for fuels with different volatilities ($\dot{m}_{a_{in}}=0.1$ kg/s, $A_s=0.02$ m^2, $A_d=0.04$ m^2, Pin=100 kPa Tin=600 K, $\mathrm{Re}_{in}=52400$, $S=0.76$, $\mathrm{SMD}_i=52$ μm, $A/F=60$): (*a*) comparison of combustion efficiency and second law efficiency (%); and (*b*) process irreversibilities (J/s).

Spray Cone Angles	Combustion efficiencies			Second law efficiencies		
	n hexane	kerosene	n dodecane	n hexane	kerosene	n dodecane
60^0	91.30	67.10	58.71	62.55	76.45	81.13
80^0	95.40	96.92	94.81	56.11	70.64	74.44
100^0	98.62	93.86	91.30	50.04	68.25	68.38

(*a*)

Spray Cone Angle	n hexane			kerosene			n dodecane		
	I_g	I_d	I	I_g	I_d	I	I_g	I_d	I
60^0	21018	12330	33348	14680	5702	20382	10192	6391	16583
80^0	21154	17930	39084	22963	2454	25417	21481	1474	22955
100^0	20466	24019	44485	19865	7613	27478	16189	12484	28673

(*b*)

a higher inlet pressure for the process of spray combustion is not thermodynamically meaningful from the view point of conservation of both the quantity and quality of energy.

Influence of Spray Parameters on Combustion Efficiency and Second Law Efficiency for Fuels With Different Volatilities.

Influence of Spray Cone Angle. It is observed from Table 3(*a*) that, the combustion efficiency for a higher volatile fuel (*n* hexane) is very high and increases marginally with the spray cone angle. For fuels of lower volatility (kerosene and *n* dodecane), the combustion efficiency is very low at a lower spray cone angle of 60 deg. However when the spray cone angle of the lower volatile fuels is increased from 60 deg to 80 deg, there is a considerable increase in combustion efficiency followed by a slight decrease with a further increase in spray cone angle to 100 deg. This can be physically explained as follows.

At a lower spray cone angle of 60 deg, the penetration of fuel droplets is relatively high. The poor rate of droplet vaporization, in case of fuels with lower volatility, may lead to a situation where a class of vaporizing droplets may reach the downstream location beyond the primary zone where burning is less conducive due to a lower temperature because of excess air. This does not happen in case of a higher volatile fuel because of higher rate of fuel vaporization. When the spray cone angle is increased (ψ=80 deg, 100 deg) most of the droplet classes, for all fuels, strike the combustor wall due to their large radial dispersions. According to the assumed stick model, droplets striking the wall stick and undergo a complete vaporization there itself. This causes an effective mixture of air and fuel vapor within the primary zone and hence results in an increase in combustion efficiency. The increase is substantial for a lower volatile fuel because many of the droplets which could have escaped the primary zone before complete vaporization in case of lower spray cone angle, have in fact been trapped within the primary zone due to wall sticking at higher spray cone angle. For a higher volatile fuel, the situation is a little different. Due to a rapid rate of fuel vaporization, almost all the droplets are trapped within the primary zone for their complete vaporization at all the spray cone angles. However, an increase in spray cone angle involves more combustion air within the spray to enhance the process of mixing between the fuel vapor and air and thus produces a slight increase in combustion efficiency.

It is observed from Table 3(*a*) that the second law efficiency (η_{II}) decreases with an increase in spray cone angle (ψ) for all fuels. Again at a given ψ, the value of η_{II} increases with a decrease in fuel volatility. The decrease in the value of η_{II} with ψ is due to the increase in total thermodynamic Irreversibility, $\dot{I}$ of the process (Table 3(*b*)) for a given flow availability at the inlet. However an interesting picture is obtained, if we look into the variation of different irreversibility components, $\dot{I}_g$, and $\dot{I}_d$ with ψ for fuels of different volatilities. It is observed from Table 3(*b*) that for the higher volatile fuel (*n*-hexane), an increase in ψ from 60 deg to 100 deg increases the irreversibility rate, $\dot{I}_d$ due to inter-phase transport processes, while the irreversibility rate $\dot{I}_g$, contributed by the gas phase, remains almost the same. In case of lower volatile fuels (kerosene and *n*-dodecane), an increase in ψ from 60 deg to 80 deg increases the value of $\dot{I}_g$ considerably while the value of $\dot{I}_d$ is reduced. But with a further increase in ψ from 80 deg to 100 deg, the value of $\dot{I}_g$ is reduced while the value of $\dot{I}_d$ is considerably increased. This can be explained physically as follows.

For a higher volatile fuel, an increase in the value of ψ causes larger radial dispersions of fuel droplets and involves more air circulating within the spray in enhancing the rate of droplet vaporization and thus causes an increase in the value of $\dot{I}_d$. In case of lower volatile fuels, an increase in the value of ψ produces two contrasting effects in the rate of droplet vaporization. With an increase in the value of ψ, a large class of droplets strikes the wall and vaporizes while sticking to the wall. Therefore the rate of inter-phase transport processes is reduced due to a reduction in the droplet surface area available for such processes. On the other hand, an increase in the value of ψ, reduces the undue droplet penetration. The droplets under this situation, are retained within an effective burning region in the primary zone, and are exposed to a much steeper temperature and concentration gradients at the interface, for which the rates of inter-phase transport processes are increased. When the value of ψ is increased from 60 deg to 80 deg, the influence of wall sticking of droplets in the rate of inter-phase transport processes dominates in reducing the value of $\dot{I}_d$, while for an increase in the value of ψ from 80 deg to 100 deg, the influence of droplet penetration on inter-phase transport rates dominates in increasing the value of $\dot{I}_d$.

Influence of Initial SMD. It is observed from Table 4(*a*), that the combustion efficiency increases for all fuels when the initial

Table 4 Influences of initial SMD on combustion efficiencies and process irreversibilities for fuels with different volatilities ($\dot{m}_{a_{in}}=0.1$ kg/s, $A_s=0.02$ m^2, $A_d=0.04$ m^2, Pin=100 kPa Tin=600 K, Re$_{in}$=52400, $S=0.76$, SMD$_i$=52 μm, $A/F=60$): (*a*) comparison of combustion efficiency and second law efficiency (%); and (*b*) process irreversibilities (J/s).

Initial SMD (μm)	Combustion efficiencies			Second law efficiencies		
	n hexane	kerosene	n dodecane	n hexane	kerosene	n dodecane
25	92.62	88.90	86.32	59.62	76.35	80.69
50	95.40	96.92	94.81	56.11	70.64	74.44
75	94.20	95.61	93.53	53.70	66.15	72.79

(*a*)

Initial SMD (μm)	n hexane			kerosene			n dodecane		
	I_g	I_d	I	I_g	I_d	I	I_g	I_d	I
25	23188	12773	35961	17442	3029	20471	11717	5257	16974
50	21154	17930	39084	22963	2454	25417	21418	1474	22955
75	20240	20985	41225	23346	2014	26360	22476	1243	23719

(*b*)

SMD (SMD$_i$), is increased from 25 μm to 50 μm. However, with a further increase in the value of SMD$_i$ from 50 μm to 75 μm, the combustion efficiency suffers a marginal decrease for all the fuels.

With an increase in SMD$_i$, the rate of droplet vaporization per unit mass is reduced but at the same time, the spray penetration is increased. In the lower range of SMD$_i$ the spray penetration is more important from the viewpoint of combustion efficiency. An increase in combustion efficiency takes place so long the penetration of the droplets in the gas phase increases, but the droplets remain almost within the primary zone where burning rate of fuel is more effective. For still higher penetration, droplets may reach to a downstream location beyond the primary zone, where burning is less conducive due to lower temperature because of additional air. This results in a reduction in combustion efficiency.

It is further observed from Table 4(*a*) that the second law efficiency decrease with an increase in initial SMD of the fuel spray. The decrease in the value of η_{II} with the SMD$_i$ is attributed to an increase in total process irreversibility $\dot{I}$, while the flow availability at the inlet remains the same, since the incoming species (air and fuel vapor) and their thermodynamic states remain the same.

It is interesting to observe from Table 4(*b*) that for a higher volatile fuel (*n* hexane), an increase in SMD$_i$ increases the Irreversibility $\dot{I}_d$ due to inter-phase transport processes but reduces irreversibility $\dot{I}_g$ due to gas phase transport processes; but it is just the opposite in case of fuels with lower volatilities. The increase in the value of $\dot{I}_d$ with the SMD$_i$ for a higher volatile fuel, can be physically attributed to the enhanced rates of inter-phase transport processes and vaporization of coarser droplets because of their better penetration and mixing in the gas phase. While, on the other hand, the enhanced inter-phase transports and better mixing of fuel vapor in the ambience makes the gas phase more homogeneous and brings about a slight decrease in the value of $\dot{I}_g$ due to gas phase transport processes. In case of lower volatile fuels, larger penetration of fuel droplets, beyond the primary zone with an increase in SMD$_i$ reduces the rate of inter-phase transport processes and hence in the value of $\dot{I}_d$. An increase in the value of $\dot{I}_g$ takes place accordingly.

Conclusion

A comparative study on the variations in combustion efficiency and second law efficiency along with the various components of exergy losses of a spray combustion process in a gas turbine combustor has been made for fuels with different volatilities at different operating conditions to throw light on the trade off between the effectiveness of combustion and the lost work due to thermodynamic irreversibilities in the process of combustion. The major observations are as follows:

An increase in fuel volatility increases combustion efficiency only at a higher pressure for any given inlet temperature and swirl. The combustion efficiency is uninfluenced by the inlet swirl at its lower pressure, while it decreases with an increases in inlet swirl when the pressure of inlet air is high. The second law efficiency increases with a decrease in fuel volatility and an increase in combustor pressure. At a higher combustor pressure, an increase in inlet air swirl decreases both the combustion efficiency and second law efficiency.

When the spray cone angle is increased, the combustion efficiency increases drastically for a lower volatile fuel, followed by a marginal decrease, while for a higher volatile fuel, the influence of spray cone angle on combustion efficiency is relatively marginal. The second law efficiency decreases with an increase in spray cone angle for all the fuels considered.

The combustion efficiency increases with an increase in initial SMD of fuel spray up to a value of 50 μm, but a further increase in initial SMD causes a decrease in combustion efficiency. The second law efficiency shows a monotonic decreasing trend with initial SMD.

The optimum design of the combustor is based on a trade off between η_c and η_{II} for an overall energy economy. The relative weightage of η_c and η_{II} to be assigned in the process of optimization depends on the relative saving in the cost of energy quantity over the energy quality for a specific application. This is a task of energy management in practice where the information provided by the present paper will serve as the fundamental inputs.

Nomenclature

$\dot{A}$ = rate of flow availability
A_s = slot area of secondary air inlet
A_d = slot area of dilution air inlet
a = specific flow availability
b = size parameter of Rosin-Rammler function
c_p = specific heat at constant pressure
C_{fs} = mean fuel vapor mass fraction at the droplet surface
C_j = mean mass fraction of j^{th} species
d = droplet diameter
d_i = droplet diameter of i^{th} class of droplet

$d_{\min i}$ = minimum diameter of i^{th} droplet class
$d_{\max i}$ = maximum diameter of i^{th} droplet class
D = combustor diameter
D_{eff} = effective mass diffusivity
$\dot{E}$ = entropy generation rate
h = enthalpy of formation
$\bar{h}$ = molar enthalpy
Δh_f = enthalpy of formation
$\Delta \bar{h}_f$ = molar enthalpy of formation
I = rate of Irreversibilities
$I_b(T)$ = black body radiation intensity at a temperature, T
M = molecular weight
m = mass
$\dot{m}_{f_t}$ = rate of fuel injection
Nu = Nusselt number
p = pressure
Pr = Prandtl number
q_i^r = radiative heat flux in x_i direction
R = radius of the combustor
Re = Reynolds number
r = radial location
s = entropy
$\bar{s}$ = molar entropy
S = Swirl number
$\acute{S}$ = gas phase mass source term due to droplets
Sc = Schmidt Number
Sh = Sherwood Number
$\acute{S}_C$ = gas phase species conservation equation source term
$\acute{S}_E$ = gas phase energy conservation equation source term due to evaporation and combustion of liquid droplets.
$\acute{S}_M$ = gas phase momentum source term due to momentum exchange with the droplets
SMD = Sauter Mean Diameter
t = time
T = mean temperature
U_i = mean velocity in x_i direction
U_z = mean axial velocity
x = mole fraction
V_i = velocity in x_i direction
y = molar concentration of species
z = axial location

Greek Letters

α_{eff} = effective thermal diffusivity
μ_{eff} = effective viscosity
μ_t = eddy viscosity
ρ = gas phase density
ψ = spray cone angle
λ = stoichiometric coefficient

Subscripts

i = initial/index of tensor notation
j = index of tensor notation
in = inlet
e = exit
f, F = fuel
P = product
r = reference quantitity

Superscripts

d = droplet phase
f = fuel
g = gas phase

References

[1] Faeth, G. M., 1983, ''Evaporation and Combustion of Sprays,'' Prog. Energy Combust. Sci., **9**, pp. 1–76.
[2] Faeth, G. M., 1987, ''Mixing, Transport and Combustion in Sprays,'' Prog. Energy Combust. Sci., **13**, pp. 293.
[3] Sirignano, W. A., 1983, ''Fuel Droplet Vaporization and Spray Combustion Theory,'' Prog. Energy Combust. Sci., **9**, pp. 291.
[4] Sirignano, W. A., 1986, ''The Formulation of Spray Combustion Models: Resolutions Compared to Droplet Spacing,'' ASME J. Heat Transfer , **108**, pp. 633.
[5] Sirignano, W. A., 1988, ''An Integrated Approach to Spray Combustion Model Development,'' Combust. Sci. Technol., **58**, pp. 231.
[6] Dash, S. K., Sengupta, S. P., and Som, S. K., 1991, ''Transport Processes and Associated Irreversibilities in Droplet Evaporation,'' Am. Inst. Aeronaut. Astronaut. J. Thermo Physics and heat Transfer, **5**(3), pp. 366–371.
[7] Dash, S. K., and Som, S. K., 1991, ''Transport Processes and Associated Irreversibilities in Droplet Combustion in a Convective Medium,'' Int. J. Energy Res., **15**, pp. 603.
[8] Puri, I. K., 1992, ''Second Law Analysis of Convective Droplet Burning,'' Int. J. Heat Mass Transf., **35**, pp. 2571.
[9] Hiwase, S. D., Datta, A., and Som, S. K., 1998, ''Entropy Balance and Exergy Analysis in the Process of Droplet Combustion,'' J. Phys. D, **31**, pp. 1601.
[10] Dash, S. K., and Som, S. K., 1993, ''Thermodynamics of Spray Evaporation,'' J. Phys. D, **26**, pp. 574.
[11] Dunbar, W. R., and Lior, N., 1994, ''Sources of Combustion Irreversibility,'' Combust. Sci. Technol., **103**, pp. 41.
[12] Westbrook, C. K., and Dryer, F. L., 1981, ''Simplified Reaction Mechanisms for the Oxidation of Hydrocarbon Fuels in Flames,'' Combust. Sci. Technol., **27**, pp. 31–45.
[13] Magnussen, B. F., Hjertager, B. H., 1977, ''On Mathematical Modeling of Turbulent Combustion With Special Emphasis on Soot Formation and Combustion,'' *Sixteenth Symposium (International) on Combustion*, The Combustion Institute, pp. 719–727.
[14] Ozisik, M. N., 1973, *Radiative Heat Transfer*, Wiley, New York.
[15] Sparrow, E. M., Cess, R. D., 1978, *Radiation Heat Transfer*, Hemisphere, Washington DC.
[16] Clift, R., Grace, J. R., and Weber, M. E., 1978, *Bubbles, Drops and Particles*, Academic Press, New York.
[17] Ranz, W. E., and Marshall, W. R., Jr., 1952, ''Evaporation From Drops: Part II,'' Chem. Eng. Prog., **48**, pp. 173–180.
[18] Mugele, R. A., and Evans, H. D., 1951, ''Droplet Size Distribution in Sprays,'' Ind. Eng. Chem., **43**, 1317–1324.
[19] Hirt, C. W., and Cook, J. L., 1972, ''Calculating Three Dimensional Flows Around Structures and over Rough Terrain,'' J. Comput. Phys., **10**, pp. 324–341.
[20] Harlow, F. H., and Welch, J. E., 1965, ''Numerical Computation of Time Dependent Viscous Incompressible Flow of Fluid with a Free Surface,'' Phys. Fluids, **8**(12), pp. 2182–2190.
[21] Cameron, C. D., Brouwer, J., Wood, C. P., and Samuelson, G. S., 1989, ''A Detailed Characterization of Velocity and Thermal Fields in a Model Can Combustor With Wall Jet Injection,'' ASME J. Eng. Gas Turbines Power, **3**, pp. 31–40.
[22] Chang, K. C., and Chen, C. S., 1993, ''Development of a Hybrid k-ε Turbulence Model for Swirling Recirculating Flows Under Moderate to Strong Swirl Intensities,'' Int. J. Numer. Methods Fluids, **16**, pp. 421.
[23] Dallenback, P. A., 1986, ''Heat Transfer and Velocity Measurements in Turbulent Swirling Flow Through an Abrupt Axi-symmetric Expansion,'' Ph.D thesis, Arizona State University, Tempe, A2.
[24] Khalil, K. H., El Mahallawy, F. M., and Moneib, H. A., 1977, ''Effect of Combustion Air Swirl on the Flow Pattern in a Cylindrical Oil Fired Furnace,'' *Sixteenth Symposium (International) on Combustion*, The Combustion Institute., pp. 135–141.
[25] Moran, M. J., and Shapiro, H. N., 1988, *Fundamentals of Engineering Thermodynamics*, John Wiley, New York.
[26] Hirschfelder, J. C., Curtiss, C. F., and Bird, R. B., 1954, *Molecular Theory of Gases and Liquids*, John Wiley, New York.

Hong-Shun Li

Gilles Flamant
e-mail: gilles.flamant@imp.cnrs.fr

Institut de Science et de Génie des Matériaux
et Procédés,
IMP-CNRS, BP 5-Odeillo,
66125 Font-Romeau Cédex,France

Ji-Dong Lu
National Laboratory of Coal Combustion,
Huazhong University of Science & Technology,
Wuhan 430074, P.R. China

Reduction of False Scattering of the Discrete Ordinates Method

A novel method, the Double Rays Method (DRM), is proposed to capture the discontinuous nature of the radiation intensity, in order to reduce false scattering of the discrete ordinates method (DOM). Numerical tests demonstrate that the DRM successfully removes false scattering in all the two-dimensional test problems discussed in this paper. The effect of false scattering on the computational results in two-dimensional situations is investigated with the DRM. False scattering plays a double role: when the boundary emits radiation in a limited number of directions, or when the irradiation comes from a limited number of directions, it produces a smeared intensity field and radiative heat flux distribution, and thus must be removed. In the case of diffuse boundary, however, false scattering plays a useful role and thus should be retained. [DOI: 10.1115/1.1495518]

Keywords: *Heat Transfer, Modeling, Numerical Methods, Radiation, Scattering*

1 Introduction

In the last two decades, the discrete ordinates method (DOM) has become more and more popular in radiative heat transfer computations because it has several desirable features: easy coding, computational economy, good accuracy, flexible marching procedures, etc. Up to now, the DOM has been successfully applied to various radiation problems, such as radiation transfer in Cartesian, cylindrical, and spherical coordinates, curvilinear system, complex or irregular geometry, combined heat transfer, and non-gray problems, to name but a few. The efficiency of the DOM is constantly improved; new methods for selecting the discrete ordinate quadratures [1–7] and for solving radiation transfer equations [8–15] have been proposed. Another kind of DOM, the finite-volume method [16,17], was also proposed and has found wide applications.

The DOM, however, still has two shortcomings: ray effect and false scattering [18]. To eliminate ray effect, Ramankutty and Crosbie [19] used a modified differential approximation, in which the radiation intensity is divided into two parts. For the same purpose, more recently, Baek et al. [20] used a combined Monte-Carlo and Finite-Volume Method. However, as discussed by Thynell [21], false scattering is much more difficult to handle, and additional approaches for eliminating false scattering should be developed. Pessoa-Filho and Thynell [10] proposed an approximate technique to eliminate false scattering, but this method is different from the standard DOM. The differencing scheme in Ref. [8] and the hybrid scheme in Ref. [15] can also partially reduce false scattering. To our knowledge, since Chai et al. [18] first presented a detailed analysis on ray effect and false scattering associated with the DOM, there has been no report of successful removal of such false scattering. The purpose of this study is to propose a new method, the Double Rays Method (DRM), to capture the discontinuous nature of the radiation intensity field, in order to remove or minimize false scattering. Then the DRM is used to investigate how false scattering influences the computational results.

2 Reduction of False Scattering

As analyzed by Chai et al. [18], false scattering occurs once the spatial discretization is performed over domains where the intensity is discontinuous. Thus, to eliminate false scattering, one should consider the discontinuous nature of the radiation intensity field. Several scholars employed the Fredholm integral form of the equation of transfer [22,23] for this purpose. Unfortunately, as analyzed in Refs. [10] and [21], the discontinuity cannot be completely eliminated by this equation. Since its solution often requires an evaluation of a singular kernel, hence, false scattering may occur. The purpose of this section is just to define a method that can effectively handle discontinuous boundary conditions. In addition, as concerns the spatial integration of the RTE, false scattering cannot be eliminated by the cell-averaged schemes (namely, the diamond and step schemes, etc.) [18,24], and thus other methods must be found. In this work, the discrete ordinate interpolation method (DOIM) [9] is used, even though the DOIM still suffers from false scattering due to its unsuitable treatment of the discontinuous intensity field.

2.1 Basic Idea of the DRM: Improved Treatment of Discontinuous Boundary Conditions.

For ease of presentation, let us begin the analysis from the example problem 2 in Ref. [18]: consider a square enclosure with four black walls and a non-participating medium. The bottom half of the left wall is hot, and its top half and the other three walls are cold. The objective of this test is to compute the radiation distribution for the radiation component, which is at an angle $\theta=60$ deg to the grid lines, and parallel to the x-y plane, as shown in Fig. 1. The shadowing region is the region with an intensity of unity, and the intensity is zero in the rest of the enclosure. Let us consider the computation of the intensity at point D, I_{D}. As shown in Fig. 1, this beam comes from point B, which is located between two nodal points A and C. According to the DOIM [9], to compute I_{D} it is necessary to determine the intensity at its upstream point B, I_{B}. This intensity can be obtained with linear interpolation between nodal points A and C [9]:

$$I_{\mathrm{B}}=I_{\mathrm{A}}+\frac{x_{\mathrm{B}}-x_{\mathrm{A}}}{x_{\mathrm{C}}-x_{\mathrm{A}}}(I_{\mathrm{C}}-I_{\mathrm{A}}) \tag{1}$$

The intensity at point C, I_{C}, is already known ($I_{\mathrm{C}}=0$), the remaining problem is to determine I_{A}. If the real boundary condition is $I_{\mathrm{A}}=0$, then, $I_{\mathrm{B}}=0$. Since the medium is transparent, then $I_{\mathrm{D}}=I_{B}=0$. This is identical with the physically real distribution (as in Fig. 1, I_{D} is equal to zero). However, if the real boundary condition is $I_{\mathrm{A}}=1$, and Eq. (1) is still used to calculate I_{B}, then, obviously, I_{B} is not equal to zero, and thus I_{D} is not equal to zero either. As a result, false scattering occurs.

In a similar test problem in Ref. [9], Cheong and Song assumed that $I_{\mathrm{A}}=0.5$ (i.e., average value of unity and zero), but this still resulted in false scattering [9]. Note that 0.5 is correct: if a min-

---

Contributed by the Heat Transfer Division for publication in the JOURNAL OF HEAT TRANSFER. Manuscript received by the Heat Transfer Division October 6, 2000; revision received May 9, 2002. Associate Editor: A. Majumdar.

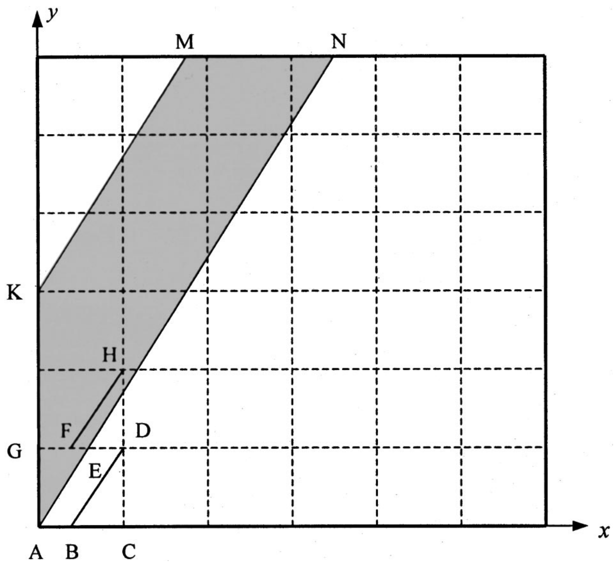

Fig. 1 Test problem and the method for interpolation

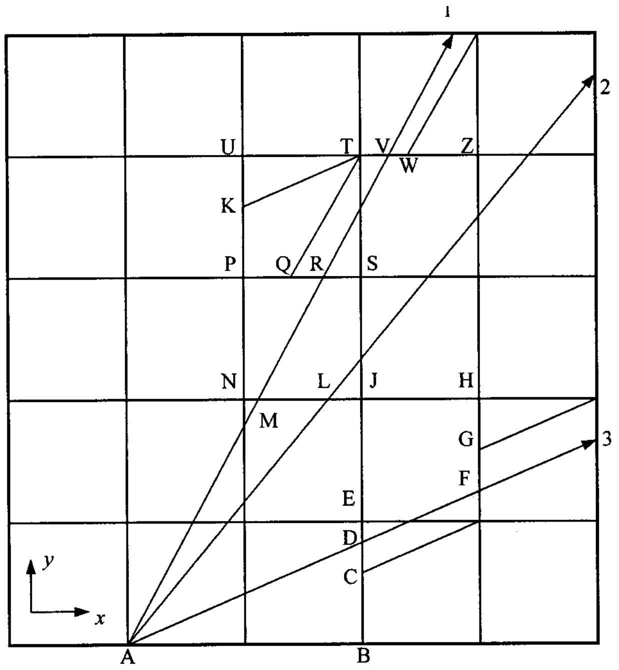

Fig. 2 The double rays method

iature radiometer is put at a position close to point A and on the direct line A-E (actually, it is a plane) to measure the intensity at point A, within the "pencil" solid angle that the radiometer receives, half is filled with the radiation with the intensity of unity, and the other half is zero; as a result, the "measured value" is 0.5. However, keep in mind that Eq. (1) can give a prediction of second order precision only in a continuously changing intensity field. If the variation of the intensity is non-continuous, Eq. (1) may produce serious error. If $I_A = 1$, the intensity field has a step change at point A: at point (0,0), the intensity is equal to unity, but at point $(0^+,0)$ (here "0^+" means a positive infinitesimal, as in the following), it becomes zero. Thus, if Eq. (1) is still used to calculate I_B, it will produce an incorrect result; consequently, false scattering occurs.

Based on the above analyses, the basic idea of the DRM is to conduct the interpolation between point $(0^+,0)$ and point C, since the intensity is continuous in this region, namely

$$I_B = I_{\mathrm{Aright}} + \frac{x_B - x_A}{x_C - x_A}(I_C - I_{\mathrm{Aright}}) \tag{2}$$

where I_{Aright} is the intensity at point $(x_A + 0, y_A)$, i.e., at point $(0^+,0)$. In this way, no matter how much the intensity at point (0,0) is, I_B is always equal to zero; thus $I_D = I_B = 0$. This is identical with the physically real solution. Similarly, to calculate I_H, it is necessary to determine I_F. The interpolation is conducted between point G and point $(x_E - 0, y_E)$ (here "+/−0" means to add/subtract an infinitesimal, as in the following), instead of between points G and D, because the intensity is non-continuous in the region between points G and D. Namely

$$I_F = I_G + \frac{x_F - x_G}{x_E - x_G}(I_{\mathrm{Eleft}} - I_G) \tag{3}$$

where I_{Eleft} is the intensity at point $(x_E - 0, y_E)$, as in Fig. 1. It is equal to unity, since the medium is non-participating. Thus $I_F = 1$, and $I_H = I_F = 1$, also the physically real solutions. Following the above method, one node by one node, all the intensities can be calculated. The final computational result is identical with the physically real distribution, without any false scattering occurring.

Now the above principle is applied to the example problem 1 in Ref. [18]. The situation is the same as the example problem in Fig. 1, but the radiation direction is normal to the left wall. In Fig. 4 of Ref. [18], it is shown that the diamond scheme produces overshoot and negative intensities. Here, the diamond scheme is used, but note that the intensity field has a step change at $y = 0$ and $y = 3\Delta y$. Namely, the intensity is zero at $y = 0$, and unity at $y = 0^+$; it is unity at $y = 3\Delta y$, and zero at $y = 3\Delta y + 0$. Thus, when the diamond spatial differencing scheme is used to extrapolate the boundary intensity at $y = \Delta y$, then the intensity at $y = 0^+$, instead of at $y = 0$, should be employed. Similarly, the same treatment is applied to all nodes at $y = 3\Delta y$ to extrapolate the boundary intensity at $y = 4\Delta y$. In this way, the final result obtained with the diamond scheme is also identical with the physically real solution: no overshoot, no negative intensity (since it is very easy to understand the above analysis, this result is not shown here for brevity, the reader may refer to Fig. 4(a) in Ref. [18] for details).

2.2 General Situations: The Double Rays Method (DRM).

In the above two example problems, there is only one discrete direction, and the medium is non-participating. A general situation in a two-dimensional rectangular enclosure (participating medium, more discrete directions than one) is shown in Fig. 2. For illustrative purposes, we assume there is only one discontinuous boundary point, A, namely, the boundary condition has a step change at point A. The straight lines, A-1, A-2, and A-3, are the projection on x-y plane of the discrete directions in the first octant emitting from point A (only three directions are shown for illustrative purpose; note that the discrete directions in the fifth octant coincide with the above straight lines because of the symmetry in z-direction). Each straight-line represents two rays (the present method is named the Double Rays Method for this reason), i.e., one ray starts from point $(x_A - 0, y_A)$, while the other one starts from point $(x_A + 0, y_A)$. For example, the straight-line A-1 represents the following two rays (projection on the x-y plane): the first one starts from point $(x_A - 0, y_A)$, passes points $(x_M - 0, y_M)$, $(x_R - 0, y_R)$, $(x_V - 0, y_V)$ in sequence, and reaches point $(x_1 - 0, y_1)$. For ease of reference, this ray is hereafter labeled Ray *A-1a*. Meanwhile, the second ray starts from $(x_A + 0, y_A)$, passes points $(x_M + 0, y_M)$, $(x_R + 0, y_R)$, $(x_V + 0, y_V)$ in sequence, and reaches point $(x_1 + 0, y_1)$. Hereafter, this ray is labeled Ray *A-1b*. The purpose of the double rays is to capture the discontinuous nature of the radiation intensity field, which is due to the discontinuous boundary at point A and to the discretization of the angular variable of the DOM. Note that the discrete direction in the second octant emitting from point A are not shown in Fig. 2 for clarity, but they are treated in the same way.

How does the DRM capture the discontinuous nature of the intensity field? Let us take the above Rays *A-1a* and *A-1b* as an example. They start from points $(x_A - 0, y_A)$ and $(x_A + 0, y_A)$, respectively. Since point A is a discontinuous boundary point, then $I_{1\mathrm{Rleft}} \neq I_{1\mathrm{Rright}}$ ($I_{1\mathrm{Aleft}}$ and $I_{1\mathrm{Aright}}$ are the intensities in A-1 direction at point $(x_A - 0, y_A)$ and $(x_A - 0, y_A)$, respectively; the rest may be inferred by analogy). Thus, at any position on Ray *A-1a*, say at point $(x_R - 0, y_R)$, the intensity in A-1 direction is not equal to the corresponding intensity at its "twin" point $(x_R + 0, y_R)$, i.e., $I_{1\mathrm{Rleft}} \neq I_{1\mathrm{Rright}}$. By this way is recorded the step change of the radiation intensity across the straight A-1. Meanwhile, the region in which an interpolation is conducted is always limited at one side of the straight line A-1; for example, the Eq. (5) in the following. In this way, the discontinuous nature of the radiation intensity in the discrete direction A-1 that is due to the discontinuous boundary point A is respected.

Attention is now focused on the procedure for solving the radiation transfer equations. To solve the discrete transfer equations, an iterative procedure must be used. As aforementioned, in the present work, the DOIM [9] is still used to solve the equations. Thus, all the procedures, such as the marching direction of the iteration, and so on, are the same as the DOIM [9] except for two differences. The first one is that the regions of linear interpolation may be different from the DOIM: in the DOIM the region of interpolation is always between two nodal points, whereas in the present work, the region of interpolation is subject to the DRM. The second difference is that in the DOIM, the discontinuous nature of the radiation across the straight lines A-1, A-2, and A-3 is not considered, whereas in the present work it is considered. Moreover, the intensities on all the double rays, such as Rays *A-1a* and *A-1b* mentioned above, will be computed with iteration. For the sake of brevity, in the following analyses, only these two differences are analyzed in details; the reader may refer to [9] for details about the DOIM.

Consider the first difference mentioned above. For example, to use the DOIM to predict the intensity in A-1 direction at point T in Fig. 2, I_{1T}, it is necessary to calculate the intensity at its upstream point Q, I_{1Q}, with the interpolation. According to the DOIM [9], the linear interpolation is conducted between nodal points P and S

$$I_{1Q} = I_{1P} + \frac{x_Q - x_P}{x_S - x_P}(I_{1S} - I_{1P}) \tag{4}$$

Then, I_{1T} is determined with the exponential scheme [9]. However, since the intensity is discontinuous in the region between nodal points P and S (the radiation intensity distribution experiences a step change at point R), the above interpolation will result in false scattering. Thus in the DRM, the region of interpolation is changed to be between points $(x_R - 0, y_R)$ and P, as listed in Table 1,

$$I_{1Q} = I_{1P} + \frac{x_Q - x_P}{x_R - x_P}(I_{1\mathrm{Rleft}} - I_{1P}) \tag{5}$$

where $I_{1\mathrm{Rleft}}$ is the intensity in A-1 direction at point $(x_R - 0, y_R)$. However, note that if there is not a discontinuous change in radiation intensity between the two nodal points, then the interpolation is still conducted between them. For example

$$I_{3K} = I_{3P} + \frac{y_K - y_P}{y_U - y_P}(I_{3U} - I_{3P}) \tag{6}$$

Since the intensity in A-3 direction is continuously changing between points P and U (as in Fig. 2, the straight line A-3 does not pass through this region).

In the above Eq. (5), obviously, before I_{1Q} is predicted, one must know the intensity at points $(x_R - 0, y_R)$, $I_{1\mathrm{Rleft}}$. Unfortunately, since the medium is participating, this intensity is unknown, and thus it is necessary to determine it with iteration. This leads to the aforementioned second difference between the DOIM [9] and the present work. Concerning this difference, the most important question is how to compute the intensities on the double rays the straight lines A-1, A-2, and A-3 stand for.

Table 1 Method for the interpolation in Fig. 2

Position	Intensity	region of interpolation
C	$I_{1C}{}^{*}, I_{2C}$	(x_B, y_B) — (x_E, y_E)
C	I_{3C}	(x_B, y_B) — $(x_D, y_D\ \text{-}0)$
G	I_{3G}	$(x_F, y_F + 0)$ — (x_H, y_H)
M	I_{2M}	(x_N, y_N) — $(x_L\text{-}0, y_L)$
M	I_{3M}	(x_N, y_N) — (x_J, y_J)
L	I_{1L}	$(x_M + 0, y_M)$ — (x_J, y_J)
L	I_{3L}	(x_N, y_N) — (x_J, y_J)
Q	I_{1Q}	(x_P, y_P) — $(x_R\text{-}0, y_R)$
W	I_{1W}	$(x_V + 0, y_V)$ — (x_Z, y_Z)

* subscript 1 stands for the intensity in the discrete directions A-1, subscript C means at point C. The rest may be inferred by analogy.

The general iterative procedures are the following (take the two rays the straight line A-1 represents as the example). First, to predict the intensities at the points on the aforementioned Ray *A-1a*, the iterative direction is along its propagating direction: from point A to point 1. For example, to predict the intensity in the A-1 direction at point $(x_R - 0, y_R)$, one must compute the intensities for all the discrete directions at point $(x_R - 0, y_R)$ and its upstream point $(x_M - 0, y_M)$. At the upstream point, the intensity in the A-1 direction has already been predicted; consequently, the interpolation is unnecessary. The radiation intensity in A-2 direction experiences a step change at point L, thus the linear interpolation is conducted between points $(x_L - 0, y_L)$ and N, as listed in Table 1, namely:

$$I_{2M} = I_{2\mathrm{Mright}} = I_{2\mathrm{Mleft}} = I_{2N} + \frac{x_M - x_N}{x_L - x_N}(I_{2\mathrm{Lleft}} - I_{2N}) \tag{7}$$

However, the radiation intensity in A-3 direction is continuously changing between nodal points N and J, thus the linear interpolation is conducted between them

$$I_{3M} = I_{3\mathrm{Mright}} = I_{3\mathrm{Mleft}} = I_{3N} + \frac{x_M - x_N}{x_J - x_N}(I_J - I_{3N}) \tag{8}$$

The intensities in the discrete directions in the second, third, and fourth octants at point $(x_M - 0, y_M)$ are obtained with the linear interpolation similar to Eq. (8).

Similarly, the intensities in all other discrete directions at point $(x_R - 0, y_R)$ can also be obtained with linear interpolation between points P and S. Then the intensity in A-1 direction at point $(x_R - 0, y_R)$ can be predicted with the exponential scheme

$$I_{1R} = I_{1M}\exp(-\beta_{av}\Delta s) + S_{av}/\beta_{av}[1 - \exp(-\beta_{av}\Delta s)] \tag{9}$$

$$\Delta s=(y_R-y_M)/\eta_1 \tag{10}$$

where β_{av} and S_{av} are the average values of the corresponding parameters at points M and R, and the latter is determined using Eq. (11) introduced in the following. In this way, one points by one point one can predict the intensity in the A-1 direction at all the points on the Ray *A-1a*.

Then, the same procedures are repeated to predict the intensities in A-1 direction at all the points on Ray *A-1b*. But note that each point on Ray *A-1b* shares the same intensities in all the discrete directions except for A-1 direction with its "twin" point on Ray *A-1a*, and they also share the same incident radiation and source function. For example, the point (x_R+0,y_R) on Ray *A*-1*b* and its "twin" point (x_R-0,y_R) on Ray *A-1a* share the same incident radiation and source function for A-1 direction:

$$G=2w_1(I_{1\mathrm{Rleft}}+I_{1\mathrm{Rright}})/2+\sum_{i=2,n}2w_iI_{1\mathrm{Rleft}} \tag{11}$$

$$S_1=\kappa I_{bR}+(\sigma_s/4\pi)\left[2\Phi_1w_1(I_{1\mathrm{Rleft}}+I_{1\mathrm{Rright}})/2+\sum_{i=2,n}2\Phi_iw_iI_{1\mathrm{Rleft}}\right] \tag{12}$$

Note that, for the situation in Fig. 2.

$$I_{i\mathrm{Rleft}}=I_{i\mathrm{Rright}}\quad(i=2,n) \tag{13}$$

where w_i is the weight of the discrete direction A-*i*, and n is the total number of the discrete directions in the first to fourth octants (note the symmetry of two-dimensional problems). It is easy to understand the above Eqs. (11)–(13) by recalling the discussion in subsection 2.1.

Then the same procedures are repeated to predict the intensities on all other double rays emitting from point A (in all other discrete directions in the first and second octants). After all these intensities on the double rays are predicted, the above interpolating method (some typical regions of interpolation are listed in Table 1) is used to predict the nodal intensities in all the discrete directions, and the iterative procedures are the same as the DOIM [9]. Then the above procedures are repeated again and again until the iteration precision is satisfied. Finally, the discontinuous changes in heat flux at points 1, 2, and 3 can also be computed, whereas the DOIM [9] cannot provide these data.

2.3 Accuracy of the DRM. Since the DRM uses a linear interpolation, and the linear DOM is also a scheme of second order precision [9], thus the numerical precision of the DRM is of second order too.

3 Results

Two cases are solved and compared with physically exact solutions: participating medium and non-participating medium, in order to test the DRM. Before beginning the discussion, note the difference between "NUMERICALLY exact solution of the discrete ordinate equations" and "PHYSICALLY exact solution." The former is the exact solution satisfying the discrete ordinate equations, while the latter is the real solution of the physical problem. Obviously, the former may not be equal to the latter, since the discrete ordinate equations are merely the discrete representation of the continuous directional variation of the radiation intensity.

3.1 Non-Participating Medium and Diffuse Boundaries (Test Problem 3). Here, the example problem 3 in Ref. [18] is chosen, since it is a very illustrative one. Consider a two-dimensional rectangular enclosure with three black walls and non-participating medium, the top and bottom walls' length is six, and the two sidewalls' length is three. A section of the top wall is hot (from $x=5$ to $x=6$), while the rest of the top wall and the other three walls are cold. The objective of this problem is to compute the *y*-direction dimensionless heat flux distribution on the bottom wall. In the following analyses, only LSO S_2- and S_4-approximations are employed, because it is easy to know the numerically exact solutions of the discrete ordinate equations of these two quadrature sets (needless to day, these exact solutions are free of false scattering). For S_2 set, the numerically exact solution is that the heat flux is zero everywhere except for the region between $x=2$ to $x=3$ where it is equal to 0.5; this is due to the discrete direction of $\xi=\eta=-0.5$ [18]. To facilitate the presentation, the direction cosines of LSO S_4 are listed in Table 2. The numerically exact solution of the S_4 set will also be equal to zero everywhere except for three regions, i.e., $x=(2,3)$, (4.0277, 5.0277), (5.9773, 6), in which the heat flux is equal to 0.09863, 0.30275, and 0.30275, respectively. This is due to the three discrete directions coming from the hot section, namely, the first and second directions in the third octant (see Table 2), and the second direction in the fourth octant (ξ=0.2958759, η=−0.9082483).

Table 2 Discrete ordinates for LSO S_4-approximation

direction	ξ	η	μ	w
1	0.2958759	0.2958759	0.9082483	$\pi/6$
2	0.2958759	0.9082483	0.2958759	$\pi/6$
3	0.9082483	0.2958759	0.2958759	$\pi/6$

Figure 3 illustrates the heat flux distributions on the bottom wall obtained with the DRM. To facilitate the comparison, solutions obtained with the step scheme by a 26×26 points grid are also illustrated in the figure. As shown in Fig. 3, the solutions obtained with the DRM using S_2 and S_4-approximations are identical with the numerically exact solutions of the discrete ordinate equations in the above paragraph (the numerically exact solution for S_2-approximation is not shown in the figure for clarity). On the contrary, the solution using the step scheme exhibits a continuous heat flux distribution due to false scattering. However, the physically exact solution is a continuous distribution without any bump. Thus, from this standpoint, false scattering is helpful to remedying ray effect; of course, this does not mean that ray effect is eliminated, as pointed out in Ref. [18]. In fact, obviously, the physically exact solution should exhibit the maximum heat flux at $x=5.5$ (not shown in Fig. 3 for clarity). Yet, the above two solutions with S_2 and S_4-approximations and the step scheme do not

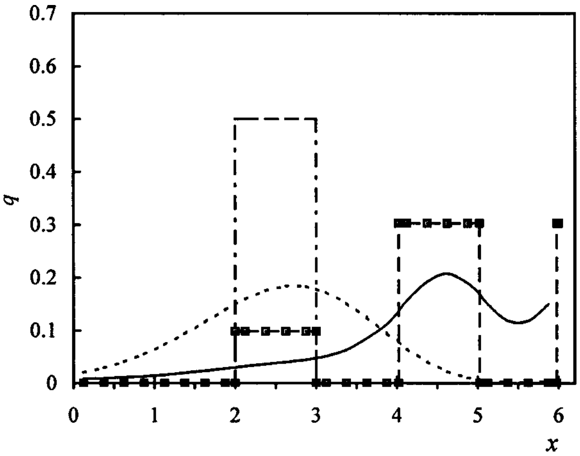

Fig. 3 Dimensionless heat flux distribution on the bottom wall for the example problem 3 in Ref. [18], obtained with ——— LSO S_2 and the step scheme, — LSO S_4 and the step scheme, — – LSO S_2 and the DRM, – – LSO S_4 and the DRM, ■ numerically exact solution of the discrete ordinate equations of LSO S_4

Table 3 Dimensionless heat flux on the top wall for test problem 4 obtained with the DRM

Position, x	physically exact solution [22]*	this work, with S_4	this work, with S_8
0.0	0.893	0.8869	0.8860
0.1	0.827	0.8233	0.8230
0.2	0.796	0.7886	0.7920
0.3	0.777	0.7670	0.7748
0.4	0.767	0.7563	0.7656
0.5	0.764	0.7531	0.7626
0.6	0.767	0.7563	0.7656
0.7	0.777	0.7670	0.7748
0.8	0.796	0.7886	0.7920
0.9	0.827	0.8233	0.8230
1.0	0.893	0.8869	0.8860

* By linear interpolation to corresponding x

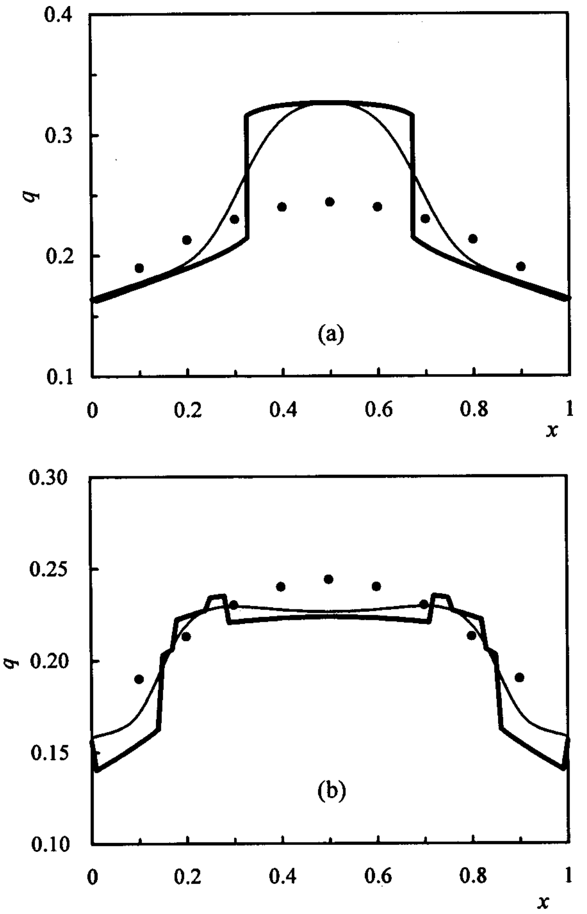

Fig. 4 Dimensionless heat flux distribution on the top wall for test problem 4: (*a*) using LSO S_4 approximation and 101×101 grid points; and (*b*) using LSO S_8 approximation and 101×101 grid points. ▬ obtained with the DRM, — obtained with the step scheme, ● physically exact solution [22]

predict this result; in fact the solution obtained with the S_4-approximation and the step scheme displays a dip at about $x = 5.5$.

If one uses the example problem 4 in Ref. [18] to further test the DRM, the results are also identical with the numerically exact solutions of the discrete ordinate equations. These results prove that, in the case of non-participating medium, the DRM can thoroughly remove false scattering.

3.2 Participating Medium and Diffuse Boundary (Test Problem 4). Consider a purely scattering uniform medium in a two-dimensional black square enclosure, the bottom wall is hot while the other three are cold, the lengths of the walls are one, and the scattering coefficient of the medium is unity; hereafter, this problem is referred to as test problem 4. This particular case is selected because the physically exact solution is available in the literature, for example, Ref. [22]. It has also been used as a benchmark by many researchers [1,2,4,10,19].

First, the dimensionless heat flux distributions on the bottom wall predicted with the DRM using LSO S_4 and S_8-approximations and a 101×101 points grid are compared with the physically exact solution [22], see Table 3. The iterative precision of these results is 1.0×10^{-15} (using the double precision of FORTRAN code, as for all the following results) and the corresponding iterative numbers are 23 and 24 times for LSO S_4 and S_8-approximations respectively. As listed in Table 3, with an increment of the order of S_N-approximation, the predicted heat flux approaches the physically exact solution. The highest relative error of the results with S_8-approximation is 0.78 percent (at $x = 0.0$ and $x = 1.0$, i.e., the two discontinuous boundary points). This good agreement confirms the numerical precision of the DRM.

In this test problem, predicting the heat flux distribution on the top wall is a severe test. Figure 4 shows the dimensionless heat flux distribution obtained with the DRM using LSO S_4 and S_8-approximations, as well as the results obtained with the step scheme. Figure 5 illustrates the corresponding dimensionless heat flux in y-direction along the centerline normal to the bottom wall.

In Fig. 4(*a*) the solution using the DRM and S_4-approximation exhibits a sharp rise or drop of 0.1006737 at $x = 0.32577$ and $x = 0.67423$, respectively. Ray tracing analysis reveals that these sharp changes are due to ray effect. As shown in Fig. 6, the boundary has a step change at points A and B. The sharp rise in heat flux at $x = 0.32577$ on the top wall is due to radiation beam A-2, whose direction cosines (ξ_2, η_2, μ_2) are equal to (0.2958759, 0.9082483, 0.2958759), i.e., the second discrete direction in Table 2. The sharp drop at $x = 0.67423$ is due to radiation beam B-5, whose direction cosines (ξ_2, η_2, μ_2) are equal to (0.2958759, 0.9082483, 0.2958759). In fact, the intensity can be divided into two parts [19], namely

$$I_i = I_{wi} + I_{mi} \tag{14}$$

Here subscript "i" stands for the ith discrete direction, I_{wi} is the direct intensity component due to the emission and reflection at the walls, and I_{mi} is the intensity due to the contribution of the medium by emission of scattering. Consider the radiation beam A-2: it reaches point 2 on the top wall after traveling an optical path of $1/\eta_2$ (note that the medium is uniform). Thus when it reaches the top wall, its direct intensity component becomes

$$I_{w2} = I_0 \exp(-1/\eta_2) \tag{15}$$

with

$$I_0 = \sigma T_1^4/\pi \tag{16}$$

here T_1 is the temperature of the bottom wall. I_{w2} contributes to the y-direction dimensionless heat flux on the top wall:

$$\begin{aligned} q_{w2} &= w_2 \eta_2 I_{w2}/(\sigma T_1^4) = (\pi/3)\cdot 0.9082483 \cdot I_0 \\ &\quad \cdot \exp(-1.0/0.9082483)/(\sigma T_1^4) = 0.1006737 \end{aligned} \tag{17}$$

As a result, this produces a sharp rise of 0.1006737 in the dimensionless heat flux at point 2 ($x_2 = 0.32577$, $y_2 = 1$) on the top wall.

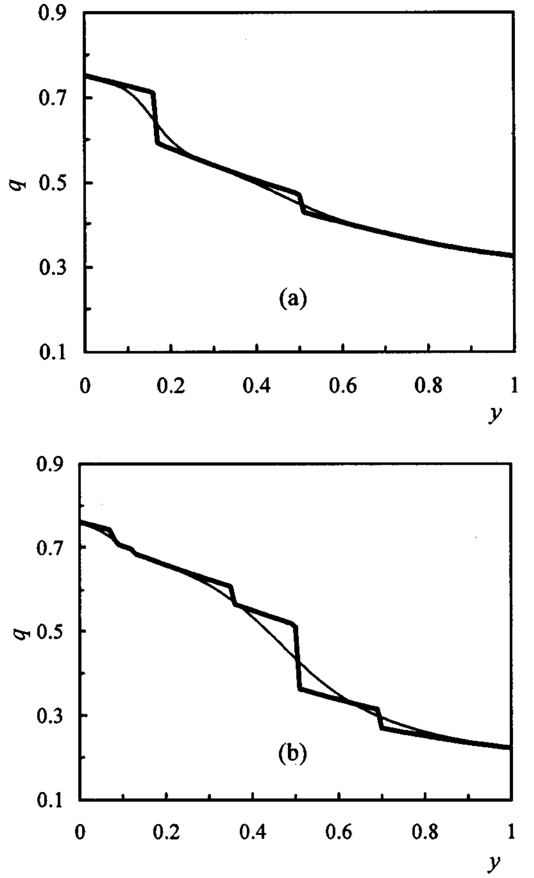

Fig. 5 Dimensionless heat flux in *y*-direction along the centerline normal to the bottom wall for test problem 4: (*a*) using LSO S_4 approximation and 101×101 grid points; and (*b*) using LSO S_8 approximation and 101×101 grid points. ▬ obtained with the DRM, — obtained with the step scheme.

The result from Eq. (17) is surprisingly identical with the aforementioned value predicted by the DRM (note that in the DRM the intensity is not separated into the aforementioned two components). This identity is achieved in all other discrete directions, without exception; no matter what quadrature set is used. This identity not only demonstrates that false scattering has been completely eliminated in this test problem, but also indicates the DRM is numerically precise (here the relative error for q_{w2} is zero).

In Fig. 5(*a*), the heat flux using S_4-approximation has a sharp drop at $y=0.16$ and $y=0.5$. Obviously, these bumps are also due to the ray effects: as shown in Fig. 6, the bump at $y=0.16$ (i.e., at point C) is due to the beams A-3 and B-6, while the bump at $y=0.5$ (i.e., at point D in Fig. 6) is due to the beams A-1 and B-4. Meanwhile in Fig. 5(*b*), the heat flux using S_8-approximation exhibits more bumps; the drop at $y=0.5$ is the strongest one. The reason for these bumps is that, among the ten discrete directions in the first octant of the LSO S_8 quadrature set (this set is available in many references, for example, Ref. [3]), two are located on the plane $\phi=\pi/4$. Moreover, the sum of the weights of these two directions is 0.6329538, which corresponds to 40.3 percent of the total weight of the first octant (i.e., $\pi/2$)! As a result, this produces a strong variation at $y=0.5$. Moreover, the top wall cannot "see" such an amount of radiation except at the two corners (as a consequence, the heat flux distribution in Fig. 4(*b*) turns upwards at $x=0$ and $x=1$); this is obviously not very reasonable. Further examination of other quadrature sets reveals that though the standard discrete ordinate quadrature sets have the advantage of rotational symmetry, too high weights are concentrated on the plane of $\phi=\pi/4$. For example, in the quadrature set of S_8-approximation, just one direction, $\xi=\eta=\mu=0.5773503$, its weight ($=0.4617179$) makes up 29.4 percent of the total. Needless to day, this enhances ray effect.

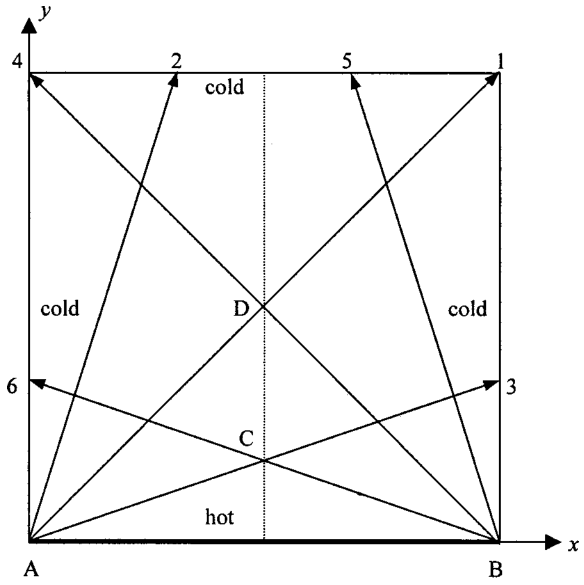

Fig. 6 Analysis on the ray effects in Figs. 4(*a*) and 5(*a*)

3.3 Participating Medium and Diffuse Boundary (Test Problem 5). In the above two subsections, the step scheme and the DRM are used. In this subsection, the linear DOIM [9] will be used to further examine the effect of false scattering. For ease of presentation, we first present some explanations about false scattering associated with these two spatial schemes. It has been shown that the DOIM also "suffers from" false scattering [9]. However, we found that, for two-dimensional problems, the DOIM does not produce false scattering in the discrete directions that satisfy $\xi/\eta=\Delta x/\Delta y$. Here Δx and Δy are the grid size in x and y-directions, respectively. But the DOIM produces false scattering in all other directions. If $\Delta x=\Delta y$, then the DOIM does not produce false scattering in all the directions that satisfy $\phi=45$ deg ("selective false scattering"). This point will not be demonstrated

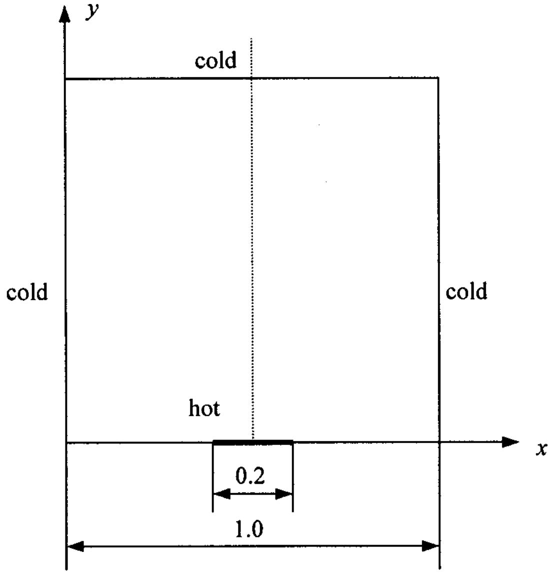

Fig. 7 Test problem 5

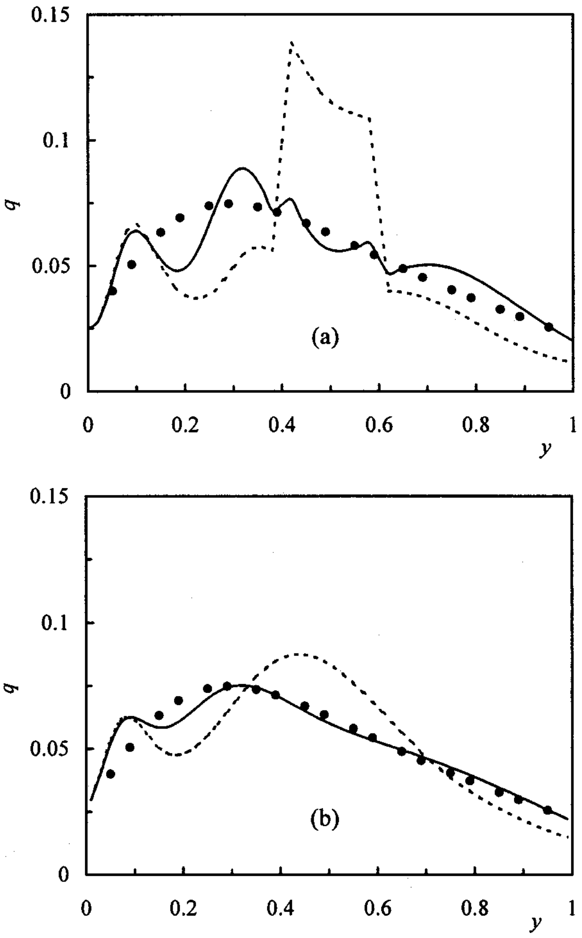

Fig. 8 Dimensionless heat flux on the right wall for test problem 5: (*a*) using the DOIM [9] and a 50×50 grid; (*b*) using the step scheme and a 50×50 grid (— using LSH S_{10} quadrature set [3]; - - - - - using LSO S_8 quadrature set; ● exact solution (using the Monte Carlo Method)

here, since it can be easily verified from the data in Ref. [9]. On the contrary, the step scheme produces false scattering in all the discrete directions [18,24].

Now, consider the test problem 5 shown in Fig. 7. The situation is similar to test problem 4, but only a section 0.2 long at the center of the bottom wall is hot. This problem was also used as a test case in Ref. [19]. Figure 8 shows the dimensionless heat flux distributions on the right wall for test problems 5, obtained with LSO S_8 and LSH S_{10} quadrature sets [3] using the linear DOIM [9] and the step scheme, as well as the physically exact solution obtained with the Monte Carlo Method. When the DOIM scheme is applied, the intensities at $x=0.4$ and $x=0.6$ are treated as Cheong and Song [9] did (i.e., assumed to be 0.5). As shown in Fig. 8(*a*), the result with LSO S_8 and the DOIM exhibits a sharp change at $y=0.4$ and $y=0.6$, respectively. Ray tracing analysis reveals that this is due to two reasons. The first one is ray effect: the effect of the two rays located on the plane $\theta=45$ deg (here, $\Delta x=\Delta y$) and the too high weights associated with them (see the analyses in subsection 3.2). The second one is selective false scattering: although the DOIM produces false scattering in all other directions, it does not produce false scattering in the directions that satisfy $\phi=45$ deg. On the contrary, since the step scheme produces false scattering on all the discrete directions [18,24], it greatly reduces the fluctuations in the heat flux (see Fig. 8(*b*)) and the results are closer to the physically exact solution than the results in Fig. 8(*a*). Especially for the results with LSH S_{10} set, the bumps at $y=0.4$ and 0.6 in Fig. 8(*a*) are not observed in Fig. 8(*b*). Figure 8(*a*) reveals that even if a scheme does not produce false scattering in only one or two discrete directions, ray effect may be strong. Thus Fig. 8 proves again that false scattering effectively reduces unwanted bumps due to ray effect; in other words, it plays a useful role. Thus it is better to retain false scattering in the case of diffuse boundary conditions.

3.4 Other Boundary Conditions. Now let us analyze test problem 4 and the results in Fig. 4(*a*) from an opposite point of view: assume that the hot bottom wall is not a diffuse surface but, on the contrary, that it REALLY emits radiation in the same directions as the discrete directions of the S_4-approximation (i.e., 12 directions in the half solid angle range of 2π), and that the radiative heat flux in each direction is the same as the flux in the corresponding direction of the S_4-approximation for diffuse surface. Then, in this case, the physically real heat flux distribution on the top wall will be close to the result obtained with the DRM in Fig. 4(*a*). In other words, the physically exact solution REALLY has a bump at $x=0.32577$ and $x=0.67423$. However, the result obtained with the step scheme does not show these bumps; on the contrary, the step scheme smears these sharp changes (see Fig. 4(*a*)). In this case, false scattering becomes a shortcoming and must be removed. The results in Figs. 3, 4(*b*), 5, and 7 can also be analyzed in the same way; all these analyses give the same conclusion as above. In fact, this is also the conclusion stated in Ref. [18].

4 Conclusion

From the above studies, the following conclusions are drawn:

1. In all the test problems discussed in this paper (two-dimensional), with non-participating or participating medium), the DRM effectively captured the discontinuous nature of the intensity field that is due to the discontinuous boundary points and to the discretization of the angular variable, and false scattering was thoroughly removed using the DRM.
2. Previously, false scattering was thought to be a "shortcoming" [9,10,15,18,21,24]; however, the above analyses show that false scattering plays a double role. In the case of diffuse boundary, it plays a useful role, and makes the computational results close to the physically exact solutions. Thus, it will be better to retain it. However, when the boundary emits radiation in a limited number of directions, or when the irradiation comes from a limited number of directions (e.g., collimated irradiation), it produces smeared intensity field and radiative heat flux distribution, thus it really becomes a shortcoming, and it must be removed. Under these circumstances the DRM predicts more accurately than other methods.

Acknowledgment

The authors are grateful to AFCRST (Sino-French Association for Scientific and Technological Research) for their financial aid.

Nomenclature

G = dimensionless incident radiation
I = dimensionless radiation intensity
q = dimensionless heat flux
S = dimensionless source function
w = weights in quadrature
β = extinction coefficient
Φ = scattering phase function
ϕ = azimuthal angle
σ_s = scattering coefficient
ζ,η,μ = direction cosines with respect to x, y, z-axes, respectively

Subscript

(capital letters) = at corresponding points in Fig. 1 or Fig. 2
b = black body

References

[1] Fiveland, W. A., 1987, ''Discrete Ordinate Methods for Radiative Heat Transfer in Isotropically and Anisotropically Scattering Media,'' ASME J. Heat Transfer , **109**, pp. 809–812.

[2] Truelove, J. S., 1987, ''Discrete-Ordinates Solutions of the Radiative Transport Equation,'' ASME J. Heat Transfer, **109**(4), pp. 1048–1051.

[3] Fiveland, W. A., 1991, ''The Selection of Discrete Ordinate Quadrature Sets for Anisotropic Scattering,'' in *Fundamental of Radiation Heat Transfer*, ASME HTD-Vol. 160, ASME, New York, pp. 89–96.

[4] El Wakil, N., and Sacadura, J. F., 1992, ''Some Improvements of the Discrete Ordinates Method for the Solution of the Radiative Transport Equation in Multidimensional Anisotropically Scattering Media,'' in *Developments of Radiative Heat Transfer*, ASME HTD-Vol. 203, ASME, New York, pp. 119–127.

[5] Thurgood, C. P., Pollard, A., and Becker, H. A., 1995, ''The T_N Quadrature Set for the Discrete Ordinate Method,'' ASME J. Heat Transfer, **117**(4), pp. 1068–1070.

[6] Koch, R., Krebs, W., Wittig, S., and Viskanta, R., 1995, ''Discrete Ordinates Quadrature Scheme for Multidimensional Radiative Transfer,'' J. Quant. Spectrosc. Radiat. Transf., **53**(4), pp. 353–372.

[7] Li, B.-W., Yao, Q., Cao, X.-Y., and Cen, K.-F., 1998, ''A New Discrete Ordinate Quadrature Scheme for Three-Dimensional Radiative Heat Transfer,'' ASME J. Heat Transfer , **120**(2), pp. 514–518.

[8] Liu, F., Becker, H. A., and Polland, A., 1996, ''Spatial Differencing Schemes of the Discrete Ordinates Method,'' Numer. Heat Transfer, Part B, **30**(1), pp. 23–43.

[9] Cheong, K.-B., and Song, T.-H., 1997, ''An Alternative Discrete Ordinates Method With Interpolation and Source Differencing for Two-Dimensional Radiative Transfer Problem,'' Numer. Heat Transfer, Part B, **32**(1), pp. 107–125.

[10] Pessoa-Filho, J. B., and Thynell, S. T., 1997, ''An Approximate Solution to Radiative Transfer in Two-Dimensional Rectangular Enclosures,'' ASME J. Heat Transfer, **119**(4), pp. 738–745.

[11] Sakami, M., and Charrette, A., 1998, ''A New Differencing Scheme for the Discrete Ordinates in Complex Geometry,'' Rev. Gen. Therm., **37**(3), pp. 440–449.

[12] Mohamad, A. A., 1998, ''Local Analytical Discrete Ordinate Method for the Solution of the Radiative Transfer Equation,'' Int. J. Heat Mass Transf., **39**(9), pp. 1859–1864.

[13] Fiterman, A., and Ben-Zvi, R., 1999, ''Dots: Pseudo-Time-Stepping Solution of the Discrete Equations,'' Numer. Heat Transfer, Part B, **35**(1), pp. 163–183.

[14] Selcuk, N., and Kirbas, G., 2000, ''The Method of Lines Solution of the Discrete Ordinates Method for Radiative Heat Transfer in Enclosures,'' Numer. Heat Transfer, Part B, **37**(1), pp. 107–125.

[15] Kim, Il-K., and Kim, W.-D., 2001, ''A Hybrid Spatial Differencing Schemes for Discrete Ordinates Method in 2D Rectangular Enclosures,'' Int. J. Heat Mass Transf., **4**(4), pp. 575–586.

[16] Raithby, G. D., and Chui, E. H., 1990, ''A Finite-Volume Method for Predicting a Radiative Heat Transfer in Enclosures with Participating Media,'' ASME J. Heat Transfer , **112**(2), pp. 415–423.

[17] Chai, J. C., Lee, H. S., and Patankar, S. V., 1994, ''Finite-Volume Method for Radiation Heat Transfer,'' J. Thermophys. Heat Transfer, **8**(3), pp. 419–425.

[18] Chai, J. C., Lee, H. S., and Patankar, S. V., 1993, ''Ray Effect and False Scattering in the Discrete Ordinates Method,'' Numer. Heat Transfer, Part B, **24**(2), pp. 373–389.

[19] Ramankutty, M. A., and Crosbie, A. L., 1997, ''Modified Discrete Ordinates Solution of Radiative Transfer in Two-Dimensional Rectangular Enclosures,'' J. Quant. Spectrosc. Radiat. Transf., **57**, pp. 107–140.

[20] Baek, S. W., Byun, D. Y., and Kang, S. J., 2000, ''The Combined Monte-Carlo and Finite-Volume Method for Radiation in a Two-Dimensional Irregular Geometry,'' Int. J. Heat Mass Transf., **43**(13), pp. 2337–2344.

[21] Thynell, S. T., 1998, ''Discrete-Ordinates Method in Radiative Heat Transfer,'' Int. J. Eng. Sci., **35**(12–14), pp. 1651–1675.

[22] Crosbie, A. L., and Schrenker, R. G., 1984, ''Radiative Transfer in a Two-Dimensional Rectangular Medium Exposed to Diffuse Radiation,'' J. Quant. Spectrosc. Radiat. Transf., **31**(4), pp. 339–372.

[23] Thynell, S. T., and Özisik, N. N., 1987, ''Radiation Transfer in Isotropically Scattering, Rectangular Enclosures,'' J. Thermophys. Heat Transfer, **1**(1), pp. 69–76.

[24] Chai, J. C., Patankar, S. V., and Lee, H. S., 1994, ''Evaluation of Spatial Differencing Practices for the Discrete Ordinates Method,'' J. Thermophys. Heat Transfer, **8**(1), pp. 140–144.

Investigation of Circumferential Variation of Heat Transfer Coefficients During In-Tube Evaporation for R-22 and R-407C Using Liquid Crystal

Seok Ho Yoon
Ph.D. candidate

Min Soo Kim
e-mail: minskim@snu.ac.kr

School of Mechanical and
Aerospace Engineering,
Seoul National University,
Seoul 151-742, Korea

Heat transfer coefficients during evaporation in a horizontal smooth tube for R-22 and R-407C (R-32/125/134a, 23/25/52 wt.%) have been measured using thermochromic liquid crystal. Focus has been put on the circumferential variation of heat transfer coefficients at several cross-sections of the test tube with inner diameter of 11.3 mm for several vapor qualities of refrigerant. The inner wall temperatures were calculated by one dimensional heat conduction equation from the measured outer wall temperatures, which were obtained using an image processing technique with thermochromic liquid crystal (TLC). The relation between measured temperature and color information (Red-Green-Blue values) of thermochromic liquid crystal was calibrated by a neural network method. Results show that circumferential variation of heat transfer coefficients for R-22 is quite large with the highest heat transfer coefficient at the top of the tube. For zeotropic mixture of R-407C, similar trend has been observed with less difference between the heat transfer coefficients at the top and bottom than that of R-22. [DOI: 10.1115/1.1484110]

Keywords: *Evaporation, Heat Transfer, Image Processing, Refrigeration*

1 Introduction

Environmental issues of global warming and ozone depletion by CFC and HCFC refrigerants have driven us to find and develop new alternative refrigerants. Extensive studies on alternative refrigerants have already been carried out for their thermophysical properties and their performances in refrigerators, air-conditioners, heat pumps, etc. Since two-phase heat transfer is a main mechanism of energy transfer in these systems, investigation of evaporation and condensation heat transfer has been carried out and enhancement of heat transfer has been constantly pursued which, in turn, will improve system performance. In designing a new machine with new alternative refrigerants, it is a prerequisite to get information on two-phase heat transfer for new refrigerants.

Until now, several experiments and theoretical studies have been done for in-tube evaporation of new alternative refrigerants. Measurements of heat transfer coefficients along test tubes have been the most frequent studies (Wang et al. [1]; Shin et al. [2]; Kim et al. [3]; Choi et al. [4]; Kattan et al. [5]), and several correlations based on experimental data have been proposed for the purpose of heat exchanger design and analysis (Gungor and Winterton [6]; Jung et al. [7]; Kandlikar [8,9]; Kattan et al. [10]). When the circumferential variations of heat transfer coefficients at one cross section of the tube are considered, there are some studies based on the measurements at several positions around the circumference (Ross et al. [11]; Jung et al. [12]; Yoshida et al. [13]; Niederkrüger et al. [14]; Boyd et al. [15]; Shin et al. [16]; Kattan et al. [5]; Choi et al. [4]). In most cases, it is quite usual to measure tube wall temperatures at 3 or 4 locations of test section (i.e., top, one or two sides, and bottom) using thermocouples and calculate the average value to get a local heat transfer coefficient as a representation of heat transfer coefficient at one axial position. However, there always are limitations on the number of measuring points using thermocouples, and conduction loss through the thermocouple wire tends to reduce the accuracy of the measurement. The circumferential heat transfer coefficients differ around the circumference mainly because of the liquid film thickness change due to gravity, flow patterns, and composition shift for zeotropic refrigerant mixtures. Even though circumferential heat transfer variation will not fully explain these phenomena, it is quite important to investigate the circumferential heat transfer coefficient change, and to compare this with the locally averaged heat transfer coefficient from 3 or 4 point measurements.

Thermochromic liquid crystals exhibit all colors of the visible spectrum for specified temperature range. Recently, quantitative measurements using liquid crystals were carried out in a convective heat transfer study by Camci et al. [17], and it is found that a very accurate quantitative approach is possible when a linear hue versus temperature relation for a certain range is used. It is noteworthy that Matsumoto et al. [18] used a neural network method in their calibration to get a relation between RGB signals and temperatures. In this study, neural network method is also used for color-to-temperature transformation, because an accurate calibration curve over a wide temperature range can be obtained by considering a strong non-linear relation between color images (RGB signals) and temperatures when compared with the hue-temperature method. The advantage of this technique is the possibility to get two dimensional temperature distributions over the circumference and for some axial length simultaneously.

The main objective of this study is to investigate a local circumferential variation of heat transfer coefficients during in-tube evaporation. It includes a comparison of the measured data with existing heat transfer correlations. In this study, an imaging technique using thermochromic liquid crystal (TLC) is used to measure an almost continuous variation of outer wall temperatures during in-tube evaporation of pure R-22 and zeotropic refrigerant mixture of R-407C (R-32/125/134a, 23/25/52 wt %). Circumferential variation of heat transfer coefficients for these two refrigerants at several vapor qualities is provided.

Contributed by the Heat Transfer Division for publication in the JOURNAL OF HEAT TRANSFER. Manuscript received by the Heat Transfer Division March 27, 2000; revision received April 1, 2002. Associate Editor: T. Y. Chu.

2 Wall Temperature Measurement Using Liquid Crystal

Image Processing System. First of all, wall temperature measurement using liquid crystal is described in this section. Since the color of liquid crystal varies uniquely as temperature changes, it is required to get color information of the liquid crystal to be incorporated with the temperature of the wall of a test section. As the liquid crystal film was attached on the outer wall of the test tube in a very thin layer while keeping the tube temperature near the ambient air, it is quite acceptable that the temperature of liquid crystal is very close to that of the wall. Color image processing technique is used for obtaining color information of liquid crystal, which means colors of liquid crystal that appear on the outer wall of the test section are observed by a CCD camera to get red-green-blue (RGB) information at the spot of interest. The CCD camera sends analog (NTSC) signals to the frame grabber in a computer, which converts analog signals to digitized image of 640×480 pixels. However, only 5×5 pixels around the spot of interest which is perpendicular to the camera angle have been used for color to temperature conversion, where each pixel has digitized RGB values ranging from 0 to 255. For the measurement at other positions around the circumference, camera has been rotated by keeping a perpendicular orientation to the tube surface. As an illumination system, halogen lamp of 100 W with ring-type optical fiber was used.

Calibration. To measure a temperature using thermochromic liquid crystal, the relation between the color of liquid crystal and the temperature of the test section should be known. A test section for calibration was made of a quartz tube, where thermochromic liquid crystal film and copper foil were attached on the inner wall of the quartz tube. Five thermocouples were attached on the copper foil inside the quartz tube. Single phase water flows through the test tube at the maximum rate of about 0.2 kg/s so that the temperature change in the test section would be negligible while maintaining a designated temperature. Thermochromic liquid crystal used in this study is a cholesteric-type that has an event temperature range from 10°C (red) to 20°C (blue). The lighting source during the calibration is positioned 25 deg off from the CCD camera viewing direction, which is the same as in the main experiments to minimize the effects of illumination angle to the test surface on temperature measurement. When steady state is reached, the image capturing with CCD camera and the temperature measurement using thermocouples are carried out simultaneously.

Color to Temperature Transformation. Typical example of RGB values for liquid crystals in this study versus measured temperatures is presented in Fig. 1. RGB values obtained from the test as shown in Fig. 1 are then normalized with their mathematical sum to represent the observer-independent color values as stated by Camci et al. [17]. The normalized RGB values are defined as in the following Eq. (1).

$$r=\frac{R}{R+G+B},\quad g=\frac{G}{R+G+B},\quad b=\frac{B}{R+G+B} \tag{1}$$

Instead of calibrating RGB values obtained from the captured image to the measure temperature, normalized RGB values (rgb) are used for the calibration. In this study, neural network method is introduced to formulate the relation between color information and temperature. An exemplary neuron in the neural network is shown in Fig. 2(a). With given inputs of x_k's, the output $f(s)$ of the neuron is given by Eq. (2);

$$f(s)=\frac{1}{1+\exp(-u_0 s)},\qquad s=\sum_{k=1}^{3} x_k w_k+c \tag{2}$$

where c is an offset for the neuron, w_k's are weighting coefficients, and u_0 is a constant, which is given as 0.5. A neuron has an ability to learn the relation between given inputs and their corresponding outputs as stated by Kimura et al. [19]. The structure of neural network used in this study is depicted in Fig. 2(b). The weighting coefficients (w_k) and offset (c) between two neurons are optimized to get best results for the normalized calculated temperature, θ_C from the measured temperature, θ_M, where the normalized temperature is shown in Eq. (3).

$$\theta=\frac{T-T_{\min}}{T_{\max}-T_{\min}} \tag{3}$$

where $T_{\max}$ is the maximum event temperature of 20°C and $T_{\min}$ represents the minimum event temperature of 10°C. The optimized weighting coefficients and offsets are listed in Table 1, based on normalized RGB values and normalized reference tem-

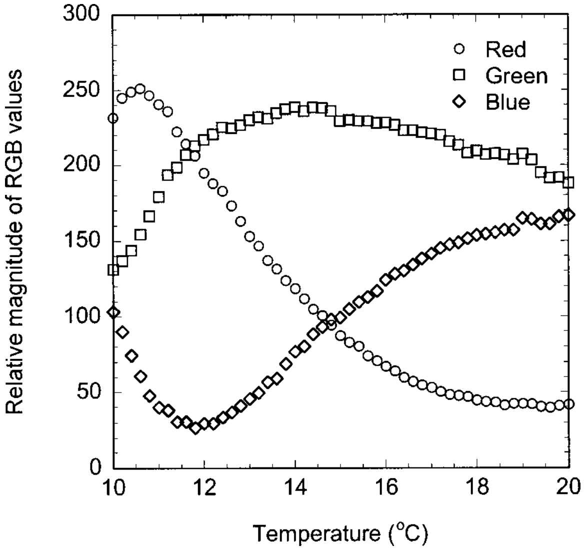

Fig. 1 Relative magnitude of RGB values as a function of temperature

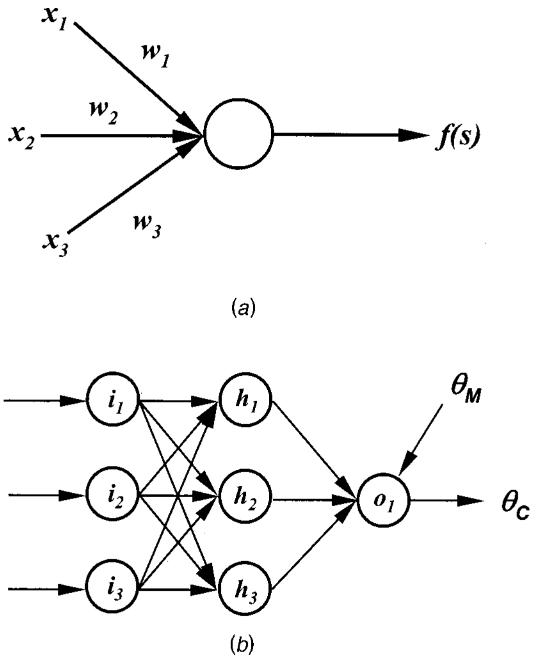

Fig. 2 (a) An exemplary neuron; and (b) neural network used for calibration

Table 1 Optimized weighting coefficients and offsets of the neural network in this study

Weighting coefficient		Offset	
path	value	path	value
$i_1 \rightarrow h_1$	-2.204163	$i_k \rightarrow h_1$	-1.198521
$i_2 \rightarrow h_1$	3.667228		
$i_3 \rightarrow h_1$	-2.582375		
$i_1 \rightarrow h_2$	-2.232578	$i_k \rightarrow h_2$	-2.283305
$i_2 \rightarrow h_2$	3.419837		
$i_3 \rightarrow h_2$	3.145532		
$i_1 \rightarrow h_3$	4.555921	$i_k \rightarrow h_3$	-0.855518
$i_2 \rightarrow h_3$	-7.220535		
$i_3 \rightarrow h_3$	-0.620283		
$h_1 \rightarrow o_1$	10.534632	$h_k \rightarrow o_1$	-0.868899
$h_2 \rightarrow o_1$	0.398910		
$h_3 \rightarrow o_1$	1.274797		

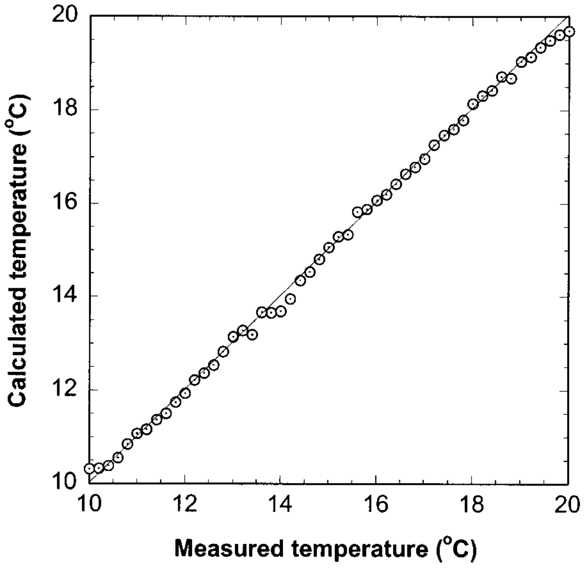

Fig. 3 Comparison of the measured temperatures with the calculated values using a neural network

peratures that are used for calibration. Once the optimal values of weighting coefficients and offsets are obtained, neural network system can calculate a normalized temperature using normalized RGB values. The calibration results are shown in Fig. 3 and it is clear that the calculated temperatures agree very well with the measured temperatures. The maximum deviation between the calculated temperatures and the measured temperatures is 0.3 K and rms of the deviation is about 0.1 K.

3 Experiment

Experimental Apparatus. Experimental apparatus for evaporative heat transfer study is designed to get circumferential distribution of heat transfer coefficients inside a horizontal smooth tube from the wall temperature measurement using thermochromic liquid crystal which is attached outside of the test tube. The schematic diagram of experimental apparatus is shown in Fig. 4. The test rig is composed of magnetic gear pump (Tuthill, TXCM26MCNK) for refrigerant circulation, liquid receiver, chiller, heat exchanger for subcooling the refrigerant, pre-heater, mass flow meter (Oval, D012S-SS-200), and heat transfer test section. In addition to these, CCD camera (Panasonic, KR-222) for capturing color images, illumination system and computer with frame grabber (Matrox, Meteor) become part of the test setup. The magnetic gear pump circulates the subcooled liquid from the liquid receiver to the pre-heater, and the pre-heater is installed to adjust the inlet quality of the refrigerant to the desired value. The mass flow meter is installed before the pre-heater to measure the flow rate of the refrigerant in the liquid phase.

Figure 5 represents the schematic diagram of the heat transfer test section. Seamless stainless steel tube is used as a heat transfer test section with inner and outer diameters of 11.3 and 12.7 mm, respectively. Thermochromic liquid crystal is attached on the outer wall of the test tube where black paint is painted between the outer wall and the layer of thermochromic liquid crystal. The test section is surrounded by quartz tube for insulation, since the thermal conductivity of quartz tube is about one tenth of that of stainless steel tube. In addition to this, the temperature difference between the surroundings of the test section and the outer wall of the tube has been kept within 2°C. The heat is generated from the tube since AC voltage has been directly applied to the test tube and the amount of heat transferred to the refrigerant at the test section is measured by a powermeter. Pressure taps are drilled at the inlet and outlet of the test section to measure the pressures of the refrigerant.

Test Conditions. Mass flux of refrigerant flow and heat flux to the test section are major factors which affect evaporative heat transfer of refrigerant. Test section inlet temperature of the refrigerant was also varied to investigate the influence of refrigerant temperature on heat transfer. The experiment in the high vapor quality region above 0.6 has not been performed to protect thermochromic liquid crystal from a burn-out. Test conditions in this study are shown in Table 2 for R-22 and R-407C.

Data Reduction. Prior to the measurement, a steady state should be reached while operating the chiller to condense the refrigerant that was evaporated in the main test section. During the test, refrigerant temperatures at the inlet and outlet of the test section were measured together with the pressures at the same positions. Mass flow rate of refrigerant and heat flux to the test section were also measured, and all the measured values were transmitted to personal computer through multi-channel recorder using GPIB interface. Data were saved into a file during the steady state operation when the maximum deviations of temperature, mass flux, and pressure from the mean values were less than 0.1°C, 3 kg/m^{2}s, and 2 kPa, respectively. The saturation temperatures of refrigerants were calculated from the measured pressure by using a modified Carnahan-Starling-DeSantis equation of state (Huber et al. [20]). For mixtures, vapor quality, which was obtained from the energy balance in the preheater section, was additionally used to calculate the local temperature together with the pressure at the test section. The difference between the measured temperature of refrigerant and the calculated temperature from pressure measurement was less than 0.15°C. The colors of the liquid crystal appearing at the outer wall of the test section were observed by the CCD camera, and when steady state was reached, the images were saved for an analysis.

Heat transfer coefficient is defined as in Eq. (4).

$$h = \frac{q''}{T_{wi} - T_{\text{sat}}} \tag{4}$$

where q'' is the heat flux to the test section and T_{wi} is the inner wall temperature calculated by one dimensional heat conduction equation from measured outer wall temperatures which were obtained with thermochromic liquid crystal using an image processing technique.

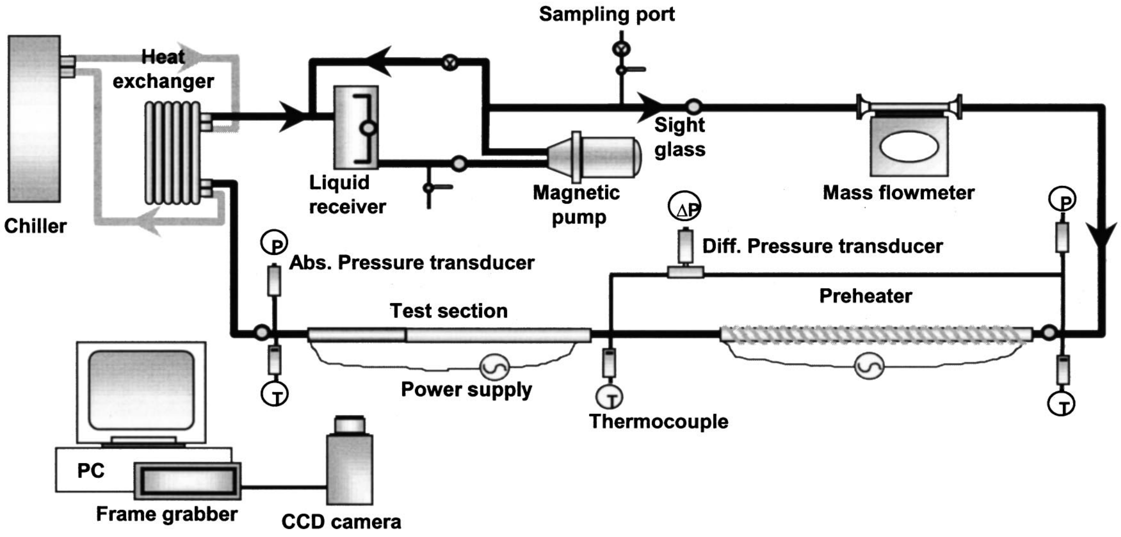

Fig. 4 Schematic diagram of experimental apparatus for measuring circumferential heat transfer coefficient

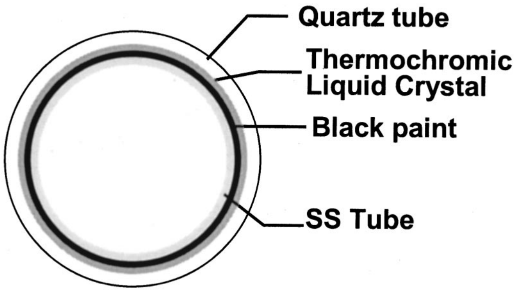

Fig. 5 Cross sectional view of the test section

Table 2 Test conditions in this study for circumferential measurement of heat transfer coefficient

	R-22	R-407C
Heat flux (kW/m^2)	3.6	3.6
Mass flux (kg/m^{2}s)	100 ~ 300	200 ~ 300
Test section average pressure (kPa)	660 ~ 695	760 ~ 790
Test section inlet temperature (℃)	9.5 ~ 10.5	9.5 ~ 10.5
Vapor quality	0.05 ~ 0.55	0.1 ~ 0.6

4 Results and Discussion

Energy Balance Test. Energy balance tests in the test section have been done to check the accuracy in heat flux measurement. The basic idea is to compare the heat given to the refrigerant with the heat gain by the refrigerant, which is R-22 in this case. Only liquid phase flow was used in energy balance test for simplicity and easiness to measure the temperature difference before and after the test section. Absolute average of deviation calculated by Eq. (5) was 0.7 % for 100 data points.

$$E_Q=\frac{1}{N}\sum_{i=1}^{N}\left|\frac{Q_{C,i}-Q_{M,i}}{Q_{C,i}}\right|\times 100(\%) \tag{5}$$

where Q_M is the measured heat rate using a wattmeter, and Q_C is the sensible heat rate calculated by the mass flow rate and temperature change of refrigerant in the test section. Actually, Q_M is the heat rate generated in the test tube made of stainless steel when the electric current was applied to the tube.

For comparison of the measured heat transfer coefficient in the single phase flow, Dittus-Boelter's correlation (Dittus and Boelter [21]) for single phase heat transfer was used. Absolute average deviation of 4.1 % was obtained when calculated with Eq. (6) for 100 data points.

$$E_h=\frac{1}{N}\sum_{i=1}^{N}\left|\frac{h_{C,i}-h_{M,i}}{h_{C,i}}\right|\times 100(\%) \tag{6}$$

where h_M is the measured single phase heat transfer coefficient, and h_C is the calculated heat transfer coefficient using Dittus-Boelter's correlation. In measuring the single phase heat transfer coefficient, the refrigerant temperature was measured directly by the thermocouple, and the tube wall temperature was obtained from the color information using the liquid crystal.

Circumferential Variations of Inner Wall Temperature With Respect to Quality. Circumferential variations of inner wall temperatures and heat transfer coefficients at several vapor qualities for R-22 and R-407C were obtained. Figures 6 and 7 show inner wall temperatures and refrigerant temperatures at several circumferential locations for R-22 and R-407C. Circumferential variation of inner wall temperatures together with refrigerant temperature at quality near 0.25 are shown for R-22 and R-407C in Fig. 6 with mass flux G of 200 kg/m^{2}s and heat flux q'' of 3.6 kW/m^2. The inner wall temperature at the top is lower than that at the bottom, because of the different liquid film thickness caused by gravity for both cases of R-22 and R-407C. For R-22 as shown in Fig. 6(*a*), the liquid film at the top is thinner than that at the bottom, which represents that the inner wall temperature at the top will be lower if we assume the liquid-vapor interface temperature is uniform and the heat generation is also uniform along the tube. However, for the case of R-407C, the inner wall temperature is higher than that of R-22, which means the wall superheat difference at the top and bottom for R-407C is not so great as that of R-22. This is mainly because of the composition difference in the local liquid film of refrigerant. If zeotropic refrigerant mixtures are considered, more volatile component will easily evaporate, which means there exists a concentration gradient near the interface. In the liquid phase near the interface, there is a higher concentration of less volatile component, which will generally reduce the evaporation of more volatile component. As a result, the temperature at the interface differs at the top and at the bottom. When this effect of preferential evaporation is purely considered, the

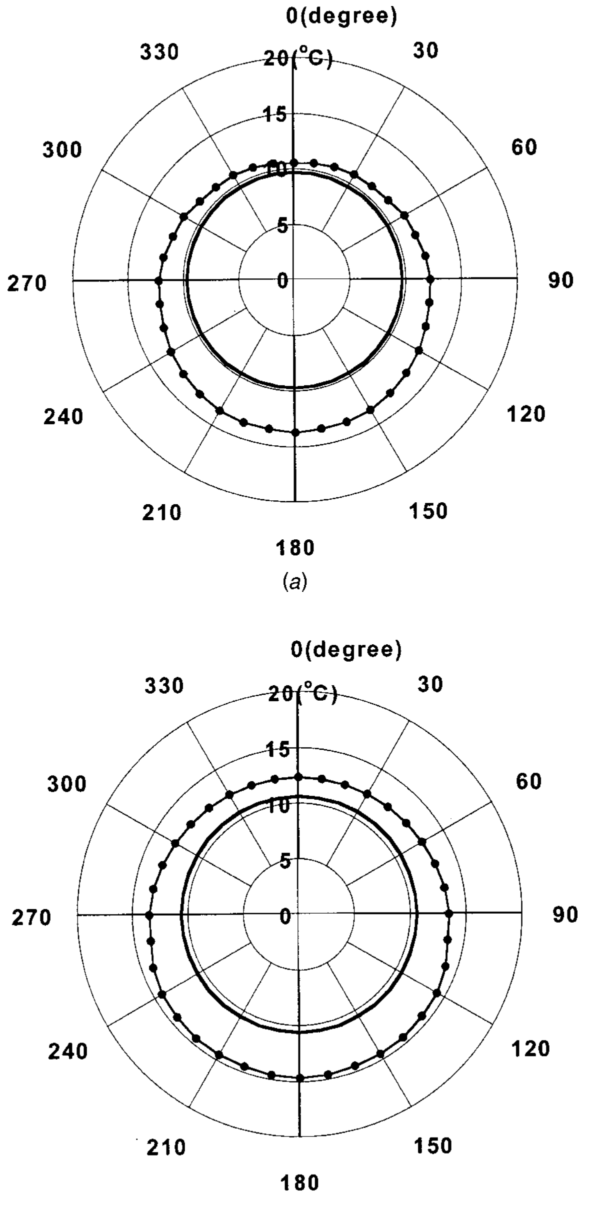

(a)

(b)

Fig. 6 Circumferential variation of inner wall temperatures at quality near 0.25 for R-22 and R-407C: (*a*) R-22; $G=200$ kg/m^2 s; $q''=3.6$ kW/m^2; $P_{sat}=670$ kPa; $x=0.26$; and (*b*) R-407C; $G=200$ kg/m^2 s; $q''=3.6$ kW/m^2; Psat=760 kPa; $x=0.24$

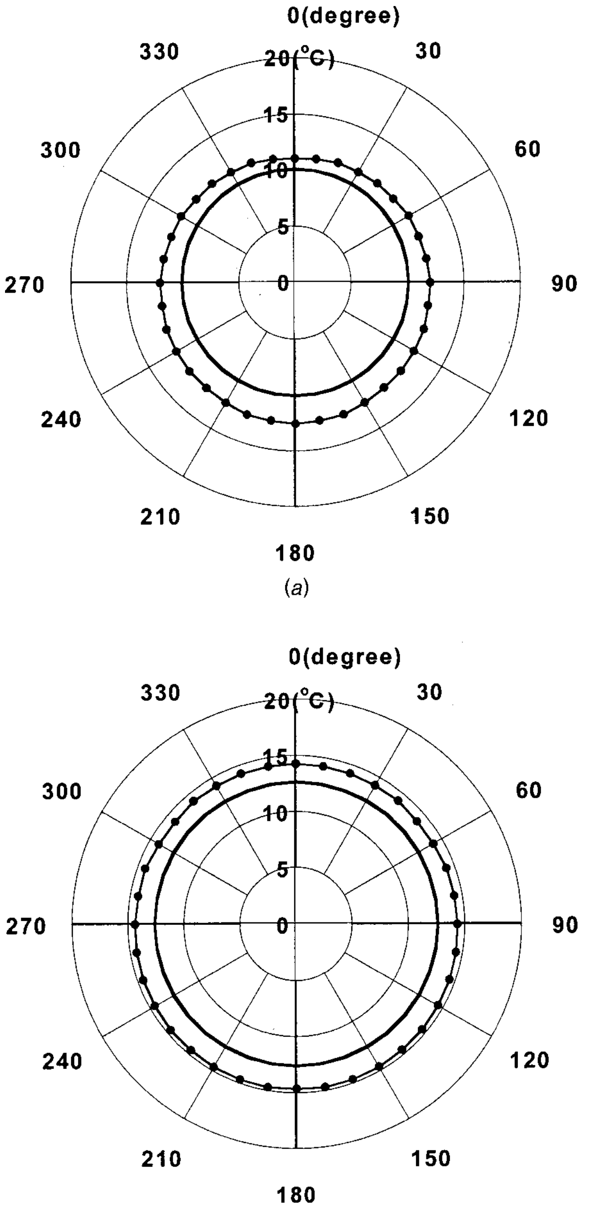

(a)

(b)

Fig. 7 Circumferential variation of inner wall temperatures at quality near 0.50 for R-22 and R-407C: (*a*) R-22; $G=200$ kg/m^2 s; $q''=3.6$ kW/m^2; $P_{sat}=670$ kPa; $x=0.46$; and (*b*) R-407C; $G=200$ kg/m^2 s; $q''=3.6$ kW/m^2; $P_{sat}=760$ kPa; $x=0.54$

interface temperature at the top tends to be lower than that at the bottom (Jung et al. [12]). However, in practical point of view, it is very hard to measure or estimate the local interface temperature, therefore the equilibrium temperature for a given pressure and a mass quality is generally used for the determination of heat transfer coefficient.

Circumferential variations of inner wall temperatures at vapor quality near 0.5 for R-22 and R-407C are shown in Fig. 7 with mass flux G of 200 kg/m^{2}s and heat flux q'' of 3.6 kW/m^2. As quality increases, the liquid film thickness becomes thinner and more uniform along the circumference. Therefore, the difference between the inner wall temperature at the top and that at the bottom is reduced for both cases of R-22 and R-407C. But still, the difference between these two positions exists due to the effect of gravity on the liquid film especially for R-22. A circumferential variation of inner wall temperature for R-407C is quite decreased when compared with that for R-22, which represents the inner wall temperature for R-407C is also affected by a preferential evaporation of more volatile component in the refrigerant mixture.

Circumferential Variation of Heat Transfer Coefficient With Respect to Vapor Quality. Circumferential variation of heat transfer coefficient versus vapor quality for R-22 are shown in Fig. 8 when saturation pressure is 670 kPa, mass flux is 200 kg/m^{2}s, and heat flux is 3.6 kW/m^2. For R-22, the heat transfer coefficient at the top of the test tube is greater than that at the bottom, because of the different liquid film thickness along the circumference. When vapor velocity increases due to evaporation in the test section, the liquid film thickness becomes thinner and more uniform along the circumference until it reaches a dryout

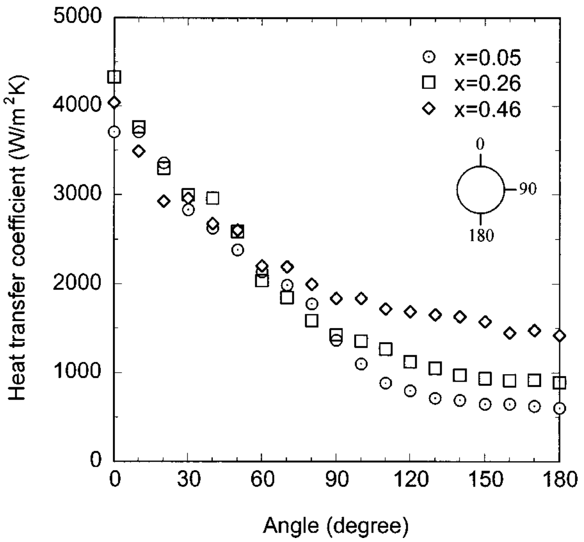

Fig. 8 Circumferential variation of heat transfer coefficients at several vapor qualities of R-22 ($G=200$ kg/m^2 s; $q''=3.6$ kW/m^2; $P_{sat}=670$ kPa)

point. Therefore, heat transfer coefficient increases as quality increases in the test range, which is thought mostly in the annular flow regime and the difference between the heat transfer coefficient at the top and that at the bottom is accordingly reduced.

Circumferential variation of heat transfer coefficient for R-407C is shown in Fig. 9 for the refrigerant pressure of 760 kPa, mass flux of 200 kg/m^{2}s, and heat flux of 3.6 kW/m^2. Circumferential variation of heat transfer coefficient for R-407C is quite different from that of R-22. The heat transfer coefficient for R-407C at the top is slightly higher than that at the bottom, which is due to the combined effects of the film thickness change and the preferential evaporation at the interface. As vapor quality increases, the local heat transfer coefficients along the circumference are elevated due to higher mean velocity of the refrigerant. At low quality region, the ratio of heat transfer coefficients at the top and at the bottom is greater compared with the case at high quality region.

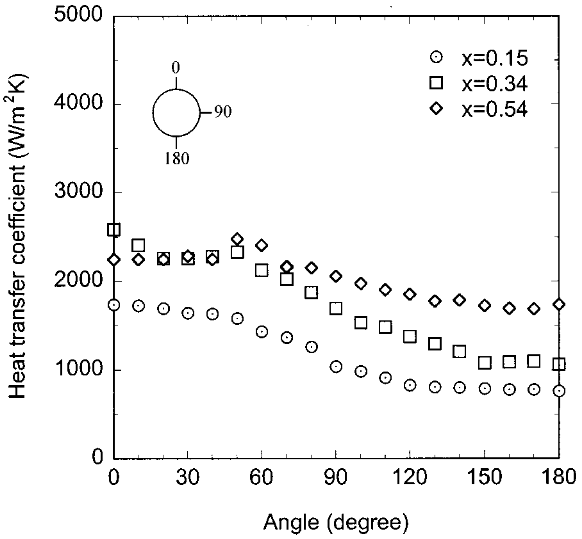

Fig. 9 Circumferential variation of heat transfer coefficients at several vapor qualities of R-407C ($G=200$ kg/m^2 s; $q''=3.6$ kW/m^2; $P_{sat}=760$ kPa)

It should be noted that the average of circumferential temperature distribution is quite different from the local heat transfer coefficient measurement using wall-attached thermocouples normally at the top, bottom, or side positions of the tube. Concerning the measurement of heat transfer coefficients around the circumference using thermocouples, there are some data in the literature previously listed, however, it is very hard to compare directly with them mainly due to the different test conditions. One of the acceptable methods is to compare the circumferentially-averaged heat transfer coefficient with that obtained by a 4-point (top, bottom, and two sides) average value using the corresponding data obtained in this study with liquid crystals. This is quite reasonable since the temperature measured by liquid crystal has been calibrated with the thermocouple measurement with a maximum deviation of 0.3 K (rms deviation of 0.1 K) as shown in Fig. 3. For R-22, the difference between the circumferentially-averaged value and the 4 point average is about 5 %, and for R-407C it is about 2 %.

Comparison With Several Correlations. Figure 10 shows circumferential variation of heat transfer coefficients at specified test conditions and it is compared with in-tube heat transfer correlations (Gungor and Winterton [6]; Kandlikar [8]; Kattan et al.

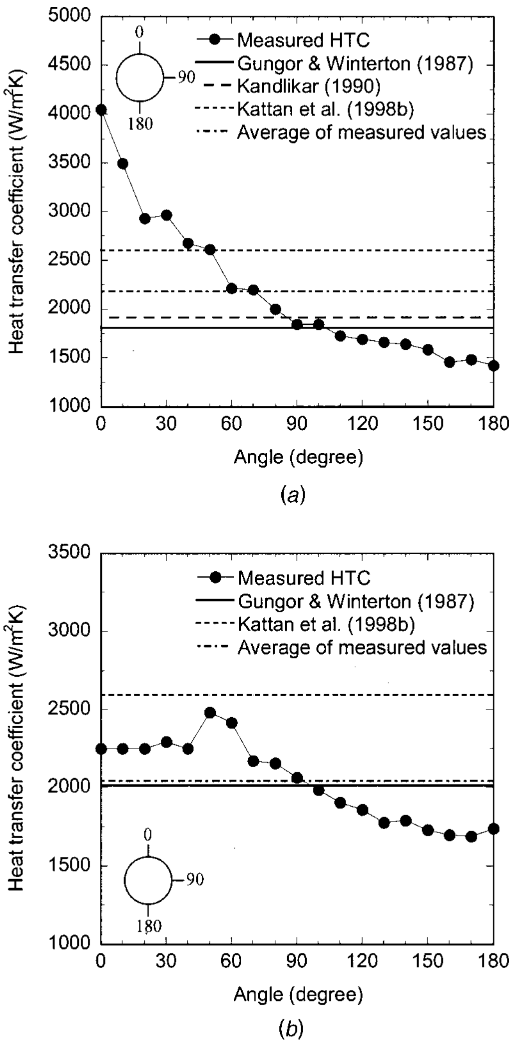

(*a*)

(*b*)

Fig. 10 Circumferential variation of heat transfer coefficients and comparison with correlations for R-22 and R-407C: (*a*) R-22; $G=200$ kg/m^2 s; $q''=3.6$ kW/m^2; $P_{sat}=670$ kPa; $x=0.46$; and (*b*) R-407C; $G=200$ kg/m^2 s; $q''=3.6$ kW/m^2; $P_{sat}=760$ kPa; $x=0.54$

[10]) for R-22. For R-407C, the correlations of Gungor and Winterton [6], and that of Kattan et al. [10] are used together with a correlation for refrigerant mixtures proposed by Thome and Shakir [22]. In Fig. 10(*a*), a very high value of heat transfer coefficient is obtained especially at the top during the horizontal in-tube evaporation of R-22 (mass flux of 200 kg/m^2s; heat flux of 3.6 kW/m^2; pressure of 670 kPa; quality of 0.46), and the maximum deviation of 88 % from the average is observed at this point. The average deviation between the average of measured circumferential heat transfer coefficient and the correlation by Gungor and Winterton [6] relative to the average of measured values is -9.4 % and absolute average deviation is 21.7 %. The average deviation between the average of measured circumferential heat transfer coefficient and the correlation by Kandlikar [8] using the fluid dependent parameter of 1.0 for stainless steel tube is -4.0 % and absolute average deviation is 22.8 %. The average deviation from the correlation of Kattan et al. [10] relative to the experimental value is 30.6 %, and the absolute average deviation is 39.9 %. Figure 10(*b*) shows measured heat transfer coefficients for R-407C (mass flux of 200 kg/m^2s; heat flux of 3.6 kW/m^2; pressure of 760 kPa; quality of 0.54), the values from the correlations by Gungor and Winterton [6], and by Kattan et al. [10]. The average deviations between the values from the correlation and the measured values relative to the measurement result for R-407C were 0.2 % and 29.2 %, and the absolute average deviation is 11.4 % and 29.2 % for Gungor and Winterton [6], and Kattan et al. [10], respectively.

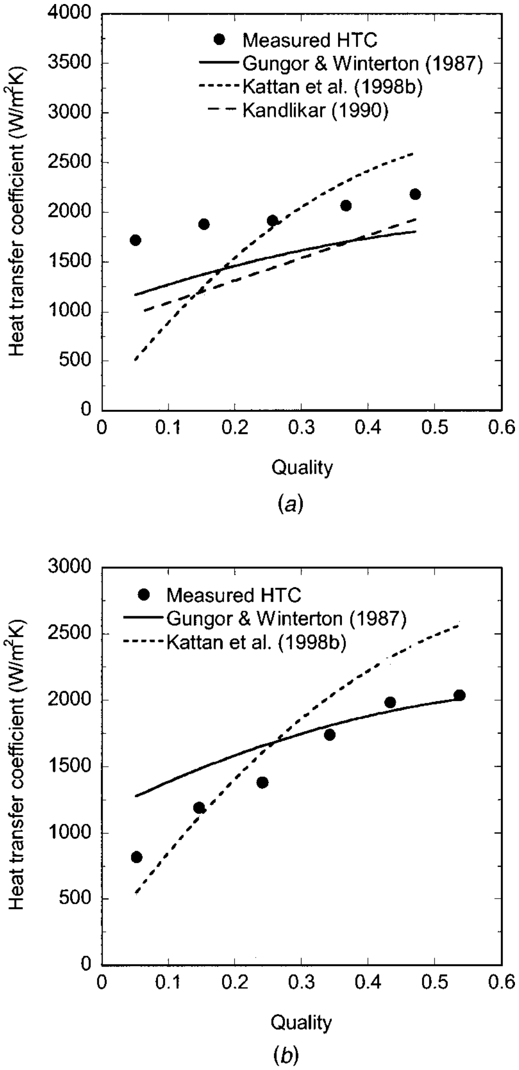

Fig. 11 Variation of average heat transfer coefficients with respect to quality and comparison with correlations for R-22 and R-407C: (*a*) R-22; $G=200$ kg/m^2 s; $q''=3.6$ kW/m^2; $P_{sat}=670$ kPa; and (*b*) R-407C; $G=200$ kg/m^2 s; $q''=3.6$ kW/m^2; $P_{sat}=760$ kPa

The comparison of test results with the correlations mentioned above for several qualities up to about 0.55 is shown in Fig. 11, where one data point represents the average of 36 heat transfer coefficients measured along the circumference. The RMS (root mean square) deviation between the locally averaged heat transfer coefficient from the measurement for R-22 and the correlation by Gungor and Winterton [6] is 22.2 %. That by Kandlikar [8] and by Kattan et al. [10] is 28.1 % and 36.2 %, respectively. For R-407C, the correlation by Kattan et al. [10] shows RMS deviation of 21.7 %, and that by Gungor and Winterton [6] exhibits 27.2 % relative to the circumferentially averaged heat transfer coefficient. From the comparison in the test range of this study, the correlation by Gungor and Winterton [6] and that by Kattan et al. [10] is quite acceptable in predicting local heat transfer coefficients.

5 Concluding Remarks

Evaporative heat transfer characteristics for R-22 and R-407C in a horizontal smooth tube have been experimentally investigated. The circumferential variation of heat transfer coefficient was focused on, and thermochromic liquid crystal was used to measure the outer wall temperature of the test tube. Heat transfer coefficients along the circumference were obtained for several vapor qualities. Experimental results were compared with a correlation for heat transfer coefficient proposed by Gungor and Winterton [6], Kandlikar [8], and Kattan et al. [10]. Some conclusions from this study are drawn as follows.

1 Circumferential variation of outer wall temperature and corresponding heat transfer coefficient for R-407C was quite different from that for R-22. The heat transfer coefficient for R-22 at the top of the test tube is much greater than that at the bottom because of the different liquid film thickness due to gravity. However, the heat transfer coefficient for R-407C at the top of the test tube is slightly higher than that at the bottom, which is due to the combining effects of liquid film thickness and the preferential evaporation of more volatile component near the vapor-liquid interface. There has been a difference between the circumference averaged heat transfer coefficient and the average value based on the measured data at the top, bottom, and two sides.

2 As the vapor quality increases, the heat transfer coefficients generally increase, and the ratio of heat transfer coefficient at the top and that at the bottom is reduced. This reduction is quite evident at higher vapor quality for both pure R-22 and zeotropic refrigerant mixture, R-407C. Quite amount of an increase in heat transfer coefficient with respect to quality was found at the bottom of the tube.

3 Measured experimental data were compared with the existing correlations proposed by Gungor and Winterton [6], Kandlikar [8], and Kattan et al. [10]. The RMS deviation between locally averaged heat transfer coefficient and that from the correlation by Gungor and Winterton [6] was 22.2 % for R-22 and 27.2 % for R-407C in the vapor quality range of this study. When Kandlikar's correlation [8] was used for R-22, the RMS deviation is 28.1 %. The RMS deviation of the correlation by Kattan et al. [10] is 36.2 % for R-22, but if the lower quality region is not considered, the predictions become much better. For R-407C, it shows 21.7 % of RMS deviation.

4 In calculating the heat transfer coefficients using the outer wall temperature measurement during in-tube evaporation, the thermochromic liquid crystal film is one of good tools to measure circumferential or even two dimensional wall temperature distribution. However, caution should be given to the measurement for the curved surface, i.e., outer wall of the tube, and the color-to-temperature calibration process.

Acknowledgments

This work has been supported by Korea Science and Engineering Foundation (1999-1-304-006-3) and by the Brain Korea 21 project of the Ministry of Education.

Nomenclature

c = offset in Eq. (2)
G = mass flux (kg/m^{2}s)
h = heat transfer coefficient (kW/m^{2}K)
P = pressure (kPa)
Q = transferred heat (kW)
q'' = heat flux (kW/m^2)
RGB = red, green, blue
rgb = red, green, blue (normalized value)
T = temperature (°C)
E = average deviation
w = weighting coefficient in Eq. (2)
x = vapor quality
θ = normalized temperature, defined in Eq. (3)

Subscripts

M = measured value
C = calculated value
wi = inner wall
sat = saturated state
h = heat transfer coefficient

Appendix A Uncertainty Analysis

Uncertainty evaluation of heat transfer coefficient is performed in accordance with a 95 % confidence interval to satisfy ANSI/ASME PTC 19.1.

Heat transfer coefficient is determined as shown in the following equation.

$$h=\frac{q''}{T_{wi}-T_{\text{sat}}}$$

The total experimental uncertainty in the measurement is classified by bias error and precision error. The 95 % confidence uncertainty of heat transfer coefficients is calculated from as follows.

$$U_h=\sqrt{B_h^2+P_h^2}$$

$$\text{bias limit}\quad \left(\frac{B_h}{h}\right)^2=\left(\frac{B_{q''}}{q''}\right)^2+\left(\frac{B_{T_{wi}}}{\Delta T}\right)^2+\left(\frac{B_{T_{\text{sat}}}}{\Delta T}\right)^2$$

$$\text{precision limit}\quad \left(\frac{P_h}{h}\right)^2=\left(\frac{P_{q''}}{q''}\right)^2+\left(\frac{P_{T_{wi}}}{\Delta T}\right)^2+\left(\frac{P_{T_{\text{sat}}}}{\Delta T}\right)^2,$$

$\Delta T=T_{wi}-T_{\text{sat}}$, where heat flux supplied to test section, q'', is

$$q''=\frac{VI\ \cos\phi}{A}$$

Because power factor, $\cos\phi$ is near to 1 and heat transfer area, A, is constant, the bias limit and precision limit of heat flux is as follows.

$$\text{Bias limit}\quad \left(\frac{B_{q''}}{q''}\right)^2=\left(\frac{B_V}{V}\right)^2+\left(\frac{B_I}{I}\right)^2$$

$$\text{Precision limit}\quad \left(\frac{P_{q''}}{q''}\right)^2=\left(\frac{P_V}{V}\right)^2+\left(\frac{P_I}{I}\right)^2$$

Therefore, uncertainty of heat transfer coefficient, U_h, is determined as follows.

$$\frac{U_h}{h}=\sqrt{\left(\frac{B_h}{h}\right)^2+\left(\frac{P_h}{h}\right)^2}$$

$$\text{bias limit}\quad \left(\frac{B_h}{h}\right)^2=\left(\frac{B_V}{V}\right)^2+\left(\frac{B_I}{I}\right)^2+\left(\frac{B_T wi}{\Delta T}\right)^2+\left(\frac{B_{T_{\text{sat}}}}{\Delta T}\right)^2$$

$$\text{precision limit}\quad \left(\frac{P_h}{h}\right)^2=\left(\frac{P_V}{V}\right)^2+\left(\frac{P_I}{I}\right)^2+\left(\frac{P_{T_{wi}}}{\Delta T}\right)^2+\left(\frac{P_{T_{\text{sat}}}}{\Delta T}\right)^2$$

1 Uncertainty of power measurement,
$U_{q''}$ $B_V/V=0.02$ % from rms voltage measurement

$$\frac{B_I}{I}=(0.2^2+0.1^2)^{0.5}=0.22\ \ \%$$

rms current measurement 0.2 %
Clamp meter accuracy 0.1 %

$$\frac{P_{q''}}{q''}=\left(\left(\frac{P_V}{V}\right)^2+\left(\frac{P_I}{I}\right)^2\right)^{0.5}=1.21\ \ \%$$

2 Uncertainty of inner wall temperature measurement, $U_{T_{wi}}$

$$\frac{B_{T_{wi}}}{\Delta T}=(5^2+0.05^2+1.0^2)^{0.5}=5.1\ \ \%$$

T-type thermocouple error 0.1°C
DC voltage measurement 0.05 %
Color-temperature conversion 1.0 %

$$\frac{P_{T_{wi}}}{\Delta T}=2.5\ \ \%$$

3 Uncertainty of saturation temperature measurement, $U_{T_{\text{sat}}}$
Uncertainty of saturation temperature is determined as shown in the following equation.

$$U_{T_{\text{sat}}}=\left.\frac{dT}{dP}\right|_{\text{sat}}\times U_p$$

$$\frac{B_{P_{\text{sat}}}}{P_{\text{sat}}}=0.25\ \ \%,\qquad \frac{P_{P_{\text{sat}}}}{P_{\text{sat}}}=0.3\ \ \%$$

$$\frac{B_{T_{\text{sat}}}}{\Delta T}=4.3\ \ \%,\qquad \frac{P_{T_{\text{sat}}}}{\Delta T}=5.18\ \ \%$$

4 Calculation of uncertainty of heat transfer coefficient

After evaluating the bias and precision errors, the uncertainty of heat transfer coefficient is calculated as follows.

$$\frac{B_h}{h}=\sqrt{\left(\frac{B_V}{V}\right)^2+\left(\frac{B_I}{I}\right)^2+\left(\frac{B_{T_{wi}}}{\Delta T}\right)^2+\left(\frac{B_{T_{\text{sat}}}}{\Delta T}\right)^2}$$
$$=(0.2^2+0.22^2+5.1^2+4.3^2)^{0.5}=6.68\ \ \%$$

$$\frac{P_h}{h}=\sqrt{\left(\frac{P_V}{V}\right)^2+\left(\frac{P_I}{I}\right)^2+\left(\frac{P_{T_{wi}}}{\Delta T}\right)^2+\left(\frac{P_{T_{\text{sat}}}}{\Delta T}\right)^2}$$
$$=(1.21^2+2.5^2+5.18^2)^{0.5}=5.88\ \ \%$$

$$\frac{U_h}{h}=\sqrt{\left(\frac{B_h}{h}\right)^2+\left(\frac{P_h}{h}\right)^2}=\sqrt{6.68^2+5.88^2}=8.9\ \ \%$$

References

[1] Wang, C. C., Kuo, C. S., Chang, Y. J., and Lu, D. C., 1996, ''Two-Phase Flow Heat Transfer and Friction Characteristics of R-22 and R-407C,'' ASHRAE Trans., **102**, Part 1, pp. 830–838.
[2] Shin, J. Y., Kim, M. S., and Ro, S. T., 1996, ''Correlation of Convective Boiling Heat Transfer in a Horizontal Tube for Pure Refrigerants and Refrigerant Mixtures,'' Korean Journal of Air-Conditioning and Refrigeration Engineering, **8**(9), pp. 254–266.
[3] Kim, S. H., Kwak, K. M., Bai, C. H., and Chung, M., 1997, ''An Experimental Study on Nucleate Boiling of Ternary Refrigerant R407C,'' Korean Journal of Air-conditioning and Refrigeration Engineering, **9**(3), pp. 276–283.
[4] Choi, T. Y., Kim, Y. J., Kim, M. S., and Ro, S. T., 2000, ''Evaporation Heat

Transfer of R-32, R-134a, R-32/134a, and R-32/125/134a inside a Horizontal Smooth Tube,'' Int. J. Heat Mass Transf., **43**, pp. 3651–3660.
[5] Kattan, N., Thome, J. R., and Favrat, D., 1998, ''Flow Boiling in Horizontal Tubes: Part 2-New Heat Transfer Data for Five Refrigerants,'' ASME J. Heat Transfer, **120**, pp. 148–155.
[6] Gungor, K. E., and Winterton, R. H. S., 1987, ''Simplified General Correlation for Flow Saturated Boiling and Comparisons of Correlations with Data,'' Chem. Eng. Res. Des., **65**, pp. 148–156.
[7] Jung, D. S., McLinden, M., Radermacher, R., and Didion, D., 1989, ''A Study of Flow Boiling Heat Transfer with Refrigerant Mixture,'' Int. J. Heat Mass Transf., **9**(1), pp. 1751–1764.
[8] Kandlikar, S. G., 1990, ''A General Correlation for Saturated Two-phase Flow Boiling Heat Transfer Inside Horizontal and Vertical Tubes,'' ASME J. Heat Transfer, **112**, pp. 219–228.
[9] Kandlikar, S. G., 1998, ''Boiling Heat Transfer with Binary Mixtures: Part II—Flow Boiling in Plain Tubes,'' ASME J. Heat Transfer, **120**, pp. 388–394.
[10] Kattan, N., Thome, J. R., and Favrat, D., 1998, ''Flow Boiling in Horizontal Tubes: Part 3-Development of a New Heat Transfer Model Based on Flow Pattern,'' ASME J. Heat Transfer, **120**, pp. 156–165.
[11] Ross, H., Radermacher, R., and Di Marzo, M., 1987, ''Horizontal Flow Boiling of Pure and Mixed Refrigerants,'' Int. J. Heat Mass Transf., **30**(5), pp. 979–992.
[12] Jung, D. S., McLinden, M., Radermacher, R., and Didion, D., 1989, ''Horizontal Flow Boiling Heat Transfer Experiments with a Mixture of R22/R114,'' Int. J. Heat Mass Transf., **32**, pp. 131–145.
[13] Yoshida, S., Mori, H., Matsunaga, T., and Ohishi, K., 1991, ''Heat Transfer to Non-Azeotropic Mixtures of Refrigerants Flowing in a Horizontal Evaporator Tube,'' *ASME/JSME Thermal Eng. Proc.*, **2**, pp. 295–300.
[14] Niederkrüger, M., Steiner, D., and Schlünder, E.-U., 1992, ''Horizontal Flow Boiling Experiments of Saturated Pure Components and Mixtures of R846-R12 at High Pressures,'' Int. J. Refrig., **15**(1), pp. 48–58.
[15] Boyd, R. D., Smith, A., and Turknett, J., 1995, ''Two-Dimensional Wall Temperature Measurements and Heat Transfer Enhancement for Top-Heated Horizontal Channels With Flow Boiling,'' Exp. Therm. Fluid Sci., **11**, pp. 372–386.
[16] Shin, J. Y., Kim, M. S., and Ro, S. T., 1997, ''Experimental Study on Forced Convective Boiling Heat Transfer of Pure Refrigerants and Refrigerant Mixtures in a Horizontal Tube,'' Int. J. Refrig., **20**, pp. 267–275.
[17] Camci, C., Kim, K., Hippensteele, S. A., and Poinsatte, P. E., 1993, ''Evaluation of a Hue Capturing Based Transient Liquid Crystal Method for High-Resolution Mapping of Convective Heat Transfer on Curved Surfaces,'' ASME J. Heat Transfer , **115**, pp. 311–318.
[18] Matsumoto, R., Kikkawa, S., and Senda, M., 1997, ''Effect of Pin Fin Arrangement on Endwall Heat Transfer,'' JSME Int. Journal, Series B, **40**(1), pp. 142–151.
[19] Kimura, I., Kuroe, Y., and Ozawa, M., 1993, ''Application of Neural Networks to Quantitative Flow Visualization,'' J. Flow Visualization and Image Processing, **1**, pp. 261.
[20] Huber, M., Gallagher, J., McLinden, M., and Morrison, G., 1996, NIST Thermodynamic Properties of Refrigerants and Refrigerant Mixtures Database (REFPROP) Version 5.0, National Institute of Standards and Technology, U.S.A.
[21] Dittus, F. W., and Boelter, L. M. K., 1930, *University of California (Berkeley) Publications of Engineering*, **2**, University of California, Berkeley, CA, pp. 443.
[22] Thome, J. R., and Shakir, S., 1987, ''A New Correlation for Nucleate Pool Boiling of Aqueous Mixtures,'' AIChE Symp. Ser., **83**(257), pp. 46–51.

Evaporation of Water Droplets Placed on a Heated Horizontal Surface

Orlando E. Ruiz
e-mail: orlando-e_ruiz@hp.com
Hewlett Packard,
Pen Technology & Manufacturing Center,
Solutions Development Group,
P.O. Box 4048,
Agüadilla, PR 00605

William Z. Black
e-mail: william.black@me.gatech.edu
Regents Professor
Georgia Institute of Technology,
George W. Woodruff School of
Mechanical Engineering,
Atlanta, GA 30332-0405

A numerical analysis of the evaporation process of small water droplets with diameters of 1 mm or less that are gently deposited on a hot isothermal solid surface has been performed. This study considers the internal fluid motion that occurs as a result of the thermocapillary convection in the droplet and it determines the effect of fluid motion on the heat transfer between the drop and the solid surface. This study is particularly relevant because the internal fluid motion has not been considered in previous numerical and analytical models presented in the literature. To assess the effects of internal fluid motion, the model results are compared to numerical results provided by a heat conduction model that neglects the fluid motion. The Navier-Stokes and Thermal Energy equations are solved using the Artificial Compressibility Method with Dual Time Stepping. Boundary-fitted grids are used to track the changes in the droplet surface shape during the evaporation process. The numerical simulations have demonstrated that the internal fluid motion provides vastly different temperature distributions in the drop compared to the results from the heat conduction model that neglects fluid motion. The evolution of the droplet geometry was simulated from an initial spherical-shaped cap until the contact angle was close to the receding contact angle. [DOI: 10.1115/1.1494092]

Keywords: Computational, Convection, Droplet, Evaporation, Thermocapillary

Introduction

Dropwise evaporative cooling is the process by which a single fluid droplet impacts a heated surface and cools by latent heat absorption which transforms the liquid into the vapor phase. The heat transfer rate during the evaporation process is much greater than traditional air cooling techniques. Dropwise evaporative cooling of a hot surface is widely used in many areas of engineering. For instance, this technique is applied in metallurgical applications, nuclear thermal management, electronic industries, and fire suppression systems. The microelectronics industry has been a major motivating influence on the research in the spray-cooling field. The thermal loads projected for future microelectronic technologies are beyond the capabilities of traditional air cooling systems. As a result, droplet evaporation has received consideration as a means to provide the high heat flux cooling that is necessary to maintain microelectronic packages at reasonable temperatures.

To understand the thermal interaction of the spray with the heated surface, a substantial amount of experimental research has been conducted to optimize the parameters of the spray cooling process. Some researchers have studied the spray cooling process by proposing theoretical and numerical models of the dropwise evaporation process. These models have been expanded based on statistical arguments to describe the spray cooling process as the collective influence of independent drops [1]. During the past two decades, researchers have modeled this process by considering heat transfer by conduction as the dominating mode of thermal energy transport and they have neglected motion of the fluid in the droplet. Various experimental studies [2–5] have demonstrated that the droplet evaporation process is a combination of the interaction among the coupled fluid dynamics, surface chemistry, and heat transfer. Most of the theoretical and numerical dropwise evaporation models have neglected the effects of fluid motion within the liquid droplets. An exception is the work of Lorenz and Mikic [6], were the effects of the thermocapillary flow in the condensation process of hemispherical water drops was determined to be insignificant. These models have considered simplifying assumptions regarding the shape of the droplet during the evaporation process, contact angle behavior, and liquid-solid interface thermal conditions.

The physical processes that take place during the droplet evaporation are complicated and consist of conjugate heat transfer between the solid and the liquid, convective fluid motion within the droplet, free surface flow, contact line motion, and surface evaporation. The heat transfer interaction between the solid and the liquid is complicated and it is based on the fact that as the droplet evaporates, the contact line travels over the heated surface making the contact surface vary with time. When droplets are placed on a solid metallic surface with a high thermal conductivity, the surface temperature changes are very small during the droplet lifetime [1,7]. For these cases, the contact surface can be treated as an isothermal boundary. This simplification allows concentrating on the transport processes in the evaporating droplet without the added complexity of the solid-liquid thermal interaction.

Convective fluid motion within the droplet can be attributed to the interaction between buoyant and thermocapillary convection cells. During the evaporation process, buoyant convection may occur as a result of the density stratification in the fluid. The thermocapillary convection is the result of an instability due to surface tension gradients at the droplet free surface. These gradients occur as a result of a non-uniform temperature distribution at the free surface. The colder fluid has higher surface tension and it pulls the warmer fluid which has a lower surface tension. This behavior sets up viscous forces in the fluid at the free surface which drag adjacent fluid layers toward the cooler regions of the droplet.

In this study the droplet evaporation process is investigated from a numerical standpoint. The value of a droplet evaporation model as a starting point for more complex spray cooling models has been proven consistently by previous researchers [1,5,8]. The difficulty of measuring local heat fluxes, temperature distributions within the droplet, and the evolution of the droplet geometry has created a need to model this process. There are several benefits to

---

Contributed by the Heat Transfer Division for publication in the JOURNAL OF HEAT TRANSFER. Manuscript received by the Heat Transfer Division March 5, 2001; revision received May 7, 2002. Associate Editor: P. S. Ayyaswamy.

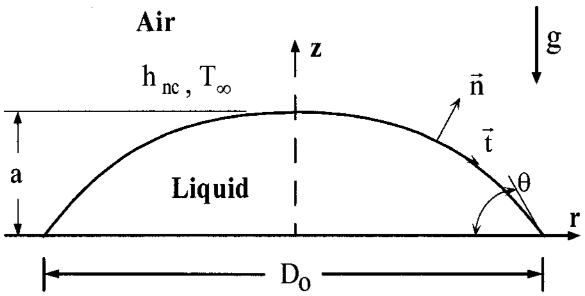

Fig. 1 Droplet geometry

this type of model. It can be used to study several parameters such as initial surface temperature, liquid subcooling, solid material thermal properties, and fluids of interest in spray cooling. A droplet evaporation model also can be used to determine optimum droplet parameters, evaporation time, heat transfer rates and temperature distributions, as well as the effect of droplet geometry on heat transfer rates.

A numerical model that assumes a small diameter liquid droplet gently deposited on a heated substrate was developed during this study. The droplet is initially shaped as a spherical cap as shown in Fig. 1. The model considers the evaporation process that takes place after the droplet impacts the substrate, spreads, and reaches an equilibrium geometry. The fluid motion that takes place in the droplet due to the thermocapillary convection effects has been modeled. This study considers the evaporation process for substrate surface temperatures for which nucleate boiling is suppressed and the contact surface with the solid remains isothermal.

A numerical model of an evaporating droplet presents many challenges. During the process, surface tension gradients along the droplet surface initiate thermocapillary flow. This flow develops convection cells below the drop surface with dimensions of the order of the droplet radius. Since the droplet surface is an interface between the liquid and the surrounding gas, free surface flow occurs. These types of problems tend to be numerically complex because the free surface position is not known a priori and must be determined from the flow field solution. The liquid-gas interface terminates at a contact line with the solid. For viscous fluids, the proper boundary condition at surfaces where a liquid and a solid are in contact is the well known no-slip condition. The fluid adheres to the solid and has the same velocity of the solid where the contact occurs. At contact lines, this boundary condition appears to break down based on a balance of the forces involved in the contact line motion. As a result, the motion of the contact line is still an active area of investigation, both experimentally and theoretically.

Another challenge that must be faced in developing a numerical model of the droplet evaporation process is the issue of time scales. The motion of the fluid develops on a time scale that is much less than the time scale of the evaporation process. The difference in these two time scales for water drops could be as large as six orders of magnitude. From a computational standpoint, this substantially complicates the analysis because the simulations must be performed on the smaller of the two time scales. As a result, a very large number of numerical iterations must be carried out before the evaporation effects have an impact on the thermal and flow fields.

Droplet Evaporation Model

Based on experimental observations of Zhang and Yang [2], Rymkiewicz and Zapalowicz [3], and Di Marzo and Evans [9], gently deposited water drops assume an initial equilibrium shape as a spherical cap. The gravity effects are small compared to the surface tension effects on the droplet shape. Based on this argument and various experimental studies in the literature [2,3,9] and visualizations studies that we have performed, we have neglected the gravity effects on the droplet shape in this study. The initial contact angle depends on many factors such as the surface material properties, surface finish, temperature, and contamination of the surface. For water drops on stainless steel surfaces, contact angles approaching 90 deg have been measured experimentally by Qiao and Chandra [10] and Chandra et al. [11]. Bernardin et al. [12] reported that for aluminum surfaces, water droplets assumed a spherical cap shape with an initial static contact angle approaching 90 deg for surface temperatures up to 120°C.

The assumption of an isothermal surface is applicable for surfaces with high thermal conductivity, such as aluminum and copper. This assumption simplifies the analysis because it permits a study of the influence of the fluid motion inside the drop on the evaporation process without the complexity of studying the transient interaction between the solid and the liquid. Figure 1 provides a sketch of the geometry that has been considered in the present model. The contact diameter (D_o), also called wetted diameter, is kept constant during most of the evaporation process. The apex dimension (a) and the contact angle (θ) are allowed to vary as the volume of the drop decreases due to evaporation. The droplet has been modeled in a cylindrical coordinate system with the radial coordinate (r) along the horizontal direction and the axial coordinate (z) along the vertical direction. In the absence of thermal or mechanical loads in the circumferential direction, the process is assumed to be axisymmetric without swirl.

To determine the effects of internal fluid motion on the evaporation process, a comparison between two numerical models with and without fluid motion has been performed. The numerical model that accounts for the fluid motion will be referred from this point on as the convection model and the numerical model without fluid motion will be referred as the conduction model. The goal of this study is to accurately model the thermal convection effects during the process and to understand the impact of convective motion on the evaporation rates of small drops. Previous numerical models of evaporating drops have neglected the internal fluid motion. This study extends the scientific understanding of the evaporation process by modeling the fluid motion and its effects on the thermal field within the drops.

Convection Model. The heat transfer and fluid motion in the droplet are governed by the Navier-Stokes and the Conservation of Energy equations. Since no gradients or motion in the circumferential direction will be considered, the equations can be simplified for an axisymmetric coordinate system. The dimensionless Navier-Stokes and Conservation of Energy equations for a fluid with constant properties and an axisymmetric domain are the following:

$$\frac{1}{r}\frac{\partial(ru)}{\partial r}+\frac{\partial v}{\partial z}=0 \tag{1}$$

$$\frac{\partial u}{\partial t}+\frac{1}{r}\frac{\partial(ru^2)}{\partial r}+\frac{\partial(uv)}{\partial z}=-\frac{\partial P}{\partial r}-\frac{1}{r\,\mathrm{Re}}\frac{\partial}{\partial r}\left(r\frac{\partial u}{\partial r}\right)+\frac{u}{r^2\,\mathrm{Re}}-\frac{1}{\mathrm{Re}}\frac{\partial}{\partial z}\left(\frac{\partial u}{\partial z}\right) \tag{2}$$

$$\frac{\partial v}{\partial t}+\frac{1}{r}\frac{\partial(ruv)}{\partial r}+\frac{\partial(v^2)}{\partial z}=-\frac{\partial P}{\partial z}+\frac{1}{r\,\mathrm{Re}}\frac{\partial}{\partial r}\left(r\frac{\partial v}{\partial r}\right)+\frac{1}{\mathrm{Re}}\frac{\partial}{\partial z}\left(\frac{\partial v}{\partial z}\right)+\frac{\mathrm{Ra}}{\mathrm{Re}^2\,\mathrm{Pr}}T \tag{3}$$

$$\frac{\partial T}{\partial t}+\frac{1}{r}\frac{\partial(ruT)}{\partial r}+\frac{\partial(vT)}{\partial z}=\frac{1}{r\,\mathrm{Re}\,\mathrm{Pr}}\frac{\partial}{\partial r}\left(r\frac{\partial T}{\partial r}\right)+\frac{1}{\mathrm{Re}\,\mathrm{Pr}}\frac{\partial}{\partial z}\left(\frac{\partial T}{\partial z}\right). \tag{4}$$

The velocity field expressed in axisymmetric cylindrical coordinates has u and v components in the radial (r) and axial (z)

directions respectively. The variables P and T correspond to the pressure and temperature respectively. Since the evaporation process is slow and the fluid velocities are not expected to be large, the viscous dissipation term that typically appears in the Conservation of Energy equation can be neglected. A body force term in the axial direction has been used to characterize the natural convective motion of the fluid during the transient evaporation process. Since the fluid is assumed incompressible, the buoyant convection effects are modeled using the Boussinesq approximation. For small drops, this mode of convection can be insignificant in comparison to the thermocapillary convection in the drop. However, this body force term can become relevant in situations involving large drops in which the thermocapillary effects are less important. The governing equations were dimensionalized based on the length scale (R_o), velocity scale (U_{sc}), and temperature difference ($\Delta T = T_H - T_\infty$). The pressure was made dimensionless based on the dynamic pressure scale (ρU_{sc}^2). The dimensionless numbers Re, Pr, and Ra result from selecting these scales.

The droplet is initially at a quiescent state, and the fluid temperature is assumed to be at a uniform ambient temperature T_∞. The initial fluid velocity is assumed to be zero. The boundary conditions of the fluid domain are specified at three locations, the contact surface with the heated solid, the free surface, and the axis of symmetry. The contact surface boundary conditions enforce no-slip, no fluid penetration through the surface, and the equivalence of the liquid and solid surface temperature distributions at the contact surface. These boundary conditions are as follows:

$$u(r,0,t) = 0 \tag{5}$$

$$v(r,0,t) = 0 \tag{6}$$

$$T(r,0,t) = T_H. \tag{7}$$

where T_H is the temperature of the heated surface.

At the axis of symmetry, the boundary conditions state that no fluid penetrates this boundary and zero radial derivatives of temperature and axial fluid velocity are imposed. The symmetry boundary conditions are summarized as follows:

$$u(0,z,t) = 0 \tag{8}$$

$$\left.\frac{\partial v}{\partial r}\right|_{(0,z,t)} = 0 \tag{9}$$

$$\left.\frac{\partial T}{\partial r}\right|_{(0,z,t)} = 0. \tag{10}$$

The free surface boundary conditions are complex since this boundary deforms and moves inward as the liquid evaporates at the interface. Conservation of mass at the free surface equates the mass flux of the liquid that moves to the free surface with the mass flux of liquid that evaporates. A normal stress balance considers the local pressure difference across the interface to be equal to the sum of the surface tension stress and the normal viscous stress. A balance between viscous and surface tension forces must be enforced in a direction tangent to the free surface to incorporate the thermocapillary convection effects. Finally, the thermal boundary condition enforces a balance of conduction with natural convection and evaporative mass transfer to the environment. These boundary conditions have been derived based on a relatively slow evaporation process in which the thermal conductivity, viscosity, and density of the vapor phase are much smaller than the liquid phase properties. These boundary conditions are summarized as follows,

$$\rho(\vec{V} - \vec{V}_I) \cdot \vec{n} = m'' \tag{11}$$

$$P - P_\infty = -\kappa\sigma + \vec{n} \cdot (\underline{\underline{S}} \cdot \vec{n}) \tag{12}$$

$$\vec{t} \cdot (\underline{\underline{S}} \cdot \vec{n}) = \nabla\sigma \cdot \vec{t} \tag{13}$$

$$-k\nabla T \cdot \vec{n} = h_{nc}(T - T_\infty) + m'' h_{fg}. \tag{14}$$

The local mean curvature term in the normal stress boundary condition can be calculated by taking the divergence of the unit normal vector at the free surface as follows [13],

$$\kappa = -\nabla \cdot \vec{n}. \tag{15}$$

The evaporative mass flux is calculated based on the product of the mass transfer coefficient, h_m, and the difference between the saturated vapor density at the free surface ($\rho_{\text{vap,sat}}$) and the vapor density in the surrounding environment ($\rho_{\text{vap},\infty}$),

$$m'' = h_m(\rho_{\text{vap,sat}}(T) - \rho_{\text{vap},\infty}). \tag{16}$$

The saturated vapor density depends only on the local free surface temperature. The vapor density on the surrounding environment depends on the species concentration in the far field from the liquid drop. For the purpose of this study, the environment surrounding the droplet was assumed to be dry air and therefore the concentration of the vapor in the far field was assumed to be zero. The vapor density is a thermodynamic property of the fluid and is tabulated as a function of temperature and pressure in many references [14]. The mass transfer coefficient is determined based on the analogy between heat and mass transfer [15] using the following relationship,

$$h_m = \frac{h_{nc}}{\rho_{\text{air}} c_{p,\text{air}} \text{Le}^{2/3}} \tag{17}$$

The natural convection heat transfer rate between the droplet surface and the surrounding air is very small because both the surface area and the temperature difference between the droplet surface and the surrounding air are small. Given this condition, the Nusselt number can be approximated by its conduction limit value of 2.0 [16–18]. This simplified boundary condition reduced the complexity associated in determining the external flow field and the external thermal convection in a stagnant surrounding. The droplet shape varies as it evaporates and the heat transfer coefficient is expected to depend directly on the droplet geometry. This simplified boundary condition did not affect adversely the numerical results for the cases considered in this study. It is expected that for larger drops, the external convection may be more significant as compared to the present cases due to the larger surface area in contact with the surrounding fluid. As a result, an appropriate Nusselt number correlation must be used to account for the droplet geometry variation as the volume decreases.

During the droplet evaporation process, the liquid surface temperature varies due to the absorption of latent heat, conduction and convection of heat from the solid surface, and the heat transfer with the surroundings. The surface temperature inhomogeneity initiates Marangoni convection due to the surface tension dependence on temperature. The surface tension usually depends on the scalar fields in the system (e.g., electrical fields and temperature fields) as well as on the concentration of foreign materials on the interface. Since the temperature field is the focus of this study, an equation of state must be considered for the surface tension. The most common approach is to characterize this dependence by a linear law as follows [19],

$$\sigma = \sigma_o - \left|\frac{d\sigma}{dT}\right|(T - T_o), \tag{18}$$

where σ_o is the reference surface tension at the reference temperature T_o, and $|d\sigma/dT|$ is a constant that depends on the fluid.

As the fluid warms, buoyant convection occurs within the droplet. During the evaporation process there is an interaction of the Marangoni and buoyant convection which makes it difficult to select a characteristic velocity scale for the problem. Since the velocities associated with buoyant convection are expected to be smaller than the fluid velocities due to Marangoni convection, the selected velocity scale is based on the dominant mode of convection. The Marangoni velocity scale is selected based on a scale analysis performed on the tangential stress boundary condition, Eq. (13). The Marangoni velocity scale represents a balance between surface tension gradients at the interface and the shear stresses generated by them [20]

$$U_{sc}=\frac{\left|\frac{d\sigma}{dT}\right|\Delta T}{\mu}. \tag{19}$$

When this velocity scale is used, the Reynolds number is defined as follows:

$$\mathrm{Re}=\frac{\left|\frac{d\sigma}{dT}\right|\Delta T R_o}{\nu\mu}=\frac{\mathrm{Ma}}{\mathrm{Pr}}, \tag{20}$$

and the Marangoni number is defined as

$$\mathrm{Ma}=\frac{\left|\frac{d\sigma}{dT}\right|\Delta T R_o}{\mu\alpha}. \tag{21}$$

In addition to scaling the governing equations, the initial and boundary conditions must be scaled as well. The scaled initial conditions for the drop are the following,

$$\tilde{u}(\tilde{r},\tilde{z},0)=0 \tag{22}$$

$$\tilde{v}(\tilde{r},\tilde{z},0)=0 \tag{23}$$

$$\tilde{T}(\tilde{r},\tilde{z},0)=0. \tag{24}$$

The contact surface boundary conditions are scaled as follows:

$$\tilde{u}(\tilde{r},0,\tilde{t})=0 \tag{25}$$

$$\tilde{v}(\tilde{r},0,\tilde{t})=0 \tag{26}$$

$$\tilde{T}(\tilde{r},0,\tilde{t})=1. \tag{27}$$

The axis of symmetry boundary conditions take the following form:

$$\tilde{u}(0,\tilde{z},\tilde{t})=0 \tag{28}$$

$$\left.\frac{\partial\tilde{v}}{\partial\tilde{r}}\right|_{(0,\tilde{z},\tilde{t})}=0 \tag{29}$$

$$\left.\frac{\partial\tilde{T}}{\partial\tilde{r}}\right|_{(0,\tilde{z},\tilde{t})}=0. \tag{30}$$

Finally, the scaled free surface boundary conditions produce the following dimensionless expressions:

$$\tilde{V}_n-\tilde{V}_{I,n}=\tilde{m}'' \tag{31}$$

$$\tilde{P}=-\frac{\tilde{\kappa}}{\mathrm{Re}}\left(\frac{1}{\mathrm{Ca}}-\tilde{T}\right)+\frac{2}{\mathrm{Re}}\left(\frac{\partial\tilde{V}_n}{\partial n}-\tilde{\vec{V}}\cdot\frac{\partial\vec{n}}{\partial n}\right) \tag{32}$$

$$\frac{\partial\tilde{V}_t}{\partial n}+\frac{\partial\tilde{V}_n}{\partial s}-\tilde{\vec{V}}\cdot\left(\frac{\partial\vec{t}}{\partial n}+\frac{\partial\vec{n}}{\partial s}\right)=-\frac{\partial\tilde{T}}{\partial s} \tag{33}$$

$$-\frac{\partial\tilde{T}}{\partial n}=\mathrm{Bi}\,\tilde{T}+\frac{\mathrm{Ma}}{\mathrm{Ja}}\tilde{m}''. \tag{34}$$

The normal and tangential partial derivatives are $\partial/\partial n$ and $\partial/\partial s$, respectively. The new dimensionless numbers that result from the scaling of these boundary conditions are the Biot number (Bi), capillary number (Ca), and the Jacob number (Ja).

During the droplet evaporation process, various modes of thermal energy transport are coupled. The fluid motion in the drop allows for thermal energy transport by means of a convection process. Also, a portion of the thermal energy is transported through heat diffusion and the droplet surface experiences a temperature reduction due to the latent heat absorbed as a result of evaporation on the surface. Each of these thermal transport processes has a time scale associated with it. The thermal convection in the fluid occurs due to a combination of the thermocapillary and buoyancy effects. Based on the previous scaling analysis, the Marangoni velocity scale was chosen to model the dominant mode of convection in the process. A time scale associated with this convection mode, called the Marangoni time scale, is defined as follows:

$$t_{\mathrm{Ma}}=\frac{R_o\mu}{\left|\frac{d\sigma}{dT}\right|\Delta T}. \tag{35}$$

The thermal diffusion occurs at a much slower rate than the Marangoni convection and the time scale associated with the thermal diffusion is the thermal diffusion time scale that is defined as follows,

$$t_{\mathrm{diff}}=\frac{R_o^2}{\alpha}. \tag{36}$$

The evaporation process also occurs at a much slower rate than the Marangoni convection. A time scale for this process can be derived based on a thermal energy balance between conduction and evaporative mass transfer at the free surface. The evaporation time scale is defined here as follows,

$$t_{\mathrm{evap}}=\frac{R_o^2\rho h_{fg}}{k\Delta T}. \tag{37}$$

The Marangoni time scale is on the order of 10^{-5} to 10^{-6} second for very small water droplets while the evaporation time scale is larger by five to six orders of magnitude. For a larger temperature difference (ΔT), the evaporation process occurs faster and the velocity associated with the thermocapillary process is larger. This vast difference in time scales presents a computational challenge because the governing equations must be scaled based on the Marangoni time scale to accurately resolve the convection process. As a result, the number of computational time steps that must be accumulated before the drop experiences significant evaporation is extremely large.

Conduction Model. To determine the importance of the internal fluid motion on the droplet evaporation process, a heat conduction model was formulated. The purpose of this model was to provide information on the temperature distribution within the drop in the absence of fluid motion. The results were compared with the solution of the convection model to determine the effects of the fluid motion on the evaporation process. The governing equation describing the thermal process in an evaporating droplet in the conduction model is the Heat Conduction Equation. Assuming that the process is axisymmetric and the liquid has constant properties, the Heat Conduction Equation can be written in cylindrical coordinates as follows:

$$\frac{1}{\alpha}\frac{\partial T}{\partial t}=\frac{1}{r}\frac{\partial}{\partial r}\left(r\frac{\partial T}{\partial r}\right)+\frac{\partial^2 T}{\partial z^2}. \tag{38}$$

Since the conduction model shares the same thermal initial and boundary conditions as the convection model, these equations will only be mentioned here. The fluid is initially at uniform ambient temperature T_∞. The contact surface is isothermal at temperature T_H, Eq. (7). The axis of symmetry boundary condition was shown previously in Eq. (10). Finally, the free surface thermal balance was presented in Eq. (14). Temperature, length, and time scales are chosen as before to nondimensionalize these equations. The temperature is scaled based on the temperature difference between the heated plate and the ambient temperature. The chosen length scale is the initial contact radius R_o. The time scale for the Heat Conduction Equation is typically based on the diffusion time scale. However, in this analysis the time scale is selected equal to the Marangoni time scale so that the results can be compared on a one-to-one basis with the results provided from droplet evaporation model that includes fluid motion. Based on these scaling quantities, the governing equation for the conduction model in dimensionless form is

$$\frac{\partial \tilde{T}}{\partial \tilde{t}} = \frac{1}{\mathrm{Ma}}\left[\frac{1}{\tilde{r}}\frac{\partial}{\partial \tilde{r}}\left(\tilde{r}\frac{\partial \tilde{T}}{\partial \tilde{r}}\right) + \frac{\partial^2 \tilde{T}}{\partial \tilde{z}^2}\right]. \tag{39}$$

The initial and boundary conditions are scaled in a similar fashion as the convection model.

Numerical Method

The numerical techniques used to solve both the convection and conduction models described in the previous section are based on the Finite Difference Method. Boundary-fitted non-uniform grids were used to represent the physical domain and to track the droplet surface as the domain deforms and shrinks due to evaporation. A generalized curvilinear coordinate transformation was used to map the physical grid into a stationary uniform grid. The governing equations and boundary conditions are transformed from the physical coordinates r and z to the generalized curvilinear coordinates ξ and η as shown in Fig. 2. As a result of the transformation, the governing partial differential equations become more complex and contain additional terms that account for the geometric transformation and the grid motion. For details of the geometric transformation and the resulting partial differential equations, refer to Ruiz [21]. The benefit of the transformation results from the fact that the boundaries become coordinate lines in the computational domain. The boundary conditions are transformed and applied on these coordinate lines. This approach reduces the difficulty of implementing boundary conditions especially on boundaries that move and deform. In addition, the presence of coordinate lines at the boundaries permits moving boundaries such as free surfaces to be located with considerable accuracy.

The Artificial Compressibility method was used to solve for the fluid velocities and temperature distribution in the droplet domain. This numerical technique was first introduced by Chorin [22] to obtain steady-state solutions to the incompressible Navier-Stokes equations. The method has been used with much success by many investigators. The Artificial Compressibility method has also been extended to obtain time accurate solutions of the incompressible Navier-Stokes equations by using the Dual-Time Stepping approach [23]. In this study, the formulation of Rogers and Kwak [24] has been extended to couple the Conservation of Energy Equation and simultaneously solve for the temperature and velocity fields. The numerical scheme is implicit and second order accurate in time. The convection derivatives were approximated using a third order upwind flux-difference splitting approach [25] and the viscous derivatives were approximated using second order central differences in a collocated grid. Source terms were evaluated at the cell centers. Second order accurate forward and backward differences were used to approximate the partial derivatives in the boundary conditions.

The system of equations was marched iteratively between physical time-steps by using a Line Relaxation approach [26]. At the end of a physical time step, a converged solution was obtained when the dimensionless discrete divergence was below 10^{-4} and the dimensionless variables variation between sub-iterations was below 10^{-8}. The grid was generated at every physical time-step using an algebraic grid generation approach. Specifically, a transfinite interpolation method based on the four-boundary scheme [27,28] was used to generate the boundary-fitted grid at each physical time-step.

Results

The numerical simulations were accomplished using a computer code developed during the course of this investigation. The computer code was validated for numerical accuracy by comparison with the numerical solutions to several benchmark problems [21]. In this study, the effects of three major variables on the evaporation process were considered. These variables are the initial droplet contact diameter D_o, initial droplet contact angle θ_o, and the heated surface temperature T_H. The initial droplet diameter was assigned a value of either 1.0 mm or 0.1 mm. The size was selected because droplets within this range of sizes are obtained in many spray cooling applications. The initial contact angle was assigned a value of 90 deg or 60 deg. The heated surface temperature was set at either 80°C or 100°C. These temperatures are low enough so that nucleate boiling does not occur at the contact surface. The ambient temperature T_∞ was assumed to be constant with a value equal to 20°C. Table 1 shows these variables and the dimensionless parameters relevant to this problem (Ma,Ca,Bi,Pr,Re). In addition to the eight primary cases (1–8), two additional cases (9 and 10) for droplets with similar initial volumes and different contact angles were also considered. Based on the selection of the primary variables, the maximum Marangoni number considered was approximately 152,000 and the smallest was approximately 7000. The values for the Ca, Bi, and Pr numbers do not vary significantly since they are based almost entirely on fluid properties. The Reynolds number is equal to the ratio of the Marangoni and the Prandtl number and its value covers a range between approximately 2300 and 68,500.

The time scale associated with the thermocapillary convection is at least five orders of magnitude smaller than the evaporation time scale. The evaporation time scale characterizes the thermal interaction at the droplet surface and the deformation of the droplet shape. In this study, the difference in time scales and their significance in the numerical process has been used as an advantage. Based on numerical studies, the evolution of both the temperature and flow fields is characterized by the Marangoni time scale. Both fields become "stationary" before the deformation of the free surface can affect them. The deformation process occurs at a much slower rate that is based on the evaporation time scale.

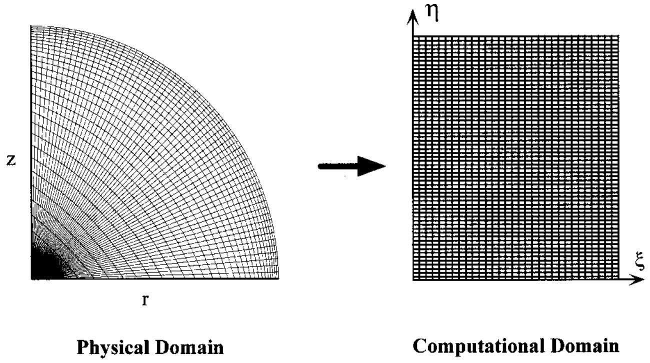

Fig. 2 Generalized curvilinear coordinate transformation

Table 1 Simulation variables and dimensionless parameters ($T_\infty = 20°C$)

Case	D_o (mm)	θ_o	T_H (°C)	Ma	Ca	Bi	Pr	Re
1	1.0	90°	80	70061	0.143	0.0428	2.988	23447
2	1.0	90°	100	119049	0.191	0.0417	2.219	53650
3	1.0	60°	80	70061	0.143	0.0428	2.988	23447
4	1.0	60°	100	119049	0.191	0.0417	2.219	53650
5	0.10	90°	80	7006	0.143	0.0428	2.988	2345
6	0.10	90°	100	11905	0.191	0.0417	2.219	5365
7	0.10	60°	80	7006	0.143	0.0428	2.988	2345
8	0.10	60°	100	11905	0.191	0.0417	2.219	5365
9	1.276	60°	100	151928	0.191	0.0417	2.219	68467
10	0.128	60°	100	15193	0.191	0.0417	2.219	6847

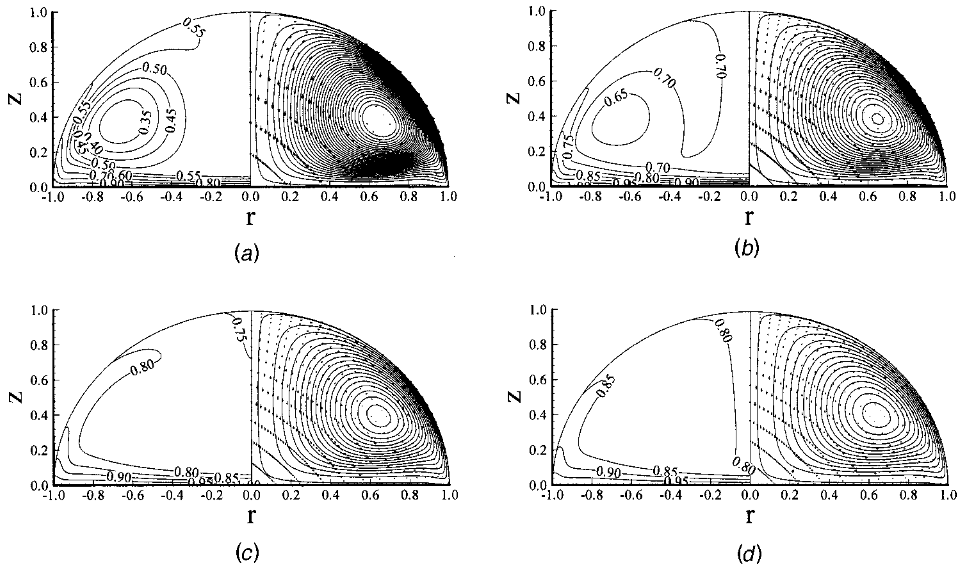

Fig. 3 Short time solution: Isotherm and Streamfunction contours (with velocity vectors superimposed) for a 0.1 mm initial contact diameter water drop on a 100°C heated surface. Initial contact angle=90 deg. Environment: $T_\infty = 20°C$, dry air: (*a*) 0.5 ms, (*b*) 1.0 ms, (*c*) 1.5 ms, and (*d*) 2.0 ms.

To obtain numerical solutions in a reasonable time, the numerical simulations of the convection model were performed in two stages. During the first stage, the governing equations were numerically integrated using a small integration time step to solve the short time transient evolution of the temperature and flow fields. A dimensionless integration time step Δt of 0.1 was sufficiently accurate for the present computations. This value corresponds to a dimensional time step of 0.1 times the Marangoni time scale. This first stage of the numerical simulation is characterized by a heating period in which the drop temperature increases due to heat transfer with the solid surface. During the same time frame, the flow field develops and affects the heating process and temperature field within the drop. The solution evolves until the thermal and flow field changes are very small. At this point in time, the isotherm and streamfunction contours appear to have reached their steady state distributions. For the drop sizes selected in this study, this process occurs during approximately the first five percent of the total evaporation time. The mass loss and volume changes that occur during this stage are small. As this nearly asymptotic state is approached, the temperature and flow field solutions resemble the steady-state solutions obtained by solving the problem without droplet mass loss and without free surface deformation.

This type of simulation will be referred to as the short time solution. The number of physical time steps required to complete the short time solution depends on the Marangoni time scale. Based on these short time simulations, a small amount of the droplet mass evaporates during the evolution of the thermal and flow fields. The numerical simulations were performed using six processors on an SGI Origin2000 parallel platform. The large drops ($D_o = 1.0\,\mathrm{mm}$) required on the order of 264 hours of computational time while the small drops ($D_o = 0.1\,\mathrm{mm}$) required between 120 to 144 hours for these short time solutions.

The second stage of the numerical solution which is referred to as the long time solution is characterized by changes in the drop geometry and volume due to the evaporation effects. Very small changes occur in the temperature and flow fields as these fields adjust to changes in the drop geometry. During this stage the solution is advanced using a larger integration time step than was used during the short time solution. The larger integration time step is carefully chosen so that it does not jeopardize the solution accuracy and stability. A dimensionless integration time step of 10.0 was used for the large diameter drops and it was 1.0 for the small drops. These integration time steps allowed the solution to advance at a faster rate and permitted a more economical solution for the thermal and flow fields. A long time solution for a droplet evaporation case required between 96 to 120 hours of runtime on the SGI Origin2000 parallel platform. The short and long time transient solutions were patched together to obtain a complete history of the evaporation process.

To determine the proper grid resolution required for the simulations in this investigation, a grid resolution study was performed. During the grid resolution study, the droplet evaporation problem was solved using four different grids with increasing levels of grid refinement. The four grids used had refinement levels of 61×31, 91×46, 121×61, and 181×91 points in the ξ and η directions respectively. Each refinement level approximately doubled the total number of grid points. Based on a comparison of the velocity profiles, temperature profiles, average Nusselt number, and apex temperature, the 121×61 grid was selected as an acceptable resolution level to perform all the numerical simulations. This resolution level provided reasonable accuracy without an excessive number of grid points. The 181×91 grid was not used due to the greater storage constraints and due to the excessive computational time requirements that would be required with this level of grid refinement.

Thermal and flow solutions are shown below that are based on the selection of one of the droplet evaporation cases. The case that was selected for this comparison consists of a water droplet initially at room conditions ($T_\infty = 20°C$). The droplet has an initial contact radius of 0.1 mm and an initial contact angle of 90 deg. The heated surface temperature T_H is maintained at 100°C. This corresponds to case 6 in Table 1. The results of the other cases in Table 1 are not presented because the results of case 6 show the same trends and characteristics and due to space limitations. Isotherm and streamfunction contours have been used to quantify the changes in the thermal and flow fields for both the short and long time solutions. Isotherm contours are also shown for the conduction model based on the same conditions used for the convection model.

Short Time Solution. Figure 3 shows a time sequence of the isotherm and streamfunction contours throughout the water droplet for the conditions identified as Case 6 in Table 1. These con-

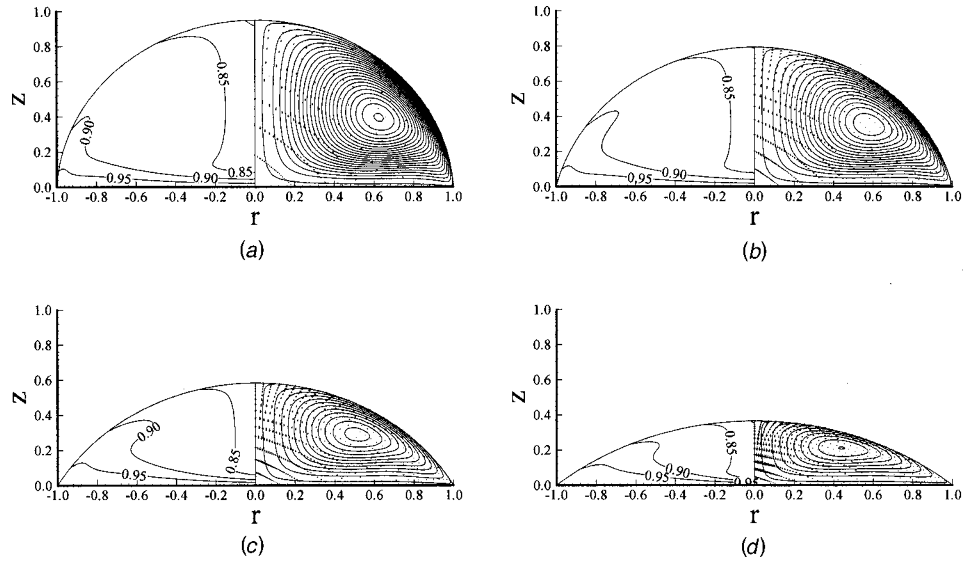

Fig. 4 Long time solution: Isotherm and Streamfunction contours (with velocity vectors superimposed) for a 0.1 mm initial contact diameter water drop on a 100°C heated surface. Initial contact angle=90 deg. Environment: $T_\infty = 20°C$, dry air: (*a*) 5 ms, (*b*) 20 ms, (*c*) 40 ms, and (*d*) 60 ms.

tours represent the evolution of the thermal and flow fields during the initial transient period described by the short time solution. The short time solution for case 6 has a total duration of 5.23 ms. The isotherm contours shown are for 0.5, 1.0, 1.5, and 2.0 ms after the start of the evaporation process. During approximately the initial 1.5 ms of the evaporation process, the violent startup of the thermal and flow fields cause the cold fluid in the drop to be entrained inside a circulation cell. The droplet surface warms very fast due to the strong thermal convection that occurs early in the heating process. The isotherms are concentrated near the contact surface ($z=0$) demonstrating the existence of a thermal boundary layer near this boundary. The isotherms meet the axis of symmetry orthogonally due to the symmetry required at that boundary. As time increases (>2.0 ms), the changes in thermal field occur at a slower rate and a nearly steady temperature distribution results. A small amount of the total droplet volume has left due to evaporation during this time. For times greater that 2.0 ms, the isotherms are less concentrated near the contact surface when compared to the initial startup process. The temperatures inside the drop are well above the initial isothermal temperature that existed at time=0.

A circulation cell with a size of the order of the contact radius of the drop was observed in all the cases considered in this study. Since the model assumes axial symmetry about the vertical axis, the circulation cell forms a toroid in three-dimensional space. During the startup process, the radial and axial location of the center of circulation shifts with time. The motion of the cell center decays until the flow field becomes nearly stationary. The circulation cell pulsates and moves during this initial transient. This pulsating behavior can be observed using computer animations of the isotherms and viewing the streamfunction contours as a function of time.

During the short time solution large temperature and velocity gradients occurred at the contact surface with the solid. The flow field was characterized by a tangential velocity distribution at the droplet surface while the fluid traveled from the contact line to the droplet apex. The flow field at the axis of symmetry consisted of cooler fluid and it resembled an impingement type flow. The temperature distribution inside the droplet showed very curved isotherms demonstrating the strong influence of the flow field on the thermal process. The isotherms were concentrated near the contact surface with the solid providing evidence of the large temperature gradients at this boundary. The changes in the droplet volume due to the evaporation process were very small during the short time solution interval.

The instantaneous contours displayed in this section show the relevant features that occur during the startup process. The streamfunction contour lines exhibit a curved pattern near the contact line ($r=R_{CL}$). Also, the streamfunction contour lines are concentrated near the droplet surface. This is clear evidence of the high velocity gradients that exist near the droplet surface. The surface tension gradient along the droplet surface results in a tangential stress that drags the fluid layers next to the surface toward cooler regions. The streamfunction contours decrease in magnitude away from the center of circulation as can be seen from the increased spacing between contour lines. As time increases, the velocity of the fluid throughout the drop decreases until a nearly steady velocity field is established.

Long Time Solution. The long time solution results of the evaporation process presented in this section are a continuation of the short time solution results for the same conditions identified in the previous section (Case 6). For this simulation, the numerical calculations were continued until a physical time of approximately 72.1 ms had transpired. The contact angle predicted at this time was approximately 26.0 deg and the volume remaining in the drop was 17.6 percent of the original volume. Since the contact angle is greater than the receding angle which is approximately 10 deg for water on a metallic surface [12], the contact line remained at the same location throughout the entire time of the simulation. The convergence of the numerical computations deteriorated beyond 72.1 ms. Beyond this time, the grid became very distorted. Grid distortion is inevitable because as the contact angle approaches the receding angle, the droplet resembles a thin film. Based on personal experimental observations of small water droplets evaporating on heated surfaces, the deformation process at these low contact angles becomes non-symmetric and the symmetry assumed in the model is no longer valid. Rymkiewicz and Zapalowicz [3] and Chandra et al. [11] have also observed this behavior.

It is possible that the circumferential component of the velocity is no longer insignificant from this point on. The numerical model assumes that the problem is axisymmetric with no circumferential motion. Experience with other numerical problems (e.g., the flow over a backward facing step and the axisymmetric sudden expan-

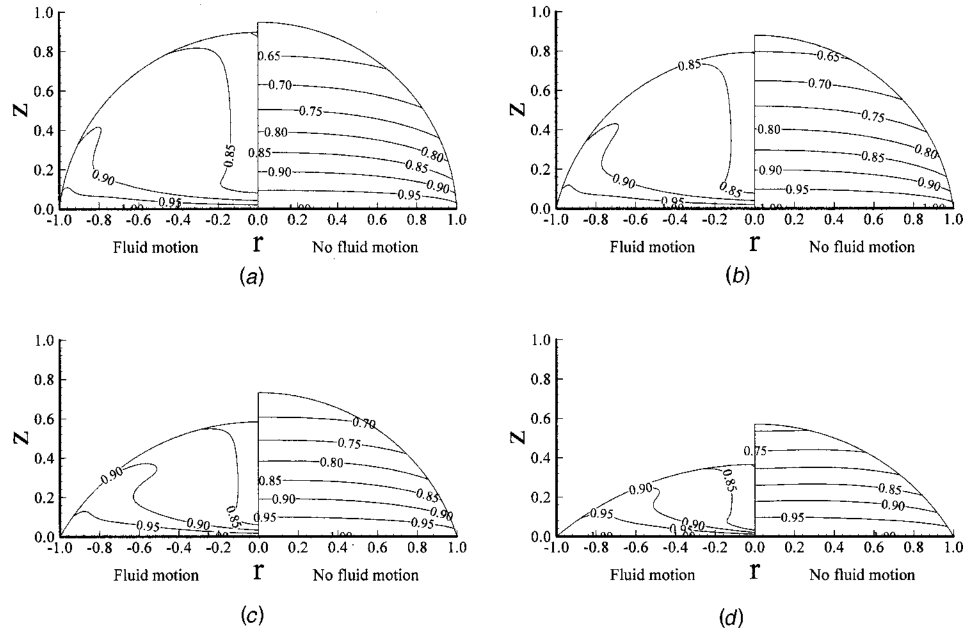

(*a*) (*b*)

(*c*) (*d*)

Fig. 5 Isotherm contours comparison between the numerical solutions with fluid motion and without fluid motion for a water drop with an initial contact diameter of 0.1 mm, 100°C heated surface, and initial contact angle=90 deg. Environment: $T_\infty = 20°C$, dry air: (*a*) 10 ms, (*b*) 20 ms, (*c*) 40 ms, and (*d*) 60 ms.

sion flow) using the present formulation has shown that the convergence deteriorates as the flow field becomes three-dimensional. Therefore difficulty with the convergence of the numerical computations may be one way of detecting a transition in the flow field. Though the numerical formulation takes into account the non-orthogonal contributions in the fluxes and on the boundary conditions, there will be some discretization error associated with the distortion of the grids.

Figure 4 shows long time instantaneous isotherm and streamfunction contours for this case. The contours are shown at times of 5, 20, 40, and 60 ms. These contours show the long time changes in the droplet geometry and their effects on the temperature distribution in the drop. As the evaporation process occurs, the droplet volume decreases as demonstrated by the decrease in the droplet apex height and the motion of the droplet surface. The position of the isotherms changes to satisfy the energy balance at the boundaries. No significant variation occurs in the isotherm spacing near the contact surface. The isotherms are very distorted near the droplet free surface indicating a strong influence of the fluid motion in the thermal process. The contour lines meet the axis of symmetry orthogonally as expected. The streamfunction contours show that only one cell remains during the time interval of the simulation. The center of the circulation cell moves down as the cell size decreases and the droplet surface compresses the circulation cell against the contact surface.

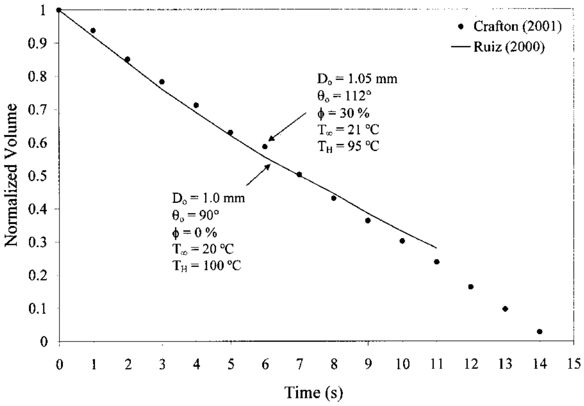

Fig. 6 Water droplet normalized volume comparison with experimental data of Crafton [29]

Conduction Model. Figure 5 show instantaneous contours of the dimensionless temperature distribution in the drop based on the results of the convection and conduction models. The isotherm contour lines for the conduction model are almost horizontal in contrast with the distorted isotherms that are observed in the convection model results. As the droplet evaporates, the contour lines adjust to the new shape and the boundary conditions. The isotherms intersect the axis of symmetry orthogonally, as expected. When these results are compared with the long time solution (time >5 ms) of the convection model, it can be noticed that the conduction model underpredicts the speed of the evaporation process. The temperature levels inside the drop predicted by the conduction model are lower in the top half of the drop throughout most of the process compared to the predictions of the convection model. The influence of the fluid motion produces a warmer droplet surface. Since the evaporative mass flux is based on the local temperature distribution at the droplet surface, a warmer surface will result in a larger evaporative mass flux. Therefore, the convection model predicts a faster evaporation rate from the surface of the drop as demonstrated in Fig. 5.

Droplet Volume. In Figure 6 a comparison of the normalized droplet volume is made with the experimental data from Crafton [29]. The normalized droplet volume is defined as the current droplet volume divided by the initial droplet volume. The experimental data considers a water droplet with an initial contact diameter of 1.05 mm and initial contact angle of 112 deg placed on an aluminum surface at 95°C. The surroundings of the droplet were at 21°C and a relative humidity of 30 percent. The numerical results are in close agreement with the experimental data. The comparison demonstrates that the normalized volume decreases in a relatively linear fashion as time elapses.

Conclusions

A numerical study of the evaporation process of small water droplets on hot isothermal solid surfaces has been performed. The present numerical study has taken into account the effects of fluid motion on the evaporation of small droplets by modeling the thermocapillary convection that occurs during the process. Most of the experimental studies in the literature have concentrated on larger drops and temperatures above saturation for which nucleate boiling occurs. No other simulations in the current literature have considered the internal fluid motion and the droplet geometrical changes that occur during the evaporation process.

A computational strategy consisting of modeling the evaporation process in two solution stages called the short and long time solutions was implemented. The short time solution showed large changes in the thermal and flow fields with small changes in the geometry due to evaporation. In addition, the short time solution showed that the temperature and flow fields become stationary after the initial transient period. The long time solution showed no significant variation in the thermal and flow fields as the geometry changed due to the evaporation of the water drop. This computational strategy of dividing the solution in a short time and a long time solution has been successful because of the asymptotic trend of the thermal and flow fields during the short time solution. As a result, the computational strategy allowed the advance of the long time solution using larger integration time steps without compromising the numerical accuracy and reducing the total solution time.

The simulations using the convection model were terminated when the contact angle approached the receding angle. The numerical convergence deteriorated as the droplet contact angle approached the receding angle value of 10 deg. There is a possibility that this convergence deterioration is a result of the numerical model being incompatible with the assumption of an axisymmetric flow field and deformation process when the contact line motion starts. Experimental observation has shown that the evaporation process becomes asymmetric as the contact line motion occurs. The numerical convergence deterioration that occurs when the contact angle approaches the receding angle seems to indicate that the axisymmetric assumption is no longer appropriate. Perhaps, a three-dimensional model that takes into account the circumferential fluid motion is better suited to model the contact angle transition and the asymmetric deformation process that occurs when the contact line moves.

The conduction model results were compared with the results of the convection model. The conduction model predicted slower rates of change of the droplet volume, height, and contact angle. The conduction model predicted larger values of the volume, height, and contact angle compared to the convection model at corresponding times. Based on these comparisons, it is obvious that fluid motion plays a very important role in the transport processes during the evaporation process of small water drops in horizontal surfaces. The fluid motion significantly affects the thermal field in the droplet, and the temperature distribution at the droplet surface determines the rate of mass loss due to evaporation. A model without fluid motion underpredicts the rate of change of the droplet mass and overpredicts the evaporation times.

The numerical results were in close agreement with experimental data of the normalized volume for gently deposited small water droplets. The close agreement with the experimental results suggests that using the Reynolds Analogy and the conduction limit ($\mathrm{Nu}=2.0$) to determine the mass transfer coefficient at the free surface had no adverse impact on the droplet volume predictions. These results demonstrate the applicability of the numerical model to predict the droplet shape evolution as the fluid evaporates. This type of model can be used to predict temperature distributions and fluid velocities in small drops were non-invasive measuring techniques are unfeasible and very difficult to accomplish.

Nomenclature

a = droplet apex
Bi = Biot number, $\mathrm{Bi}=h_{nc}k/R_o$
Ca = capillary number, $\mathrm{Ca}=|d\sigma/dT|\Delta T/\sigma_o$
c_p = liquid specific heat
D_o = initial contact diameter
$D_{\text{vap-air}}$ = binary diffusion coefficient of the vapor species into air
g = acceleration of gravity
h_{fg} = latent heat of vaporization
h_m = mass transfer coefficient
h_{nc} = natural convection heat transfer coefficient
Ja = Jacob number, $\mathrm{Ja}=h_{fg}/c_p\Delta T$
k = liquid thermal conductivity
k_{air} = air thermal conductivity
Le = Lewis number, $\mathrm{Le}=\alpha_{\text{air}}/D_{\text{vap-air}}$
m = droplet mass
m'' = mass flux across the droplet surface
Ma = Marangoni number, $\mathrm{Ma}=|d\sigma/dT|\Delta TR_o/\mu\alpha$
$\vec{n}$ = unit normal vector to the droplet surface
Nu = Nusselt number, $\mathrm{Nu}=h_{nc}D/k_{\text{air}}$
P = pressure
Pr = Prandtl number, $\mathrm{Pr}=\nu/\alpha$
r = radial coordinate
Ra = Rayleigh number, $\mathrm{Ra}=g\beta\Delta TR_o^3/\nu\alpha$
Re = Reynolds number, $\mathrm{Re}=U_{sc}R_o/\nu$
R_o = initial contact radius
$\underline{\underline{S}}$ = viscous stress tensor
T = temperature
t = time
t_{diff} = thermal diffusion time scale
t_{evap} = evaporation time scale
T_H = heated surface temperature
t_{Ma} = Marangoni time scale
$\vec{t}$ = unit tangential vector to the droplet surface
Δt = physical time increment
ΔT = temperature difference scale
u,v = radial and axial velocity components
U_{sc} = velocity scale
$\vec{V}$ = velocity vector
z = axial coordinate
$\sim$ = denotes a dimensionless quantity

Greek

α = liquid thermal diffusivity
α_{air} = air thermal diffusivity
ε_{sv} = convergence parameter for the state vector pseudotime variation
θ = contact angle
κ = local mean curvature
μ = liquid dynamic viscosity
ν = liquid kinematic viscosity
ξ, η, τ = computational space coordinates
$\rho_{\text{vap,sat}}$ = saturated density of the vapor at the surface temperature
$\rho_{\text{vap},\infty}$ = vapor density in the ambient
σ = surface tension

Subscript

∞ = ambient condition
air = air property
I = interface
n = normal component
o = reference state
t = tangential component

References

[1] Liao, Y., 1992, ''Dropwise Evaporative Cooling of Solid Surfaces,'' Ph.D. thesis, University of Maryland, College Park, MD.
[2] Zhang, N., and Yang, Wen-Jei, 1982, ''Natural Convection in Evaporating Minute Drops,'' ASME J. Heat Transfer, **104**, pp. 656–662.
[3] Rymkiewicz, J., and Zbigniew, Z., 1993, ''Analysis of the Evaporation Process for Water Droplet on Flat Heated Surface,'' Int. Commun. Heat Mass Transfer, **20**, pp. 687–697.
[4] Yang, Wen-Jei, 1975, ''Theory on Vaporization and Combustion of Liquid Drops of Pure Substances and Binary Mixtures on Heated Surfaces,'' Institute of Space and Aeronautical Science, University of Tokyo, Report No. 535, pp. 423–455.
[5] Bonacina, C., Del Giudice, S., and Comini, G., 1979, ''Dropwise Evaporation,'' ASME J. Heat Transfer, **101**, pp. 441–446.
[6] Lorenz, J. J., and Mikic, B. B., 1970, ''The Effect of Thermocapillary Flow on Heat Transfer in Dropwise Condensation,'' ASME J. Heat Transfer, **92**, pp. 46–52.
[7] Di Marzo, M., Tartarini, P., Liao, Y., Evans, D., and Baum, H., 1993, ''Evaporative Cooling Due to a Gently Deposited Droplet,'' Int. J. Heat Mass Transf., **36**, pp. 4133–4139.
[8] Tio, K.-K., and Sadhal, S. S., 1992, ''Thermal Analysis of Droplet Spray Evaporation from a Heated Solid Surface,'' ASME J. Heat Transfer, **114**, pp. 220–226.
[9] Di Marzo, M., and Evans, D. D., 1987, ''Evaporation of a Water Droplet Deposited on a High Thermal Conductivity Solid Surface,'' *Proceedings of the 24th National Heat Transfer Conference and Exhibition, Heat and Mass Transfer in Fire*, Pittsburgh, PA, pp. 11–18.
[10] Qiao, Y. M., and Chandra, S., 1995, ''Evaporative Cooling and Enhancement by Addition of a Surfactant to Water Drops on a Hot Surface,'' *ASME National Heat Transfer Conference*, Portland, Oregon, **2**, pp. 63–71.
[11] Chandra, S., Di Marzo, M., Qiao, Y. M., and Tartarini, P., 1996, ''Effect of Liquid-Solid Contact Angle on Droplet Evaporation,'' G Ital. Med. Lav Ergon, **27**, pp. 141–158.
[12] Bernardin, J. D., Mudawar, I., Walsh, C. B., and Franses, E. I., 1997, ''Contact Angle Temperature Dependence for Water Droplets on Practical Aluminum Surfaces,'' Int. J. Heat Mass Transf., **40**, pp. 1017–1033.
[13] Aris, R., 1962, *Vectors, Tensors, and the Basic Equations of Fluid Mechanics*, Prentice-Hall, Inc., Englewood Cliffs, NJ.
[14] Black, W. Z., and Hartley, J. G., 1996, *Thermodynamics*, HarperCollins College Publishers, New York, NY.
[15] Incropera, F. P., and DeWitt, D. P., 1990, *Fundamentals of Heat and Mass Transfer*, John Wiley & Sons, New York.
[16] Yang, W., 1978, ''Mechanics of Droplet Evaporation on Heated Surfaces,'' Lett. Heat Mass Transfer **5**, pp. 151–166.
[17] Kreith, F., and Black, W. Z., 1980, *Basic Heat Transfer*, Harper & Row, NY, p. 259.
[18] Mills, A. F., 1999, *Basic Heat & Mass Transfer*, Prentice Hall Inc., NJ.
[19] Carey, V. P., 1992, *Liquid-Vapor Phase Change Phenomena—An Introduction to the Thermophysics of Vaporization and Condensation Processes in Heat Transfer Equipment*, Hemisphere Publishing Corporation, Washington.
[20] Ostrach, S., 1982, ''Low-Gravity Fluid Flows,'' Annu. Rev. Fluid Mech., **14**, pp. 313–345.
[21] Ruiz, O. E., 2000, ''Numerical Analysis of the Dropwise Evaporation Process,'' Ph.D. thesis, Georgia Institute of Technology, Atlanta, GA.
[22] Chorin, A. J., 1967, ''A Numerical Method for Solving Incompressible Viscous Flow Problems,'' J. Comput. Phys., **2**, pp. 12–26.
[23] Merkle, C. L., and Athavale, M., 1987, ''Time-Accurate Unsteady Incompressible Flow Algorithm Based on Artificial Compressibility,'' AIAA Paper 87-1137-CP.
[24] Rogers, S. E., Kwak, D., and Kiris, C., 1989, ''Numerical Solution of the Incompressible Navier-Stokes Equations for Steady-State and Time-Dependent Problems,'' AIAA Paper 89-0463.
[25] Rogers, S. E., and Kwak, D., 1991, ''An Upwind Differencing Scheme for the Incompressible Navier-Stokes Equations,'' Appl. Numer. Math., **8**, pp. 43–64.
[26] Rogers, S. E., 1995, ''A Comparison of Implicit Schemes for the Incompressible Navier-Stokes Equations with Artificial Compressibility,'' AIAA Paper 95-0567.
[27] Vinokur, M., and Lombard, C. K., 1983, ''Algebraic Grid Generation with Corner Singularities,'' *Advances in Grid Generation*, ASME FED Vol. 5, K. N. Ghia and U. Ghia, eds., New York, pp. 99–106.
[28] Shih, T. I-P., Bailey, R. T., Nguyen, H. L., and Roelke, R. J., 1991, ''Algebraic Grid Generation for Complex Geometries,'' Int. J. Numer. Methods Fluids, **13**, pp. 1–31.
[29] Crafton, E. F., 2001, ''Measurements of the Evaporation Rates of Heated Liquid Droplets,'' M.S. thesis, Georgia Institute of Technology, Atlanta, GA.

A Cavity Activation and Bubble Growth Model of the Leidenfrost Point

John D. Bernardin
Assoc. Mem. ASME

Issam Mudawar
e-mail: mudawar@ecr.purdue.edu
Fellow ASME

Boiling and Two-Phase Flow Laboratory,
School of Mechanical Engineering,
Purdue University,
West Lafayette, IN 47907

This study presents a new mechanistic model of the Leidenfrost point (LFP); the minimum liquid/solid interface temperature required to support film boiling on a smooth surface. The model is structured around bubble nucleation, growth, and merging criteria, as well as surface cavity size characterization. It is postulated that for liquid/solid interface temperatures at and above the LFP, a sufficient number of cavities (about 20 percent) are activated and the bubble growth rates are sufficiently fast that a continuous vapor layer is established nearly instantaneously between the liquid and the solid. The model is applicable to both pools of liquid and sessile droplets. The effect of surface cavity distribution on the LFP predicted by the model is verified for boiling on aluminum, nickel and silver surfaces, as well as on a liquid gallium surface. The model exhibits good agreement with experimental sessile droplet data for water, FC-72, and acetone. While the model was developed for smooth surfaces on which the roughness asperities are of the same magnitude as the cavity radii (0.1–1.0 μm), it is capable of predicting the boundary or limiting Leidenfrost temperature for rougher surfaces with good accuracy.

[DOI: 10.1115/1.1470487]

Keywords: *Boiling, Bubble Growth, Cavities, Heat Transfer*

1 Introduction

The competitive demands of industry for products with enhanced material properties which can be manufactured more efficiently and with greater cost effectiveness are continually shaping and advancing processing techniques. For example, processing of aluminum alloys has received considerable attention from the automobile and aerospace industries because of such attributes as high strength-to-weight ratio, corrosion resistance, and recyclability. However, the replacement of steel components with aluminum alloy counterparts has been restricted, in part, by limited knowledge of the heat transfer aspects associated with quenching of extrusions, castings, forgings, and other heat treated parts.

Quenching involves rapid cooling of a part to control microstructural development and hence dictates material properties [1]. Figure 1 shows a typical temperature-time history of an aluminum part during a quench. The curve is divided into four distinct regimes, each possessing unique heat transfer characteristics. In the high temperature, or film boiling regime, the quench proceeds rather slowly as liquid-solid contact is prevented by the formation of an insulating vapor blanket. The lower temperature boundary of this regime is referred to as the Leidenfrost point (LFP), below which partial liquid-solid contact increases cooling rate. As discussed by Bernardin and Mudawar [1], most of the material transformations for aluminum alloys occur at temperatures above the LFP, while warping and distortions are caused by thermal stresses resulting from the large cooling rates at temperatures below the LFP. Consequently, accurate knowledge of the Leidenfrost temperature and the parameters which govern its behavior is paramount to controlling the quenching process and subsequent material properties. It must be emphasized that boiling is an interfacial phenomenon. Consequently, the Leidenfrost temperature corresponds to that of the liquid-solid interface at the LFP, which may differ significantly from temperatures within the solid.

In a previous study by the authors [2], a fairly comprehensive experimental assessment of the Leidenfrost phenomenon was performed, which included data for acetone, benzene, FC-72, and water on heated aluminum surfaces with various surface finishes. The same study also explored the effects of surface material (copper, nickel, silver, and aluminum), liquid subcooling, liquid degassing, surface roughness, and chemical residue on the Leidenfrost point. In addition, several Leidenfrost point models developed over the past four decades were reviewed and assessed. These models include hypotheses adopted from different disciplines, such as hydrodynamic instability theory, metastable physics, thermodynamics, and surface chemistry. Table 6 of Ref. [2] reveals these models fail to accurately and consistently predict the Leidenfrost temperature for sessile droplets.

The model proposed and verified in this paper is based on surface cavity size characterization as well as bubble nucleation, growth, and merging criteria. It is consistent with the relationship between surface cavities and the boiling phenomena reported in early nucleate boiling literature. In these studies, scanning electron microscopy identified micron-sized cavities on macroscopically polished surfaces and high-speed photography recorded bubble formation speculated to originate from vapor trapped within these cavities [3–5]. In conjunction with these early observations, a bubble incipience model to predict the surface superheat required to form vapor bubbles from surface cavities was developed [6–9]. The focus of continuing investigations was to correlate the observed heat flux and superheat characteristics to the number density of active cavities [4,5,10,11]. It has been well documented in these studies that as the surface superheat is increased, the number of active nucleation sites increases up to some maximum point at which bubble coalescence occurs and a vapor blanket begins to develop, covering nearly 50 percent of the surface at critical heat flux [4].

In the present study, it is hypothesized that as the Leidenfrost temperature is approached from the boiling incipience temperature, *smaller and more numerous surface cavities become activated, and the growth rate of these bubbles increases appreciably*. For liquid-solid interface temperatures at and above the LFP, a sufficient number of cavities are activated and the bubble growth rates are large enough that *liquid in immediate vicinity of the*

Contributed by the Heat Transfer Division for publication in the JOURNAL OF HEAT TRANSFER. Manuscript received by the Heat Transfer Division June 30, 2001; revision received January 7, 2002. Associate Editor: T. Y. Chu.

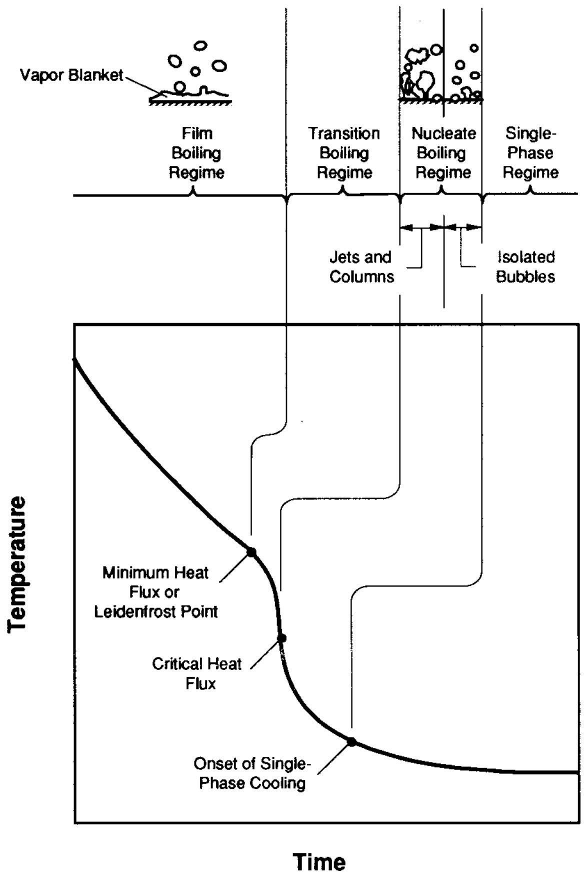

Fig. 1 Temperature-time history of a surface during quenching in a bath of liquid

surface is nearly instantaneously converted to vapor upon contact, enabling a continuous insulating vapor layer to form between the liquid and the solid.

To help explain the rationale of the proposed LFP model, Fig. 2 displays the sessile droplet evaporation time versus wall superheat, exhibiting the four distinct boiling regimes indicated in the cooling curve of Fig. 1. In this example, the interface temperature refers to that at which the liquid and the solid come in contact. Included in Fig. 2 are photographs depicting the vapor layer development for sessile water droplets approximately 2 ms after making contact with a polished aluminum surface at four interface temperatures. At an interface temperature of $T_i = 137°\mathrm{C}$, corresponding to the transition boiling regime, individual vapor bubbles occupying roughly 15 percent of the liquid-solid contact area are visible throughout the liquid film. At 151°C, approaching the LFP, the bubble density increases significantly, covering nearly 50 percent of the droplet underside. As the interface temperature increases further, bubble density also increases, signaling the formation of a continuous vapor layer beneath the droplet. The LFP corresponds to the minimum liquid-solid interface temperature required to sustain a continuous vapor layer, as suggested in Fig. 2 for $T_i = 165°\mathrm{C}$. At and above the LFP, the vapor layer beneath the droplet allows surface tension forces in the liquid to reduce the droplet's outer diameter noticeably as shown in Fig. 2 for $T_i = 180°\mathrm{C}$.

To fully appreciate the proposed model, the structure of solid surfaces and its influence on the boiling process must first be explored.

Characterization of Surfaces. A typical surface is made up of many imperfections, including pits, scratches, and bumps. In addition, there is no definite region on a particular length scale which can be considered as roughness or waviness. As mentioned by Ward [12], a surface generally exhibits self-similarity, meaning that its appearance remains basically the same over a wide range of magnifications. This behavior is described in Fig. 3(*a*), in which a hypothetical surface profile is shown at various magnifications. Surface roughness features appear to repeat themselves as the magnification is increased again and again. Based on this type

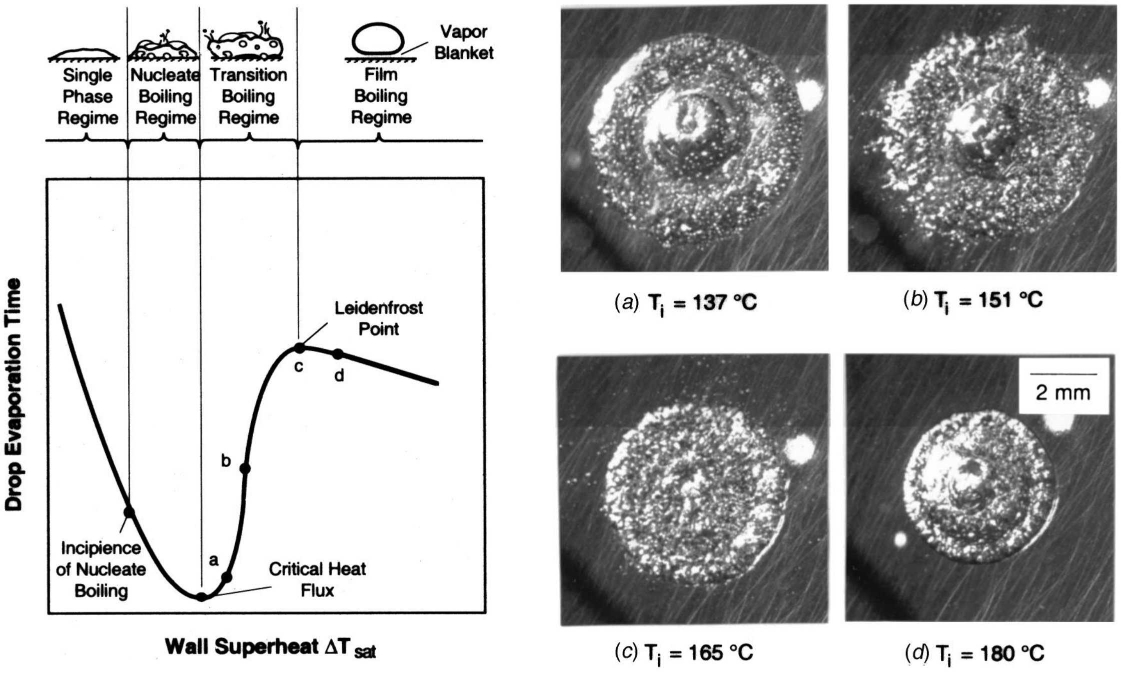

(*a*) T_i = 137 °C

(*b*) T_i = 151 °C

(*c*) T_i = 165 °C

(*d*) T_i = 180 °C

Fig. 2 Sessile droplet evaporation curve and corresponding photographs of water droplets approximately 2 ms after contact with a polished aluminum surface

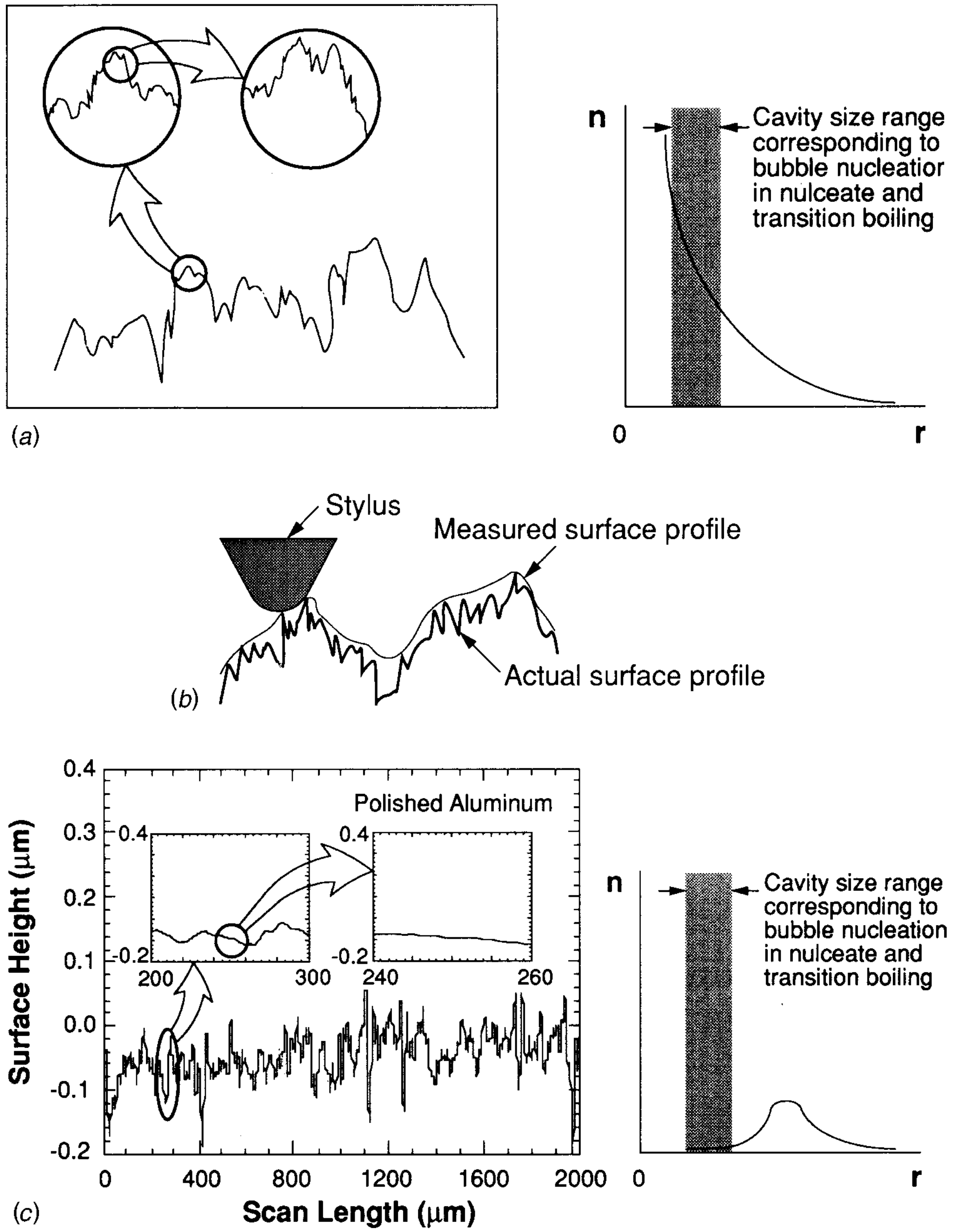

Fig. 3 Depiction of (*a*) an actual surface profile exhibiting self-similarity and the corresponding cavity size distribution, (*b*) sensitivity limitation of a stylus of a surface contact profilometer, and (*c*) a polished aluminum surface profile (with an arithmetic average surface roughness of 26 nm) measured with a contact profilometer and the corresponding cavity size distribution

of surface description, it is reasonable to conclude that the surface consists of relatively large craters, which are filled with many smaller cavities, and so on [11]. Consequently, the surface cavity sizes would be expected to fit an exponential distribution as shown in Fig. 3(*a*).

Several techniques, including surface contact profilometry, scanning electron microscopy, and various optical, electrical, and fluid methods, are available for assessing surface features [13]. As mentioned by Ward [12], each of these techniques is bandwidth limited, meaning it can only resolve surface features of a certain size interval. Figures 3(*b*) and 3(*c*) describe this limitation for a surface contact profilometer, showing how at higher magnifications the surface appears to get smoother as fine surface features are no longer detected. This resolution limit is the result of the physical size of the diamond stylus, typically having a tip radius of 1 to 10 μm. Thus, the resulting surface cavity distribution measured with such an instrument would erroneously exhibit the characteristic dome-shape of Fig. 3(*c*) commonly employed in boiling heat transfer literature. Cavities which serve as bubble nucleation sites (0.1 to 5 μm) would not be detected with a surface contact profilometer [2,11].

Scanning electron microscopy images (SEMS) help identify and characterize the cavities which serve as nucleation sites. Figure 4 displays surface cavity distributions for a polished aluminum surface determined from SEMS at two different magnifications. Each distribution is limited by the SEM magnification. However, by combining the distributions from both SEMS, a complete cavity size distribution covering the range responsible for bubble nucleation of common fluids is obtained.

In the past, a number of investigations were performed to char-

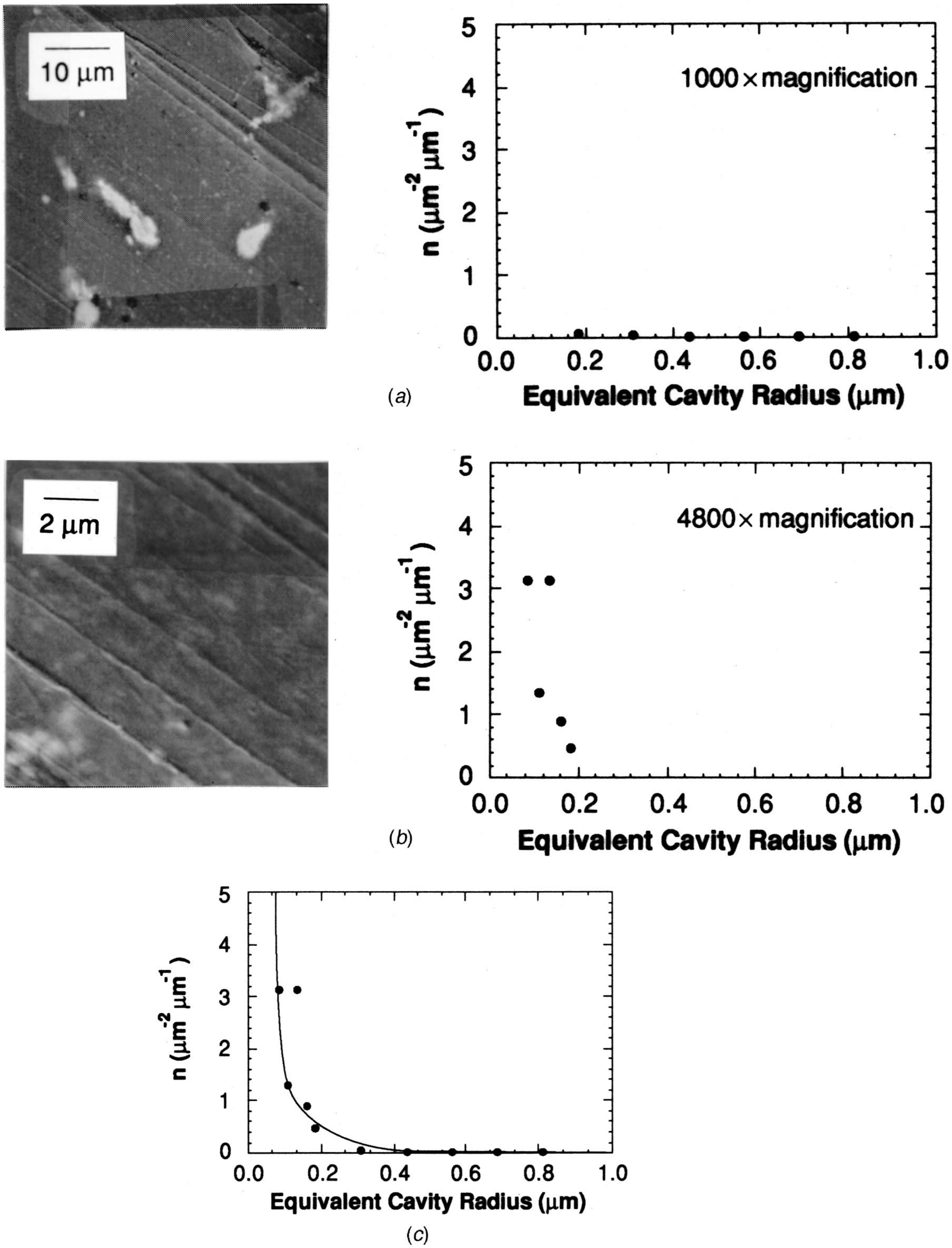

Fig. 4 Cavity size distributions for a polished aluminum surface determined from scanning electron microscopy images at (*a*) 1000× magnification, (*b*) 4800× magnification, and (*c*) combined magnifications

acterize surface features responsible for nucleate boiling to derive quantitative relationships for nc_a, the number of surface cavities which are activated [11,14–16]. More recently, Yang and Kim [17] determined nc_a using scanning electron and differential interference microscope data along with the vapor entrapment criterion (contact angle, θ, must be greater that the cone angle, ϕ, of the assumed conical-shaped cavities). Later, Wang and Dhir [18] determined the relationship between the number of surface cavities per unit area, nc, and those that become activated, nc_a, for water boiling on a polished copper surface. They also confirmed Gaertner's [19] statistical spatial distribution of active cavities. Using a Poisson distribution function, Gaertner derived the following expressions for the statistical distribution, $f(d)$, and average, $\overline{d}$, of nearest-neighbor distances, d, between cavities

$$f(d)=2\pi nc_a d\,\exp(nc_a\pi d^2) \tag{1}$$

$$\overline{d}=\frac{0.50}{\sqrt{nc_a}}. \tag{2}$$

The remainder of this paper presents the development of the new theoretically-based LFP model. Experimental data and numerical schemes required to solve the model equations are included and discussed. Finally, comparisons are made between the model predictions and empirical data to demonstrate both the robustness and accuracy of this model.

2 LFP Model Development

The methodology used to construct the present LFP model relies upon two important aspects concerning bubble nucleation and its relationship to surface temperature and cavity shape and distribution. First, based upon earlier bubble nucleation criteria [6–9], increasing surface superheat beyond the boiling incipience temperature causes both larger and smaller surface cavities to activate and bubble growth rates to increase. Secondly, for a typical polished surface, there is an exponential increase in the number of surface cavities with decreasing cavity mouth radius [17,18], as shown in Fig. 3.

In the present study, the authors postulate that at some large liquid-solid interface temperature corresponding to the LFP, a sufficient number of cavities will activate to produce enough vapor to separate the liquid from the solid, and hence, induce film boiling. Discussed below are the various sub-models used to support the overall LFP model. In the next section, a solution procedure based upon these sub-models is outlined.

Bubble Nucleation. The criteria for bubble nucleation from cavities have been rigorously investigated theoretically and verified experimentally by many researchers. The significant aspects of the bubble nucleation model are outlined below. In the development that follows, it is assumed that the surface cavities are conical.

The pressure drop across a spherical bubble interface of radius r is given as

$$P_g-P_f=\frac{2\sigma}{r}. \tag{3}$$

A relation for the liquid superheat, ΔT_{sat}, required to provide the necessary gas pressure, P_g, for initiation of bubble growth can be found by integrating the Clausius-Clapeyron equation along the saturation line,

$$\int_{P_{f,\text{sat}}}^{P_{g,\text{sat}}} dP=\int_{\tau_{\text{sat}}}^{T_{\text{sat}}+\Delta T_{\text{sat}}}\frac{h_{fg}}{Tv_{fg}}\,dT. \tag{4}$$

By substituting Eq. (3) for the pressure difference ($P_{g,\text{sat}}-P_{f,\text{sat}}$) and holding the latent heat of vaporization and specific volume difference constant, Eq. (4) can be integrated to give the following expression for the surface superheat temperature required to initiate the growth of a hemispherical vapor bubble of radius r,

$$T_{\text{rsh}}=T_{\text{sat}}\exp\left(\frac{2\sigma v_{fg}}{rh_{fg}}\right). \tag{5}$$

By assuming constant values for h_{fg} and v_{fg} (evaluated at the mean temperature $(T_{\text{rsh}}+T_{\text{sat}})/2$), integrating Eq. (4) produces a difference of only 6 percent (for water and a surface superheat temperature of 190 °C) from the results obtained by substituting temperature-dependent properties and performing the more complicated integration.

The superheat available for bubble nucleation is provided by the transient heat diffusion following contact of the liquid with the heated surface. For a relatively short duration over which rapid bubble nucleation occurs at high superheats, the contact between the liquid and solid can be modeled as one-dimensional transient conduction between two semi-infinite bodies. The transient temperature distribution in the liquid, or the available superheat, $T_{\text{ash}}(y,t)$, is given by [20]

$$T_{\text{ash}}=T_i+(T_f-T_i)\,\text{erf}\left(\frac{y}{2\sqrt{\alpha_f t}}\right). \tag{6}$$

where the interface temperature, T_i, is

$$T_i=\frac{(k\rho c_p)_s^{1/2}T_s+(k\rho c_p)_f^{1/2}T_f}{(k\rho c_p)_s^{1/2}+(k\rho c_p)_f^{1/2}}. \tag{7}$$

y is the distance into the liquid measured normal to the liquid-solid interface, and T_s and T_f are, respectively, the surface and liquid temperatures prior to the contact.

The minimum condition necessary for bubble nucleation is met when the available superheat at a distance y from the solid surface, is equal to the required superheat for a hemispherical bubble whose radius, r, is equal to y. This condition is represented by equating the required and available superheats from Eqs. (5) and (6), respectively:

$$T_{\text{sat}}\exp\left(\frac{2\sigma v_{fg}}{rh_{fg}}\right)=T_i+(T_f-T_i)\,\text{erf}\left(\frac{r}{2\sqrt{\alpha_f t}}\right). \tag{8}$$

Cavity Size Distribution. Surface cavities and other defects, typically on the order of 1 to 10 μm, have long been known to be highly influential in controlling nucleate boiling by serving as nucleation sites. In this study, scanning electron microscopy (SEM) was utilized to characterize the surface cavity distributions of macroscopically polished surfaces from which empirical Leidenfrost temperature measurements were made [2]. NIH Image, an image processing and analysis program for the Macintosh was utilized in conjunction with digitized SEM images of the polished surfaces to determine the number and sizes of the surface cavities. The program determined the mouth area of each irregular cavity, and then calculated an equivalent circular cavity mouth radius which would provide an equal mouth area.

From inspection of various SEM images at different magnifications, it was apparent that the number of cavities per unit area, n, having an equivalent mouth radius between r and $r+\Delta r$, could be fit by the exponential function

$$n=a_1\exp(-a_2 r). \tag{9}$$

Using the scanning electron microscopy images of the various surfaces used in this study, the following curve fits were obtained over a cavity size range of 0.07 to 1.0 μm:

$$n=3.379\exp(-10.12r)\quad\text{(aluminum)} \tag{10a}$$

$$n=4.597\exp(-12.20r)\quad\text{(nickel)} \tag{10b}$$

$$n=13.16\exp(-16.07r)\quad\text{(silver)}, \tag{10c}$$

where the units for n and r are sites.μm^{-2}.μm^{-1} and μm, respectively. The curve fits had acceptable least square residuals with a worst case value of 0.87.

The cumulative number of surface cavities in the radius interval $r_{\min}\leq r\leq r_{\max}$, is then obtained through integration,

$$nc=\int_{r_{\min}}^{r_{\max}} n(r)\,dr=\frac{a_1}{a_2}[\exp(-a_2 r_{\min})-\exp(-a_2 r_{\max})]. \tag{11}$$

Bubble Growth. Due to the relatively high superheat and short duration over which vapor is created in the film boiling regime, it is believed the rapid bubble growth will be initially dominated by inertia rather than heat diffusion. For this condition, bubble growth is described by the Rayleigh equation (neglecting

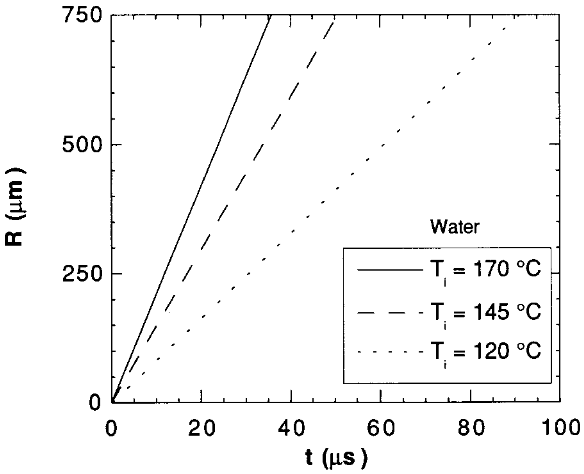

Fig. 5 Temperature dependence of vapor bubble growth for water as predicted by the numerical solution to the Rayleigh equation

viscous effects) which can be derived from the momentum equation for incompressible and irrotational flow [21], or from energy conservation principles [22], incorporating the pressure drop across a spherical interface, $2\sigma/R$.

$$R\ddot{R}+\frac{3}{2}\dot{R}^2=\frac{1}{\rho_f}\left[(P_g-P_\infty)-\frac{2\sigma}{R}\right], \tag{12}$$

where $\dot{R}$ and $\ddot{R}$ are, respectively, the first and second derivatives of bubble radius with respect to time, and P_∞ is the liquid pressure far from the bubble interface. While no analytical solution to the Rayleigh equation exists, an asymptotic solution ($R \gg R_o$) which neglects surface tension forces, has been obtained [22,23].

However, for early stages of bubble growth, surface tension forces cannot be neglected. Consequently, Eq. (12) must be solved to accurately describe these early stages of bubble growth. In solving the differential Rayleigh equation, the following intermediate step

$$d(R^{3/2}\dot{R})=\frac{1}{\rho_f}\left(\Delta P-\frac{2\sigma}{R}\right)R^{1/2}dt=\frac{1}{R^{3/2}\dot{R}}\,d\left[\frac{\Delta P}{\rho_f}\frac{R^3}{3}-\frac{\sigma R^2}{\rho_f}\right] \tag{13}$$

was used in the present study to reduce Eq. (12) to the following integral

$$t=\int_0^R \frac{dR}{\left[\frac{2}{3\rho_f}(P_g-P_\infty)-\frac{2\sigma}{\rho_f R}\right]^{0.5}} \tag{14}$$

Figure 5 displays the numerically predicted temperature dependence for bubble growth for surface temperatures corresponding to nucleate, transition, and film boiling of water. As expected, the growth rate increases appreciably with increasing surface temperature.

The bubble growth predicted by Eq. (14) is similar to the rapid inertia-controlled growth examined numerically and analytically by Lee and Merte [24] and Bankoff and Mikesell [26], respectively. The bubble growth rates displayed in Fig. 5 are also very similar to data for bubble growth in superheated water presented in the same references. The hemispherical bubble geometry adopted in the present model for the inertia-controlled growth is consistent with the description given by Carey [27].

Interaction of the Thermal Boundary Layer and the Growing Bubbles. As will be shown in the next section, the bubble growth predicted by the numerical solution to the Rayleigh equation is several orders of magnitude faster than that of the thermal boundary layer. Therefore, it is assumed the early stage of bubble growth is described by the solution to the Rayleigh Eq. (14) until the bubble dome reaches the maximum bubble stability point in the growing thermal boundary layer predicted by Eq. (8), after which the bubble growth is controlled by this slower diffusion rate of the thermal boundary layer. This two-staged bubble growth model is fairly consistent with the numerical bubble growth model of Lee and Merte [24], which predicts a rapid inertia-controlled bubble growth that converges to a much slower thermally controlled growth as the bubble expands.

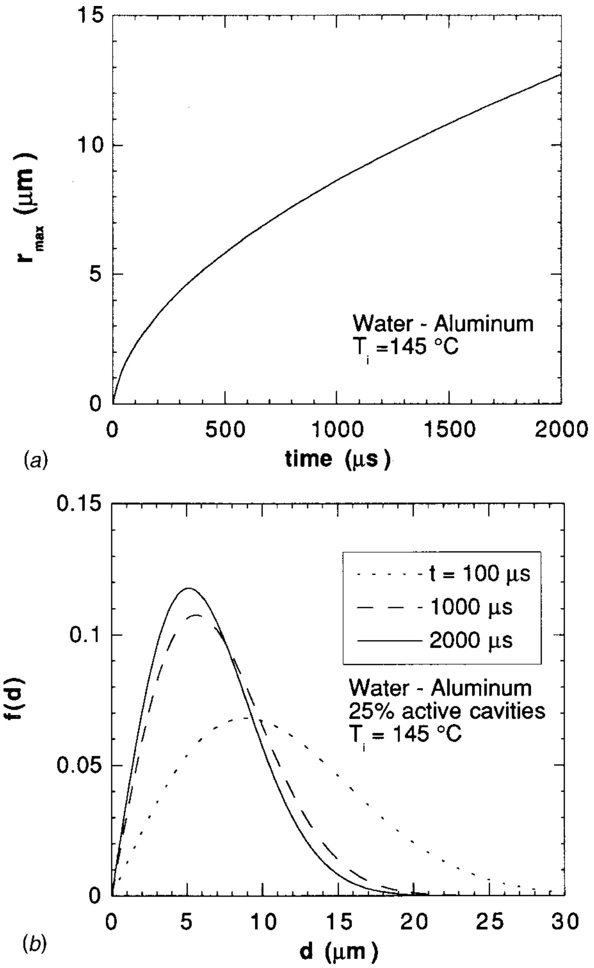

Fig. 6 (*a*) Transient maximum cavity activation and bubble radius and (*b*) nearest-neighbor cavity distances for 25 percent cavity activation at three different times following liquid-solid contact for water on a polished aluminum surface with an interface temperature of 145°C

At interface temperatures well above the boiling point of the liquid, the number of active surface cavities and the bubble growth rates can become significantly large that bubble interference begins to take place. Figure 6 describes this interference for water in contact with a polished aluminum surface with an interface temperature of 145°C. Figure 6(*a*) displays the transient maximum stable bubble radius supported by the growing thermal boundary layer as predicted by Eq. (8). Figure 6(*b*) shows the nearest-neighbor distance distribution given by Eq. (1) and the transient cumulative cavity density for a polished aluminum surface 100, 1000, and 2000 μs following liquid-solid contact. In Fig. 6(*b*), it is assumed that only 25 percent of the surface cavities satisfy the vapor entrapment criterion and serve as nucleation sites, an estimate consistent with the findings of Yang and Kim [17] and Wang and Dhir [18].

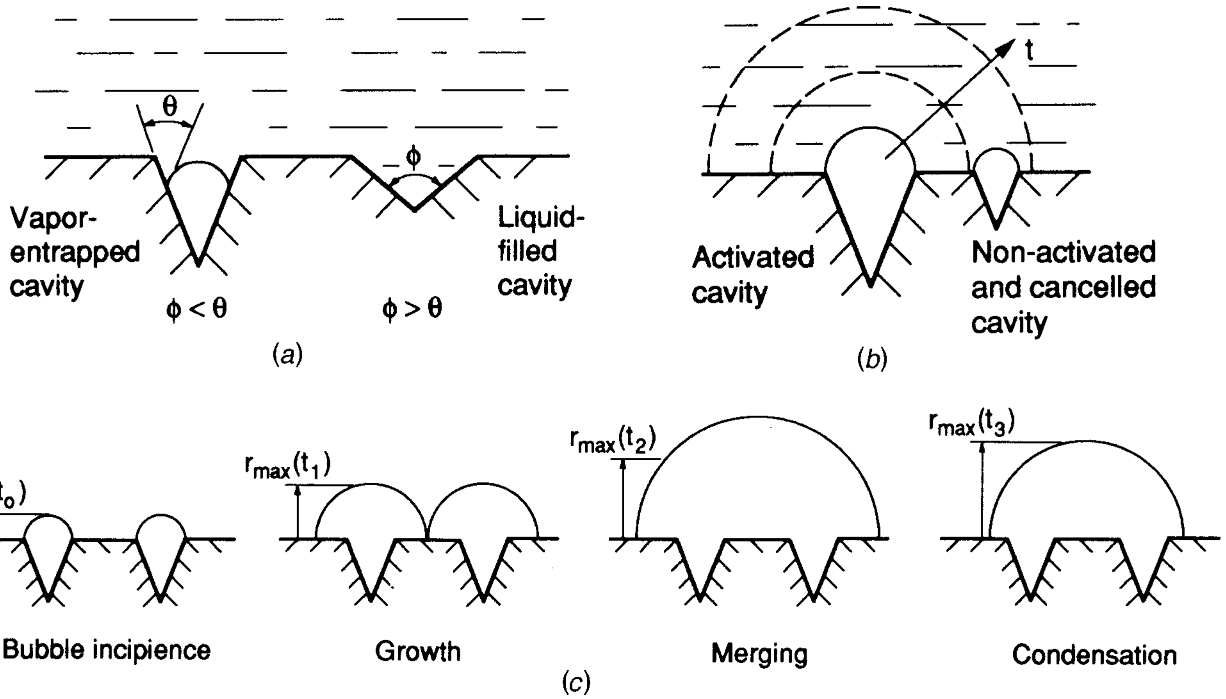

Fig. 7 Schematic representation of different forms of cavity cancellation: (*a*) poor vapor entrapment, (*b*) neighbor bubble overgrowth, and (*c*) bubble merging

In comparing Figs. 6(*a*) and 6(*b*), it is apparent that the bubble radius exceeds half of the nearest-neighbor distance for a large percentage of the active cavities, a condition which is necessary for two bubbles to interfere with one another. This trend increases significantly as time progresses. However, not all cavities will participate equally in this process. Because of several cancellation effects discussed below, only a small fraction of the cavities will activate to form bubbles which grow until they begin to interfere with bubbles from neighboring cavities.

Figure 7 is a schematic representation of different forms of surface cavity cancellation which occur before or during the development of the vapor layer. Figure 7(*a*) displays the vapor entrapment mechanism for conical surface cavities. When the liquid initially makes contact with the solid surface, only those cavities with a cone angle smaller than the advancing contact angle will entrap vapor and serve as bubble nucleation sites [25]. Two other types of cavity cancellation occur during bubble growth from nucleation sites. As illustrated in Fig. 7(*b*), a bubble from an activated cavity can overgrow a non-activated, vapor entrapped cavity, thus canceling it out as a nucleation site. Two growing bubbles may collide and merge as depicted in Fig. 7(*c*). In this case, the bubbles, represented as hemispheres for simplicity, may form a single larger bubble which extends beyond the stability limit of the thermal boundary layer, causing condensation and bubble shrinkage to temporarily occur. The net effect is the cancellation of an active bubble source by bubble merging.

It should be noted that the LFP model described in this paper is applicable to sessile as well as impinging droplets. In addition, since the model is constructed around cavity activation and bubble growth arguments, and not on the expanse of the surrounding liquid, it should be applicable to pool boiling as well.

3 LFP Model Solution Procedure

Upon contact between a sessile droplet and a heated surface, a thermal boundary layer begins to develop in the liquid. At some time t_o, the thermal boundary layer would have grown sufficiently large to satisfy the bubble nucleation criterion for conical-shaped cavities with a mouth radius r_o as shown in Fig. 8(*a*). For a polished surface, this radius is typically well within the range of cavity radii available on the surface. As time progresses and thermal boundary layer thickens, all cavities within a specific cavity radius interval are activated. This interval is given by the two roots of Eq. (8), namely, $r_{\min}(t)$ and $r_{\max}(t)$, as displayed in Fig. 8(*b*), where $r_{\max}$ is the radius of the largest activated cavity at a given instant, not the largest cavity on the surface. Similarly, $r_{\min}$ is the smallest activated cavity.

Table 1 presents curve fits for $r_{\min}(t)$ and $r_{\max}(t)$ obtained by solving Eq. (8) over a 2 ms time interval for a variety of fluids and liquid-solid interface temperatures. These curve fits were used in the remainder of the LFP model calculations to determine the Leidenfrost temperature for sessile droplets.

Assuming only a fraction, ψ, of the cavities actively participate in the growth of the vapor layer due to the cancellation effects described in the previous section, and that bubbles grow from cavities as hemispheres, the time dependence of the cumulative number of activated cavities per unit area can be found by integrating the cavity size distribution over the radius limits $r_{\min}(t)$ and $r_{\max}(t)$:

$$nc_a(t) = \psi \int_{r_{\min}(t)}^{r_{\max}(t)} a_1 \exp(-a_2 r) dr$$

$$= \psi \frac{a_1}{a_2} \{\exp(-a_2 r_{\min}(t)) - \exp(-a_2 r_{\max}(t))\}. \quad (15)$$

Since the inertia-controlled bubble growth rate predicted by Eq. (14) is orders of magnitude greater than the thermal boundary layer growth rate, it is assumed all bubbles initiated with $r_o < r_{\max}(t)$ will rapidly grow to $r_{\max}(t)$, the maximum stable hemispherical bubble radius supported by the growing thermal boundary layer. A hemispherical bubble will not be stable for sizes beyond $r_{\max}(t)$ as condensation on the leading front of the growing bubble would significantly reduce its growth rate [26]. This is consistent with bubble incipience model of Hsu [7] and the experimental results of Clark et al. [3]. Consequently, the limiting condition considered here is that once the bubbles reach the thermal boundary layer limit of $r_{\max}(t)$ they will continue to grow at

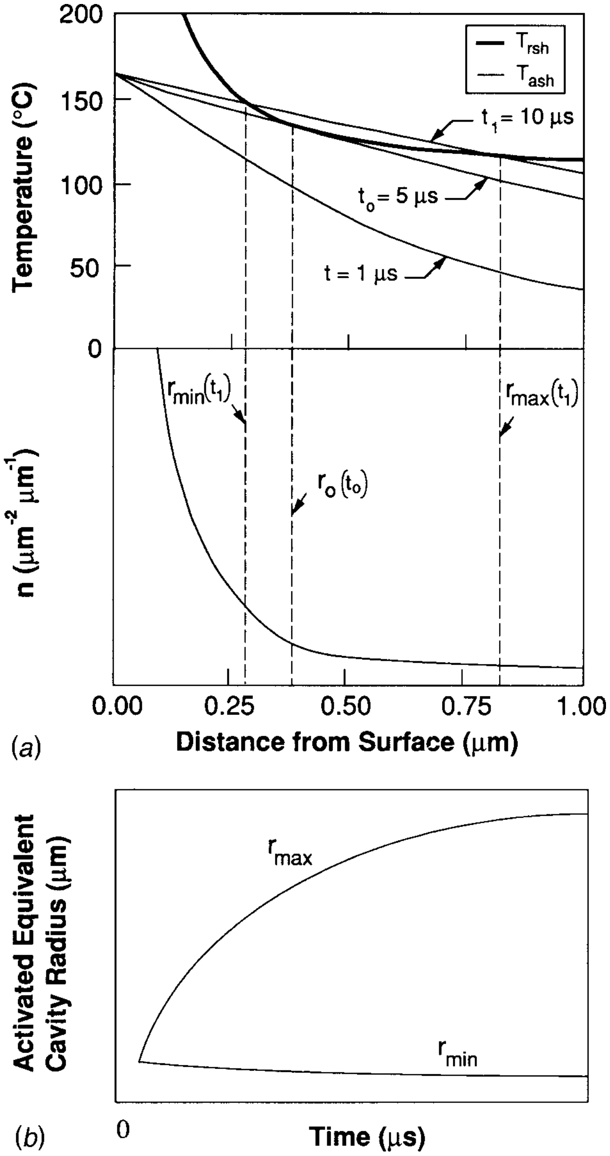

Fig. 8 Transient cavity nucleation model including (*a*) cavity nucleation superheat criteria and corresponding cavity size distribution with transient activation window, and (*b*) transient maximum and minimum active cavity radii for water in contact with a hot surface with an interface temperature of 165°C

Table 1 Active cavity radii equations for sessile droplets of various liquids in contact with a hot surface for different interface temperatures

Fluid (T_{sat} °C)	T_i (°C)	r_{min} (µm)	r_{max} (µm)
Acetone (56)	95	$0.200\ t^{-0.022}$	$0.275\ t^{0.511}$
	115	$0.097\ t^{-0.015}$	$0.349\ t^{0.506}$
	135	0.051	$0.401\ t^{0.505}$
FC-72 (56)	70	$1.085\ t^{-0.161}$	$0.037\ t^{0.661}$
	85	$0.168\ t^{-0.032}$	$0.148\ t^{0.532}$
	100	$0.081\ t^{-0.012}$	$0.207\ t^{0.512}$
	115	$0.049\ t^{-0.010}$	$0.242\ t^{0.506}$
Water (100)	145	$0.606\ t^{-0.051}$	$0.162\ t^{0.573}$
	165	$0.251\ t^{-0.019}$	$0.304\ t^{0.521}$
	185	$0.141\ t^{-0.012}$	$0.389\ t^{0.509}$

the same rate as the thermal boundary layer, i.e., $\dot{r}_{\max}(t)$. This two-stage growth is consistent with the bubble growth findings of Lee and Merte [24].

Given this bubble growth model, the time-dependent percent area coverage of the liquid-solid interface by vapor, $AB\%(t)$, is then given by

$$AB\%(t)=nc_a(t)\pi r_{\max}^2(t) \tag{16}$$

which, upon substitution of Eq. (15), gives

$$AB\%(t)=\psi\frac{a_1}{a_2}\{\exp(-a_2r_{\min}(t)) - \exp(-a_2r_{\max}(t))\}\pi r_{\max}^2(t). \tag{17}$$

To determine the cavity cancellation parameter, ψ, in Eq. (17), the vapor layer development in Fig. 2 corresponding to 137°C was compared to vapor layer predictions of the LFP model. A value of 0.05 for ψ resulted in a 15 percent vapor layer coverage, consistent with the 14.5 percent value for $T_i=137$°C in Fig. 2 determined with the image analysis software. A value of 0.05 for ψ indicates that even if 25 percent of the cavities satisfy the vapor entrapment criterion, as discussed previously and illustrated in Fig. 6, only 20 percent of these nucleation sites actively participate in the vapor layer growth; the remaining sites being canceled out by the effects illustrated in Fig. 7. Based on this comparison, a value of 0.05 for ψ was used consistently for all subsequent calculations presented in this study. Due to the complex shapes of surface features and the limited means of analyzing these shapes, it is extremely difficult to characterize the surface cavities which serve as potential nucleation sites. In addition, the contact angle used for the vapor entrapment criterion is highly dependent on the spreading velocity of the liquid, surface contamination, as well as surface roughness [28]. Since the present models for surface characterization and bubble nucleation are limited in their degree of accuracy, a more accurate means of determining the percent of actively participating surface cavities, ψ, is currently unavailable and warrants further investigation. Nevertheless, it should be emphasized that while the choice of ψ will influence the vapor layer growth rate, the strong temperature-dependence of the latter, $\Delta AB\%/\Delta t$, which is used to identify the LFP in the present model, is still very well preserved.

4 LFP Model Assessment

Figure 9(*a*) shows the temperature dependence of the transient vapor layer growth for a sessile water droplet on a polished aluminum surface with the cavity distribution given by Eq. (10*a*). The time for complete vapor layer development ($AB\%=100$) is shown to rapidly decrease as the interface temperature is increased from 145 to 185°C. While the model predicts an eventual 100 percent vapor layer growth for the interface temperature of 145°C, other effects such as bubble departure and liquid motion which are not accounted for in the model, would interrupt this development within a few milliseconds of liquid-solid contact,

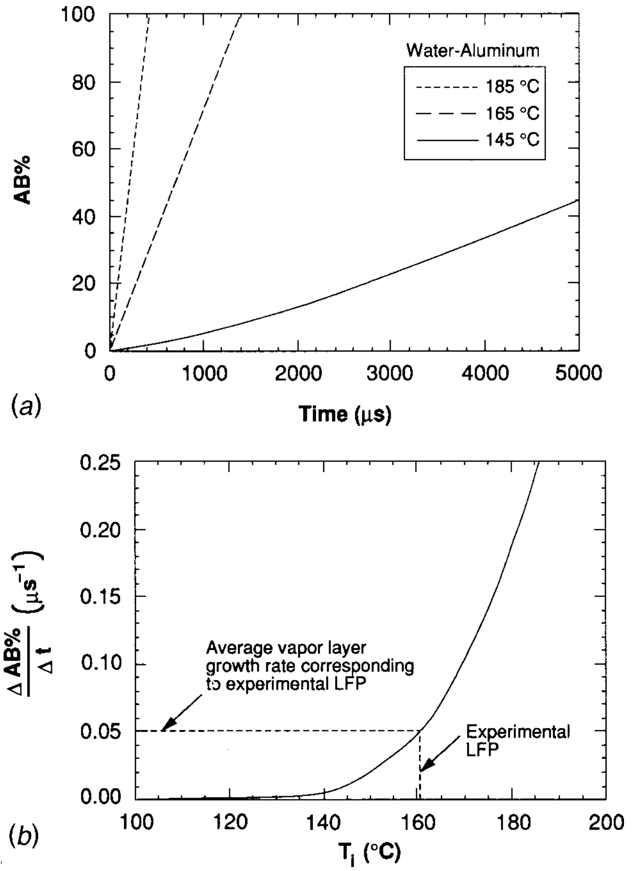

Fig. 9 Temperature dependence of the (*a*) transient vapor layer coverage and (*b*) average vapor layer growth rate for a sessile water droplet on a polished aluminum surface

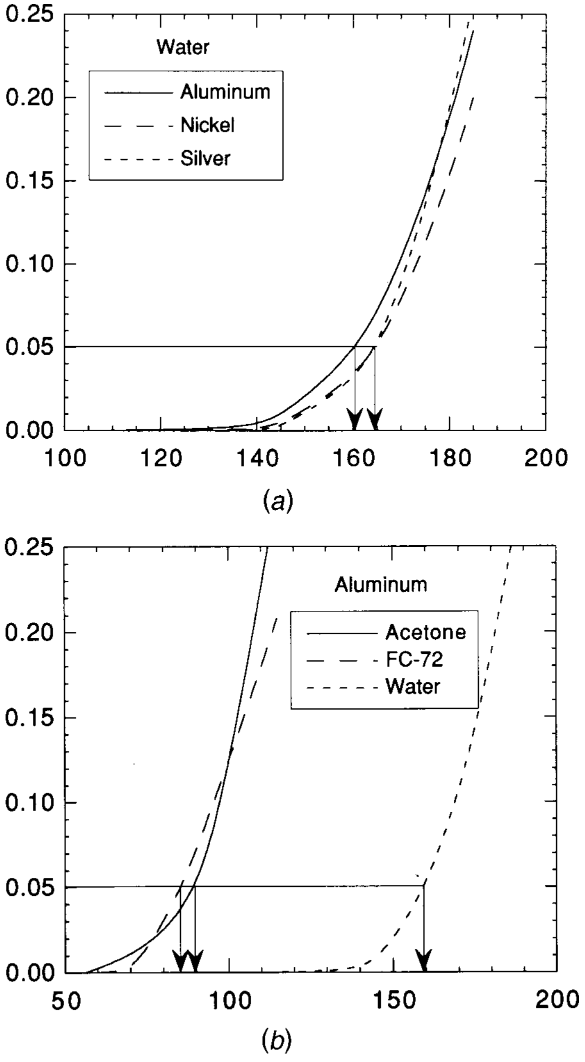

Fig. 10 Average vapor layer growth rate for sessile droplets of (*a*) water on various polished metallic surfaces and (*b*) acetone, FC-72, and water on polished aluminum

and hence prevent film boiling from occurring. Figure 9(*b*) presents the trend observed in Fig. 9(*a*) in a slightly different manner. Figure 9(*b*) shows that as the interface temperature increases beyond the liquid saturation temperature, the average vapor layer growth rate will increase exponentially. Intuition suggests that at some minimum interface temperature, the LFP, the average vapor layer growth rate will become sufficiently high to support film boiling. To determine the minimum average vapor layer growth rate required to support film boiling, experimental LFP data for sessile water droplets on aluminum were employed. The water-aluminum system was used earlier in the model development to determine the percentage of actively participating surface cavities and this system was also highly scrutinized in an experimental study of the LFP [2]. Shown in Fig. 9(*b*) is the experimentally determined Leidenfrost temperature of 162°C ($T_s = 170$°C) for sessile water droplets on aluminum which corresponds to an average vapor layer growth rate of 0.05. This value of the average vapor layer growth rate was used throughout the LFP model assessment of different liquid-solid systems.

This same technique, as described by Carey [27], has been used to determine the critical vapor bubble formation rate needed to sustain homogeneous nucleation within a superheated liquid. In the homogeneous nucleation superheat limit model, the vapor bubble formation rate increases exponentially with increasing liquid temperature, much like the vapor blanket growth rate in the present study. Carey explains how empirical data were used to determine a critical vapor bubble formation rate, and how this single bubble formation rate was used to determine the homogeneous nucleation superheat limit of several different liquids including water.

Figures 10(*a*) and 10(*b*) display, respectively, the average vapor layer growth rate versus interface temperature for sessile water droplets on various metallic surfaces and sessile acetone, FC-72, and water droplets on aluminum. Using these plots and an average vapor layer growth rate of 0.05, the LFP was determined for each of these fluid-solid systems. These LFP model predictions are compared to measured values [2] in Table 2. Excellent agreement is obtained for all cases except acetone, where the agreement is only fair. Even so, these results are quite promising considering the large differences in the wetting characteristics as well as the thermodynamic and thermal properties of the fluids and solids used in the comparison. In addition, the differences between the LFP predictions and present measurements are significantly smaller than the majority of previous LFP predictive tools presented in [2]. The difference exhibited for acetone on aluminum may be due to the limitation imposed on the number of actively participating cavities, accounted for in the parameter ψ in Eq. (17). As discussed earlier, the existing techniques for modeling vapor entrapment and bubble nucleation as well as characterization of surface cavities are limited and warrant continued study. Adopting newer techniques may lead to a more accurate means of determining the number of actively participating cavities and hence further strengthen the present LFP model.

Table 2 Comparison of measured Leidenfrost temperatures [2] and predictions based on the present LFP model for acetone, FC-72, and water on various polished metallic surfaces

Fluid	Polished Surface Material	T_{leid} (°C) (LFP model)	T_{leid} (°C) (measured)
Acetone	Aluminum	90	132
FC-72	Aluminum	87	89
Water	Nickel	165	161
	Silver	165	169
	Aluminum	162	162

Further Justifications of the LFP Model and Application to Rough Surfaces. For a perfectly smooth surface which is void of all surface cavities, the current LFP model predicts that the liquid can be heated to an infinitely high temperature and film boiling would never be reached. Realistically, the maximum temperature that the liquid can be heated to, above which it is instantaneously converted to vapor, is referred to as the kinetic or thermodynamic superheat limit. Methods to predict this superheat limit, which is well above the Leidenfrost temperature of the liquid-solid systems presented earlier in this study, can be found elsewhere [29].

Gallium, a liquid metal with a melting point of 29.8°C and density of 5900 $\mathrm{kg.m^{-3}}$, was used in the present study to provide a smooth liquid surface nearly free of defects. Using a thermal monitoring system consisting of a temperature controller, cartridge heater, and thermocouple, sessile droplet evaporation experiments, similar to those described in [2], were performed to determine the LFP of water on liquid gallium. Results revealed a gallium temperature of 260°C was needed to provide a water/gallium interface temperature of 222°C corresponding to the LFP. Impurities in the gallium caused by oxidation and contaminant metals were speculated to provide a few heterogeneous nucleation sites which prevented the water from obtaining its maximum superheat temperature limit of 273°C predicted using the thermodynamic homogeneous nucleation model [30], or 310°C according to the kinetic homogeneous nucleation model [27]. However, the results do indicate that a dramatic reduction in surface cavities greatly increases the Leidenfrost temperature, which is in agreement with the present LFP model.

While this model was developed for polished surfaces, it also provides a limiting condition for surfaces possessing roughness features orders of magnitude larger than the cavity radii responsible for bubble nucleation (0.1 to 1 μm). The model effectively predicts a lower limit to the Leidenfrost temperature for sessile droplets and pools of liquid. Contamination and surface roughness will act to increase the Leidenfrost temperature by requiring a thicker vapor layer to inhibit liquid-solid contact. This is supported by experimental data for sessile droplets of different liquids on surfaces of various roughnesses [2].

5 Conclusions

This study presented a new theoretically based LFP model which was constructed around vapor bubble nucleation, growth, and interference criteria, along with surface cavity size characterization. After evaluating the model with an extensive experimental database, the following key conclusions can be drawn about its validity and use:

1. The number of surface cavities which act as bubble nucleation sites increases exponentially with increasing liquid-solid interface temperature.
2. Bubble growth rates predicted by the solution to the Raleigh equation are several orders of magnitude greater than the growth rate of the thermal boundary layer for conditions consistent with film boiling of common fluids. Consequently, the bubbles emanating from active surface cavities grow instantaneously to the maximum allowable radius as predicted by bubble nucleation theory, and thereafter, grow at the rate of the diffusing thermal boundary layer.
3. For interface temperatures at and above the LFP, the present model predicts the number of active sites and bubble growth rates are large enough that a complete vapor layer is established between the liquid and solid almost instantaneously upon contact.
4. The present model is substantiated by a large experimental data base for sessile droplets, provided the surface roughness features are on the same order of magnitude as the cavities responsible for bubble nucleation. For rougher surfaces, the model predicts a lower bound for the sessile droplets.

Acknowledgment

The authors gratefully acknowledge the support of the Office of Basic Energy Sciences of the U.S. Department of Energy (Grant No. DE-FE02-93ER14394.A003).

Nomenclature

a_1, a_2 = coefficients in cavity size distribution
AB % = percent liquid-solid interface area coverage by vapor
c_p = specific heat at constant pressure
d = nearest-neighbor cavity distance
$\overline{d}$ = average nearest-neighbor cavity distance
$f(d)$ = nearest-neighbor cavity distance distribution
h_{fg} = latent heat of vaporization
k = thermal conductivity
n = number of surface cavities per unit area per unit interval (sites $\mu\mathrm{m}^{-2}$ $\mu\mathrm{m}^{-1}$)
nc = cumulative number of surface cavities per unit area (sites $\mu\mathrm{m}^{-2}$)
nc_a = cumulative number of active surface cavities per unit area (sites $\mu\mathrm{m}^{-2}$)
P = pressure
R = bubble radius
$\dot{R}$ = first derivative of bubble radius with respect to time
$\ddot{R}$ = second derivative of bubble radius with respect to time
r = surface cavity radius
r_a = radius of active surface cavity (μm)
T = temperature
t = time
v_{fg} = specific volume difference between vapor and liquid
y = normal distance from solid surface

Greek Symbols

α = thermal diffusivity
ΔAB %/Δt = average vapor layer growth rate
ΔT_{sat} = surface superheat, $T_s - T_{\mathrm{sat}}$
ϕ = cavity cone angle
θ = contact angle
ρ = density

σ = surface tension
ψ = fraction of actively participating cavities

Subscripts

a = active
ash = available superheat
f = liquid
g = vapor
i = liquid-solid interface
leid = Leidenfrost condition
max = maximum
min = minimum
o = initial, nucleation
rsh = required superheat
s = surface, solid
sat = saturation
∞ = liquid condition far from bubble interface.

References

[1] Bernardin, J. D., and Mudawar, I., 1995, ‘‘Validation of the Quench Factor Technique in Predicting Hardness in Heat Treatable Aluminum Alloys,’’ Int. J. Heat Mass Transf., **38**, pp. 863–873.
[2] Bernardin, J. D., and Mudawar, I., 1999, ‘‘The Leidenfrost Point: Experimental Study and Assessment of Existing Models,’’ ASME J. Heat Transfer, **121**, pp. 894–903.
[3] Clark, H. B., Strenge, P. S., and Westwater, J. W., 1959, ‘‘Active Sites for Nucleate Boiling,’’ Chem. Eng. Prog., Symp. Ser., **55**, pp. 103–110.
[4] Gaertner, R. F., and Westwater, J. W., 1959, ‘‘Population of Active Sites in Nucleate Boiling Heat Transfer,’’ Chem. Eng. Prog., Symp. Ser., **55**, pp. 39–48.
[5] Kurihara, H. M., and Myers, J. E., 1960, ‘‘The Effects of Superheat and Surface Roughness on Boiling Coefficients,’’ AIChE J., **6**, pp. 83–91.
[6] Bankoff, G. S., 1959, ‘‘The Prediction of Surface Temperatures at Incipient Boiling,’’ Chem. Eng. Prog., Symp. Ser., **55**, pp. 87–94.
[7] Hsu, Y. Y., 1962, ‘‘On the Size Range of Active Nucleation Cavities on a Heating Surface,’’ ASME J. Heat Transfer, **84**, pp. 207–213.
[8] Han, C. Y., and Griffith, P., 1965, ‘‘The Mechanism of Heat Transfer in Nucleate Pool Boiling-Part I,’’ Int. J. Heat Mass Transf., **8**, pp. 887–904.
[9] Lorenz, J. J., Mikic, B. B., and Rohsenow, W. M., 1974, ‘‘The Effects of Surface Condition on Boiling,’’ *Proc. Fifth Int. Heat Transfer Conf.*, **4**, Tokyo, pp. 35–39.
[10] Gaertner, R. F., 1965, ‘‘Photographic Study of Nucleate Pool Boiling on a Horizontal Surface,’’ ASME J. Heat Transfer, **87**, pp. 17–29.
[11] Cornwell, K., and Brown, R. D., 1978, ‘‘Boiling Surface Topography,’’ *Proc. Sixth Int. Heat Transfer Conf.*, **1**, Toronto, Canada, pp. 157–161.
[12] Ward, H. C., 1982, ‘‘Profile Description,’’ in *Rough Surfaces* T. R. Thomas, ed., Longman Group, New York, pp. 72–90.
[13] Thomas, T. R., 1982, ‘‘Stylus Instruments,’’ in *Rough Surfaces* T. R. Thomas, ed., Longman Group, New York, pp. 12–70.
[14] Brown, W. T., Jr., 1967, ‘‘Study of Flow Surface Boiling,’’ Ph.D. thesis, M.I.T., Cambridge, MA.
[15] Mikic, B. B., and Rohsenow, W. M., 1969, ‘‘A New Correlation of Pool-Boiling Data Including the Effect of Heating Surface Characteristics,’’ ASME J. Heat Transfer, **91**, pp. 245–250.
[16] Bier, K., Gorenflo, D., Salem, M., and Tanes, Y., 1978, ‘‘Pool Boiling Heat Transfer and Size of Active Nucleation Centers for Horizontal Plates With Different Surface Roughness,’’ *Proc. Sixth Int. Heat Trans. Conf.*, **1**, Toronto, Canada, pp. 151–156.
[17] Yang, S. R., and Kim, R. H., 1988, ‘‘A Mathematical Model of the Pool Boiling Nucleation Site Density in Terms of the Surface Characteristics,’’ Int. J. Heat Mass Transf., **31**, pp. 1127–1135.
[18] Wang, C. H., and Dhir, V. K., 1993, ‘‘Effect of Surface Wettability on Active Nucleation Site Density During Pool Boiling of Water on a Vertical Surface,’’ ASME J. Heat Transfer, **115**, pp. 659–669.
[19] Gaertner, R. F., 1963, ‘‘Distribution of Active Sites in the Nucleate Boiling of Liquids,’’ Chem. Eng. Prog., Symp. Ser., **59**, pp. 52–61.
[20] Eckert, E. R. G., and Drake, R. M., 1972, *Analysis of Heat and Mass Transfer*, McGraw-Hill, New York.
[21] Panton, R. L., 1984, *Incompressible Flow*, John Wiley & Sons, New York.
[22] Mikic, B. B., Rohsenow, W. M., and Griffith, P., 1970, ‘‘On Bubble Growth Rates,’’ Int. J. Heat Mass Transf., **13**, pp. 657–666.
[23] Van Stralen, S. J. D., Sohal, M. S., Cole, R., and Sluyter, W. M., 1975, ‘‘Bubble Growth Rates in Pure and Binary Systems: Combined Effect of Relaxation and Evaporation Microlayers,’’ Int. J. Heat Mass Transf., **18**, pp. 453–467.
[24] Lee, H. S., and Merte, H., 1996, ‘‘Spherical Vapor Bubble Growth in Uniformly Superheated Liquids,’’ Int. J. Heat Mass Transf., **39**, pp. 2427–2447.
[25] Bankoff, S. G., 1958, ‘‘Entrapment of Gas in the Spreading of a Liquid over a Rough Surface,’’ AIChE J., **4**, pp. 24–26.
[26] Bankoff, S. G., and Mikesell, R. D., 1959, ‘‘Bubble Growth Rates in Highly Subcooled Nucleate Boiling,’’ Chem. Eng. Prog., Symp. Ser., **55**, pp. 95–102.
[27] Carey, V. P., 1992, *Liquid-Vapor Phase-Change Phenomena: An Introduction to the Thermophysics of Vaporization and Condensation Processes in Heat Transfer Equipment*, Hemisphere, New York.
[28] Bernardin, J. D., Mudawar, I., Walsh, C. B., and Franses, E. I., 1997, ‘‘Contact Angle Temperature Dependence for Water Droplets on Practical Aluminum Surfaces,’’ Int. J. Heat Mass Transf., **40**, pp. 1017–1034.
[29] Skripov, V. P., 1974, *Metastable Liquids*, John Wiley & Sons, New York.
[30] Spiegler, P., Hopenfeld, J., Silberberg, M., Bumpus, Jr., C. F., and Norman, A., 1963, ‘‘Onset of Stable Film Boiling and the Foam Limit,’’ Int. J. Heat Mass Transf., **6**, pp. 987–994.

A. K. Satapathy
e-mail: aksatapathy@rec.ori.nic.in

R. K. Sahoo

Department of Mechanical Engineering,
Regional Engineering College,
ROURKELA-769 008,
Orissa, India

Rewetting of an Infinite Slab With Uniform Heating Under Quasi-Steady Conditions

The two-dimensional quasi-steady conduction equation governing conduction controlled rewetting of an infinite slab, with one side flooded and the other side subjected to a constant heat flux, has been solved by Wiener-Hopf technique. The solution yields the quench front temperature as a function of various model parameters such as Peclet number, Biot number and dimensionless heat flux. Also, the critical (dryout) heat flux is obtained by setting the Peclet number equal to zero, which gives the minimum heat flux required to prevent the hot surface being rewetted. [DOI: 10.1115/1.1484111]

Keywords: *Analytical, Boiling, Heat Transfer, Heat Pipes, Modeling, Nuclear*

1 Introduction

The process of quenching of hot surfaces is of practical importance in nuclear and metallurgical industries. For instance, in the event of a postulated loss-of-coolant accident (LOCA) in water cooled reactors, the clad surface of the fuel elements may reach very high temperature because the stored energy in the fuel cannot be removed adequately by the surrounding steam. In order to bring the reactor to a cooled shutdown condition, an emergency core cooling system is activated to reflood the core. The time delay in re-establishing the effective cooling may result in a cladding temperature rise, significantly above the saturation temperature. If the cladding temperature rises above the rewetting temperature, a stable vapor blanket will prevent the immediate return to liquid-solid contact. Rewetting is the re-establishment of liquid contact with a hot cladding surface and, thereby, bringing it to an acceptable temperature. Also, quenching phenomenon is of considerable practical interest in many other applications such as steam generators, evaporators, cryogenic systems and metallurgical processing. The cooling process during quenching is characterized by the formation of a wet patch on the hot surface, which eventually develops into a steadily moving quench front. As the quench front moves along the hot surface, two regions can be identified: a dry region ahead of the quench front and a wet region behind the quench front. The upstream end of the solid (wet region) is cooled by convection to the contacting liquid, while its downstream end (dry region) is cooled by heat transfer to a mixture of vapor and entrained liquid droplets, called precursory cooling.

The rewetting model for a two-dimensional two-region heat transfer with a step change in heat transfer coefficient at the quench front has been solved for a single slab [1–3] or for a composite slab [4]. In the single slab model the unwetted side is considered to be adiabatic, whereas in case of a composite slab a three layer composite is considered to simulate the fuel and the cladding separated by a gas filled gap between them. The solution method commonly employed is Wiener-Hopf technique. The two-dimensional rewetting model for a single slab with a uniform heat flux and precursory cooling has been solved by an approximate integral method [5]. The one-dimensional rewetting model with a uniform heat flux has been solved for a smooth plate [6] and for both smooth and grooved plates [7], considering the dry region to be adiabatic.

The analysis of rewetting of a hot surface subjected to a boundary heat flux and the dryout induced by the heat flux is of specific interest while considering the decay heating of a nuclear fuel [5] or in the design of heat pipes for thermal radiators [6,7]. Chan and Zhang [7] observed that the existence of heat flux on the wall poses an unsteady state solution for the heat conduction equation, even after the equation is transformed to the Lagrangian coordinate moving with the quench front. In this respect, they also considered the rewetting velocity as well as the plate temperature (at far ahead of the quench front) to be time variant. In the present paper, however, precursory cooling in the dry region has been included in the boundary condition in order to consider the quasi-steady state conduction equation. Further, reported literature on analytical investigations indicates that Wiener-Hopf solution for the rewetting model with a boundary heat flux does not exist. In the present analysis, Wiener-Hopf technique has been employed because of its accuracy and computational simplicity. Besides, the advantage of using the Wiener-Hopf technique may be recognized in case of handling discontinuous boundary conditions, where the singularity due to the discontinuity can be readily resolved by decomposing an appropriate kernel function in the complex Fourier domain.

In the present study, the physical model consists of an infinitely extended vertical slab with one side flooded and the other side subjected to a uniform heat flux. The model assumes constant but different heat transfer coefficients for the wet and dry regions on the flooded side. The two-dimensional quasi-steady conduction equation governing the conduction-controlled rewetting of the infinite slab has been solved by Wiener-Hopf technique. The present solution involves the exact decomposition of the kernel function, so that the solution may be valid for all range of values of the parameters used in the model. The solution has been compared with other analytical solutions and depicted in the graphical form.

2 Mathematical Model

The two-dimensional transient heat conduction equation for the slab is

$$k\left(\frac{\partial^2 T}{\partial X^2}+\frac{\partial^2 T}{\partial Y^2}\right)=\rho C\,\frac{\partial T}{\partial t} \quad 0<X<\delta \quad 0<Y<L \quad L\to\infty \quad (1)$$

where L is the length of the slab and δ is the thickness of the slab. The density, specific heat and thermal conductivity of the slab material are ρ, C, and k respectively. The origin of the coordinate frame is at left-bottom corner of the slab. To convert this transient equation into a quasi-steady state equation, the following transformation is used:

$$\bar{x}=X \quad \bar{y}=Y-ut$$

Contributed by the Heat Transfer Division for publication in the JOURNAL OF HEAT TRANSFER. Manuscript received by the Heat Transfer Division September 8, 2000; revision received March 29, 2002. Associate Editor: T. Y. Chu.

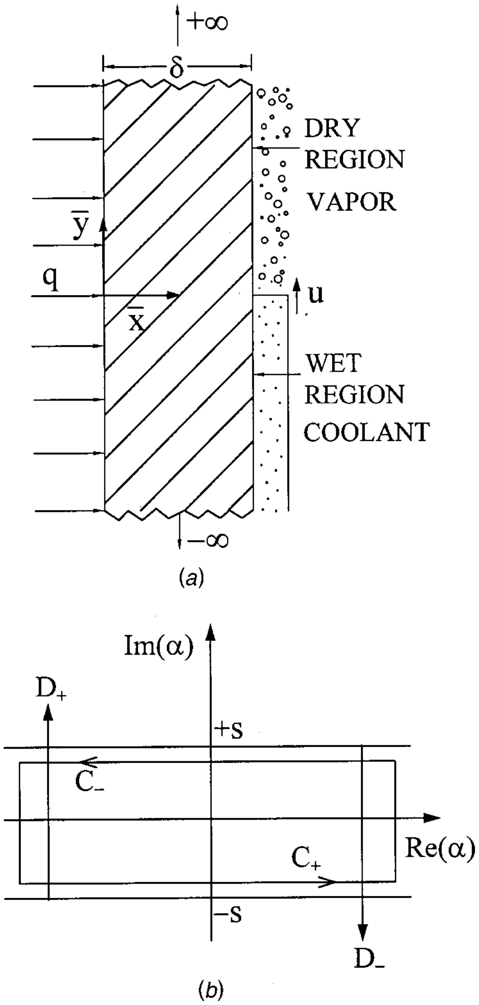

(*a*)

(*b*)

Fig. 1 (*a*) Physical domain of infinite slab; and (*b*) common strip of analyticity in the complex Fourier plane.

where u is the constant quench front velocity and $\bar{x}$, $\bar{y}$ are normal and axial coordinates respectively (Fig. 1(*a*)). Experiments have shown that, if the slab is long enough compared to the penetration depth to heat transfer field, the temperature distribution around the heat source/sink soon becomes independent of time. That is, an observer stationed at the origin of the moving $(\bar{x},\bar{y})$ coordinate system fails to notice any appreciable change in the temperature distribution around him as the front moves on. This is identified as the apparent steady state or quasi-steady state condition. Thus the transformed heat conduction equation in a coordinate system moving with the quench front is

$$\frac{\partial^2 T}{\partial \bar{x}^2}+\frac{\partial^2 T}{\partial \bar{y}^2}+\frac{\rho C u}{k}\frac{\partial T}{\partial \bar{y}}=0 \quad 0<\bar{x}<\delta \quad -\infty<\bar{y}<\infty \tag{2}$$

The above equation is the governing partial differential equation in quasi-steady state for the slab, in which $\partial T/\partial t=0$ in the moving coordinate system.

In conduction-controlled rewetting analysis, it is believed that conduction of heat along the slab from the dry region to wet region is the dominant mechanism of heat removal ahead of the quench front, which results in a lowering of the surface temperature immediately downstream of the quench front and causes the quench front to progress further. Since only axial conduction is considered, the effect of coolant mass flux, coolant inlet subcooling and its pressure gradient etc. are not accounted for explicitly, but implicitly in terms of wet region heat transfer coefficient, which is incorporated in the boundary condition. In the present analysis, the heat transfer coefficient h_1 is assumed to be constant over the entire wet region. The coolant temperature is taken to be equal to its saturation temperature T_s. On the dry side of the slab, the wall is cooled by the surrounding vapor. The heat transfer coefficient accounting for both convective and radiative cooling effects on the dry side is assumed equal to h_2, a constant, which is smaller than h_1. The temperature of the surrounding vapor is assumed equal to T_w, which can be interpreted as the initial temperature of the hot surface without a boundary heat flux. This is justified because the vapor in dry region would be superheated due to the existence of imposed surface heat flux on the wall. The rewetting (quench front) temperature is denoted by T_0.

Following Yao [5], it may be envisaged that the temperature field is sufficiently flat in the axial direction at infinity. Consequently, the first and second derivatives of temperature in $\bar{y}$-direction can be neglected at far upstream of the quench front (at $\bar{y}\rightarrow-\infty$) as well as at far downstream of the quench front (at $\bar{y}\rightarrow+\infty$). The above two assumptions are adequate to prescribe the temperature at infinity $(\bar{y}\rightarrow\pm\infty)$. The far-field boundary conditions then become

$$\begin{aligned} T&=T_s+\frac{q}{k}(\delta-\bar{x})+\frac{q}{h_1} \quad \bar{y}\rightarrow-\infty \\ T&=T_w+\frac{q}{k}(\delta-\bar{x})+\frac{q}{h_2} \quad \bar{y}\rightarrow+\infty \end{aligned} \tag{3}$$

The conventional rewetting models (without a boundary heat flux) usually assume the vapor temperature in the dry region equal to its saturation temperature so that it would be used as a sink temperature. In the presence of a boundary heat flux, however, it is well justified to assume the vapor temperature equal to the initial wall temperature because the vapor would be superheated owing to the existence of the boundary heat flux. The surface temperature of the slab at far ahead of the quench front (at $\bar{x}=\delta$, $\bar{y}\rightarrow+\infty$) can be calculated (Eq. (3)) to be equal to (T_w+q/h_2). In situations when $T_0\geqslant T_w$, the temperature of dry region wall $T(\delta,\bar{y})$ will be above T_w and, hence, the wall will be cooled by the vapor. On the other hand, for $T_0<T_w$, only a finite part of the dry region wall immediately ahead of the quench front will be less than T_w, whereas for the remaining part it will be more than T_w over an infinite length. This implies that the former part of the dry region wall of a finite length will be heated by the vapor while the latter part of an infinite length will be cooled by the vapor and the overall effect is to cool the dry region wall. Thus, on the whole, in both the situations the vapor temperature would behave as the sink temperature. Moreover, the boundary conditions in Eq. (3) suggest that precursory cooling in the dry region cannot be neglected in the case of existence of boundary heat flux on the wall. Equation (2) can be expressed in the following dimensionless form

$$\frac{\partial^2 \theta}{\partial x^2}+\frac{\partial^2 \theta}{\partial y^2}+\mathrm{Pe}\frac{\partial \theta}{\partial y}=0 \quad 0<x<1 \quad -\infty<y<\infty \tag{4}$$

The associated boundary conditions are

$$\begin{aligned} &\frac{\partial \theta}{\partial x}+Q=0 \quad \text{at } x=0 \quad -\infty<y<\infty \\ &\frac{\partial \theta}{\partial x}+B_1\theta=0 \quad \text{at } x=1 \quad y<0 \\ &\frac{\partial \theta}{\partial x}+B_2(\theta-1)=0 \quad \text{at } x=1 \quad y>0 \\ &\theta=\frac{Q}{B_1}+Q(1-x) \quad \text{at } y\rightarrow-\infty \\ &\theta=1+\frac{Q}{B_2}+Q(1-x) \quad \text{at } y\rightarrow+\infty \\ &\theta=\theta_0 \quad \text{at } x=1 \quad y=0 \end{aligned} \tag{5}$$

The non-dimensional variables used above are

$$x=\frac{\bar{x}}{\delta},\quad y=\frac{\bar{y}}{\delta},\quad \theta=\frac{T-T_s}{T_w-T_s},\quad B_1=\frac{h_1\delta}{k},\quad B_2=\frac{h_2\delta}{k},$$

$$\mathrm{Pe}=\frac{\rho C u\delta}{k},\quad Q=\frac{q\delta}{k(T_w-T_s)}\quad \text{and}\quad \theta_0=\frac{T_0-T_s}{T_w-T_s}.$$

It may be verified that for no heat flux condition with adiabatic dry side (by setting $Q=0$ $B_2=0$ and $Q/B_2=0$), the boundary conditions in Eq. (5) reduces to that of conventional two-region model (insulated dry wall and without a heating [2]). The main objective of the present analysis is to obtain the quench front temperature θ_0 in terms of wetside Biot number B_1, dryside Biot number B_2, Peclet number Pe and dimensionless heat flux Q. Although Eqs. (4) and (5) have been formulated for the case of bottom flooding, they are also valid for top flooding.

3 Analytical Solution

In order to employ the Wiener-Hopf technique, Eq. (4) is first transformed with a new variable φ, defined by $\theta(x,y)=1+(Q/B_2)+Q(1-x)-\varphi(x,y)e^{-sy}$, in which $s=\mathrm{Pe}/2$. The governing equation (Eq. (4)) then becomes

$$\frac{\partial^2\varphi}{\partial x^2}+\frac{\partial^2\varphi}{\partial y^2}-s^2\varphi=0\quad 0<x<1\quad -\infty<y<\infty \tag{6}$$

The boundary conditions can be written sequentially as

$$\frac{\partial\varphi}{\partial x}=0\quad \text{at } x=0\quad -\infty<y<\infty$$

$$\frac{\partial\varphi}{\partial x}+B_1\varphi=B_1\left[1+\frac{Q}{B_2}-\frac{Q}{B_1}\right]e^{sy}\quad \text{at } x=1\quad y<0$$

$$\frac{\partial\varphi}{\partial x}+B_2\varphi=0\quad \text{at } x=1\quad y>0 \tag{7}$$

$$\varphi=\left[1+\frac{Q}{B_2}-\frac{Q}{B_1}\right]e^{sy}\quad \text{at } y\to-\infty$$

$$\varphi=0\quad \text{at } y\to+\infty$$

3.1 Fourier Transform. Fourier transformation of a partial differential equation and of its associated boundary conditions generally results in a less complicated problem in the plane of the transformed variable. If the solution of this subsidiary problem can easily be obtained and inverted, then the transform technique is straightforward and supposed to be efficient. In the next step of the analysis, Fourier transform is used to convert the partial differential equation (Eq. (6)) to an ordinary differential equation. The Fourier transform is defined by

$$\Phi(\alpha,x)=\Phi_+(\alpha,x)+\Phi_-(\alpha,x)=\int_{-\infty}^{\infty}\varphi(x,y)e^{i\alpha y}dy \tag{8}$$

with

$$\Phi_-(\alpha,x)=\textstyle\int_{-\infty}^{0}\varphi(x,y)e^{i\alpha y}dy,$$

$$\Phi_+(\alpha,x)=\textstyle\int_{0}^{\infty}\varphi(x,y)e^{i\alpha y}dy.$$

The parameter α used above is a complex quantity. The far-field boundary conditions in Eq. (7) indicate that $\varphi(x,y)$ is of the order $\exp(sy)$ at $y\to-\infty$, whereas $\varphi(x,y)$ is of the order $\exp(-sy)$ at $y\to+\infty$. Thus, the functions $\Phi_+(\alpha,x)$, $\Phi_-(\alpha,x)$ are analytic in the domains D_+ and D_- respectively ([8], p. 78). The domains D_+ and D_- are defined (Fig. 1(*b*)) in the entire complex domain as: $D_+:\mathrm{Im}(\alpha)>-s$, $D_-:\mathrm{Im}(\alpha)<+s$. Applying the Fourier transform, Eq. (6) assumes the form

$$\frac{d^2\Phi}{dx^2}-\gamma^2\Phi=0 \tag{9}$$

in which $\gamma=(\alpha^2+s^2)^{1/2}$. The transformed boundary conditions are

$$\Phi'(\alpha,0)=0$$

$$\Phi'_-(\alpha,1)+B_1\Phi_-(\alpha,1)=-\frac{i}{\alpha-is}B_1\left[1+\frac{Q}{B_2}-\frac{Q}{B_1}\right] \tag{10}$$

$$\Phi'_+(\alpha,1)+B_2\Phi_+(\alpha,1)=0$$

where prime denotes the transform of x-derivatives of $\varphi(x,y)$. The general solution of the second order ordinary differential equation (Eq. (9)) is

$$\Phi(\alpha,x)=C_1(\alpha)\cosh\gamma x+C_2(\alpha)\sinh\gamma x \tag{11}$$

Imposing the boundary conditions of Eq. (10) into Eq. (11) yields

$$\Phi_+(\alpha,1)+\left[\frac{1+(B_1\coth\gamma)/\gamma}{1+(B_2\coth\gamma)/\gamma}\right]\Phi_-(\alpha,1)$$
$$=-\frac{i}{\alpha-is}\left(\frac{B_1\coth\gamma}{\gamma+B_2\coth\gamma}\right)\left(1+\frac{Q}{B_2}-\frac{Q}{B_1}\right) \tag{12}$$

3.2 Wiener-Hopf Technique. The technique of Wiener-Hopf, which has been fruitfully applied to the class of rewetting problems, uses the strategy of solving a functional equation (Eq. (9)) comprising of two unknown functions (Φ_+ and Φ_-) of complex variable. The crucial step in successful execution of the Wiener-Hopf technique depends on the factorization of a function, which is analytic in a strip, into the product of two functions that are analytic in the overlapping half-planes. In this context, let

$$K(\alpha)=K_+(\alpha)K_-(\alpha)=\frac{1+(B_1\coth\gamma)/\gamma}{1+(B_2\coth\gamma)/\gamma} \tag{13}$$

where the functions $K_+(\alpha)$, $K_-(\alpha)$ are analytic in the domains D_+ and D_- respectively. Now the kernel function $K(\alpha)$, in connection with Eq. (12), is to be decomposed to $K_+(\alpha)$ and $K_-(\alpha)$ in accordance with the Wiener-Hopf technique. This is accomplished by rearranging Eq. (12) to obtain

$$\frac{\Phi_+(\alpha,1)}{K_+(\alpha)}-\frac{i}{\alpha-is}\left(\frac{Q}{B_2}+\frac{1}{1-\lambda}\right)\left[\frac{1}{K_+(\alpha)}-\frac{1}{K_+(is)}\right]$$
$$=-\frac{i}{\alpha-is}\left(\frac{Q}{B_2}+\frac{1}{1-\lambda}\right)\left[K_-(\alpha)-\frac{1}{K_+(is)}\right]$$
$$-\Phi_-(\alpha,1)K_-(\alpha) \tag{14}$$

where $\lambda=B_2/B_1$. In Eq. (14), each side characterizes the same "entire function", through its representation in the upper and lower halves of the α-plane. Since $\Phi_+(\alpha,1)$ and $\Phi_-(\alpha,1)$ tend to zero at infinity in their half planes of analyticity, while $K_+(\alpha)$ and $K_-(\alpha)$ remain bounded, it follows that the entire function vanishes according to Liouville's theorem ([8], p. 27). Therefore, equating both sides of the Eq. (14) to zero, $\Phi_+(\alpha,1)$ and $\Phi_-(\alpha,1)$ are determined as

$$\Phi_+(\alpha,1)=\frac{i}{\alpha-is}\left(\frac{Q}{B_2}+\frac{1}{1-\lambda}\right)\left[1-\frac{K_+(\alpha)}{K_+(is)}\right]$$
$$\Phi_-(\alpha,1)=-\frac{i}{\alpha-is}\left(\frac{Q}{B_2}+\frac{1}{1-\lambda}\right)\left[1-\frac{1}{K_-(\alpha)K_+(is)}\right] \tag{15}$$

3.3 Quench Front Temperature. Using the above expressions of $\Phi_+(\alpha,1)$ and $\Phi_-(\alpha,1)$, quench front temperature may be obtained by inverting the Fourier transform (Eq. (8)). Such an attempt may become tedious because, in order to carry out the Fourier inversion, it would be necessary to evaluate the residues of the function $\Phi(\alpha,1)$ in the complex domain. Alternatively, in the present paper θ_0 has been calculated in a simplified approach [1] as follows.

$$\Phi_+(\alpha,1)=\int_0^\infty \varphi(1,y)e^{i\alpha y}dy$$

$$=\frac{i}{\alpha}\varphi(1,0)-\frac{1}{i\alpha}\int_0^\infty \frac{\partial\varphi(1,y)}{\partial y}e^{i\alpha y}dy \qquad (16)$$

In the limit $\alpha\rightarrow\infty$, the second integral appearing in Eq. (16) vanishes since the quantity $\partial\varphi/\partial y$ is bounded [1]. Then, by virtue of Eqs. (15)–(16) and invoking an assumption that $K_+(\alpha)$ approaches unity as $\alpha\rightarrow\infty$ (the assumption will be validated later), we obtain

$$\varphi(1,0)=\lim_{\alpha\rightarrow\infty}[-i\alpha\Phi_+(\alpha,1)]=\left(\frac{Q}{B_2}+\frac{1}{1-\lambda}\right)\left[1-\frac{1}{K_+(is)}\right] \qquad (17)$$

The quench front temperature then becomes

$$\theta_0=1+Q/B_2-\varphi(1,0)=\frac{1}{K_+(is)}\left[\frac{Q}{B_2}+\frac{1}{1-\lambda}\right]-\frac{\lambda}{1-\lambda} \qquad (18)$$

Now the function $K_+(is)$ may be expressed as an "infinite product series" or as a "contour integral." While the former leads to evaluation of the eigen values of a certain transcendental equation, the latter leads to an integral expression which is seemingly more convenient for numerical computation. On applying the Cauchy residue theorem within the strip, the function $\ln K(\alpha)$ can be represented by the following contour integral.

$$\ln K(\alpha)=\ln K_+(\alpha)+\ln K_-(\alpha)$$

$$=\frac{1}{2\pi i}\int_{C_+}\frac{\ln K(\xi)}{\xi-\alpha}d\xi-\frac{1}{2\pi i}\int_{C_-}\frac{\ln K(\xi)}{\xi-\alpha}d\xi \qquad (19)$$

where C_+/C_- is an infinite contour lying inside the strip and passing below/above the point α (Fig. 1(*b*)). It may be noted that, due to the asymptotic nature of $\ln K(\alpha)$ function (the order of $\ln K(\alpha)$ being $1/\alpha$), the contribution of vertical sides of the contour to the integral vanishes at $\mathrm{Re}(\alpha)\rightarrow\pm\infty$. Equation (19) can be succinctly written as

$$\ln K_\pm(\alpha)=\pm\frac{1}{2\pi i}\int_{C_\pm}\frac{\ln K(\xi)}{\xi-\alpha}d\xi \qquad (20)$$

from which it follows that $K_\pm(\alpha)=1$ as $\alpha\rightarrow\infty$, as assumed earlier. In order to evaluate the function $K_+(is)$, the contour C_+ may be shifted to the real axis to yield

$$\ln K_+(is)=\frac{1}{2\pi i}\int_{-\infty}^{+\infty}\frac{\ln K(\xi)}{\xi-is}d\xi \qquad (21)$$

Further, as the functions $\ln K(\xi)$, $\xi\ln K(\xi)$ exhibit even and odd properties respectively, Eq. (21) thereby reduces to

$$\ln K_+(is)=\frac{s}{\pi}\int_0^\infty\frac{\ln K(\xi)}{\xi^2+s^2}d\xi \qquad (22)$$

For computational purposes it is advantageous to transform ξ, by $\xi=s\tan\Omega$, to finally obtain the quench front temperature

$$\theta_0=\frac{1}{K_+(is)}\left[\frac{Q}{B_2}+\frac{B_1}{B_1-B_2}\right]-\frac{B_2}{B_1-B_2} \qquad (23)$$

in which,

$$K_+(is)=\exp\left[\frac{1}{\pi}\int_0^{\pi/2}\ln\left\{\frac{1+(B_1\coth s\sec\Omega)/s\sec\Omega}{1+(B_2\coth s\sec\Omega)/s\sec\Omega}\right\}d\Omega\right].$$

It is of interest to examine the limiting solution of the above equation for the case that has been investigated by Olek [2], namely, the rewetting of an infinite slab without any heating or precursory cooling. By assigning $Q=0$, $B_2=0$ and $Q/B_2=0$ in Eq. (23), the expression for θ_0 reduces to exactly the same as that of Olek [2] which, in turn, substantiates the present solution.

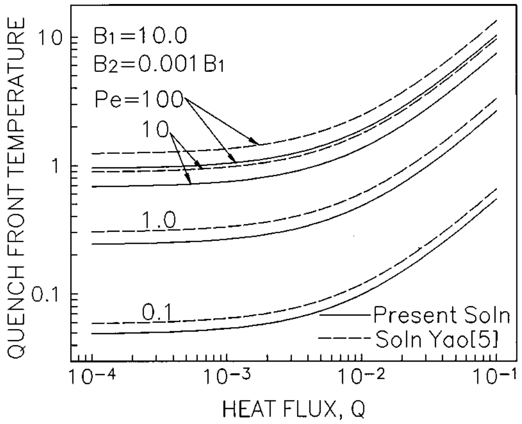

Fig. 2 Quench front temperature for various heat flux and Peclet number

3.4 Critical Heat Flux. The quench front temperature at the critical (dryout) heat flux has been deduced by specifying $s=0$ in Eq. (23). Thus, $K_+(is)$ simplifies to

$$K_+(is)=\exp\left[\frac{1}{\pi}\int_0^{\pi/2}\ln(B_1/B_2)d\Omega\right]=\sqrt{\frac{B_1}{B_2}} \qquad (24)$$

The quench front temperature at the critical heat flux is finally determined as

$$\theta_0=\frac{Q}{\sqrt{B_1B_2}}+\frac{\sqrt{B_2}}{\sqrt{B_1}+\sqrt{B_2}} \qquad (25)$$

The heat flux Q appearing in Eq. (25) may be regarded as the critical heat flux Q_{cri}, which characterizes the maximum allowable heat input to a slab to inhibit the dryout of the coolant.

4 Results and Discussion

Numerical values of the quench front temperature are obtained from the expressions in Eqs. (23) and (25), for a practical range of model parameters B_1, B_2, Pe and Q. For this purpose, the integral appearing in Eq. (23) has been numerically calculated by Simpson's 1/3 rule with 101 equally spaced base points. Experimental investigations on quenching [9] reveal the existence of four distinct heat transfer regimes along the wall, the regimes being demarcated by the characteristic hot surface temperature. These four zones are: forced convection of subcooled liquid, nucleate boiling, wet and dry transition boiling and film boiling. Quench front is observed to exist in the transition zone. The heat transfer coefficient in the transition zone is shown to be 10^5–10^6 W/m^2-K and the vapor cooling heat transfer coefficient in the film boiling zone is in the order of 10^2 W/m^2-K. In the present analysis the values of h_1 and h_2 are adopted from the experimental results of Barnea et al. [9]. Hence the values of h_2 are set equal to $10^{-3}h_1$ and, therefore, $B_2=10^{-3}B_1$.

The variation of quench front temperature with heat flux and Peclet number is shown in Fig. (2), for a fixed value of Biot number. Here θ_0 is found to increase with increase in Peclet number. With fixed material properties and dimensions, Peclet number and Biot number represent the quench front velocity and the heat transfer coefficient respectively. For prescribed values of heat flux and Biot number, θ_0 increases with increase in quench front velocity. This may be due to the fact that a higher relative velocity between the slab and the coolant allows less time for sufficient heat transfer to take place, resulting in a higher value of θ_0. The above trend also reflects the fact that, for the same rewetting rate,

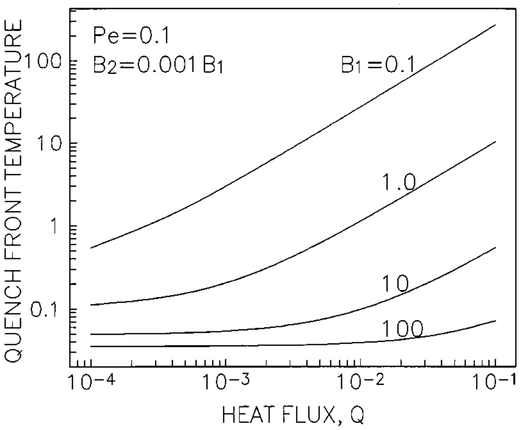

Fig. 3 Quench front temperature for various heat flux and Biot number

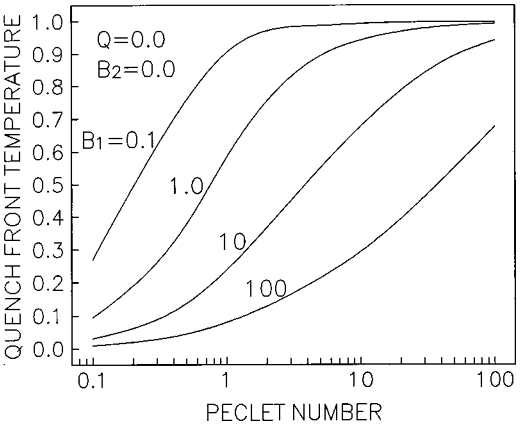

Fig. 5 Quench front temperature for various wetside Biot number and Peclet number without heating and precursory cooling

an increasing slab thermal diffusivity tends to reduce θ_0 whereas the increasing slab thickness has the opposite effect. Further, for a fixed Peclet number, θ_0 increases with increase in Q. Apparently, a higher heat flux causes more heat transfer to the slab and hence this would increase θ_0.

The dependence of quench front temperature on Biot number and dimensionless heat flux is shown in Fig. (3), where θ_0 decreases with increase in Biot number for a given Pe and Q. A higher Biot number results in a higher heat transfer coefficient. This enhanced heat transfer coefficient may cause to decrease θ_0. The above trends are in obvious accord with the predictions based on physical ground. In all cases, θ_0 decreases as Biot number increases, reflecting the fact that a quench front progresses more easily when the heat transfer to the coolant is increased. On a similar ground, conversely, one would conclude that an increasing Q has the opposite effect on the quench front velocity.

The dependence of quench front temperature on Biot number and dimensionless heat flux is shown in Fig. (4), with Pe=0. The physical meaning of Pe=0 is that the quench front ceases to move when Q approaches its critical value. This is the case that the surface can no longer be wetted. For $Q > Q_{\mathrm{cri}}$, the quench front will reverse its direction and the wetted surface will be dried. In this case, the slab will be heated by a heat flux that exceeds the maximum heat removal capacity by convection and boiling and, thus, dryout would occur. Further, the present solution has been compared with those of Yao [5] in Fig. (2) and in Fig. (4). The results are in good agreement with those in [5] for lower values of Biot and Peclet numbers while the deviation becomes more pronounced as Biot and Peclet numbers become large. In Yao's [5] analysis, the temperature distribution along the width of the slab was assumed to be quadratic and with this assumption, the solution was obtained for a two-dimensional conduction model. Apparently, the solution may deviate at higher Biot and Peclet numbers due to the above approximation. Finally, the model is reduced to the conventional model (by setting $Q=0$, $B_2=0$ and $Q/B_2=0$) and illustrated in Fig. (5). As expected, θ_0 increases with increase in Peclet number and with decrease in Biot number.

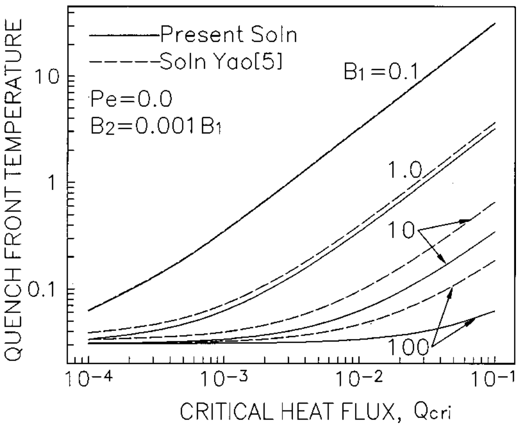

Fig. 4 Quench front temperature at the critical heat flux

The Wiener-Hopf technique yields a solution for the quench front temperature (Eq. (23)), which is more elegant and accurate than results obtained by other analytical methods. In particular, Wiener-Hopf solution is superior to the one by separation of variables, since it overcomes the accuracy problems due to slow convergence of the series expansions that stem from discontinuity of the surface heat flux at the quench front [2]. The technique makes use of decomposing a kernel function in the complex Fourier plane so as to resolve the singularity arising out of discontinuous boundary conditions at the quench front, as in the case of a rewetting problem. The explicit formula for the quench front temperature obtained in the present study is valid for all Biot and Peclet numbers. However, the present model is limited to small Peclet numbers with regard to heat pipes. This is due to the fact that, in the case of large Peclet numbers, a thermal boundary layer is formed near the cooling surface of a heat pipe and this has not been incorporated in the present model. Besides, large Biot numbers are usually associated with large Peclet numbers, unless the internal heating is large. Since the internal heating effect is also not considered in the model, the present analysis is limited to both small Biot and Peclet numbers in case of heat pipes.

5 Conclusion

An analytical solution for rewetting of an infinite slab with a uniform heating has been obtained, employing the Wiener-Hopf technique. In general, quench front temperature is found to increase with increase in Peclet number and dimensionless heat flux, and with decrease in Biot number. The boundary conditions in the present formulation require liquid/vapor temperatures and liquid/vapor heat transfer coefficients as input parameters, these limitations being inherent in a conduction-controlled rewetting model. The arbitrariness of the choice of their values may be eliminated if a conjugate heat transfer model is considered, where the energy equations of solid, liquid and vapor regions need to be solved simultaneously.

Nomenclature

B = Biot number
C = specific heat
h = heat transfer coefficient
k = thermal conductivity
L = length of the slab
Pe = Peclet number
q = heat flux
Q = dimensionless heat flux
s = half of the Peclet number
t = time
T = temperature
u = quench front velocity
X, Y = physical coordinates
$\bar{x}, \bar{y}$ = coordinates in quasi-steady state
x, y = dimensionless coordinates in quasi-steady state

Greek Alphabets

δ = thickness of the slab
λ = ratio of dryside to wetside Biot numbers
θ = dimensionless temperature
ρ = density

Subscripts

0 = quench front
1 = wet region
2 = dry region
s = saturation
w = initial wall condition

References

[1] Levine, H., 1982, "On a Mixed Boundary Value Problem of Diffusion Type," Appl. Sci. Res., **39**, pp. 261–276.
[2] Olek, S., 1988, "On the Two-region Rewetting Model with a Step Change in the Heat Transfer Coefficient," Nucl. Eng. Des., **108**, pp. 315–322.
[3] Tien, C. L., and Yao, L. S., 1975, "Analysis of Conduction Controlled Rewetting of a Vertical Surface," ASME J. Heat Transfer, **97**, pp. 161–165.
[4] Olek, S., 1994, "Quenching of a Composite Slab," Int. Commun. Heat Mass Transfer, **21**, pp. 333–344.
[5] Yao, L. S., 1976, "Rewetting of a Vertical Surface with Internal Heat Generation," AlChE Symposium Series: Solar and Nuclear Heat Transfer, **73**, pp. 46–50.
[6] Peng, X. F., and Peterson, G. P., 1992, "Analysis of Rewetting for Surface Tension Induced Flow," ASME J. Heat Transfer, **114**, pp. 703–707.
[7] Chan, S. H., and Zhang, W., 1994, "Rewetting Theory and the Dryout Heat Flux of Smooth and Grooved Plates with a Uniform Heating," ASME J. Heat Transfer, **116**, pp. 173–179.
[8] Roos, B. W., 1969, *Analytical Functions and Distributions in Physics and Engineering*, John Wiley and Sons, New York.
[9] Barnea, Y., Elias, E., and Shai, I., 1994, "Flow and Heat Transfer Regimes during Quenching of Hot Surfaces," Int. J. Heat Mass Transf., **37**, pp. 1441–1453.

A Natural Circulation Model of the Closed Loop, Two-Phase Thermosyphon for Electronics Cooling

S. I. Haider

Yogendra K. Joshi

G. W. Woodruff School of Mechanical Engineering,
Georgia Institute of Technology,
Atlanta, GA 30332

Wataru Nakayama

Therm Tech International,
920-7 Higashi Koiso, Oh-Iso Machi,
Kanagawa 255-0004, Japan

This study presents a model for the two-phase flow and heat transfer in the closed loop, two-phase thermosyphon (CLTPT) involving co-current natural circulation. The focus is on CLTPTs for electronics cooling that exhibit complex two-phase flow patterns due to the closed loop geometry and small tube size. The present model is based on mass, momentum, and energy balances in the evaporator, rising tube, condenser, and the falling tube. The homogeneous two-phase flow model is used to evaluate the friction pressure drop of the two-phase flow imposed by the available gravitational head through the loop. The saturation temperature dictates both the heat source (chip) temperature and the condenser heat rejection capacity. Thermodynamic constraints are applied to model the saturation temperature, which also depends upon the local heat transfer coefficient and the two-phase flow patterns inside the condenser. The boiling characteristics of the enhanced structure are used to predict the chip temperature. The model is compared with experimental data for dielectric working fluid PF-5060 and is in general agreement with the observed trends. The degradation of condensation heat transfer coefficient due to diminished vapor convective effects, and the presence of subcooled liquid in the condenser are expected to cause higher thermal resistance at low heat fluxes. The local condensation heat transfer coefficient is a major area of uncertainty. [DOI: 10.1115/1.1482404]

Keywords: *Cooling, Electronics, Heat Transfer, Thermosyphons, Two-Phase*

Introduction

We report on the modeling of the two-phase flow and heat transfer in the closed loop, two-phase thermosyphon (CLTPT) involving co-current natural circulation. Most of the available modeling literature deals with two-phase thermosyphons with counter-current circulation within a closed, vertical, wickless heat pipe arrangement. A need was felt to develop a model for design and optimization of CLTPTs for microelectronics applications. These devices allow not only large heat removal capability from discrete electronic devices, but also provide considerable flexibility in the placement of the condenser and evaporator.

Figure 1 shows a schematic diagram of the experimental setup described by Yuan et al. [1] to which the present model results are compared. Their CLTPT consists of four major components; the evaporator, the rising tube, the condenser, and the falling tube. A micro fabricated three-dimensional boiling enhancement structure within the evaporator is attached to its bottom wall. The terms ‘‘rising’’ and ‘‘falling’’ describe the general fluid flow direction through the connecting tubes in a natural circulation thermosyphon where condenser is placed at a higher elevation than the evaporator. Figure 1 shows four distinct thermodynamic states along the loop as S1 (evaporator outlet), S2 (condenser inlet), S3 (condenser outlet), and S4 (evaporator inlet). To simplify the analysis, the evaporator wall thickness is neglected. As a result, the square base of the enhanced boiling structure is in intimate contact with the heat generating chip surface. This plane termed as the ‘‘wall,’’ is the reference plane with which the various elevations of the thermosyphon are measured to reflect the respective gravitational heads. The desired range of the wall temperature is typically 80–95°C for microelectronics applications.

A modeling methodology based on mass, momentum, and energy balances is presented, which also utilizes thermodynamic constraints in the four major components of the thermosyphon loop. The fluid absorbs heat by boiling inside the evaporator enclosure. The resulting two-phase flow rises up from the evaporator through a vertical tube, bends by 90 deg, and then undergoes condensation by passing through a naturally cooled fin-tube heat exchanger. Depending upon the inlet vapor quality, flow rate, saturation and ambient temperatures, and the condenser inside/outside heat transfer characteristics, the flow may or may not completely condense within the available condenser length. If the condensation is not complete by the condenser outlet, the falling tube will experience a higher pressure drop due to two-phase flow and will yield a smaller gravitational head due to vapor presence. As a result, the evaporator will receive both vapor and liquid, the entire thermosyphon would operate at a constant saturation temperature/pressure, and all heat transfer in the evaporator would be latent. On the other hand, if the condensation is complete, it would be followed by a subcooled liquid core toward the condenser outlet. The presence of a subcooled liquid core in the condenser would deteriorate the condenser's heat transfer performance, the condenser outlet would be at a temperature less than the saturation temperature, the falling tube would experience single-phase pressure drop and would give rise to a maximum gravitational head at the evaporator, and some of the heat addition in the evaporator would be sensible.

After rejecting heat in the condenser, the condensate then flows vertically downward through the falling tube, bends by 90 deg, and enters the evaporator. As no heat losses are considered through the connecting tubes, the vapor quality, void fraction, and temperature remain constant along the rising and falling tubes. The difference between the gravitational heads of the liquid-rich falling tube and the vapor-rich rising tube causes the natural circulation of the two-phase flow through the loop. The homogeneous two-phase flow model is used to evaluate the two-phase

---

Contributed by the Heat Transfer Division for publication in the JOURNAL OF HEAT TRANSFER. Manuscript received by the Heat Transfer Division August 28, 2001; revision received April 4, 2002. Associate Editor: F. B. Cheung.

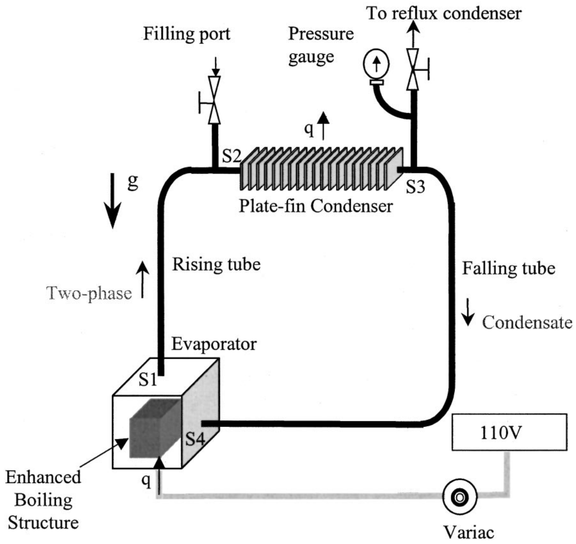

Fig. 1 Schematic of the experimental setup of the co-current, closed loop, two-phase thermosyphon

friction pressure drop along the loop. An established natural convection correlation is used for the condenser air-side plate-fin geometry. Nonetheless, the local in-tube condensation heat transfer coefficient is an area of uncertainty due to its lack of sensitivity to the vapor convective effects, and the laminar to turbulent Reynolds number range encountered during condensation in the present set-up.

Saturation temperature that couples the evaporator and condenser is identified as a key variable, as it dictates both the heat source (chip) temperature and the condenser's capacity to reject heat to the ambient. Thermodynamic constraints are reconciled with the thermophysical balances in an attempt to model the system saturation temperature, which strongly depends upon the prediction of the local condensation heat transfer coefficient and the void fractions in the system components. To the best of our knowledge, this is the first attempt to model the saturation temperature in a CLTPT as a function of heat transfer, fluid flow, and thermodynamic characteristics of the system. The experimentally observed boiling characteristics of the enhanced structure reported by Yuan et al. [1] are used in the model to predict the wall temperature.

Literature Survey

The available modeling literature on two-phase thermosyphons is dedicated to the closed, gravity assisted, two-phase thermosyphons (GATPTs). They are vertical, wickless heat pipes whose lower and upper sections, separated by an adiabatic section, serve as the evaporator and condenser, respectively. The working fluid absorbs heat in the evaporator section, and the vapor rises up to the condenser section where it rejects heat to the ambient by condensing on the vertical pipe wall. The liquid then flows downward on the wall under the effect of gravity as a thin film whose thickness is much smaller than the pipe diameter. The counter-current liquid and vapor streams are well separated. A survey of GATPTs by El-Genk and Saber [2] shows ethanol, acetone, R-11, and R-113 as working fluids of interest, wall heat fluxes of 0.99–52.62 kW/m^2, filling ratios of 0.01–0.62, inner diameters of 6–37 mm, evaporator section height of 50–609.6 mm, and vapor temperature of 261–352 K.

The typical GATPT length scales are much larger than that in the present CLTPT arrangement. Because of their smaller size, loop geometry, and liquid film thickness of the order of the diameter of the condenser tubing, CLTPTs also face more complex two-phase flow patterns and higher pressure and temperature rises from the initial ambient condition. In the following, we present a brief overview of the GATPT modeling literature in order to relate it to the saturation temperature modeling in the present CLTPT geometry. Modeling saturation temperature in the present CLTPT is very important because of the level of rise of the vapor pressure in the operating heat flux range. The successful prediction of the chip wall temperature is critically dependent on the saturation temperature.

Harley and Faghri [3] modeled a GATPT arrangement using the mass, momentum, and energy balances, and solving them for the well-separated, counter-current liquid and vapor flows due to a Nusselt type condensation on the wall. The maximum temperature variation in their thermosyphon is only 6 C in the test range. They modeled the saturation temperature as the falling condensate film interface temperature that drives the conjugate heat transfer through the film and the wall. They solved the vapor momentum balance and the velocity field by using a guessed pressure field. Then, they used the Clasius-Clapeyron equation to find the new saturation temperature corresponding to the new pressure, and applied the general gas law to find the new vapor density. The coupling between the heat transfer and the flow geometry was used to determine the correct saturation pressure and temperature fields on the interface. In a similar analysis of Zuo and Gunnerson [4], operating saturation temperature was specified and not modeled.

El-Genk and Saber [5] studied the effect of initial filling ratio and vapor temperature on the design and operation of closed two-phase thermosyphons of the inside diameter range 15–45 mm and the evaporator length range 0.5–2.0 m. They gave special emphasis to calculating the operating filling ratio by applying mass balances to the individual components of the thermosyphon. They also calculated the axial distribution of the liquid film thickness along the condenser, evaporator, and adiabatic sections. A significant effect on the thermosyphon performance was found due to the pressure dependence of the latent heat of vaporization. However, in their model the saturation temperature is not modeled as a function of heat input, but is rather treated as an independent parameter set for parametric study. Vincent and Kok [6] simulated an oil-cooled closed-loop thermosyphon using 375 kg water for a 1 MW industrial application. They applied a control-volume based energy and momentum balance, but did not deal with the thermodynamics of the thermosyphon. The saturation temperature was treated as an independent parameter in their parametric study, though it varied from 90°C to 250°C.

Wang and Ma [7] modeled and conducted experiments on inclined two-phase thermosyphons. They concluded that when the liquid filling is larger than 10 percent, the liquid filling and vapor pressure will affect the condensation heat transfer in the thermosyphon. They concluded the existence of an optimum angle of inclination between 30–50 deg from the horizontal. They also reported other investigations where an optimum angle of inclination was found between 10–50 deg. An improved gravity-assisted drainage could reduce the condenser thermal resistance, which is the dominant part in the present system, and result in a lower wall (chip) temperature. Their work indirectly shows that different saturation temperatures can be realized for the same heat flux input and same initial fill ratio, depending upon the mode of heat transfer realized in the condenser.

Present Two-Phase Thermosyphon Model

A rationally based thermosyphon model was developed by satisfying the mass, momentum, and energy balances, as well as the thermodynamic constraints. The model utilized the visual observations made by Yuan et al. [1] for the rising tube, falling tube, and the evaporator. A steady-state thermosyphon operation is assumed and a one-dimensional analysis is performed. The pressure drops in the rising and falling tubes are modeled using the homogeneous two-phase flow model, which assumes equal liquid and vapor phase velocities. All two-phase flow parameters are cross-section averaged, with vapor assumed to be an ideal gas in ther-

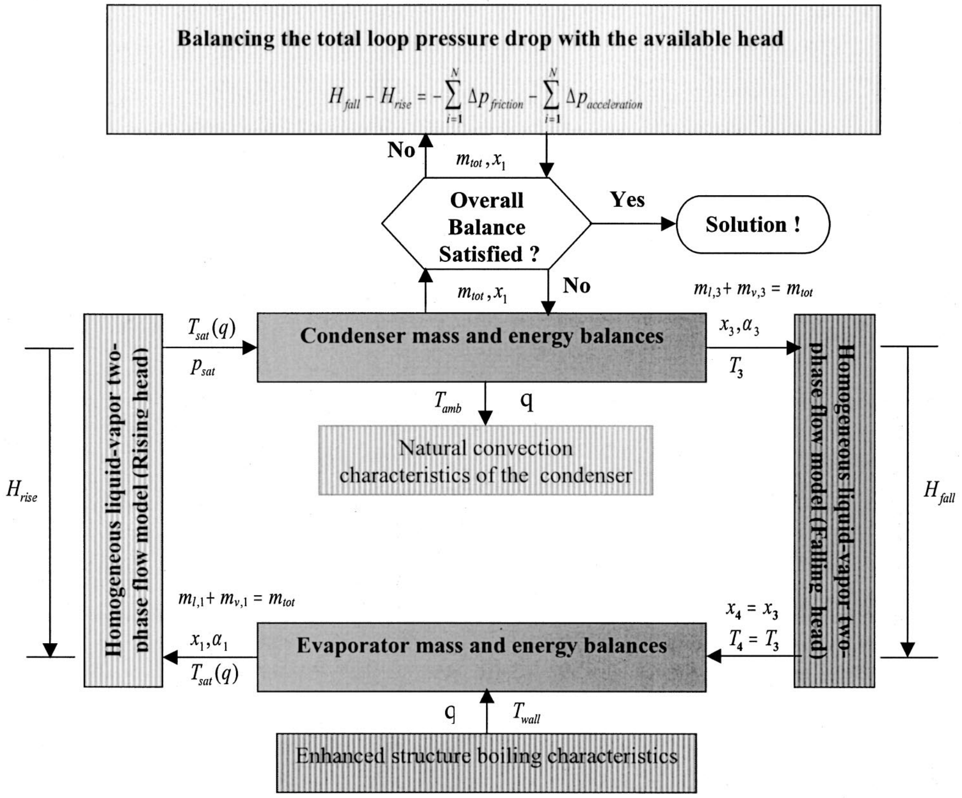

Fig. 2 Mass, momentum, and energy balance iterations in the thermosyphon model

modynamic equilibrium with the liquid phase. The model neglects pressure drops in the evaporator and the condenser; as well as the heat losses from the rising and falling tubes. The neglected quantities are believed to be of the order of magnitude of the uncertainties involved in predicting similar quantities in other parts of the thermosyphon. The model assumes constant liquid/vapor thermophysical properties with the exception of vapor density that varies with saturation temperature and pressure that are, in turn, interdependent.

Figure 2 shows a summary of the present two-phase thermosyphon model. The figure reflects two distinct iterations coupled through two key design parameters; the total two-phase mass flow rate circulating through the loop and the vapor quality at the evaporator outlet. The first iteration is based on the overall momentum balance. This means that the sum of the friction and acceleration pressure drops in the entire thermosyphon loop must be equal to the available gravitational pressure head—the driving force behind the natural circulation—which is the liquid-rich falling tube gravitational head minus the vapor-rich gravitational head of the evaporator and the rising tube. The homogeneous two-phase flow model was used to evaluate the two-phase friction pressure drops in the system. The first iteration backs out a *total* two-phase mass flow rate whose circulation through the loop would satisfy the overall pressure balance along the loop.

The second iteration decomposes the *total* two-phase flow rate into the *vapor* and *liquid* parts by solving the individual mass and energy balances on the evaporator and the condenser. This also requires the knowledge of the air-side natural convection characteristics of the condenser. The experimentally observed boiling characteristics of the enhanced boiling structure are also built in the model that allows us to predict the wall temperature for a given saturation temperature. In the entirety, the model looks for the values of the total mass flow rate and the evaporator outlet quality that would satisfy both iterations, i.e., the overall mass, momentum and energy balance as well as the thermodynamic constraints.

Overall Loop Pressure Balance. The general formulation of the idealized one-dimensional steady-sate, two-phase flow pressure gradient in an inclined tube can be found in Carey [8] as follows:

$$-\left(\frac{dp}{dz}\right) = -\frac{p}{A}\left(\frac{dA}{dz}\right) - \left(\frac{dp}{dz}\right)_{fr} + [(1-\alpha)\rho_l + \alpha\rho_v]g \sin\theta + \frac{1}{A}\frac{d}{dz}\left[\frac{G^2x^2A}{\rho_v\alpha} + \frac{G^2(1-x)^2A}{\rho_l(1-\alpha)}\right] \quad (1)$$

The above equation accounts for the conservation of mass with possible phase change; individual momentum transports of both liquid and vapor phases during two-phase flow, as well as the interfacial shear force balance.

Assuming an adiabatic flow through the rising and falling tubes with constant area of cross-section leads to a constant quality and a constant void fraction. This eliminates the acceleration terms, and the following equation results:

$$-\left(\frac{dp}{dz}\right) = -\left(\frac{dp}{dz}\right)_{fr} + [(1-\alpha)\rho_l + \alpha\rho_v]g \sin\theta \quad (2)$$

Thus, the overall pressure gradient in the rising and falling tubes is a sum of the friction and gravitational pressure gradients. The friction pressure gradient term includes the combined effect of both liquid and vapor phases.

Let H_{pump} be the pumping head (Pa) available to the loop through an external power source. In that case, H_{pump} would act opposite to the gravitational, frictional, and acceleration pressure losses. Therefore, the following equation can be written:

$$H_{\text{pump}}+\sum_{i=1}^{N}\ \Delta p_{fr}+\sum_{i=1}^{N}\ \Delta p_{gr}+\sum_{i=1}^{N}\ \Delta p_{\text{acc}}=0 \tag{3}$$

where N is the total number of distinct pressure drop components in the closed loop. We are following a sign convention that H_{pump} is positive; Δp_{fr} is always negative; Δp_{gr} is positive in a falling component and negative in a rising component; and Δp_{acc} is positive if the flow decelerates and negative if the flow accelerates. The above equation is a formal way of expressing the fairly established methodology for modeling mass flow rate through the closed loops, e.g., by Cammarata et al. [9] and Tengblad [10].

As the gravitational pressure change is positive for the falling tube and negative for the rising tube and the evaporator, Eq. 3 can be rewritten as:

$$H_{\text{pump}}+(H_{\text{fall}}-H_{\text{rise}})=-\sum_{i=1}^{N}\ \Delta p_{fr}-\sum_{i=1}^{N}\ \Delta p_{\text{acc}} \tag{4}$$

where both H_{fall} and H_{rise} are the *magnitudes* of the falling and rising gravitational pressure heads that would act in tandem with any externally imposed H_{pump}. In the absence of any externally imposed head H_{pump}, as is the case at present, the difference between the falling and rising heads would be the sole driver of the natural circulation through the two-phase thermosyphon. The two-phase pressure drop is neglected inside the horizontal condenser, as are fitting pressure drops in the system and entrance/exit pressure losses.

Rising and Falling Tube Pressure Drops. During the thermosyphon operation, the rising tube experiences two-phase flow while the falling tube is filled with two-phase flow or saturated liquid returning back to the evaporator, depending upon whether the condensation is complete.

Homogeneous Two-phase Flow Model. The homogeneous two-phase flow model was used to analyze the flow characteristics in the rising and falling tubes. The model treats the two-phase as a single phase with mean fluid properties that are functions of the corresponding liquid and vapor properties and the quality. This also means assuming equal liquid and vapor velocities, i.e., no slip $(S=1)$. The flow through the rising and falling tubes is considered adiabatic, so temperature, vapor quality, and void fraction remain unchanged along the rising and falling tubes.

Considering the two-phase flow as an equivalent single phase flow, the frictional part of the overall pressure gradient in Eq. 2 is evaluated using the following conventional form:

$$-\left(\frac{dp}{dz}\right)_{fr}=\frac{2f_{tp}G^{2}}{\bar{\rho}d_{h}} \tag{5}$$

where f_{tp} is the effective two-phase friction factor, and the mean two-phase density is defined as a function of liquid and vapor densities, and vapor quality (x) as follows:

$$\frac{1}{\bar{\rho}}=\frac{x}{\rho_{v}}+\frac{1-x}{\rho_{l}} \tag{6}$$

The mass velocity G (kg/m^2/s) is given by:

$$G=\frac{\dot{m}_{\text{tot}}}{A}=\frac{\dot{m}_{l}+\dot{m}_{v}}{A} \tag{7}$$

The hypothetical single-phase pressure gradient considering the entire two-phase flow at the liquid density, is evaluated for benchmarking purposes, as follows:

$$-\left(\frac{dp}{dz}\right)_{lo}=\frac{2f_{lo}G^{2}}{\rho_{l}d_{h}} \tag{8}$$

Both f_{tp} and f_{lo} are evaluated using the following conventional forms for laminar $(\text{Re}<2{,}300)$ and turbulent flows, respectively.

$$f=16.0\ \text{Re}^{-1.0} \tag{9}$$

$$f=0.079\ \text{Re}^{-0.25} \tag{10}$$

The Reynolds numbers for the liquid-only and two-phase flows are defined as.

$$\text{Re}_{lo}=\frac{\text{Gd}_{h}}{\mu_{l}} \tag{11}$$

$$\text{Re}_{tp}=\frac{\text{Gd}_{h}}{\bar{\mu}} \tag{12}$$

We used the following expression for the two-phase mean viscosity proposed by McAdams et al. [11].

$$\frac{1}{\bar{\mu}}=\frac{x}{\mu_{v}}+\frac{1-x}{\mu_{l}} \tag{13}$$

More details and references on the homogeneous flow model can be found in Collier [12].

Modeling the System Saturation Temperature. A unique aspect of the present model is its ability to predict the saturation temperature in the CLTPT. Thermodynamic considerations are important as the saturation temperature and pressure vary significantly with the heat flux due to the volumetric constraints of the two-phase thermosyphon.

The vapor density for PF-5060, a perflourocarbon (Perfluoro-2-methylpentane, C_6F_{14}) with a molecular weight 338.04, was computed by using the general gas law. This helped estimate the total charge, m_{charge}, in the system using the initial fill ratio at the ambient saturation condition. We used the following empirical equation for the inter-conversion of p_{sat} and T_{sat} for PF-5060

$$\log_{10}(p_{\text{sat}})=a-\frac{b}{(T_{\text{sat}}+273.15)-c} \tag{14}$$

where $a=4.04938$, $b=1108.035$, $c=56.584$ and, p_{sat} and T_{sat} are in bar and degree C, respectively. The equation was found from NIST (CAS Registry Number 355-04-4), and relates the PF-5060 experimental data on saturation pressure and temperature within the range, -19.22 C to 177.96 C. It was preferred over the classical Clasius-Clapeyron equation, as it accounts for the dependencies of i_{fg} and ρ_l on saturation state.

So far, we have no information on either the saturation temperature or pressure during the thermosyphon operation. We propose the heat balance coupling between the evaporator and the condenser as the missing link to the solution of saturation temperature. The balance, which would relate the saturation temperature with the heat flux, is implicit in the present model. Summarily, T_{sat} is iteratively solved to the value that would be low enough to absorb the heat input in the evaporator and high enough to reject the same in the condenser, for the imposed flow circulation. In addition to the condenser heat transfer characteristics, the prediction of T_{sat} also requires the knowledge of the condenser void fraction as a function of the initial system filling ratio, and the operating void fractions of the rising tube, falling tube, and the evaporator. This way the mass balance gives an estimate of the amount of liquid in the condenser that has to match with the liquid film distribution dictated by the condensation characteristics along the condenser wall. Thus, for a given initial charge in the thermosyphon, m_{charge}, the following overall mass balance needs to be satisfied in terms of the component volumes and their predicted operating void fractions.

$$m_{\text{charge}}=\sum_{i=1}^{4}\ [\rho_{l}(1-\alpha_{i})+\rho_{v}\alpha_{i}]V_{i} \tag{15}$$

The evaporator and condenser void fractions are dictated by the heat flux input and the respective condenser heat transfer characteristics. The above equation implicitly reconciles the heat transfer rates and the void fractions in a way that leads to the saturation temperature. Intuitively the saturation temperature should be a function of the condenser heat transfer characteristics, besides the system initial filling ratio, and the heat flux. This was corroborated by blowing a fan over the condenser, and noting that the saturation temperature dropped by about 5°C around 40 W/cm^2 wall heat flux.

Tube Length Required for Complete Condensation. As the in-tube condensation heat transfer coefficient $h_i(x)$ varies along the condenser length due its dependence on vapor quality, a differential analysis was performed to determine the variation of vapor quality (x) along the condenser length (z). The analysis was based on a condensing vapor-liquid mass balance causing a change in quality (dx) along a differential tubing element of length dz; and the rejection of the associated latent heat from the condensing fluid to the ambient air through the wall of the element under the tube inside and outside heat transfer characteristics. The resulting formulation is as follows.

$$-\dot{m}_{\mathrm{tot}} i_{fg}\left(\frac{dx}{dz}\right)=\frac{\pi F(T_{\mathrm{sat}}-T_{\mathrm{amb}})}{\left[\dfrac{1}{h_i(x)D_i}+\dfrac{\ln\left(\dfrac{D_o}{D_i}\right)}{2k}+\dfrac{1}{\eta h_o D_{o,\mathrm{eff}}}\right]} \tag{16}$$

The rectangular plate fin array attached to the condenser tubing to enhance the natural convection heat transfer constitutes parallel vertical channels that are open to the ambient air from all sides. We used a semi-empirical model from Bar-Cohen and Rohsenow [13] for the air-side free convection heat transfer coefficient h_o within the channels. As no more than a few degrees of subcooling is anticipated, a constant h_o is justified for the entire condenser tubing.

The effective outside diameter $D_{o,\mathrm{eff}}$ accounts for the effect of the outside surface geometry in terms of the tube outside diameter D_o, the rectangular fin height (H), width (W), spacing (S), and thickness (t), as follows.

$$D_{o,\mathrm{eff}}=\frac{1}{\pi(S+t)}\left[\left(2HW-\frac{\pi}{2}D_o^2\right)+\pi D_o S+2t(W+H)\right] \tag{17}$$

We used the following correlation from Ananiev et al. [14] for local in-tube condensation heat transfer coefficient, as required by Eq. 16

$$h_i(x)=h_{lo}\sqrt{\frac{\rho_l}{\overline{\rho(x)}}} \tag{18}$$

where the liquid-only heat transfer coefficient h_{lo} is computed from the typical single-phase heat transfer correlations assuming the entire two-phase flow to be liquid. The same liquid-only heat transfer coefficient would also be applicable to the subcooled region, if it existed. For turbulent flow, we use.

$$\frac{h_{lo,\mathrm{tur}}d_h}{k_l}=0.021\,\mathrm{Re}_{lo}^{0.8}\,\mathrm{Pr}^{0.43} \tag{19}$$

For laminar flow with a constant heat flux boundary condition, we use.

$$\frac{h_{lo,\mathrm{lam}}d_h}{k_l}=4.36 \tag{20}$$

Using Eq. 6 for the homogeneous flow mean two-phase density, the local condensation heat transfer coefficient from Ananiev et al. [14] is rewritten as a function of the local vapor quality, as follows.

$$h_i(x)=h_{lo}\sqrt{1+\left(\frac{\rho_l}{\rho_v}-1\right)x} \tag{21}$$

Using the above $h_i(x)$ equation gave the following closed form solution of Eq. 16 for the local vapor quality (x) along the condenser length (z) applicable within the condensation region ($x_{c,i} \leqslant x \leqslant x_{c,o}$).

$$Az=B(x_{c,i}-x)+C\left(\sqrt{1+\left(\frac{\rho_l}{\rho_v}-1\right)x_{c,i}}-\sqrt{1+\left(\frac{\rho_l}{\rho_v}-1\right)x}\right) \tag{22}$$

where

$$A=\frac{\pi F(T_{\mathrm{lat}}-T_{\mathrm{amb}})}{\dot{m}_{\mathrm{tot}} i_{fg}} \tag{23}$$

$$B=\frac{\ln\left(\dfrac{D_o}{D_i}\right)}{2k}+\frac{1}{\eta h_o D_{o,\mathrm{eff}}} \tag{24}$$

$$C=\frac{2}{h_{lo}D_i\left(\dfrac{\rho_l}{\rho_v}-1\right)} \tag{25}$$

Equation 22 gives the following condenser tubing length required for complete condensation ($x=0$).

$$L_{cc}=\frac{Bx_{c,i}}{A}+\frac{C}{A}\left(\sqrt{1+\left(\frac{\rho_l}{\rho_v}-1\right)x_{c,i}}-1\right) \tag{26}$$

The flow at the condenser outlet may be two-phase, saturated, or subcooled depending upon whether the available condenser tubing length L_c is less than, equal to, or greater than L_{cc}, respectively.

Condenser Outlet Thermodynamic State. Assuming that no heat is rejected and no phase change occurs in the rising and falling tubes, the evaporator outlet thermodynamic state is expected to be the same as the one at the condenser inlet ($T_{c,i}=T_{c,o}$; $x_{c,i}=x_{c,o}$), and vice versa ($T_{e,i}=T_{c,o}$; $x_{e,i}=x_{c,o}$). For steady-state thermosyphon operation, the above assumption also establishes equalities in the latent and sensible heat transfer in the evaporator and the condenser, i.e, $q_{c,\mathrm{lat}}=q_{e,\mathrm{lat}}$ and $q_{c,\mathrm{sen}}=q_{e,\mathrm{sen}}$. However, there are two possible scenarios for applying the overall condenser heat balance depending upon whether the condensation is complete or not. First, we compute the condenser length required for complete condensation L_{cc} using Eq. 26. If L_{cc} is less than the available condenser tubing length L_c, the remaining condenser length is filled with subcooled liquid. On the other hand, if L_{cc} turns out to be larger than L_c, the entire condenser is filled with two-phase flow.

Complete Condensation. In this scenario, the available condenser tubing length is sufficient for complete condensation, and the condenser outlet vapor quality is zero ($x_{c,o}=0$). Here, first, the latent heat added in the evaporator is rejected in the condensation length of the condenser tubing at a constant saturation temperature while vapor quality decreases. Once the condensation process is complete, the sensible heat added in the evaporator is rejected in the remaining length of the condenser tubing, which is filled with sub-cooled liquid. The condenser outlet temperature and the amount of sensible heat rejected by the condenser are dictated by a balance between the heat transfer characteristics of the subcooled section and the subcooled liquid's capacity to reject heat, as follows.

The sensible heat, $q_{c,\mathrm{sen}}$, rejected by the sub-cooled liquid section of length L_{sub} to the ambient air is as follows

$$q_{c,\text{sen}}=\frac{\pi L_{\text{sub}}F_{\text{sub}}(LMTD_{\text{sub},cf})}{\left[\dfrac{1}{h_{lo}D_i}+\dfrac{\ln\left(\dfrac{D_o}{D_i}\right)}{2k}+\dfrac{1}{\eta h_{\text{sub},o}D_{o,\text{eff}}}\right]} \tag{27}$$

where the counter-flow log-mean-temperature difference for the subcooled section is defined in terms of the condenser inlet, outlet, and ambient temperatures as follows.

$$\text{LMTD}_{\text{sub},cf}=\frac{(T_{c,i}-T_{\text{amb}})-(T_{c,o}-T_{\text{amb}})}{\ln\left(\dfrac{T_{c,i}-T_{\text{amb}}}{T_{c,o}-T_{\text{amb}}}\right)} \tag{28}$$

Therefore, the following specific heat balance also has to hold.

$$q_{c,\text{sen}}=\dot{m}_{\text{tot}}c_{p,l}(T_{c,i}-T_{c,o}) \tag{29}$$

Thus, the amount of sensible heat addition in the evaporator is dictated by the degree of subcooling attained in the condenser.

Incomplete Condensation. Here, the available condenser tubing length is not sufficient for all the vapor to condense, and the condenser outlet is two-phase that also suggests a constant temperature throughout the condenser $(T_{c,o}=T_{c,i})$. Thus, no subcooled liquid core exists and no sensible heat rejection is involved here; and the entire thermosyphon operates at a constant saturation temperature/pressure. The condenser outlet vapor quality $x_{c,o}$ can be obtained by solving Eq. 22 for the known total condenser length L_c, as follows.

$$AL_c=B(x_{c,i}-x_{c,o})+C\left[\sqrt{1+\left(\frac{\rho_l}{\rho_v}-1\right)x_{c,i}}-\sqrt{1+\left(\frac{\rho_l}{\rho_v}-1\right)x_{c,o}}\right] \tag{30}$$

Condenser Vapor Volume. The model assumes an annular two-phase flow all along the condensation length. A liquid film of mean thickness δ growing on the tube wall surrounds the vapor core that diminishes in size due to condensation. The peripheral variation in the liquid film thickness due to gravity is considered insignificant for volumetric calculations. The local void fraction, α, at a general location z is defined in terms of the local mean film thickness $\delta=\delta(z)$ and the condenser tube inside diameter D_i, as follows:

$$\alpha=\frac{(D_i-2\delta)^2}{D_i^2} \tag{31}$$

Using this expression, a differential vapor volume along the condensation length turns out to be

$$dV_v=\frac{\pi}{4}D_i^2\alpha dz \tag{32}$$

Using the following expression for local homogeneous flow void fraction

$$\alpha=\frac{\left(\dfrac{\rho_l}{\rho_v}\right)x}{1+\left(\dfrac{\rho_l}{\rho_v}-1\right)x} \tag{33}$$

along with the $z=z(x)$ formulation in Eq. 22, Eq. 32 can be rewritten as:

$$\frac{dV_v}{dx}=\frac{-\pi D_i^2}{4A}\left[\frac{B\left(\dfrac{\rho_l}{\rho_v}\right)x}{1+\left(\dfrac{\rho_l}{\rho_v}-1\right)x}+\frac{C\left(\dfrac{\rho_l}{\rho_v}-1\right)\left(\dfrac{\rho_l}{\rho_v}\right)x}{2\left(1+\left(\dfrac{\rho_l}{\rho_v}-1\right)x\right)^{3/2}}\right] \tag{34}$$

Integrating the above expression from the maximum vapor quality $x_{c,i}$ at the condenser inlet through the minimum vapor quality $x_{c,o}$ generally occurring at the condenser outlet, we get the following formulation of the total vapor core volume in the condenser.

$$\begin{aligned}V_{v,\text{cond}}=\frac{\pi D_i^2}{4A}\Bigg\{&\frac{B\left(\dfrac{\rho_l}{\rho_v}\right)(x_{c,i}-x_{c,o})}{\left(\dfrac{\rho_l}{\rho_v}-1\right)}\left[1-\frac{1}{\left(\dfrac{\rho_l}{\rho_v}-1\right)(x_{c,i}-x_{c,o})}\right.\\&\left.\times\ln\left(\frac{\left(1+\left(\dfrac{\rho_l}{\rho_v}-1\right)x_{c,i}\right)}{\left(1+\left(\dfrac{\rho_l}{\rho_v}-1\right)x_{c,o}\right)}\right)\right]+\frac{C\left(\dfrac{\rho_l}{\rho_v}\right)}{\left(\dfrac{\rho_l}{\rho_v}-1\right)}\\&\times\left[\left(\sqrt{1+\left(\frac{\rho_l}{\rho_v}-1\right)x_{c,i}}-\sqrt{1+\left(\frac{\rho_l}{\rho_v}-1\right)x_{c,o}}\right)\right.\\&\left.-\left(\frac{1}{\sqrt{1+\left(\dfrac{\rho_l}{\rho_v}-1\right)x_{c,o}}}-\frac{1}{\sqrt{1+\left(\dfrac{\rho_l}{\rho_v}-1\right)x_{c,i}}}\right)\right]\Bigg\}\end{aligned} \tag{35}$$

As the above formulation is developed in terms of inlet and outlet vapor qualities, it is also valid for the case of complete condensation with minimum vapor quality $x_{c,o}(=0)$ occurring before the condenser outlet.

Evaporator Mass and Energy Balances. The following mass balance was applied at the evaporator inlet and outlet.

$$\dot{m}_{tot}=\dot{m}_{v,i}+\dot{m}_{l,i}=\dot{m}_{v,o}+\dot{m}_{l,o} \tag{36}$$

The overall evaporator heat transfer was, in general, assumed to be divided into latent and sensible parts.

$$q_e=q_{e,\text{lat}}+q_{e,\text{sen}} \tag{37}$$

In case of a complete condensation in the condenser, sensible heat must be added in the evaporator to compensate for the sensible heat rejection from the condenser subcooled liquid core $(q_{e,\text{sen}}=q_{c,\text{sen}}\neq 0)$. On the other hand, if the condensation is not complete, there would be no sensible heat rejection from the condenser or addition in the evaporator $(q_{e,\text{sen}}=q_{c,\text{sen}}=0)$. In the evaporator, the sensible heat is added first to the subcooled liquid returning from the condenser to bring its temperature up to the saturation level. Once the saturation temperature is reached, further heat addition to the fluid is latent and increases its vapor quality through boiling on the enhanced surface.

The following latent heat balance also needs to be satisfied in the evaporator.

$$q_{e,\text{lat}}=\dot{m}_{\text{tot}}i_{fg}(x_{e,o}-x_{e,i}) \tag{38}$$

Evaporator Gravitational Pressure Drop. In the absence of a reliable model to predict the two-phase friction and acceleration pressure drops through the cubic evaporator enclosure, we only considered the gravitational pressure change in the evaporator. Following Tengblad [10], we assumed the evaporation rate to be uniform all along the evaporator. So, the well-mixed vapor quality increases linearly along the evaporator height, z, as follows.

$$x=x_i+\left(\frac{x_o-x_i}{\Delta H}\right)z \tag{39}$$

where ΔH is the change in the elevation (gravitational level) from the inlet to the outlet of the evaporator.

Using the above idealization with the homogeneous flow mean density given by Eq. 6, the gravitational pressure drop in the evaporator turns out to be, as follows.

$$\Delta p_{gr} = -g \int_{o}^{\Delta H} \overline{\rho} dz$$

$$= \frac{-\rho_l g \Delta H}{\left(\frac{\rho_l}{\rho_v} - 1\right)(x_o - x_i)} \ln\left[\frac{\left(1 + \left(\frac{\rho_l}{\rho_v} - 1\right)x_o\right)}{\left(1 + \left(\frac{\rho_l}{\rho_v} - 1\right)x_i\right)}\right] \quad (40)$$

Even though the above expression is apparently derived for the evaporator, it is equally applicable to the other thermosyphon parts such as the rising and falling tubes. In case of upward flow through the evaporator or the rising tube, ΔH is positive that results in a negative Δp_{gr} or a drop in the gravitational pressure head. For the downward flow through the falling tube, ΔH is negative that signifies a positive Δp_{gr} or a rise in pressure.

Using Eq. 39 with Eq. 33 for local homogeneous void fraction, the overall void fraction of the evaporator is modeled as

$$\overline{\alpha}_e = \frac{1}{x_o - x_i} \int_{x_i}^{x_o} \alpha dx = \frac{\frac{\rho_l}{\rho_v}}{\left(\frac{\rho_l}{\rho_v} - 1\right)} \left[1 - \frac{1}{\left(\frac{\rho_l}{\rho_v} - 1\right)(x_o - x_i)} \times \ln\left(\frac{\left(1 + \left(\frac{\rho_l}{\rho_v} - 1\right)x_o\right)}{\left(1 + \left(\frac{\rho_l}{\rho_v} - 1\right)x_i\right)}\right)\right] \quad (41)$$

Evaporator Enhanced Boiling Surface Characteristics. Experiments by Yuan et al. [1] were conducted with the dielectric fluid PF-5060. The following relation between the wall heat flux (W/cm^2) and the wall superheat (K) was found by curve-fitting their observed boiling data for 50% initial fill height.

$$q_w = 1.2263(T_w - T_{\text{sat}})^{1.1578} \quad (42)$$

The above fit corresponds to a maximum spread of ±2.5 C in the wall superheat and a maximum spread of ±4.5 W/cm^2 in the wall heat flux, due to the uncertainty in the experimental data. The above equation obtained with the highly confined boiling enhancement structure does not represent a typical boiling curve, and rather suggests a roughly constant evaporator heat transfer coefficient not very sensitive to the wall superheat. We expect two reasons for this unconventional trend. First, as opposed to the typical pool boiling curve, every data point corresponds to a different system pressure. Secondly, the above equation may also reflect any suppression caused by the convective effects of the condensate returning to the evaporator. It appears that the dynamic situation in the evaporator is more similar to flow boiling than pool boiling. As the equation is based on actual data, it implicitly accounts for the pressure variation and any boiling suppression involved.

The wall heat flux, q_w, and the wall temperature, T_w, in the above empirical equation are based on the projected base area of the cubic enhanced structure. In the present study this also simulates the footprint area of the heat dissipating chip to which the enhanced boiling structure would be attached. Using this area, the overall heat transfer input to the evaporator, $Q_w(W)$, could be evaluated. In the present model, Eq. 42 is used to predict the wall temperature for the input heat flux and the computed T_{sat}. Finally, for the given ambient temperature, T_{amb}, the overall thermal resistance of the thermosyphon is evaluated as.

$$R_{\text{tot}} = \frac{T_w - T_{\text{amb}}}{Q_w} \quad (43)$$

Parametric Study

An interesting feature of the present model is its highly coupled nature, which has created a very iterative computational environment. For example, to perform the mass and energy balances on the evaporator, one needs to know whether the condensation is complete or not and whether subcooled liquid or a two-phase flow should be expected at the evaporator inlet. Conversely, the same balances on the condenser require the knowledge of heat addition in the evaporator. Besides, the evaporator and condenser balances require the mass flow rate that is not known until the pressure balances are applied, which in turn require the vapor qualities that are not known until the evaporator/condenser mass and energy balances have been applied. We used the commercially available software Engineering Equation Solver (EES) [15] to solve this system of coupled non-linear equations.

The model predictions are compared with experimental data for dielectric working fluid PF-5060. As shown in Fig. 1, the rectangular loop in the present experimental setup lies in a vertical plane with the exception of the horizontal condenser, which is oriented perpendicular to the vertical plane. The two-tube-pass condenser has 75 cm long aluminum tubing, and is naturally cooled by ambient air using an array of aluminum plate fins attached to its 8.5 mm outside-diameter tubing. The 0.16 mm thick rectangular fins are 60 mm high and 27 mm wide with 4.34 mm spacing. An overall fin efficiency (η) of 0.70, and a correction factor (F) of 0.90 are used for the present computations. The thermosyphon data were taken by boiling the working fluid PF-5060 over a cubic enhanced structure confined inside an 8 cm^3 evaporator. A 3.125 mm inside diameter transparent tygon tubing is used as flexible rising and falling tubes that connect the plexiglass evaporator to the 6.9 mm inside diameter condenser tubing. More details on the experimental procedure, or the magnified geometry of the condenser, evaporator and the micro-fabricated enhanced boiling structure can be obtained from Yuan et al. [1].

The condenser elevation and the separation between the rising and falling tubes are adjustable. The tested condenser elevation is 30 cm above the chip surface. For a 30 cm×30 cm arrangement, the total thermosyphon fluid volume is 44.41 cm^3. The volume distribution among the evaporator, the rising tube, the condenser, and the falling tube is 16.4 percent, 10.1 percent, 63.1 percent, 10.3 percent, respectively. For a 50 percent initial fill height at an ambient temperature of 23.4 C, the total initial liquid and vapor volumes are 11.86 cm^3 and 32.55 cm^3, respectively. A 0 percent initial fill height means that the evaporator is completely filled but there is no liquid in the rising tube; while a 100 percent fill height means that the rising tube is completely filled up to the end of the 90 deg bend but there is no liquid in the horizontal section of the rising tube. The 23.4 C ambient temperature corresponds to a saturation pressure of 0.2703×10^5 Pa compared to an atmospheric pressure of 1.01325×10^5 Pa. Using a constant liquid density, $\rho_1 = 1680\,\text{kg/m}^3$ with the computed vapor density $\rho_v = 3.71\,\text{kg/m}^3$, the liquid and vapor masses are 19.93×10^{-3} kg and 0.12×10^{-3} kg, respectively. Thus, the total fluid mass in the system is 20.05×10^{-3} kg. The following figures show various predictions by the present model over the tested heat flux range of 5.9–40.2 W/cm^2. They demonstrate the capabilities of the model, and provide the estimate of the quantities of interest.

Figure 3 shows that the variation of available gravitational head between 2272 Pa to 3452 Pa, and the total mass flow rate between 2.6×10^{-3} kg/s to 3.2×10^{-3} kg/s it is able to impose through the loop. Figure 4 shows the predicted condenser inlet/outlet vapor qualities, and shows an almost complete condensation throughout the test range. As expected, as heat flux increases, the evaporator outlet vapor quality increases. Whether the condensation is complete would strongly depend upon the condensation correlation and the void fraction model used. A less than 1.0 evaporator outlet vapor quality, as suggested by Fig. 4, is in accordance with our visual observations. We were able to make the visual observation

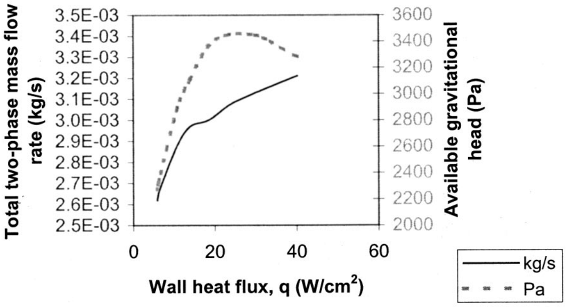

Fig. 3 Available gravitational pressure head and loop mass flow rate

as the plexiglass evaporator and the connecting tygon tubings are transparent. We did experimentally observe a liquid-vapor two-phase plug/slug flow leaving the evaporator and rising through the vertical tygon tubing to the condenser throughout the test range. We were able to clearly see significant liquid fraction being pulled into the vertical tygon tubing throughout the heat flux test range of practical interest. Because of the dynamic boiling activity on the micro-fabricated cubic boiling structure inside the evaporator, the generated vapor drags some of the saturated liquid inside the evaporator into the vertical tygon tubing. So, the re-circulatory two-phase flow involves some liquid that is neither evaporated nor condensed. Thus, our flow visualizations are consistent with the predicted evaporator outlet quality to be significantly less than unity that still corresponds to significantly high void fraction due to the liquid-vapor density difference.

Figure 5 shows that all heat transfer is latent throughout the tested range, which again implies that condensation is either just completed or is incomplete at the condenser outlet. On the contrary, if the applied condenser were long enough to condense all generated vapor before the condenser outlet, the condensed liquid would be subcooled by the time it would reach the condenser outlet and the evaporator inlet. Then, a part of the heat conducted through the enhanced boiling structure would be used to sensibly heat the returning subcooled liquid up to the saturation temperature corresponding to the evaporator pressure. We accounted for the possible sensible heat transfer through the sub-cooled liquid region, as its impact on the prediction of condenser void fraction could far outweigh its numerical significance relative to the latent part.

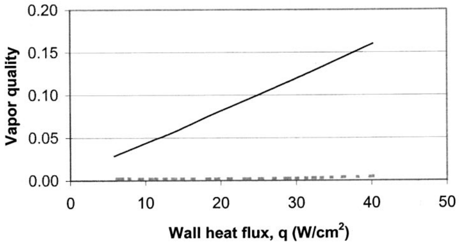

Fig. 4 Condenser inlet and outlet vapor qualities

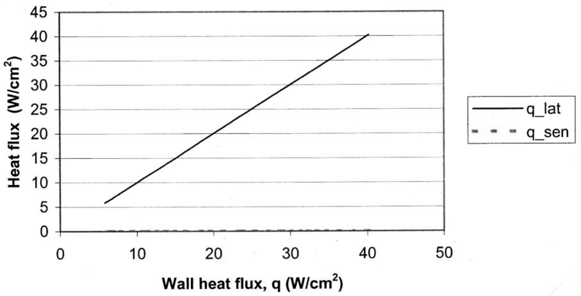

Fig. 5 Latent and sensible contributions to the heat flux

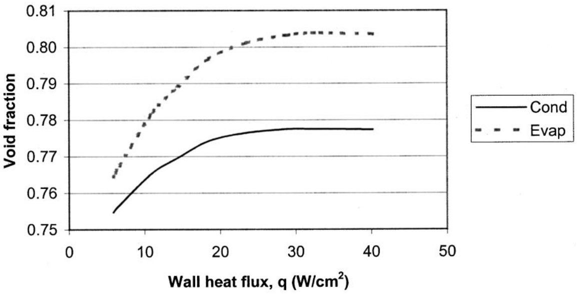

Fig. 6 Condenser and evaporator overall void fractions

Figure 6 shows a void fraction variation of 4.0 percent in the evaporator and 2.3 percent in the condenser over the entire heat flux range tested. As a related observation from the model, the overall void fraction of the system does not change significantly. At 23.4 C ambient temperature, the initial void fraction of the system was 73.29 percent while at 55.2 C saturation temperature, it became 73.62 percent. Thus, about 0.45 percent of the initial liquid volume was evaporated to increase the vapor density by three folds to 11.25 kg/m^3. The corresponding change of 0.33 percent in the system void fraction is negligible, with the possibility that individual void fractions may vary rather significantly in the evaporator, condenser, and rising and falling tubes.

As shown in Fig. 6, the model predicts an asymptotic plateauing of the condenser and evaporator overall void fractions starting around 25–30 W/cm^2. As Figs. 4 and 5 have shown an almost complete condensation at the condenser outlet throughout the test range, the falling tube is filled with liquid phase returning to the evaporator with very little vapor. For an almost constant liquid volume in the system, the overall void fraction of the rising tube would also start plateauing around 25–30 W/cm^2. Thus, the overall void fraction of each of the four thermosyphon components becomes constant above 25–30 W/cm^2 heat flux. Further rise of saturation temperature and pressure, caused by increasing heat flux, would compress additional vapor in the same vapor volume in the rising tube, which explains the drop of available gravitational pressure head as shown in Fig. 3. However, an increased mass flow rate with higher vapor quality is predicted to remove the increasing heat flux, and is sustained by a rather declining available pressure head due to the non-linear dependence of the pressure drop on vapor quality and void fraction that are on the rise, as suggested by Eq. 5 through 13 of the homogeneous two-phase flow model.

Figure 7 shows various predicted Reynolds numbers. It can be seen that the *liquid-only* Reynolds numbers for the 3.175 mm dia rising and falling tubes, and the 6.9 mm dia. condenser tube are within the laminar range, and are fairly insensitive to the heat flux. However, the Reynolds number of the vapor core is turbulent over

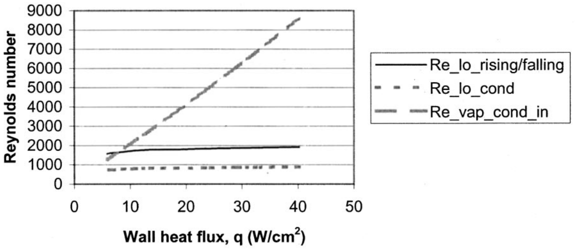

Fig. 7 Two-phase flow Reynolds numbers

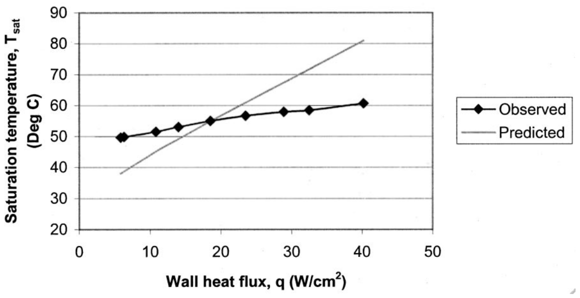

Fig. 8 A comparison between the predicted and observed saturation temperatures

the tested heat flux range, and varies by a factor of eight over the tested heat flux range of 5.9–40.2 W/cm^2. The finding suggests a turbulent vapor core in the middle surrounded by a laminar liquid film on the condenser wall. This suggests a need to assess the role of the turbulent vapor convective effects, as well as the no-slip condition between the *mean* liquid and vapor velocities in the condenser. Contrary to the currently used homogeneous flow assumption, the mean liquid and vapor velocities may be different due to separated flow in the condenser, especially, at high heat fluxes. Sudden expansion at the condenser inlet could change the void fraction without changing the quality.

Figure 8 compares the observed and predicted saturation temperatures. It is believed that the discrepancy in the predicted and measured saturation temperatures is caused by a combined effect of the uncertainties in the condensation heat transfer and the individual void fractions. The saturation temperature was measured by using thermocouples inside the liquid pool of the evaporator. It is worth emphasizing that the present model did not introduce any empirical constant. An underprediction of T_{sat} at low heat fluxes and an over prediction at high heat fluxes suggests that we may be using a higher condensation heat transfer coefficient at low heat flux and a lower heat transfer coefficient at higher heat flux. It may be due to the fact that Ananiev correlation does not account for the factor of eight variation in the vapor core Reynolds number. The use of liquid-only Reynolds number in annular two-phase flow tends to hide the convective effects of the vapor core by lumping the laminar liquid and turbulent vapor flow rates together. This also shows the importance of correctly predicating the local condensation heat transfer coefficient, which is recognized as a major area of uncertainty in the present model. It is quite possible that for the present thermosyphon setup, the condensation heat transfer coefficient may not follow the large tube condensation correlations due to the laminar condenser operation and surface tension effects. The possibility of existence of subcooled liquid film within the condensation length, i.e., in the laminar liquid layer beneath the saturated liquid-vapor interface, cannot be ruled out. This way subcooled liquid could still exist even though there may not be a 100 percent liquid filled subcooled core right before the condenser outlet.

Conclusions

The present paper proposes an analytical approach to modeling the closed loop two-phase thermosyphon (CLTPT) performance. The model identifies the fundamental elements, and has a closure in the form of the prediction of the system saturation temperature. The model is compared with experimental data for dielectric working fluid PF-5060 and is in general agreement with the observed trends. The simulation results for the given experimental setup and the test range suggest an annular two-phase flow with a turbulent vapor core in the middle surrounded by a laminar liquid film on the condenser wall. The results predict all heat transfer in the condenser and evaporator to be latent. Simulations show a void fraction variation of 4.0 percent in the evaporator and 2.3 percent in the condenser over the entire heat flux range tested, compared to a corresponding 0.33 percent change in the overall system void fraction.

Currently, there are two major uncertainties in the model. The first uncertainty is inducted by using a conventional condensation heat transfer correlation developed for large tubes. With an almost constant evaporator heat transfer coefficient, the observed trends in the total thermal resistance are caused by the condensation thermal resistance. At low heat flux, the condensation heat transfer coefficient is expected to be poor due to small vapor flow rates. As heat flux increases, so does the vapor flow rate in the core, which should drive the condensation heat transfer coefficient up. The currently used Ananiev correlation does not account for an order of magnitude variation in the convective effects in the vapor core inside the condenser. More realistic predictions are expected once better condensation correlations are used that are sensitive to the vapor convective effects. Thus, a deteriorating condenser heat transfer coefficient can explain higher thermal resistances observed at lower heat fluxes. The second uncertainty stems from using a homogeneous flow assumption of equal *mean* liquid and vapor velocities inside the condenser, i.e., slip factor $S=1$. This is clearly not the case for the condenser, where the vapor velocity could considerably change over the tested heat flux range due to the well-separated annular flow. The introduction of a slip factor is bound to affect the void fraction prediction throughout the thermosyphon.

It is concluded that with all basic features of the model successfully identified, the key lies in using the two-phase heat transfer correlation developed for small diameter horizontal tubes and validated with fluids similar to PF-5060, such as R-113.

Acknowledgment

The present research is sponsored through the DARPA HERETIC Program under contract N00164-99-C-0039, managed by Dr. Dan Radack and Dr. Elias Towe. This work was done when the authors were at the University of Maryland, College Park.

Nomenclature

c_p = specific heat, J/kg/K
d_h = hydraulic diameter, *m*
D_i = Tube-inside diameter, *m*
D_o = Tube-outside diameter, *m*
f = friction factor
F = heat exchanger correction factor for the cross flow effect
g = acceleration due to gravity, m/s^2
G = two-phase flow mass velocity, kg/m^2/s
h_i = Condenser inside heat transfer coefficient, W/m^2/K
h_o = Condenser outside heat transfer coefficient, W/m^2/K
H = magnitude of the gravitational pressure head, Pa
i_{fg} = latent heat of vaporization, J/kg
k = thermal conductivity, W/m/K
L = tube length, *m*
m = coolant mass, kg
$\dot{m}$ = mass flow rate, kg/s
LMTD = log-mean temperature difference, *K*
p = pressure, Pa
Pr = Prandtl number
q = heat flux, W/cm^2
Q = total heat input, *W*
R = thermal resistance, K/W
Re = Reynolds number
T = temperature, degree C
V = volume, m^3
x = two-phase flow vapor quality
z = general location along the condenser tubing, *m*

Greek Letters

α = void fraction
δ = local condensate liquid film thickness, m
η = condenser fin efficiency
μ = viscosity, kg/m/s
θ = tube inclination with the horizontal, radian
ρ = density, kg/m^3

Subscript

acc = acceleration
amb = ambient
c = condenser
cc = complete condensation
cf = counter flow
e = evaporator
fall = falling tube
fr = frictional
gr = gravitational
i = inlet
l = liquid
lat = latent
lo = liquid-only
o = outlet
rise = rising tube
sat = saturation
sen = sensible
sub = subcooling
tot = total
tp = two-phase
v = vapor
w = wall, i.e, chip surface

References

[1] Yuan, L., Joshi, Y. K., and Nakayama, W., 2001, ''Effect of Condenser Location and Tubing Length on the Performance of a Compact Two-Phase Thermosyphon,'' *Proc. 2001 ASME International Mechanical Engineering Conference and Exposition, Session on Heat Pipes and Multiphase Heat Transfer in Electronic System*, November 11–16, New York, NY.
[2] El-Genk, M. S., and Saber, H. H., 1998, ''Heat Transfer Correlations for Liquid Film in the Evaporator of Enclosed, Gravity-Assisted Thermosyphons,'' ASME J. Heat Transfer, **120**, pp. 477–484.
[3] Harley, C., and Faghri, A., 1994, ''Complete Transient Two-Dimensional Analysis of Two-Phase Closed Thermosyphons Including the Falling Condensate Film,'' ASME J. Heat Transfer, **116**, pp. 418–426.
[4] Zuo, Z. J., and Gunnerson, F. S., 1994, ''Numerical Modeling of the Steady-state Two-Phase Closed Thermosyphon,'' Int. J. Heat Mass Transf., **37**(17), pp. 2715–2722.
[5] El-Genk, M. S., and Saber, H. H., 1999, ''Determination of Operation Envelopes for Closed, Two-phase Thermosyphons,'' Int. J. Heat Mass Transf., **42**, pp. 889–903.
[6] Vincent, C. C. J., and Kok, J. B. W., 1992, ''Investigation of the Overall Transient Performance of the Industrial Two-Phase Closed Loop Thermosyphon,'' Int. J. Heat Mass Transf., **35**, No. 6, pp. 1419–1426.
[7] Wang, J. C. Y., and Ma, Y., 1991, ''Condensation Heat Transfer Inside Vertical and Inclined Thermosyphons,'' ASME J. Heat Transfer, **113**, pp. 777–780.
[8] Carey, Van P., 1992, *Liquid-Vapor Phase-change Phenomena*, Hemisphere Publishing Corporation.
[9] Cammarata, G., Fichera, A., Froghieri, M., Misale, M., and Xibilia, M. G., 1999, ''A New Modeling Methodology of Natural Circulation Loop for Stability Analysis,'' *Single and Two-Phase Natural Circulation, Proceedings of EUROTHERM SEMINAR No. 63*, September 6–8, 1999, Genoa, Italy.
[10] Tengblad, N., 1996, ''Cooling of Electronic Components with Closed Loop Two-Phase Thermosiphons,'' Engineering Licentiate Thesis, The Royal Institute of Technology, Stockholm, Sweden, pp. 17–50, Chap. 3.
[11] McAdams, W. H., Woods, W. K., and Heroman, Jr., L. C., 1942, ''Vaporization Inside Horizontal Tubes—II—Benzene-Oil Mixtures,'' Trans. ASME, **64**, p. 193.
[12] Collier, J. G., 1981, *Convective Boiling and Condensation*, Second Edition, pp. 30–34. McGraw-Hill Book Company (UK) Ltd.
[13] Bar-Cohen, A., and Rohsenow, W. M., 1984, ''Thermally Optimum Spacing of Vertical Natural Convection Cooled, Parallel Plates,'' ASME J. Heat Transfer, **106**, p. 116.
[14] Ananiev, E. P., Boyko, L. D., and Kruzhilin, G. N., 1961, ''Heat Transfer in the Presence of Steam Condensation in a Horizontal Tube,'' *Proc. 1st Int. Heat Transfer Conf.*, part II, p. 290.
[15] *Engineering Equation Solver* (EES), F-Chart Software, www.fChart.com.

Heat Transfer Characteristics of Melting Ice Spheres Under Forced and Mixed Convection

Y. L. Hao

Y.-X. Tao
e-mail: ytao@eng.fiu.edu

Department of Mechanical Engineering,
Florida International University,
Miami, FL 33199

An experimental investigation is conducted to characterize melting and heat transfer during convective melting of an ice sphere in horizontally flowing water. The shape changes of melting ice spheres with time at different velocities and supply temperatures of water and at different initial ice temperatures are recorded using a digital video camcorder. From the recorded images, the time variations of local melting rate, local heat transfer coefficient and local Nusselt number at various angular positions are obtained. The effects of water temperature and velocity on these local parameters are analyzed and the total melting rate and average heat transfer coefficient are determined. Guided by a shape factor characterizing the particle shape variation, an empirical correlation for average Nusselt number in convective melting of a solid particle is obtained. The experimental results provide important particle-level information needed to improve the accuracy of numerical models for convective melting of a single particle or packed particles. [DOI: 10.1115/1.1494090]

Keywords: *Heat Transfer, Melting, Mixed Convection*

1 Introduction

Melting of ice or solid bodies occurs in many important engineering and environmental applications such as material processing, space applications and water resource and energy conversion and conservation. Tkachev [1] examined the melting of ice spheres as well as vertical and horizontal cylinders using photographic techniques. Merk [2] obtained a boundary layer solution and predicted a minimum Nusselt number of the melting of ice spheres using the von Karman-Pohlhausen integral method. Schenk and Schenkels [3] observed the region of dual flow around an ice sphere produced by freezing a 3-mm-thick ice layer onto a hollow copper sphere of diameter 3.2 cm, and determined the subsequent melting rate from pictures obtained during free-convection melting in water. The results provided an equation for the Nusselt number in terms of the Grashof and Prandtl numbers. Vanier and Tien [4] conducted experiments on free-convection melting of a submerged ice sphere in water, focusing on boundary layer motion existing at 4°C. Accelerated melting in the bottom region of the sphere was due to heavy circulation in the wake of the boundary layer flow. This resulted in the formation of a scallop at the bottom. Eskandari [5] and Eskandari et al. [6] reported on a series of experiments to study forced convection heat transfer from a flowing stream of water over an ice sphere, and developed two relationships to describe the process. Anselmo [7,8] performed an extensive theoretical and numerical analysis of the melting of a solid sphere partially or fully submerged in a pool of its own melt. Anselmo accounted for variation in heat transfer coefficient due to change in sphere diameter and flow condition. Mukherjee et al. [9] conducted a visualization study on melting of an ice sphere in a pool of water using dyed ice. Aziz et al. [10] used the weighing method to obtain experimental data on heat transfer between a sphere and forced convective water, and presented an empirical correlation. Mcleod et al. [11] conducted a visualization study of melting of a wax sphere in hot water. They calculated the melting rate using a simple theoretical analysis which estimates melt layer thickness and the heat flux from the fluid.

The previous studies mentioned above focus mainly on either the melting process of a sphere in a pool of liquid or heat transfer between fluid and sphere in a flowing liquid. To our knowledge, there has been no complete study on the full melting process of a sphere in a flowing liquid, especially where the shape of the solid changes considerably from that of a sphere. In order to fill this gap, Hao and Tao [12] presented the visualization and qualitative analysis of convective melting process of ice spheres and ice cylinders and examined the influence of water velocity. They further reported more detailed flow visualization based on the particle image velocimetry (PIV) technique (Hao and Tao [13]). In their study, the distributions of velocity, streamline, and vorticity around the ice sphere are obtained for different upstream velocities and temperatures. The focus is on flow characteristics around the melting ice sphere and effects of velocity and temperature. The visualization of the melting of a dyed ice sphere is also conducted to qualitatively investigate the motion of the melt and the mixing with mainstream. These results are very helpful in understanding the interaction between fluid and melting solid particles, and lay a foundation for this paper to examine the melting and heat transfer characteristics of ice particles in flowing water.

2 Experimental Setup and Procedure

The experiments are performed in a horizontal, open channel made of Plexiglas. The experimental setup, similar to the one presented in Hao and Tao [13], as shown in Fig. 1, consists of a closed and forced water circulation loop and a temperature control circulation loop. A MARCH TE-7R-MD pump moves water from the reservoir and discharges it into the head tank, from which the water flows into the channel. Water flows downstream in the channel past the sphere, which is mounted near the middle of the channel, and is then routed back to the reservoir. The discharge line has a gate valve and a John C. Ernst Co S100 flow meter to control and measure the flow rate of water. Water temperature is controlled by a refrigerated circulator with a measured fluctuation of ±0.1°C during a typical experiment.

The dimensions of the test section are 500×152×216 mm (L ×W×H), as shown in Fig. 2. A uniform velocity at the inlet of the test section is attained by the use of a flow straightener made of Duocel aluminum foam. An overflow plate is placed at the downstream location to control the water level. Using the gate placed at

---

Contributed by the Heat Transfer Division for publication in the JOURNAL OF HEAT TRANSFER. Manuscript received by the Heat Transfer Division October 24, 2001; revision received April 16, 2002. Associate Editor: C. Amon.

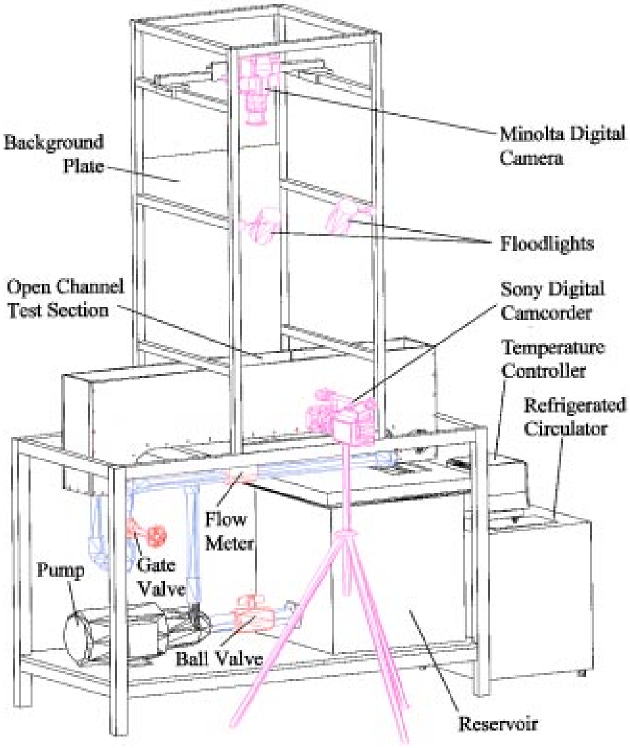

Fig. 1 Schematic of the test apparatus

the exit location instead of the overflow plate can also control the water level. A water level of 130 mm can be achieved in the present study. Twelve thermocouples are mounted at the inlet, test section, and exit so that the water temperature can be measured at different locations along the flow direction. A pair of thermocouples is placed in the center of the ice sphere to measure the central temperature of the ice sphere during the melting process. A computer with OMEGA DAS-TC/B data acquisition system is used to record the thermocouples' readings during tests.

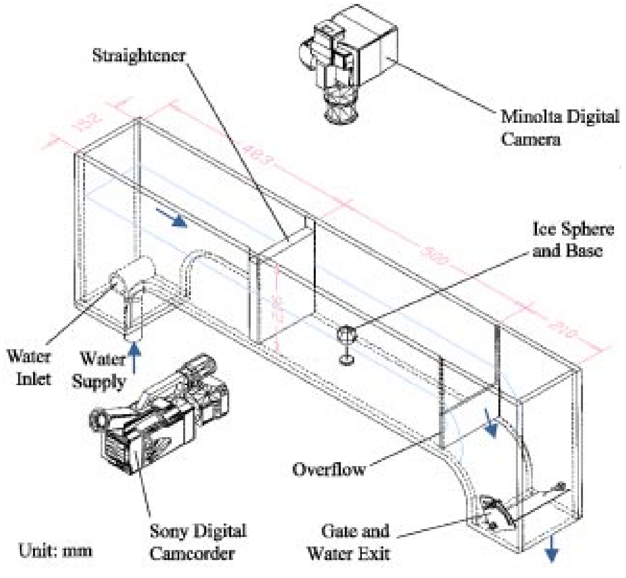

Fig. 2 Test section

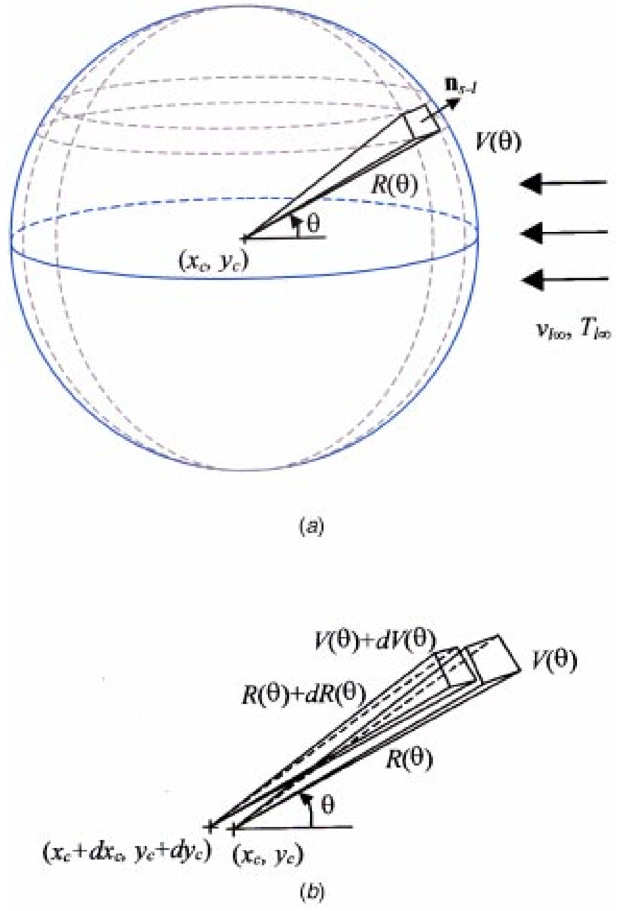

Fig. 3 Volume element in the ice sphere and volume elements between t and $t+dt$

The ice sphere is made by freezing filtered tap water in two hemispherical moulds. A thin plastic straw is sandwiched in the sphere to allow the sphere to be fixed on a movable base made of stainless steel. In this study, the diameter of the ice sphere is 36 mm, and the diameter of the thin plastic straw is 2 mm. The insert length of the straw into the sphere is about 18 mm. A pair of thermocouples is placed in the center of ice sphere through the plastic straw. The Plexiglas walls of the test section allow optical access for photography and the passage of light. A Sony DCR-VX1000 digital camcorder is used to continuously record the image from the front side, as shown in Fig. 1 and Fig. 2. A Minolta RD-175 digital camera is used to intermittently take pictures from the top. To obtain a clear image of the ice sphere, an ivory white background plate is vertically placed at 200 mm from the backside of the test section. Two 45-Watt Philips reflector floodlights are mounted above the front side of the test section. One floodlight illuminates the ice sphere from the upper front side, and another illuminates the background plate.

During a typical test, the pump is activated and a steady, open-channel flow is established at the desired flow rate and temperature by adjusting the opening of the gate valve and using the refrigerated circulator. The digital video camcorder and the computer data acquisition system begin to record video images and temperatures. The test begins when the sphere, fixed on the movable basis by a thin plastic straw, is placed into the horizontal water flow, and it ends when any remaining ice breaks away from the plastic straw and drifts downstream. After the test is finished, the shape data of the ice particle in the melting process can be obtained from the digital video images on the computer by using an image analysis software. The maximum uncertainty of the dimensional measurements is ±0.2 mm.

As illustrated in Fig. 3(a), we consider an ice sphere situated in a horizontal flow of water from the right. The local mass melting rate can be determined in terms of the volume variation of volume element on the ice surface. As a result of the shape change and different local melting rates at different locations on the surface, the centroid of the particle does not stay at a fixed physical location referenced to the ground. To take this into account and also to find a simple yet accurate way to calculate the local melting rate, we define a time dependent, geometric center of the ice particle at a given time by finding the intersection of the maximum *x*-direction linear dimension and maximum *y*-direction linear dimension lines on the center plane image (recall that the particle is symmetrical about the vertical center plane). At a given time interval from t to $t+dt$, the particle center moves from (x_c, y_c) to (x_c+dx_c, y_c+dy_c), as illustrated in Fig. 3(*b*). The corresponding volume element of the ice particle at an angular position, θ, defined at the moving origin, therefore changes from $V(\theta)$ to $V(\theta)+dV(\theta)$. Accordingly, the radius changes from $R(\theta)$ to $R(\theta)+dR(\theta)$. This treatment, although arbitrary, allows easy data reduction and presentation using spherical coordinates with the origin coinciding with the above-defined geometric center of ice sphere, as shown in Fig. 3(*a*). Therefore, it follows that the local melting rate per unit surface area at an angular position θ (measured from the horizontal centerline), $\dot{m}''(\theta)$, can be determined as follows:

$$\dot{m}''(\theta) = -\frac{\rho_s dV(\theta)}{\Delta A_s(\theta) dt} = -\rho_s\left(\frac{dR(\theta)}{dt} + \cos\theta\frac{dx_c}{dt} + \sin\theta\frac{dy_c}{dt}\right). \tag{1}$$

where $\Delta A_s(\theta)$ is the surface area element at θ. The second and third terms in the right-hand side parenthesis of the above equation results from the aforementioned definition of the moving geometric center (origin) as a result of shape change. The variations of radius as a function of an angular position, $R(\theta)$, and coordinates of the geometric center, x_c and y_c, with time t can been obtained directly from the digital video images of the ice particle in the melting process.

The heat transfer from the liquid to the solid-liquid interface is controlled by convection in the present study. The local heat flux at an angular position θ can be determined by applying an energy balance to the ice surface element

$$q(\theta) = h(\theta)(T_{l\infty} - T_{li}) = \dot{m}''(\theta)h_{ls} + q_s(\theta) \tag{2}$$

where $h(\theta)$ is the local heat transfer coefficient at the angular position θ. On the right side of above equation, the first term is the latent heat absorption rate, and the second term is the heat flux conducted into the ice particle to raise the internal temperature. The conduction heat flux will equal zero after the internal temperature of ice particle increases to the surface temperature that maintains at the melting temperature, 0°C. When the ice shape is spherical, the total heat transfer rate conducted into the ice is determined by

$$Q_s = \int_0^R 4\pi r^2 \rho_s c_{ps}\frac{\partial T_s}{\partial t}dr. \tag{3}$$

The transient temperature distribution $T_s(r,t)$ in the solid spherical region has been obtained under the condition that the initial temperature of the ice sphere is uniform and the surface temperature is maintained at the constant temperature (Gebhart [14]). The shape of melting ice gradually becomes irregular because the local melting rate is not uniform over the surface of ice (Hao and Tao [12]), so that it is impossible to obtain the analytical solution of $T_s(r,t)$ and also very difficult and complex to obtain the numerical solution of $T_s(r,t)$. To find an alternative solution, we first perform an analytical calculation for a spherical particle under the same temperature condition as in the present study. It is found that the temperature gradient is nearly zero in the interior of ice sphere except for a very thin layer under the surface, and the temperature difference in the interior of ice sphere is less than 0.02°C. Based on this, we simplify the problem by introducing the following equation:

$$Q_s = \rho_s c_{ps}(\overline{T_s} - T_{si})\frac{dV_s}{dt} + \rho_s c_{ps} V_s \frac{d\overline{T_s}}{dt}, \tag{4}$$

where $\overline{T_s}$ is the average internal temperature of the ice particle. We approximate $\overline{T_s}$ by using the center temperature measured in the melting process. T_{si} is the ice temperature at the surface of the ice, which is equal to the melting temperature of ice, $T_{si} = T_{li} = 0°\text{C}$. Equation (4) is applicable to both the spherical and nonspherical shapes of the ice particle during the melting process. Also based on the analytical solution mentioned above, we may assume that the heat flux conducted into the ice particle is uniform on the particle surface. It then follows that

$$q_s(\theta) = \overline{q_s} = Q_s/A_S. \tag{5}$$

The local heat transfer coefficient can be determined from Eq. (2) after the local melting rate and the conduction heat flux are determined,

$$h(\theta) = \frac{1}{T_{l\infty} - T_{li}}[\dot{m}''(\theta)h_{ls} + q_s(\theta)]. \tag{6}$$

The total melting rate over the surface of ice sphere can be obtained by integrating the local melting rate over the surface of ice sphere. We can also experimentally determine the total melting rate by measuring the volume change of the ice sphere over time based on

$$\dot{m} = -\rho_s\frac{dV_s}{dt}. \tag{7}$$

The average heat transfer coefficient over the surface of the ice particle can be determined by

$$\overline{h} = \frac{\dot{m}h_{ls} + Q_s}{A_S(T_{l\infty} - T_{li})}. \tag{8}$$

Uncertainties were present in various experimental measurements. The maximum random uncertainties in temperature, timing, dimension and coordinates, and flow rate of water measurements are ±0.5°C, ±0.5 s, ±0.2 mm, and ±2.0 percent, respectively. Based on the method of Kline and McClintock [15], the maximum uncertainties in the shape change, melting rate, heat transfer coefficient, Reynolds number, Grashof number, Nusselt number, and Stefan number are estimated to be ±2.66 percent, ±4.98 percent, ±5.16 percent, ±4.66 percent, ±4.17 percent, ±7.82 percent, and ±4.0 percent, respectively.

3 Results and Discussion

3.1 General Characteristics. The typical video pictures of the ice sphere in the melting process are shown in Fig. 4. The top-view images obtained from the experiment reveal that the shape change of ice sphere in the traverse direction to the flow is very symmetrical about the vertical center plane, as shown in Fig. 4(*b*). Therefore, in the following discussion, we focus our attention to local melting and heat transfer from the side view, which shows significant deviation from symmetry in the vertical direction.

Figure 5(*a*) shows the typical shape change of a melting ice sphere, viewed from the side, with time for forced convection dominated conditions ($\text{Gr}_0/\text{Re}_0^2 < 1$). In Fig. 5(*a*), *x* stands for the coordinate in the horizontal direction, and *y* is in the vertical direction. Water flows horizontally from the right side to the left side. As will be discussed later, there exists a second upper boundary layer separation point due to the discharge of melt near the

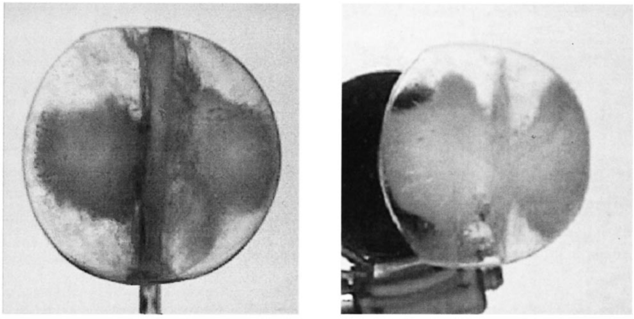

(*a*) (*b*)

Fig. 4 Typical video pictures of the ice sphere in the melting process (water flows horizontally from the right side to the left side): (*a*) Side view; (*b*) top view.

rear portion of the surface, as shown in Fig. 5(*b*) where the shapes of the particle have been plotted in the spherical coordinate system with the center of the particle coinciding with the origin. Figure 6 shows the history of temperature measured by the thermocouples at the inlet of test channel and in the center of ice particle for the same case as in Fig. 5. The time variations of total heat transfer rate, total latent heat of fusion and heat conducted into the inside of ice particle over the surface of ice particle are shown in Fig. 7.

Upon immersion into flowing water with a temperature higher than the phase change temperature (0°C), the ice sphere begins to melt, and its surface temperature remains at the phase change temperature. When the initial temperature of ice is lower than 0°C, heat is transferred as a result of the temperature difference between ice and water, causing the ice on the surface to melt and the sphere's internal temperature to increase, as shown in Fig. 6. The heat conducted into the ice decreases with the increase in the internal temperature, as shown in Fig. 7. When the internal temperature of the ice sphere rises to 0°C, the heat from water to ice equals the latent heat for ice melting, and the ice temperature remains constant at 0°C. Finally, the thermocouple probe placed in the center of the ice sphere is exposed to flowing water as the ice reduces to a critical size. The temperature measured by the probe then quickly rises as shown by the final segment of curve 2 in Fig. 6. When the remaining ice breaks away from the plastic straw and drifts downstream, the test ends.

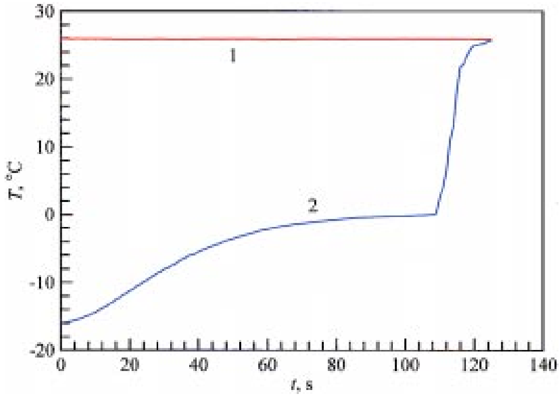

Fig. 6 Temperature-time histories at the inlet and the ice center: $T_{l0}=26°\mathrm{C}$, $v_{l\infty}=0.06\ \mathrm{m/s}$, $T_{s0}=-16°\mathrm{C}$, $d_0=36\ \mathrm{mm}$, $\mathrm{Gr}_0/\mathrm{Re}_0^2=0.319$. 1—inlet; 2—center of ice.

As shown in a preceding paper (Hao and Tao [13]), the non-uniform flow field around the sphere results in different interaction among mass, momentum, and energy between ice particle and flow at different local locations on the ice surface. These differences cause the shape of a convectively melting ice sphere to become irregular in later stages, as shown in Fig. 5. This situation may occur in many practical processes. The model prediction and empirical correlations from the existing studies in open literature do not include this type of melting process. To characterize the shape change during the melting process, we show in Fig. 8 the equivalent spherical diameter based on the same volume and the equivalent spherical diameter based on the same surface area. The difference of these two diameters increases as ice shapes becomes more irregular. We define the shape factor based on the two diameters as follows:

$$\phi=\frac{d_V^3}{d_s^3} \tag{9}$$

This dimensionless parameter varies between 0 and 1. The shape factor equals 1 when a particle is spherical. The shape factor will be less than 1 when a particle becomes non-spherical, which means that an irregularly shaped particle has a larger surface area than a sphere with the same volume. The variation of shape factor in the melting process is also shown in Fig. 8. It

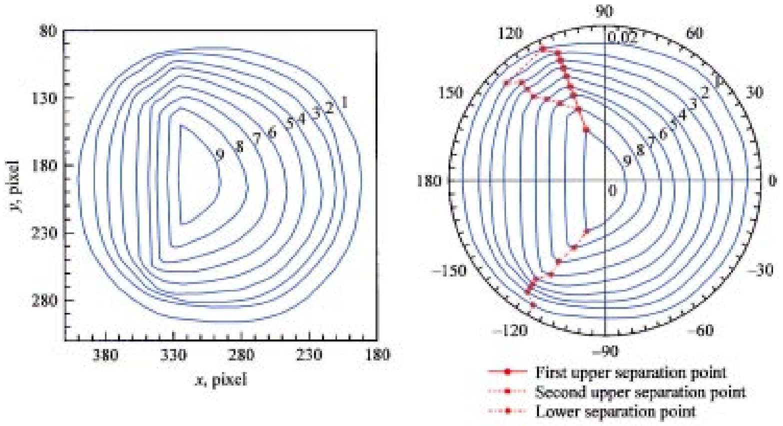

(*a*) (*b*)

Fig. 5 Shape change of ice particle in the melting process: $T_{l0}=26°\mathrm{C}$, $v_{l\infty}=0.06\ \mathrm{m/s}$, $T_{s0}=-16°\mathrm{C}$, $d_0=36\ \mathrm{mm}$, $\mathrm{Gr}_0/\mathrm{Re}_0^2=0.319$. 1—0 s; 2—20 s; 3—35 s; 4—50 s; 5—65 s; 6—80 s; 7—95 s; 8—110 s; 9—125 s: (*a*) In Cartesian coordinates; (*b*) in spherical coordinates with the center of particle coinciding with the origin.

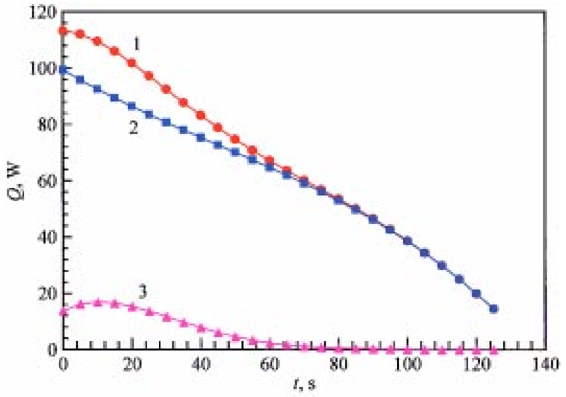

Fig. 7 Variations of total heat transfer rate, total latent heat for fusion, and total conducted heat into the inside with time in the melting process: $T_{l0}=26°\mathrm{C}$, $v_{l\infty}=0.06$ m/s, $T_{s0}=-16°\mathrm{C}$, $d_0=36$ mm, $\mathrm{Gr}_0/\mathrm{Re}_0^2=0.319$. 1—convective heat transfer from water to interface; 2—total latent heat for fusion; 3—heat conducted into the inside of ice.

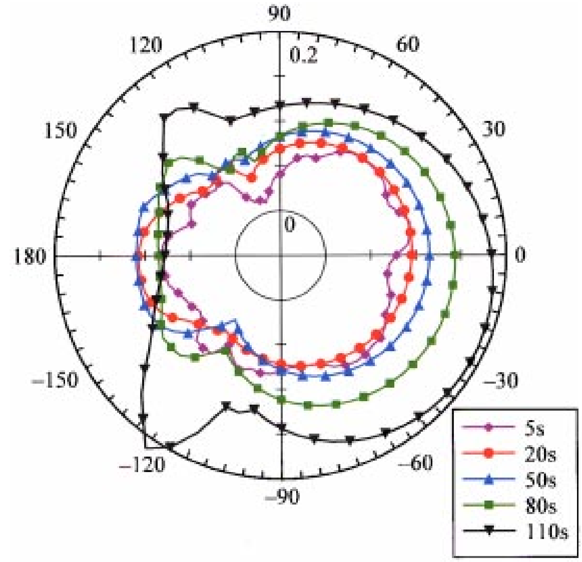

Fig. 9 Local melting rate $\dot{m}''(\theta)$ at different time in the melting process: $T_{l0}=26°\mathrm{C}$, $v_{l\infty}=0.06$ m/s, $T_{s0}=-16°\mathrm{C}$, $d_0=36$ mm, $\mathrm{Gr}_0/\mathrm{Re}_0^2=0.319$.

indicates that a spherical ice particle gradually changes its shape and deviates from initial spherical shape as convective melting of the particle continues.

3.2 Local Melting Rate and Heat Transfer Coefficient.

3.2.1 Low Gr_0/Re_0^2 *(<1).* The local melting rate, local heat transfer coefficient, and local Nusselt number in the same case as in Figs. 5 to 8 are shown in Figs. 9–11. The test conditions are maintained at a water velocity of 0.06 m/s, a water temperature of 26°C, an initial ice temperature of −16°C, an initial ice diameter of 36 mm, and an initial Reynolds number of 1793. For these test results, the ratio of corresponding $\mathrm{Gr}/\mathrm{Re}^2$ is less than unity, indicating an inertia-dominant flow. In the figures, the positive value of the angular coordinate θ stands for the angle measured from the horizontal centerline to the upper surface and the negative value of θ represents the angle to the lower side.

The local melting rate and local heat transfer coefficient are distributed irregularly at first when the water flow is disturbed after the ice particle with the stainless steel basis is suddenly placed in the water flow. The first 5 seconds of the curve shown in Figs. 9 and 10 represents this irregular distribution. After stable water flow resumes, the local melting rate and local heat transfer coefficient distribute more smoothly. The initial transient period lasts about 10 to 15 seconds within the range of the present testing conditions. The variations in the local heat transfer coefficient includes the effect of heat conducted into the ice when the internal temperature is lower than the melting temperature during the early melting period. The highest value of conducted heat rate is less than 20 percent of the total heat rate from the water to the ice, as shown in Fig. 7. For the results shown in Figs. 9 and 10, the trend of local heat transfer coefficient is almost the same as that of the local melting rate. This means that the conduction effect is generally not significant except for a short early effective period. The effect of the heat conduction, or the conduction effective time period, does increase slightly with a decrease in the initial temperature of ice particle.

The variation of the local Nusselt number with θ at different time is shown in Fig. 11. The local Nusselt number decreases with

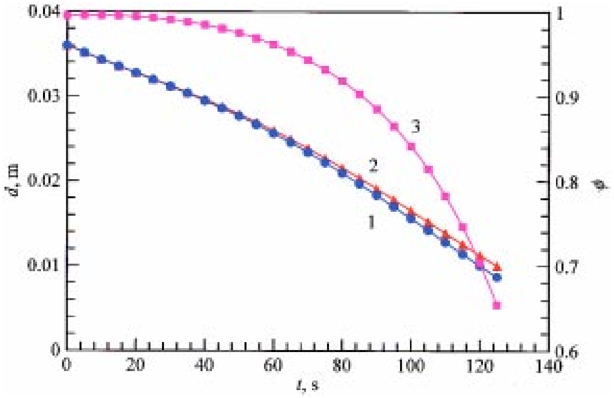

Fig. 8 Variation of diameters and shape factor with time in the melting process: $T_{l0}=26°\mathrm{C}$, $v_{l\infty}=0.06$ m/s, $T_{s0}=-16°\mathrm{C}$, $d_0=36$ mm, $\mathrm{Gr}_0/\mathrm{Re}_0^2=0.319$. 1—diameter based on volume of ice, d_V; 2—diameter based on surface area of ice, d_s; 3—shape factor, ϕ.

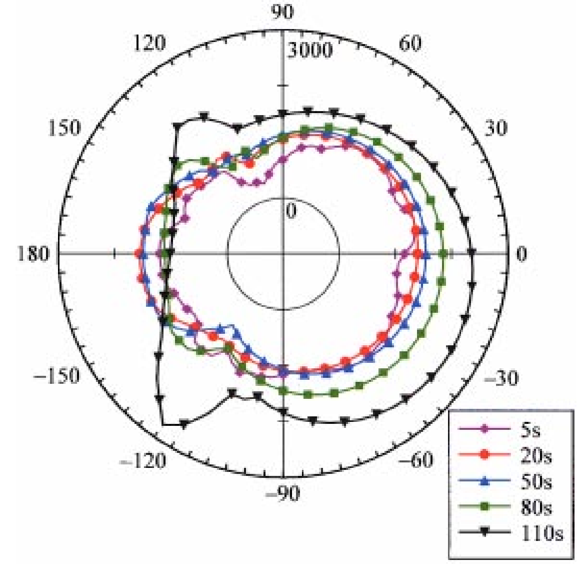

Fig. 10 Local heat transfer coefficient $h(\theta)$ at different time in the melting process: $T_{l0}=26°\mathrm{C}$, $v_{l\infty}=0.06$ m/s, $T_{s0}=-16°\mathrm{C}$, $d_0=36$ mm, $\mathrm{Gr}_0/\mathrm{Re}_0^2=0.319$.

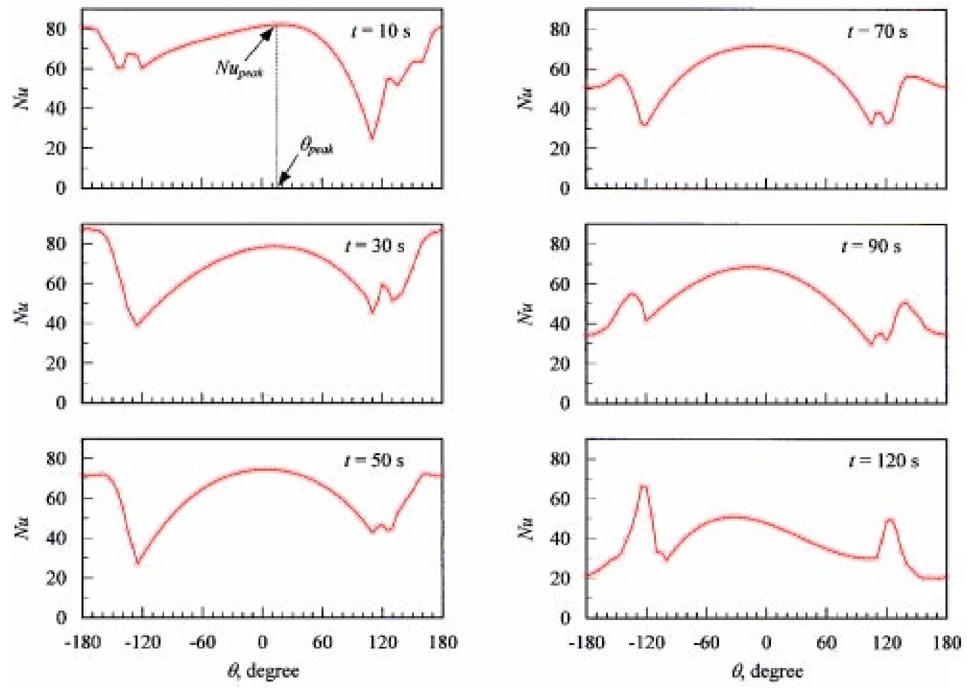

Fig. 11 Local Nusselt number Nu(θ) at different time in the melting process: $T_{l0}=26°\mathrm{C}$, $v_{l\infty}=0.06$ m/s, $T_{s0}=-16°\mathrm{C}$, $d_0=36$ mm, $\mathrm{Gr}_0/\mathrm{Re}_0^2=0.319$.

time over almost all the surface except for the regions around $\theta\approx130$ deg and $\theta\approx-130$ deg in the final melting period. This trend is contrary to the local melting rate and local heat transfer coefficient, since the effects of volume diameter, which decreases with the melting of ice particle as shown in Fig. 8, are also included. The Reynolds number, which also includes the effect of size change during the melting process, decreases from the initial value of 1793 to the final value of 439 in this case.

After the initial stage, the stable boundary layer is formed over the most surface of ice sphere except for the region beyond the separation point (Hao and Tao [13]). The characteristics of heat transfer are strongly influenced by the nature of boundary layer development on the surface. The local Nusselt number decreases with increasing $|\theta|$ from the horizontal centerline to $\theta\approx110$ deg and $\theta\approx-120$ deg as a result of boundary layer development along the ice surface (Fig. 11). The local Nusselt number reaches the minimum on the upper and lower surface ($\theta\approx110$ deg and $\theta\approx-120$ deg, respectively), due to the separation of the boundary layer there. Beyond the separation point the local Nusselt number increases with increasing $|\theta|$ and even reaches a slightly higher value than that over the front surface because considerable disturbance exists near the rear surface of the ice sphere, where wake eddies sweep the surface. The strong local heat transfer results in a relatively high local melting rate over the rear surface in the earlier stage, as shown in Fig. 9. Therefore, the rear shape of the ice sphere gradually flattens and eventually becomes completely flat, as shown in Fig. 5. The variation of the local Nusselt number with θ on the upper surface is characterized by two minima before $t=100$ s. This is because secondary separation of the boundary layer happens on the upper surface (also see Fig. 5(*b*). The most significant feature of the boundary layer with melting that differs from that without melting is that the melt from the surface discharges into the boundary layer. The strong disturbance enhances the heat transfer in the region just beyond the separation point, causing further melting. The higher density of the melt with respect to the mainstream causes the melt on the upper surface to flow downward along the upper surface but quickly mixes backward into the mainstream (recall $\mathrm{Gr}_0/\mathrm{Re}_0^2<1$) and forms a new boundary layer beyond the first upper separation point. The development of new boundary layer causes the heat transfer to weaken, and the local Nusselt number decreases until it finally reaches the secondary minimum at $\theta\approx130$ deg, where the new boundary layer separates (see Fig. 5(*b*) for the second upper separation point). It is worth mentioning that for a non-melting sphere, the separation point usually appears at about $\theta\approx80$ deg for the same Re range.

In Fig. 11, $\mathrm{Gr}_0/\mathrm{Re}_0^2=0.319$; therefore we still see some thermal buoyancy effect on the lower surface of the melting particle as the melt discharges from the surface. The downward motion of the melt induced by thermal buoyancy prevents from the reattachment of boundary layer beyond the lower separation point, as compared with the formation of new boundary layer beyond the first upper separation point (see Fig. 5). Therefore, no secondary separation, or the second minimum of local Nusselt number, appears on the lower side. Before the lower separation point, the downward free convection also makes the boundary layer on the lower surface thicker than that on the upper side. That can explain why the local Nusselt number of lower surface is smaller than that of upper surface during $t=30\sim60$ s.

Another feature implied in Fig. 11 is that shape changes due to the melting further influence heat transfer by changing the flow pattern around the particle. The shape of the ice sphere gradually changes into a scallop shape because the higher heat transfer causes higher melting rate on the front and rear surfaces. In turn, the flow pattern around the ice gradually changes, along with changes in the curvature of the front surface and the maximum radius in the cross direction of water flow. The most obvious change on heat transfer is that of the local Nusselt number, which decreases from a maximum to a minimum on the rear surface ($\theta=180$ deg) while the rear shape of the ice changes from spherical to flat during the entire melting process. The surface contour beyond the location of the maximum radius experiences a sudden change when the rear shape of ice becomes flat. As a result the boundary layer cannot continue to develop. Therefore, the separation point always appears at the position of the maximum radius in the traverse direction of water flow when the rear shape of ice

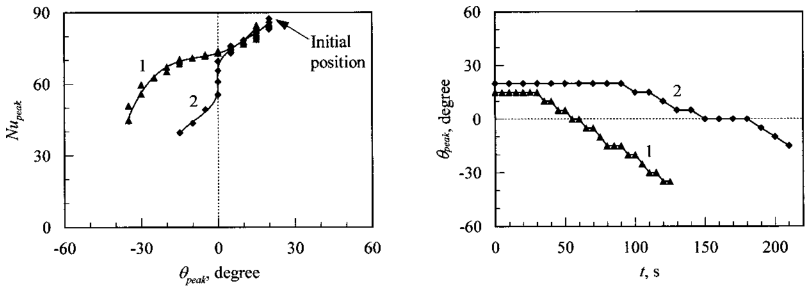

(*a*) (*b*)

Fig. 12 Peak local Nusselt number $\mathrm{Nu}_{\mathrm{peak}}$ and the location θ_{peak} during the melting process: 1—$T_{l0}=26°\mathrm{C}$, $v_{l\infty}=0.06$ m/s, $T_{s0}=-16°\mathrm{C}$, $d_0=36$ mm, $\mathrm{Gr}_0/\mathrm{Re}_0^2=0.319$, 2—$T_{l0}=16°\mathrm{C}$, $v_{l\infty}=0.06$ m/s, $T_{s0}=-16°\mathrm{C}$, $d_0=36$ mm, $\mathrm{Gr}_0/\mathrm{Re}_0^2=0.093$.

becomes a flat. The strong disturbance beyond the separation point can be isolated in a small region so that a high local Nusselt number remains there and even slightly increases during the final period of melting. The influence of disturbance is weakening in the region near $\theta=180$ deg while the rear shape of ice becomes flat, resulting in a gradual decrease in the local Nusselt number. The phenomenon of secondary separation on the upper surface (illustrated by the second upper minimum point on the curve in Fig. 11) also gradually disappears. The reduced heat transfer on the lower front surface in the earlier period results in a lower melting rate than that of the upper front side, and as a result the curvature of the lower front surface gradually becomes slightly bigger than that of upper front surface in the final period. The shape change also causes the flow over the lower front surface to flow faster than that over the upper front side. Therefore, the local Nusselt number on the lower front surface gradually becomes higher than that on the upper front surface during the final period.

The above discussion may lead us to conclude that during convective melting the melting layer on the ice surface is being mixed with the boundary layer flow resulting from the main flow. The combined convective mass transfer and heat transfer (which includes both forced and free convection), along with the particle shape change, complicate the distribution of local Nusselt number, as shown in Fig. 11, and reveal multiple flow separation points. Even before flow separation occurs, the combined mass and heat transfer play an important role in the local Nusselt number distribution. If we define a peak Nusselt number, $\mathrm{Nu}_{\mathrm{peak}}$, the maximum value of the Nusselt number over the portion of surface where the boundary layer is attached, as shown in Fig. 11, and its corresponding location, θ_{peak}, we can plot $\mathrm{Nu}_{\mathrm{peak}}$ as a function of θ_{peak}, as shown in Fig. 12(a). For $\mathrm{Gr}_0/\mathrm{Re}_0^2=0.319$, it can be seen that the peak Nusselt number decreases with θ_{peak} (from about 15 deg to -35 deg); i.e., shifting from the upper surface to the lower surface. This trend corresponds to the time history of the melting process as shown in Fig. 12(*b*). Initially, θ_{peak} remains at about 15 deg upper surface and gradually moves downwards. For the lower $\mathrm{Gr}_0/\mathrm{Re}_0^2(=0.093)$, there exists a period when θ_{peak} remains at zero degree, similar to the forced flow around a non-melting sphere. These complex features need further study and theoretical analysis.

Effect of Flow Velocity

Figure 13 shows the results at a water temperature of 16°C, an initial ice temperature of $-9°\mathrm{C}$, an initial ice diameter of 36 mm, and a water velocity of 0.06 m/s and 0.04 m/s ($\mathrm{Re}_0=1558$ and 1039, respectively), to demonstrate the influence of water velocity on the melting process. The variations of radius, local melting rate, and local Nusselt number with θ is plotted in the time sequence of 50, 100, 150, and 200 second, respectively, to make more original experimental data available. The increase in water velocity enhances the heat transfer between the water and the surface of ice, resulting in an increase in the local melting rate, as shown in Fig. 13(*b*). As a result the size of the ice in the case of $v_{l\infty}=0.06$ m/s is smaller than in the case of $v_{l\infty}=0.04$ m/s, as shown in Fig. 13(*a*). Changes in the local Nusselt number are determined by changes in the local heat transfer coefficient and the ice diameter, based on the equivalent sphere volume. The local Nusselt number for the case of $v_{l\infty}=0.06$ m/s is initially higher than in the case of $v_{l\infty}=0.04$ m/s, as shown in Fig. 13(*c*). As time elapses, the local Nusselt number for the higher water velocity becomes smaller. This is due to the fact that the decrease in the size is faster for the 0.06 m/s case, resulting in a decrease in the time-dependent Re (for example, at $t=200$ s in Fig. 13(*c*)).

Effect of Flow Temperature

Figure 14 shows another set of test results for observing the effects of water temperature. The tests are also conducted at the water velocity of 0.06 m/s, the initial ice temperature of $-16°\mathrm{C}$, and the initial ice diameter of 36 mm. Two water temperatures of 30°C and 16°C are selected, yielding $\mathrm{Re}_0=1895$ and 1558, respectively. The results indicate that the increase in water temperature results in an increase in local melting rate and a decrease in melting time, as shown in Fig. 14(*a*) and (*b*). The local Nusselt number for high water temperature is smaller than that for lower water temperature at the same time, especially in the later period of the melting process, as shown in Fig. 14(*c*), because the size decreases rapidly in high water temperature.

3.2.2 *High* $\mathit{Gr}_0/\mathit{Re}_0^2(>6)$.

For a melting process with a high $\mathrm{Gr}_0/\mathrm{Re}_0^2$, the shape variation of the ice sphere is significantly different. This is due to the strong influence of thermal buoyancy as visualized in Hao and Tao [13]. Figure 15 shows the results at a low water velocity of 0.01 m/s, water temperature of 21°C, initial ice temperature of $-3°\mathrm{C}$, initial ice diameter of 36 mm, and initial Reynolds number of 279. The initial Grashof number is 5.43×10^5, and the initial $(\mathrm{Gr}_0/\mathrm{Re}_0^2)$ reaches 6.98. The thermally induced density difference between the cold melt and mainstream causes a strong downward flow in the region behind the ice sphere and a downward extension of the wake. The upper separation point moves towards the rear of ice sphere. The effects of separation and disturbance caused by separation are relatively weak. The melt from the surface moves into the boundary layer and further weakens these effects. Therefore, no significant drop in local melting rate is observed at $\theta\approx110$ deg and $\theta\approx-130$ deg, as shown in Fig. 15(*b*); instead a relatively uniform distribution of local melting rate over the rear surface of ice sphere is found. This type of distribution of local melting rate does not cause the ice sphere become scallop-shaped. The shape instead changes into an ellipsoid from the side view, in which the minor axis is in the horizontal direction, and the major axis is in the vertical direction, as shown in Fig. 15(*a*). On the contrary, in the cases with higher initial Reynolds numbers the lowest local melting rate appears in

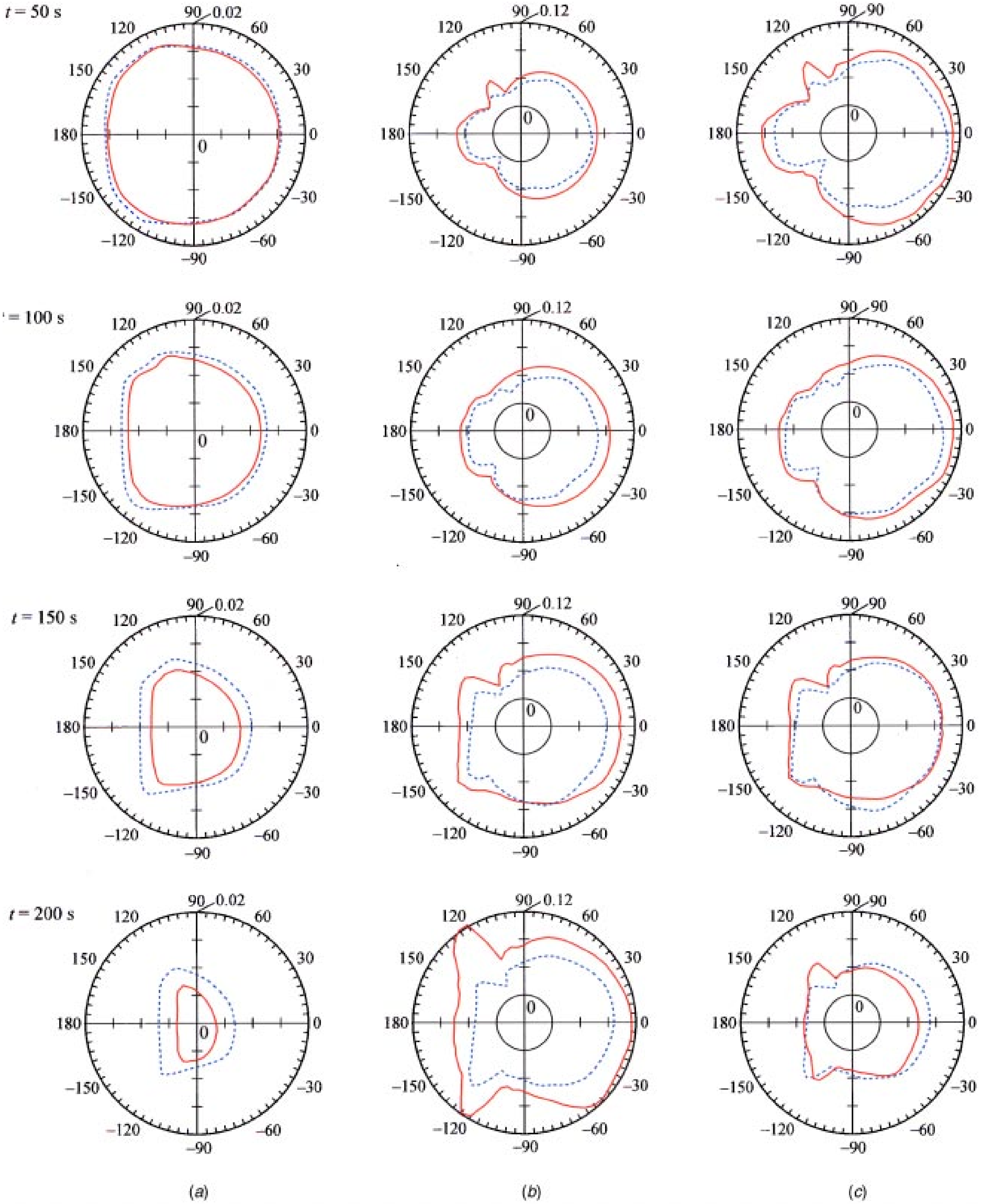

(*a*) (*b*) (*c*)

Fig. 13 Compared experimental results at different water velocities: —— $T_{l0}=16°C$, $v_{l\infty}=0.06$ m/s, $T_{s0}=-9°C$, $d_0=36$ mm, $Gr_0/Re_0^2=0.093$. ------ $T_{l0}=16°C$, $v_{l\infty}=0.04$ m/s, $T_{s0}=-9°C$, $d_0=36$ mm, $Gr_0/Re_0^2=0.209$. (*a*) *R*; (*b*) $\dot{m}''$; (*c*) Nu.

the regions near the separation points, and the relative higher local melting rates occurs in the rear portion. This kind of distribution of local melting rate corresponds to the shape change into scallop. Further details in the flow characteristics for high Gr/Re^2 cases can be found in Hao and Tao [13].

The variation of local heat transfer coefficient with θ at different times is shown in Fig. 15(*c*). In this case, the trend in local heat transfer coefficient is almost the same as that of local melting rate because the initial ice temperature is slightly lower than 0°C, and the influence of heat conducted into inside of ice particle is relative small. The variation of local Nusselt number with θ at different times is shown in Fig. 15(*d*). In general, the local Nusselt

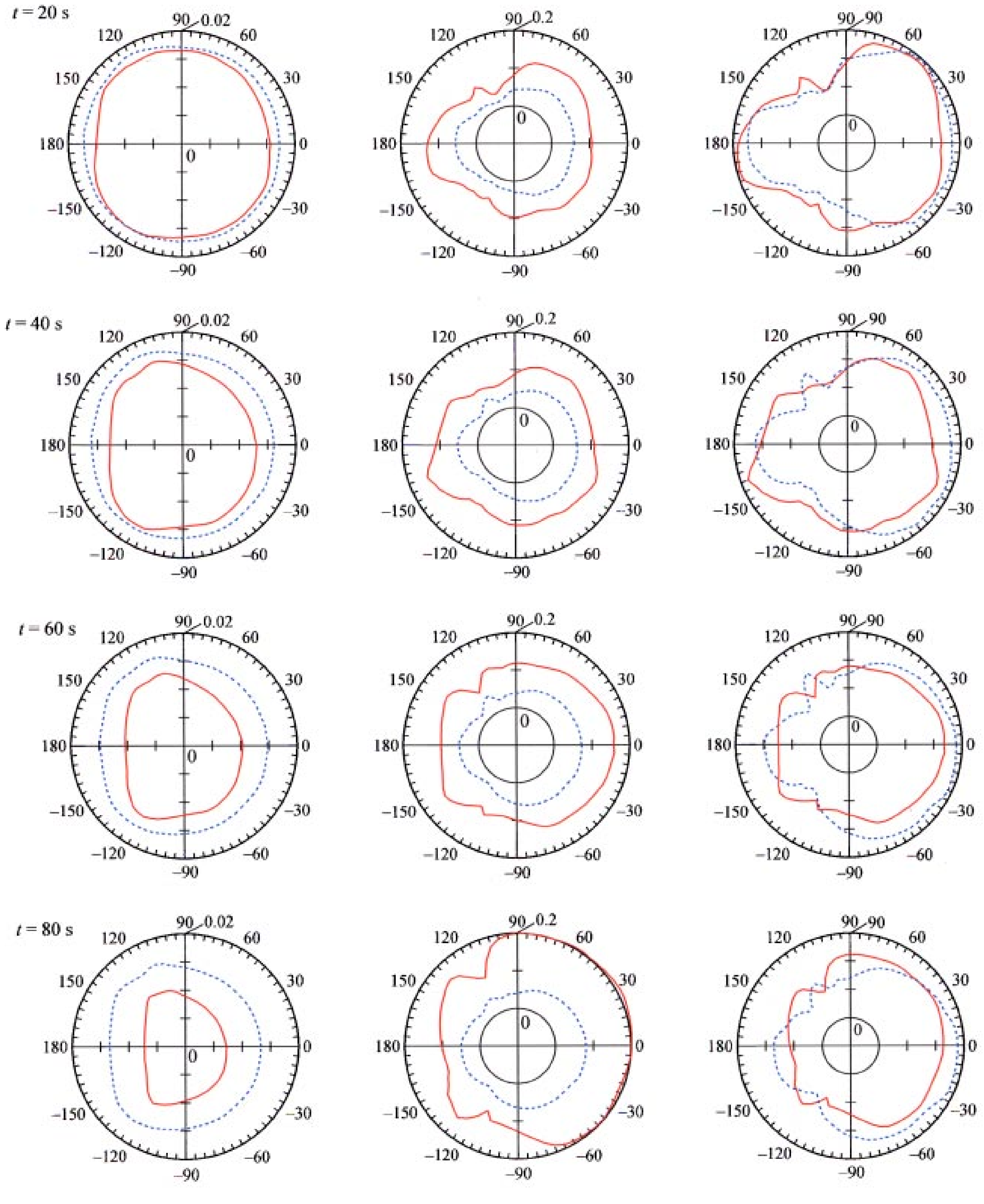

(a) (b) (c)

Fig. 14 Compared experimental results at different water temperatures: —— $T_{l0}=30°\mathrm{C}$, $v_{l\infty}=0.06$ m/s, $T_{s0}=-9°\mathrm{C}$, $d_0=36$ mm, $\mathrm{Gr}_0/\mathrm{Re}_0^2=0.440$. ------ $T_{l0}=16°\mathrm{C}$, $v_{l\infty}=0.06$ m/s, $T_{s0}=-9°\mathrm{C}$, $d_0=36$ mm, $\mathrm{Gr}_0/\mathrm{Re}_0^2=0.093$. (*a*) R; (*b*) $\dot{m}''$; (*c*) Nu.

number decreases as time elapses, contrary to that of local melting rate and local heat transfer coefficient, which increase. This is because the local Nusselt number is defined by the time dependent equivalent sphere diameter that decreases at a rate much faster than the increased rate of local heat transfer coefficient.

3.3 Total Melting Rate and Average Heat Transfer Coefficient. The variations of total melting rate and average heat transfer coefficient with time at different water velocities are shown in Figs. 16 and 17. All six tests are conducted at a supply water temperature of 16°C, initial ice temperature of −8°C, and

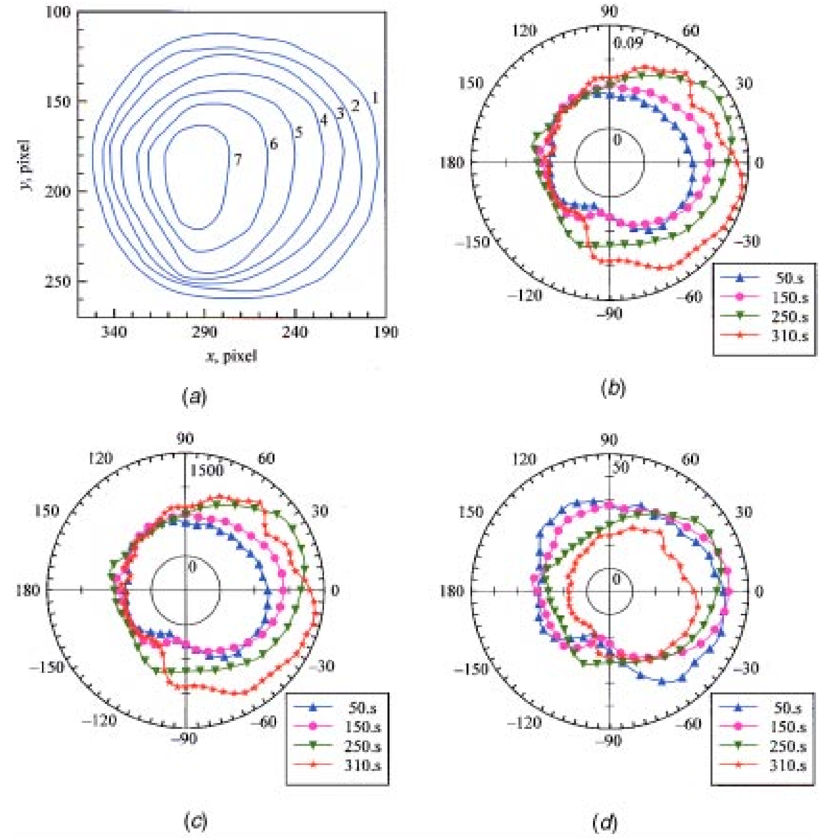

Fig. 15 Experimental results at a slow water velocity: $T_{l0}=21°\mathrm{C}$, $v_{l\infty}=0.01$ m/s, $T_{s0}=-3°\mathrm{C}$, $d_0=36$ mm, $\mathrm{Gr}_0/\mathrm{Re}_0^2=6.98$. (*a*) Shape change; (*b*) $\dot{m}''$; (*c*) h; (*d*) Nu.

initial ice diameter of 36 mm. The water velocities are varied from 0.01 to 0.06 m/s. The increase in the water velocity enhances the convection heat transfer between water and ice surface resulting in an increase in the total melting rate and average heat transfer coefficient.

The volume and surface area of ice decrease over time. The melting rate is the highest when the melting process begins, as shown in Fig. 16. The melting rate gradually decreases over time as the volume and surface area of the particle decrease. The trend of the decrease in melting rate with the elapse of time is stronger for higher velocity of water. At a high velocity the melting rate may be lower than at lower velocity near the end of the melting process because the decrease in volume and surface area of ice is more pronounced than the influence of increase in water velocity.

The trends of variation of the average heat transfer coefficient with time are similar in all experimental results with different velocities, as shown in Fig. 17. The average heat transfer coefficient increases with time during the early melting period because the size of the ice decreases as the melting continues. In the final period, the shape of the ice becomes very irregular, and the convective heat transfer between water and ice surface is weakened, especially in the rear where the shape becomes flat. This causes a reduction in the average heat transfer coefficient.

As discussed in the above section, free convection caused by

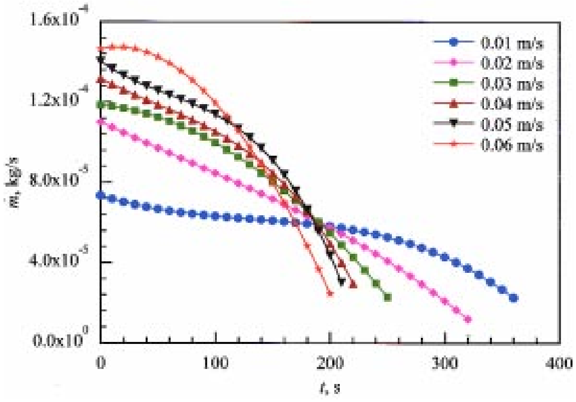

Fig. 16 Variation of melting rate of ice particle with time at different water velocities: $T_{l0}=16°\mathrm{C}$, $T_{s0}=-8°\mathrm{C}$, $d_0=36$ mm.

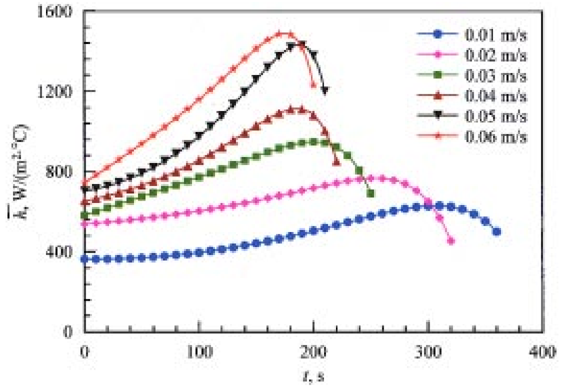

Fig. 17 Variation of average heat transfer coefficient with time at different water velocities: $T_{l0}=16°\mathrm{C}$, $T_{s0}=-8°\mathrm{C}$, $d_0=36$ mm.

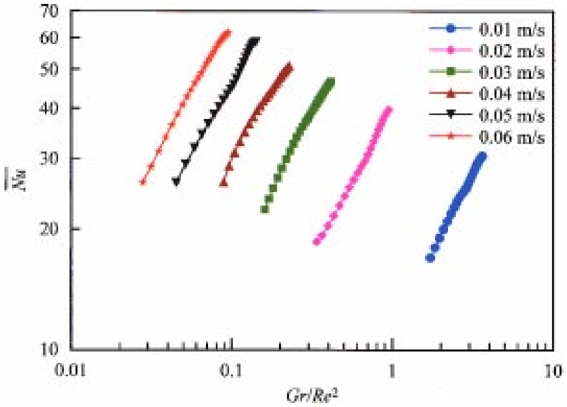

Fig. 18 Variation of Nusselt number as a function of $(\mathrm{Gr}/\mathrm{Re}^2)$ at different water velocities: $T_{l0}=16°\mathrm{C}$, $T_{s0}=-8°\mathrm{C}$, $d_0=36\ \mathrm{mm}$.

the density difference between the cold melt and the mainstream has an important effect on the heat transfer between the water and the ice surface and the melting process. Figure 18 shows the Nusselt number based on the average heat transfer coefficient and volume diameter as a function of $(\mathrm{Gr}/\mathrm{Re}^2)$ at different water velocities. For a given velocity, the Nu-Gr/Re^2 relation actually shows a similar dependence on the ice size for all the cases. Figures 19, 20, and 21 show the variation of melting rate and average heat transfer coefficient with time and Nusselt number as a function of $(\mathrm{Gr}/\mathrm{Re}^2)$, respectively, for the melting ice particles under different supply water temperatures. All the five tests are conducted at the water velocities of 0.06 m/s, the initial ice temperature of $-8°\mathrm{C}$, and the initial ice diameter of 36 mm. The water temperatures are varied at 11, 16, 21, 26, and 30°C, respectively.

All those results show a strong correlation among Nu, Gr, Re, and Ste (temperature effect). To develop an empirical correlation, we conduct a total of thirty tests with water velocity of 0.01 to 0.10 m/s and water temperature of 4 to 30°C. Some of them were repeated to test the repeatability of the experiments under identical conditions. The qualitative results of repeating tests agree reasonably well, and no detectable differences in main quantitative results are found. The regression analysis yields the following empirical correlation for the average Nusselt number in a melting process,

$$\overline{\mathrm{Nu}}=\frac{\overline{h}d_V}{k_{l0}}=0.118\mathrm{Re}^{0.431}\mathrm{Gr}^{0.0898}\mathrm{Pr}^{0.748}\mathrm{Ste}^{-0.167} \qquad (10)$$

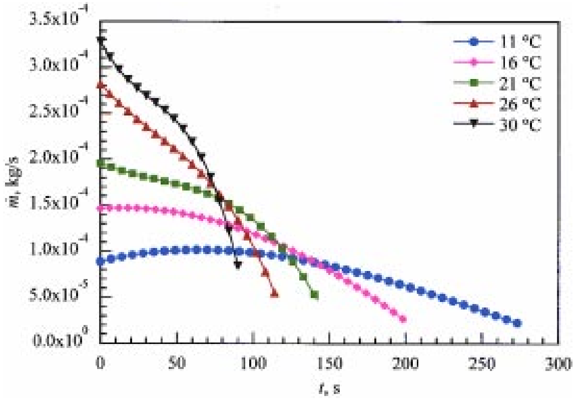

Fig. 19 Variation of melting rate of ice particle with time at different water temperatures: $v_{l\infty}=0.06\ \mathrm{m/s}$, $T_{s0}=-8°\mathrm{C}$, $d_0=36\ \mathrm{mm}$.

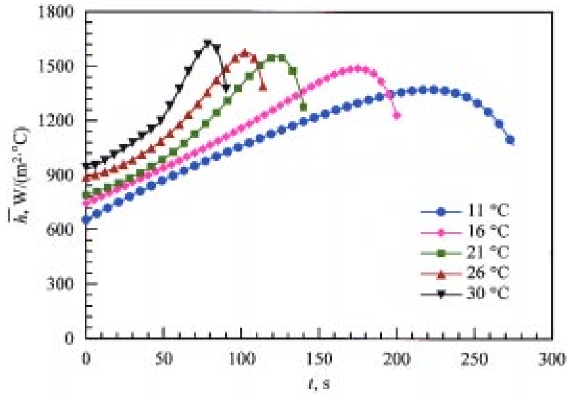

Fig. 20 Variation of average heat transfer coefficient with time at different water temperatures: $v_{l\infty}=0.06\ \mathrm{m/s}$, $T_{s0}=-8°\mathrm{C}$, $d_0=36\ \mathrm{mm}$.

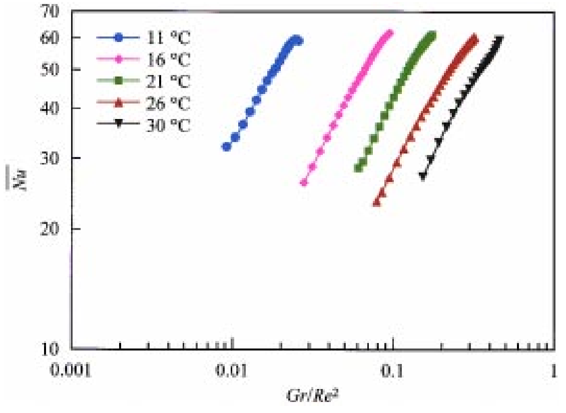

Fig. 21 Variation of Nusselt number as a function of $(\mathrm{Gr}/\mathrm{Re}^2)$ at different water temperatures: $v_{l\infty}=0.06\ \mathrm{m/s}$, $T_{s0}=-8°\mathrm{C}$, $d_0=36\ \mathrm{mm}$.

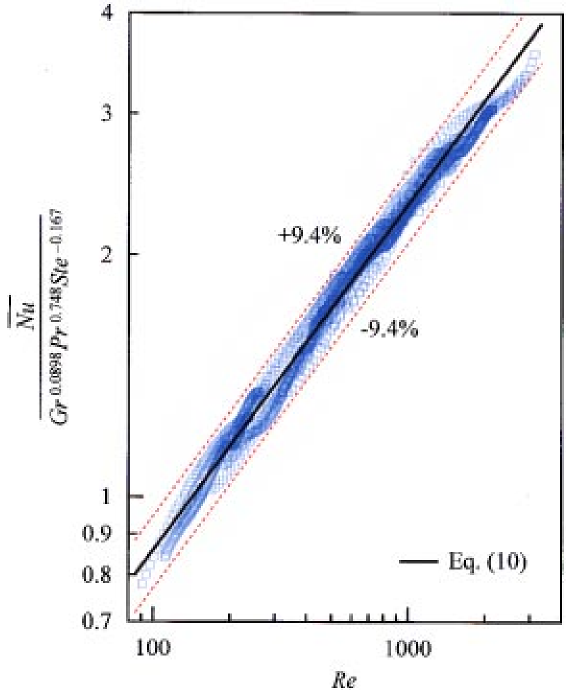

Fig. 22 Correlation and all of results for dimensionless average heat transfer coefficient in the present study: $T_{l0}=4\sim30°\mathrm{C}$, $v_{l\infty}=0.01\sim0.10\ \mathrm{m/s}$, $T_{s0}=-23\sim0°\mathrm{C}$, $d_0=36\ \mathrm{mm}$.

which is valid for

$$80 \leqslant \mathrm{Re} \leqslant 3200 \quad 0.0016 \leqslant \mathrm{Gr}/\mathrm{Re}^2 \leqslant 6.98$$

$$7.91 \leqslant \mathrm{Pr} \leqslant 12.69 \quad 0.05 \leqslant \mathrm{Ste} \leqslant 0.39$$

$$0.007 \leqslant d_V \leqslant 0.036 \ \mathrm{m} \quad 0.65 \leqslant \phi \leqslant 1$$

Each of the properties (ρ_{l0}, μ_{l0}, c_{pl0}, k_{l0}, and β_{l0}) in the dimensionless numbers is evaluated at the film temperature, $T_f = (T_{l\infty} + T_m)/2$. The R-squared value for Eq. (10) is 0.9378. The comparison of the experimental data with the values calculated by Eq. (10) is shown in Fig. 22. The deviation for all test data is within ±9.4 percent.

Summary and Conclusions

The melting and heat transfer characteristics of the convective melting of an initially spherical ice particle in horizontally flowing water have been studied experimentally to arrive at quantitative results. Based on the experimental results, the following conclusions have been drawn:

1 The trends of the local heat transfer coefficient are almost identical to those of the local melting rate on the ice surface. The rate of change in local heat transfer coefficient is slightly lower than that of local melting rate in the early-stage of melting process. The local heat transfer coefficient includes the effect of heat conduction into the inside of ice. Although the conduction effect is generally not significant except for a short early effective period, the effective time period of heat conduction does increase with the decrease in the initial temperature of ice particle.

2 For $\mathrm{Gr}_0/\mathrm{Re}_0^2 < 1$ and at a given time during the early melting period, a typical distribution of local Nusselt number over the front portion of the ice sphere exhibits a peak local Nusselt number ($\mathrm{Nu}_{\mathrm{peak}}$) at a location ($\theta_{\mathrm{peak}}$) starting from the upper surface, then decreases with increasing θ from θ_{peak}, and reaches minima at the upper and lower surfaces at an angular location of about 110 deg to 130 deg, depending on the flow velocity, and −120 deg near the separation point. The location θ_{peak} for $\mathrm{Nu}_{\mathrm{peak}}$ shifts from the upper surface towards the lower surface as melting proceeds. There exist two flow separation points on the upper surface and one separation point on the lower surface of a melting particle, resulting from combined mass and heat transfer and particle shape change. The second separation point on the upper rear surface corresponds to a second minimum value on the local Nusselt number distribution curve. For high $\mathrm{Gr}_0/\mathrm{Re}_0^2$ (>6) cases, thermal buoyancy effects become more pronounced. The local Nusselt number distribution does not show a second separation point on the upper surface of the melting particle.

3 $\mathrm{Gr}_0/\mathrm{Re}_0^2$ also correlates to the shape variation of the ice sphere in the melting process. The shape over the rear ice sphere becomes flat and the overall shape of the ice changes into a scallop when $\mathrm{Gr}_0/\mathrm{Re}_0^2$ is small (less than 1). With a high $\mathrm{Gr}_0/\mathrm{Re}_0^2$ (>6), the shape over the rear of ice sphere does not become flat and the shape of ice sphere changes into an ellipse from the side view. Further investigation is needed to define more precisely the criteria of distinguishing these two different types of shape change.

4 The increase in water velocity results in an increase in the local melting rate and the local heat transfer coefficient and a decrease in the total melting time. The increase in water temperature results in an increase in the local melting rate and the local heat transfer, which eventually causes the local Nusselt number to decrease because of the decrease in the particle size.

5 The average heat transfer coefficient first increases with time and later rapidly decreases. The average heat transfer coefficient increases with the velocity and temperature of water except near the end of melting period.

6 An empirical correlation that can be used to calculate the average heat transfer coefficient in a melting process is obtained. This correlation considers the irregular shape of ice. A shape factor that indicates the irregularity of particle shape in melting process is defined.

Acknowledgments

The supports from NASA (Grant No. NAG3-1797) and NSF (Grant No. HR67206268) are greatly appreciated.

Nomenclature

A_s = surface area of ice particle, m^2
c_p = specific heat, J/kg K
d_s = surface diameter, m
d_V = volume diameter, m
Gr = Grashof number, $g_0 \beta_{l0} \rho_{l0}^2 d_V^3 (T_{l\infty} - T_m)/\mu_{l0}^2$
g = gravitational acceleration, m/s^2
h = local heat transfer coefficient, W/m^2 K
h_{ls} = latent heat of fusion, J/kg
k = thermal conductivity of water, W/m K
$\dot{m}$ = total melting rate, kg/s
$\dot{m}''$ = local melting rate, kg/m^2 s
Nu = local Nusselt number, $h d_V / k_{l0}$
Pr = Prandtl number, $\mu_{l0} c_{pl0} / k_{l0}$
Q = total heat transfer rate, W
q = heat flux, W/m^2
R = outside radius, m
Re = Reynolds number, $\rho_{l0} v_{l\infty} d_V / \mu_{l0}$
r = radius coordinate inside ice, m
Ste = Stefan number, $c_{pl0}(T_{l\infty} - T_m)/h_{ls}$
T = temperature, °C
t = time, s
V = volume, m^3
v = velocity, m/s
x, y = coordinates, m

Greek Symbols

β = coefficient of thermal expansion, K^{-1}
θ = angle from the horizontal centerline, degree
μ = viscosity, Pa·s
ρ = density, kg/m^3
ϕ = shape factor, d_V^3/d_s^3

Subscripts

0 = at the inlet; initial; respective value of property in dimensionless number
c = center of particle
l = liquid, water
i = interface
m = phase change
s = solid, ice
∞ = mainstream

Other

— = average

References

[1] Tkachev, A. G., 1953, "Heat Exchange in Melting and Freezing of Ice," in *Problem of Heat Transfer During Change of Phase: A Collection of Articles*, AEC-tr-3405, translated from Russian, State Power Press, pp. 169–178.
[2] Merk, H. J., 1953, "The Influence of Melting and Anomalous Expansion on the Thermal Convection in Laminar Boundary Layers," Appl. Sci. Res., **4**, pp. 435–452.
[3] Schenk, I., and Schenkels, F. M., 1968, "Thermal Free Convection from an Ice Sphere in Water," Appl. Sci. Res., pp. 465–476.
[4] Vanier, Cr. R., and Tien, C., 1970, "Free Convection Melting of Ice Spheres," AIChE J., **16**, pp. 76–82.
[5] Eskandari, V., 1981, "Forced Convection Heat Transfer from Ice Spheres in Flowing Water," *Master's thesis*, University of Toledo, Toledo, OH.
[6] Eskandari, V., Jakubowski, G. S., and Keith, T. G., 1982, "Heat Transfer from Spherical Ice in Flowing Water," Joint AIAA/ASME Fluids, Plasma, Thermophysics, and Heat Transfer Conference, St Louis, MO, ASME 82-HT-58, pp. 1–5.

[7] Anselmo, A., Prasad, V., and Koziol, J., 1991, ''Melting of a Sphere when Dropped in a Pool of Melt with Applications to Partially-Immersed Silicon Pellets,'' *Heat Transfer in Metals and Containerless Processing and Manufacturing*, ASME HTD Vol. 162, pp. 75–82.

[8] Anselmo, A., Prasad, V., Koziol, J., and Gupta, K. P., 1993, ''Numerical and Experimental Study of a Solid-pellet Feed Continuous Czochralski Growth Process for Silicon Single Crystals,'' J. Cryst. Growth, **131**, pp. 247–264.

[9] Mukherjee, M. K., Shih, J., and Prasad, V., 1994, ''A Visualization Study of Melting of an Ice Sphere in a Pool of Water,'' 1994 International mechanical Engineering Congress and Exposition, The Winter Annual Meeting, ASME 94-WA/HT-14, Chicago, Illinois, November 6–11, 1994.

[10] Aziz, S. A., Janna, W. S., and Jakubowski, G. S., 1995, ''Forced Convection Heat Transfer From an Isothermal Melting Ice Sphere Submerged in Flowing Water,'' ASME HTD-Vol. 317-1, pp. 213–217.

[11] McLeod, P., Riley, D. S., and Sparks, R. S. J., 1996, ''Melting of a Sphere in Hot Fluid,'' J. Fluid Mech., **327**, pp. 393–409.

[12] Hao, Y. L., and Tao, Y. X., 1999, ''Convective Melting of a Solid Particle in a Fluid,'' *Proceedings of the 3rd ASME/JSME Joint Fluids Engineering Conference*, San Francisco, California, July 18–23, 1999, FEDSM99-7091, pp. 1–6.

[13] Hao, Y. L., and Tao, Y. X., 2001, ''Melting of Solid Sphere Under Forced and Mixed Convection: Flow Characteristics,'' ASME J. Heat Transfer, **123**, pp. 937–950.

[14] Gebhart, B., 1993, *Heat Conduction and Mass Diffusion*, McGraw-Hill, Inc., New York, Chap. 4.

[15] Kline, S. L., and McClintock, F. A., 1953, ''Describing Uncertainties in Single-Sample Experiments,'' Mech. Eng. (Am. Soc. Mech. Eng.), **75**, pp. 3–8.

Dominique Baillis
e-mail: domino@cethil.insa-lyon.fr

Jean-François Sacadura

Center de Thermique de Lyon (CETHIL),
UMR CNRS 5008,
Institut National des Sciences Appliquées de
Lyon,
20, avenue Albert Einstein 69621,
Villeurbanne Cedex,
France

Directional Spectral Emittance of a Packed Bed: Influence of the Temperature Gradient in the Medium

Recently a new experimental set-up for measuring the directional spectral emittance has been developed. Both sides of packed opaque spheres are simultaneously heated with identical power laser beams (CO_2 10.6 μm) and the isothermal condition in the medium is assumed. In this paper we consider the coupled conduction-radiation equations to investigate the effect of the temperature nonuniformity on the calculated value of the emittance and to verify if the isothermal assumption is valid. Moreover, the sensitivity of the emittance and the temperature profile to the values of parameters (such as the porosity, the face temperatures, and the particle hemispherical reflectivity, etc.) is studied. [DOI: 10.1115/1.1466459]

Keywords: Heat Transfer, High Temperature, Modeling, Packed Beds, Participating Media, Porous Media, Properties, Radiation

Introduction

Radiative heat transfer through semi-transparent media (absorbing, emitting and scattering media) is governed by the Radiative Transfer Equation (RTE). The RTE is stated in terms of radiation intensity, a scalar that varies with spatial location, direction, and wavelength, and is coupled through temperature to the energy conservation equation. The RTE is an integro-differential equation with relatively few analytical solutions. A wide variety of approximate and computational techniques have therefore been developed to solve the RTE. Moreover, experiments to measure intensity have been developed. An extensive review of the radiative transfer in dispersed media dealing with theoretical prediction and experimental studies was carried out by Viskanta and Mengüc [1] and by Baillis and Sacadura [2]. Radiative heat transfer prediction depends upon accurate material property information in addition to accurate RTE modelling techniques, and the properties themselve continue to be an important source of uncertainty. To this end, radiative heat transfer through relatively simple media such as packed bed spheres has received much attention. A general review of radiation heat transfer in packed beds was given by Kaviany [3].

Kamiuto [4] proposed a correlated-scattering theory to determine radiative properties of a packed bed consisting of relatively large spheres. Singh and Kaviany [5] showed that the radiative properties for a bed of large opaque spheres can be obtained from the independent properties by scaling the optical thickness while leaving the albedo and the phase function unchanged. These authors also concluded from this study that the results obtained from the correlated scattering theory of Kamiuto do not generally show good agreement with the results obtained from the Monte Carlo method. Jones et al. [6] measured the spectral directional distribution of radiation intensity at the exposed boundary of a packed bed of opaque spheres using a direct radiometric technique. The purpose of these measurements was to provide an experimental data base of radiative intensity with which to correlate intensity field solutions of the radiative equation in packed beds. Recently Lopes et al. [7] have developed a new experimental set up for measuring the directional spectral emittance. Both sides of the sample are simultaneously heated with identical power laser beams (CO_2 10.6 μm) and the isothermal condition in the medium is assumed. Directional spectral emittances have been measured for packed beds of oxidized bronze spherical particles. Experimental results have been compared with emittances calculated by solving the radiative transfer equation using the discrete ordinates method. Radiative properties are predicted using the geometric optics theory combined with a correlated scaling factor for large size parameter proposed by Singh and Kaviany [5].

In this paper, the coupled conduction-radiation equations are considered in order to investigate the effect of the temperature non-uniformity on the calculated value of the emittance, and to verify if the isothermal assumption is valid. Moreover, results obtained from uncorrelated and correlated radiative properties are compared. An analysis of sensitivity of parameters such as porosity, particle diameter, and surface temperature on the temperature profile and on emittance results is also studied here.

Firstly, the two samples of packed bed of oxidized bronze spherical particles studied are described. Then emittance measurements are briefly recalled. Then the model of coupled conduction-radiation is described. Finally, results obtained from two samples are presented and discussed.

Packed Spheres Systems

The participating porous medium considered in this study is a mono-dispersion of spherical particles of oxidized bronze. It is assumed that the packing geometry is random. When heated, the bronze oxidizes and a black oxide forms on the particle boundary surface. In order to ensure that oxide growth does not continue during measurements, the samples are heated in a furnace at 923 K for 72 hours. Two different samples are studied. For each medium, spheres are assumed to have a nominal uniform diameter, as specified by the supplier. The dimensional characteristics of the two samples are given in Table 1.

Emittance Measurement

Emittance measurements are briefly recalled here, more details can be found in Lopes et al. [7]. The experimental set up (Fig. 1, Ref. [8]) was developed to minimize the temperature gradient inside the medium. Indeed, both sides of the sample are simulta-

---

Contributed by the Heat Transfer Division for publication in the JOURNAL OF HEAT TRANSFER. Manuscript received by the Heat Transfer Division December 15, 2000; revision received October 12, 2001. Associate Editor: R. D. Skocypec.

Table 1 Sample data

Sample number	Sample Thickness L (mm)	Porosity δ	Sphere diameter d (μm)	Face Temperatures (K)
A	2.94	0.3112	300	890
B	4.91	0.3876	400	888

neously heated with a high power laser (4 kW, CO_2 10.6 μm) which was split into two identical beams using a beam splitter (50 percent − 50 percent ± 1 percent). The power of both laser beams is measured by a calorimeter. Energy distribution of the laser beam is homogenized using two copper tubes with a square opening and with side-faces buffed as a mirror. The sample temperature is determined by a pyrometer. Values obtained are given in Table 1. Uncertainties of temperatures have been estimated to be less than 3.5 percent.

The directional spectral emittance can be defined as the ratio of the spectral fluxes emitted by the sample and by the reference blackbody. The radiometer Heimann KT4S collects the heat flux emitted by the sample and by a reference blackbody at the same temperature, within the same spectral range and solid angle (Fig. 1). The radiometer is mounted on a rotating arm allowing the measurement of the radiation emitted by the sample at several angles. Different narrow band infrared filters are used to measure spectral emitted radiation. The area of the sample surface heated by the laser beams is 12×12 mm. Uncertainties of emittance measurements have been estimated to be less than 11 percent.

Theoretical Emittance Model-Combined Conduction-Radiation Heat Transfer

Governing Equations. Lopes et al. [7] have considered the medium as isothermal. In this paper our aim is to verify the validity of this hypothesis. It is necessary to solve the energy conservation equation to determine the complete temperature field to be input in the RTE. The oxidized bronze spherical packed bed used in the experiment is considered as a finite plane parallel square slab. The medium can be treated as one-dimensional. The one-dimensional, radiation/conduction energy equation is:

$$-\frac{\partial}{\partial y}\left(k_b\frac{\partial T}{\partial y}\right)+4\pi\beta_\lambda\int_{\lambda=0}^{\infty}(1-\omega_\lambda)I_{\lambda b}d\lambda-2\pi\beta_\lambda\int_{\lambda=0}^{\infty}(1-\omega_\lambda)\int_{\mu=-1}^{1}I_\lambda d\mu d\lambda=0 \tag{1}$$

The bed thermal conductivity can be obtained by using parallel-series models from the thermal conductivity of the bed particle (bronze), the thermal conductivity of the interstitial medium (air) being negligible:

$$k_b=\frac{1}{2}(1-\delta)k_{\text{bronze}} \tag{2}$$

The bronze conductivity, k_{bronze} is given by the relation:

$$\log k_{\text{bronze}}=C_0+C_1\log T+C_2(\log T)^2+C_3(\log T)^3 \tag{3}$$

with $C_0=-37.8999$, $C_1=43{,}3167$, $C_2=-15{,}8575$, $C_3=1{,}9488$. Equation (1) is solved with the measured temperature boundary conditions $(T(0),T(\tau_0))$.

For a one-dimensional semi-transparent medium with azimuthal symmetry the RTE is written:

$$\mu\frac{\partial I_\lambda(\tau,\mu)}{\partial\tau}+I_\lambda(\tau,\mu)=S_\lambda(\tau,\mu,T) \tag{4}$$

where the source term is:

$$S_\lambda(\tau,\mu,T)=(1-\omega_\lambda)I_{\lambda b}(T)+\frac{\omega_\lambda}{2}\left(\int_{-1}^{1}I_\lambda(\tau,\mu')p(\mu',\mu)d\mu'\right)$$

On the bed's surface, the incoming boundary condition intensity is taken as the sum of the blackbody radiation at the temperature of the surroundings $I_{b\lambda}(T=293\text{ K})$ and the collimated normally incident radiation I_0 incoming from the power laser at the wavelength 10.6 μm.

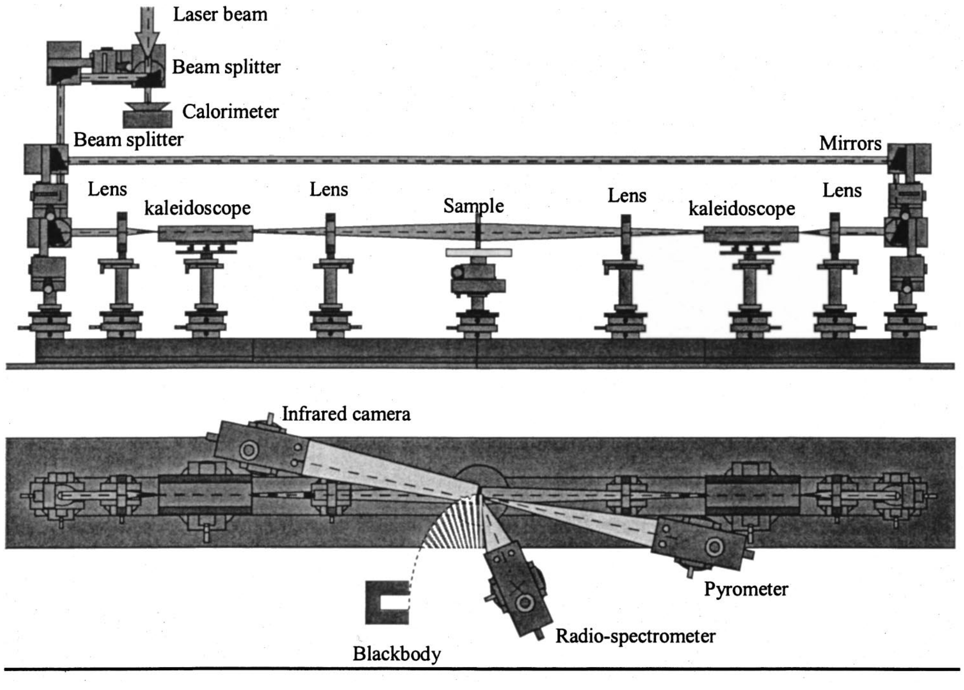

Fig. 1 Emittance measurement system (Lopes et al. [11])

$$\lambda=10.6\mu m\begin{cases}\tau=0\rightarrow\begin{cases}I_\lambda(0,\mu)=I_0+I_{b\lambda}(T=293K)\mu_0\leqslant\mu\leqslant 1\\ I_\lambda(0,\mu)=I_{b\lambda}(T=293K)\quad 0<\mu<\mu_0\end{cases}\\ \tau=\tau_o\rightarrow\begin{cases}I_\lambda(\tau_0,\mu)=I_0+I_{b\lambda}(T=293K)-1\leqslant\mu\leqslant-\mu_0\\ I_\lambda(\tau_0,\mu)=I_{b\lambda}(T=293K)-\mu_0<\mu<0\end{cases}\end{cases}\tag{5.a}$$

$$\lambda\neq 10.6\mu m\begin{cases}\tau=0\rightarrow I_\lambda(0,\mu)=I_{b\lambda}(T=293K)0\leqslant\mu\leqslant 1\\ \tau=\tau_o\rightarrow I_\lambda(\tau_0,\mu)=I_{b\lambda}(T=293K)-1\leqslant\mu\leqslant 0\end{cases}\tag{5.b}$$

$$I_0=P/(2\pi(1-\cos\theta_0)S)\tag{6}$$

with P, the power laser received by the sample $P=625$ W,

θ_0, the divergence half angle of the incident collimated beam $\theta_0=2.5$ deg,

S, the sample surface $S=1.44\ 10^{-4}$ m^2. Numerical calculations have shown that blackbody radiation at the temperature of the surroundings incoming on the sample face can be neglected.

The directional spectral emittance of the medium is defined as:

$$\varepsilon_\lambda(0,\mu)=\frac{I_\lambda(0,\mu)}{I_{\lambda b}(T(0))}\quad\mu<0\tag{7}$$

Solution Method. The discrete ordinates method (DOM) associated with the control volume method is used to solve the coupled radiation conduction equations (Doermann [9]). A quadrature over 24 directions is adopted in the DOM. The spherical space is discretized into 12 directions for the positive range of μ and 12 other symmetric directions for the negative μ. This quadrature is precise and adapted to our case. Indeed the incident radiative flux on the sample being collimated, a first zone in which is the collimated beam is considered ($\mu_0\leqslant\mu\leqslant 1$). After this zone, in the interval ($0\leqslant\mu\leqslant\mu_0$) a combination of two Gaussian quadrature with 11 directions is used (Nicolau [10]). A linear scheme (diamond) (Doermann [9]) is employed to evaluate the radiative intensity in the control volume. The spectral integrations in Eq. (1) are computed by solving Eq. (4) for constant spectral band intensities between 1.3 μm and 16.3 μm. 153 bands are considered. The general solution algorithm is iterative. An initial temperature-linearized form is adopted. The RTE is solved iteratively using a marching algorithm starting from the boundary faces. The spatial domain is discretised in control volume. A variable discretization of Tchebycheff with a grid concentration near boundaries is used. The dimension of the volume j is given by: $\Delta y_j=1/2\{\cos[(j-1)\pi/ny]-\cos[j\pi/ny]\}$ with ny the number of control volumes. A grid sensitivity study indicated that 90 control volumes are sufficient to achieve a converged solution for both samples.

Radiative Properties. The spherical particles have a size parameter $x(x=\pi d/\lambda)$ larger than 59, wavelengths being less than 15.8 μm and particles diameter being larger than 300 μm. When the particle size parameter x is much larger than unity, the geometrical optics theory can be used to predict radiative properties. If a packed bed consists of large diffuse spheres, then the independent uncorrelated radiative properties become (Brewster [11]):

$$p(\mu)=(8/3\pi)(\sqrt{1-\mu^2}-\mu\cos^{-1}\mu)\tag{8}$$

$$\omega_u=\rho_\lambda\tag{9}$$

$$\beta_u=1.5f_v/d\tag{10}$$

To take into account the dependent effects due to the overlapping particles for a bed of large opaque spheres, Singh and Kaviany [5] proposed scaling factors so that the independent radiative properties can be scaled to give the dependent properties of the particulate media. The scaling factor γ proposed by Singh and Kaviany [5] is evaluated by finding the ratio of the slopes calculated by the Monte Carlo method and by independent theory. The scaling factor scales the extinction coefficient, leaving the phase function and the albedo unchanged:

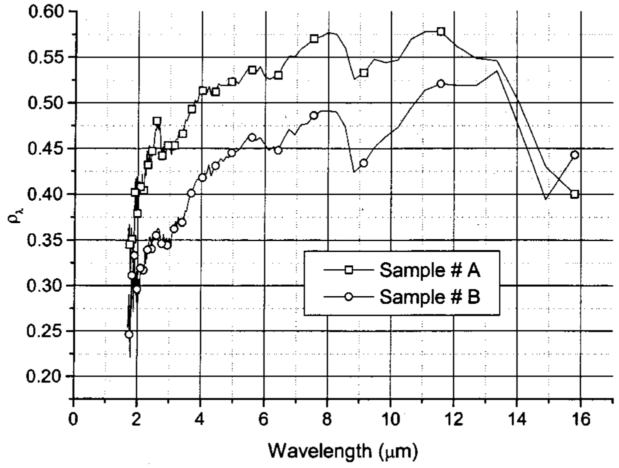

Fig. 2 Particle hemispherical reflectivity for Samples A and B (Lopes et al. [7])

$$\beta_c=\gamma\beta_u\tag{11}$$

The values of γ for $f_v<0.7$ can be obtained from the following polynomial expression (Singh and Kaviany [5]):

$$\gamma=1+1.84f_v-3.15f_v^2+7.2\,f_v^3\tag{12}$$

The particle spectral hemispherical reflectivity (ρ_λ) has been determined for the two samples studied by Lopes et al. [7] from an identification method (Gauss method of linearization) applied to bidirectional spectral reflectance data obtained from an experimental device using a Fourier transform infrared spectrometer. The ρ_λ values obtained for the two samples are shown in Fig. 2

Results-Influence of Parameters

Different cases carried out for the two different packed beds of oxidized bronze spherical particles are studied. All cases presented show numerical results, except case 1, which shows experimental results obtained by Lopes et al. [7]. The reference case (case 3) is the solution of the coupled conduction-radiation heat transfer model described before, the data are those of Table 1, the bed conductivity (k_b) is given by Eqs. (2 to 3), radiative properties are correlated (Eqs. 8 to 12), and the emittance is defined by Eq. (7). For other cases when not specified, the data are the same as those of reference case.

Case 1: experimental results
Case 2: isothermal medium
Case 3: reference case
Case 4: in the emittance calculation (Eq. 7), the blackbody emission is $I_{\lambda b}(T(\tau_0/2))$ instead of $I_{\lambda b}(T(0))$
Case 5: radiative coefficients are uncorrelated (Eqs. 8, 9, 10)
Case 6: porosity $\delta=\delta$ (Table 1) ±5 percent δ (Table 1)

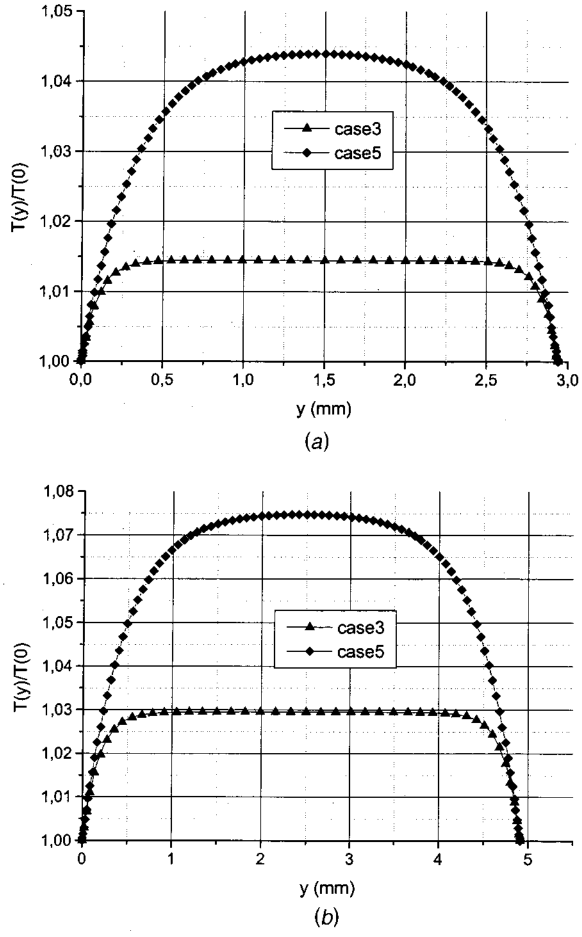

(*a*)

(*b*)

Fig. 3 (*a*) Sample A-temperature profile for cases 3 and 5; and (*b*) Sample B-temperature profile for cases 3 and 5.

Case 7: particle diameter $d=d$ (Table 1) ±5 percent d (Table 1)
Case 8: thickness of medium $L=L$ (Table 1) ±5 percent L (Table 1)
Case 9: particle hemispherical reflectivity $\rho_\lambda=\rho_\lambda$ (Fig. 2) ±5 percent ρ_λ (Fig. 2)
Case 10: bed thermal conductivity $k_b=k_b$ (Eq. 2) ±5 percent k_b (Eq. 2)
Case 11: $T(0)=T(0)$ (Table 1) ±5 percent $T(0)$ (Table 1), $T(\tau_0)=T(\tau_0)$ (Table 1) ±5 percent $T(\tau_0)$ (Table 1)
Case 12: incident laser power $P=625$ W±5 percent 625 W

Emittance obtained from different cases are compared especially for the wavelength, 3 μm, for which high intensity values are measured.

Temperature Gradient and Its Influence on Emittance Results. To study the influence of taking into account the coupled conduction-radiation heat transfer, the reference case 3 is compared to the isothermal case 2. In Fig. 3, normalized temperatures $(T/T(0))$ of case 3 are shown. The normalized temperature of isothermal case 2 being $T/T(0)=1$, the relative deviation between the temperatures normalized of case 3 and case 2 is less than 3 percent for Sample B and less than 1.5 percent for Sample A (Figs. 3(*a*, *b*)). The temperature gradient is more important for Sample B than for Sample A due to the fact that Sample B is thicker than Sample A, and Sample B extinction coefficient ($\beta=5968.8\ \mathrm{m}^{-1}$) is smaller than the Sample A extinction coefficient ($\beta=10765.4\ \mathrm{m}^{-1}$) (extinction coefficients being calculated from the radiative properties model (Eqs. 10, 11)).

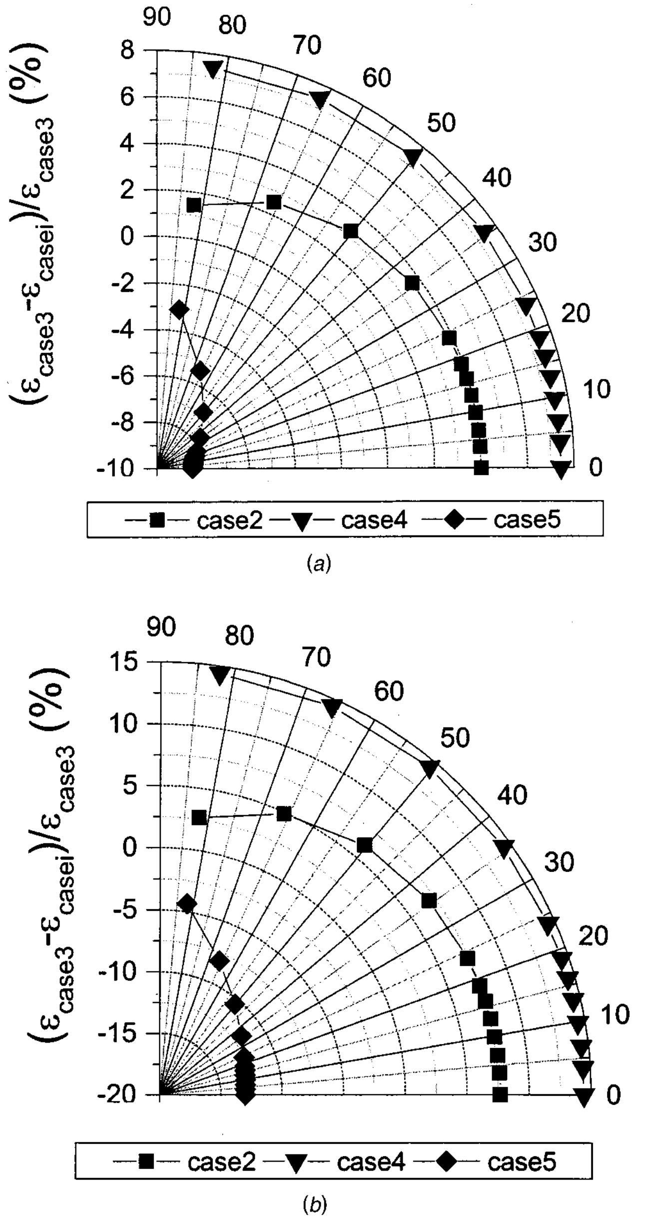

(*a*)

(*b*)

Fig. 4 (*a*) Sample A-relative deviation between the emittance of case 3 and one of cases $i=2,4,5$ for $\lambda=3\ \mu$m; and (*b*) Sample B-relative deviation between the emittance of case 3 and one of cases $i=2,4,5$ for $\lambda=3\ \mu$m.

For Sample B the relative deviation between emittance of the case 3 and that of the case 2 is less than 7.7 percent (Fig. 4(*b*)); for Sample A these relative deviations are smaller, they are less than 4 percent (Fig. 4(*a*)). As is expected, reference case 3 emittances are closest to experimental case 1 emittances for Sample B (Fig. 5(*b*)). For Sample A, the emittances of isothermal case 2 are closer to the experimental case 1 emittances (Fig. 5(*a*)). This fact can be explained by experimental uncertainties. Indeed they have been estimated to be on the order of 11 percent (Lopes et al. [7]) and deviations between experimental case 1 emittances and those obtained from case 2 or 3 remains less than this value.

The agreement between theoretical and experimental emittances confirms the validity of the value of the bed conductivity obtained from the simple parallel-series model. Larger values of bed conductivity could also be valid, in which case the temperature gradient would decrease and emittance results would be nearer to case 2 emittances. On the contrary for smaller values of

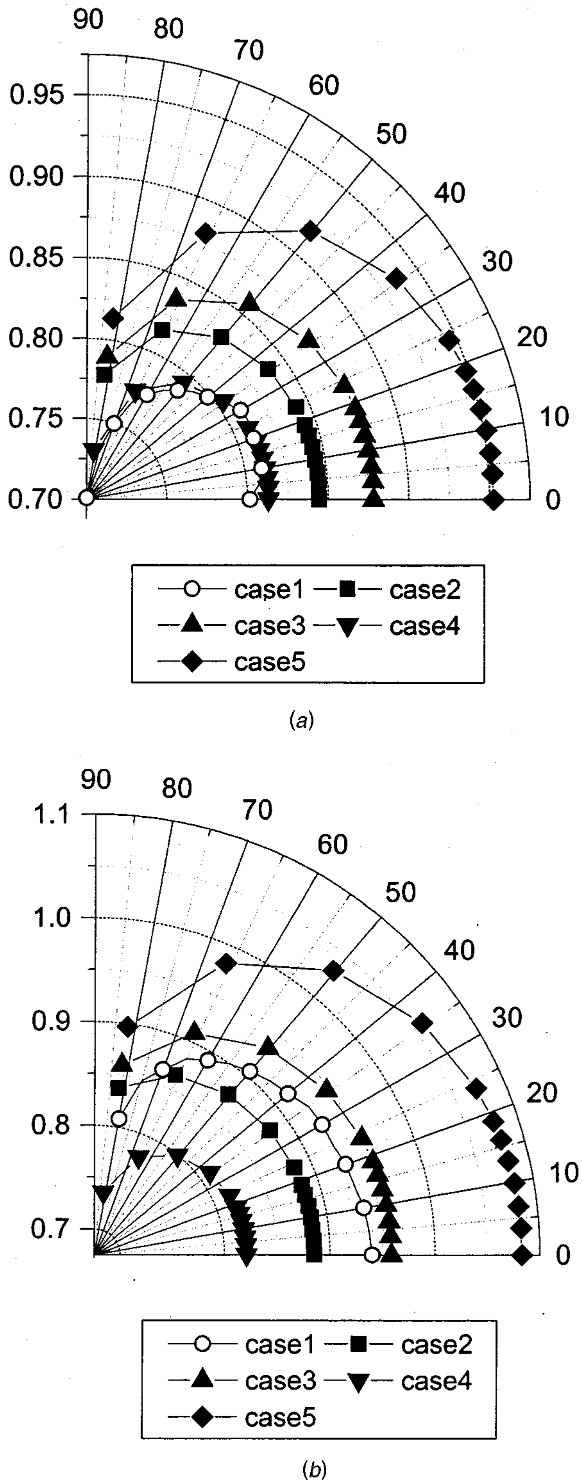

(*a*)

(*b*)

Fig. 5 (*a*) Sample A emittance polar distribution for $\lambda = 3\ \mu$m; and (*b*) Sample B emittance polar distribution for $\lambda = 3\ \mu$m.

bed conductivity the gradient temperature would increase and theoretical emittance would increase resulting in theoretical emittance further from experimental ones.

To better study the influence of the temperature gradient inside the medium, case 4 is considered, where the blackbody intensity is calculated with the temperature at spatial position $\tau_0/2$ instead of boundary temperature. The relative deviation between the emittance of reference case 3, and that of case 4 is 14.5 percent for Sample B (Fig. 4(*b*)). For Sample A the relative deviation is 7.5 percent (Fig. 4(*a*)). As a result, the weak temperature gradient has a significant influence on emittance calculation, especially for Sample B.

Comparison Between Results Obtained From Correlated and Uncorrelated Radiative Properties. When the radiative properties are uncorrelated (case 5), the extinction coefficient is 2.6 times smaller than in the case of correlated radiative properties (due to the gamma factor, $\gamma = 2.6$). As a result, the temperature inside the medium and therefore emittance are higher for case 5 than for case 3. The maximum relative deviation between the temperature of case 5 and the isothermal case 2 ($T/T(0) = 1$) is 7.5 percent for Sample B and 4.5 percent for Sample A (Figs. 3(*a*, *b*)). It can be noted that radiative properties, when uncorrelated, have a significant influence on the temperature gradient in the medium.

A maximum deviation on emittance of 13 percent is observed between cases 3 and 5 in the direction $\theta = 0$deg for Sample B, and 8.5 percent for Sample A (Figs. 4(*a*, *b*)). Moreover, it can be observed that emittances for case 5 are very far from the experimental ones (Fig. 5). Therefore, the use of the Singh and Kaviany correlation seems to be appropriate and necessary.

Sensitivity of Emittance and Medium Temperature to Temperature Boundary Conditions and Thermophysical Properties. The computed temperatures and intensities are functions of the temperature boundary conditions and of the thermophysical properties.

The sensitivities of temperature to each parameter are functions of the spatial position. The relative variation of normalized temperature $\Delta T'/T'$ are calculated for parameter variation $\Delta x_i/x_i = \pm 5$ percent (cases 6 . . . 12). A same value of parameter variation is used for each parameter in order to compare parameter sensitivities. The value of ±5 percent represents the maximum parameter uncertainty. The sensitivities of medium temperature to hemispherical reflectivity and sample thickness are smallest, and they are greatest for the porosity and boundaries temperature (Figs. 6, 7). Sensitivities are less than 0.35 percent for Sample B and less than 0.14 percent for Sample A. As a result, uncertainties on data should not induce a significant variation on the temperature gradient.

The sensitivities of the emittance to each parameter are functions of wavelength and direction. Figures 8, 9 show the sensitivities of emittance ($\Delta\varepsilon_\lambda/\varepsilon_\lambda$) as a function of the angle θ and for $\lambda = 3\ \mu$m. Except for the reflectivity sensitivity that is maximum for the direction $\theta = 82$deg, other parameter sensitivities are maximum for the normal direction to the sample, $\theta = 0$deg. It can be observed that sensitivity to sample thickness is nearly zero, this is due to the fact that sample thickness is sufficiently large. The sensitivities are the largest for the following parameters: porosity (δ), boundary temperatures ($T(0), T(\tau_0)$) and hemispherical reflectivity (ρ_λ). For Sample A, the hemispherical reflectivities sensitivity is larger than the porosity and the faces temperatures sensitivities, while for Sample B, these sensitivities are on the same order. This is due to the fact that the extinction coefficient β is higher for the Sample A resulting in a smaller sensitivity to the boundary temperatures and porosity. The emittance sensitivities remains weak; they are less than 1.8 percent. Hence uncertainties on data do not induce significant variation on the emittance calculation; emittances remain very near to those of case 3.

Conclusions

An experimental setup for measuring the directional spectral emittance has been recently developed. The isothermal condition in the medium has traditionally been assumed. In this paper, the coupled conduction-radiation equations are considered in order to investigate the effect of temperature non-uniformity on the calculated value of the emittance and to analyze the sensitivities of temperature gradient and emittance to parameters.

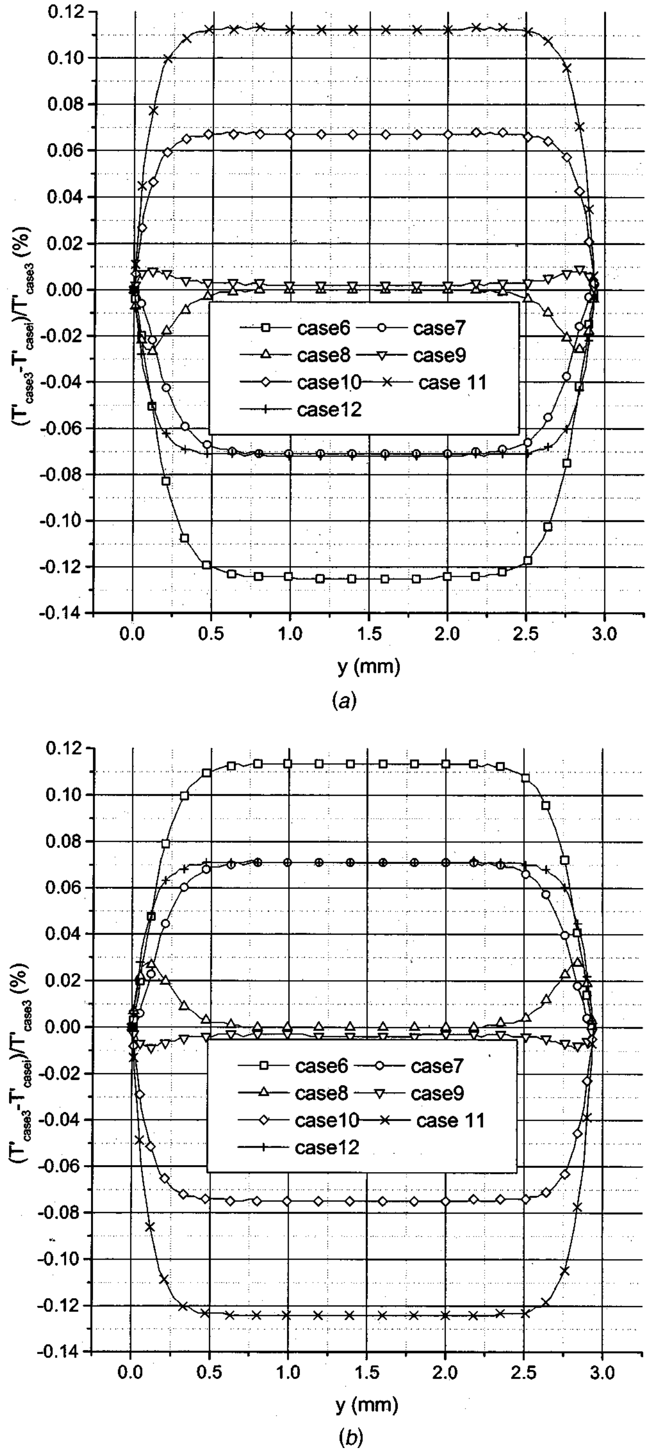

(*a*)

(*b*)

Fig. 6 Sample A-relative deviation between the normalized temperature profiles T' of case 3 and cases $i=6$ to 12: (*a*) $\Delta x_i/x_i=+5$ percent; and (*b*) $\Delta x_i/x_i=-5$ percent.

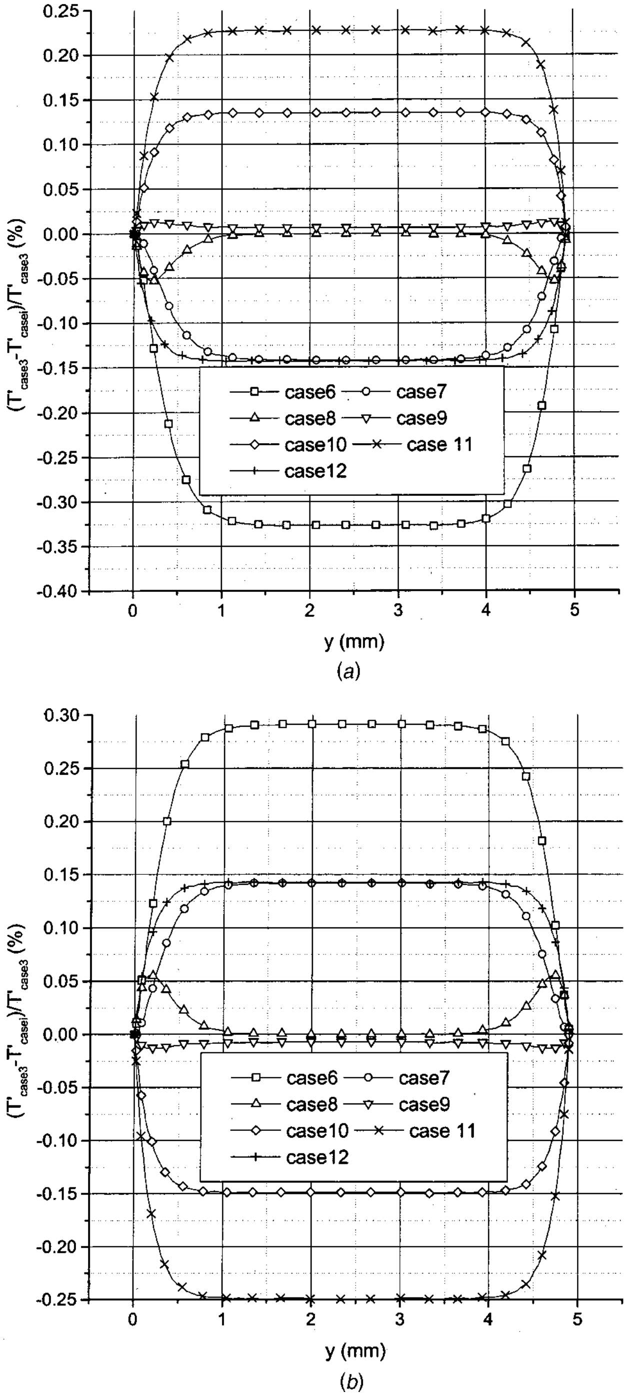

(*a*)

(*b*)

Fig. 7 Sample B-relative deviation between the normalized temperature profiles T' of case 3 and cases $i=6$ to 12: (*a*) $\Delta x_i/x_i=+5$ percent; and (*b*) $\Delta x_i/x_i=-5$ percent.

The largest temperature gradient is observed for case B, it remains less than 3 percent and induces a variation on emittance of 7.7 percent in the direction near 0 deg. Weak gradient temperatures are observed for samples considered in this study. The temperature gradient inside the medium is dependent on the thickness, on the bed conductivity and on the extinction coefficient of the sample. For samples with other radiative and conductive properties, the temperature gradient could be larger. Simulations are strongly recommended to verify the validity of experimental results based on the isothermal assumption.

Comparison between emittance results obtained from correlated and uncorrelated radiative properties confirms that the use of the Singh and Kaviany correlation is suitable and necessary. If radiative properties are not correlated, the deviation between theoretical and experimental emittance is significant.

The sensitivity of temperature gradient and emittance to variation in parameters such as porosity, particle dimension, sample thickness, particle hemispherical reflectivity, bed thermal conduc-

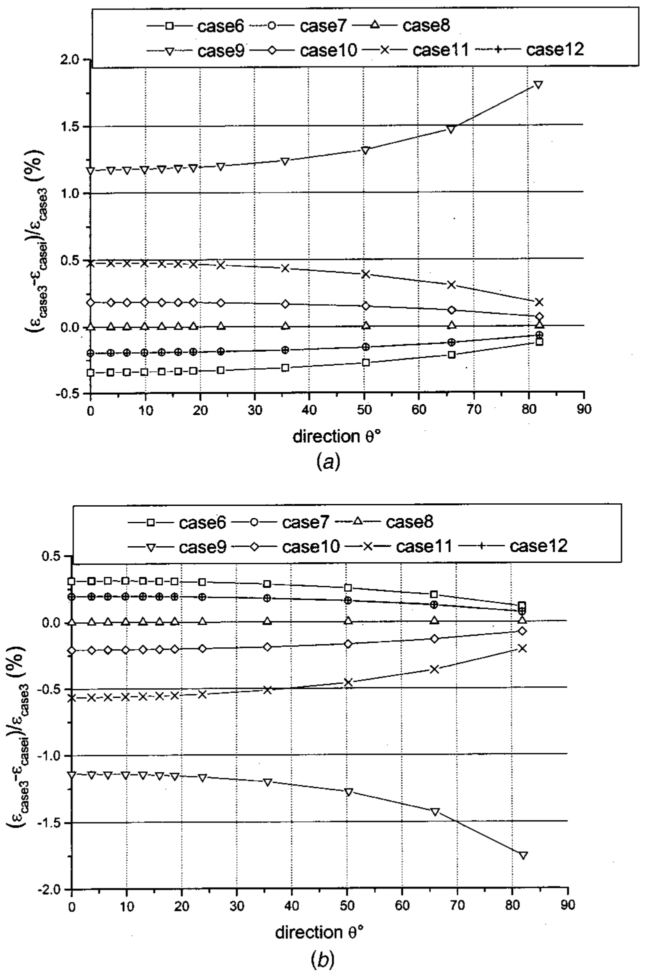

(a)

(b)

Fig. 8 Sample A-relative deviation between the emittance of case 3 and one of cases $i=6$ to 12 for $\lambda=3\ \mu$m: (*a*) $\Delta x_i/x_i=+5$ percent; and (*b*) $\Delta x_i/x_i=-5$ percent.

tivity, face temperature and laser power remain weak. Uncertainties of these parameters do not induce significant uncertainties on emittance calculation. The more sensitive parameters for emittance are the porosity, the surface temperatures and the hemispherical reflectivity. Overall, the identification of porosity and hemispherical reflectivity, or alternatively β and ω_λ, at different temperatures and different wavelengths from emittance measurements will be difficult due to the weak sensitivities.

Nomenclature

d = $2r$, particle diameter
F = quadratic difference
fv = volume fraction
I = intensity
$I_{\lambda b}$ = spectral blackbody intensity
k_b = bed thermal conductivity
L = thickness of a participating medium
N = number of directions in discrete ordinates method (DOM)
P = laser power received by the sample
p = phase function
R = reflectance
S = term source
T = absolute temperature
T' = normalized temperature ($T'=T/T(\tau=0)$)
U = uncertainties
x = $=2\pi r/\lambda$, size parameter

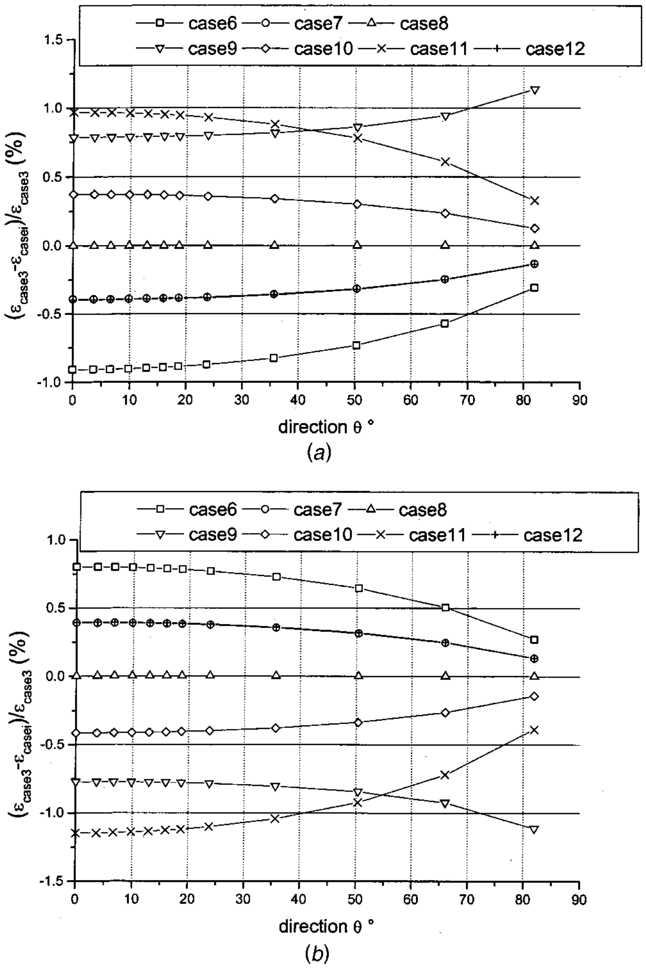

(a)

(b)

Fig. 9 Sample B-relative deviation between the emittance of case 3 and one of cases $i=6$ to 12 for $\lambda=3\ \mu$m: (*a*) $\Delta x_i/x_i=+5$ percent; and (*b*) $\Delta x_i/x_i=-5$ percent.

Greek Symbols

β = extinction coefficient
δ = porosity
θ = angle of direction of propagation as measured from the normal of the sample
ε = emittance
γ = scaling factor
μ = $\cos\theta$
ρ = particle hemispherical reflectivity
τ = optical coordinate
τ_0 = optical thickness of the sample
Ω = solid angle
ω = albedo

Subscripts

b = blackbody
c = correlated
e = experimental
t = theoretical
u = uncorrelated
λ = wavelength

Abbreviations

DOM = Discrete Ordinates Method
RTE = Radiative Transfer Equation

References

[1] Viskanta, R., and Mengüç, M. P., 1989, ''Radiative Transfer in Dispersed Media,'' ASME Appl. Mech. Rev., **42**(9), pp. 241–259.

[2] Baillis, D., and Sacadura, J. F., 2000, ''Thermal Radiation Properties of Dispersed Media: Theoretical Prediction and Experimental Characterization,'' J. Quant. Spectrosc. Radiat. Transf., **67**, pp. 327–363.

[3] Kaviany, M., 1995, *Principles of Heat Transfert in Porous Media*, 2nd ed., Springer-Verlag.

[4] Kamiuto, K., 1990, ''Correlated Radiative Transfer in Packed-Sphere Systems,'' J. Quant. Spectrosc. Radiat. Transf., **43**(1), pp. 39–43.

[5] Singh, B. P., and Kaviany, M., 1992, ''Modeling Radiative Heat Transfer in Packed Beds,'' Int. J. Heat Mass Transf. **35**(6), pp. 1397–1405.

[6] Jones, P. D., McLeod, D. G., and Dorai-Raj, D. E., 1996, ''Correlation of Measured and Computed Radiation Intensity Exiting a Packed Bed,'' J. Heat Transfer, **118**, pp. 94–102.

[7] Lopes, R., Moura, L. M., Baillis, D., and Sacadura, J. F., 2001, ''Directional Spectral Emittance of a Packed Bed: Correlation Between Theoretical Prediction and Experimental Data,'' J. Heat Transfer, **123**(2), pp. 205–416.

[8] Lopes, R., Moura, L. M., Delmas, A., and Sacadura, J.-F., 1998, ''Directional Spectral Emittance of Ceramic Material: Theoretical Prediction Compared to Experimental Data,'' 7th AIAA/ASME Joint Thermophysics and Heat Transfer Conference, Albuquerque, New Mexico.

[9] Doermann, D., 1995, ''Modélisation des transferts thermiques dans des matériaux semi-transparents de type mousse *à* pores ouverts et prédiction des propriétés radiatives,'' Ph.D. thesis, n° 95 ISAL. 0010, INSA de Lyon, France.

[10] Nicolau, V. P., 1994, ''Identification des propriétés radiatives des matériaux semi-transparents diffusants,'' Ph.D. thesis, n° 94 ISAL. 0001, INSA de Lyon, France.

[11] Brewster, M. Q., 1992, *Thermal Radiative Transfer and Properties*, John Wiley and Sons, New York, Inc., pp. 301–336.

R-22 and Zeotropic R-22/R-142b Mixture Condensation in Microfin, High-Fin, and Twisted Tape Insert Tubes

F. J. Smit
Ph.D. student
Rand Afrikaans University,
Johannesburg, South Africa

J. P. Meyer
e-mail: JPMeyer@postino.up.ac.za
Mem. ASME
Professor
University of Pretoria,
Department of Mechanical and
Aeronautical Engineering,
Pretoria, 0002, South Africa

Using mixtures of the zeotropic refrigerant mixture R-22/R-142b, a series of experiments was performed to determine the sectional and average heat transfer coefficients. Experiments were also conducted to compare three different heat transfer enhancement methods to that of smooth tubes. They were microfins, twisted tapes, and high fins. Measurements at different mass fluxes were obtained at six refrigerant mass fractions from 100 percent R-22 up to a 50 percent/50 percent mixture of R-22/R-142b. All condensation measurements were conducted at an isobaric inlet pressure of 2.43 MPa. This pressure corresponds to a saturation temperature of 60°C for R-22. The measurements were taken in 9.53 mm outer diameter smooth tubes and microfin tubes with lengths of 1603 mm. The heat transfer coefficients were determined with the Log Mean Temperature Difference equations. It was found that microfins were more suitable as an enhancement method than twisted tubes or high fins. Also, that the heat transfer coefficients and pressure drops decrease as the mass fraction of R-142b increases. [DOI: 10.1115/1.1484394]

Keywords: *Condensation, Enhancement, Finned Surfaces, Refrigeration, Tubes*

Introduction

Microfin tubes perform outstanding in enhancing heat transfer and are widely used to save energy in the air-conditioning and refrigeration industries. For this reason, its heat transfer characteristics have been extensively studied over the past 20 years. Detailed literature reviews are presented by Bergles [1,2] and Thome [3]. According to Thome the heat transfer enhancement of microfin tubes (relevant to condensation), can be explained by:

1. the increase in wetted surface area per unit length which usually ranges from 1.4 to 1.9, depending on the number of fins, their height and shape, and the helix angle;
2. an increase in liquid phase convective heat transfer due to the fins;
3. the increase in wetting around the circumference of the tube at low mass fluxes due to capillary forces, which maintain the flow in the completely wetted wall regime rather than the partly dry wall regime of stratified flow;
4. an effect of swirl on mist flow at low qualities that increases turbulence and forces entrained liquid droplets to the wall.

In spite of the number of published studies, there is a huge demand for further experimental research in order to test new microfin tubes and refrigerants. Manufacturers of air-conditioning and refrigeration equipment that use microfin tubes in their products usually offer different refrigerants depending on where the manufacturer and customer are located. Manufacturers in Europe tend to offer R-134a for air-conditioning and natural refrigerants such as ammonia and propane for refrigeration and process cooling. Japanese manufacturers offer R-134a, R-404A, and R-407C. In Thailand and China they offer R-22 ($CHClF_2$) units. Manufacturers in the USA offer many refrigerants, and although many options are available, R-22 remains extremely popular.

In nonindustrialized countries where air-conditioning, heat pump and refrigeration equipment is being developed, that is not usually manufactured in industrialized countries, HCFCs are still being used for new equipment under development such as hot-water heat pump heaters. Especially R-22 is very popular and it seems at this stage as if it will be used up to the year 2040, if allowed by legislation and if the cost stays reasonable.

The refrigerant R-22 in hot-water heat pumps is especially used in countries with a mild climate in winter, that have no natural gas and where electrical heating is usually used for the heating of water. Heating of water with heat pumps is very energy-efficient. Savings of approximately 67 percent can be realised, compared to heating with direct electrical resistance heaters [4,5]. Hot-water heat pumps are vapor compression cycles, which use water-cooled condensers for the heating of hot water. The most widely used refrigerant for hot-water heat pumps is R-22 with which a maximum hot-water temperature of 60°C to 65°C is possible with approximately the same condensing temperatures. This is possible by making use of the refrigerant's superheat, which is approximately at a temperature of 120°C at the compressor outlet. The maximum condensation temperature is limited by the maximum condensing pressure to control the amount of wear in the compressor bearings, the load on the bearings, and to keep the lubrication oil from decomposing at higher compressor discharge temperatures.

Although hot-water temperatures of 60°C to 65°C are adequate for domestic use, they are low when compared to temperatures that can be produced by fossil fuel and direct electric resistance systems. This limits the potential applications of hot-water heat pumps. Smit and Meyer [6] as well as Johannsen [7] showed analytically that a zeotropic mixture of R-22 and R-142b ($CClF_2CH_3$) could be used to obtain higher temperatures. A hot-water outlet temperature of 120°C is possible if only R-142b is used. The disadvantage of using only R-142b is that its heating capacity is 15% lower and its heating COP (coefficient of performance) is 7% lower when compared to R-22. Furthermore, it is flammable, but the flammability is decreased by adding R-22. A mixture of 60% R-22 with 40% R-142b to 80% R-22 with 20% R-142b by mass, is usually recommended. With these mixtures the heating capacities are about the same as when just R-22 is used, but the COP is increased while hot-water temperatures of

---

Contributed by the Heat Transfer Division for publication in the JOURNAL OF HEAT TRANSFER. Manuscript received by the Heat Transfer Division August 21, 2000; revision received April 5, 2002. Associate Editor: T. Y. Chu.

80°C (80%/20% R-22/R-142b) to 90°C (60%/40% R-22/R-142b) can be achieved. Mixtures of R-22 with R-142b form zeotropic mixtures with glides of 7°C and 5°C for 60% and 80% R-22 respectively.

Literature searches by Smit [8], Kebonte [9] and Bukasa [10] showed that apparently no detailed literature on heat transfer coefficients for microfin tubes at the recommended mass fractions of R-22 with R-142b at a dew point temperature of 60°C or more has been published. In addition, it seems as if no detailed data on condensation exist for the mixture of R-22/R-142b. Meyer et al. [11] published on average condensation coefficients at this high condensing temperature but in the annulus of coiled tube-in-tube heat exchangers. Shizuya et al. [12] published on sectional heat transfer coefficients for smooth tubes, but only for a mass fraction ratio of 50/50.

The first objective of this work was to determine the sectional and average heat transfer coefficients of the zeotropic mixture R-22 with R-142b for microfin tubes at the following mass fractions: 90%/10%, 80%/20%, 70%/30%, 60%/40% and 50%/50%. The heat transfer coefficients were to be determined at an inlet pressure of 2.43 MPa. At this pressure the dew point temperature for condensation will vary between 60°C (100% R-22) and 85.6°C (50% R-22). During these measurements, the average pressure drops were also to be determined. The second objective was to compare three different heat transfer enhancement methods, namely: microfins, twisted tapes and high fins to that of smooth tubes.

Test Facility

A test facility was specifically constructed to measure in-tube condensation of pure refrigerants and refrigerant mixtures. The characteristics of R-22 and the R-22/R-142b mixtures considered, as calculated from the REFPROP [13] database, are given in Table 1. The overall test facility is shown in Fig. 1. It was a vapor compression refrigeration and/or heat pump system. The compressor was a hermetically sealed, reciprocating type with a nominal cooling capacity of 10 kW. An oil separator was connected parallel to the compressor with a bypass line. By manually controlling the flow through the bypass line and through the oil separator the oil mass fraction in the refrigerant could be controlled. Refrigerant liquid samples were taken downstream of the after-condenser and analyzed for oil mass fraction according to the ANSI/ASHRAE 41.4 [14] standard. For this study, full use was made of the oil separator and only results of oil mass fractions less than 0.1% were used.

The test condenser consisted of eight separate coaxial double tube condensers in series labeled *A*, *B*, *C*, up to *N*, where $N=8$, as shown in Fig. 1. The inner tube of each smooth tube test section was a hard-drawn refrigeration copper tube with an inner diameter of 8.11 mm and an outer diameter of 9.53 mm (3/8 inch). The microfin tube test sections had the same outside diameter but the inner diameter was 8.92 mm. It also had 60 helically ribbed microfins at a helix angle of 18 deg with an area ratio of 1.59 (fin area divided by inner diameter area without fins). The fins had a triangular profile with a rounded tip. The fin height was 0.203 mm and the included angle of the fins was 51 deg. A profile of the microfin tube is shown schematically in Fig. 2. The twisted tape test section consisted of a 9.53 mm outer diameter smooth tube with a 0.3 mm thick plate helically twisted to a twist ratio of 3. The twist ratio is the axial pitch for a 180° turn of the tape divided by the tube diameter. The width of the twisted tape was 7.9 mm. The high fin (or internally finned) test section was a 9.52 mm outer diameter tube with 6 fins with a height of 0.6 mm, thickness of 0.2 mm, area ratio of 1.26 and a spiral angle of 18 deg. The cross sectional shape of the fins was rectangular. The inner tube diameter measured at the roots of the fins was 8.87 mm. The profile of the high fin is shown schematically in Fig. 3.

Spacers were used halfway in each test section to keep the inner tubes from bending. The heat transfer length of each section was 1603 mm and the distance between pressure drop measuring points 1900 mm. The outer tube for all the test sections was also a hard-drawn copper tube with an inner diameter of 17.27 mm and an outer diameter of 19.05 mm (3/4 inch). The thermal conductivity of all tubes was 339 W/m°C. Sight-glasses were installed between all the test sections to observe the refrigerant quality visually. All test sections were well insulated with 13 mm of armoflex inside a 50 mm glass wool box to prevent heat leakage effectively. A bypass line was connected parallel to the test condenser to control the refrigerant mass flow through the test sections. A water-cooled after-condenser was used to ensure that only liquid refrigerant enters a coriolis mass flowmeter with an error of ±0.1%. The sight-glasses before and after the coriolis flowmeter were to ensure that only liquid flow through it. A filter drier followed it, and also a hand-controlled expansion valve for controlling the evaporating temperature. A water-heated evaporator was used as well as a suction accumulator on the low-pressure side to complete the refrigerant loop.

Two main water loops were used, one flowing through the condensing side and one flowing through the evaporating side. On the condensing side the water was kept constant at a temperature

Table 1 Thermodynamic properties at different mass fractions of the R-22/R142b mixture at a pressure of 2.43 MPa

Mass fraction R-22 [%]	100	90	80	70	60	50
T_f [°C]	60	63.23	66.64	70.53	74.64	79.10
T_g [°C]	60	65.72	71.07	76.13	80.97	85.64
Temperature glide [°C]	0	2.49	4.43	5.60	6.33	6.54
T_c [°C]	96.15	100.95	105.75	110.35	114.75	119.05
P_c [MPa]	4.990	5.0	4.988	4.954	4.899	4.822
ρ_f [kg/m^3]	1030	1013	995.6	977.7	959.5	940.8
ρ_g [kg/m^3]	111.6	110.8	110.7	111.0	111.8	112.9
μ_f [μPa.s]	107.6	107.2	106.5	105.5	104.2	102.6
μ_g [μPa.s]	14.97	14.94	14.88	14.81	14.73	14.65
h_{fg} [kJ/kg]	139.9	141.3	142.0	141.9	141.2	139.7
c_{pf} [kJ/kg.K]	1.539	1.548	1.561	1.578	1.598	1.624
c_{pg} [kJ/kg.K]	1.287	1.287	1.302	1.327	1.358	1.399
k_f [W/m.K]	0.06763	0.06641	0.06516	0.06389	0.06258	0.06125
k_g [W/m.K]	0.01636	0.01708	0.01767	0.01833	0.01904	0.01982
σ [N/m]	0.00351	0.00367	0.00377	0.00382	0.00380	0.00372

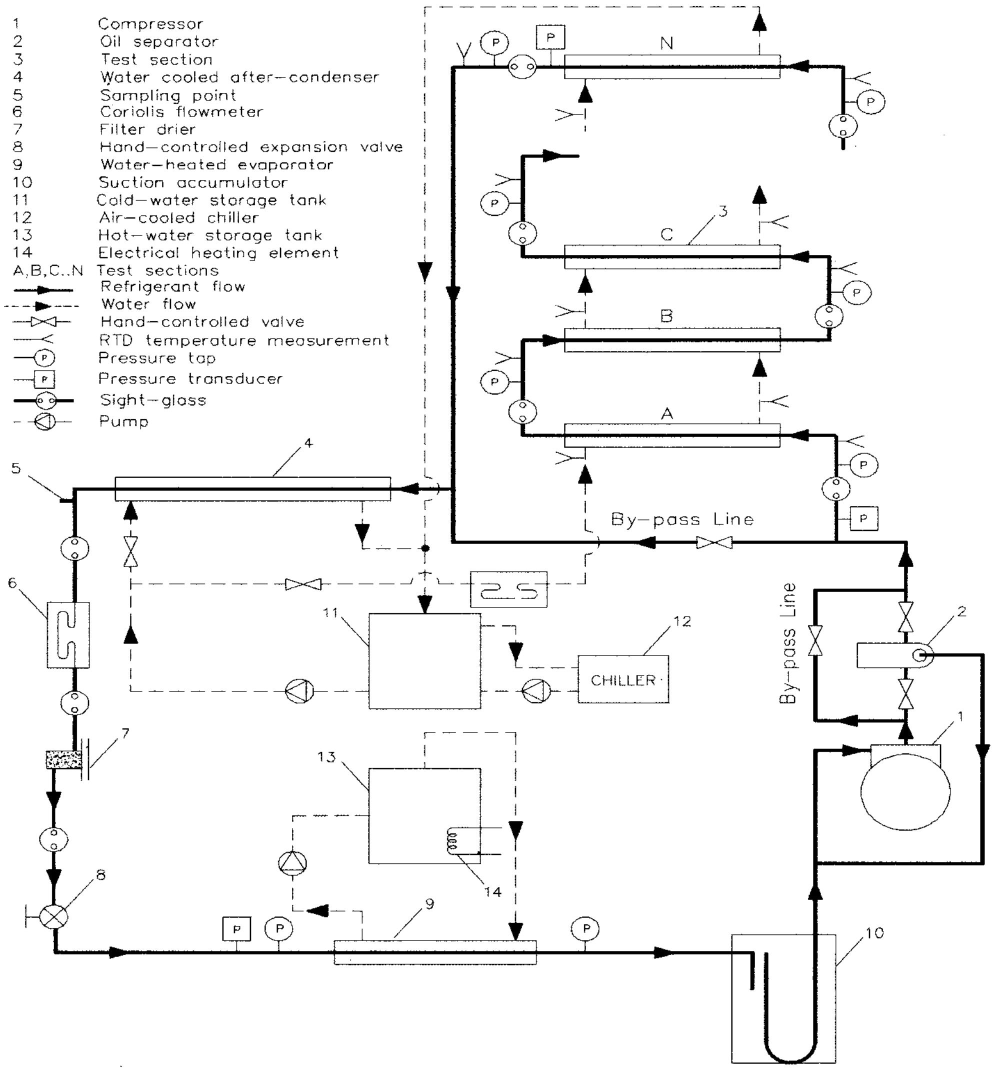

Fig. 1 Schematic of test facility

of 10°C to 85°C (depending on the experiments conducted) in a 1000-liter insulated storage tank connected to a 15 kW chiller. The water flow rate through the test sections could be controlled with a hand-controlled valve. The flow rate of the water through the test sections was measured with a coriolis mass flowmeter with an error of ±0.2%. The control of the water inlet temperature made it possible to have more control over the average refrigerant quality in a specific test section. The measuring could be done on more equally spaced quality values. For different refrigerants and mass fluxes, comparisons were possible at approximately the same quality values. A similar flow loop was used on the evaporating side, also with an insulated 1,000 liter storage tank but connected to a 20 kW electric resistance heater. This water was also kept constant at a temperature of 8°C to 30°C, depending on the experiments conducted. By increasing or decreasing the temperature of the water through the evaporator, the refrigerant density at the compressor inlet and thus refrigerant mass flow could also be changed. The water temperatures in both loops could be thermostatically controlled at a constant temperature with an error of ±1°C. As the storage capacities of the two tanks were rela-

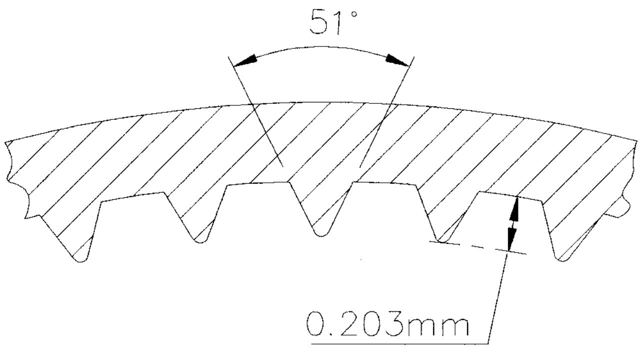

Fig. 2 Profile of the microfin tube (9.53 mm outer diameter)

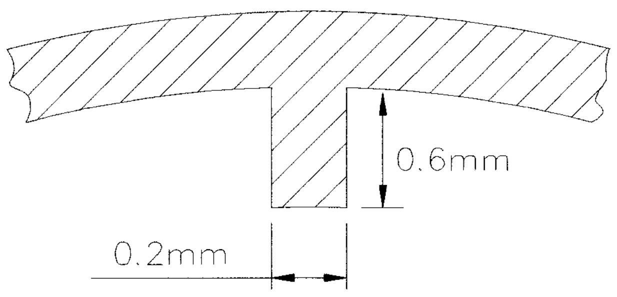

Fig. 3 Profile of the high fin tube (9.52 mm outer diameter)

tively large, the source and sink temperatures were very stable which helped in obtaining quick steady state conditions during experiments.

Temperatures were measured with resistance temperature devices (RTDs) mounted longitudinally on the outside of the tubes. The RTDs were strapped firmly in position with tape and were also insulated on the outside to prevent heat losses to the environment. The RTDs were calibrated to measure temperature differences with errors less than ±0.1°C. Temperatures were measured at the locations shown in Fig. 1. At each of these locations, three RTDs were located at the top, sides and bottom of the tube to take care of any circumferential temperature variation. The average temperature of the three values was used, with the side RTD weighted double, as the average temperature measurement. Absolute pressures on the high-pressure side were measured with a 160-mm dial pressure gauge with a range of 0 to 2500 kPa. The gauge was calibrated to an error of ±5 kPa. Pressure differences were measured with a differential pressure transducer with a range of 0 to 60 kPa, calibrated to an error of ±0.05% of full scale. For small pressure drops, another differential pressure transducer, connected parallel to the first, was used with a range of 0 to 10 kPa. It was also calibrated to an error of ±0.05% of the reading.

Data Reduction

Annulus Heat Transfer Coefficient. Before the test condenser was connected to the experimental set-up shown in Fig. 1, the annulus heat transfer coefficient of each section was determined individually in a water-to-water configuration. The annulus heat transfer coefficient was determined by using the modified Wilson plot technique [15]. For each test section at least 20 data points were used, all with an energy balance of less than ±2% (the average heat transfer between the inside heat transfer and outside heat transfer was used as the reference). Before the test condenser was connected into the experimental set-up it was dried with high flows of nitrogen and evacuated several times to a pressure of less than 6 Pa. Once connected and charged with R-22, it was operated for a period of 14 days during which time the refrigerant charge and filter drier were changed twice. This was to eliminate possible water moisture in the inner tube from the Wilson plot experiments before the experiments in this study were conducted.

Heat Transfer Coefficient. Assuming no fouling, the ''sectional'' heat transfer coefficient (which is the regionally average for each section) was obtained from:

$$h_i=\frac{1}{\left(\frac{1}{U_o}-\frac{A_o\ln(R_0/R_i)}{2\pi kL}-\frac{1}{h_o}\right)\frac{A_i}{A_o}} \tag{1}$$

The sectional heat transfer coefficients were integrated along the total length of the condenser using the trapezoid rule to obtain the integrated average heat transfer coefficient. The overall heat transfer coefficient was calculated from the sensible heat gain of the water and the logarithmic mean temperature difference as follows

$$\dot{Q}=U_oA_o\Delta T_{\mathrm{LMTD}} \tag{2}$$

where

$$\dot{Q}=\dot{M}_wc_{pw}(T_{\mathrm{out}}-T_{\mathrm{in}}) \tag{3}$$

The logarithmic temperature difference was calculated by

$$\Delta T_{\mathrm{LMTD}}=\frac{(T_{r,\mathrm{in}}-T_{w,\mathrm{out}})-(T_{r,\mathrm{out}}-T_{w,\mathrm{in}})}{\ln[(T_{r,\mathrm{in}}-T_{w,\mathrm{out}})/(T_{r,\mathrm{out}}-T_{w\mathrm{in}})]} \tag{4}$$

Refrigerant temperatures in Eq. 4 were from actual measurements and the first superheated section was ignored as well as consecutive sections if the refrigerant entered as superheated.

Quality. In the first test section, Q_w was equated to the refrigerant enthalpy change to obtain the outlet enthalpy (which is also the inlet enthalpy for the next test section) as it was assumed that no heat losses occured through the insulation, so that

$$h_{\mathrm{out}}=\frac{\dot{Q}_w}{\dot{M}_r}+h_{\mathrm{in}} \tag{5}$$

where h_{in} is the refrigerant inlet enthalpy for the first or second test-section obtained from a refrigerant database [19] using its inlet pressure and temperature as the inlet enthalpy was usually in the superheat region. Usually the outlet of the second test section was in the two-phase region. Then the outlet enthalpy of the second test section was used in Eq. 5 in the place of h_{in}. The inlet and outlet enthalpies of each test section as well as the enthalpies of saturated vapor and liquid were used to determine the inlet and outlet qualities. Hence, the sectional vapor quality is

$$x=\frac{h-h_f}{h_g-h_f} \tag{6}$$

The average between the inlet and outlet qualities of each test section was used to determine the average refrigerant quality of the test section. For the mixtures, REFPROP [19] was used to calculate the enthalpy change of the particular mixture along the dew point temperature curve in the above calculations.

Pressure Drop Experiments. To limit the scope of this study only the sectional pressure drops for 100% R-22 in smooth and enhanced tubes were measured. Only average pressure differences were measured for refrigerant mixtures from 90%/10% R-22/R-142b to 50%/50% R-22/R-142b.

Experimental Uncertainty. A propagation of error analysis [16] was performed to determine the uncertainty in the measured sectional heat transfer coefficients. Using this method, the uncertainty for the sectional heat transfer coefficients was found to range from a low of ±4% at the highest heat flux to a high of ±20% at the lowest heat flux. Uncertainties in the average heat transfer coefficients ranged from ±7% to ±13% over the mass flux range reported. To ensure low experimental uncertainties the mass flow rates of the water in the annulus were adjusted to ensure that the relative values of the heat transfer coefficients determined from the Wilson plot method do not influence the heat transfer coefficients in the inner tube negatively.

Experimental Results

Verification of the Experimental Procedure and R-22 Results. The heat transfer coefficients and pressure drops were verified to be accurate by first taking measurements with R-22 in both smooth and microfin tubes and comparing the results with literature, as shown in Figs. 4–7. The measurements were taken at saturation temperatures of 40°C or 50°C, whichever was the highest from measurements published in literature and which were thoroughly tested against the results of other studies. In Fig. 4 the measured sectional heat transfer coefficients were compared to those of Eckels and Tesene [17] at a mass flux of 400 kg/m^{2}s and a saturation temperature of 50°C. The measurements of Eckels and Tesene were also for a smooth tube with an inner diameter of 8.11 mm and the same microfin size and configuration were used as in this study. For smooth tubes, the sectional heat transfer coefficients of the present study underpredicted the sectional heat transfer coefficients by approximately 9% on average, with a maximum error of approximately 36% at a quality of approximately 83%, when compared to those of Eckels and Tesene. For microfin tubes, the comparison was better than for smooth tubes. The sectional heat transfer coefficients of the present study also underpredicted the sectional heat transfer coefficients by approxi-

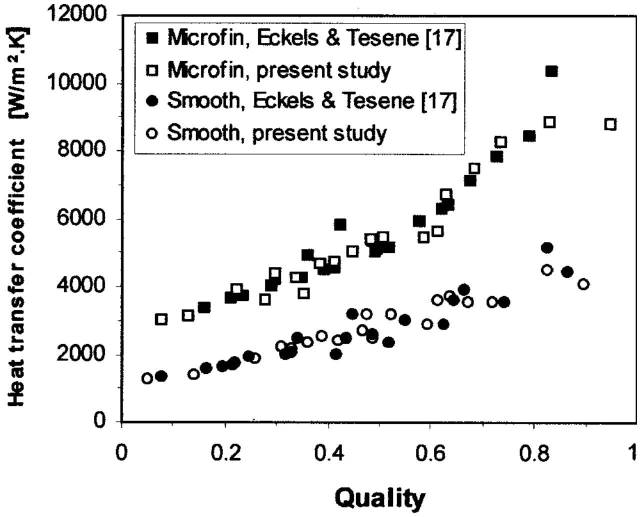

Fig. 4 Comparison between literature and measured heat transfer coefficients of R-22 condensing in smooth and microfin tubes at a mass flux of 400 kg/m^2.s and a saturation temperature of 50°C

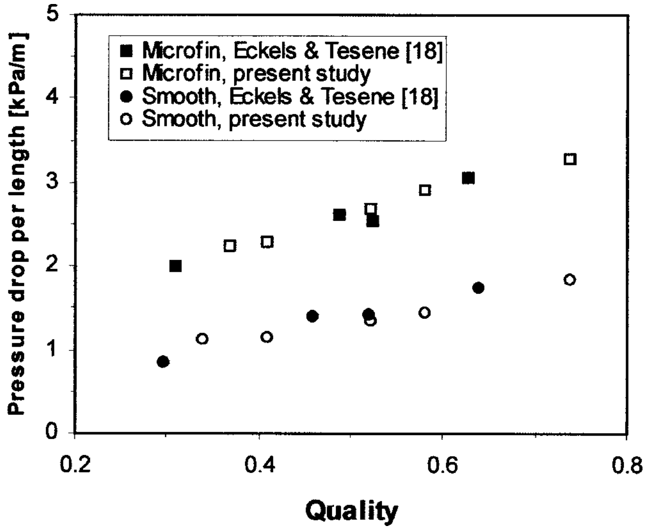

Fig. 6 Comparison between literature and measured pressure gradients of R-22 condensing in smooth and microfin tubes at a mass flux of 250 kg/m^2.s and a saturation temperature of 50°C

mately 4% on average, with a maximum error of approximately 18% at a quality of 83%, when compared to those of Eckels and Tesene.

Figure 5 shows the average heat transfer coefficient for R-22 at a saturation temperature of 40°C. Results were obtained over a mass flux range of 89 kg/m^2.s to 645 kg/m^2.s for smooth tubes and from 100 kg/m^2.s to 650 kg/m^2.s for microfin tubes. The inlet qualities were 85% to 90% and the average exiting quality was 10% (also, for most of the other experiments in the following section when heat transfer enhancement and refrigerant mass fractions were considered). Also shown on the plot are results obtained by Eckels and Tesene [17], with similar test tubes, also at a saturation temperature of 40°C. For smooth tubes, the present study overpredicted the average heat transfer coefficients by approximately 6% on average, with a maximum error of 18% at a mass flux of 89 kg/m^2.s. For microfin tubes, the agreement is better than for smooth tubes. The heat transfer coefficients are overpredicted by approximately 2% on average and the maximum error is 3% at a mass flux of approximately 100 kg/m^2.s

The pressure drop per unit length at a saturation temperature of 50°C for smooth and microfin tubes is shown in Fig. 6. The pressure drop per unit length is calculated by dividing the total pressure drop by the length between pressure taps. The active heat transfer length in each of the test sections is 1,604 mm, while pressure tap to pressure tap length is 1,900 mm. The pressure gradients were measured between an inlet quality of approximately 75% and an outlet quality of approximately 30%. All the results of the present study are within 10% of the measurements of Eckels and Tesene [18].

The pressure drops during condensation at a saturation temperature of 40°C for the smooth and microfin tubes compared to measurements of Eckels and Tesene [18] are given in Fig. 7. The pressure drops were measured with an approximate inlet quality of 90% and an outlet quality of 10% (also, for most of the other experiments in the following section when heat transfer enhance-

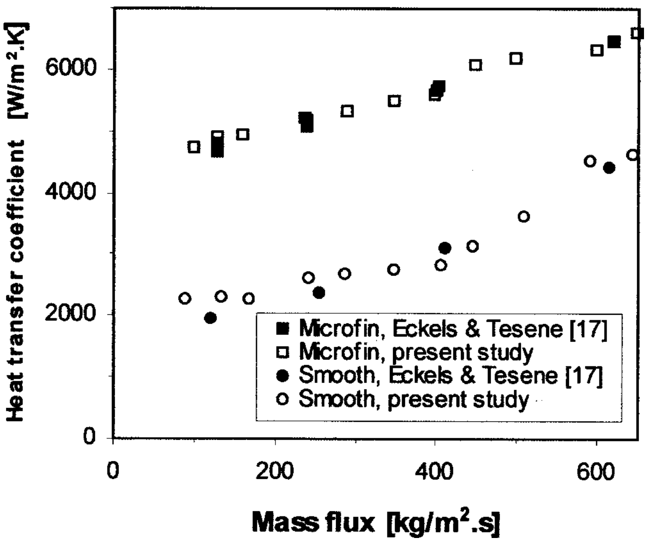

Fig. 5 Comparison between literature and measured average heat transfer coefficients of R-22 as function of mass flux in smooth and microfin tubes at a saturation temperature of 40°C

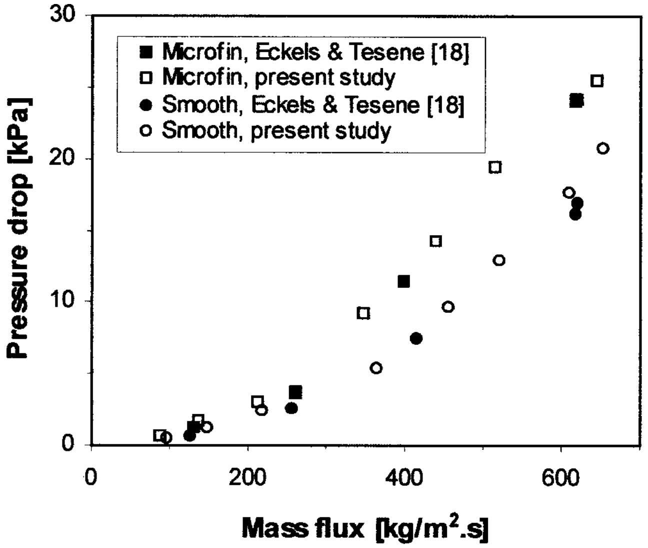

Fig. 7 Comparison between literature and measured pressure drops of R-22 as function of mass flux in smooth and microfin tubes at a saturation temperature of 40°C

ment and refrigerant mass fractions are considered) over a mass flux range of 88 kg/m^2.s to 654 kg/m^2.s. For both tubes, it was estimated that the results of the present study are all within 10% of the measurements of Eckels and Tesene.

Enhancement Methods. Measurements were conducted for a wide range of mass fractions, ranging from 100% R-22 to a 50%/50% mixture (on a mass basis) of R-22 with R142b. The results shown in Fig. 8 and 9 are for a mass fraction of 70%/30% as it was very representative of all the mass fractions considered. Measurements were conducted between mass fluxes of 135 kg/m^2.s to 774 kg/m^2.s. An inlet pressure of 2.43 MPa was used for all experiments. At this pressure the dew point temperature was 76.13°C and the bubble point temperature was 70.53°C.

From Fig. 8 follows that the average heat transfer coefficient increases with the use of twisted tapes, high fins and microfins compared to the heat transfer coefficient of a smooth tube. The heat transfer coefficients are increased by approximately 46%, 87% and 113% on average compared to those of smooth tubes, using respectively twisted tapes, high fins and microfins. However, at high mass fluxes of 500 kg/m^2.s and higher, the difference in heat transfer coefficients of high fins and microfins is not significant.

The pressure drops for the different types of enhancement methods are shown in Fig. 9. On average the pressure drops of microfin tubes are 38% higher than those of smooth tubes. High fin tubes increase the pressure drop by 81% in comparison to smooth tubes and twisted tapes increase the pressure drop by 148%. The microfin tube is therefore the best performer of the enhancement methods considered, if taking into consideration its huge increase in heat transfer coefficient and moderate increase in pressure drop. This result was expected and corresponds with lots of work on the advantages of microfin tubes as a heat transfer enhancement method as is also shown in a recent review article by Liebenberg et al. [19]. Therefore, only the results of the microfin tubes are given and discussed further on in this paper.

Mass Fraction of R-22/R-142b. In Figs. 10–12 the sectional heat transfer coefficients are given for smooth and microfin tubes. The coefficients are for different refrigerant mass fractions at mass fluxes of 100 kg/m^2.s (Fig. 10), 300 kg/m^2.s (Fig. 11), and 600

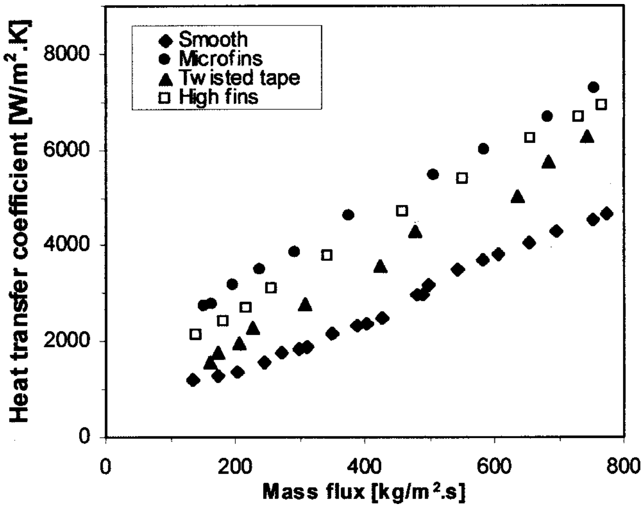

Fig. 8 Average heat transfer coefficients for R-22/R-142b (mass fraction of 70 percent/30 percent) during condensation at a dew point temperature of 76.13°C for different heat transfer enhancement methods and a smooth tube

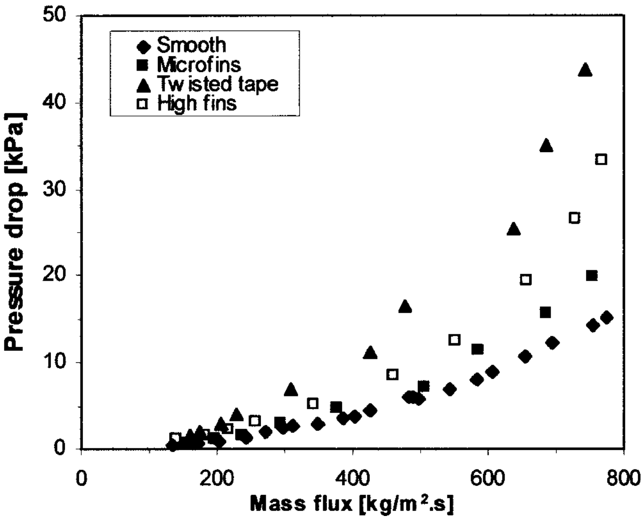

Fig. 9 Average pressure drop for R-22/R-142b (mass fraction of 70 percent/30 percent) during condensation at a dew point temperature of 76.13°C for different heat transfer enhancement methods and a smooth tube

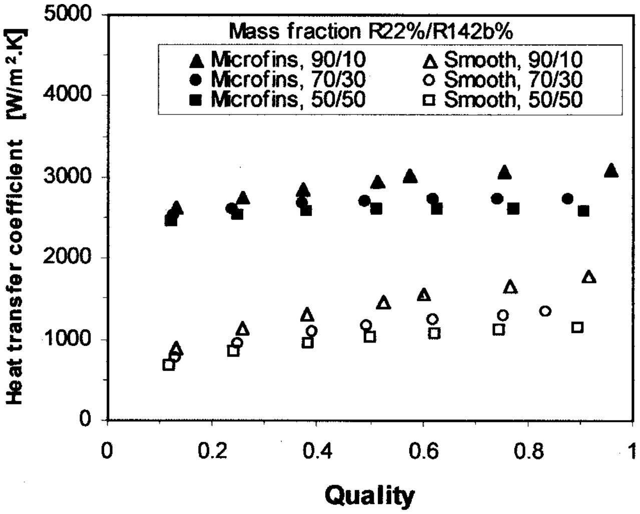

Fig. 10 Sectional heat transfer coefficients in smooth and microfin tubes at different mass fractions of R-22/R-142b at a mass flux of 100 kg/m^2.s

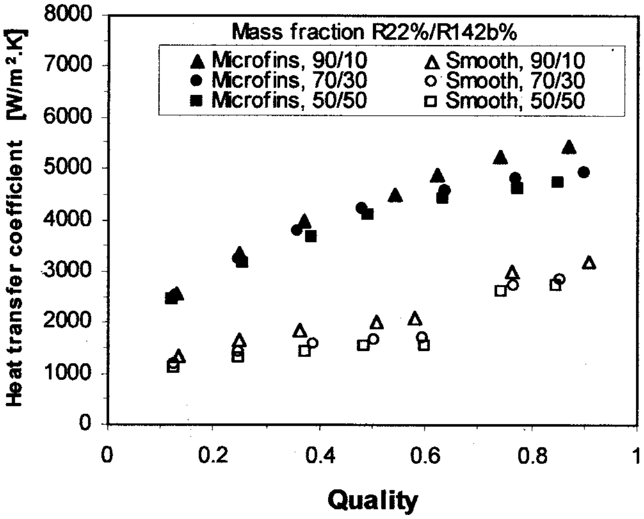

Fig. 11 Sectional heat transfer coefficients in smooth and microfin tubes at different mass fractions of R-22/R-142b at a mass flux of 300 kg/m^2.s

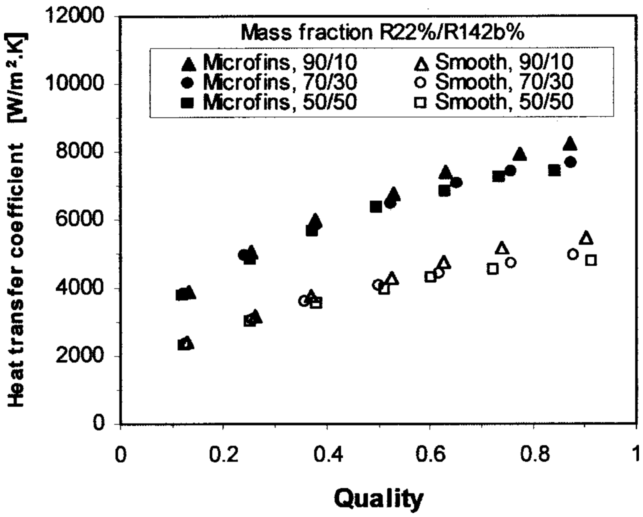

Fig. 12 Sectional heat transfer coefficients in smooth and microfin tubes at different mass fractions of R-22/R-142b at a mass flux of 600 kg/m^2.s

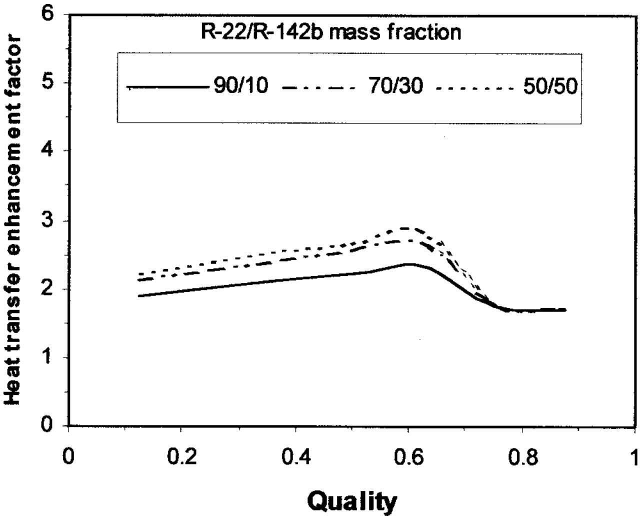

Fig. 14 Heat transfer enhancement factor at a mass flux of 300 kg/m^2.s for different refrigerant mass fractions

kg/m^2.s (Fig. 12). Only the results for mass fractions of 90%/10%, 70%/30%, and 50%/50% of R-22/R-142b are given. Measurements were also taken for mass fractions of 100%, 80%/20% and 60%/40% but are not given as the results in Figs. 10–12 are sufficient for discussion purposes. All the measurements were conducted at an inlet pressure of 2.43 MPa. Therefore the dew point temperatures were 65.72°C (90%/10%), 76.13°C (70%/30%) and 85.64°C (50%/50%). The corresponding temperature glides were 2.49°C, 5.60°C, and 6.54°C.

All the results show that the sectional heat transfer coefficients decrease as the mass fraction of R-142b increases. For smooth tubes the heat transfer coefficient decreases by approximately 30% on average as the R-22 mass fraction decreases from 90% to 50%. For microfin tubes the decrease is very similar at 27%. According to Cavallini et al. [20] this decrease is due to an increase in mass transfer thermal resistance. This resistance can be accounted for by the corrections of Silver [21], and Bell and Ghaly [22], which can be approximated to

$$h_m \approx [1/h + x c_{pg}(\Delta T / h_{fg} / h_g)]^{-1} \qquad (7)$$

where h_m is the corrected heat transfer coefficient for a zeotropic mixture, referred to the temperature difference in saturation which varies between the dew point and bubble point temperatures. h is the heat transfer coefficient of a pure fluid and h_g is the heat transfer coefficient of the vapor phase flowing alone in an internally enhanced tube calculated by a correlation given by Ravigururajan and Bergles [23]. The specific heat of the gas phase is c_{pg} and the temperature glide is ΔT, while the enthalpy change during isobaric condensation of the mixture is h_{fg}. The term on the right-hand side in the square brackets of Eq. 7, represents mass transfer thermal resistance. This term increases by 188% as the mass fraction of the R-22/R-142b mixture decreases from 90% to 50%, and is therefore the reason why the heat transfer coefficients decreased as the mass fraction of R-142b was increased.

It can also be deduced from the results in Figs. 10–12 that the sectional heat transfer coefficients increase as the mass flux increases. Also, that the heat transfer coefficients of the microfin tubes are higher than those of smooth tubes at the same mass fluxes as can be expected (and as also determined in the previous section).

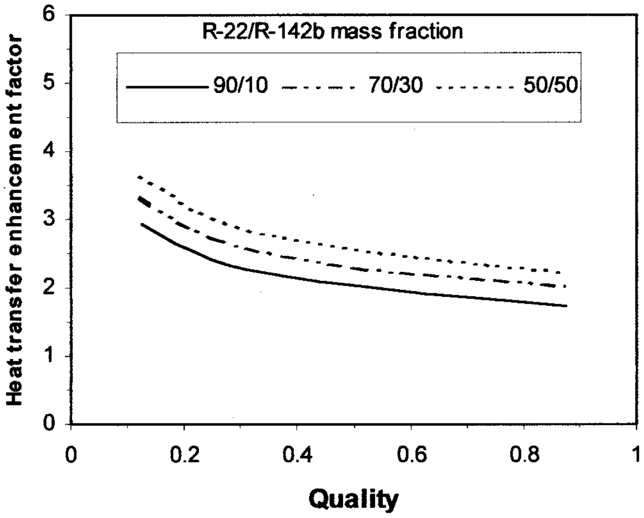

Fig. 13 Heat transfer enhancement factor at a mass flux of 100 kg/m^2.s for different refrigerant mass fractions

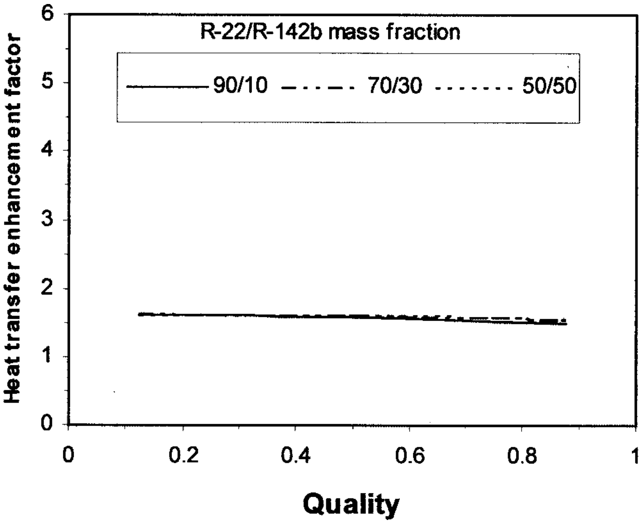

Fig. 15 Heat transfer enhancement factor at a mass flux of 600 kg/m^2.s for different refrigerant mass fractions

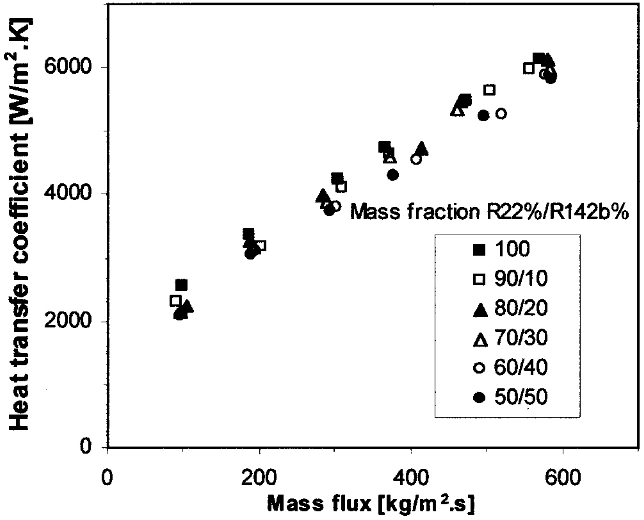

Fig. 16 Average heat transfer coefficients in the microfin tube as function of mass flux for different refrigerant mass fractions

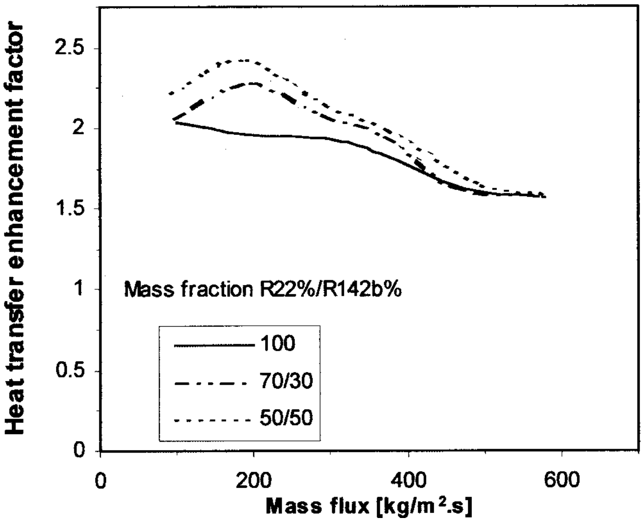

Fig. 18 Average heat transfer enhancement factor as function of mass flux for different refrigerant mass fractions

By fitting polynomials in the data in Figs. 10–12 and dividing the heat transfer coefficients of the microfin tubes by the heat transfer coefficients of the smooth tubes, the heat transfer enhancement factors were obtained at mass fluxes of 100 kg/m^2.s (Fig. 13), 300 kg/m^2.s (Fig. 14) and 600 kg/m^2.s (Fig. 15). The results are shown in Figs. 13–15 for three different mass fractions of R-22/R-142b.

At low mass fluxes of approximately 100 kg/m^2 (Fig. 13) all the heat transfer enhancement factors vary between 1.8 and 3.6. At a mass flux of 300 kg/m^2.s (Fig. 14) the heat transfer enhancement factors vary between 1.7 and 2.9, and at a mass flux of 600 kg/m^2.s (Fig. 15), they vary between 1.5 and 1.6. The highest heat transfer enhancement factors therefore occur at lower mass fluxes. The reason being that the microfin tube ensures that the flow regime stays annular for a longer period before it changes to a stratified/wavy flow regime. The microfins therefore prevent the liquid to accumulate at the bottom of the tube due to gravity for a longer period. As the mass flux increases, the flow regime will stay annular for even a longer period as can be deduced from Figs. 14 and 15. The reason is that the influence of gravity forces on the condensing liquid at the tube surface is negligible in comparison to the inertia forces. The advantage of microfins therefore decreases as the mass flux increases.

In Fig. 16 the average heat transfer coefficients in the microfin tube are given as function of mass flux for different refrigerant mass fractions. The heat transfer coefficients increase approximately linearly with mass flux. In general, the heat transfer coefficient of R-22 is the highest and decreases as the mass fraction of R-142b is increased. At mass fluxes of approximately 100 kg/m^2.s the heat transfer coefficient of the 50%/50% mixture of R-22/R-142b is approximately 20% lower than that of 100% R-22. At higher mass fluxes of 600 kg/m^2.s the differences decrease to only 5%.

The influence of refrigerant mass fraction on pressure drop for the microfin tube is much more significant than on the average heat transfer coefficient, as can be deduced from Fig. 17. The pressure drop increases almost quadratic with mass flux. This observation corresponds with that of Shao and Granryd [24] which suggests $\Delta p = \text{constant}.G^2$. The pressure drop for R-22 is the highest and decreases significantly as the mass fraction of R-142b

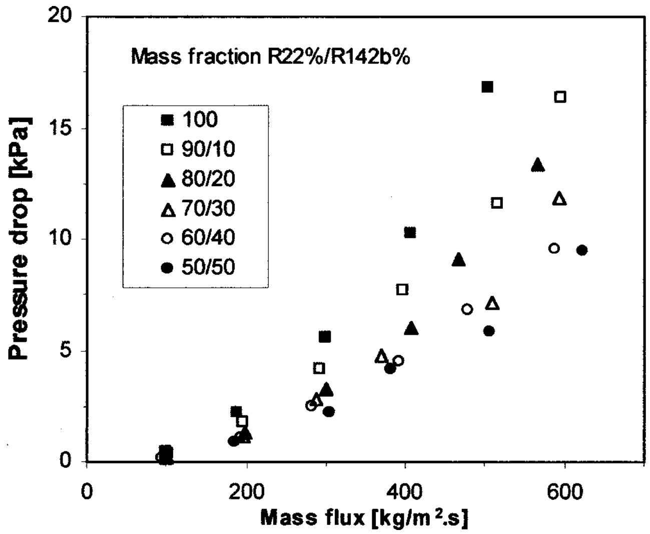

Fig. 17 Pressure drop in the microfin tube as function of mass flux for different refrigerant mass fractions

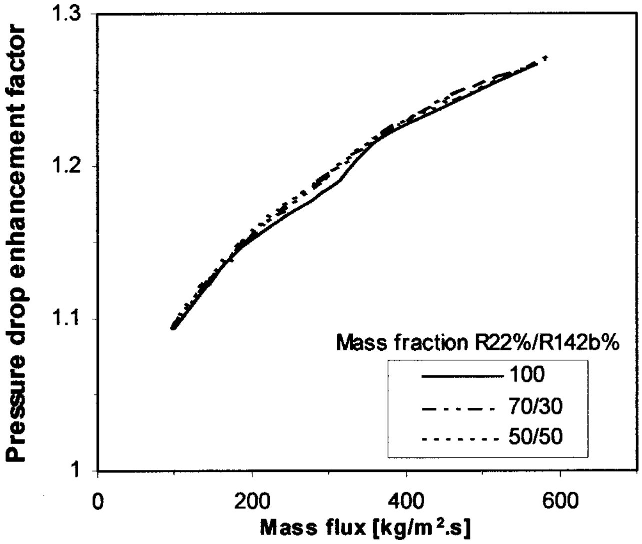

Fig. 19 Pressure drop enhancement factor as function of mass flux for different refrigerant mass fractions

is increased. On average, the pressure drop decreases with approximately 50% if the mass fraction of R-142b is increased to 50%.

The heat transfer enhancement factor in microfin tubes compared to that in smooth tubes is considered in Fig. 18 as function of mass flux. The maximum heat transfer enhancement occurs at low mass fluxes of 100 kg/m^2.s to 300 kg/m^2.s. For mass fluxes of 80 kg/m^2.s to 300 kg/m^2.s the heat transfer enhancement factors vary between approximately 2 and 2.5. At higher mass fluxes of more than 300 kg/m^2.s they decrease to approximately 1.5. In general, the heat transfer enhancement factor increases as the mass fraction of R-22 is decreased. According to Shao and Granryd [24], the non-ideal properties of mixtures are mainly responsible for heat transfer degradation which includes the diffusion resistance due to concentration difference, the local non-equilibrium state between the phases, enhanced also by the slip in the liquid-vapor interface, etc. Again, this effect is more dominant at lower mass fluxes than at higher mass fluxes.

The pressure drop enhancement factor (Fig. 19) increases with mass fluxes from approximately 1.1 at 100 kg/m^2.s to 1.27 at 600 kg/m^2.s. This increase is small in comparison to the large increase in mass flux. It is also shown that the pressure drop enhancement factor increases as the mass fraction of R-142b increases.

Conclusions

The performance of different refrigerant mixtures, varying in mass fraction from 100% R-22 with increases in steps of 10% of R-142b, up to a 50%/50% mixture of R-22/R-142b was determined for 9.53 mm microfin tubes. Average and sectional heat transfer coefficients were measured over a range of mass fluxes, qualities and dew point temperatures from 60°C to 85.64°C. For all these tests the inlet pressure was kept constant at 2.43 MPa. Measurements were also taken on three different heat transfer enhancement methods, namely microfins, twisted tubes, and high fins. The heat transfer enhancements were compared to those of a smooth tube.

When heat transfer enhancement methods were investigated, it was found that microfin tubes are more suitable for heat transfer enhancement of R-22/R-142b mixtures, than twisted tapes or high fins. The heat transfer coefficients were increased by approximately 46%, 87%, and 113% on average compared to those of smooth tubes, using respectively twisted tapes, high fins and microfins. However, at high mass fluxes of 500 kg/m^2.s and higher, the difference in heat transfer coefficients of high fins and microfins is not significant.

Comparing pressure drops showed that on average the pressure drops of microfin tubes were 38% higher than those of smooth tubes. High fin tubes increased the pressure drop by 81% in comparison to smooth tubes and twisted tapes that increased the pressure drop by 148%. The microfin tube was therefore the best performer of the enhancement methods considered, if taking into consideration its huge increase in heat transfer coefficient and moderate increase in pressure drop.

From the measurements on microfin tubes at different mass fractions of R-22/R-142b, it was found that:

1. the sectional heat transfer coefficients decrease as the mass fractions of R-142 are increased;
2. the highest heat transfer enhancements of microfin tubes compared to smooth tubes are at low mass fluxes and the benefit of microfins decreases as the mass flux increases;
3. the average heat transfer coefficients decrease as the mass fraction of R-142b is increased;
4. the average pressure drop is strongly influenced by the refrigerant mass fraction and that the pressure drop decreases as the mass fraction of R-142b is increased.

Acknowledgments

Support for this project was provided by the Rand Afrikaans University, NRF and Eskom.

Nomenclature

U = overall heat transfer coefficient

Subscripts

c = critical
exp = experimental
g = gas
i = inner or in-tube
in = inlet of test section
LMTD = logarithmic mean temperature difference
m = corrected
o = outer or annulus side
out = outlet of test section
r = refrigerant
w = water

References

[1] Bergles, A. E., 1999, "Enhanced Heat Transfer: Endless Frontier, or Mature and Routine?," Enhanced Heat Transfer, **6**, pp. 79–99.
[2] Bergles, A. E., Jensen, M. K., and Shome, B., 1996, "The Literature on Enhancement of Convective Heat and Mass Transfer," Enhanced Heat Transfer, **4**, pp. 1–6.
[3] Thome, J. R., 1996, "Boiling of New Refrigerants: A State-of-the-Art Review," Int. J. Refrig., **19**(7), pp. 435–457.
[4] Meyer, J. P., and Greyvenstein, G. P., 1991, "Hot Water for Homes in South Africa," Energy—The International Journal, **16**(7), pp. 1039–1044.
[5] Meyer, J. P., and Greyvenstein, G. P., 1992, "Hot Water for Large Residential Units, Hospitals and Laundries with Heat Pumps in South Africa: A Technoeconomic Analysis," Energy, Conversion, and Management, **33**, pp. 135–143.
[6] Smit, F. J., and Meyer, J. P., 1998, "Investigation of the Potential Effect of Zeotropic Refrigerant Mixture on Performance of a Hot-Water Heat Pump," ASHRAE Trans., **104**, (Part 1A), pp. 387–394.
[7] Johannsen, A. F. B., 1992, "Potential of Non-Azeotropic Refrigerant Mixtures for Water-Heating Heat Pumps in South Africa," Department of Mineral and Energy Affairs, Report no. ED 8807, Pretoria, South Africa.
[8] Smit, F. J., 1996, "The Influence of a Non-Azeotropic Refrigerant Mixture on the Performance of a Hot-Water Heat Pump," M. Eng. dissertation, Rand Afrikaans University, Johannesburg, South Africa.
[9] Kebonte, S. A., 1999, "Condensation Heat Transfer and Pressure Drop Coefficients of R22/R142b in a Water Cooled Helically Coiled Tube-in-Tube Heat Exchanger," M. Eng. dissertation, Rand Afrikaans University, Johannesburg, South Africa.
[10] Bukasa, J. M., 1999, "Average Boiling Heat Transfer and Pressure Drop Coefficients of R22/R142b in a Helically Coiled Water Heated Tube-in-Tube Heat Exchanger," M.Eng. dissertation, Rand Afrikaans University, Johannesburg, South Africa.
[11] Meyer, J. P., Bukasa, J. M., and Kebonte, S. A., 2000, "Average Boiling and Condensation Heat Transfer Coefficients of the Zeotropic Refrigerant Mixture R22/R142b in a Coaxial Tube-in-Tube Heat Exchanger," ASME J. Heat Transfer, **122**, pp. 186–188.
[12] Shizuyo, M., Itoh, M., and Hijrkata, K., 1995, "Condensation of Nonazeotropic Binary Refrigerant Mixtures Including R-22 as a More Volatile Component Inside a Horizontal Tube," ASME J. Heat Transfer, **117**, pp. 538–543.
[13] NIST, 1998, "NIST Thermodynamic and Transport Properties of Refrigerants and Refrigerant Mixtures Database," (REFPROP Ver. 6.01), National Institute of Standards and Technology, Gaithersburg, MD.
[14] ANSI/ASHRAE 1996, ASHRAE STANDARD 41.4, "Standard Method for Measurement of Proportion of Lubricant in Liquid Refrigerant," American Society of Heating, Refrigerating and Air-Conditioning Engineers, Atlanta, GA.
[15] Briggs, D., and Young, E., 1969, "Modified Wilson Plot Technique for Obtaining Heat Transfer Correlations for Shell and Tube Heat Exchangers," Chem. Eng. Prog., Symp. Ser., **65**(2), pp. 35–45.
[16] Kline, S., and McClintock, F., 1953, "Describing Uncertainties in Single-Sample Experiments," Mech. Eng. (Am. Soc. Mech. Eng.), **75**, pp. 3–8.
[17] Eckels, S. J., and Tesene, B. A., 1999, "A Comparison of R-22, R-134a, R-410a, and R-407c Condensation Performance in Smooth and Enhanced Tubes: Part I, Heat Transfer," ASHRAE Trans., **105**, Pt. 2
[18] Eckels, S. J., and Tesene, B. A., 1999, "A Comparison of R-22, R-134a, R-410a, and R-407c Condensation Performance in Smooth and Enhanced Tubes: Part II, Heat Transfer," ASHRAE Trans., **105**, Pt. 2.
[19] Liebenberg, L, Bergles, A. E., and Meyer, J. P., 2000, "A Review of Refrigerant Condensation in Horizontal Micro-fin Tubes," *Proceedings of the ASME Advanced Energy Systems Division, International Mechanical Engineering*

Congress and Exhibition, November 5–10, Orlando, Florida, AES-Vol. 40, pp. 155–168.

[20] Cavallini, A., Del Col, D., Doretti, L., Longo, G. A., and Rosetto, L., 2000, ‘‘Heat Transfer and Pressure Drop During Condensation of Refrigerants Inside Horizontal Enhanced Tubes,’’ Int. J. Refrig., **23**(4), pp. 4–25.

[21] Silver, L., 1947, ‘‘Gas Cooling with Aqueous Condensation,’’ Trans. Inst. Chem. Eng., **25**, pp. 30–42.

[22] Bell, K. J., and Ghaly, M. A., 1973, ‘‘An Approximate Generalized Design Method for Multicomponent/Partial Condenser,’’ AIChE Symp. Ser., **69**, pp. 72–79.

[23] Ravigururajan, T. S., and Bergles, A. E., 1985, ‘‘General Correlations for Pressure Drop and Heat Transfer for Single Phase Turbulent Flow in Internally Ribbed Tubes,’’ ASME HTD, **52**, pp. 9–20.

[24] Shao, D. W., and Granryd, E., 1998, ‘‘Experimental and Theoretical Study on Flow Condensation With Non-Azeotropic Refrigerant Mixtures of R32/R134a,’’ Int. J. Refrig., **12**(3), pp. 230–246.

Effectiveness Correlations for Heat and Moisture Transfer Processes in an Enthalpy Exchanger With Membrane Cores

L. Z. Zhang
e-mail: BeLzhang@polyu.edu.hk

J. L. Niu

Department of Building Services Engineering,
The Hong Kong Polytechnic University,
Kowloon, Hong Kong

The performance correlations for the effectiveness of heat and moisture transfer processes in an enthalpy exchanger with membrane cores are presented. The physical phenomena relevant to the heat and moisture transfer in these devices have been used to develop a novel set of correlations based on the relevant dimensionless parameters. The total enthalpy effectiveness can be calculated from sensible effectiveness, latent effectiveness, and the ratio of latent to sensible energy differences across the unit. Studies show that the sensible effectiveness is a function of NTU, the number of transfer units for heat; while the latent effectiveness is a function of NTU_L*, the number of transfer units for moisture. The relations between* NTU_L *and NTU are derived and studied with the proper separation of moisture resistance for membranes. This newly developed dimensionless parameter,* NTU_L*, is to summarize the sorption characteristics of membrane material, the exchanger configurations, as well as the operating conditions. A number of experimental results on an enthalpy exchanger with novel hydrophilic membrane cores has been used to valid these correlations.* [DOI: 10.1115/1.1469524]

Keywords: Dehumidification, Heat Transfer, Moisture, Membrane, Exchanger

1 Introduction

Mechanical ventilation with heat recovery is often considered as one of the key elements of a low energy residential building in various climates [1]. In the past, researches were only focused on the recovery of sensible heat [2–4] by neglecting the treatment of humidity for ventilation air. These systems usually employ traditional heat exchangers such as fixed plates, sensible heat exchange wheels, heat pipes, and coil run-around loop heat exchangers, of which the performance is easy to predict. However, in recent years, increasing attention has been paid to energy recovery, or enthalpy recovery, in which both the sensible and the latent heat are recovered. The latent load constitutes a large fraction of the total thermal load for an air-conditioned building, and thus it is more significant to recover the latent heat, as well as the sensible heat.

The present techniques for enthalpy recovery rely on the alternate sorption and regeneration of desiccant materials, either in the form of cycling packed beds or rotary wheels. San [5] investigated the heat and mass transfer in a set of two-dimensional cross-flow regenerative beds. The effects of operating conditions and outdoor climate conditions on the enthalpy effectiveness are numerically studied. Simonson and Besant [6] proposed a numerical model for the heat and moisture transfer in energy wheels during sorption, condensation, and frosting conditions, and the sensitivity of condensation and frosting to wheel speed and desiccant type are studied. Simonson and Besant [7,8] also investigated the performances of energy wheels both numerically and experimentally in detail. The fluctuations of sensible and latent effectiveness with various operating temperatures and humidities are discussed in their research.

These studies are very interesting and they are certainly helpful to improve the system efficiency. However, due to the low thermal conductivity of desiccants, the regeneration of desiccants is very slow and energy consuming, which may in return sacrifice the efficiency in energy recovery. Furthermore, cycling beds are bulky and the maintenance of rotating wheels is problematic.

Membrane-based enthalpy exchanger is another alternative for enthalpy recovery. This concept is just like an air-to-air sensible heat exchanger. But in place of traditional metal heat exchange plates, novel hydrophilic membranes are used, through which both heat and moisture are transferred simultaneously. Since the permeation of moisture through the membrane is in a continuous manner, no regeneration is required. Furthermore, it is very easy to construct and implement, therefore it is more promising. It should be noted that membranes have been used in air dehumidification for a long time, see Pan et al. [9]; Asaeda and Du, [10]; Wang et al. [11]; Cha, et al. [12]; to name but a few, and some energy recovery exchangers have been patented by a couple of companies. However, the theoretical studies of hydrophilic membrane-based enthalpy recovery exchangers are still scarce [13,14].

To optimize the membrane system, the effectiveness of enthalpy exchange under various conditions should be calculated. Due to the complex coupling between heat and moisture transfer, there is no simple design methodology available for the membrane-based enthalpy exchanger. Finite difference simulations, which have been used to study the sensitivity of performance to outside conditions [13,15], is time consuming and inconvenient for engineers to estimate and select efficient membrane enthalpy recovery devices that provide greater life cycle cost savings. Therefore it is imperative to develop some simple correlations that could predict the sensible and latent effectiveness by summarizing the couplings between the performance and the sorption characteristics of membrane material, and the operating conditions. This is the objective of this research.

2 Basic Equations

A cross-flow enthalpy exchanger with membrane cores is shown in Fig. 1. Two air streams- the supply and the exhaust flow

---

Contributed by the Heat Transfer Division for publication in the JOURNAL OF HEAT TRANSFER. Manuscript received by the Heat Transfer Division July 1, 2001; revision received November 6, 2001. Associate Editor: C. T. Avedisian.

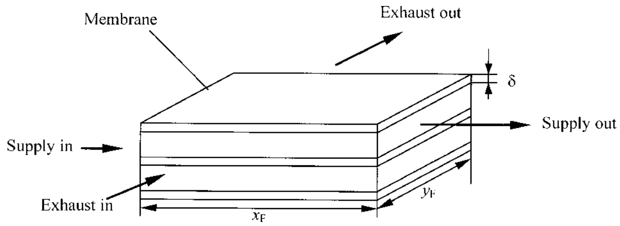

Fig. 1 Schematic of a cross-flow enthalpy exchanger with membrane cores

in thin, parallel, alternating membrane layers, in order to transfer heat and moisture from one air stream to the other. In air conditioning, the supply is usually the outside fresh air and the exhaust is the room air that needs to be discharged to the outside. The enthalpy exchanger is just like a traditional plate-type heat recuperator. The only difference is that hydrophilic membranes are used in place of metal plates. The governing dimensionless equations for simultaneous heat and moisture transfer in enthalpy exchangers, based on the assumptions listed in Table 1, are as follows:

Supply

$$\frac{\partial T_s}{\partial x^*}=2\mathrm{NTU}_s(T_{ms}-T_s) \tag{1}$$

$$\frac{\partial \omega_s}{\partial x^*}=2\mathrm{NTU}_{\mathrm{Ls}}(\omega_{ms}-\omega_s) \tag{2}$$

Exhaust

$$\frac{\partial T_e}{\partial y^*}=2\mathrm{NTU}_c(T_{me}-T_e) \tag{3}$$

$$\frac{\partial \omega_e}{\partial y^*}=2\mathrm{NTU}_{\mathrm{Le}}(\omega_{me}-\omega_e) \tag{4}$$

where

$$x^*=\frac{x}{x_F},\quad y^*=\frac{y}{y_F},$$

$$\mathrm{NTU}_s=\frac{n_s h_s x_F y_F}{\dot{m}_s c_{ps}}=\frac{h_s A_{\mathrm{tot}}}{\dot{m}_s c_{ps}},\quad \mathrm{NTU}_e=\frac{n_e h_e x_F y_F}{\dot{m}_c c_{pe}}=\frac{h_e A_{\mathrm{tot}}}{\dot{m}_c c_{pe}},$$

$$\mathrm{NTU}_{\mathrm{Ls}}=\frac{k_s A_{\mathrm{tot}}}{\dot{m}_s},\quad \mathrm{NTU}_{\mathrm{Le}}=\frac{k_e A_{\mathrm{tot}}}{\dot{m}_e},$$

where T_{ms} and T_{me} are the temperature of membrane in supply side and exhaust side, respectively, ω is moisture uptake in air streams, x and y are coordinates, h is convective heat transfer coefficient, k is convective mass transfer coefficient, $\dot{m}$ is mass flow rate of dry air, x_F and y_F are lengths of flow channels, n is the number of channels. The subscript "s" means "in supply side". Previous studies found that the temperature difference between the two sides of membrane is very small due to the small thickness of membrane [13]. So it is reasonable to assume that $T_{ms}=T_{me}=0.5(T_s+T_e)$.

Table 1 Assumptions used in governing equations

1. There is no lateral mixing of the two air streams.
2. Heat conduction and vapor diffusion in the two air streams are negligible compared to energy transport and vapor convection by bulk flow.
3. Adsorption of water vapor and membrane material is in equilibrium adsorption-state.
4. Both the heat conductivity and the water diffusivity in the membrane are constants.
5. Heat and moisture transfer is one-dimensional in membrane.

The effect of axial fluid conduction is totally negligible for Pe (Peclet number)=100, and is quite small even for Pe=10. In practical applications axial conduction is frequently of considerable significance for laminar flow of liquid metals, which have very low Prandtl numbers. For gases axial conduction can be of importance only at extremely low Reynolds numbers [16]. Generally speaking, assumption (2) is valid when the Peclet number is bigger than 2. The present values of Peclet number in this case are from 11 to 60.

From assumptions (1) and (2), it is seen that heat and moisture transfer is one-dimensional and along the flow direction. However, due to the cross-flow arrangements, the temperature and humidity distributions in the air streams are two-dimensional.

The above dimensionless parameters are the commonly recognized Number of Transfer Units. They give an insight into the characteristics of heat and moisture exchange between fluids and surfaces.

Moisture flow rate through the membrane:

$$\dot{m}_w=D_{wm}\frac{\theta_{ms}-\theta_{me}}{\delta} \tag{5}$$

where θ_{ms}, θ_{me} are moisture uptake in membrane at two surfaces (kg.kg^{-1}), δ is the membrane thickness, and D_{wm} is the water diffusivity in membrane (kgm^{-1}s^{-1}).

The equilibrium between the membrane and moisture at its surface can be expressed with a general sorption curve as

$$\theta=\frac{w_{\max}}{1-C+C/\phi} \tag{6}$$

where $w_{\max}$ represents the maximum moisture content of the membrane material (i.e., moisture uptake when $\phi=100$ percent) and C determines the shape of the curve and the type of sorption.

The parameters of θ, ϕ, and ω can be correlated by ideal gas state equation and psychrometric relations.

The convective heat transfer coefficients are obtained from Nusselt correlations [17] and the mass transfer in boundary layers is often described by Sherwood correlations. By using the well-known Chilton-Colburn Analogy [18]

$$\mathrm{Sh}=\mathrm{Nu}\cdot\mathrm{Le}^{-1/3} \tag{7}$$

We have

$$k=\frac{h}{c_{pa}}\mathrm{Le}^{-1/3} \tag{8}$$

For ventilation air and vapor mixture, which is always near atmospheric states, the Lewis number, Le, varies in the range of 1.19 to 1.22, see Ref. [17].

Analogous to the heat transfer effectiveness commonly used in heat exchanger analysis, the concept of effectiveness can be applied to the heat and moisture transfer processes in a membrane based enthalpy exchanger. For a constant specific heat and heat of phase change, the effectiveness is defined as

Sensible effectiveness

$$\varepsilon_s=\frac{(\dot{m}c_{pa})_s(T_{si}-T_{so})}{(\dot{m}c_{pa})_{\min}(T_{si}-T_{ei})} \tag{9}$$

Latent effectiveness

$$\varepsilon_L=\frac{(\dot{m}c_{pa})_s(\omega_{si}-\omega_{so})}{(\dot{m}c_{pa})_{\min}(\omega_{si}-\omega_{ei})} \tag{10}$$

Enthalpy transfer effectiveness, i.e., total energy transfer effectiveness

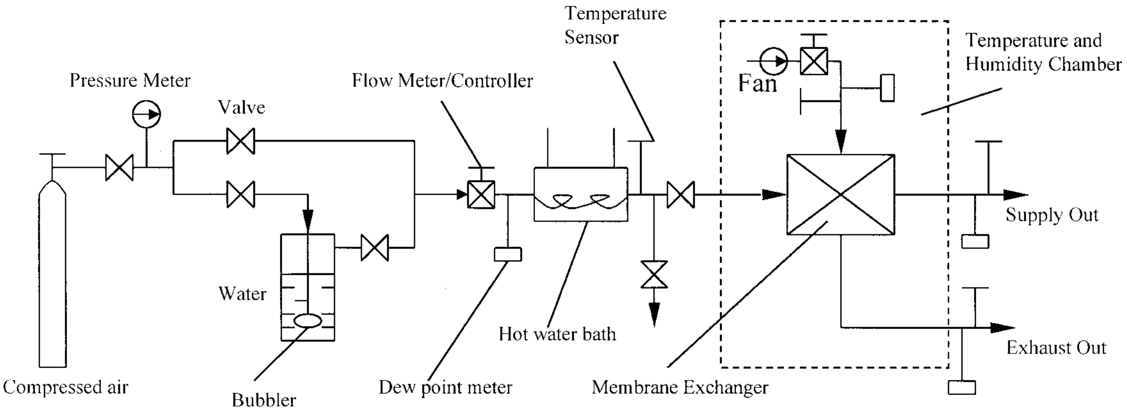

Fig. 2 Schematic of the experimental setup

$$\varepsilon_{\text{tot}}=\frac{\dot{m}_s(H_{si}-H_{so})}{\dot{m}_{\min}(H_{si}-H_{ei})} \tag{11}$$

where H is the specific enthalpy of air, and it is calculated by [7]

$$H=c_{pa}T+\omega(2501+1.86T) \tag{12}$$

where T is in °C.

The third term in Eq. (12) usually has a less than 3 percent effect, thus it can be neglected. Then the enthalpy effectiveness can be further simplified as

$$\varepsilon_{\text{tot}}=\frac{\varepsilon_s+\varepsilon_L H^*}{1+H^*} \tag{13}$$

where

$$H^*=\frac{2501(\omega_{si}-\omega_{ei})}{c_{pa}(T_{si}-T_{ei})}\approx 2501\frac{\Delta\omega}{\Delta T} \tag{14}$$

where H^* is essentially a ratio of latent to sensible energy differences between the inlets of two air streams flowing through the enthalpy exchanger. H^* can in theory vary from $-\infty$ to $+\infty$, but varies typically from -6 to $+6$ for enthalpy recovery in HVAC applications. From above equation, it is clear that the total enthalpy effectiveness is not a simple algebraic average of sensible and latent effectiveness. When $H^*=1$, $\varepsilon_{\text{tot}}=(\varepsilon_s+\varepsilon_L)/2$. As $H^*\to\infty$, $\varepsilon_{\text{tot}}\to\varepsilon_L$; as $H^*\to 0$, $\varepsilon_{\text{tot}}\to\varepsilon_s$; as $H^*\to -1$, $\varepsilon_{\text{tot}}\to\pm\infty$.

3 Experimental

Enthalpy exchange experiments were performed on a cross-flow membrane exchanger with the apparatus shown schematically in Fig. 2. The supply air flows from a compressed air bottle and the exhaust air is supplied from a large humidity and temperature chamber. For the supply air, humidity is adjusted to the desired point by humidifying air through a bubbler immersed in a bottle of water and subsequently mixing it with a dry air stream. The temperature is controlled to the desired point by a hot water bath. The experimental effectiveness is obtained by measuring the temperatures and humidities at the inlets and outlets of two air streams. Temperature is measured by platinum resistance and humidity is measured by chilled-mirror dew point meter. Air mass flow rate is measured and controlled at two values: 0.01 kg/s and 0.05 kg/s. The uncertainties of measurement are: 0.2°C for temperature; 2 percent for humidity; and 5–10 percent for air flow rate. The maximum uncertainties for the tested sensible effectiveness are: 16.8 percent for air mass flow rate of 0.01 kg/s and 12.2 percent for 0.05 kg/s flow rate respectively. The maximum uncertainties for the latent effectiveness are 9.8 percent for air mass flow rate of 0.01 kg/s and 5.2 percent for 0.05 kg/s respectively. A large fraction of the uncertainties came from the uncertainties in air-flow-rate measurement. However, for most of the test results, the uncertainties are less than 5 percent because most of the temperature differences between the two inlets are bigger than 1.5°C and/or the humidity differences are greater than 3.4 g/kg. Before the test, tracer gas is used to detect the cross-over of air streams.

The membranes used are a novel hydrophilic polymer membrane developed and supplied by one of our vendors. It is a modification of poly(vinylchloride) (PVC) membrane by cross-linking it with a selective coating and a 0.02 μm pore diameter porous base material. The final membrane thickness is 20 μm and the composite material has an average degree of polymerization of 480. For the applications of such membranes in heat and moisture transfer, the influences of the microstructure on the performance are reflected by the sorption curve of the material (including shape and sorption potential) and the diffusivity of water in membrane. The sorption curve for the membrane material is measured in a constant temperature and humidity chamber and is shown in Fig. 3. As can be seen, it is a third-type sorption curve that is more sensitive to humidity with increasing humidities. For this material, $C=2.5$, $w_{\max}=0.23$ kg/kg. The effective diffusivity is found to be 2.16×10^{-8} kgm^{-1} s^{-1} from the product manual.

The configurations of the membrane exchanger are: width, 0.5 m; length, 0.5 m; number of membranes for each side, 15; height of flow channels, 5 mm. The exchanger is in cross-flow arrangements, for easy of sealing and construction.

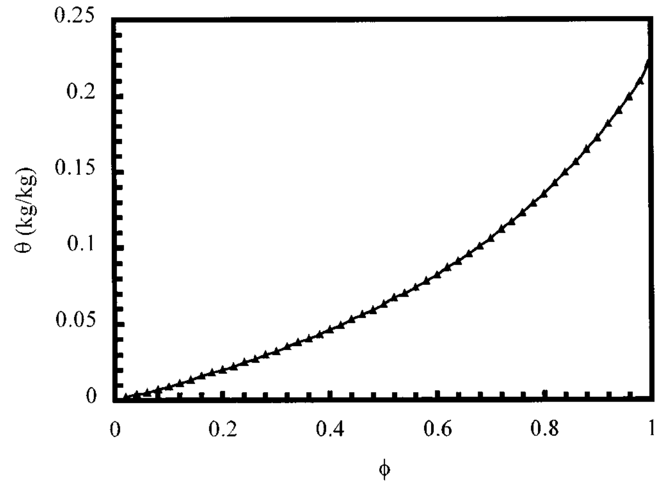

Fig. 3 Sorption curve for the membrane material, $C=2.5$, $w_{\max}=0.22$

4 Development of Effectiveness Correlations

A total number of transfer units is used to reflect the sensible heat transfer in an exchanger. For the membrane exchanger that has equal area on both sides, the total number of transfer units for sensible heat is

$$\mathrm{NTU}=\frac{A_{\mathrm{tot}}U}{(\dot{m}c_{pa})_{\min}}$$

where U is the total heat transfer coefficient. Its general form is

$$U=\left[\frac{1}{h_s}+\frac{\delta}{\lambda}+\frac{1}{h_e}\right]^{-1} \tag{15}$$

The term in the middle is the thermal resistance of membrane, which value is around 0.005 $\mathrm{m^2K/kW}$. Other two terms are convective thermal resistance. Their values are in the order of 40 $\mathrm{m^2K/kW}$, or 8000 times larger than membrane resistance. Therefore, membrane resistance for heat transfer can be neglected.

The sensible effectiveness is a function of two dimensionless parameters, NTU and $R_1=(\dot{m}c_{pa})_{\min}/(\dot{m}c_{pa})_{\max}$, the ratio of minimum to maximum heat capacity rate of two air streams. For unmixed cross flow, it can be expressed as [17]

$$\varepsilon_s=1-\exp\left[\frac{\exp(-\mathrm{NTU}^{0.78}R_1)-1}{\mathrm{NTU}^{-0.22}R_1}\right] \tag{16}$$

This empirical equation is fairly accurate except at the extremes of the variables.

A form similar to Eq. (16) for latent effectiveness may be derived if the moisture resistance for membrane could be clarified and estimated.

The moisture flow rate through the membrane can also be expressed as

$$\dot{m}_W=k_s(\omega_s-\omega_{ms})=k_e(\omega_{me}-\omega_e) \tag{17}$$

$$\theta_{me}=\theta_{ms}+\left.\frac{\partial\theta}{\partial\phi}\right|_{ms}\Delta\phi=\theta_{ms}+\left.\frac{\partial\theta}{\partial\phi}\right|_{ms}(\phi_{me}-\phi_{ms}) \tag{18}$$

Substituting Eq. (18) into Eq. (5), we have

$$\dot{m}_W=\frac{D_{wm}}{\delta}\left(\frac{\partial\theta}{\partial\phi}\right)_{ms}(\phi_{ms}-\phi_{me}) \tag{19}$$

Using Clapeyron equation to represent the saturation vapor pressure and assuming a standard atmospheric pressure of 101325 Pa gives the relation between humidity and relative humidity as

$$\frac{\phi}{\omega}=\frac{e^{5294/(T+273.15)}}{10^6}-1.61\phi \tag{20}$$

where the second term on the right side of the equation will generally have less than a 5 percent effect, thus it can be neglected. Thus the relation between ϕ and ω is expressed by

$$\phi=\frac{e^{5294/(T+273.15)}}{10^6}\,\omega \tag{21}$$

Substituting Eq. (21) into Eq. (19), we have

$$\dot{m}_W=\frac{D_{wm}}{\delta}\left(\frac{\partial\theta}{\partial\phi}\right)_{ms}\frac{e^{5294/(T+273.15)}}{10^6}(\omega_{ms}-\omega_{me}) \tag{22}$$

From Eq. (17), two equations can be deduced

$$\omega_{ms}=\omega_s-\dot{m}_w/k_s \tag{23}$$

$$\omega_{me}=\omega_c+\dot{m}_w/k_c \tag{24}$$

Substituting above two equations into Eq. (22) to eliminate ω_{ms} and ω_{me} gives

$$\dot{m}_W=\frac{1}{\gamma_{\mathrm{tot}}}(\omega_s-\omega_e) \tag{25}$$

or

$$\dot{m}_W=U_L(\omega_s-\omega_e)$$

where

$$\gamma_{\mathrm{tot}}=U_L^{-1}=\frac{1}{k_s}+\gamma_m+\frac{1}{k_e} \tag{26}$$

and

$$\gamma_m=\frac{\delta}{D_{wm}}\,\frac{10^6}{e^{(-5294/T)}\left(\frac{\partial\theta}{\partial\phi}\right)_{ms}} \tag{27}$$

It is indicated that γ_{tot}, the total moisture transfer resistance, has an expression similar to thermal resistance where the first and the third term are the convective resistance on the supply side and exhaust side respectively. The middle term, γ_m, is the moisture diffusive resistance in membrane. U_L can be called the total moisture transfer coefficient for the device.

The differentiation of Eq. (6) gives

$$\frac{\partial\theta}{\partial\phi}=\frac{w_{\max}C}{(1-C+C/\phi)^2\phi^2} \tag{28}$$

The Eq. (27) can be further simplified as

$$\gamma_m=\frac{\delta}{D_{wm}}\,\psi \tag{29}$$

$$\psi=\left.\frac{10^6(1-C+C/\phi)^2\phi^2}{e^{(5294/T)}w_{\max}C}\right|_{ms} \tag{30}$$

where the coefficient of diffusive resistance for membrane, ψ, is co-determined by the operating conditions and the slope of sorption curves of membrane material.

Similar to the definition of total number of transfer units for heat, the total number of transfer units for moisture can be written as

$$\mathrm{NTU}_L=\frac{A_{\mathrm{tot}}U_L}{(\dot{m})_{\min}} \tag{31}$$

The comparison of total transfer units for moisture and sensible heat, assuming equal specific heats for two air streams, gives

$$\beta=\frac{\mathrm{NTU}_L}{\mathrm{NTU}}=\frac{U_Lc_{pa}}{U} \tag{32}$$

Substituting Eqs. (15), (26), (27), into Eq. (32) suggests that

$$\beta=\frac{\left(1+\frac{h_s}{h_e}\right)+\frac{\delta h_s}{\lambda}}{\left(1+\frac{h_s}{h_e}\right)+\frac{\delta}{D_{wm}}\psi k_s} \tag{33}$$

where, $(\delta h_s/\lambda)$ is several orders smaller than other terms, mainly due to the small thickness of membranes, so it can be neglected. The above equation can be further simplified into

$$\beta=\frac{\left(1+\frac{h_s}{h_e}\right)}{\left(1+\frac{h_s}{h_e}\right)+\frac{\gamma_m}{1/k_s}} \tag{34}$$

In most cases, the enthalpy recovery is implemented with balanced flows, i.e., the two air streams have the same flow rates. Therefore, the convective heat transfer coefficients would have the same value on both sides of membrane result from similar fluid fields. Consequently, Eq. (34) can be written in

$$\beta = \frac{1}{1+\alpha} \tag{35}$$

where

$$\alpha = \frac{\gamma_m}{\gamma_c} \tag{36}$$

$$\gamma_c = \frac{2}{k_s} \tag{37}$$

where γ_c is the convective moisture transfer resistance, and α is the ratio of diffusive resistance to convective resistance for membrane. As can be seen, the total number of transfer units for moisture can be estimated from the total number of transfer units for sensible heat, and ratio of diffusive to convective moisture resistance. As $\alpha \to \infty$, $\mathrm{NTU}_L \to 0$, no moisture can be permeated through the membrane. In this case, the "membrane" is like a metal plate. On the other hand, as $\alpha \to 0$, $\mathrm{NTU}_L \to \mathrm{NTU}$, $\epsilon_L = \epsilon_s$. If $\alpha = 1$, $\mathrm{NTU}_L = \mathrm{NTU}/2$. Under the current operating conditions, the values of α vary from 2 to 10 (see Fig. 6), which implies that membrane resistance for moisture transfer cannot be neglected.

Similar to the deduction of Eq. (16) for sensible heat transfer, the correlation for latent effectiveness can be written as

$$\varepsilon_L = 1 - \exp\left[\frac{\exp(-\mathrm{NTU}_L^{0.78} R_2) - 1}{\mathrm{NTU}_L^{-0.22} R_2}\right] \tag{38}$$

$$\mathrm{NTU}_L = \beta \cdot \mathrm{NTU} \tag{39}$$

$$R_2 = \dot{m}_{\min} / \dot{m}_{\max} \tag{40}$$

A more detailed set up of the analogy between Eqs. (38) and (16) can be seen in the appendix. The latent effectiveness correlations for other flow arrangements, such as concurrent flow and counter flow, can also be derived from those corresponding correlations for sensible effectiveness, using the definition of Eq. (35). The value of relative humidity of membrane in supply side, which is determined by latent effectiveness (permeation rate), needs to be known before the calculation of diffusive resistance for membrane γ_m and the diffusive to convective ratio α. Iterations are performed to obtain a converged solution for ϕ_{ms}.

5 Results and Discussion

To demonstrate the suitability of the correlations in predicting the effectiveness, sensible and latent effectiveness are calculated with the proposed correlations and compared with experimental results, as shown in Figs. 4 and 5 respectively. To make more extensive comparisons, simulation results with a finite difference model proposed by Zhang and Jiang [13] are also plotted in the two figures. The uncertainty for the finite difference results is less than 1 percent with a grid size of 2 mm.

From Figs. 4 and 5, it is obvious that both the sensible and the latent effectiveness are properly represented by the correlation from the present study. The largest discrepancies between the predictions by the correlation and the experimental data result from the cases with the smallest air flow rate, where the uncertainties of the experimental data are the biggest. The average errors between the predicted and experimental results are 7.3 percent and 8.6 percent for sensible and latent effectiveness respectively.

For a given exchanger, the sensible effectiveness is a fixed value at the specified flow rates. However the latent effectiveness will be affected by the two important dimensionless factors proposed in this study: the ratio of diffusive to convective resistance (α), and the ratio of total number of transfer units of moisture to that of sensible (β). The values of α and β are in turn affected by the membrane material types and operating inlet conditions. The

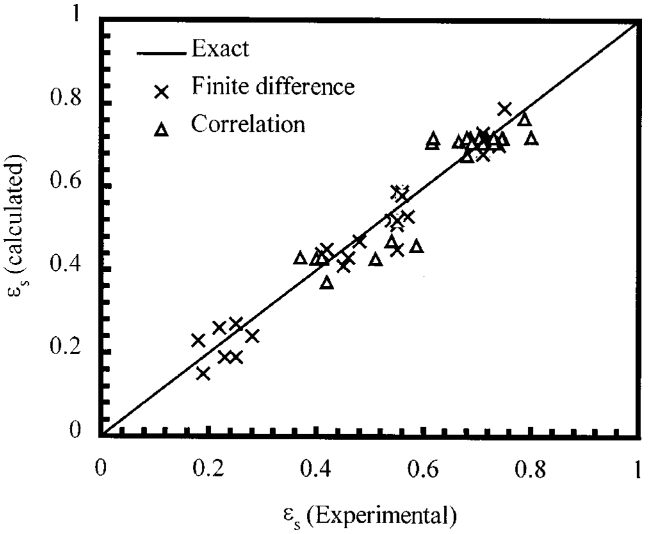

Fig. 4 Calculated and experimental sensible effectiveness for a cross-flow membrane enthalpy exchanger

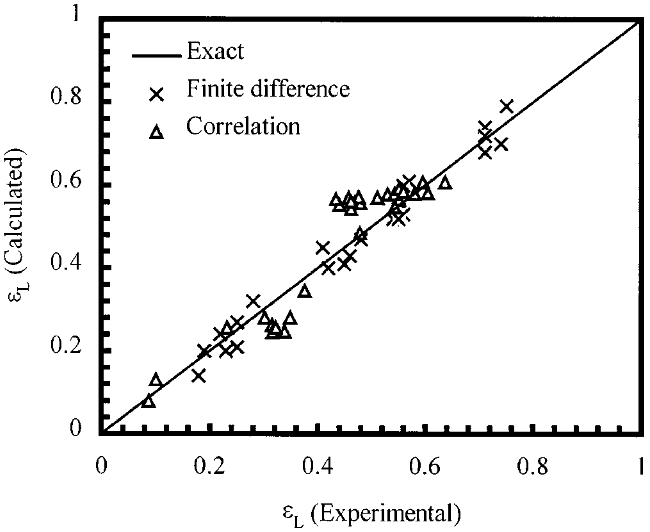

Fig. 5 Calculated and experimental latent effectiveness for a cross-flow membrane enthalpy exchanger

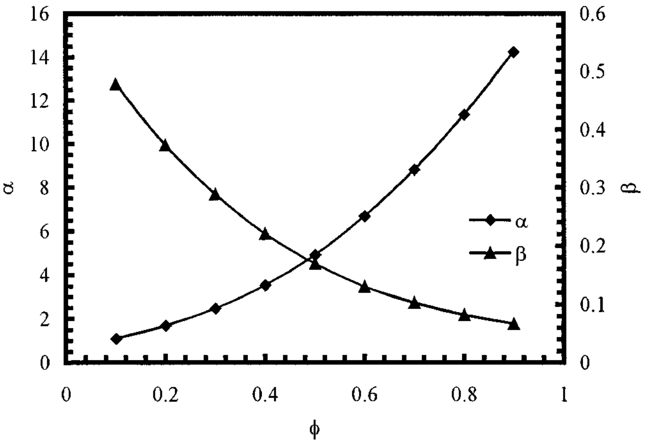

Fig. 6 Variations of α and β with increasing inlet relative humidity for first-type ($C=0.1$) membrane material

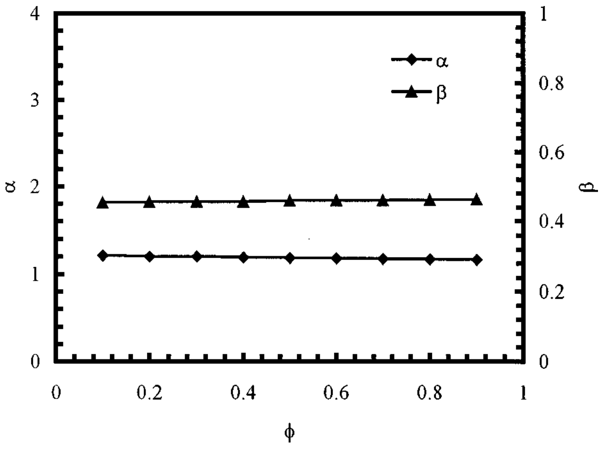

Fig. 7 **Variations of α and β with increasing inlet relative humidity for linear type ($C=1.0$) membrane material**

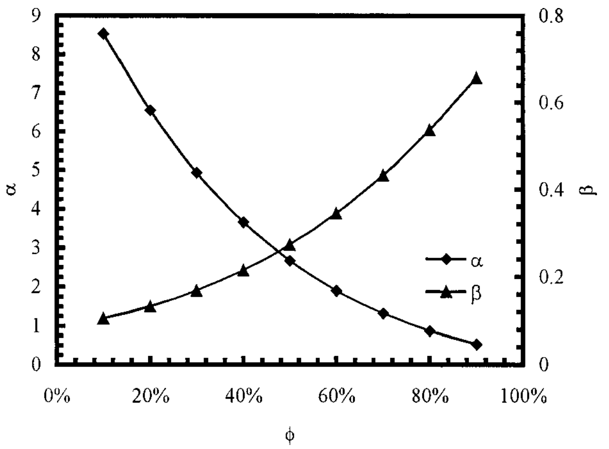

Fig. 8 **Variations of α and β with increasing inlet relative humidity for third-type ($C=10$) membrane material**

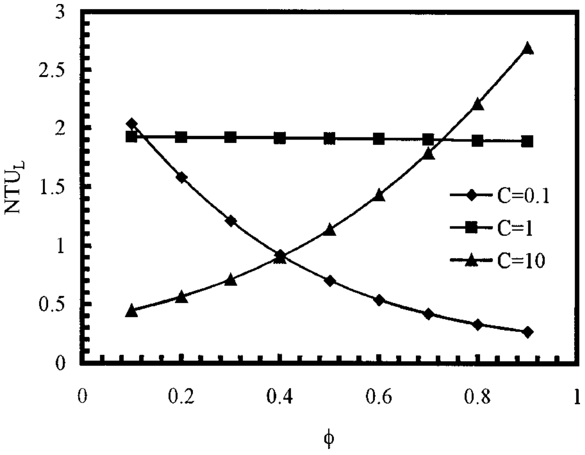

Fig. 9 **Variations of NTU_L with relative humidity for different membranes, NTU=4.2**

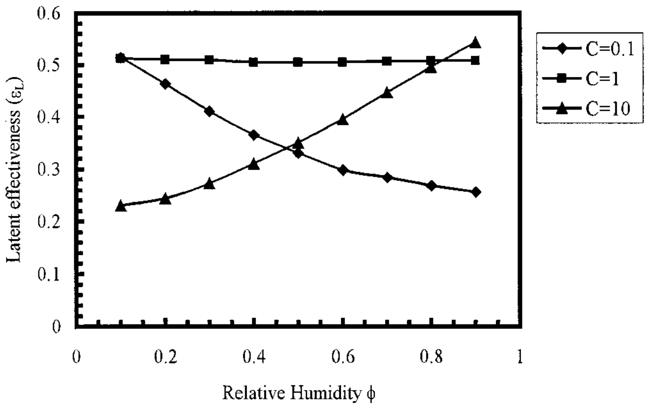

Fig. 10 **Latent effectiveness for three types of membranes, NTU=4.2**

variations of α and β with increasing inlet relative humidities of the supply air are plotted in Figs. 6–8, for three kinds of membrane material that are most often used.

The value of α and β with linear type membrane does not change with inlet relative humidity. However, for first-type membrane material, α increases from around 0.5 at 10 percent RH to 15 at 90 percent RH, while for third-type membrane, α decreases from 8.6 at 10 percent RH to 0.4 at 90 percent RH. The bigger the α, the larger the β and the latent effectiveness.

Figure 9 demonstrates the variations of NTU_L, when NTU is kept constant, with different inlet humidities. The value of NTU_L decreases and increases for first-type and third-type material, with increasing inlet humidity respectively. The trends of resulting latent effectiveness are the same as those of NTU_L, which can be deduced from Eq. (31), see Fig. 10. For the linear type material, the NTU_L and the latent effectiveness will not change with the outside conditions. The number of transfer units for moisture would keep at 0.45 times of that for sensible heat for this material.

The above discussions suggest that an enthalpy exchanger with linear type membrane cores always performs better than those with other membrane cores. For example, to obtain a latent effectiveness of 0.6 under an inlet humidity of 50 percent, NTU_L should be at least 2.0, which means that the minimum values of NTU required for the exchanger are: 4.44 with linear type; 8 with third-type; and 11.1 with first-type membrane. A smaller NTU usually makes the enthalpy exchanger more compact and cheaper.

6 Conclusions

Enthalpy recovery with new hydrophilic membranes has potentially extensive uses in energy efficient buildings. To evaluate the system performance, the effectiveness correlations are proposed. By separating the moisture resistance through membranes and building up an analogy between the number of transfer units for moisture and that for sensible heat, the latent effectiveness correlation is written in a form very similar to the empirical correlation for sensible effectiveness that can be easily found in many literatures. A comparison with established experimental results shows that the correlations correctly predict the influences of the design variables on the performance of the membrane system. The studies also find that the ratio of diffusive to convective resistance (α) determines the number of transfer units for moisture, with a fixed value of the number of transfer units for sensible heat. The ratio α reflects the couplings between the moisture transfer and the sorption characteristics of membrane material and the operating conditions. For a given number of transfer units for sensible heat, enthalpy exchangers with linear type membrane cores would have the highest transfer units for moisture, which in return results in the highest latent effectiveness.

Acknowledgment

This research is funded by the Research Grant Council of the Hong Kong SAR Government and the postdoctoral fellowship of the Hong Kong Polytechnic University.

Nomenclature

A = transfer area (m^2)
C = constant in sorption curve
c_p = specific heat (kJkg^{-1}K^{-1})
D_{wm} = diffusivity of water in membrane (kgm^{-1}s^{-1})
H = specific enthalpy (kJ/kg)
H^* = ratio of latent to sensible energy differences between the inlets of two air streams
h = convective heat transfer coefficient (kWm^{-2}K^{-1})
k = convective mass transfer coefficient (kgm^{-2}s^{-1})
$\dot{m}$ = mass flow rate of air streams (kg/s)
$\dot{m}_W$ = mass flow rate of moisture flow (kgm^{-2}s^{-1})
NTU = number of transfer units
Nu = Nusselt number
n = number of channels
R = ratio for heat/mass capacity
Sh = Sherwood number
T = temperature (°C)
U = total heat transfer coefficient (kWm^{-2}K^{-1})
U_L = total mass transfer coefficient (kgm^{-2}s^{-1})
$w_{\max}$ = maximum water uptake of desiccant (kgkg^{-1})
x, y = coordinates (m)
x^*, y^* = nondimensional coordinates
x_F = length of supply channel (m)
y_F = length of exhaust channel (m)

Greek Letters

ψ = coefficient of moisture diffusive resistance in membrane (CMDR)
λ = thermal conductivity of membrane (kWm^{-1}K^{-1})
θ = moisture uptake in membrane (kgkg^{-1})
ε = effectiveness
γ = resistance (m^{2}K/k W for thermal and m^{2}s/kg for moisture)
ϕ = relative humidity
δ = thickness of membrane (m)
ω = moisture content (kg moisture/kg dry air)
α = ratio of diffusive to convective moisture resistance for membrane
β = ratio of total number of transfer units for moisture to that for sensible heat

Subscripts

a = air
c = convective
e = exhaust
i = inlet
L = latent, moisture
m = membrane, diffusive
s = supply, sensible
o = outlet
tot = total
w = water

Appendix

Deduction of effectiveness correlations

Considering a cross-flow membrane exchanger with only one flow channel. At any point in the exchanger a heat and mass balance for an infinitely small volume *dxdy* can be written from Eq. (15) and Eq. (25) as

$$dq = U(T_s - T_e)dxdy \tag{A1}$$

$$d\dot{m}_W = U_L(\omega_s - \omega_e)dxdy \tag{A2}$$

Equation (*A*1) is a basic heat transfer equation, and Eq. (*A*2) has been widely employed as a mass permeation model through a membrane in chemical industry [19].

Across the elements x_F and y_F units in length the energy and moisture balances yield

$$dq = -\frac{(\dot{m}c_{pa})_s}{y_F}\frac{\partial T_s}{\partial x}dxdy \tag{A3}$$

$$dq = \frac{(\dot{m}c_{pa})_e}{x_F}\frac{\partial T_e}{\partial y}dxdy \tag{A4}$$

$$d\dot{m}_W = -\frac{\dot{m}_s}{y_F}\frac{\partial \omega_s}{\partial x}dxdy \tag{A5}$$

$$d\dot{m}_W = \frac{\dot{m}_e}{x_F}\frac{\partial \omega_e}{\partial y}dxdy \tag{A6}$$

Combining Eqs. (*A*1) and (*A*3) and then Eqs. (*A*1) and (*A*4) gives

$$\frac{Uy_F}{(\dot{m}c_{pa})_s}(T_s - T_e) = -\frac{\partial T_s}{\partial x} \tag{A7}$$

$$\frac{Ux_F}{(\dot{m}c_{pa})_e}(T_s - T_e) = \frac{\partial T_e}{\partial y} \tag{A8}$$

Similarly, combining Eqs. (*A*2) and (*A*5) and then Eqs. (*A*2) and (*A*6) gives

$$\frac{U_L y_F}{\dot{m}_s}(\omega_s - \omega_e) = -\frac{\partial \omega_s}{\partial x} \tag{A9}$$

$$\frac{U_L x_F}{\dot{m}_e}(\omega_s - \omega_e) = \frac{\partial \omega_e}{\partial y} \tag{A10}$$

Differentiating Eqs. (*A*7) and (*A*8) with respect to *y* and *x* and taking their sum gives

$$\frac{Ux_F}{(\dot{m}c_{pa})_e}\frac{\partial(T_s - T_e)}{\partial x} + \frac{Uy_F}{(\dot{m}c_{pa})_s}\frac{\partial(T_s - T_e)}{\partial y} = -\frac{\partial^2(T_s - T_e)}{\partial x \partial y} \tag{A11}$$

Similarly, differentiating Eqs. (*A*9) and (*A*10) with respect to *y* and *x* and taking their sum gives

$$\frac{U_L x_F}{\dot{m}_e}\frac{\partial(\omega_s - \omega_e)}{\partial x} + \frac{U_L y_F}{\dot{m}_s}\frac{\partial(\omega_s - \omega_e)}{\partial y} = -\frac{\partial^2(\omega_s - \omega_e)}{\partial x \partial y} \tag{A12}$$

Let dimensionless variables

$$\theta_1 = \frac{T_s - T_e}{T_{si} - T_{ei}}, \quad \theta_2 = \frac{\omega_s - \omega_e}{\omega_{si} - \omega_{ei}}, \quad x^* = \frac{x}{x_F}, \quad y^* = \frac{y}{y_F}$$

and substituting in Eqs. (*A*11), (A12),

$$\frac{Ux_F y_F}{(\dot{m}c_{pa})_e}\frac{\partial \theta_1}{\partial x^*} + \frac{Ux_F y_F}{(\dot{m}c_{pa})_s}\frac{\partial \theta_1}{\partial y^*} = -\frac{\partial^2 \theta_1}{\partial x^* \partial y^*} \tag{A13}$$

$$\frac{U_L x_F y_F}{\dot{m}_e}\frac{\partial \theta_2}{\partial x^*} + \frac{U_L x_F y_F}{\dot{m}_s}\frac{\partial \theta_2}{\partial y^*} = -\frac{\partial^2 \theta_2}{\partial x^* \partial y^*} \tag{A14}$$

with

$$\text{NTU}_a = \frac{Ux_F y_F}{(\dot{m}c_{pa})_e}, \quad \text{NTU}_b = \frac{Ux_F y_F}{(\dot{m}c_{pa})_s},$$

$$\text{NTU}_{La} = \frac{U_L x_F y_F}{\dot{m}_e}, \quad \text{NTU}_{Lb} = \frac{U_L x_F y_F}{\dot{m}_s}$$

Eqs. (*A*13) and (*A*14) become

$$\text{NTU}_a\frac{\partial \theta_1}{\partial x^*} + \text{NTU}_b\frac{\partial \theta_1}{\partial y^*} + \frac{\partial^2 \theta_1}{\partial x^* \partial y^*} = 0 \tag{A15}$$

$$\text{NTU}_{La}\frac{\partial \theta_2}{\partial x^*} + \text{NTU}_{Lb}\frac{\partial \theta_2}{\partial y^*} + \frac{\partial^2 \theta_2}{\partial x^* \partial y^*} = 0 \tag{A16}$$

Initial condition: $\theta_1(0,0) = \theta_2(0,0) = 1$

Mason [20] obtained a solution for Eq. ($A15$) in the form of an infinite series by employing the Laplace transformation as following:

$$\theta_1(x^*,y^*)=e^{-(\mathrm{NTU}_a)y^*+(\mathrm{NTU}_b)x^*}\sum_{n=0}^{\infty}\left[\frac{(\mathrm{NTU}_a)(\mathrm{NTU}_b)x^*y^*}{(n!)^2}\right]^n \tag{A17}$$

Since Eqs. ($A15$) and ($A16$) are the same form of differential equations. They are identical if NTU_a is replaced by NTU_{La} and NTU_b by NTU_{Lb}. Therefore, the solution to Eq. ($A16$) can be written as

$$\theta_2(x^*,y^*)=e^{-(\mathrm{NTU}_{La})y^*+(\mathrm{NTU}_{Lb})x^*}\sum_{n=0}^{\infty}\left[\frac{(\mathrm{NTU}_{La})(\mathrm{NTU}_{Lb})x^*y^*}{(n!)^2}\right]^n \tag{A18}$$

The overall heat transferred in the exchanger is the integral of Eq. ($A17$)

$$Q=Ux_Fy_F(T_{si}-T_{ei})\int_0^1\int_0^1\theta_1(x^*,y^*)dx^*dy^* \tag{A19}$$

The overall moisture transferred in the exchanger is the integral of Eq. ($A18$)

$$M_w=U_Lx_Fy_F(\omega_{si}-\omega_{ei})\int_0^1\int_0^1\theta_2(x^*,y^*)dx^*dy^* \tag{A20}$$

If we define

$$\mathrm{NTU}=\frac{Ux_Fy_F}{(\dot{m}c_{pa})_{\min}},\quad \mathrm{NTU}_L=\frac{U_Lx_Fy_F}{(\dot{m})_{\min}}$$

$$R_1=\frac{(\dot{m}c_{pa})_{\min}}{(\dot{m}c_{pa})_{\max}},\quad R_2=\frac{\dot{m}_{\min}}{\dot{m}_{\max}}$$

$$\Omega_1=\int_0^1\int_0^1\theta_1(x^*,y^*)dx^*dy^*,$$

$$\Omega_2=\int_0^1\int_0^1\theta_2(x^*,y^*)dx^*dy^*$$

$$\varepsilon_s=\frac{Q}{(\dot{m}c_{pa})_{\min}(T_{si}-T_{ei})},\quad \varepsilon_L=\frac{M_W}{\dot{m}_{\min}(\omega_{si}-\omega_{ei})}$$

then

$$\varepsilon_s=\mathrm{NTU}\Omega_1 \tag{A21}$$

$$\varepsilon_L=\mathrm{NTU}_L\Omega_2 \tag{A22}$$

$$\Omega_1=\frac{1}{(\mathrm{NTU}_a)(\mathrm{NTU}_b)}\sum_{n=0}^{\infty}f(\mathrm{NTU}_a)f(\mathrm{NTU}_b) \tag{A23}$$

$$\Omega_2=\frac{1}{(\mathrm{NTU}_{La})(\mathrm{NTU}_{Lb})}\sum_{n=0}^{\infty}f(\mathrm{NTU}_{La})f(\mathrm{NTU}_{Lb}) \tag{A24}$$

where

$$f(z)=1-e^{-z}\sum_{m=0}^{n}\frac{z^m}{m!} \tag{A25}$$

There are two cases:

If $(\dot{m}c_{pa})_e=(\dot{m}c_{pa})_{\min}$, then $\mathrm{NTU}_a=\mathrm{NTU}$, and $\mathrm{NTU}_b=R_1\mathrm{NTU}$

If $(\dot{m}c_{pa})_e=(\dot{m}c_{pa})_{\max}$, then $\mathrm{NTU}_a=R_1\mathrm{NTU}$, and $\mathrm{NTU}_b=\mathrm{NTU}$

In both cases, Eq. ($A21$) can be replaced by the relationship

$$\varepsilon_s=\frac{1}{R_1(\mathrm{NTU})}\sum_{n=0}^{\infty}\left[1-e^{-\mathrm{NTU}}\sum_{m=0}^{n}\frac{(\mathrm{NTU})^m}{m!}\right]\times\left\{1-e^{-R_1(\mathrm{NTU})}\sum_{m=0}^{n}\frac{[R_1(\mathrm{NTU})]^m}{m!}\right\} \tag{A26}$$

Similarly, for moisture effectiveness, we have

$$\varepsilon_L=\frac{1}{R_2(\mathrm{NTU}_L)}\sum_{n=0}^{\infty}\left[1-e^{-\mathrm{NTU}_L}\sum_{m=0}^{n}\frac{(\mathrm{NTU}_L)^m}{m!}\right]\times\left\{1-e^{-R_2(\mathrm{NTU}_L)}\sum_{m=0}^{n}\frac{[R_2(\mathrm{NTU}_L)]^m}{m!}\right\} \tag{A27}$$

We can see at this step that the moisture effectiveness has the same form of expression with sensible effectiveness. The only differences are that NTU is replaced by NTU_L and R_1 is replaced by R_2.

For heat transfer, Eq. ($A26$) is too complicated, since it has infinite series. Therefore, Kays and London [21] used following empirical equation to represent the sensible effectiveness as

$$\varepsilon_s=1-\exp\left[\frac{\exp(-R_1(\mathrm{NTU}^{0.78})-1}{R_1\mathrm{NTU}^{-0.22}}\right] \tag{A28}$$

Similarly, Eq. (27), which is similar to Eq. (26), could be approximated with

$$\varepsilon_L=1-\exp\left[\frac{\exp(-R_2\mathrm{NTU}_L^{0.78})-1}{R_2\mathrm{NTU}_L^{-0.22}}\right] \tag{A29}$$

References

[1] Dorer, V., and Breer, D., 1998, ''Residential Mechanical Ventilation Systems: Performance Criteria and Evaluations,'' Energy Build., **27**(3), pp. 247–255.

[2] Dhital, P., Besant, R. W., and Schoenau, G. J., 1995, ''Integrating Run-Around Heat Exchanger Systems Into the Design of Large Office Buildings,'' ASHRAE J., **101**(2), pp. 979–991.

[3] Johnson, A. B., Besant, R. W., and Schoenau, G. J., 1995, ''Design of Multi-Coil Run-Around Heat Exchanger Systems for Ventilation Air Heating and Cooling,'' ASHRAE Trans., **101**(2), pp. 967–978.

[4] Manz, H., Huber, H., Schalin, A., Weber, A., Ferrazzini, M., and Studer, M., 2000, ''Performance of Single Room Ventilation Units With Recuperative or Regenerative Heat Recovery,'' Energy Build., **31**(1), pp. 37–47.

[5] San, J. Y., 1993, ''Heat and Mass Transfer in a Two-Dimensional Cross-Flow Regenerator With a Solid Conduction Effect,'' Int. J. Heat Mass Transf., **36**(3), pp. 633–643.

[6] Simonson, C. J., and Besant, R. W., 1998, ''Heat and Moisture Transfer in Energy Wheels During Sorption, Condensation, and Frosting Conditions,'' ASME J. Heat Transfer, **120**, pp. 699–708.

[7] Simonson, C. J., and Besant, R. W., 1999, ''Energy Wheel Effectiveness: Part I—Development of Dimensionless Groups,'' Int. J. Heat Mass Transf., **42**, pp. 2161–2170.

[8] Simonson, C. J., and Besant, R. W., 1999b, ''Energy Wheel Effectiveness: Part II—Correlations,'' Int. J. Heat Mass Transf., **42**, pp. 2171–2185.

[9] Pan, C. Y., Jensen, C. D., Bielech, C., and Habgood, H. W., 1978, ''Permeation of Water Vapor Through Cellulose Triacetate Membranes in Hollow Fiber Form,'' J. Appl. Polym. Sci., **22**, pp. 2307–2323.

[10] Asaeda, M., and Du, L. D., 1986, ''Separation of Alcohol/Water Gaseous Mixtures by Thin Ceramic Membrane,'' J. Chem. Eng. Jpn., **19**, pp. 72–77.

[11] Wang, K. L., Mccray, S. H., Newbold, D. D., and Cusseler, E. L., 1992, ''Hollow Fiber Air Drying,'' J. Membr. Sci., **72**, pp. 231–244.

[12] Cha, J. S., Li, R., and Sirkar, K. K., 1996, ''Removal of Water Vapor and VOCs From Nitrogen in a Hydrophilic Hollow Fiber Gel Membrane Permeator,'' J. Membr. Sci., **119**, pp. 139–153.

[13] Zhang, L. Z., and Jiang, Y., 1999, ''Heat and Mass Transfer in a Membrane-Based Energy Recovery Ventilator,'' J. Membr. Sci., **163**, pp. 29–38.

[14] Zhang, Y. P., Jiang, Y., Zhang, L. Z., Deng, Y. C., and Jin, Z. F., 2000, ''Analysis of Thermal Performance and Energy Saving Effect of Membrane Based Heat Recovery Ventilator,'' Energy-The International Journal, **25**(6), 515–527.

[15] Zhang, L. Z., Jiang, Y., and Zhang, Y. P., 2000, ''Membrane-Based Humidity Pump: Performance and Limitations,'' J. Membr. Sci., **171**, pp. 207–216.

[16] Kays, W. M., and Crawford, M. E., 1993, *Convective Heat and Mass Transfer*, McGraw-Hill New York, pp. 432–435.

[17] Incropera, F. P., and Dewitt, D. P., 1990, *Fundamentals of Heat and Mass Transfer*, 3rd ed., Wiley, New York, pp. 416–420, 556–557.

[18] Taylor, R., and Krishna, R., 1993, *Multicomponent Mass Transfer*, John Wiley & Sons, New York, pp. 278–279.

[19] Scovazzo, P., Burgos, J., Hoehn, A., and Todd, P., 1998, ''Hydrophilic Membrane-Based Humidity Control,'' J. Membr. Sci., **149**, pp. 69–81.

[20] Kern, D. Q., and Kraus, A. D., 1972, *Extended Surface Heat Transfer*, McGraw-Hill, New York, pp. 617–621.

[21] Kraus, A. D., Aziz, A., and Welty, J., 2001, *Extended Surface Heat Transfer*, John Wiley & Sons, New York, pp. 471.

On the Potential for Homogeneous Nucleation of Salt From Aqueous Solution in a Natural Convection Boundary Layer

Kenneth A. Smith
e-mail: kas@mit.edu
Department of Chemical Engineering,
Massachusetts Institute of Technology,
77 Massachusetts Avenue, Room 66-540,
Cambridge, MA 02139

Marc Hodes[1]
Department of Mechanical Engineering,
Massachusetts Institute of Technology,
77 Massachusetts Avenue,
Cambridge, MA 02139

Peter Griffith
e-mail: pgrif@mit.edu
Department of Mechanical Engineering,
Massachusetts Institute of Technology,
77 Massachusetts Avenue, Room 7-044,
Cambridge, MA 02139

Recent studies have examined the rate of salt deposition by natural convection on a cylinder heated above the solubility temperature corresponding to the concentration of salt in the surrounding solution at conditions typical of the Supercritical Water Oxidation (SCWO) process (Hodes et al. [1,2], Hodes [3]). The total deposition rate of salt on the cylinder is the sum of the rate of deposition at the salt layer-solution interface (SLSI) formed on the cylinder and that within the porous salt layer. The rate of deposition at the SLSI cannot be computed without determining whether or not salt nucleates homogeneously in the adjacent (natural convection) boundary layer. A methodology to determine whether or not homogeneous nucleation in the boundary layer is possible is presented here. Temperature and concentration profiles in the boundary layer are computed under the assumption that homogeneous nucleation does not occur. If, under this assumption, supersaturation does not occur, homogeneous nucleation is impossible. If supersaturation is present, homogeneous nucleation may or may not occur depending on the amount of metastability the solution can tolerate. It is shown that the Lewis number is the critical solution property in determining whether or not homogeneous nucleation is possible and a simple formula is developed to predict the Lewis number below which homogeneous nucleation is impossible for a given solubility boundary and set of operating conditions. Finally, the theory is shown to be consistent with experimental observations for which homogeneous nucleation is absent or present. [DOI: 10.1115/1.1494089]

Keywords: *Crystal Growth, Cylinder, Heat Transfer, Mass Transfer, Natural Convection, Phase Change*

Introduction

Supercritical Water Oxidation (SCWO), oxidation in water at temperatures and pressures exceeding the critical temperature (374°C) and critical pressure (221 bar) of pure water, is an effective technology for the remediation of hazardous organic wastes. Reviews of SCWO technology have been provided by Tester et al. [4] and, more recently, by Gloyna and Li [5]. Widespread commercialization of SCWO continues to be hindered by scale buildup (fouling) by "sticky" salts. (See, for example, Shaw and Dahmen [6].) Various salts are commonly present in SCWO feeds or produced during neutralization of halogen-containing wastes. These salts precipitate from solution due to the low dielectric constant of water at SCWO conditions. Precipitated salts can form agglomerates and coat internal surfaces and, if left uncontrolled, plug SCWO reactors or transport lines.

Recently, rates of deposition from aqueous salt solutions to a heated cylinder at near-supercritical conditions have been measured by Hodes et al. [1,3] in the (visually accessible) test cell described by Hurst et al. [7]. The solutions were preheated to about 5°C below the solubility temperature corresponding to the concentration of salt in the bulk solution surrounding the cylinder and the temperature of the cylinder was increased beyond this solubility temperature to drive deposition. The total deposition rate of salt on the cylinder is the sum of the deposition rate at the salt layer-solution interface (SLSI) formed on the cylinder plus that within the porous salt layer. The dominant transport mode for deposition at the SLSI is (laminar) natural convection [3]. Deposition rates at the SLSI have been computed by Hodes et al. [2,3] under the assumption that dissolved salt is transported to it by molecular diffusion (with advection) and that it subsequently nucleates heterogeneously. A methodology to determine whether or not homogeneous nucleation in the boundary layer is possible is presented here and applied to the experimental conditions.

Molecular diffusion coefficients for salts in supercritical water (SCW) are necessary to calculate deposition rates in SCWO systems and compute the solution Lewis numbers needed to apply the results developed below. Butenhoff et al. [8] measured the molecular diffusion coefficient of sodium nitrate in SCW. It ranged, for example, from $1.06{*}10^{-8}$ to $2.17{*}10^{-8}\ \mathrm{m^2/sec}$ as pressure was increased from 271.6 to 600.0 bar at 400°C in a 1 molal aqueous sodium nitrate solution. These are the only data available for molecular diffusion coefficients of salts in SCW. Lamb et al. [9] measured the self diffusion coefficient in SCW over the 400 to 700°C temperature range and 199 to 1459 bar pressure range. Molecular diffusion coefficients in gases and liquids are normally on the order of 10^{-5} and $10^{-9}\ \mathrm{m^2/s}$, respectively [10]; and those measured by Butenhoff et al. [8] and Lamb et al. [9] in SCW lie between those for gases and liquids. Butenhoff et al. [8] also measured the thermal diffusivity of the sodium nitrate-water solutions. Lewis numbers were between about 5 and 7 throughout the temperature (400–500°C), pressure (270–1000 bar) and concentration (0.25–3.0 molal) space investigated by Butenhoff et al. [8].

---

[1] Current address is: Bell Laboratories, Lucent Technologies, 700 Mountain Ave., Rm. 1C-433A, Murray Hill, NJ 07974, Hodes@lucent.com

Contributed by the Heat Transfer Division for publication in the JOURNAL OF HEAT TRANSFER. Manuscript received by the Heat Transfer Division October 20, 2000; revision received April 18, 2002. Associate Editor: J. Georgiadis.

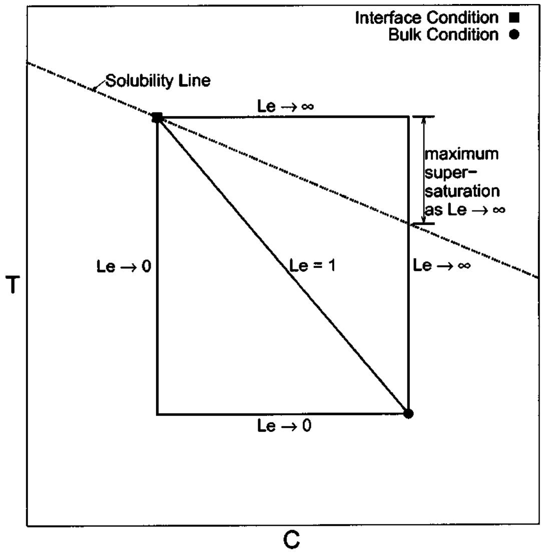

Fig. 1 Loci of temperature-concentration states connecting bulk and SLSI conditions for selected Lewis numbers. Below the solubility line is a one phase fluid region and above it a two phase, solid-fluid region.

Armellini et al. [11] performed shock-crystallization experiments to simulate the rapid precipitation of salts at typical SCWO conditions. Measured particle diameters for sodium sulfate and sodium chloride precipitates typically ranged from 1 to 20 microns and 5 to 100 microns, respectively, for the flow conditions investigated by Armellini et al. [11]. Brownian diffusion coefficients of particles in this size range may be calculated from the Stokes-Einstein equation and are several orders of magnitude smaller than the corresponding molecular diffusion coefficients. Moreover, the laminar natural convection mass transfer coefficient (h_m) for transport of salt from the bulk solution to the SLSI scales as the mass diffusion coefficient to the 3/4 power. Thus, if molecular clusters of salt nucleate homogeneously in the boundary layer and grow to Brownian-sized particles which diffuse to the SLSI, the deposition rate will be substantially slower than if salt molecules diffuse to the SLSI and then nucleate heterogeneously. Even when both particles and molecules diffuse to the SLSI, one expects that the deposition rate will be slower than for pure molecular diffusion because formation and growth of Brownian particles depletes the driving force for molecular diffusion.

The potential for homogeneous nucleation of salt in the natural convection boundary layer around the SLSI is investigated here. A qualitative relationship between the Lewis number of the aqueous salt solution, the phase boundary curve, and the potential for homogeneous nucleation is developed first. Then quantitative criteria are developed in order to predict whether or not supersaturation and/or homogeneous nucleation will occur within the boundary layer. The criteria are then applied to the conditions in the aforementioned deposition experiments. Next, characteristics of aqueous salt solutions conducive to supersaturation and/or homogeneous nucleation within the boundary layer are identified and specific solutions with such characteristics are discussed. Finally, the results of a nucleation experiment using lithium carbonate are presented.

Qualitative Relationship Between Lewis Number and Nucleation Mechanism

Figure 1 illustrates the relationship between the Lewis number of the aqueous salt solution, the phase boundary and the nucleation mechanism in the boundary layer. It shows a bulk solution condition, SLSI condition and a phase boundary which separates a one phase fluid region from a solid-fluid region. The phase boundary shown is linear, but the physics elucidated here also apply to a phase boundary with curvature. Throughout this paper, saturation conditions are assumed to exist at the SLSI. Trajectories of temperature-concentration (T,C) states connecting the bulk and SLSI conditions corresponding to solution Lewis numbers of 0, 1, and ∞ are also shown in Fig. 1. Note that Fig. 1 does not correspond to a constant heat flux boundary condition at the SLSI because the temperature difference between the SLSI and bulk solution is then a function of the thermophysical properties of the fluid, i.e., Lewis number, etc. This figure represents fixed temperatures at the SLSI and bulk conditions.

The ratio of the thermal boundary layer thickness to the concentration boundary layer thickness scales as a (positive) fractional power of Lewis number. Consequently, as the Lewis number approaches zero, the thermal boundary layer thickness becomes vanishingly small relative to the concentration boundary layer thickness and salt (solute) concentration decreases from its bulk value to its SLSI value at the bulk temperature. Analogously, temperature increases from its bulk value to its SLSI value at the SLSI concentration. The Le→∞ trajectory in Fig. 1 is analogous to that for Le→0. The rectangle bounded by the Le→0 and Le→∞ trajectories envelopes the physically plausible (T,C) states which may exist between the bulk and SLSI conditions. When the Lewis number equals one, dimensionless salt concentration equals dimensionless temperature throughout the boundary layer and a straight line connects the bulk and SLSI conditions. (Rigorously, this assumes that the non-dimensional boundary conditions for the energy and species equations are the same.) If homogeneous nucleation within the boundary layer is to be possible, the locus of (T,C) states within the boundary layer must cross the solubility line. Thus, if the phase boundary is linear and $\mathrm{Le} \leqslant 1$, homogeneous nucleation is not possible.

If nucleation does not occur in the boundary layer, the salt concentration corresponding to a given temperature must increase with solution Lewis number because of the reduced thickness of the concentration boundary layer relative to the thermal boundary layer. Moreover, beyond some critical Lewis number (Le_c), salt concentration will exceed the solubility concentration at the corresponding temperature; and supersaturation and/or homogeneous nucleation must occur. As the Lewis number is increased beyond its critical value, the amount of potential supersaturation increases and, therefore, homogeneous nucleation becomes more likely. In the limit as Le→∞, all of the flow field surrounding the heated cylinder is at the bulk concentration; hence, the level of potential supersaturation is at a maximum throughout the boundary layer. At sufficiently high levels of supersaturation, a metastable limit is surpassed and salt will precipitate from solution; however, metastable limits for solutes of interest are currently unavailable.

If constant power is supplied to the cylinder and salt is allowed to accumulate on it, the critical Lewis number will increase with time because the temperature of the SLSI decreases as its area increases. Figure 2 shows three successive loci of (T,C) states connecting a bulk condition to three respective SLSI conditions. The loci were computed from the analysis presented below and correspond to a solution for which $\mathrm{Le}=100$, $\mathrm{Pr}=0.72$, and $\tilde{N}$ (defined below) is of order 1. (The Prandtl number of (pure) water at a pressure of 250 bar is plotted in Fig. 3 by using thermophysical property data from the NIST Steam Tables [12]. For temperatures ranging from 200°C to 700°C it is between 0.79 and 2.0, except in the interval from 376°C to 405°C where it increases to about 8 at 385°C.) At the highest SLSI temperature shown in Fig. 2, the Lewis number of the solution exceeds the critical Lewis number and supersaturation and/or homogeneous nucleation occurs in the boundary layer. As the deposition process continues, a condition is reached such that the solution Lewis number equals the critical Lewis number. Finally, at the lowest SLSI temperature, the solution Lewis number is below the critical value and saturation conditions exist only at the SLSI.

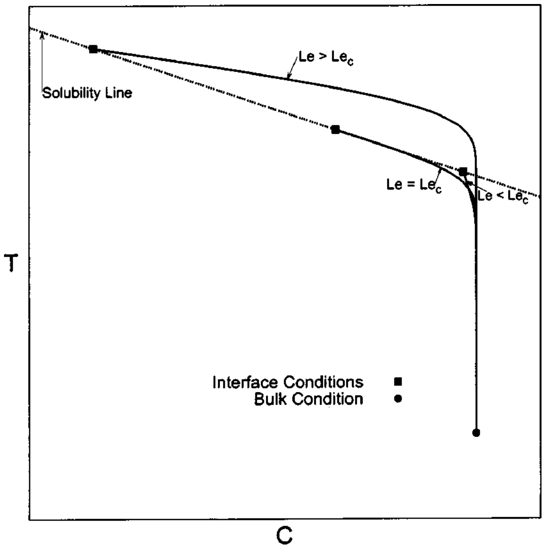

Fig. 2 Loci of (T,C) states connecting a bulk condition to three successive SLSI conditions. Loci correspond to Le=100, Pr=0.72, and $\tilde{N}$=O[1]

As steady-state conditions are approached, the SLSI concentration approaches the bulk concentration and the critical Lewis number approaches infinity. Since the Lewis number of any solution is finite, eventually salt must be transported to the SLSI exclusively by molecular diffusion. It is noted that, even if supersaturation is not present in the natural convective boundary layer formed adjacent to the nominal SLSI, nucleation is not necessarily confined to this nominal interface. Indeed, analyses suggest that a significant amount of heterogeneous nucleation and deposition occurs within the porous salt layer formed around the heated cylinder ([2,3]). The relationship between the solution Lewis number, the phase boundary, and the nucleation mechanism also applies to the analogous problem for which solubility increases with temperature and solute is deposited on a cooled cylinder as in the problem of fog formation.

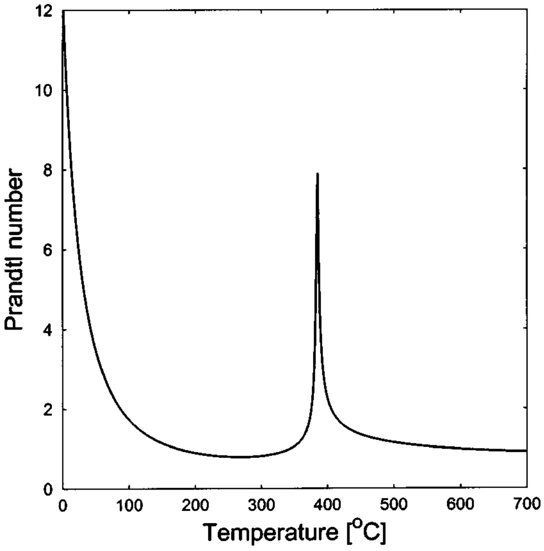

Fig. 3 Prandtl number of pure water versus temperature at a pressure of 250 bar

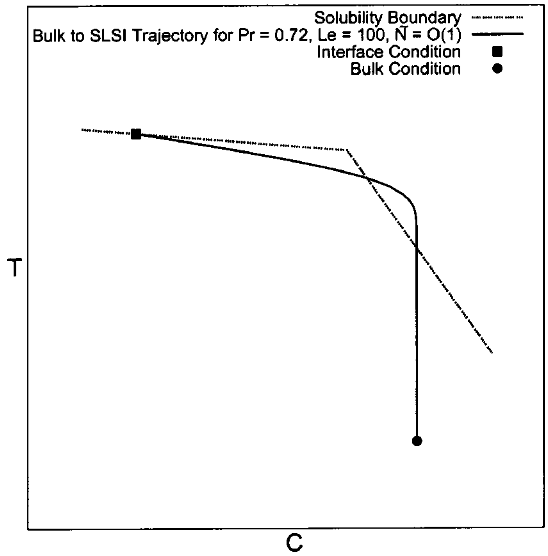

Fig. 4 Hypothetical set of conditions for which supersaturation and/or homogeneous nucleation occurs in the boundary layer, but $dT/dC|_i < dT/dC|_{\mathrm{sat},i}$

Quantitative Nucleation Criteria

A sufficient criterion for supersaturation and/or homogeneous nucleation to occur in the boundary layer is that dT/dC in the solution at the SLSI exceeds dT/dC of the phase boundary at the SLSI, i.e.,

$$\left.\frac{dT}{dC}\right|_i > \left.\frac{dT}{dC}\right|_{\mathrm{sat},i} \tag{1}$$

Although this criterion is necessary for supersaturation and/or homogeneous nucleation to occur for most systems, exceptions are possible. A phase boundary and trajectory of (T,C) states (at Pr =0.72, Le=100, $\tilde{N}$=O [1]) connecting bulk and SLSI conditions for which supersaturation and/or homogeneous nucleation must occur, but for which Eq. 1 is not satisfied, is shown in Fig. 4. In the usual case for which Eq. 1 applies, it follows from the definitions of the Nusselt and Sherwood numbers that the criterion for supersaturation and/or homogeneous nucleation to occur is:

$$\frac{\mathrm{Nu}_x}{\mathrm{Sh}_x} < \frac{C_i - C_B}{T_i - T_B}\left.\frac{dT}{dC}\right|_{\mathrm{sat},i} \tag{2}$$

In this paper, the SLSI is modeled as a constant temperature vertical flat plate adjacent to a double-diffusive natural convection boundary layer. Since saturation conditions are assumed at the SLSI, its concentration is also constant. The boundary conditions in the bulk solution are constant temperature and concentration and it follows that the ratio $\mathrm{Nu}_x/\mathrm{Sh}_x$ is a function of Le, Pr, and $\tilde{N}$ [13]. The dimensionless buoyancy parameter, $\tilde{N}$, is, for a parcel of fluid adjacent to the plate, simply the ratio of the concentration and temperature induced buoyancy forces, i.e.,

$$\tilde{N} = \frac{\beta^*(\rho_{A,i} - \rho_{A,\infty})}{\beta(T_i - T_\infty)} \tag{3}$$

where ρ_A is salt concentration in kg of salt per m^3 of solution. The volumetric coefficient of thermal expansion (β) and the species expansion coefficient (β^*) are defined by

$$\beta = -\frac{1}{\rho}\left.\frac{\partial \rho}{\partial T}\right|_{P,C} \tag{4}$$

$$\beta^* = -\frac{1}{\rho}\frac{\partial \rho}{\partial \rho_A}\bigg|_{P,T} \tag{5}$$

and a convenient form of the Grashof number is

$$\mathrm{Gr}_x = \frac{g\beta(T_i - T_\infty)x^3}{\nu^2} \tag{6}$$

For $\mathrm{Le} \gtrsim 1$, the ratio $\mathrm{Sh}_x/\mathrm{Nu}_x$ scales as approximately the Lewis number to the 1/3 power and, thus, an appropriate expression for it is

$$\frac{\mathrm{Nu}_x}{\mathrm{Sh}_x} = \frac{\Omega}{\mathrm{Le}^{1/3}}, \tag{7}$$

where Ω is a weak function of Le, Pr, and $\tilde{N}$. The critical Lewis number beyond which supersaturation and/or homogeneous nucleation occurs becomes:

$$\mathrm{Le}_c = \left[\frac{\Omega(T_i - T_B)}{(C_i - C_B)\left.\dfrac{dT}{dC}\right|_{\mathrm{sat},i}}\right]^3 \tag{8}$$

When the solution Lewis number equals 1, Ω equals 1 for all Pr and $\tilde{N}$ because the analogy between heat and mass transfer applies. At $\mathrm{Pr} = 0.7$ and $\tilde{N} = 0.5$, which are characteristic of the aforementioned deposition experiments [3], Ω equals 0.78 at $\mathrm{Le} = 14.29$ based on the results of Gebhart and Pera [13]. (Ω equals 0.86 for $\mathrm{Pr} = 7.0$, $\tilde{N} = 0.5$ and $\mathrm{Le} = 14.29$, i.e., it is in the same range even for the maximum Prandtl number of SCW at a pressure of 250 bar.) Based on the foregoing values, it is reasonable to assume that Ω equals approximately 0.9 for $1 \lesssim \mathrm{Le} \lesssim 15$, $1 \lesssim \mathrm{Pr} \lesssim 10$ and $\tilde{N} \simeq 0.5$. However, for the deposition experiments, the critical value of the Lewis number may be very much greater than 15 as shown below. Thus, an expression for Ω has been developed for the case in which $\mathrm{Le} \to \infty$.

Following Gebhart and Pera [13], it is convenient to introduce a similarity variable, η

$$\eta = \frac{y}{x}\left(\frac{\mathrm{Gr}_x}{4}\right)^{1/4} \tag{9}$$

and to express the stream function in terms of it

$$\Psi(x,y) = \left[4\nu\left(\frac{\mathrm{Gr}_x}{4}\right)^{1/4}\right] f(\eta) \tag{10}$$

The momentum, energy and species equations then become[2]

$$f''' + 3ff'' - 2f'^2 + \phi_T + \tilde{N}\phi_{\rho A} = 0 \tag{11}$$

$$\phi_T'' + 3\mathrm{Pr} f \phi_T' = 0 \tag{12}$$

$$\phi_{\rho A}'' + 3\mathrm{Sc} f \phi_{\rho A}' = 0 \tag{13}$$

subject to

$$f(0) = f'(0) = f'(\infty) = 1 - \phi_T(0) = 1 - \phi_{\rho A}(0) = \phi_T(\infty) = \phi_{\rho A}(\infty) = 0 \tag{14}$$

where dimensionless temperature and concentration are defined as

$$\phi_T = \frac{T - T_\infty}{T_i - T_\infty} \tag{15}$$

$$\phi_{\rho A} = \frac{\rho_A - \rho_{A,\infty}}{\rho_{A,i} - \rho_{A,\infty}} \tag{16}$$

Since, for $\mathrm{Le} \to \infty$ and $\mathrm{Pr} = \mathrm{O}(1)$, the mass transfer boundary layer is thin when compared with either the momentum or the thermal boundary layer thicknesses, the function $f(\eta)$ in Eq. 13 may be expanded in a Taylor series in which only the first nonzero term is retained for the "inner" problem, i.e., within the mass transfer boundary layer. In terms of a new spatial variable $\zeta = \eta \mathrm{Sc}^{1/3}$, the similarity formulation for the "inner" problem becomes

$$\frac{d^3 f}{d\zeta^3} - \frac{1}{2}[f''(0)]^2\ \mathrm{Sc}^{-5/3}\zeta^2 + \mathrm{Sc}^{-1}[\phi_T + \tilde{N}\phi_{\rho A}] = 0 \tag{17}$$

$$\frac{d^2\phi_T}{d\zeta^2} + \frac{3}{2}\mathrm{Le}^{-1} f''(0)\zeta^2 \frac{d\phi_T}{d\zeta} = 0 \tag{18}$$

$$\frac{d^2\phi_{\rho A}}{d\zeta^2} + \frac{3}{2} f''(0)\zeta^2 \frac{d\phi_{\rho A}}{d\zeta} = 0 \tag{19}$$

Equation 17 shows that $d^3 f/d\zeta^3$ is of order Sc^{-1} for $\tilde{N} \lesssim \mathrm{O}(1)$. It follows that the next term in the Taylor expansion for f (in terms of η) is smaller by a factor of $\mathrm{Sc}^{1/3}$ and is therefore negligible in the limit as $\mathrm{Sc} \to \infty$. Equation 19 can therefore be solved for $\phi_{\rho A}$ in terms of $f''(0)$. Moreover, $f''(0)$ can be obtained directly from the solution for the "outer" problem for which $\zeta \gg 1$ and $\eta = \mathrm{O}$ [1]. In this region, $\phi_{\rho A} \cong 0$ so Eqs. 11 and 12 become:

$$f''' + 3ff'' - 2f'^2 + \phi_T = 0 \tag{20}$$

$$\phi_T'' + 3\mathrm{Pr} f \phi_T' = 0 \tag{21}$$

subject to the boundary conditions on f and ϕ_T in Eq. 14. These equations are the conventional ones which apply in the absence of mass transfer and the tabulation of Gebhart [14] provides values for $f''(0)$ as a function of Pr.

To obtain the Sherwood number, Eq. 19 may be integrated once to give

$$\frac{d\phi_{\rho A}}{d\zeta} = K\exp\left[-\frac{1}{2}\mathrm{Sc} f''(0)\zeta^3\right] \tag{22}$$

and then integrated again. Application of the boundary conditions to the result of the second integration gives

$$K\int_0^\infty \exp\left[-\frac{1}{2}f''(0)\zeta^3\right]d\zeta = -1 \tag{23}$$

or

$$K = \frac{-3}{\Gamma(1/3)}\left[\frac{f''(0)}{2}\right]^{1/3} \tag{24}$$

where the gamma function ($\Gamma(z)$) is defined as (Abramowitz and Stegun [15])

$$\Gamma(z) = \int_0^\infty t^{z-1}e^{-t}dt \tag{25}$$

Finally,

$$h_m = -\mathcal{D}_{AB}\frac{\partial\phi_{\rho A}}{\partial\zeta}\bigg|_{y=0}\frac{\partial\zeta}{\partial y} \tag{26}$$

or

$$\mathrm{Sh}_x = 0.62849[f''(0)]^{1/3}\mathrm{Sc}^{1/3}\mathrm{Gr}_x^{1/4} \tag{27}$$

The effect of Prandtl number on the Sherwood number is embedded in the constant $f''(0)$. Gebhart and Pera [13] provide $f''(0)$ for $\mathrm{Pr} = 0.7$ and 7.0 as 0.67890 and 0.45069 respectively. The resulting Sherwood numbers are

---

[2] At the conditions in the deposition experiments, scale analysis shows that the Boussinesq approximation applies, the flow is quasi-steady, and the normal velocity at the SLSI is negligible [3]. All of these assumptions are made by Gebhart and Pera [13] to arrive at Eqs. 11 through 14. It is noted that the analysis by Gebhart and Pera [13] was slightly more general. The approach adopted here corresponds to Gebhart and Pera's result for $n = 0$, $P = 1$, and $Q = 0$.

Table 1 Summary of Ω values and their ranges of applicability

Pr	Sc	Le	$\tilde{N}$	Ω
All	Pr	1	All	1
0.7	10.0	14.29	0.5	0.78
0.7	$\rightarrow\infty$	$\rightarrow\infty$	O[1]	0.72
7.0	100.0	14.29	0.5	0.86
7.0	500	71.43	0.5	0.83
7.0	$\rightarrow\infty$	$\rightarrow\infty$	O[1]	0.81

$$\mathrm{Sh}_x = 0.536\mathrm{Le}^{1/3}\mathrm{Ra}_x^{1/4} \quad \text{for Pr}=0.7,\ \mathrm{Le}\rightarrow\infty,\ \tilde{N}=\mathrm{O}[1] \tag{28}$$

$$\mathrm{Sh}_x = 0.567\mathrm{Le}^{1/3}\mathrm{Ra}_x^{1/4} \quad \text{for Pr}=7.0,\ \mathrm{Le}\rightarrow\infty,\ \tilde{N}=\mathrm{O}[1] \tag{29}$$

Sherwood numbers at other Prandtl numbers may be computed using the tabulation of $f''(0)$ as a function of Prandtl number available in Gebhart et al. [14]. When the Lewis number equals one, the heat and mass transfer analogy applies and $\mathrm{Sh}_x = \mathrm{Nu}_x$. At Le=1 and Pr=Sc=0.7, for example, $\mathrm{Sh}_x = \mathrm{Nu}_x = 0.386\mathrm{Ra}_x^{1/4}$ (Gebhart and Pera [13]) and thus the constant in Eq. 28 (0.536) is 39 percent too high as a consequence of the Taylor series approximation for $f(\eta)$ in the "inner" region. Actually, a 39 percent error is surprisingly small considering that Sc is only 0.7. Moreover, the results of the Gebhart and Pera [13] study at, for example, Pr=7 and Sc=500, may be used to validate Eq. 27 for high Sc numbers. When Eq. 27 is used, the constant which multiplies $\mathrm{Gr}_x^{1/4}$ is found to be high by 1.9 percent, low by 0.3 percent, and low by 3.8 percent for $\tilde{N}$ equal to 0.5, 1, and 2 respectively relative to the results of Gebhart and Pera [13] for Pr=7 and Sc=500. Values of Ω calculated from the foregoing results have been summarized in Table 1. The most striking observation which emerges from the comparison is the simple fact that Ω does not vary much.

Given the value of K, Eq. 22 can also be integrated to provide the solute concentration profile in the boundary layer. The result is

$$\phi_{\rho A} = 1 - P\left(\frac{1}{3}, \frac{f''(0)\mathrm{Sc}\,\eta^3}{2}\right) \quad \text{for Le}\rightarrow\infty \quad \text{and} \quad \tilde{N}=\mathrm{O}[1] \tag{30}$$

where $P(a,x)$ is the incomplete gamma function defined by Abramowitz and Stegun [15]. Loci of temperature-concentration states in the boundary layer may be computed from this result, together with those of Ostrach [16] and others for $\phi_T(T)$. Although the asymptotic expressions for Sherwood number (Eq. 27) and $\phi_{\rho A}$ (Eq. 30) were developed in the limit as Le→∞, they also apply at physically realistic Le numbers. The form of the species equation given by Eq. 19 could, following Lèvêque [17], have been obtained by assuming a linear velocity profile in the concentration boundary layer. This "Lèvêque approach" suggests a procedure by which the requirement that $\mathrm{Sc}^{1/3}$ be much greater than one may be made more quantitative. In particular, it is apparent that the method cannot be appropriate if the concentration boundary layer extends beyond the point at which the velocity is a maximum. Thus, a rough criterion may be obtained by using Eq. 30 to determine the thickness of the concentration boundary layer (by determining the value of $\mathrm{Sc}f''(0)\eta^3$ at which the dimensionless concentration is 0.01) and comparing the result with the value of η at which the velocity is a maximum. This procedure requires that Sc exceed 8 for Pr=0.7 and 25 for Pr=7.0. In each case, the value is rather modest. This is consistent with the observation above that the Sherwood number expression given by Eq. 28 is "surprisingly" accurate even at Pr=Sc=0.7.

Table 2 Prediction of critical Lewis numbers at the beginning of the deposition experiments and after 6 and 12 minutes of run time. Relevant temperatures and concentrations at the beginning of the experiments are also provided.

SALT -	C_{in} wt%	T_{Bo} °C	T_{io} °C	C_{Bo} wt%	C_{io} wt%	Le_c at 0^+, 6, 12 min
Na_2SO_4	2	363.3	373.2	1.51	0.42	4.8, 7.2, 18.0
Na_2SO_4	4	355.0	365.6	3.51	2.42	7.2, 12.1, 18.0
Na_2SO_4	6	347.7	358.5	5.52	4.43	9.5, 17.8, 28.1
Na_2SO_4	8	340.8	352.4	7.54	6.29	9.7, 18.7, 30.5
K_2SO_4	2	374.7	383.9	1.64	0.76	132, 628, 2342
K_2SO_4	4	372.0	381.8	3.48	2.19	51, 222, 714
K_2SO_4	6	369.0	379.1	5.44	4.01	41, 177, 557
K_2SO_4	8	366.1	376.6	7.36	5.68	28, 113, 327

Application of Theory to Experiments

Based on the results of the preceding analyses, Ω is set equal to 0.72 to provide a conservative estimate of the minimum critical Lewis numbers in the deposition experiments run by Hodes et al. [1]. The calculations are conservative in that Ω is at least 0.72 in accordance with Table 1 and the critical Lewis number is proportional to Ω^3. Based on the results of the Butenhoff et al. [8] study discussed above, Lewis numbers of aqueous sodium sulfate and potassium sulfate solutions are likely about 5 at the experimental conditions. Critical Lewis numbers at the beginning of the sodium sulfate and potassium sulfate deposition experiments and 6 and 12 minutes into each run are provided in Table 2. There is a modest cross flow of aqueous salt solution past the heated cylinder and the "inlet" concentration of salt (C_{in}) is that of the solution entering the test cell. The values of C_i, C_B, and T_i have been extracted from the modeling results of Hodes [3] and T_B has been measured by Hodes et al. [1]. At the beginning of the sodium sulfate deposition experiments, the critical Lewis number ranges from 4.8 to 9.7. It is unlikely that the Lewis numbers of the aqueous sodium sulfate solutions substantially exceed 4.8, if at all. After 12 minutes of run time have elapsed, the critical Lewis numbers range from 18.0 to 30.5. It is highly unlikely that the Lewis numbers of the aqueous sodium sulfate solutions are as high as 18.0. Few, if any, particles were observed in the boundary layer formed around the heated cylinder during the sodium sulfate deposition experiments (Hodes [3]) which is consistent with the critical Lewis numbers in Table 2. At the beginning of the potassium sulfate deposition experiments, the critical Lewis numbers range from 28 to 132. It is extremely unlikely that the Lewis numbers of the aqueous potassium sulfate solutions exceed 28. Thus the fact that particles were not observed during the potassium sulfate deposition experiments is consistent with the theory.

The critical Lewis numbers as a function of run time corresponding to the experiments in which the sodium sulfate and potassium sulfate concentrations in the inlet stream were 4 wt percent are plotted in Fig. 5. After only thirty minutes the critical Lewis number has increased by factors of about 6 and 250 at conditions corresponding to the sodium sulfate and potassium sulfate runs, respectively. The increase in the critical Lewis number for the potassium sulfate conditions over the same time interval is substantially larger because the thermophysical properties of the solutions are significantly different.[3] Even if homogeneous nucleation in the boundary layer were to occur at the beginning of a sodium sulfate experiment, it is evident from Fig. 5 that it would cease long before steady state conditions were reached. Homogeneous nucleation could dramatically increase the time required to establish steady state conditions, however. The very low Brown-

---

[3] Both experiments were run at a pressure of 250 bar which is substantially above the critical pressure of pure water (221 bar). However, the temperature of the potassium sulfate solution around the heated cylinder is very close to the critical temperature of pure water (374°C) as per Table 2.

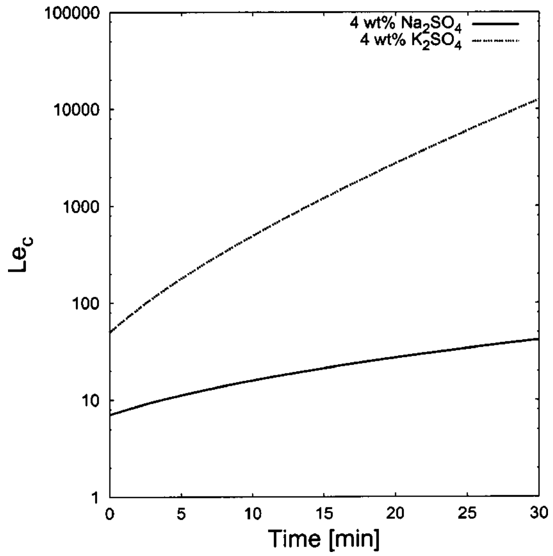

Fig. 5 Critical Lewis number as a function of time for the sodium sulfate and potassium sulfate deposition experiments in which the concentration of salt in the inlet stream was 4 wt percent

ian diffusion coefficients of particles would substantially retard deposition until enough salt accrued on the heated cylinder for the nucleation mechanism to be predominantly heterogeneous.

Trajectories of temperature-composition states which connect the bulk solution condition to the SLSI condition when the inlet concentration of sodium sulfate or potassium sulfate in the inlet stream was 4 wt percent are plotted in Figs. 6 and 7 respectively. The bulk and SLSI conditions shown correspond to the beginning of the experiments. When the Lewis number of the solution is 100 or larger, we assume that Eq. 30 applies and plot complete trajectories (for Pr=0.72); otherwise, partial trajectories are plotted by expressing Eq. 7 as:

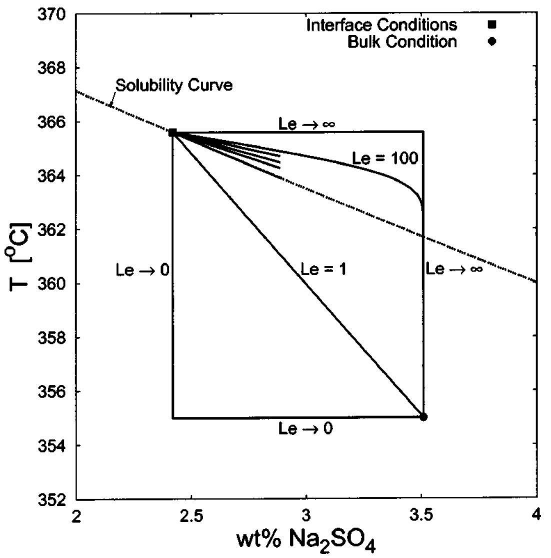

Fig. 6 Trajectories of (T,C) states connecting bulk and SLSI conditions at the beginning of the sodium sulfate deposition experiments for which C_{in} equals 4 wt percent. Unlabeled trajectories correspond to Le=15, 50.6, and 75, respectively, between the Le=1 and Le=100 trajectories.

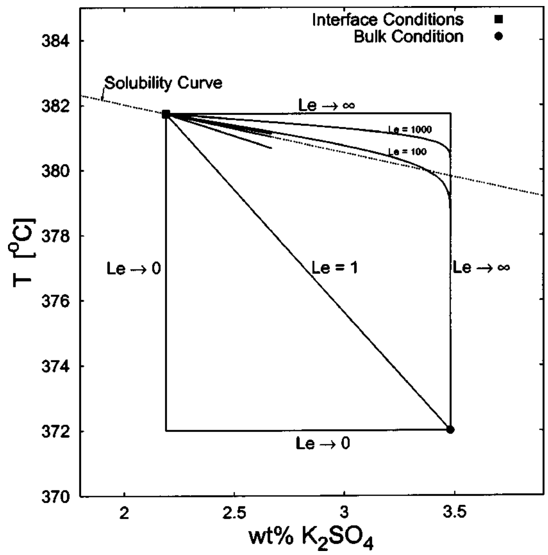

Fig. 7 Trajectories of (T,C) states connecting bulk and SLSI conditions at the beginning of the potassium sulfate deposition experiments for which C_{in} equals 4 wt percent. Unlabeled trajectories correspond to Le=7.2, 15, 25, and 50 respectively between the Le=1 and Le=100 trajectories.

$$\left.\frac{dT}{dC}\right|_i=\frac{\Omega}{\mathrm{Le}^{1/3}}\frac{T_i-T_B}{C_i-C_B} \tag{31}$$

where Ω is set equal to 0.72.

The four partial trajectories between Le=1 and Le=100 in Fig. 6 correspond to Le=7.2, 15, 25, and 50 respectively. The critical Lewis number at the beginning of the (4 wt percent inlet concentration) sodium sulfate deposition experiments equals 7.2 as indicated in the figure. It is likely that the Lewis number of the aqueous sodium sulfate solution is about equal to this critical Lewis number and this is consistent with few, and often zero, particles being observed in the sodium sulfate deposition experiments. The three partial trajectories shown in Fig. 7 for the potassium sulfate experiments between Le=1 and Le=100 correspond to Le=15, 50.6, and 75 respectively. The critical Lewis number is 50.6. The actual Lewis number of the aqueous potassium sulfate solution is likely to be much less than this value and, thus, the fact that particles were not observed during the potassium sulfate deposition runs is consistent with the nucleation theory. It is noted that even at a Lewis number equal to 1000, less than 2°C of (possible) supersaturation is predicted and therefore homogeneous nucleation may not occur.

Candidates for Homogeneous Nucleation

Since high Lewis number aqueous salt solutions are conducive to supersaturation and/or homogeneous nucleation in the boundary layer, large molecular diameter/mass salts are prime candidates for homogeneous nucleation. The uranyl fluoride-water (UO_2F_2-H_2O) system, for example, is one worthy of consideration. Uranyl fluoride is a rather large molecule with a molecular mass of 308.02 gm/gmol as compared to 142.04 and 174.27 gm/gmol for sodium sulfate and potassium sulfate respectively and all three salts precipitate from solution at similar temperatures. Thus, it is likely that the Lewis numbers of aqueous uranyl fluoride solutions exceed those of aqueous sodium sulfate and potassium sulfate solutions, making supersaturation and/or homogeneous nucleation more likely as well. Marshall et al. [18] determined the temperature-composition equilibrium diagram for the UO_2F_2-H_2O system and Hodes [3] outlines how nucleation experiments could be performed.

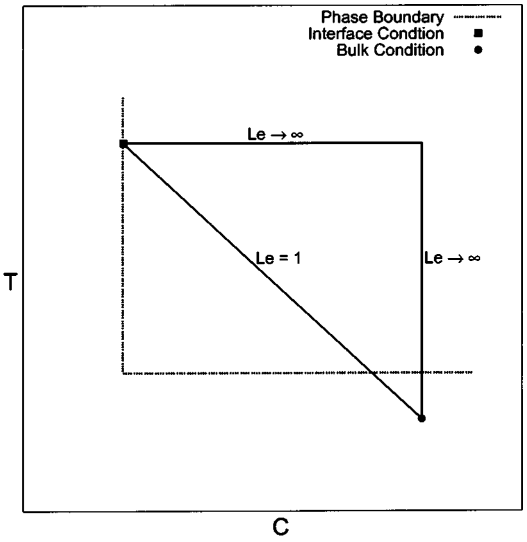

Fig. 8 Idealized phase boundary conducive to homogeneous nucleation in the boundary layer and trajectories connecting bulk and SLSI conditions for Le=1 and Le→∞

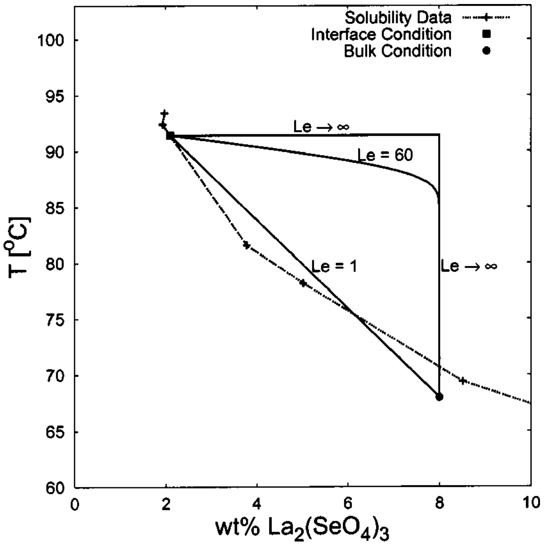

Fig. 9 Lanthanum selenate solubility data (Friend [21]) and trajectories connecting bulk and SLSI conditions at Le=1, Le =60, and Le→∞

Generally, Lewis numbers of binary gas mixtures are about two orders of magnitude smaller than those of binary liquid solutions. For example, Lewis numbers of mixtures of air with various species are of order 1, while those of ordinary aqueous solutions are of order 100 ([13]). Hence, salts which precipitate from aqueous solutions at liquid-like densities are prime candidates to homogeneously nucleate in the boundary layer. The solubility of many salts in water decreases substantially over temperature ranges below 150°C, i.e., at liquid-like conditions. Some examples include sodium orthophosphate [Na_3PO_4], magnesium sulfate [$MgSO_4$], lanthanum selenate [$La_2(SeO_4)_3$] and lithium carbonate [Li_2CO_3] (Linke [19]; Stephen and Stephen [20]). The latter two salts are subsequently discussed in some detail. In addition to the Lewis number of the aqueous salt solution, the phase boundary can also dramatically affect the probability that salt will homogeneously nucleate in the boundary layer. The shape of the hypothetical phase boundary shown in Fig. 8, for example, is extremely conducive to homogeneous nucleation. Interestingly, the shape of this idealized phase boundary is identical to that of the Le→0 trajectory connecting bulk and SLSI conditions shown in Fig. 1.

The solubility of lanthanum selenate in water was determined in a study by Friend [21] and is shown in Fig. 9. (Pressures were not reported.) The phase boundary mimics the idealized phase boundary in Fig. 8 to a significant degree. Moreover, lanthanum selenate is a very large molecule with a molecular mass of 706.69 gm/gmol. Trajectories which connect a bulk condition to a SLSI condition corresponding to Le=1 and Le=60 are also shown in Fig. 9. To compute the Le=60 trajectory, the solution Prandtl number was set equal to 2 which is that of pure water in the relevant temperature range. (Thus Sc=120 and Eq. 30 is valid.) Even at a Lewis number of one, supersaturation and/or homogeneous nucleation is expected to occur. Given the very large size of the lanthanum selenate molecule, a Lewis number of 60 or higher is quite likely. At a Lewis number of 60, 20°C of supersaturation would occur at the proposed conditions in the absence of homogeneous nucleation in the boundary layer. Thus lanthanum selenate is a prime candidate to nucleate homogeneously in the boundary layer formed around the SLSI.

Linke [19] compiled the solubility data for lithium carbonate in water shown in Fig. 10 from sources dating back to the late 19th century. Based on these data, a nucleation experiment was conducted in an effort to validate, at least for one salt, the theory developed in this paper at conditions where a salt would be expected to become supersaturated and/or nucleate homogeneously in the boundary layer. The measured bulk solution and cylinder temperatures have an uncertainty of ±4.2°C and the uncertainty of the cell pressure measurement is ±0.15 MPa ([3]).

An aqueous lithium carbonate (1 wt percent) solution preheated to 53°C was circulated through the flow system described by Hurst et al. [7] in which the test cell was visually accessible and illuminated by white light. (The pressure in the experiment was 250 bar.) Power supplied to the heated cylinder within the bulk solution increased the measured surface temperature to about 71°C and the SLSI condition which would be achieved if deposition were to occur in the absence of homogeneous nucleation is labeled "Theoretical Initial SLSI Condition" in Fig. 10. A trajectory corresponding to Le=60 and Pr=2 which connects the initial bulk and theoretical initial SLSI conditions is also shown. (Since lithium carbonate precipitates from solution at liquid-like densities, a Lewis number of at least 60 is a reasonable expectation.) At

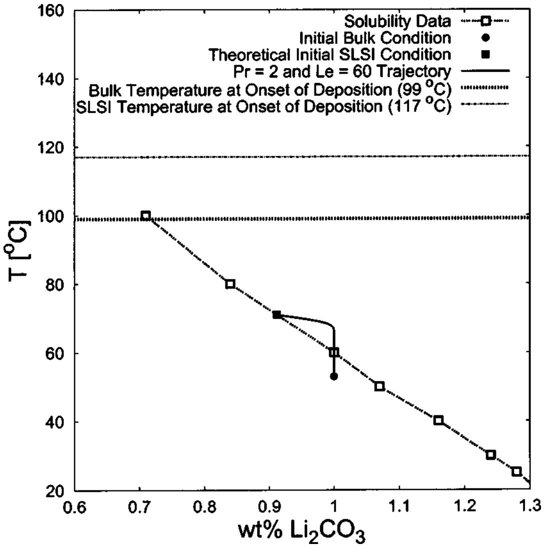

Fig. 10 Lithium carbonate solubility data (Linke [19]) and trajectory connecting bulk and SLSI conditions at Le=60. Solubility boundary separates one phase fluid region from two phase, solid-fluid region.

Le=60, about 10°C of supersaturation is predicted to occur in the absence of homogeneous nucleation. However, deposition and/or nucleation were not observed at these conditions during one hour of elapsed time. Metastability within the aqueous lithium carbonate solution may explain why deposition and/or nucleation were not observed at these conditions. Thus, in an effort to overcome metastability in case it were present, the bulk temperature of the solution in the cell was gradually ramped upward at the rate of approximately 1°C/min. At a bulk temperature of about 99°C and heated cylinder surface temperature of about 117°C, deposition began. Moreover, bright bursts of light were observed around the heated cylinder and especially in the plume above it at a frequency of about 0.5–3 hertz throughout the deposition process which was allowed to continue for about one hour. Very probably, the bright bursts of light were reflected from lithium carbonate particles which homogeneously nucleated in the boundary layer. Nothing resembling these bright bursts of light was observed during the sodium sulfate and potassium sulfate deposition experiments.

Conclusions

A model has been developed to predict whether or not homogeneous nucleation and/or supersaturation would occur in a natural convection boundary layer around a cylinder heated beyond the solubility temperature corresponding to the concentration of salt in the surrounding aqueous salt solution. It was shown that the Lewis number is the critical property in determining whether or not homogeneous nucleation is possible and a simple formula was developed to predict the Lewis number below which homogeneous nucleation is not possible for a given solubility boundary and set of operating conditions. The model was applied to the conditions for which sodium sulfate and potassium sulfate deposition experiments were run by Hodes et al. [1] and yielded consistent results, i.e., homogeneous nucleation was predicted to be absent. Attributes of aqueous salt solutions which increase the likelihood of homogeneous nucleation were identified. A lithium carbonate deposition experiment was performed at conditions for which homogeneous nucleation was expected and evidence strongly suggests that it occurred.

Nomenclature

C = salt concentration [wt percent]
$\mathcal{D}_{AB}$ = mass diffusion coefficient [m^2/s]
f = dimensionless function of η defined by stream function
g = acceleration due to gravity [m/s^2]
Gr = Grashof number
h_m = mass transfer coefficient [m/s]
Le = Lewis number
$\tilde{N}$ = dimensionless buoyancy parameter
Nu = Nusselt number
Pr = Prandtl number
Ra = Rayleigh number
Sc = Schmidt number
Sh = Sherwood number
T = temperature [°C]
u = x-direction velocity [m/s]
v = y-direction velocity [m/s]
x = coordinate direction parallel to gravity
y = coordinate direction perpendicular to gravity

Greek Symbols

β = volumetric coefficient of thermal expansion [1/°C]
β^* = species expansion coefficient [m^3/kg A]
η = dimensionless similarity parameter (Eq. 9)
ν = kinematic viscosity [m^2/s]
Ω = $\mathrm{Nu}_x \mathrm{Le}^{1/3}/\mathrm{Sh}_x$
ρ = density [kg/m^3]
ρ_A = solute (salt) concentration [kg A/m^3]
$\phi_{\rho A}$ = dimensionless salt concentration
ϕ_T = dimensionless temperature
Ψ = stream function [m^2/s]
ζ = spatial variable ($\eta \mathrm{Sc}^{1/3}$)

Subscripts

A = salt component of solution
B = bulk
c = critical
i = salt layer-solution interface (SLSI)
in = inlet to test cell
o = beginning of experiment
P = pressure
sat = saturation

References

[1] Hodes, M., Smith, K. A., Hurst, W. S., Bowers, Jr., W., Griffith, P., and Sako, K., 2002, ‘‘Solubilities and Deposition Rates in Aqueous Sulfate Solutions at Elevated Temperatures and Pressure,’’ submitted to Int. J. Heat Mass Transfer.
[2] Hodes, M., Smith, K. A., and Griffith, P., 2002, ‘‘A Natural Convection Model for the Rate of Salt Deposition from Near-Supercritical, Aqueous, Salt Solutions,’’ submitted to J. Heat Transfer.
[3] Hodes, M., 1998, ‘‘Measurements and Modeling of Deposition Rates from Near-Supercritical, Aqueous, Sodium Sulfate and Potassium Sulfate Solutions to a Heated Cylinder,’’ Ph.D. thesis, Massachusetts Institute of Technology, Cambridge, MA.
[4] Tester, J. W., Holgate, H. R., Armellini, F. J., Webley, P. A., Killilea, W. R., Hong, G. T., and Barner, H. E., 1991, ‘‘Supercritical Water Oxidation Technology: A Review of Process Development and Fundamental Research,’’ ACS Symp. Ser., **518**.
[5] Gloyna, E. F., and Li, L., 1998, ‘‘Supercritical Water Oxidation for Wastewater and Sludge Remediation,’’ *Encyclopedia of Environmental Analysis and Remediation*, R. A. Meyers, ed., John Wiley and Sons, Inc., pp. 4780–4797.
[6] Shaw, R. W., and Dahmen, N., ‘‘Destruction of Toxic Organic Materials Using Super-Critical Water Oxidation: Current State of the Technology,’’ *Supercritical Fluids: Fundamentals and Applications*, E. Kiran, P. G. Debenedetti and C. J. Peters, eds., Kluwer Academic Publishers, Dordrecht, The Netherlands.
[7] Hurst, W. A., Hodes, M. S., Bowers, Jr., W., Bean, V. E., Maslar, J. E., Smith, K. A., and Griffith, P., 2002, ‘‘Optical Flow Cell and Apparatus for Solubility, Salt Deposition and Raman Spectroscopic Studies in Aqueous Solutions near the Water Critical Point,’’ J. Supercrit. Fluids, **22**(2), pp. 157–166.
[8] Butenhoff, T. J., Goemans, M., and Buelow, S. J., 1996, ‘‘Mass Diffusion Coefficients and Thermal Diffusivity in Concentrated NaNO$_3$ Solutions,’’ J. Phys. Chem., **100**, pp. 5982–5992.
[9] Lamb, W. J., Hoffman, G. A., and Jonas, J., 1981, ‘‘Self-Diffusion in Compressed Super-Critical Water,’’ J. Chem. Phys., **74**(12), pp. 6875–6880.
[10] Fogler, H. S., 1992, *Elements of Chemical Reaction Engineering*, Prentice Hall.
[11] Armellini, F. J., Tester, J. W., and Hong, G. T., 1994, ‘‘Precipitation of Sodium Chloride and Sodium Sulfate in Water from Sub- to Supercritical Conditions: 150 to 550°C, 100 to 300 bar,’’ J. Supercrit. Fluids, **7**, pp. 147–158.
[12] Harvey, A. H., Peskin, A. P., and Klein, S. A., 2000, ‘‘NIST/ASME Steam Properties: Version 2.2,’’ U.S. Department of Commerce.
[13] Gebhart, B., and Pera, L., 1971, ‘‘The Nature of Vertical Natural Convection Flows Resulting from the Combined Buoyancy Effects of Thermal and Mass Diffusion,’’ Int. J. Heat Mass Transf., **14**, pp. 2025–2050.
[14] Gebhart, B., Jaluria, Y., Mahajan, R., and Sammakia, B., 1988, *Buoyancy-Induced Flows and Transport*, Hemisphere Publishing Corporation.
[15] Abramowitz, M., and Stegun, I. A., 1965, *Handbook of Mathematical Functions*, Dover Publications.
[16] Ostrach, S., 1953, ‘‘An Analysis of Laminar Free-Convection Flow and Heat Transfer about a Flat Plate Parallel to the Direction of the Generating Body Force,’’ Technical Report 1111, NACA.
[17] Lèvêque, J., 1928, Annales des Mines, **12**(13), pp. 305 and 381.
[18] Marshall, W. L., Gill, J. S., and Secoy, C. H., 1954, ‘‘Phase Equilibria of Uranium Trioxide and Aqueous Hydrofluoric Acid in Stochiometric Concentrations,’’ J. Am. Chem. Soc., p. 4279.
[19] Linke, W., 1958, *Solubilities of Inorganic and Metal-Organic Compounds: A Compilation of Solubility Data from the Periodical Literature*, D. Van Nostrand Company Inc.
[20] Stephen, H., and Stephen, T., 1963, *Solubilities of Inorganic and Organic Compounds: Volume 1-Binary Systems*, Macmillan.
[21] Friend, J. A. N., 1932, ‘‘The Selenates of Lanthanum and Their Solubilities in Water,’’ J. Chem. Soc., p. 1597.

Thermal Aspects in the Continuous Chemical Vapor Deposition of Silicon

Hoseon Yoo
Department of Mechanical Engineering,
Soongsil University,
Seoul 156-743, Korea

Yogesh Jaluria
Fellow ASME
e-mail: jaluria@jove.rutgers.edu
Department of Mechanical
and Aerospace Engineering,
Rutgers, The State University of New Jersey,
New Brunswick, NJ 08854

This paper deals with the continuous chemical vapor deposition of silicon in a horizontal cold wall reactor, paying special attention to a moving susceptor. A two-dimensional numerical model, which accounts for variable properties, thermal diffusion, radiative heat exchange among surfaces, and conjugate heat transfer between the gas and susceptor, is developed and validated. Scale analysis for the susceptor energy balance enables the identification of the characteristic parameters and the prediction of their qualitative effects before carrying out a detailed analysis. The results from the scale analysis are found to be consistent with the numerical predictions. The results show that the present continuous system is characterized by two newly defined parameters: conductance ratio and susceptor parameter. A pair of performance curves that relate the deposition efficiency to each parameter successfully provide the susceptor-related design conditions. It is also revealed that there exists an optimum length of heating zone that maximizes the deposition efficiency. [DOI: 10.1115/1.1482084]

Keywords: Conjugate, Heat Transfer, Mass Transfer, Radiation, Thin Films, Vapor Deposition

Introduction

Chemical vapor deposition (CVD) is an important method for manufacturing thin films. Since thin films prepared by CVD have many attractive features, such as large area coverage, good control of film structure and composition, and conformal deposition, the technology is being employed in a variety of areas. Engineering applications include the fabrication of microelectronic circuits, wear- and corrosion-resistant coatings, recording media, solar cells, and optical devices. In view of ever increasing demands on the deposition performance, one of the most important issues in the future CVD technology is the productivity. The requirement of higher throughputs necessitates new or refined designs in CVD systems.

From the viewpoint of processing, most of the previous studies on CVD have dealt with batch systems, where a limited number of substrates or wafers placed on a stationary or rotating susceptor are processed at one time. A number of existing reactors that have evolved to meet the requirements, especially deposition uniformity, arising from various applications belong to the same category. Research efforts for modeling transport phenomena occurring in these reactors and chemical reactions involved in deposition processes have been reviewed by Jensen et al. [1], Kleijn [2], and Mahajan [3]. The productivity of batch processing is essentially limited by downtime associated with product loading, reactor startup, and shutdown.

One of the ways to improve production throughput in CVD systems is to adopt continuous processing. The feasibility and utility of continuous processing have been exploited in a number of industrial applications. Yamaji et al. [4] reported that their continuous CVD siliconizing line succeeded in the manufacture of a silicon-coated steel sheet. Stevenson and Matthews [5] suggested design criteria for continuous processing of a plasma-assisted physical vapor deposition (PVD) equipment through cost analysis. Onabe et al. [6] prepared superconducting tapes using a continuous CVD technique. In addition, continuous CVD processing has been actively applied to coatings of glass [7] and fiber [8,9]. These works have addressed experimental conditions, film properties, conceptual designs, or equipment development, but have lacked detailed descriptions of processes and transport phenomena occurring in the reactor, that are needed for appropriate understanding and modeling of continuous systems.

Recently, Chiu and Jaluria [10,11] have proposed two types of continuous CVD systems based on a horizontal reactor, modeled deposition processes, and assessed their feasibility as alternatives to batch processing. One of these systems, where a finite thickness susceptor moves along the reactor bottom wall in a straight channel horizontal reactor [11], is somewhat simpler and more flexible. Such a layout allows for uninterrupted operation, precluding the concern with downtime. Moreover, film uniformity is not of primary concern since the susceptor moving at a constant speed, under steady state, experiences the same amount of deposition over the entire reactor length. This system resembles practically used injector-based atmospheric CVD reactor [12,13] in that they commonly adopt a moving susceptor, on which wafers are continuously and compactly placed, to achieve uniform deposition and high throughput. Although some basic aspects have already been presented, the continuous system needs to be revisited for better understanding of its nature and for obtaining the performance characteristics applicable to design. In addition, the effects of conjugate heat transfer and susceptor motion need to be quantified.

Motivated by such necessity, the present study considers the same continuous system as the previous work [11]. The prospect of its adoption in the practical process seems to be encouraging since it is simpler in layout than the injector-based reactor mentioned earlier. We investigate transport phenomena and chemical reactions accompanying the deposition process while paying special attention to the moving susceptor. The numerical model encompasses variable properties, thermal diffusion, radiative exchange among surfaces, and conjugate heat transfer between the gas phase and moving solid susceptor. A useful feature of this work lies in the use of scale analysis, as complementary to the numerical simulation, in identifying the characteristic parameters and analyzing the predicted results. In order to represent the performance of continuous CVD processing, a deposition efficiency is defined and interpreted. The characteristics and importance of

---

Contributed by the Heat Transfer Division for publication in the JOURNAL OF HEAT TRANSFER. Manuscript received by the Heat Transfer Division August 17, 2001; revision received March 19, 2002. Associate Editor: C. Amon.

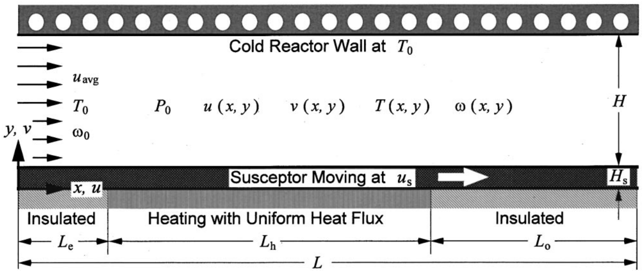

Fig. 1 Schematic of the present continuous chemical vapor deposition system

newly defined parameters, as well as of performance curves expressed as a function of these parameters, are discussed in detail. The optimization of the process in terms of the heat supplied to the system is also addressed.

Analysis

Physical System. The continuous CVD system dealt with in this study is depicted in Fig. 1. It is a horizontal reactor, where a finite thickness susceptor is allowed to move along the bottom wall. The moving finite thickness susceptor models the combination of wafers (or substrates) and a thin conveyor belt carrying compactly placed wafers on it. Continuous deposition processing is made possible by such susceptor motion. Silicon deposition from silane (SiH_4) diluted in hydrogen (H_2) carrier gas is chosen, not only because there have been extensive studies on its chemistry [2,3,14–16], but also because experimental data for model validation are readily available [17].

Gases flow in and out of the reactor at the atmospheric pressure P_0. Note here that continuously moving susceptors are particularly suited for atmospheric reactors due to easier sealing [12,13]. The susceptor moves at a constant speed u_s in the direction of bulk gas flow. The bottom wall consists of three zones: entrance, heating, and outlet, the first and last of which are thermally insulated. A uniform heat flux is supplied to the susceptor through the heating zone, enabling silane to react and deposit silicon onto the surface. The upper reactor wall is composed of silica and mirror-like coating on the outer surface, being radiatively opaque. In order to prevent unwanted deposition, the upper wall is water cooled to the ambient temperature. Due to conduction and heat conveyed by the susceptor motion, chemical vapor deposition can take place all along the reactor length, which makes the length of heating zone an important variable. For a given total heat input, as an example, changes in the length of the heating zone give rise to different temperature profiles, thereby altering the overall growth rates.

The present study focuses primarily on the moving susceptor. All operating conditions and geometric factors, except those relevant to the susceptor, are fixed at typical values [11,17,18]. The reactor channel is taken as 0.02 m high by 0.7 m long ($H\times L$). Gas enters the reactor at the average velocity (u_{avg}) of 0.175 m/s under $P_0=1$ atm and $T_0=300$ K. The cold wall temperature (T_0) is also set at 300 K. The partial pressure of silane (P_{SiH_4}) at the inlet is taken as 124.1 Pa, from which the inlet mass fraction ω_0 is calculated. A total heat input (Q_t) of 30 kW is chosen so that the susceptor surface temperature attains the experimental conditions in the presence of radiation heat exchange [17]. Finally, the lengths of entrance (L_e) and heating zones (L_h) are taken as 0.1 and 0.3 m, respectively, unless specified otherwise.

Mathematical Model. In horizontal CVD reactors two-dimensional modeling is valid if the channel width-to-height (aspect) ratio is large and forced convection is dominant [19]. For the system under consideration, buoyancy effects were earlier shown to be negligible.[11] Assuming that the present reactor is wide enough, we can employ a two-dimensional model. In describing two-dimensional steady-state transport phenomena occurring in the reactor, some commonly accepted assumptions have been introduced [1–3,14]. The flow is taken as laminar with negligible viscous dissipation effects. Note that the present operating conditions correspond to the Reynolds number of 32 when based on the inlet conditions and channel height. The gases are regarded as ideal and non-participating for thermal radiation. Since silane is highly diluted in a single carrier gas, the dilute mixture approximation can be invoked. It is a known fact that variable property and Soret effects are important in cold wall horizontal CVD reactors [18]. Despite its negligible effect, the buoyancy term is retained for the completeness of modeling.

In order to place the main focus on thermal characteristics associated with the susceptor motion, a simple, lumped overall surface reaction is adopted, precluding complicated gas phase reactions. Although many studies aimed at developing CVD chemistry models for silicon deposition from silane-hydrogen have been carried out, there is no established model that is commonly accepted in this area and many uncertainties are involved in using the different models [14,18]. In conjunction with the present susceptor arrangement, two additional issues need to be considered. One is that radiative loss from the susceptor surface is expected to be a dominant heat transport mode when a prescribed heat flux is imposed from the bottom. The other is that conjugate heat exchange between the susceptor and gas phase may affect the surface temperature at which chemical reaction takes place. For a proper prediction of deposition processes, both of these should be incorporated in the model.

Owing to the dilute mixture approach, the governing equations and boundary conditions are substantially simplified. A single concentration equation is enough to describe mass transfer because silane is the only gas species involved in the reaction. Since general versions of the formulation are available elsewhere [1–3,14], specific equations applicable to the present system are listed in the following:

$$\frac{\partial(\rho u)}{\partial x}+\frac{\partial(\rho v)}{\partial y}=0 \tag{1}$$

$$\frac{\partial(\rho u\phi)}{\partial x}+\frac{\partial(\rho v\phi)}{\partial y}=\frac{\partial}{\partial x}\left(\Gamma\frac{\partial\phi}{\partial x}\right)+\frac{\partial}{\partial y}\left(\Gamma\frac{\partial\phi}{\partial y}\right)+S_\phi \tag{2}$$

where the general dependent variable ϕ, diffusion coefficient Γ, and source terms S_ϕ are defined as

$$\phi=u,v,T,\ \text{and}\ \omega \tag{3}$$

$$\Gamma=\mu,\mu,k/c_p,\ \text{and}\ \rho D \tag{4}$$

$$S_u=-\frac{\partial P}{\partial x}+\frac{\partial}{\partial x}\left(\mu\frac{\partial u}{\partial x}\right)+\frac{\partial}{\partial y}\left(\mu\frac{\partial v}{\partial x}\right)-\frac{2}{3}\frac{\partial}{\partial x}\left[\mu\left(\frac{\partial u}{\partial x}+\frac{\partial v}{\partial y}\right)\right] \tag{5}$$

$$S_v=-\frac{\partial P}{\partial y}+\frac{\partial}{\partial x}\left(\mu\frac{\partial u}{\partial y}\right)+\frac{\partial}{\partial y}\left(\mu\frac{\partial v}{\partial y}\right)-\frac{2}{3}\frac{\partial}{\partial y}\left[\mu\left(\frac{\partial u}{\partial x}+\frac{\partial v}{\partial y}\right)\right]-\rho g \tag{6}$$

$$S_T=\frac{k}{c_p^2}\left(\frac{\partial T}{\partial x}\frac{\partial c_p}{\partial x}+\frac{\partial T}{\partial y}\frac{\partial c_p}{\partial y}\right)+S_r \tag{7}$$

$$S_\omega=\frac{\partial}{\partial x}\left(D^T\frac{\partial\ln T}{\partial x}\right)+\frac{\partial}{\partial y}\left(D^T\frac{\partial\ln T}{\partial y}\right) \tag{8}$$

While the flow and mass transfer equations are solved in the gas phase only ($H_s\leqslant y\leqslant H_s+H$), the energy equation applies to the combined susceptor-gas region ($0\leqslant y\leqslant H_s+H$) to incorporate conjugate heat transfer. The boundary conditions are specified so as to cope with such situations. At the inlet, the flow is assumed to be fully developed, giving rise to a parabolic profile. The susceptor as well as the gas enter the reactor at the ambient temperature. The flow, temperature, and concentration are regarded as fully developed at the exit, so that zero gradient conditions are applied there. At the susceptor surface, the gas obeys the dilute mixture approximation, and a species balance on silane yields the mass transfer boundary condition. The upper wall is kept cold, and is regarded as impermeable. Those conditions are expressed as follows:

$$u=(6u_{\mathrm{avg}}-3u_s)(\tilde{y}-\tilde{y}^2)+u_s(1-\tilde{y});\;\; v=0;\;\; T=T_0;$$
$$\omega=\omega_0 \quad \text{at} \quad x=0 \tag{9}$$

$$\frac{\partial u}{\partial x}=0;\;\; v=0;\;\; \frac{\partial T}{\partial x}=0;\;\; \frac{\partial \omega}{\partial x}=0 \quad \text{at} \quad x=L \tag{10}$$

$$u=u_s;\;\; v=0;\;\; \rho D\frac{\partial \omega}{\partial y}+D^T\frac{\partial \ln T}{\partial y}=M_{\mathrm{SiH}_4}\mathfrak{R} \quad \text{at} \quad y=H_s \tag{11a}$$

$$-k_s\frac{\partial T}{\partial y}=q_w \quad \text{in} \quad L_e<x<L_e+L_h$$

$$\text{and} \quad \frac{\partial T}{\partial y}=0 \quad \text{elsewhere at } y=0 \tag{11b}$$

$$u=0;\;\; v=0;\;\; T=T_0;\;\; \rho D\frac{\partial \omega}{\partial y}+D^T\frac{\partial \ln T}{\partial y}=0 \quad \text{at} \quad u=H_s+H \tag{12}$$

where $\tilde{y}=(y-H_s)/H$ and $q_w=Q_t/L_h$.

Although several sophisticated models for radiation heat transfer in a horizontal CVD reactor have been proposed, e.g., [20,21], a fairly simple one that retains only the basic feature is employed here. Assuming that the inlet and outlet openings are black surfaces at the ambient temperature, the reactor can be treated as an enclosure. The susceptor surface needs to be subdivided due to the nonuniform temperature, whereas each of the other isothermal surfaces is taken as a single area element. Let N be the number of subdivisions in the x-direction, then $N+3$ surface elements constitute the enclosure. Since the gases are nonparticipating, the net-radiation method [22] for an enclosure can be used to obtain the net radiative loss from each surface, for which both the upper reactor wall and the susceptor surface are assumed to be opaque and gray. The energy balance for surface n in terms of radiosity is

$$q_{o,n}+\frac{1-\varepsilon_n}{\varepsilon_n}\sum_{j=1}^{N+3}F_{n-j}(q_{o,n}-q_{o,j})=\sigma T_n^4 \tag{13}$$

Once the radiosity $q_{o,n}$ is known, the net radiative loss $q_{r,n}$ is calculated by

$$q_{r,n}=\frac{1-\varepsilon_n}{\varepsilon_n}(\sigma T_n^4-q_{o,n}) \tag{14}$$

This loss is incorporated into the energy equation via the source term as $S_r=-q_r\times$(radiating area/volume) in every susceptor subdivision located along the surface. Of course, $S_r=0$ elsewhere.

Deposition Model. In the present system, there are large temperature variations along the susceptor surface due to uneven heating, motion, and inlet conditions. This means that the deposition process cannot be simply treated as diffusion-controlled. Although gas phase reactions were excluded, the silane concentration can be influenced by the surface boundary conditions. In view of these factors, it is necessary to adopt an overall surface reaction that depends on the reactant concentration as well as the surface temperature. The mechanism proposed by Claasen et al. [15] and refined later [16] seems to meet the need. Then, the reaction rate is expressed as

$$\mathfrak{R}=\frac{rP_{\mathrm{SiH}_4}}{1+A_1P_{\mathrm{H}_2}+A_2P_{\mathrm{SiH}_4}}[\mathrm{mol-Si/m^2s}] \tag{15}$$

where the rate constant is

$$r=1.25\times10^9e^{-18500/T}[\mathrm{mol-Si/atm\,m^2s}] \tag{16}$$

In most of stationary reactors, the deposition characteristics have been represented by the local film growth rate

$$G=(M_{\mathrm{Si}}/\rho_{\mathrm{Si}})\mathfrak{R} \tag{17}$$

This quantity needs to be modified to characterize the performance in continuous processing. A dimensionless average growth rate defined as

$$\eta=\frac{\rho_{\mathrm{Si}}\overline{G}L}{\rho_0u_{\mathrm{avg}}\omega_0H(M_{\mathrm{Si}}/M_{\mathrm{SiH}_4})} \tag{18}$$

can take the place of G. This parameter indicates the ratio of the total deposition rate of silicon along the susceptor to the supply rate at the inlet. From its physical meaning, η can be termed *deposition efficiency*. The species conservation of silicon (or silane) allows us to evaluate it alternatively as [17,23].

$$\eta=1-\frac{\int_{H_s}^{H_s+H}\rho u\omega|_{x=L}dy}{\rho_0u_{\mathrm{avg}}\omega_0H} \tag{19}$$

Since the deposition efficiency includes reactor inlet conditions as well as the film growth rate, it can be used as a general performance index in CVD systems where film uniformity is not a major concern.

Scale Analysis

It would be useful, especially in a complicated system, if we can identify relevant parameters and infer their qualitative effects prior to the detailed study. To this end, a scale analysis for the susceptor energy balance is carried out. This analysis is based on the assumption that the deposition performance depends primarily on the susceptor temperature, being independent of the species concentration. Further assuming constant properties, the energy equation for the moving susceptor can be rewritten as

$$(\rho c_p)_s u_s\frac{\partial T_s}{\partial x}=k_s\left(\frac{\partial^2 T_s}{\partial x^2}+\frac{\partial^2 T_s}{\partial y^2}\right) \tag{20}$$

where the subscript s is used to denote the susceptor. Equation (20) is scaled as

$$\mathrm{Pe}\frac{(\Delta T_s)_x}{L^2}\sim\frac{(\Delta T_s)_x}{L^2}+\frac{(\Delta T_s)_y}{H_s^2} \tag{21}$$

This relation has two limiting cases depending on the magnitude of Pe. From the inlet and outlet boundary conditions, the horizontal temperature difference can be estimated as $(\Delta T_s)_x\sim T_{s,\max}-T_0$. According to the basic assumptions mentioned here, it is deduced that

$$\eta\sim\theta_s=\frac{k_{s,\mathrm{ref}}(T_{s,\max}-T_0)}{q_wL} \tag{22}$$

where the subscript ref designates the reference conditions. the scale of vertical temperature difference can be expressed in terms of the supplied heat flux s $(\Delta T_s)_y\sim q_wH_s/k_s$. Since the analysis procedure is straightforward, only the final results are presented here, i.e.,

$$\eta\sim K^{-1} \quad \text{for } \mathrm{Pe}\ll1 \tag{23}$$

$$\eta\sim S^{-1} \quad \text{for } \mathrm{Pe}\gg1 \tag{24}$$

New dimensionless parameters K and S are defined, respectively, as

$$K = \frac{k_s H_s}{k_{s,\mathrm{ref}} H_{s,\mathrm{ref}}} \tag{25}$$

$$S = \frac{(\rho c_p)_s u_s H_s}{k_{s,\mathrm{ref}}} \tag{26}$$

In view of the fact that Eq. (25) is associated with the longitudinal conduction capability of a susceptor, K is termed *conductance ratio*. Although S physically represents the dimensionless heat capacity rate of a moving susceptor, we simply call it *susceptor parameter*. Since the two parameters are defined in terms of the susceptor thickness, material properties, and speed only, the qualitative relations, Eqs. (23) and (24), remain valid regardless of the change in heat transfer between the susceptor and gas. The effect of conjugate heat transfer would appear through the quantitative dependence of η on K and S.

Although the preceding results need confirmation, it is worth noting their implications briefly at this stage. First of all, the present continuous system may be characterized by the two parameters. The susceptor Peclet number, which appears in the scaling procedure, is irrelevant to the system performance. Next, in each limiting case of Pe the deposition efficiency is expressed in terms of a single parameter. Such a feature may be of practical importance in data reduction. Finally, differently from Eq. (23), the deposition efficiency should approach a finite value as K approaches zero since $\eta < 1$ by definition.

Properties. Using the dilute mixture approximation, it is easy to evaluate both thermophysical and transport properties of gases. Since silane is present in small fractions, properties of the mixture are taken as those of the hydrogen carrier gas. The properties are allowed to vary with temperature as [11,18,24,25]

$$\rho = P_0 M_{\mathrm{H}_2}/(\mathbf{R}T) \tag{27}$$

$$c_p = 1.44\times10^4 - 2.61\times10^{-1}T + 8.67\times10^{-4}T^2 \tag{28}$$

$$\mu = \mu_0 (T/T_0)^{0.648} \tag{29}$$

$$k = k_0 (T/T_0)^{0.691} \tag{30}$$

where $\mu_0 = 8.96\times10^{-6}$ kg/ms and $k_0 = 1.83\times10^{-1}$ W/mk. The power-law dependence is also used for the binary diffusion coefficient of SiH_4–H_2 mixture

$$D = D_0 (T/T_0)^{1.70} \tag{31}$$

where $D_0 = 6.24\times10^{-5}$ m^2/s. For a dilute mixture, the thermal diffusion coefficient can be expressed as

$$D^T = \rho D a \omega \tag{32}$$

The factor a is estimated using the Holstein's approximation [26] and curve-fitted Lennard-Jones parameters [27].

The density of silicon is taken as $\rho_{\mathrm{Si}} = 2330$ kg/m^3. In response to the result of scale analysis, a set of reference conditions for the susceptor are chosen based on the previous work [11] as: $H_{s,\mathrm{ref}} = 2$ mm, $(\rho c_p)_{s,\mathrm{ref}} = 1.631\times10^6$ J/m^{3}K, and $k_{s,\mathrm{ref}} = 141.2$ W/mK. Noting that the actual susceptor is a composite element (of conveyor belt and silicon wafer), its properties do not necessarily correspond to a specific material. The susceptor properties may have wide spectra and vary diversely with temperature depending on the material combination. Their effects on the deposition process can be assessed by a parametric study as is done in this work. Those values listed here were taken for silicon at the ambient temperature as an approximation. Other numerical data used here include well-known universal constants and molecular masses, which can be found elsewhere. In view of the previous work [24], emissivities of the upper wall and susceptor surfaces are taken as 0.7 and 0.6, respectively. For the same reason as mentioned earlier, the temperature dependence of emissivity is not taken into account.

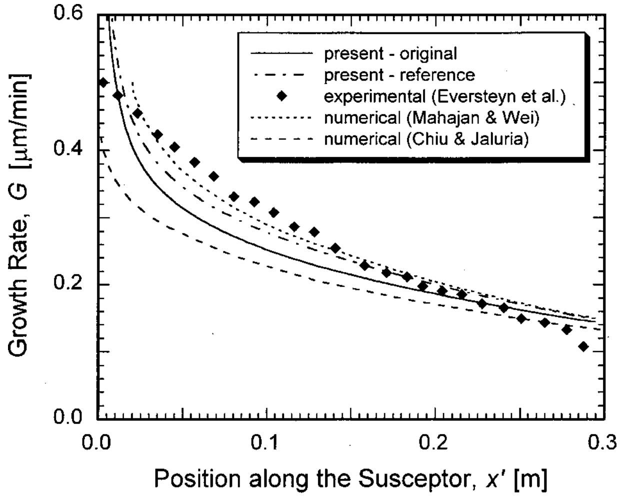

Fig. 2 Comparison of the predicted film growth rate with existing experimental data [17] and numerical results [11,18]

Numerical Method. The governing equations and boundary conditions are discretized on a nonuniform staggered grid system using a finite volume method. In correcting the pressure field, an approach similar to the SIMPLE algorithm [28] has been employed. As noted earlier, the same energy equation covers the combined susceptor-gas region along with individual property values, yielding the conjugate temperature field. Since the species conservation equation is decoupled from the others under the dilute mixture approximation, it is solved after the flow and temperature fields have converged.

A typical grid system consists of 450 streamwise and 40 transverse nodes in the gas phase. The number of transverse nodes in the susceptor material depends on the thickness considered. For a typical case of $H_s = 2$ mm, 10 nodes are used. The grid size was chosen by appropriate grid refinement so that the converged solutions are independent of the grid. It is also confirmed that the numerical results are independent of other user-specified variables such as the initial guess and convergence criteria.

Results and Discussion

A large number of simulations have been performed to investigate the influences of susceptor-related factors. The simulated cases are divided into four groups according to the susceptor material and thickness. Case A just refers to the reference conditions. Each of Cases B, C, and D designates the change in k_s, H_s, and both of k_s and H_s, respectively, while the other variables remain at the reference values.

Model Validation. In order to validate the present numerical model, two sets of the predicted local growth rate of silicon film are compared in Fig. 2 with the well-known experimental data of Eversteyn et al. [17]. For comparative discussions, the plot also includes two representative numerical results [11,18] that commonly employed two-dimensional models. A stationary, isothermal susceptor at 1323 K is used for this comparison to replicate the experimental conditions. The susceptor in Fig. 2 corresponds to the heating zone in Fig. 1. Hence, $x' = x - L_e$. One of the present predictions, the solid curve, is referred to as original because it is obtained from the model without any change. The other is a reference case for later discussion.

Except near the leading edge, the present simulation favorably (within 20 percent bound) agrees with the experimental data. The leading edge discrepancy seems to originate not from improper modeling but from mismatch in the boundary conditions between the prediction and the experiment. A steep drop in the growth rate always appears in numerical predictions employing an isothermal

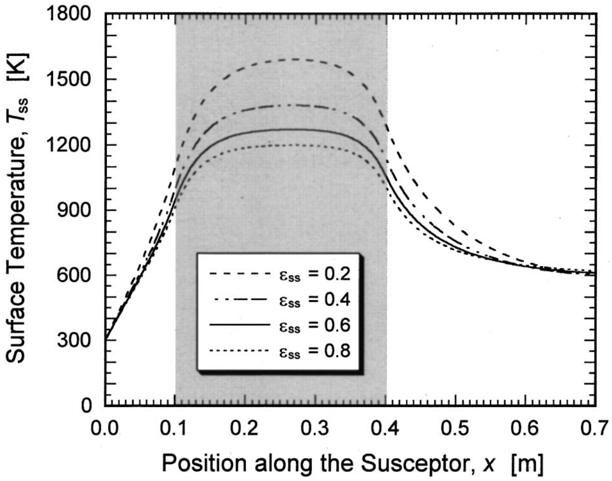

Fig. 3 Effect of the susceptor surface emissivity on the temperature distribution

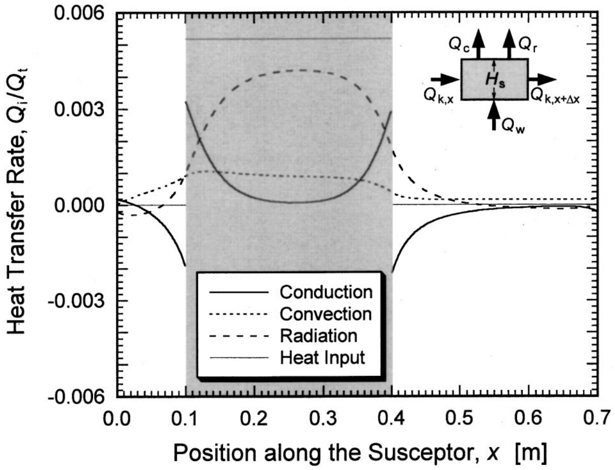

Fig. 4 A typical result of the conjugate heat transfer analysis: heat transport modes for a susceptor segment

susceptor because silane is depleted sharply from the inlet condition to a very low level there. The other numerical results confirm this aspect. In the experiment, the surface temperature at the leading and trailing edges would be lower than specified, deviating from the isothermal condition. A gradual change at the leading edge and inflective decrease at the trailing edge in the experimental growth rate support this arguement.

Regardless of models, all the numerical predictions show the same qualitative trend over the susceptor length. In terms of quantitative agreement with the experiment [17], the original curve of the present prediction appears to be inferior to the result of Mahajan and Wei [18], whereas superior to that of Chiu and Jaluria [11]. This observation, however, needs some explanations. Mahajan and Wei [18] used a larger diffusion coefficient than Eq. (31) and other studies [2,3,24], and assumed the diffusion-controlled deposition. Both of these effects are known to increase the local growth rate. Using their diffusion coefficient in the present model indeed yielded considerably higher growth rates, which are depicted as the reference case in Fig. 2. It is also known [11] that the diffusion-controlled assumption leads to faster film growth than the present reaction kinetics, Eq. (15). Note that the infinite reaction rate is just a limiting case. These facts imply that under proper conditions, the predictions might deviate farther from the experiment than seen here. Meanwhile, Chiu and Jaluria [11] neglected thermal diffusion that acts as obstructing film deposition in silane-hydrogen system. The inclusion of thermal diffusion in their model may produce lower growth rates than the plotted result. It is deduced from this discussion that the present model is capable of resolving the basic characteristics of silicon deposition occurring in a cold wall horizontal CVD reactor within a reasonable tolerance.

Radiation and Conjugate Heat Transfer. In view of their contributions, radiation and conjugate heat transfer in the present continuous system are addressed first. Results are obtained for the case of a stationary susceptor. Figure 3 demonstrates the effect of emissivity on the temperature distribution along the susceptor surface. The shaded areas in Fig. 3 and plots presented from now on indicate the part of susceptor that overlies the heating zone. Over a wide band of the susceptor surface emissivity, the curves show a similar pattern, but temperature differences among them along the heating zone are quite large. Noting that the surface temperature directly affects the deposition rates, the large differences suffice to illustrate the importance of radiation. The radiation model can also be used in reactor design to calculate the total heat input that is needed to maintain a prescribed susceptor temperature. In all the subsequent simulations, the susceptor surface emissivity is set at the previously noted value of 0.6.

The role of radiation can also be understood in Fig. 4, where a typical result of the conjugate heat transfer analysis is depicted. This is the energy balance for a susceptor segment shown in the inset of Fig. 4. Four curves represent net conduction ($Q_{k,x+\Delta x} - Q_{k,x}$), convection ($Q_c$), net radiation ($Q_r$), and heat input ($Q_w$), respectively. The heat input is $q_w \Delta x$ for a segment on the heating zone and 0 elsewhere. It is confirmed that radiation is the dominant heat transfer mode along the susceptor in the heating zone. Two discontinuities in the net conduction curve, which appear at the borders of the heating zone, correspond to each of inflexion points in the temperature distribution (see Fig. 3). Heat conduction through a thin susceptor contributes to smoothen the horizontal temperature variation. Although convection from the susceptor surface to the gas is much smaller than radiation, it may affect the deposition performance when gas phase reactions are included in the model.

Effect of Conductance Ratio. The scale analysis yielded a relation between the deposition efficiency and conductance ratio for small Peclet numbers. Its validity and utility is examined for $S=0$ because a stationary susceptor best satisfies the limiting condition of $\mathrm{Pe} \ll 1$. The local growth rates for two cases with the same value of K, but obtained from different combinations of k_s and H_s, are compared in Fig. 5. For each of $K=1/4$ and 4, Case B and C yield an identical curve despite the physical difference between them. Such indiscernible agreements appear in all other results, which confirm that the conductance ratio is indeed a characteristic parameter. On the other hand, the difference in pattern among cures that correspond to three values of K indicates that the conductance ratio may affect the overall deposition behavior.

Figure 6 delineates the stationary deposition efficiency calculated over a wide range of K and for as many combinations of k_s and H_s as possible. Cases B, C, and D with the same K are reduced to a single value of η_{st}, within a bound of numerical truncation. Although the η_{st} curve does not fit the scale relation, Eq. (23), the two results show a similar trend in that they decrease toward zero as K increases. At small values of K, however, the curve deviates far from the relation, as noted before. With decreasing the conductance ratio, the curve approaches asymptotically to the deposition efficiency for $K \rightarrow 0$. Noting that that variation of η_{st} is steep in a narrow band of K (e.g., $0.1 < \eta_{st} < 0.5$ for $1 < K < 10$), the overall deposition performance may depend

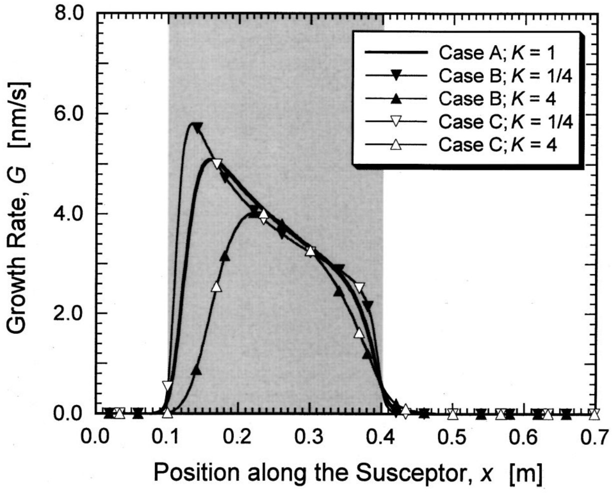

Fig. 5 Spatial variations of the film growth rate for different values and combinations of conductance ratio

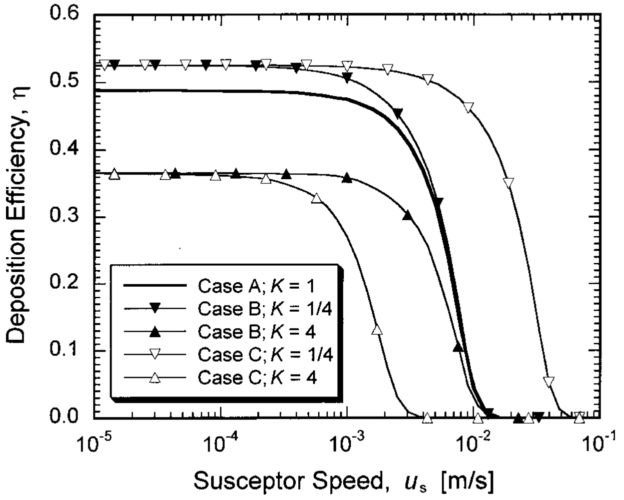

Fig. 7 Dependence of the deposition efficiency on the susceptor speed for different values and combinations of conductance ratio

strongly on the selection of susceptor. From Figs. 5 and 6, along with Eq. (23), it is evident that the conductance ratio is the only parameter representing a stationary system.

Although not shown here, the susceptor temperature over the heating zone, which primarily affects the deposition rate, decreases with increasing K, leading to the pattern of Fig. 6. The $\eta_{st}-K$ plot can be used either to estimate the deposition efficiency for a given susceptor or to select the susceptor material and thickness that meet a prescribed performance criterion.

Susceptor Speed. In the present continuous system, the susceptor speed is of fundamental importance. The deposition efficiency is readily expected to decrease as the speed increases. In order to quantify the effect of susceptor speed, η is plotted as a function of u_s in Fig. 7 for the same values of K and combinations of k_s and H_s as in Fig. 5. Regardless of the value of K, all curves show a similar pattern. As u_s increases, η is at first constant, then decreases gradually, and finally decreases sharply, approaching smoothly to zero. In the region of large u_s, on the other hand, the behavior of η is affected by both the value of K and the combination of properties used to obtain a given value. The relation between η and u_s is independent of k_s, but dependent on H_s. Such dependence is consistent with the results of scale analysis, Eqs. (24) and (26), which enable us to deduce that the deposition efficiency can be characterized by the susceptor parameter only.

When the speed u_s is converted into the susceptor parameter S according to the definition given in Eq. (26), the efficiency curves with the same value of K nearly coincide with each other. The curves for different values of K disagree with one another due to the difference in η_{st}. This problem can be resolved by normalizing η by η_{st}. Figure 8 depicts the reduced result, i.e., the relation between the normalized efficiency and susceptor parameter, for which the data are taken from Fig. 7. Although each set of data differs a little from one another, the deviations seem to be small enough to call the result a single curve. Additional calculations for the wide range of K (as in Fig. 6) and various combinations of $(\rho c_p)_s u_s$ yield the same curve. A decrease in η/η_{st} over the region of large S, where $\mathrm{Pe} \ll 1$, qualitatively agrees with the scale relation, Eq. (24). From an engineering viewpoint, this curve along with Fig. 6 can be used for susceptor design. Under the present conditions, the deposition efficiency is readily obtained for any combinations of susceptor material, thickness, and speed through a simple procedure. Once K and S are known, η_{st} and η/η_{st} can be read in Figs. 6 and 8, respectively. Multiplying them produces the required η. Therefore, with these plots, we can avoid

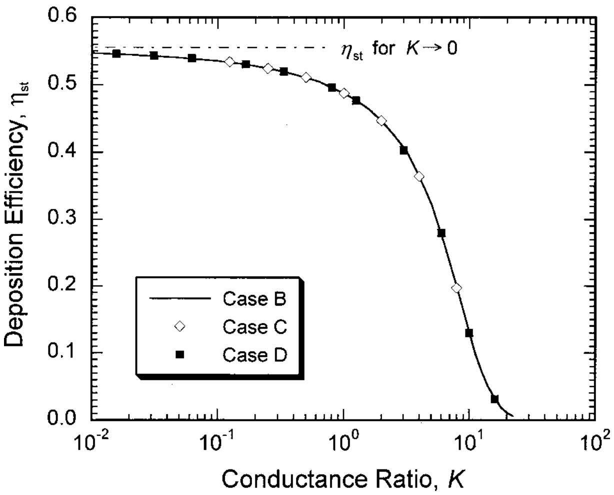

Fig. 6 Dependence of the stationary deposition efficiency on conductance ratio

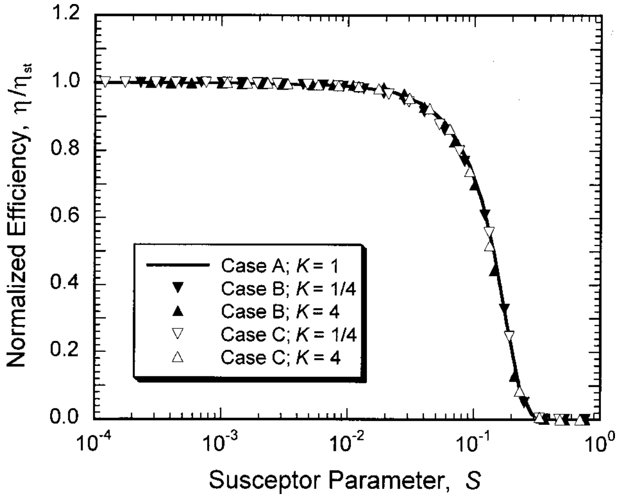

Fig. 8 Dependence of the normalized deposition efficiency on susceptor parameter

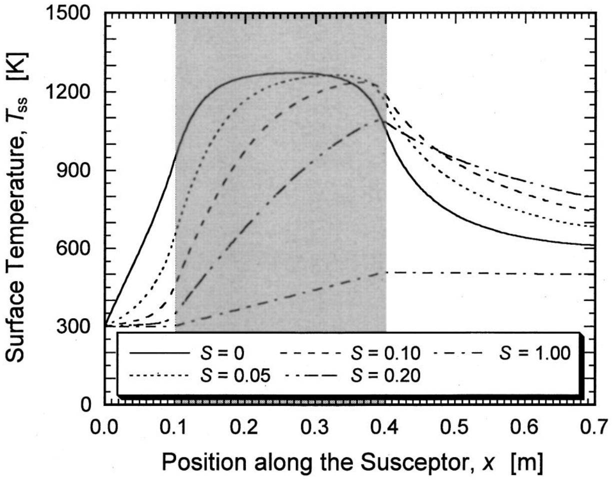

Fig. 9 Effect of susceptor parameter on the temperature distribution along the susceptor surface

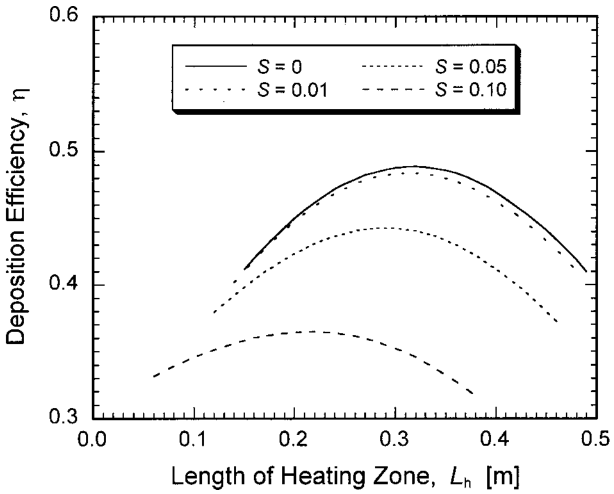

Fig. 11 Deposition efficiency as a function of heating zone length at four selected values of susceptor parameter

design conditions that result in low efficiencies. In this sense, the two curves comprise performance curves for the present continuous system.

The effect of susceptor speed on the local behavior is briefly reported here. Figure 9 presents the temperature distributions along the susceptor surface for five values of S. With increasing S (or equivalent u_s), a high temperature band narrows, the maximum value lowers and shifts downstream toward the end of heating zone, and the profile eventually becomes linear. Heat conveyed by the susceptor movement is responsible for those changes, which in turn leads to the trends seen in Fig. 8. It is unlikely that a value of S higher than 0.1 will be adopted in the design of practical systems.

Length of Heating Zone. For a given total heat input, the length of heating zone directly affects the temperature profile due to $q_w = Q_t / L_h$. The effect on the deposition performance for representative values of K and S is investigated. Figure 10 illustrates the dependence of η_{st} on L_h at four selected values of K for $S = 0$. For each K, there exists an optimum length of heating zone that maximizes the deposition efficiency. The reason is clear when we consider two limiting cases: $L_h \rightarrow 0$ and $L_h \rightarrow L$. When L_h is short, the susceptor temperature on the heating zone tends to rise high due to intensive heating, which in turn induces a large radiative loss from the surface. Although the temperature is still high, the average deposition rate becomes low because of a short deposition length. When L_h is long, the susceptor temperature becomes low, thereby heat losses being reduced. Such moderate temperature is ineffective for chemical reaction, decreasing the deposition efficiency. The optimum length $L_{h,\mathrm{opt}}$ shortens as K increases. Conduction through the susceptor is enhanced with increasing K, so that intensive heating is more effective for raising the surface temperature high enough for deposition. If conduction is suppressed with decreasing K, extensive heating yields a longer effective deposition length. A short L_h along with small K leads to a large radiative loss. This is why η_{st} for a small K decreases more sharply from the maximum on the short L_h side than on the large one.

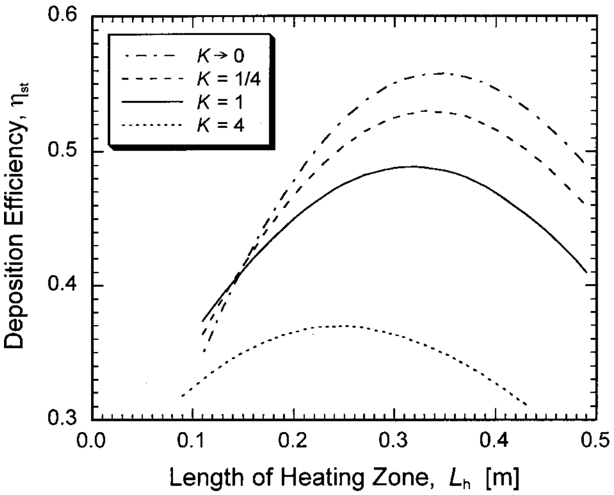

Fig. 10 Stationary deposition efficiency as a function of heating zone length at four selected values of conductance ratio

Another result is the dependence of η on L_h at representative values of S for $K = 1$, as depicted in Fig. 11. The overall picture looks similar to Fig. 10. Each curve shows an increasing-decreasing pattern, encompassing the local maximum point. The optimum length of the heating zone also shortens as S increases. The influence of S on $L_{h,\mathrm{opt}}$, however, is caused by a different mechanism from that of K. With increasing S, the width of the susceptor at high temperature narrows and the surface temperature decreases (see Fig. 9). This means that more intensive heating is needed to raise the temperature high enough for deposition. It is worth noting that the variation band of $L_{h,\mathrm{opt}}$ in both of Figs. 10 and 11 is relatively narrow. The value $L_h = 0.3$ m used so far is close to $L_{h,\mathrm{opt}}$ for a wide range of K and S. Because of the convex shape of the efficiency curve, a single value of η, other than at the maximum, corresponds to two different lengths: one is shorter, and the other longer than $L_{h,\mathrm{opt}}$. The shorter one is preferable because a smaller reactor is desirable. Other factors, such as microstructure of deposited film, conveyor drive system, and wafer loading, should be taken into account in the actual design.

In summary, the dependence of deposition performance on the length of heating zone stems from how the supplied heat is distributed along the susceptor and transported to the surroundings. Since the parameters K and S affect the distribution and transport, the efficiency curve depends on both of them. It is obvious that the radiation and conjugate heat transfer play key roles in quantifying such effects in deposition characteristics.

Conclusions

A systematic study has been carried out to investigate the performance characteristics of continuous chemical vapor deposition of silicon in a horizontal cold wall reactor, in which the main focus is placed on a moving finite thickness susceptor. The numerical model used for simulation accounts for temperature-dependent properties, thermal diffusion, radiation among surfaces, and conjugate heat transfer between the susceptor and gas. The validity and capability of the model have been confirmed by a reasonably good agreement between the predicted result and available experimental data, and a fine resolution of the coupled heat transfer. Scale analysis for the moving susceptor yield two characteristic parameters and a pair of qualitative relations, which prove to be useful for understanding the deposition behavior and analyzing the predicted data.

When the susceptor is motionless, the stationary deposition efficiency is determined by the conductance ratio only. The efficiency curve monotonically decreases that for the thin susceptor limit to zero as the conductance ratio increases. When the susceptor is in motion, the deposition efficiency, normalized by the value under stationary state conditions, is a function of the susceptor parameter only. With increasing the susceptor parameter (or speed), the normalized efficiency curve remains almost unity and then decreases sharply toward zero. This variation demonstrates the feasibility of continuous processing in that the susceptor can move up to considerable speed without sacrificing deposition efficiency. Since these two curves represent the performance characteristics of a continuous system, they can be used to determine the susceptor material, thickness, or moving speed in the design of practical systems. Finally, an optimum length of heating zone that maximizes the deposition efficiency always exists under a fixed total heat input and depends on the characteristic parameters. Adjusting the length of the heating zone, along with the use of the performance curves, can play an important role in improving the deposition efficiency of continuous CVD systems.

Acknowledgments

This work was conducted during the first author's (H.Y.) sabbatical leave. He would like to acknowledge the financial support provided by the Korea Research Foundation under Grant Number KRF-2000-EA0005 and the visiting position furnished by Rutgers University. The partial support from NSF under Grant Number DMI-96-33194 is also acknowledged.

Nomenclature

A_1 = constant in Eq. (15), $A_1 = 1.75 \times 10^3$ atm^{-1}
A_2 = constant in Eq. (15), $A_2 = 4.00 \times 10^4$ atm^{-1}
a = thermal diffusion factor
c_p = specific heat
D = binary diffusion coefficient
D^T = thermal diffusion coefficient
F = configuration factor
$\underline{G}$ = local film growth rate
G = average growth rate, $\frac{1}{L}\int_0^L G(x)dx$
g = magnitude of gravitational acceleration
H = height of reactor
H_s = susceptor thickness
K = conductance ratio
k = thermal conductivity
L = reacator length
L_e, L_h, L_o = length of entrance, heating, and outlet zones
M = molecular mass
N = number of control volumes in the x-direction
P = pressure
P_i = partial pressure of species i
Pe = Peclet number, $(\rho c_p)_s u_s L / k_s$
Q = heat transfer rate
q = heat flux
q_o = radiosity
$\mathbf{R}$ = universal gas constant
$\mathfrak{R}$ = chemical reaction rate
r = reaction rate constant
S = susceptor parameter or source term
T = temperature
u,v = velocity components in x, y-directions
u_{avg} = average gas velocity at the inlet
x, y = coordinates

Greek Letters

ε = emissivity
ϕ = stands for u, v, T, and ω
η = deposition efficiency
μ = viscosity
ρ = density
σ = Stefan-Boltzmann constant
θ = dimensionless temperature
ω = mass fraction of silane

Subscripts

0 = inlet or reference state
c = convection
k = conduction
r = radiation
ref = reference conditions
ss = susceptor surface
st = stationary susceptor
t = total
w = bottom wall

References

[1] Jensen, K. F., Einset, E. O., and Fotiadis, D. I., 1991, ''Flow Phenomena in Chemical Vapor Deposition of Thin Films,'' Annu. Rev. Fluid Mech., **23**, pp. 197–232.

[2] Kleijn, C. R., 1995, ''Chemical Vapor Deposition Processes,'' *Computational Modeling in Semiconductor Processing*, M. Meyyappan, ed., Artech House, Boston, pp. 97–229.

[3] Mahajan, R. L., 1996, ''Transport Phenomena in Chemical Vapor-Deposition Systems,'' Adv. Heat Transfer, **28**, pp. 339–425.

[4] Yamaji, T., Abe, M., Takada, Y., Okada, K., and Hiratani, T., 1994, ''Magnetic Properties and Workability of 6.5% Silicon Steel Sheet Manufactured in Continuous CVD Siliconizing Line,'' J. Magn. Magn. Mater., **133**, pp. 187–189.

[5] Stevenson, P., and Matthews, A., 1995, ''PVD Equipment Design: Concepts for Increased Production Throughput,'' Surf. Coat. Technol., **74–75**, pp. 770–780.

[6] Onabe, K., Kohno, O., Nagaya, S., Shimonosono, T., Iijima, Y., Sadakata, N., and Saito, T., 1996, ''Structure and Property of $YBa_2Cu_3O_x$ Tapes Formed on Metallic Substrate by CVD Technique,'' Mater. Trans., JIM, **37**, pp. 893–897.

[7] Gordon, R., 1997, ''Chemical Vapor Deposition of Coatings on Glass,'' J. Non-Cryst. Solids, **218**, pp. 81–91.

[8] Bansal, N., and Dickerson, R. M., 1997, ''Tensile Strength and Microstructural Characterization of HPZ Ceramic Fiber,'' Mat. Sci. Technol., **A222**, pp. 149–157.

[9] Lackey, W. J., Vaidyaraman, S., Beckloff, B. N., Moss, III, T. S., and Lewis, J. S., 1998, ''Mass Transfer and Kinetics of the Chemical Vapor Deposition of SiC onto Fiber,'' J. Mater. Res., **13**, pp. 2251–2261.

[10] Chiu, W. K. S., and Jaluria, Y., 1999, ''Effect of Buoyancy, Susceptor Motion, and Conjugate Transport in Chemical Vapor Deposition Systems,'' ASME Heat Transfer, **121**, pp. 757–761.

[11] Chiu, W. K. S., and Jaluria, Y., 2000, ''Continuous Chemical Vapor Deposition Processing with a Moving Finite Thickness Susceptor,'' J. Mater. Res., **15**, pp. 317–328.

[12] Dobkin, D. M., 2000, ''Injector-based Atmospheric Pressure Reactors,'' http://www.batnet.com/enigmatics/semiconductor_processing/CVD_Fundamentals/reactors/APCVD_ovvu.html.

[13] Silicon Valley Group, Inc., 2000, Annual Report, Securities Exch. Comm., http://www.asml.com/investors/pdf/annual_report_svg00.pdf, p. 7.

[14] Kleijn, C. R., 2000, ''Computational Modeling of Transport Phenomena and Detailed Chemistry in Chemical Vapor Deposition—A Benchmark Solution,'' Thin Solid Films, **365**, pp. 294–306.

[15] Claasen, W. A. P., Bloem, J., Valkenburg, W. G. J. N., and van den Brekel, C. H. J., 1982, ''The Deposition of Silicon from Silane in a Low-Pressure, Hot-Wall System,'' J. Cryst. Growth, **57**, pp. 259–266.

[16] Jensen, K. F., and Graves, D. B., 1983, ''Modeling and Analysis of Low Pressure CVD Reactors,'' J. Electrochem. Soc., **120**, pp. 1950–1957.

[17] Eversteyn, F. C., Severin, P. J. W., van den Brekel, C. H. J., and Peek, H. L., 1970, ''A Stagnant Layer Model for the Epitaxial Growth of Silicon from Silane on a Horizontal Reactor,'' J. Electrochem. Soc., **117**, pp. 925–931.

[18] Mahajan, R. L., and Wei, C., 1991, ''Buoyancy, Soret, Dufour, and Variable Property Effects in Silicon Epitaxy,'' ASME Heat Transfer, **113**, pp. 688–695.

[19] Quazzani, J., Chiu, K.-C.,and Rosenberger, F., 1988, ''On the 2D Modeling of Horizontal CVD Reactors and its Limitations,'' J. Cryst. Growth, **91**, pp. 497–508.

[20] Chinoy, P. B., Kaminski, D. A., and Ghandhi, S. K., 1991, ''Effects of Thermal

Radiation on Momentum, Heat, and Mass Transfer in a Horizontal Chemical Vapor Deposition Reactor,'' Numer. Heat Transfer, Part A, **19**, pp. 85–100.

[21] Kadinski, L., Makarov, Yu N., Schaefer, M., Vasil'ev, M. G., and Yuferev, V. S., 1995, ''Development of Advanced Mathematical Models for Numerical Calculations of Radiative Heat Transfer in Metalorganic Chemical Vapor Deposition Reactors,'' J. Cryst. Growth, **146**, pp. 209–213.

[22] Siegel, R., and Howell, J. R., 1992, *Thermal Radiation Heat Transfer*, 3rd ed., Hemisphere Publishing Corp., Washington, D.C.

[23] Tsai, H. C., Greif, R., and Joh, S., 1995, ''A Study of Thermophoretic Transport in a Reacting Flow with Application to External Chemical Vapor Deposition Processes,'' Int. J. Heat Mass Transf., **38**, pp. 1901–1910.

[24] Kleijn, C. R., and Hoogendoorn, C. J., 1991, ''A Study of 2- and 3-D Transport Phenomena in Horizontal Chemical Vapor Deposition Reactors,'' Chem. Eng. Sci., **46**, pp. 321–334.

[25] Moffat, H. K., and Jensen, K. F., 1988, ''Three-Dimensional Flow Effects in Silicon CVD in Horizontal Reactors,'' J. Electrochem. Soc., **135**, pp. 459–471.

[26] Holstein, W. L., 1988, ''Thermal Diffusion in Metal-Organic Chemical Vapor Deposition,'' J. Electrochem. Soc., **135**, pp. 1788–1793.

[27] Neufeld, P., Janzen, A. R., and Aziz, R. A., 1972, ''Empirical Equations to Calculate 16 of the Transport Collision Integrals $\Omega^{(l,s)*}$ for the Lennard-Jones (12-6) Potential,'' J. Chem. Phys., **57**, pp. 1100–1102.

[28] Patankar, S. V., 1980, *Numerical Heat Transfer and Fluid Flow*, Hemisphere Publishing Corp., New York.

Christopher J. Vreeman
Capstone Turbine Corporation,
21211 Nordhoff Street,
Chatsworth, CA 91311

J. David Schloz
Wagstaff Engineering,
3910 North Flora Road,
Spokane, WA 99216

Matthew John M. Krane
Member, ASME
Assistant Professor
School of Materials Engineering,
Purdue University,
West Lafayette, IN 47907

Direct Chill Casting of Aluminum Alloys: Modeling and Experiments on Industrial Scale Ingots

A continuum mixture model of the direct chill casting process is compared to experimental results from industrial scale aluminum billets. The model, which includes the transport of free-floating solid particles, can simulate the effect of a grain refiner on macrosegregation and fluid flow. It is applied to an Al-6 wt% Cu alloy and the effect of grain refiner on macrosegregation, sump profile, and temperature fields are presented. Two 45 cm diameter billets were cast under production conditions with and without grain refiner. Temperature and composition measurements and sump profiles are compared to the numerical results. The comparison shows some agreement for the grain refined case. It is believed that an incorrect assumption about the actual grain structure prevents good agreement in the non-grain refined billet. [DOI: 10.1115/1.1482089]

Keywords: *Heat Transfer, Manufacturing, Mass Transfer, Processing, Solidification*

Introduction

Direct chill casting is a semi-continuous process in which molten aluminum enters the top of a water-cooled mold, is cooled, and forms a solid ingot drawn out below (Fig. 1(*a*)). The molten aluminum begins to solidify due to the cooling effect of the mold wall. As the ingot is withdrawn from the bottom of the mold, water jets impinge on the surface, directly cooling the billet and forming a solid layer around a liquid melt, commonly referred to as the sump.

A particular defect that occurs in a wide range of casting processes, including the direct chill (DC) casting of aluminum alloys, is macrosegregation, the uncontrolled redistribution of alloying elements on the scale of the ingot during solidification. Macrosegregation in DC cast ingots can produce nonuniform mechanical properties [1], which affects the behavior of the metal during downstream forming and heat treat operations.

A commonly observed, surface-to-surface distribution of alloying elements at a transverse cross-section of a DC cast ingot reveals distinct regions of positive (solute-rich) and negative (solute-depleted) segregation [2]. Enrichment near the ingot surface is attributed to a combination of shrinkage induced flow of solute-rich liquid toward the mold wall, where solidification rates are highest, and exudation induced by local remelting of the ingot surface as the solid shell pulls away from the mold. Once a structurally sound ingot surface has formed and solidification rates have decreased, more normal segregation behavior is observed, with the solute composition increasing with decreasing radius from the solute-depleted region near the ingot surface. While this trend may be expected to continue, ingots produced by DC casting often exhibit a significant decrease in solute composition near the centerline.

Experimental studies have provided some insight into the mechanisms that control macrosegregation in DC cast ingots, especially at the centerline. Yu and Granger [2] investigated negative segregation in Al-Cu-Mg slabs and concluded that a duplex microstructure and accompanying negative segregation at the center of DC cast ingots resulted from the settling of solute-depleted, free-floating dendrites that formed near the top of the sump and were subsequently swept to the bottom of the sump by convection currents in the melt. This theory was also supported by significant positive titanium segregation at the centerline [2], which is present in grain refining particles that serve as nucleation sites for free-floating dendrites. Duplex microstructures accompanied by the negative centerline segregation have also been observed by Chu and Jacoby [3] and Dorward and Beerntsen [4], and negative centerline segregation with positive segregation of titanium was observed in ingots cast by Gariepy and Caron [5].

To model the transport phenomena which control the segregation in DC casting, single domain models have been used that implicitly couple phenomena in the melt, mushy zone, and solid regions of a solidifying ingot. Flood et al. [6] were the first to apply a single domain model for the transport phenomena in DC casting to predict macrosegregation in Al-4.5 wt% Cu billets. They assumed that the mushy zone consisted only of a rigid, permeable dendritic matrix with the solid moving at the casting speed and predicted positive segregation of copper at the center of the billet. Reddy and Beckermann [7] included the effect of free-floating dendrites of varying diameter by employing a modified version of the two-phase model developed by Ni and Beckermann [8] to simulate the DC casting of two Al-4.5 wt% Cu billets. In one case, the solid phase was assumed to form a rigid structure moving at the casting speed. In the other case, the transport of solute-depleted, free-floating dendrites was modeled assuming the solid phase formed a rigid structure at a solid volume fraction of 0.637. In the simulation with no free-floating solid, they predicted subsurface enrichment, followed by a narrow depleted region just within the surface. Positive segregation occurred at the centerline and was attributed to the buoyancy driven flow of copper-rich liquid to the bottom of the sump. In the simulation with free-floating dendrites, they predicted significant negative segregation at the centerline, which they attributed to the advection of copper-depleted dendrites to the bottom of the sump. Reddy and Beckermann were the first to include the transport of free-floating dendrites into a fully coupled, single domain, macrosegregation model of the DC casting process and to predict the resulting negative segregation at the centerline. More recently, the same authors [9] conducted further DC casting simulations of Al-4.5 wt% Cu billets to examine the effect of the grain density and interdendritic fluid flow on macrosegregation in billets devoid of free-floating dendrites. They demonstrated that, if the mushy zone consists of a rigid dendritic structure without free-floating dendrites, its permeability significantly influences macrosegregation in DC cast billets.

Vreeman et al. [10] developed a fully coupled, single-domain,

---

Contributed by the Heat Transfer Division for publication in the JOURNAL OF HEAT TRANSFER. Manuscript received by the Heat Transfer Division September 12, 2001; revision received March 26, 2002. Associate Editor: C. Amon.

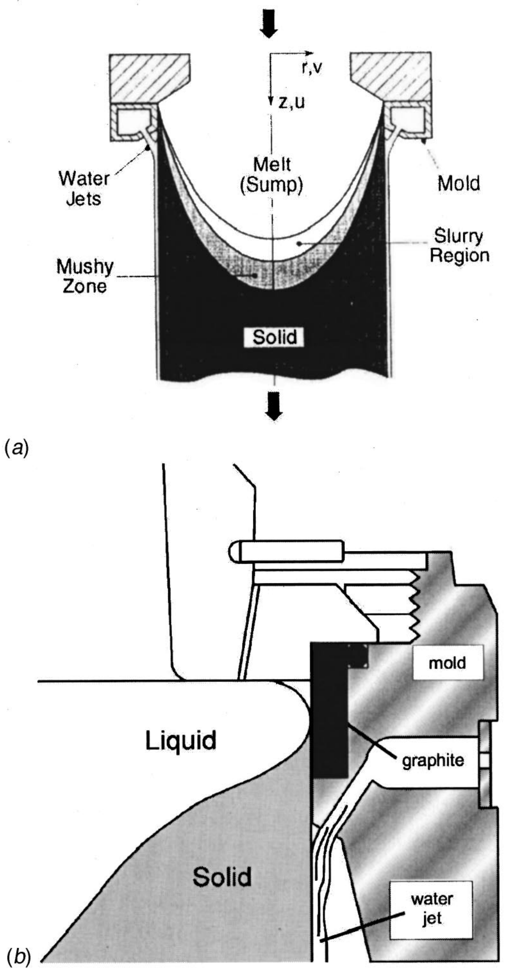

Fig. 1 (***a***) **Schematic of generic DC casting process;** (***b***) **AirSlip™ mold cross-section**

mixture model of the DC casting process which accounted for the transport of free-floating dendrites. Separate and distinct mixture momentum equations were employed to account for the different momentum transfer mechanisms in two-phase regions characterized by a slurry of free-floating dendrites and a rigid, permeable dendritic matrix saturated with interdendritic liquid. In a companion paper [11], the model was used to predict macrosegregation distributions in Al-4.5 wt% Cu and Al-6.0 wt% Mg billets and the predicted surface-to-centerline distribution of macrosegregation was found to be consistent with observations in DC cast ingots discussed above. Negative segregation at the centerline increased with an increase in the packing fraction at which free-floating dendrites are presumed to coalesce into a rigid dendritic structure. Likewise, negative segregation at the centerline and positive segregation in the enriched region increased with an increase in the characteristic diameter of the free-floating dendrites.

The objective of this study is to make a direct comparison of Vreeman's model to data taken from an industrial scale direct chill process. Two billets of an Al-6wt%Cu alloy were cast in the foundry at Wagstaff, Inc., one with and one without the use of a grain refiner to generate free-floating solid particles in the sump. Measured composition profile, temperature history, and sump profile results for the grain refined and non-grain refined billets are compared to the numerical results with and without free-floating solids.

Numerical Modeling

The numerical model is that of Vreeman et al. [10], which simulates solidification in systems with two-phase (solid-liquid) regions consisting of a slurry of free-floating dendrites above a rigid, dendritic matrix saturated with interdendritic liquid. Mixture transport equations for mass, energy, and species conservation [12] are applied in all regions of the DC cast billet as it solidifies, while the application of separate and distinct momentum equations depends on the local solid morphology [10]. The liquid metal velocities calculated in previous papers under very similar conditions were low enough to justify the assumption that the flow can be treated as laminar. In the liquid and slurry regions, for which the solid volume fraction is less than the designated *packing fraction* ($g_s < g_{s,p}$), modified versions of slurry momentum equations developed by Ni and Incropera [13] are employed (Table 1). In regions consisting of a rigid, solid structure and interdendritic liquid ($g_s \geqslant g_{s,p}$), momentum equations developed by Bennon and Incropera [12] and Prescott et al. [14] are employed to account for interdendritic fluid flow in a translating solid matrix.

The model used here to predict solid particle motion relative to the liquid flow is much simpler than some found in the literature. Wang and Beckermann [15] have developed a detailed multiphase model to account for the presence of free-floating equiaxed dendrites and their effect on composition and grain structure, linking the model to the macroscopic equations governing thermosolutal convection and heat and mass transfer. Calculations have been made, some of which were compared to experiments in salt-water solutions [16,17].

The parameter that defines the relative extent of the slurry and rigid mushy zone regions is the packing fraction, $g_{s,p}$, at which the free-floating dendrites coalesce to form a rigid dendritic structure. In general, packing fractions are not explicitly known and vary significantly from system to system. In addition to the packing fraction, a characteristic diameter of free-floating dendrites, *d*, used to calculate solid and liquid phase velocity differences, is not explicitly known [10]. In this study, $d = 75\ \mu$m was used. Lumped into this single, unchanging parameter is the real particle size distribution which varies in time and position during solidification. A rigorous determination of dendrite size variations requires implementation of an additional transport equation and a nucleation model to account for the advection and "generation" (through nucleation and/or fragmentation) of dendrites, respectively. An example of such a model is found in [7].

To model the solid-liquid interactions in the rigid mushy zone, the permeability, *K*, is assumed to be isotropic and is evaluated using the Blake-Kozeny expression, $K = \kappa_o (1 - g_s)^3 / g_s^2$. Evaluation of the permeability coefficient, κ_o for an equiaxed mushy zone relies on empirical data for flow through granular materials [18]. In this study, a permeability coefficient of $\kappa_o = 3.75 \times 10^{-11}$ m^2 is used. This value is based on a dendritic arm spacing of 75 μm, which is in the range of measured values found in DC cast billets. The thermophysical properties used in the study are shown in Table 2 and are based on values found in [19].

The model is closed by assuming thermodynamic equilibrium on the scale of individual control volumes and using the Al-Cu phase diagram, with constant equilibrium partition coefficients (Table 2) and thermodynamic relations developed by Bennon and Incropera [20] to account for both primary and eutectic solidification.

In order to obtain a steady-state solution, the energy equation was solved by itself first, with the resulting solid fraction and temperature distribution used as initial conditions for further calculations. Recognizing that converged solutions could not be obtained without the time-dependent terms in the conservation equations, transient simulations of the full model were marched forward in time with convergence rigorously enforced at each time step. While a steady state solution was obtained for the billet without free-floating dendrites ($g_{s,p} = 0$), attempts to obtain

Table 1 Mixture model transport equations [10]

Continuity	$\frac{\partial \rho}{\partial t} + \nabla \cdot \rho \vec{V} = 0$
Energy	$\frac{\partial}{\partial t}(\rho h) + \nabla \cdot (\rho \vec{V} h) = \nabla \cdot \left(\frac{k}{c_s} \nabla h \right) + \nabla \cdot \left(\frac{k}{c_s} \nabla (h_s - h) \right) - \nabla \cdot (\rho (\vec{V} - \vec{V}_s)(h_l - h))$
Species	$\frac{\partial \rho C^{Cu}}{\partial t} + \nabla \cdot \rho \vec{V} C^{Cu} = \nabla \cdot (\rho f_l D_l^{Cu}) \nabla C^{Cu} + \nabla \cdot (\rho f_l D_l^{Cu}) \nabla (C_l^{Cu} - C^{Cu}) - \nabla \cdot \rho (\vec{V} - \vec{V}_s)(C_l^{Cu} - C^{Cu})$
	Liquid & Slurry Regions $(0 \le g_s < g_{s,p})$
z - Momentum	$\frac{\partial}{\partial t}(\rho u) + \nabla \cdot (\rho \vec{V} u) = \nabla \cdot \left(\mu_l \frac{\rho}{\rho_l} \nabla u \right) - \nabla \cdot \left(\mu_l \frac{\rho f_s}{\rho_l} \nabla u_s \right) + \nabla \cdot (\bar{\mu}_s g_s \nabla u_s) - \nabla \cdot \left[\left(\frac{\rho f_s}{f_l} \right) (\vec{V} - \vec{V}_s)(u - u_s) \right]$ $+ g_s(\rho_s - \rho_l) g - g_s \rho_s g [\beta_{T,s}(T - T_o) + \beta_{S,s}(C_s^{Cu} - C_o^{Cu})] - g_l \rho_l g [\beta_{T,l}(T - T_o) + \beta_{S,l}(C_l^{Cu} - C_o^{Cu})] - \frac{\partial P}{\partial z}$
r - Momentum	$\frac{\partial}{\partial t}(\rho v) + \nabla \cdot (\rho \vec{V} v) = \nabla \cdot \left(\mu_l \frac{\rho}{\rho_l} \nabla v \right) - \mu_l \frac{\rho}{\rho_l} \frac{v}{r^2} - \nabla \cdot \left(\mu_l \frac{\rho f_s}{\rho_l} \nabla v \right) + \mu_l \frac{\rho f_s}{\rho_l} \frac{v}{r^2} + \nabla \cdot (\bar{\mu}_s g_s \nabla v) - \bar{\mu}_s g_s \frac{v}{r^2} - \frac{\partial P}{\partial r}$
	Rigid Mushy Zone & Solid Regions $(g_{s,p} \le g_s \le 1)$
z - Momentum	$\frac{\partial}{\partial t}(\rho u) + \nabla \cdot (\rho \vec{V} u) = \nabla \cdot \left(\mu_l \frac{\rho}{\rho_l} \nabla u \right) - \frac{\mu_l}{K} \frac{\rho}{\rho_l}(u - u_s) - \rho_l g [\beta_{T,l}(T - T_o) + \beta_{S,l}(C_l^{Cu} - C_o^{Cu})] - \frac{\partial P}{\partial z}$
r - Momentum	$\frac{\partial}{\partial t}(\rho v) + \nabla \cdot (\rho \vec{V} v) = \nabla \cdot \left(\mu_l \frac{\rho}{\rho_l} \nabla v \right) - \frac{\mu_l}{K} \frac{\rho}{\rho_l} v - \mu_l \frac{\rho}{\rho_l} \frac{v}{r^2} - \frac{\partial P}{\partial r}$
Liquid-Particle Interaction	$\vec{V}_s - \vec{V}_l = \frac{(1 - g_s)}{18 \mu_m}(\rho_s - \rho_l) d^2 \vec{g}$

steady state numerical solutions with free-floating dendrites ($g_{s,p} > 0$) were unsuccessful because of the unstable nature of the interaction of the fluid flow and the solid in the region of $g_{s,p}$ (see [11] for details). As the simulations proceeded forward in time, a quasi-steady state was reached where transient variations in the dependent variables reached a minimum range.

The numerical solution of the conservation equations (Table 1) is implemented through the use of a control volume formulation and the SIMPLER algorithm [21]. The procedures outlined by Bennon and Incropera [20] are used with upwind differencing to discretize all terms. Modifications are made to the differencing procedure of the so-called *advection-like source terms* in the species equation. For these terms, the discretization procedure was modified to insure that mass is conserved when both solid and liquid simultaneously cross control volume interfaces. A complete discussion of the numerical techniques used is found in [22]. The solution was carried out as described further in [11], with the exception of the thermal boundary condition. Instead of using the correlations found in [11], the temperature of the surface of the billet was determined by the measurements described below.

Experimental Methods

To understand the behavior of these billets during an actual casting process and to evaluate the performance of Vreeman's model, two 0.45 m (18 in) diameter Al-6wt%Cu billets were cast at Wagstaff's foundry in Spokane, Washington, using the Wagstaff Airslip™ process (see Fig. 1(*b*)). The alloy was induction melted and degassed with 100 percent argon, then transferred from the tilting furnace via a heated refractory trough to the mold table.

Table 2 Thermophysical properties and phase diagram data [11]

ρ_l (kg/m^3)	2491	$\beta_{T,l}$ (K^{-1})	1.17×10^{-4}
ρ_s (kg/m^3)	2573	$\beta_{T,s}$ (K^{-1})	2.25×10^{-5}
c_l (J/kg-K)	1045	$\beta_{S,l}$	-0.90
c_s (J/kg-K)	950	$\beta_{S,s}$	-0.66
h_f (kJ/kg)	387	T_{melt} (K)	933.5
k_l (W/m-K)	95	T_{eut} (K)	821.4
k_s (W/m-K)	162	C^A_{max}	0.0565
D_l^B (m^2/s)	5.0×10^{-9}	C^A_{eut}	0.33
μ_l (kg/m-s)	0.0014	k_p	0.171
$\bar{\mu}_s$ (kg/m-s)	$4.96\,\mu_l$		

The AirSlip™ mold technology is a ‘‘hot-top’’ design with a metal inlet diameter of 0.305 m (12 in). A unique feature of this technology is the use of a porous graphite ‘‘casting ring’’ that is fed with both dry air and a synthetic lubricant. This design provides minimal surface macrosegregation by reducing the degree of chill obtained within the mold bore. A specially designed cooling water array provides the necessary upward conductance and high heat transfer rate to solidify both shell and bulk of the billet.

The procedure for casting was to transfer the alloy by tilting the induction hearth, allowing the metal to fill a cavity comprised of the casting mold and a steel starter block. Following a prescribed hold time, the starter block was slowly withdrawn from the mold. The casting speed was 1 mm/s. Heat transfer for the initial 0.02 m (0.8 in.) of cast length is obtained by conduction from the molten metal through the starter block to the casting water. After this period the water then impinges on the billet surface and provides a much higher rate of cooling.

Sump depths were measured during the start phase by briefly inserting an aluminum rod into the liquid through the hot top and marking the level of the free surface of the Al alloy. When the sump depth became constant, the solidification was judged to be steady state and a thermocouple rake was inserted into the sump.

Three thermocouples were mounted on this rake and positioned near the centerline, the mid-radius, and the surface of the billet. First, a thin guide wire was introduced to provide a support for the rake. The thermocouple rake was then introduced and allowed to stabilize at the casting temperature. Following temperature stabilization the rake was ‘‘captured’’ by locating the rake to the upper-and-outermost area of the mold cavity and clamping the rake to the guide wire. The rake then moved at the casting speed and recorded the three vertical temperature profiles as it descended. Due to the inherent inaccuracy when placing thermocouples, the position of each thermocouple was established by post-cast sectioning of the billet and machining to the thermocouple tips. These final positions were found to be at $r=10$ mm, 106 mm, and 220 mm, the last of these being only a few millimeters from the surface. The uncertainty in the thermocouple measurements was estimated to be ±2°C.

Grain refiners are usually added to DC cast alloys in order to produce a more uniform grain structure in the billet. Grain refinement is normally accomplished by inoculation with ‘‘seed’’ grains and growth rate restriction. The former effect is provided by addition of either TiB_2, Ti_xC_y, or Al_3Ti, while the latter is provided by adding solute elements such as titanium that provide constitutional undercooling. Relative uniformity in grain size and equiaxed shape significantly reduces the anisotropy in the mechanical properties due to columnar grain growth that occurs without a grain refiner. The less oriented grain structure increases the ease with which these billets are rolled or extruded after casting. Two ingots were cast for this study, identical in every respect except the addition of a grain refinement process to one of them and a slight variation in composition (grain refined billet = 6.1 wt% Cu, nongrain refined billet = 5.9 wt% Cu). The grain refiner was a combination of 0.02wt% Ti (added to restrain growth rate) and 6 ppm B (added for TiB_2 inoculation) as Al-3% Ti-1%B rod. This alloy was introduced by continuously feeding a rod into the trough.

Sump profiles were obtained by two separate methods. In the case of grain-refined billet, this was accomplished by sudden addition of a molten Al-Si mixture to the hot top of the caster during steady state casting. For the nongrain-refined billet, the Al-Si mixture was replaced by molten Al-3 percent Ti-1 percentB grain refiner rod. These mixtures were chosen over more traditional methods (e.g., zinc) due to the minimal disturbance they cause in the solidification profile. The macrograph in Fig. 4 shows an example of an Al-Si sump in a grain-refined billet. The sample was prepared by slicing the billet in half, polishing the exposed surface, and etching it with a solution of 10 percent HNO_3, 10 percent HCl, and 0.1 percent HF in deionized water. Composition measurements were made using X-ray fluorescence on 20 samples, taken from each billet at 10 different radial positions. At each of the radial positions, the two samples measured were from different axial locations in the region of the billet apparently at steady-state.

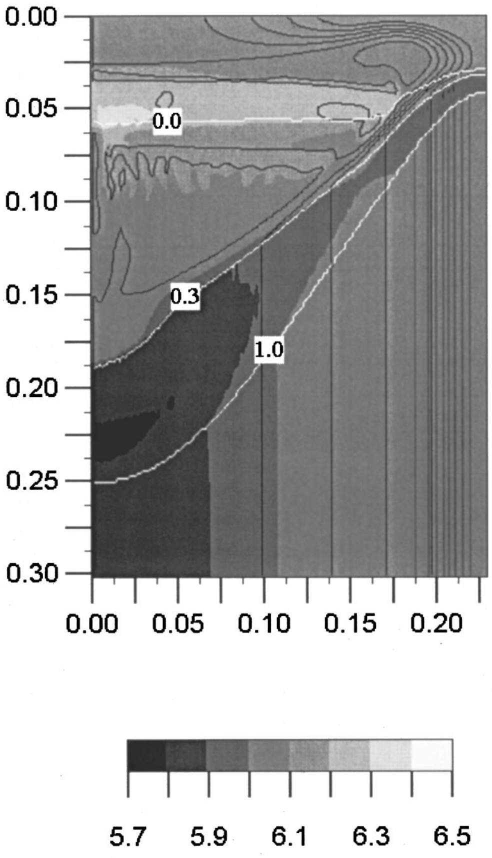

Fig. 2 **Mixture copper composition, streamlines, and solid fraction for billet with grain refiner, using experimental boundary conditions**

Results and Discussion

Predictions were made of the steady state transport phenomena in the casting of the two ingots described above. The numerical results for streamlines, composition, and fraction solid for the grain refined case are shown in Fig. 2. The streamlines show the flow being drawn from the constricted inlet almost horizontally towards the location of jet impingement on the surface. Along with the enrichment of the liquid with copper as solidification proceeds, the high rate of heat extraction under the jets is the engine which drives the buoyancy induced flow in the sump. The flow accelerates as it approaches and passes the chill, and is turned back into the billet by the formation of the rigid solid matrix. The flow then races down the interface of the rigid solid and the slurry region. As the fluid runs down towards the centerline, it is continuously entrained into the rigid mushy zone.

In these calculations, the packing fraction is set to $g_{s,P}=0.3$, which is based on observations in salt solutions and the results of numerical studies found in [11] and [23]. These works also demonstrate the sensitivity of the simulation results to the choice of packing fraction. A slurry of solid particles is formed and carried along with the flow down the rigid interface. Because the particles are formed at temperatures just below the liquidus, they are significantly depleted in copper. The movement of these particles

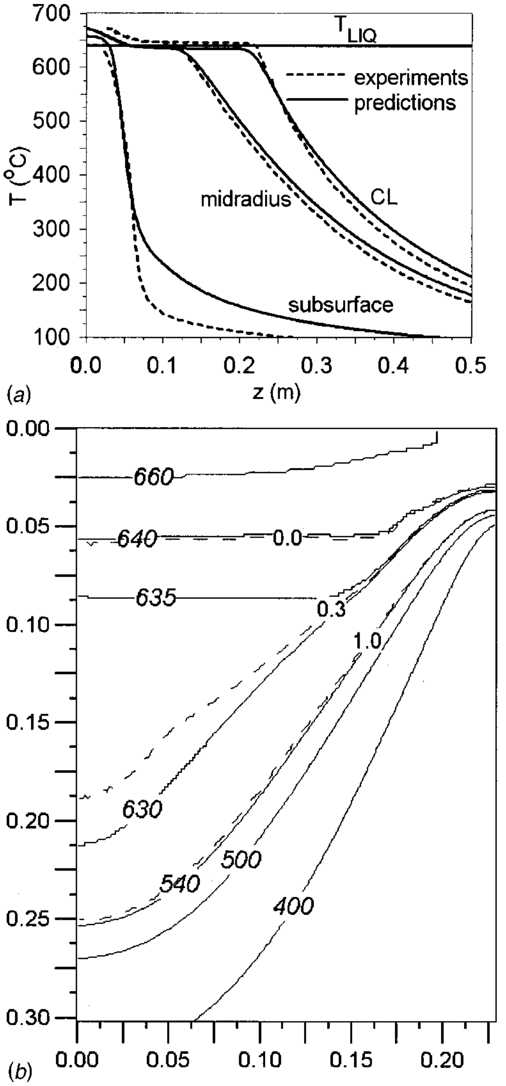

Fig. 3 Results with grain refiner: (*a*) Comparison of predicted and measured temperature profiles, and (*b*) Calculated temperature and fraction solid contours.

from where they form (near the outer radius) to where they finally join the rigid mushy zone (closer to the centerline) results in a region in the center which is deficient in copper.

A comparison of vertical temperature profiles for experiments and simulations is found in Fig. 3(*a*). At all three radial positions, the temperature decreases in the melt due to conduction towards the chill until the liquidus temperature is reached. At that point, solid begins to nucleate on the grain refiner and a solid-liquid slurry forms. Near the surface, the large heat extraction rate solidifies the alloy fast enough that the particles pack quickly and a rigid structure forms. The other two profiles behave somewhat differently, with a sudden shallowing of the temperature gradient around the liquidus temperature. This shallow gradient begins at roughly 0.06 m from the inlet and continues to approximately 0.12 m and 0.22 m for the midradius and centerline profiles, respectively. At those points the temperature gradient became markedly steeper. The reason for this behavior is found in the flow patterns described above. The liquid metal is chilled by the impinging jets and much of the metal runs down the interface at which the solid packs until it is entrained into the rigid mushy zone. This flow pattern leaves a triangular zone of weak recirculation in the center of the sump around which most of the fluid flows. This "dead zone" does contain some solid particles, as it is cooled by the colder liquid rushing underneath it, but most of the heat extracted from the ingot is taken from regions closer to the surface. The effect of this region is seen in the temperature contours in Fig. 3(*b*). Some correspondence can be found between the end of the shallow gradients in Fig. 3(*a*) and the predicted beginning of the rigid mushy zone where the fluid quickly assumes the casting speed. Both Figs. 2 and 3(*a*) present some evidence for double-diffusive flow cells in the sump, each with relatively uniform composition and temperature.

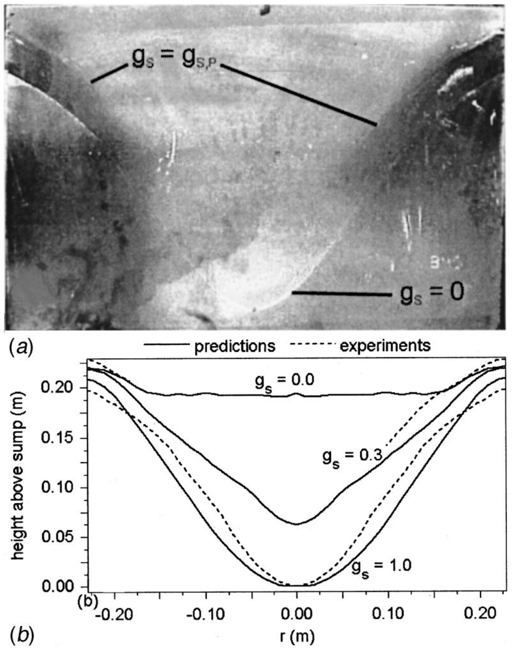

Fig. 4 Sump profiles: (*a*) Grain refined billet; and (*b*) Comparison of predictions and experiments.

An etched macrograph of the grain refined billet is compared to predictions in Fig. 4. In Fig. 4(*a*), lines representing the solidus interface ($g_S = 1.0$) and the transition between the rigid, packed solid and the slurry ($g_S = g_{S,P}$) are seen. These lines are reproduced in Fig. 4(*b*) and compared to calculations. The total sump depth is only overpredicted by approximately 5 percent, while the actual rigid mushy zone thickness at the surface is twice the calculated value near the surface. The general shape of the sump is correct, but the profiles are steeper near the center and shallower near the surface than predicted. This result suggests that the rigid mushy zone is thicker than predicted and, given the agreements in the temperature profiles, perhaps the packing fraction is slightly lower than assumed ($g_S = 0.20 - 0.25?$). Near the surface, it is possible that the packing fraction was even lower, due to the more horizontal surface, which would slow the flow and allow more time for particles to settle.

The radial composition profile is shown in Fig. 5. Near the centerline, the measured composition was up to 10 percent below the nominal value for the alloy, while numerical results predicted less than half that level of segregation there. The study of the effect of packing fraction on centerline segregation found in [11] suggests that this lower composition at the centerline could be an indication that the actual packing fraction was picked to be too low a value. However, the results for the sump temperature profiles discussed above suggest otherwise. The calculated values increased as the radius increased until a peak was reached around $r = 0.15$ m. The experiments also increased, but reached a plateau around $r = 0.07$ m. Figure 4 shows that the observed sump profiles are less steep than in the simulation near the billet surface, suggesting a greater tendency for solid particles to settle there than was predicted. As the radius decreased, the situation was reversed

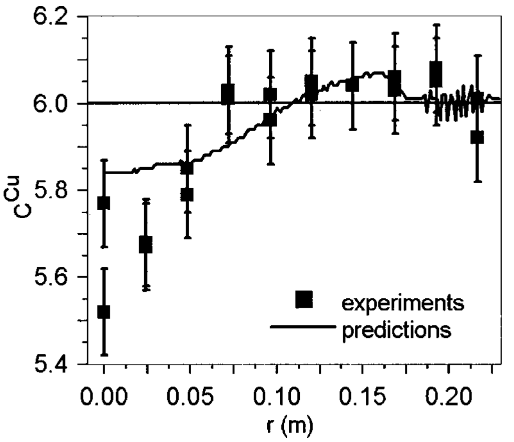

Fig. 5 Comparison of measured and calculated composition profiles for grain refined billet

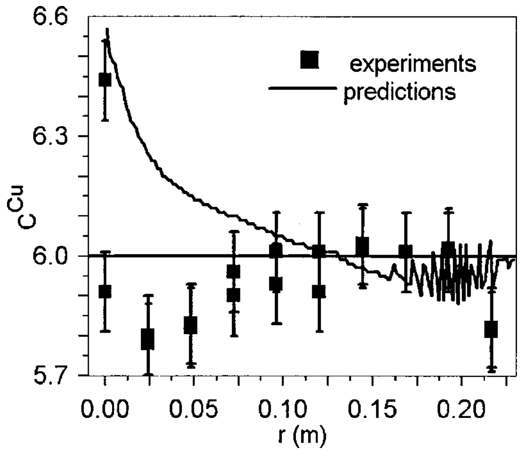

Fig. 7 Comparison of measured and calculated composition profiles for billet with no grain refiner

(predicted sump profiles were less steep than in the real billet), so copper-depleted particles are more likely to end up at the bottom of the sump at the centerline. It was noted above that the diameter of the free-floating solid particles was assumed to be fixed at 75 μm, which was picked based on typical grain sizes in the actual ingot. Using only this average leads to some uncertainty in the results. It should be noted that, in Vreeman and Incropera [11], the difference in the level of centerline macrosegregation with a variation of diameter between 25 and 100 μm was found to be approximately 2 percent of the nominal composition. Such a difference would be about 0.1 wt percent in Fig. 5, which would not account for the discrepancy between the predictions and the measurements. It should also be noted that there are some measured composition variations at given radial positions. These data, taken at different axial locations, show that the composition did vary along the axis of the billet and call into question the assumption that this process truly reaches a steady-state in the flow and composition fields.

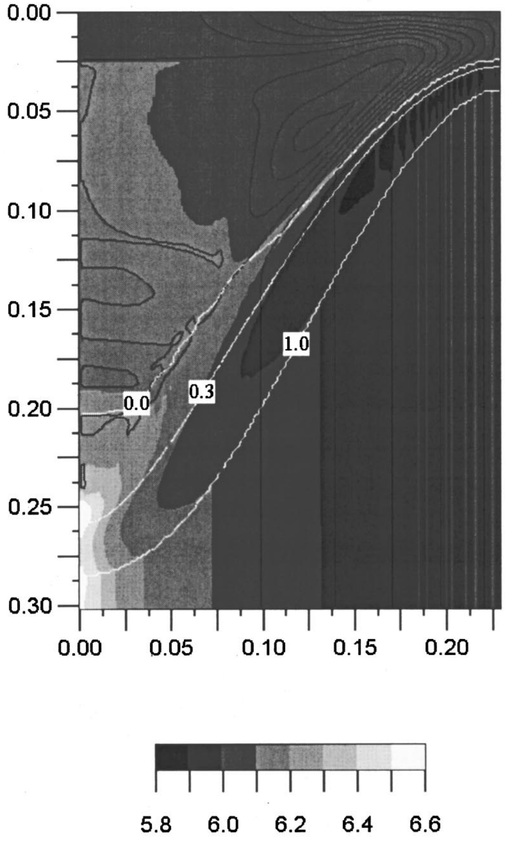

Fig. 6 Mixture copper composition, streamlines, and solid fraction for billet with no grain refiner, using experimental boundary conditions

To understand how well the model simulates the transport phenomena in a non-grain refined process, another numerical case was run with $g_{S,P}=0.0$, simulating purely columnar growth. The results were compared to experimental data from a billet cast in the same manner as above except the absence of grain refiner. Figure 6 shows the predicted composition field and streamline and fraction solid profiles. With $g_{S,P}=0.0$, the model assumes that all of the solid is rigid and moving at the casting velocity. The flow from the inlet to the chill is similar to the previous case, but, because of the much lower packing fraction, the temperature of the flow moving down along the interface of rigid mushy zone is much higher (above the liquidus temperature) than in the grain refined case. Also, with no Cu depleted solid being swept down towards the centerline by the buoyancy driven flow, only Cu enriched liquid reaches the center. This effect accounts for the predicted positive segregation at the centerline.

While the grain refined case showed very good agreement between experiments and modeling, the case with no grain refiner did not. The radial composition profile in Fig. 7 shows a marked difference between predicted and measured macrosegregation. While the predictions suggested a steady increase in composition as the radius becomes smaller, the experiments show a pattern more reminiscent of the profile in the presence of grain refiner (except at the centerline, where there is an increase in copper content). It is well known that the grain structure of these types of large billets undergo a columnar to equiaxed transition around the midradius. This change could be brought about by a slurry of solid particles in the sump generated by fragmentation of the columnar dendrites. This mechanism of particle generation would produce a much smaller slurry region and a much lower packing fraction than the grain refined billet. However, the assumption that all the solid is rigid and moves at the casting speed is not valid in the presence of such a particle cloud. At this point, attributing the discrepancy between the measured and predicted macrosegregation to a columnar to equiaxed transition is speculative and more data are needed to confirm this conclusion.

Conclusions

The continuum mixture model of Vreeman et al. [10] has been used to simulate the casting of industrial scale, 45 cm (18 in.) diameter billets of Al-6wt percentCu using Wagstaff's Airslip™ direct chill casting process. In the case with the addition of an Al-Ti-B grain refiner, some agreement was found between Vreeman's model and the measured vertical temperature profiles, sump profiles, and macrosegregation in the steady state region of the casting process. The validity of some of the assumed model parameters was discussed. It was surmised that the actual packing fraction is less that the 30 percent solid which was used in the calculations, although it must be recognized that it is likely that the packing fraction in the actual billet will vary with position and casting parameters. Without the grain refiner, the model and data do not agree as well, possibly because the grain structure in the real billet undergoes a columnar to equiaxed transition which is not accounted for in the model.

Acknowledgments

The authors wish to thank Mr. Robert Wagstaff of Wagstaff Engineering for funding the experimental portion of this research.

Nomenclature

c = specific heat [J/kg-K]
C^{Cu} = wt percent of copper
d = characteristic dendrite diameter [μm]
D = mass diffusion coefficient [m^2/s]
f = mass fraction
g = volume fraction; gravitational acceleration [m/s^2]
h = enthalpy [J/kg]
k = thermal conductivity [W/m-K]
k_p = equilibrium partition coefficient
K = permeability [m^2]
P = reduced pressure [N/m^2]
r, z = axisymmetric coordinates [m]
t = time [s]
T = temperature [K]
u = axial velocity component [m/s]
v = radial velocity component [m/s]
$\vec{V}$ = velocity vector [m/s]

Greek Symbols

β = contraction ratio
β_s = solutal expansion coefficient
β_T = thermal expansion coefficient [l/K]
μ = dynamic viscosity [kg/s-m]
ρ = density [kg/m^3]

Subscripts

i = mold inlet condition
l = liquid
liq = liquidus
m = mixture
o = reference, nominal value
p = packed, rigid structure
s = solid
S = solutal
T = thermal

References

[1] Finn, T. L., Chu, M. G., and Bennon, W. D., 1992, "The Influence of Mushy Region Microstructure on Macrosegregation in Direct Chill Cast Aluminum-Copper Round Ingots," in *Micro/Macro Scale Phenomena in Solidification*, ASME HTD-Vol. 218, C. Beckermann, et al., eds., ASME, New York, pp. 17–26.

[2] Yu, H., and Granger, D. A., 1986, "Macrosegregation in Aluminum Alloy Ingot Cast by the Semicontinuous Direct Chill (DC) Method," in *Aluminum Alloys-Their Physical and Mechanical Properties*, EMAS, United Kingdom, pp. 17–29.

[3] Chu, M. G., and Jacoby, J. E., 1990, "Macrosegregation Characteristics of Commercial Size Aluminum Alloy Ingot Cast by the Direct Chill Method," in *Light Metals 1990*, C. M. Bickert, ed., TMS, pp. 925–930.

[4] Dorward, R. C., and Beerntsen, D. J., 1990, "Effects of Casting Practice on Macrosegregation and Microstructure of 2024 Alloy Billet," in *Light Metals 1990*, C. M. Bickert, ed., TMS, pp. 919–924.

[5] Gariepy, B., and Caron, Y., 1991, "Investigation in the Effects of Casting Parameters on the Extent of Centerline Macrosegregation in DC Cast Sheet Ingots," in *Light Metals 1991*, E. L. Rooy, ed., TMS, pp. 961–971.

[6] Flood, S. C., Katgerman, L., and Voller, V. R., 1991, "The Calculation of Macrosegregation and Heat and Fluid Flows in the D.C. Casting of Aluminum Alloys," in *Modeling of Casting, Welding and Advanced Solidification Processes V*, M. Rappaz, et al., eds., TMS, pp. 683–690.

[7] Reddy, A. V., and Beckermann, C., 1995, "Simulation of the Effects of Thermosolutal Convection, Shrinkage Induced Flow, and Solid Transport on Macrosegregation and Equiaxed Grain Size Distribution in a DC Continuous Cast Al-Cu Round Ingot," in *Materials Processing in the Computer Age II*, V. R. Voller, et al., eds., pp. 89–102.

[8] Ni, J., and Beckermann, C., 1991, "A Volume-Averaged Two-Phase Model for Transport Phenomena During Solidification," Metall. Mater. Trans. B, **22B**, pp. 349–361.

[9] Reddy, A. V., and Beckermann, C., 1997, "Modeling of Macrosegregation Due to Thermosolutal Convection and Contraction-Driven Flow in Direct Chill Continuous Casting of an Al-Cu Round Ingot," Metall. Mater. Trans. B, **28B**, pp. 479–489.

[10] Vreeman, C. J., Krane, M. J. M., and Incropera, F. P., 2000, "The Effect of Free-Floating Dendrites and Convection on Macrosegregation in Direct Chill Cast Aluminum Alloys—I: Model Development," Int. J. Heat Mass Transf., **43**, pp. 677–686.

[11] Vreeman, C. J., and Incropera, F. P., 2000, "The Effect of Free-Floating Dendrites and Convection on Macrosegregation in Direct Chill Cast Aluminum Alloys—II: Predictions for Al-Cu and Al-Mg alloys," Int. J. Heat Mass Transf., **43**, pp. 687–704.

[12] Bennon, W. D., and Incropera, F. P., 1987, "A Continuum Model for Momentum, Heat and Species Transport in Binary Solid-Liquid Phase Change Systems—I: Model Formulation," Int. J. Heat Mass Transf., **30**, pp. 2161–2170.

[13] Ni, J., and Incropera, F. P., 1995, "Extension of the Continuum Model for Transport Phenomena Occurring During Metal Alloy Solidification—I: The Conservation Equations," Int. J. Heat Mass Transf., **38**, pp. 1271–1284.

[14] Prescott, P. J., Incropera, F. P., and Bennon, W. D., 1991, "Modeling of Dendritic Solidification Systems: Reassessment of the Continuum Momentum Equation," Int. J. Heat Mass Transf., **34**, pp. 2351–2358.

[15] Wang, C. Y., and Beckermann, C., 1996, "Equiaxed Dendritic Solidification With Convection: Part I. Multiscale/Multiphase Modeling," Metall. Mater. Trans. A, **27A**, pp. 2754–2764.

[16] Wang, C. Y., and Beckermann, C., 1996, "Equiaxed Dendritic Solidification With Convection: Part II. Numerical Simulations for an Al-4 wt pct Cu alloy," Metall. Mater. Trans. A, **27A**, pp. 2765–2783.

[17] Beckermann, C., and Wang, C. Y., 1996, "Equiaxed Dendritic Solidification With Convection: Part III. Comparisons With NH4Cl-H2O Experiments," Metall. Mater. Trans. A, **27A**, pp. 2784–2795.

[18] Ocansey, P., Bhat, M. S., and Poirier, D. R., 1994, "Permeability for Liquid Flow in the Mushy Zones of Equiaxed Castings," in *Light Metals 1994*, U. Mannweiler, ed., TMS, pp. 807–812.

[19] *Smithell's Metals Reference Handbook*, 1992, 7th ed., E. A. Barnes and G. B. Brook, eds., Butterworth-Heinemann, Ltd., Oxford, pp. 14.1–14.14.

[20] Bennon, W. D., and Incropera, F. P., 1988, "Numerical Analysis of Binary Solid-Liquid Phase Change Using a Continuum Model," Numer. Heat Transfer, **13**, pp. 277–296.

[21] Patankar, S., 1980, *Numerical Heat Transfer and Fluid Flow*, Hemisphere, New York, pp. 113–134.

[22] Vreeman, C. J., and Incropera, F. P., 1999, "Numerical Discretization of Species Equation Source Terms in Binary Mixture Models of Solidification and Their Impact on Macrosegregation in Semi-Continuous, Direct Chill Casting Systems," Numer. Heat Transfer, Part B, **36**(1), pp. 1–14.

[23] Vreeman, C. J., 1997, "Modeling Macrosegregation in Direct Chill Cast Aluminum Alloys," M.S. thesis, School of Mechanical Engineering, Purdue University, West Lafayette, IN.

Thermal and Electrical Energy Transport and Conversion in Nanoscale Electron Field Emission Processes

T. S. Fisher
e-mail: tsfisher@purdue.edu
Purdue University,
School of Mechanical Engineering,
1288 Mechanical Engineering Building,
West Lafayette, IN 47907-1288

D. G. Walker
Vanderbilt University
Department of Mechanical Engineering,
Box 1592, Station B,
Nashville, TN 37235

This paper considers the theory of electron field emission from nanoscale emitters with particular focus on thermal and electrical energy transport. The foundational theory of field emission is explored, and a model is presented that accounts explicitly for the energy band curvature produced by nanoscale tip emitters. The results indicate that the inclusion of band curvature strongly influences the energetic distribution of electrons for emitter radii less than 50 nm. The energy exchange process between emitted and replacement electrons is shown to allow high local energy transfer rates that can be exploited in direct thermal-to-electrical energy conversion processes. The dependence of energy conversion rates on material and operational parameters is demonstrated. Throughout the paper, opportunities for further research involving nanoscale heat transfer, materials development, and modeling are highlighted. [DOI: 10.1115/1.1494091]

Keywords: *Electronics, Energy Conversion, Heat Transfer, Microscale, Nanoscale*

1 Introduction

Prolific advances in microscale and nanoscale technologies have generated renewed scientific interest in direct thermal-to-electrical energy conversion. These advances have provided researchers with new tools to explore physical phenomena that were previously inaccessible. For example, the controlled fabrication of one- and two-dimensional nanoscale structures has fostered significant recent improvements in the efficiency and capacity of thermoelectric materials and devices [1,2]. Further, the development of thin-film heterostructures has brought thermionic energy conversion, originally a vacuum-based technology, to the solid state [3,4]. The phenomenon of electron field emission is, in some respects, similar to thermoelectric and thermionic transport. However, the thermodynamics of field emission have received less attention, although several recent theoretical papers on direct refrigeration suggest that field emission devices could operate remarkably well [5–10]. In the present work, we consider the foundations of and prospects for direct energy conversion by electron field emission and show that outstanding performance is possible with further progress in fabrication technology, modeling, and engineering.

The emission of electrons from an electrically active surface via quantum tunneling into a vacuum is commonly referred to as field emission. Fowler and Nordheim [11] provided the first theoretical treatment of field emission from planar metal surfaces. Later studies showed that emission could be substantially improved by geometric electric field enhancement provided by elongated structures, such as pyramidal or conical tips. Spindt was the first to show such enhancement using molybdenum cones [12]. Since then, the emission properties of a wide variety of metallic and semiconductor materials and structures have been studied in detail [13,14]. The emission properties of carbon-based/diamond materials, in particular, are very robust [15]. Because they do not require heating, carbon-based and other field emitters are often termed cold cathodes. However, the physical reasons behind the outstanding emission properties of carbon-based materials remain the subject of scientific inquiry [16]. Suggested applications for field emission devices include vacuum field-effect transistors, diodes and triodes, ion sources, electron guns, flat-panel displays, scanning microscopes, and many others [13].

Field emission devices are formed by placing an emitting cathode in close proximity to an anode, separated by vacuum (typically less than 10^{-5} torr). A gate electrode may also be included to modulate emission and to provide a more precise spatial separation from the cathode. Figure 1 shows a tip configuration. The cathode, anode and base electrode materials can be semiconductor (with narrow or wide band gaps) or metals. The gate is typically metallic, and the dielectric between the cathode and gate is commonly SiO_2. Field emission occurs when a sufficiently strong *local* electric field (greater than 0.5 V/Å) exists at the location of emission. Small-scale features within a low average electric field can produce a high local field. Cathode tip structures are designed to provide this field enhancement. Some field enhancement also occurs in film cathodes due to highly localized areas of emission [13].

Most prior work has focused on device operation near room temperature. In fact, the predominant theoretical foundation of field emission—basic Fowler-Nordheim theory—neglects the effects of temperature on emission characteristics. In contrast, consideration of the thermodynamics of field emission requires the inclusion of temperature effects. Fleming and Henderson [17] conducted early experiments on the energy distribution of field-emitted electrons. Their work prompted an exchange of letters with Nottingham [18,19], who predicted that field emission could produce a heating or cooling effect on the cathode, depending on the field strength. Subsequent studies by Good and Muller [20], Dyke and Dolan [21], and Gomer [22] provided a more detailed treatment of the thermodynamics of field emission.

After these early studies, relatively little work occurred on the thermodynamics of field emission for several decades. However, studies by Swanson et al. [23], Engle and Cutler [24], and Bergeret et al. [25] considered measurements of the so-called Nottingham effect [23,25] and the thermodynamics of electron emission and replacement processes [24]. In the past decade, Cutler, Miskovsky, and co-workers have studied various facets of thermodynamics in field emission processes, particularly from diamond

---

Contributed by the Heat Transfer Division for publication in the JOURNAL OF HEAT TRANSFER. Manuscript received by the Heat Transfer Division May 2, 2001; revision received November 5, 2001. Associate Editor: A. Majumdar.

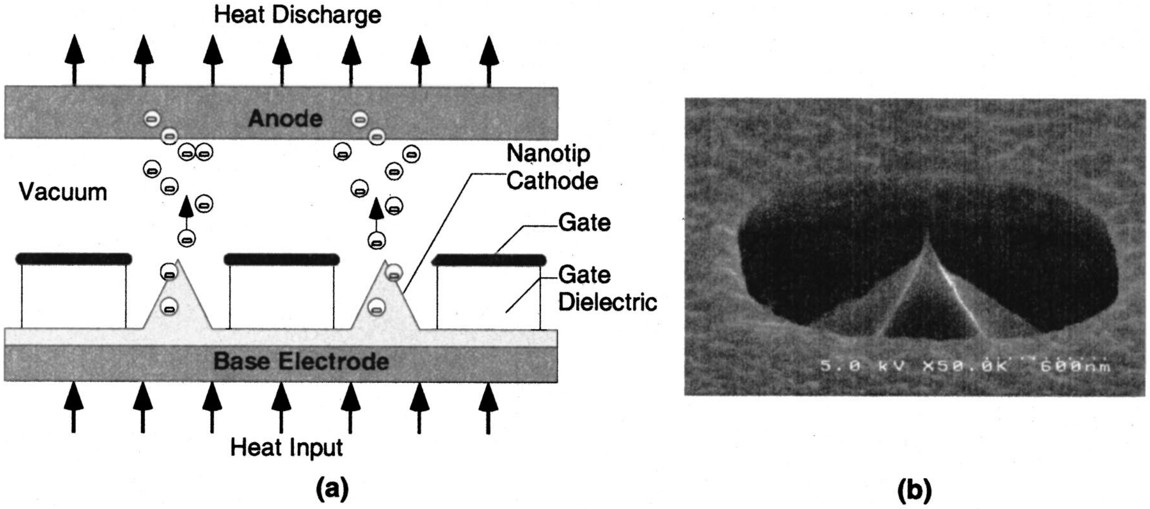

Fig. 1 Nanotips for electron field emission: (*a*) Schematic of an energy conversion system including nanotip electron emitters (cathode), gate electrode, and anode; and (*b*) Example of a polycrystalline diamond nanotip emitter surrounded by a monolithic gate. The tip radius is ~10 nm.

films, including: cathode heating mechanisms and energy exchange processes in sharp metallic emitters [26], average electron energies of emission and replacement [27,28], effects of doping [29], ballistic electron transport [30,31], and internal field emission [32–34]. This body of work has significantly advanced the theoretical understanding of energetic processes in field emission. Yet, the complexity of the physical processes involved in field emission, particularly from polycrystalline materials such as chemical vapor deposited (CVD) diamond, has prevented a thorough understanding of experimentally observed phenomena. Such understanding will be essential if the promise of energy conversion by electron field emission is to be realized.

In the present work, we review the foundational theory of nanoscale field emission with an emphasis on energy transport processes and modeling. The simplifying assumptions that are central to traditional field emission theory are presented, and their applicability to thermodynamic modeling is considered in detail. A more accurate model, which explicitly accounts for emitter-size effects and temperature dependence, is presented for thermodynamic calculations. This model is exercised over relevant parameter ranges, and its utility in interpreting experimental data is demonstrated. This work does not focus on specific energy conversion devices and systems, but rather, provides new insights into energy transport mechanisms in electron field emission from nanoscale emitters. Throughout the work, we identify opportunities for further improvements in modeling and experimental methods and highlight applications to heat transfer and energy conversion that will be important to the future development of nanoscale thermodynamic field emission devices.

2 Thermodynamics of Field Emission

2.1 The Field Emission Process. Field emission occurs when electrons tunnel through a sufficiently narrow potential barrier created by the application of a voltage bias between a cathode (negative bias) and an anode or gate electrode (positive bias). Fowler and Nordheim presented the first theory of field emission from a planar metal surface over seventy years ago [11]. Application of a voltage between planar electrodes creates a constant electric field $F=V/L$ (modified slightly by the image charge as discussed later), where V is the applied voltage and L is the distance between the electrodes. Emission from small, non-planar tips can substantially reduce the required field to produce emission by enhancing the *local* field near the emission site. This enhancement has traditionally been described within the framework of the planar field emission model by multiplying the applied field F by a field enhancement factor β [13–15] such that the local field at the tip becomes βF where β is greater than 1.

The field enhancement factor β depends strongly on small-scale structure. For tip emitters, electric field theory indicates that β is proportional to the inverse of the tip radius R [35]. Thus, the tip radius should be as small as possible to achieve low-voltage emission. However, the use of the field enhancement factor may not be appropriate for energy conversion studies. In effect, the field enhancement factor β linearizes the highly non-linear electric field near the emission surface, as illustrated in Fig. 2. In the figure, both the actual and linearized fields produce the same emission current by assumption. The linear field is necessary to arrive at the analytic current-field relation described below as the basic Fowler-Nordheim relation [see Eq. (7)]. However, the linearization does not satisfy the anode-side boundary condition on the electric potential and generally underestimates the emission flux of high-energy electrons (above the Fermi energy in Fig. 2) and overestimates the emission flux at energies below the Fermi level.

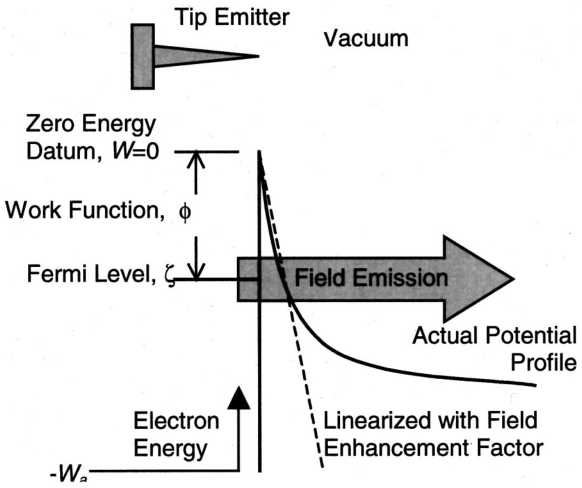

Fig. 2 Electron potential profile near a tip emitter. Solid line represents actual potential field. Dashed line represents approximate, linearized field. Both fields produce the same emission current.

For rectangular barriers, the probability of tunneling is inversely proportional to the exponential of the local potential barrier width [36]. Thus, the shape of the potential profile (which depends on the tip geometry) has a profound effect on the energy distribution of emitted electrons. Nanoscale tips produce extremely large curvature in the vacuum potential near the emission site. Tip radii of 5 nm have been reported [15]. The electrode spacing must be small to provide efficient emission and to minimize space-charge effects, which can degrade performance [37]. The combination of small tip radius R and electrode spacing can produce high emission with low applied bias. Thus, these small-scale features are essential in producing efficient, high-capacity thermal-electrical energy conversion.

In the present work, we employ a model that is more physically accurate than the basic Fowler-Nordheim approach. The present model allows for curvature of the potential field (such as shown in Fig. 2) and thus provides more accuracy in simulating the thermodynamics of field emission. Other more detailed models have been proposed [38–40], but these have typically focused on electronic applications and thus simplified the thermal considerations that are central to the present work. The one-dimensional model is based on the potential field in a spherically symmetric ball-shell system [[9,22] pp. 37–38] and takes the form:

$$V(x)=-qF(L+R)\left[1-\frac{R}{x+R}\right]+G(x) \tag{1}$$

where q is the magnitude of electron charge, F is the applied (global) field, L is the separation distance between electrodes (taken as $L=4\ \mu$m for all cases considered later), R is the *characteristic* radius of the emitter, x is the distance from the emitter, and $G(x)$ is the image potential experienced by emitting electron. This image potential for a spherical emitter tip can be expressed as [39]:

$$G(x)=\frac{-q^2}{4\pi\varepsilon_0}\frac{K-1}{K+1}\frac{R}{(2R+x)2x} \tag{2}$$

where ε_0 is permittivity of vacuum, and K is the emitter's dielectric constant. We note that this image potential neglects possible effects of surface plasmons on the tunneling electrons [41]. Subsequent results will show that the emitter radius R strongly influences the electrical and thermodynamic characteristics of field emission. The first term of Eq. (1) represents the contribution due to the applied field F and equals zero at the emission site ($x=0$). Thus, following the formalism of Good and Muller [20], the zero energy datum exists at the cathode/vacuum interface of Fig. 2 (ignoring image charge potential). The second term in Eq. (1) represents the shift in potential due to image charge [20].

2.2 Current-Voltage Behavior. The physics of field emission have been described in detail by Good and Muller [20]. The development below provides some of the major results that are central to the present work. The total emission current density J takes the form

$$J=q\int_{-W_a}^{\infty}D(W)N(W)dW \tag{3}$$

where $-W_a$ represents the bottom of the emitter's conduction band, W is the x-component of electron energy (i.e., in the direction of emission), the term $N(W)dW$ is the electron supply function, and $D(W)$ is the quantum tunneling transmission coefficient. In the present work, the transmission coefficient is calculated using the WKB approximation [42]

$$D(W)=\exp\left\{-\int_{x_1}^{x_2}\sqrt{\frac{8m}{\hbar^2}|V(x)-W|}dx\right\} \tag{4}$$

where $V(x)$ is the potential profile [see Eq. (1)], x_1 and x_2 are the zeros of $W-V(x)$, and m is the mass of an electron. We note that the WKB approximation is, in general, limited to relatively low fields; however, this approximation is retained here for the purpose of obtaining results without the need to solve Schrödinger's equation numerically for each geometric and field condition. The effect of nanoscale features on the emission current is included through the energy profile $V(x)$ in the transmission coefficient of Eq. (4). The supply function, which represents the number of electrons whose x-direction energy (W) incident on the emission surface falls within dW per second per unit area, can be formulated analytically as [20]

$$\begin{aligned}N(W)dW&=\frac{4\pi}{h^3}\left[\int_0^{\infty}f(W,\rho)\rho d\rho\right]dW\\&=\frac{4\pi mkT}{h^3}\ln\left\{1+\exp\left[\frac{-(W-\zeta)}{kT}\right]\right\}dW\end{aligned} \tag{5}$$

where h is Planck's constant, ρ is the radial electron momentum (perpendicular to the emission direction), k is Boltzmann's constant, T is the emitter temperature, ζ is the Fermi level (see Fig. 2), and $f(W,\rho)$ is the Fermi-Dirac function:

$$f(W,\rho)=\frac{1}{\exp\left(\frac{W-\zeta}{kT}+\frac{\rho^2}{2mkT}\right)+1}. \tag{6}$$

Several simplifying assumptions have been invoked historically to reduce the integral in Eq. (3) to an analytic form. As described above, the use of the field enhancement factor β linearizes the first term of Eq. (1) as $-q\beta Fx$. Also, the temperature dependence is eliminated by neglecting the spreading of the Fermi-Dirac function with increasing temperature. With these assumptions and other integration approximations [20], the current density integral can be expressed analytically as:

$$J=\frac{1.5\times10^{-6}\beta^2F^2}{\phi}\exp\left(\frac{10.4}{\phi^{1/2}}\right)\exp\left(\frac{-6.44\times10^7\phi^{3/2}}{\beta F}\right) \tag{7}$$

where J is the average current density (A/cm^2), F is the *average* applied electric field (V/cm), and ϕ is an effective work function (eV). The foregoing equation is the basic Fowler-Nordheim relation for field emission current. Note that temperature effects are absent. However, most experimental data for room-temperature emission exhibit reasonable agreement with the Fowler-Nordheim theory.

Experimental data are often plotted in so-called Fowler-Nordheim coordinates to determine unknown or uncertain parameters such as emission area, work function, and field enhancement factor by rearranging Eq. (7) as

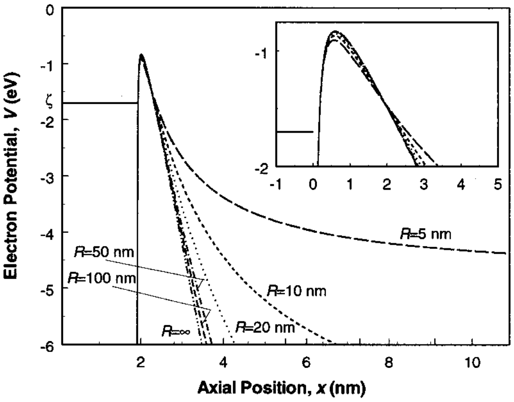

Fig. 3 Electron potential as a function of position from emitter and emitter radius. All profiles produce the same current density, $J=10$ A/cm^2. $\phi=1.7$ eV. $K=5.5$. $T=300$ K.

$$\ln\left(\frac{I}{F^2}\right)=C_0(A,\beta,\phi)+C_1(\beta,\phi)\,\frac{1}{F} \tag{8}$$

where I is the measured current, and A is the effective emission area. A linear fit of F^1 versus $\ln(I/F^2)$ enables the evaluation of the two constants C_0 and C_1, which depend on area A, field enhancement factor β, and effective work function ϕ. Thus, the formulation is underdetermined, and an assumed value is typically taken for one of the three primary variables. As discussed later, significant opportunities for advanced techniques, such as parameter estimation, exist for interpreting experimental data.

The emitter's radius R has a profound effect on the field required to produce emission. Figure 3 shows the potential field near the emitter for radii ranging from $R=5$ nm to infinity (i.e., a planar surface). We choose an effective work function of $\phi=1.7$ eV and a dielectric constant $K=5.5$ (i.e., that of diamond). The value of the work function is a convenient choice to demonstrate energy conversion processes. This choice is consistent with the minimum Schottky barrier for nitrogen-doped diamond [32] and with recent observations and analysis of emission from graphite-like grain boundary regions [43,44]. Later, results for several values of work function are considered (see Fig. 5). For each curve in Fig. 3, the average field produces a current density of 10 A/cm^2, as computed using the potential profile of Eq. (1) and numerical evaluations of the current density integral in Eq. (3). We note that the potential curves for emitter radii smaller than 50 nm exhibit large differences, while those for radii greater than 50 nm (including the planar case $R=\infty$) are quite similar. The figure indicates that the barrier width is slightly narrower in the high-energy regions (i.e., above the Fermi level) for small radii and substantially larger at lower energies for small radii. Thus, the emission radius influences the energetic distribution of emission. The required applied (average) fields range from $F=1.08\,\mathrm{V}/\mu\mathrm{m}$ for $R=5$ nm to $F=614\,\mathrm{V}/\mu\mathrm{m}$ for a planar surface ($R=\infty$). This difference in applied field strongly influences energy conversion due to the increased losses (e.g., from higher required voltages) incurred at high fields.

2.3 Energy Transport. The starting point for energy transport modeling is the current density integral of Eq. (3), from which the number of electrons emitted per unit time and area can be derived. Energy moments of this integral can provide energy transport rates. Chung et al. [27] reported related calculations for overall electron energy using numerical evaluation of double integrals. Here, we separate energy into axial (i.e., in the emission direction) and radial (i.e., perpendicular to the emission direction) components. The underlying free-electron model of the emitter material and the separability of the potential field employed here permit this spatial separation. The advantages of the present formulation are that (1) the double integral can be reduced analytically to a single integral and (2) directional information is retained that is useful in studying important problems that result from electron deposition in the gate or anode. For example, modeling and simulation of anode heating in field emission electronic devices requires an understanding of both the spatial and energetic distributions of electron energy emitted from the cathode.

The average total energy of emitted electrons can be expressed as the sum of axial and radial components, $\langle\varepsilon\rangle=\langle W\rangle+\langle\varepsilon_\rho\rangle$. The average axial energy can be calculated as

$$\langle W\rangle=\frac{1}{J}\int_{-W_a}^{\infty} qWD(W)N(W)\,dW \tag{9}$$

where the transmission function $D(W)$ and the supply function $N(W)dW$ are given in Eqs. (3) and (4), respectively. Similarly, the radial component becomes

$$\begin{aligned}\langle\varepsilon_\rho\rangle&=\frac{4\pi q}{Jh^3}\int_{-W_a}^{\infty}\int_0^{\infty}D(W)f(W,\rho)\,\frac{\rho^3}{2m}\,d\rho\,dW\\&=\frac{4\pi qm(kT)^2}{Jh^3}\int_{-W_a}^{\infty}D(W)\\&\quad\times\left(\frac{1}{2}\,\alpha(W)^2+\frac{\pi^2}{6}+\mathrm{dilog}[e^{\alpha(W)}+1]\right)dW\end{aligned} \tag{10}$$

where

$$\alpha(W)=\frac{W-\zeta}{kT} \tag{11}$$

$$\mathrm{dilog}(x)=\int_1^x\frac{\ln(t)}{1-t}\,dt. \tag{12}$$

The dilog function can be computed efficiently as a series [45].

The sum of the axial and radial energies of Eqs. (9) and (10) represents the total average energy of emitted electrons. These electrons must be replaced by others to preserve charge continuity. The difference in total average energy between emitted and replacement electrons determines whether field emission produces heating or cooling of the cathode. For example, if the average emitted energy exceeds the average replacement energy, then cooling ensues (neglecting other possible energy transport mechanisms, such as reverse emission). The energies of replacement electrons typically fall near the chemical potential ζ. Chung et al. [27] and Cutler et al. [28] showed that the average energy of replacement electrons can be several tenths of an electron volt below ζ. Again, the present formulation differs from that of Chung et al. by separating the axial and radial energy components. The average axial ($\langle W_r\rangle$) and radial ($\langle\varepsilon_{\rho r}\rangle$) replacement energies can be expressed as an integral over available energy states below the chemical potential as

$$\begin{aligned}\langle W_r\rangle&=\int_{-W_a}^{\zeta}\int_0^{\zeta-W}W\{1-f(W,\rho)[1-D(W)]\}\,d\varepsilon_\rho\,dW\int_{-W_a}^{\zeta}\int_0^{\zeta-W}\{1-f(W,\rho)[1-D(W)]\}\,d\varepsilon_\rho\,dW\\&=\frac{\int_{-W_a}^{\zeta}W\{(\zeta-W)+[1-D(W)]kT\}[\ln 2+\alpha(W)-\ln[e^{\alpha(W)}+1]]\,dW}{\int_{-W_a}^{\zeta}\{(\zeta-W)+[1-D(W)]kT\}[\ln 2+\alpha(W)-\ln[e^{\alpha(W)}+1]]\,dW}\end{aligned} \tag{13}$$

$$\langle\varepsilon_{\rho r}\rangle=\frac{\int_{-W_a}^{\zeta}\int_0^{\zeta-W}\varepsilon_\rho\{1-f(W,\rho)[1-D(W)]\}\,d\varepsilon_\rho\,dW}{\int_{-W_a}^{\zeta}\int_0^{\zeta-W}\{1-f(W,\rho)[1-D(W)]\}\,d\varepsilon_\rho\,dW}=\frac{\int_{-W_a}^{\zeta}g(W)\,dW}{\int_{-W_a}^{\zeta}\{(\zeta-W)+[1-D(W)]kT\}[\ln 2+\alpha(W)-\ln[e^{\alpha(W)}+1]]\,dW} \tag{14}$$

where

$$g(W)=\frac{(\zeta-W)^2}{2}-[1-D(W)](kT)^2\left\{\frac{\pi^2}{12}-\ln(2)\alpha(W)+\frac{1}{2}\alpha(W)^2+\mathrm{dilog}[e^{\alpha(W)}+1]\right\}. \tag{15}$$

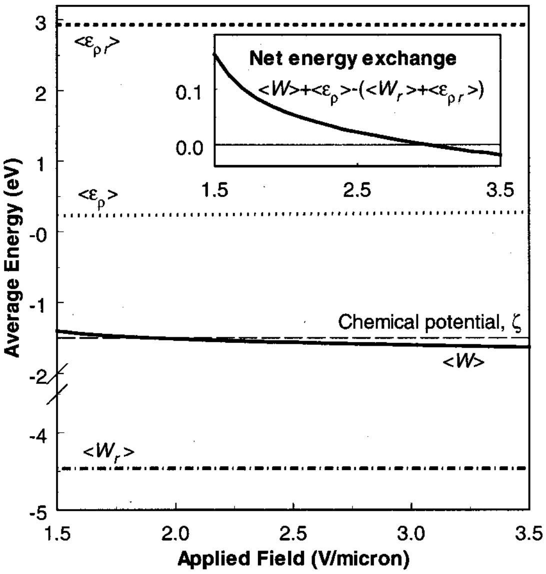

Fig. 4 Average emitted and replacement electron energies as a function applied field. Average axial emitted energy=$\langle W\rangle$. Average radial emitted energy $\langle \varepsilon_\rho\rangle$. Average axial replacement energy=$\langle W_r\rangle$. Average radial emitted energy $\langle \varepsilon_{\rho r}\rangle$. Figure inset shows net electron exchange energy as a function of applied field. Emitter characteristic radius $R=10$ nm. Work function $\phi=1.7$ eV. $K=5.5$. Temperature $T=300$ K.

Each of the integrals in Eqs. (3), (9), (10), (13), and (14) has been evaluated numerically with adaptive quadrature to a convergence to five decimal places. The combination of these integrals provides a means of evaluating the rate of energy flux q'' to or from the cathode due to electron emission. This energy flux can be expressed as the product of the electrical current density and the difference in average energy between emitted and replacement electrons:

$$q''=\frac{J}{q}[\langle W\rangle+\langle \varepsilon_\rho\rangle-(\langle W_r\rangle+\langle \varepsilon_{\rho r}\rangle)]. \tag{16}$$

The average energies described above depend on the applied field F, as shown in Figure 4 for an effective emitter radius of $R=10$ nm at a temperature $T=300$ K. For low fields, the average axial emission energies $\langle W\rangle$ are relatively high compared to the lowest possible axial energy. As the field increases, the energy decreases. The decrease in the emission energy is a consequence of the narrowing barrier width at highly populated energy states. For both axial ($\langle W_r\rangle$) and transverse ($\langle \varepsilon_{\rho r}\rangle$) replacement energies, the slight decrease in energy is a consequence of the greater number of empty low-energy states due to emission from those states. In the case of emission electrons, their average transverse energies ($\langle \varepsilon_\rho\rangle$), which must be greater than zero, tend to increase with increasing field due to the reduction in axial energies described above. This increase is a consequence of the distribution of directional energies governed by Fermi-Dirac statistics (i.e., as axial energy decreases, higher radial energy states become available). The inset of Fig. 4 shows the net electron energy exchange due to the foregoing mechanisms. The net exchange is positive at low field due primarily to the emission of high-energy electrons through the top of the potential barrier. As the field increases,

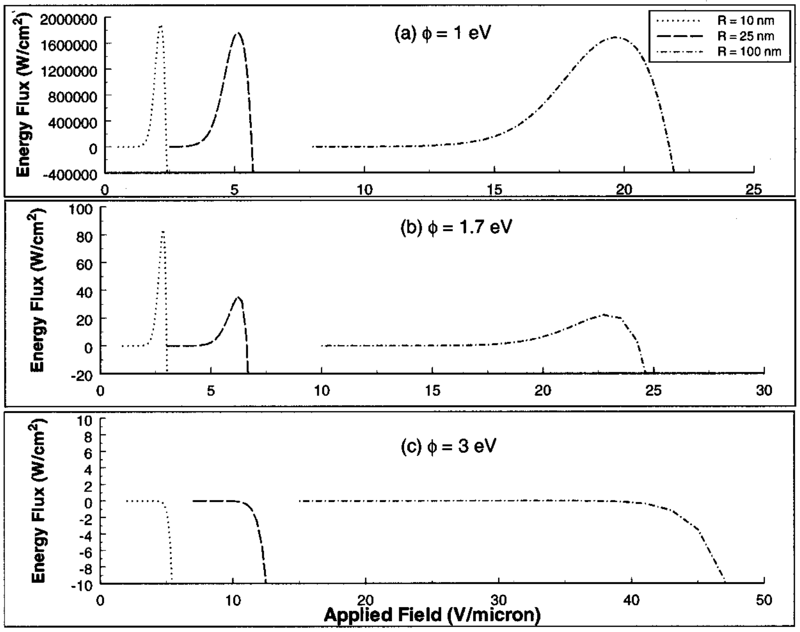

Fig. 5 Emission energy flux from the cathode as a function applied field F, emitter characteristic radius R, and work function ϕ: (*a*) $\phi=1$ eV; (*b*) $\phi=1.7$ eV; and (*c*) $\phi=3$ eV. Each part shows curves for three emitter radii, $R=10$, 25, and 100 nm. $K=5.5$. Temperature $T=300$ K.

more low-energy electrons emit, and at a field of approximately 3 V/μm, the net exchange of energy becomes negative and causes cathode heating.

Predictions from the theory outlined above suggest that substantial rates of direct electrical-thermal energy conversion and transfer are possible with field emission. The energy flux q'' from the cathode depends primarily on four parameters: (1) emitter work function ϕ, (2) characteristic emitter radius R, (3) applied field F, and (4) temperature T. As shown in Fig. 4, net exchange energies greater than 0.1 eV are possible. The net energy flux is the product of this exchange energy and the electric current density [see Eq. (16)], and consequently, even a large net energy exchange may produce little thermodynamic effect if the current density is low.

Figure 5 shows the results of this balance for three emitter radii ($R = 10$ nm, 25 nm, 100 nm) and work functions ($\phi = 1$ eV, 1.7 eV, 3 eV). For each condition, the energy flux at low fields is negligible due to the low electrical current density. As the field increases, the electrical current increases, and substantial energy flux away from the emitter is made possible by the net energy exchange between emitted and replacement electrons. As the field increases further, the energy exchange decreases and ultimately becomes negative, which causes heating. As the emitter radius increases, the peak energy flux decreases due to the downward shift in energy distribution that is inherent to larger radii (see Fig. 2). At the same time, the field range for positive energy flux grows with increasing radius due to the reduction in field enhancement. The figure also shows a strong influence of the work function. For the lowest work function, $\phi = 1$ eV, very high rates of local energy flux of order $q'' \sim 10^6$ W/cm^2 are predicted for all emitter radii. The corresponding local current densities for the maximum energy fluxes are of order $J \sim 10^7$ A/cm^2 for all radii. As the work function increases to $\phi = 1.7$ eV, the peak energy fluxes decrease significantly ($q'' \sim 10$ to 100 W/cm^2), and local current densities at the peak energy fluxes are of order $J \sim 10^4$ A/cm^2. For the largest work function, $\phi = 3$ eV, maximization of energy flux is not evident, and the energy flux is negligible or negative over the entire range of applied fields. These results indicate that low-work-function materials are necessary to enable significant energy conversion. The probability of developing materials with effective work functions as low as $\phi = 1$ eV are quite remote, and therefore the associated heat fluxes in Fig. 1(*a*) may be practically infeasible. For the case of semiconductor emitters, appropriate n-type dopants could potentially produce effective work functions near $\phi = 1.7$ eV, and we note that, in the particular case of diamond, the goal of finding suitable shallow donors has been elusive. However, several recent studies indicate some optimism in this area [46–49].

3 Discussion

Field emission from semiconductor materials can involve both internal emission from a metallic conductor into the semiconductor and external emission from the semiconductor into vacuum. For example, much recent work [32–34,50,51] on diamond emitters suggests that the interface between a base electrode (either metallic or semiconductor) and diamond (a wide-bandgap semiconductor) governs the field emission process. Therefore, the analysis of semiconductor emitters can be substantially more complicated than that of metals (such as shown in Fig. 2). However, wide-bandgap semiconductors, such as diamond, can provide substantial energy filtering effects as well as favorable structural properties, and consequently, are well suited to direct energy conversion applications.

Tunneling into the conduction band of a diamond cathode is shown schematically in the one-dimensional band diagrams of Fig. 6. Figure 6(*a*) shows the unbiased state, with slight band bending due to space charge effects [52]. The band gap, $E_g = E_C - E_V$, of diamond is 5.5 eV, and the difference between the base electrode's Fermi energy and the cathode's valence band energy for an undoped sample is $E_{FB} - E_V = 1.4$ eV, which is the energy associated with grain boundaries. Cathode doping can alter this energy difference. The effective work function ϕ_{eff} represents the axial electron energy required for an electron in the base electrode to emit into vacuum. The parameter $\chi = E_{\text{vac}} - E_C$ is the electron affinity and represents the energy required to eject an electron from the conduction band into vacuum. Numerous recent studies indicate that χ is negative (although it is shown positive in Fig. 6) when the diamond surface is terminated by hydrogen [53–56]. This negative electron affinity can significantly enhance emission.

A gate electrode can be used to extract high-energy electrons from the cathode. Figure 1 shows nanotip emitters surrounded by gate structure. Under a voltage bias (positive on the gate electrode), the electric field causes the bands in the cathode and vacuum to shift, as shown in Fig. 6(*b*). Near the base-electrode/cathode interface, significant band bending narrows the potential barrier width. This narrow barrier increases the probability of quantum tunneling, and field emission occurs. A second tunneling process may also occur at the cathode/vacuum barrier for $\chi > 0$.

The presence of internal field emission significantly complicates the task of modeling. Solid-state scattering events can alter the distribution of electrons that ultimately emit into vacuum. For polycrystalline diamond films near room temperature, Lerner et al. [31] showed that electrons can travel quasiballistically for films less than several microns in thickness. Thus, for thin films, the band structure of Fig. 6 can provide the basis for a reasonable emission model. However, neither Fowler-Nordheim theory nor the foregoing model possesses the fidelity to represent such complex profiles in detail. We note, however, that unlike basic Fowler-Nordheim theory, the present model does allow for the inclusion of size effects in thermodynamic calculations. A more rigorous approach generally requires numerical solutions to Schrödinger's equation [57], and the inclusion of multi-dimensional effects [58]. The numerical solution of Schrödinger's equation possesses the advantage of eliminating the WKB approximation in the evalua-

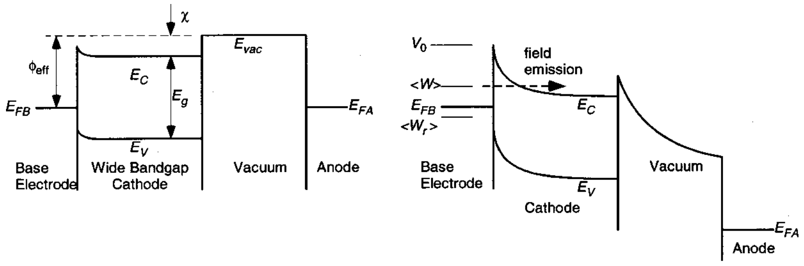

(a) at thermal equilibrium

(b) tunneling into and from the conduction band under bias

Fig. 6 Band diagrams for field emission from diamond: (*a*) Unbiased at thermal equilibrium; and (*b*) Field emission via tunneling from the base electrode to the cathode's conduction band and from the conduction band to vacuum

tion of transmission coefficients. Further, a general numerical solver would enable analysis of more complex systems, such as resonant-tunneling structures [6–8]. Advanced, multidimensional tunneling formulations have been reported [59–64] with particular application to scanning tunneling microscopy. However, to date, a combined analysis, including complex band structure, multi-dimensionality, numerically computed transmission coefficients, and energy exchange calculations has not been reported and would represent a significant achievement.

We also anticipate that, with recent and continued progress in nanoscale fabrication methods, new nanoscale materials and surfaces will require the replacement of continuum models with subcontinuum quantum models. Such models would replace the supply function $N(W)dW$ of Eq. (5). Miskovsky and co-workers have shown that discrete atomic-scale effects can strongly influence the local density of electron states from which emitting electrons originate [65]. They have also considered strong localized heating and thermoelectric effects near atomically sharp emitters [66]. Karabutov et al. [44] have postulated that two-dimensional quantum wells are responsible for the low turn-on fields of polycrystalline diamond emitters. Interestingly, the resulting current-voltage relations still closely follow Fowler-Nordheim trends. Fursey and Glazanov have compared current-voltage predictions of formulations that include nanoscale tip curvature with those from traditional Fowler-Nordheim theory [67]. A group of studies by He, Cutler, Miskovsky, and co-workers [68–71] and Jensen and co-workers [39,72] highlight the effects of nanoscale tip geometries on field emission and the commensurate shortcomings of using traditional Fowler-Nordheim theory for these small-scale devices. These studies reinforce the need for advanced treatment of nanoscale and atomic effects in the study of field emitters.

Advanced electron spectroscopy will be required to study rigorously the thermodynamics of field emission. Gadzuk and Plummer reviewed the field-emission energy distribution (FEED) technique [73]. Most such spectrometers employ hemispherical elements [74,75]. Recently, researchers have developed non-hemispherical [76] and simplified hemispherical [77] devices that offer enhanced resolution and simplicity. Electron spectroscopy has proven to be useful for studying field emission devices with electronic functions. An understanding of the electron energy distribution is particularly important in the study of anode heating, which is a significant cause of failure in high-current field emission devices [78]. For energy-conversion field-emission devices, experimental quantification of electron energy distributions will be essential.

Another area for further study involves the interpretation of experimental data and its comparison with increasingly complex models. Determination of emission parameters from the Fowler-Nordheim theory [see Eq. (7)] has historically been a heuristic process where the value of the parameters is largely dependent on the estimation procedure. The incongruous results are a feature of the models because the unknown parameters of interest are primarily non-physical and are, in general, correlated. The Fowler-Nordheim formulation of emission involves three parameters, namely the emission area (A), the work function (ϕ), and a field enhancement factor (β). However, by casting emission data into a linear form, only two parameters can be uniquely determined; two of the free parameters are linearly dependent on the third. As a result, experimenters must fix one of the free parameters using independent data and then proceed to estimate the remaining parameters using a linear regression.

One approach commonly used and described by Brodie and Schwoebel [13] is to differentiate the Fowler-Nordheim equation with respect to the applied voltage. The voltage and current are measured in experiments and the derivative of the $I-V$ characteristics can also be obtained from the data. Thus, at any point, a value for C_0 [see Eq. (8)] can be calculated, and a regression procedure is commonly employed to estimate its value. Substitution of this value back into the governing equation provides C_1. Estimates of these two factors enable estimation of two of the three unknown parameters (A, ϕ, and β) with an assumed value for the third. Estimation of these values is dubious with linear Fowler-Nordheim analysis. Also note that the estimation of the derivative of the data (dI/dV) deserves scrutiny because the differentiation of discrete points tends to magnify experimental errors [79].

A geometrically more rigorous approach to emission modeling and interpretation of experimental data has been developed by Jensen and co-workers [37,72,80]. In their work, the emission area and field enhancement are related analytically to the geometry of the tip emitter. Further, the variability of emission from multiple tips in an array is considered explicitly. It is likely that such an approach, when coupled with emission models that include band-bending effects, will provide greater efficacy in the interpretation of experiment results.

In all existing and proposed models for the interpretation of field emission data, a statistical approach can provide estimates with superior confidence as well as insights into the accuracy of estimated parameters. The sensitivity of the emission current to the free parameters can indicate the identifiability of the parameters in a given emission model. Parameter estimation techniques [81,82] represent a powerful tool for experimental interpretation and model development. Such tools are particularly suitable for field emission applications due to significant measurement noise (e.g., transient fluctuations of emission current) and the potential complexity of new theoretical and computational models. For example, the model developed herein, with the inclusion of temperature and characteristic emitter radius, presents an opportunity for more rigorous determination of physics-based emission parameters through advanced estimation methods.

The questions of total energy conversion capacity and efficiency are important to consider for the broad range of potential applications of field emission devices. The energy fluxes shown in Fig. 5 result from emission from nanoscale emitters. Both the local energy flux and the number density per unit area of nanoscale emitters will ultimately determine the total energy conversion capacity. A variety of fabrication technologies-nanodiamond pyramidal tips [83], focused ion beam molds [84], and carbon nanotubes [85]-exist that can produce tremendously high number densities of field nanoemitters. We believe that the rapidly evolving field of nanofabrication will ultimately present a wide range of fabrication options.

Ideally, the thermodynamic performance metrics, coefficient of performance for refrigeration and thermal efficiency for power generation, of field emission devices should approach that of the limiting Carnot efficiency, in a manner similar to that of vacuum thermionic devices [86]. In practice, thermal radiation and conduction losses, as well as electrical losses (e.g., in terminal leads and from Joule heating of tip emitters), would limit practical maximum efficiencies to approximately 50–70 percent of the Carnot efficiencies. This estimate is consistent with those for thermionic converters [86]. Calculations by Cutler et al. [10] suggest that the coefficient of performance of a refrigeration field emission device can exceed that of traditional thermoelectric devices. The performance can improve further through the use of gate electrodes and with retarding potentials. For power generation applications, traditional thermionic devices using metallic emitters can be highly efficient. However, the use of these materials has been limited to high temperature (>1500 K) applications because they prevent the emission of all except the highest energy electrons. In effect, thermionic converters are limited by the emitter material's work function. In contrast, the development of novel emitter materials with low work functions could make the thermionic process amenable to operation at lower temperatures due to the allowed emission of lower-energy electrons. Consequently, we believe that field emission materials and devices hold great promise for enabling the operation of a fundamentally efficient energy conversion mechanism in temperature ranges where other direct energy conversion processes lack either sufficient capacity (e.g., thermionics) or efficiency (e.g., thermoelectrics).

4 Summary and Conclusions

Field emission offers an intriguing new technical approach for direct energy conversion. This work has provided an overview of the physics of electron field emission with particular emphasis on thermal and nanoscale geometric effects. The traditional model for field emission, based on Fowler-Nordheim theory, ignores thermal effects and linearizes highly non-linear fields in order to achieve an analytic solution. The new model presented herein includes the effects of temperature and nanoscale emitter geometry. The efficacy of this approach is demonstrated by the strong effects of the characteristic emitter radius on emission (see Figs. 3 and 5).

The potential for high energy capacity and high efficiency suggests that field emission devices may find a broad range of applications; however, many technical challenges remain, particularly as new nanoscale materials and fabrication technologies emerge. As characteristic dimensions decrease below 10 nm, the continuum assumption becomes suspect, and atomic-scale modeling will be required. Further, the complex band structure of semiconductor emitters, even at continuum scales, necessitates more advanced approaches to the characterization of quantum tunneling. In order for models to be useful, important material properties, such as work functions and electron affinities, must be characterized experimentally.

Another major challenge lies in the demonstration of practical energy conversion. In order to serve useful engineering purposes, the nanoscale emission phenomenon must be scaled up to macroscopic dimensions. Thus geometric, chemical, and surface uniformity will be important considerations in any functional device. The achievement of such uniformity is a significant challenge, even in a laboratory setting.

Finally, we note that a complete study of practical thermodynamic efficiencies has not yet been reported. The similarity between field emission and thermionic emission suggests that high efficiency operation is possible. The efficiency will depend on a wide range of factors, including radiative material properties, anode work functions, and electrical resistivity of electrodes. This issue is the subject of current study by the authors.

Acknowledgments

The authors thank Professors J. L. Davidson, W. P. Kang, and A. M. Strauss for helpful conversations. This work was supported by the NSF CAREER program (Grant # CTS-9983961) and by a Vanderbilt Discovery Grant.

Nomenclature

$D(W)$ = tunneling transmission coefficient, see Eq. (4)
F = applied electric field $(V/\mu\text{m}) = V/L$
f = Fermi-Dirac function, see Eq. (6)
$G(x)$ = image charge potential (V), see Eq. (2)
h = Planck's constant$=4.1357\times10^{-15}$ eV·s
I = electrical current (A)
J = current density (A/cm^2)
K = emitter's dielectric constant
k = Boltzmann's constant$=8.617\times10^{-5}$ eV/K
L = cathode-anode separation (μm)
m = electron rest mass$=9.1095\times10^{-31}$ kg
$N(W)$ = electron supply function [s/(kg m^4)], see Eq. (5)
q = electron charge$=1.60219\times10^{-19}$ Coulomb
R = emitter characteristic radius (nm)
V = applied voltage (V)
W = axial electron energy (eV)
x = axial coordinate (m)

Greek Symbols

β = field enhancement factor, see Fig. 2
χ = electron affinity (eV), see Fig. 6
ε = dielectric constant, see Eq. (2)
ϕ = work function (eV), see Fig. 2
ζ = Fermi level (eV), see Fig. 2
ρ = radial electron momentum (kg m/s)

Subscripts

r = replacement electron value
ρ = radial direction

References

[1] Hicks, L. D., and Dresselhaus, M. S., 1993, "Effect of Quantum-Well Structures on the Thermoelectric Figure of Merit," Phys. Rev. B, **47**, pp. 12 727–12 731.
[2] Mahan, G. D., 1998, "Good Thermoelectrics," Solid State Phys., **51**, pp. 81–157.
[3] Mahan, G. D., and Woods, L. M., 1998, "Multilayer Thermionic Refrigeration," Phys. Rev. Lett., **18**, pp. 4016–4019.
[4] Shakouri, A., Lee, E. Y., Smith, D. L., Narayanamurti, V., and Bowers, J. E., 1998, "Thermoelectric Effects in Submicron Heterostructure Barriers," Microscale Thermophys. Eng., **2**, pp. 37–47.
[5] Miskovsky, N. M., and Cutler, P. H., 1999, "Microelectronic Cooling Using the Nottingham Effect and Internal Field Emission in a Diamond (Wide-Band Gap Material) Thin-Film Device," Appl. Phys. Lett., **75**, pp. 2147–2149.
[6] Tsu, R., and Greene, R. F., 1999, "Inverse Nottingham Effect Cooling in Semiconductors," Electrochem. Solid-State Lett., **2**, pp. 645–647.
[7] Korotkov, A. N., and Likharev, K. K., 1999, "Possible Cooling by Resonant Fowler-Nordheim Emission," Appl. Phys. Lett., **75**, pp. 2491–2493.
[8] Korotkov, A. N., and Likarev, K. K., 2000, "Cooling by Resonant Fowler-Nordheim Emission," Physica B, **284**, pp. 2030–2031.
[9] Fisher, T. S., 2001, "Influence of Nanoscale Geometry on the Thermodynamics of Electron Field Emission," Appl. Phys. Lett., **79**(22), pp. 3699–3701.
[10] Cutler, P. H., Miskovsky, N. M., Kumar, N., and Chung, M. S., 2000, "New Results on Microelectronic Cooling Using the Inverse Nottingham Effect. Low Temperature Operation and Efficiency," Electrochemical Society Proceedings, **2000–28**, pp. 99–111.
[11] Fowler, R. H., and Nordheim, L. W., 1928, "Field Emission From Metallic Surfaces," Proc. R. Soc. London, Ser. A, **119**, pp. 173–181.
[12] Spindt, C. A., 1968, "A Thin Film Field Emission Cathode," J. Appl. Phys., **39**, pp. 3504–3505.
[13] Brodie, I., and Schwoebel, P. R., 1994, "Vacuum Microelectronic Devices," Proc. IEEE, **82**, pp. 1006–1018.
[14] Nation, J. A., Schachter, L., Mako, F. M., Len, L. K., Peter, W., Tang, C.-M., and Rao, T., 1999, "Advances in Cold Cathode Physics and Technology," Proc. IEEE, **87**, pp. 865–889.
[15] Kang, W. P., Fisher, T. S., and Davidson, J. L., 2001, "Diamond Microemitters—The New Frontier of Electron Field Emission and Beyond," New Diamond and Frontier Carbon Technology, **11**, pp. 129–146.
[16] Robertson, J., 1999, "Mechanisms of Electron Field Emission from Diamond, Diamond-Like Carbon, and Nanostructured Carbon," J. Vac. Sci. Technol. B, **17**, p. 659.
[17] Fleming, G. M., and Henderson, J. E., 1940, "The Energy Losses Attending Field Current and Thermionic Emission of Electrons from Metals," Phys. Rev., **58**, pp. 887–894.
[18] Nottingham, W. B., 1941, "Remarks on Energy Losses Attending Thermionic Emission of Electrons from Metals," Phys. Rev., **59**, pp. 906–907.
[19] Fleming, G. M., and Henderson, J. E., 1941, "On the Energy Losses Attending Thermionic and Field Emission," Phys. Rev., **59**, pp. 907–908.
[20] Good, R. H., and Muller, E. W., 1956, "Field Emission," Handbook of Physics, **21**, pp. 176–231.
[21] Dyke, W. P., and Dolan, W. W., 1956, "Field Emission," Adv. Electron. Electron Phys., **VIII**, pp. 90–187.
[22] Gomer, R., 1961, *Field Emission and Field Ionization*, Harvard University Press, Cambridge, MA.
[23] Swanson, L. W., Crouser, L. C., and Charbonnier, F. M., 1966, "Energy Exchanges Attending Field Electron Emission," Phys. Rev., **151**, pp. 327–340.
[24] Engle, I., and Cutler, P. H., 1967, "The Effect of Different Surface Barrier Models on the Nottingham Energy Exchange Process," Surf. Sci., **8**, pp. 288–307.
[25] Bergeret, H., Septier, A., and Drechsler, M., 1985, "Nottingham Effect of a Superconducting Metal," Phys. Rev. B, **31**, pp. 149–153.
[26] Miskovsky, N. M., Park, S. H., He, J., and Cutler, P. H., 1993, "Energy Exchange Processes in Field Emission from Atomically Sharp Metallic Emitters," J. Vac. Sci. Technol. B, **11**, pp. 366–370.
[27] Chung, M. S., Cutler, P. H., Miskovsky, N. M., and Sullivan, T. E., 1994, "Energy Exchange Processes in Electron Emission at High Fields and Temperatures," J. Vac. Sci. Technol. B, **12**, pp. 727–736.
[28] Cutler, P. H., Chung, M. S., Miskovsky, N. M., Sullivan, T. E., and Weiss, B. L., 1994, "A New Model for the Replacement Process in Electron-Emission at High Fields and Temperatures," Appl. Surf. Sci., **76**, pp. 1–6.
[29] Huang, Z.-H., Cutler, P. H., Miskovsky, N. M., and Sullivan, T. E., 1995,

''Calculation of Electron Field Emission from Diamond Surfaces,'' J. Vac. Sci. Technol. B, **13**, pp. 526–530.

[30] Cutler, P. H., Huang, Z.-H., Miskovsky, N. M., D'Ambrosio, P., and Chung, M., 1996, ''Monte Carlo Study of Hot Electron and Ballistic Transport in Diamond: Low Electric Field Region,'' J. Vac. Sci. Technol. B, **14**, pp. 2020–2023.

[31] Lerner, P., Cutler, P. H., and Miskovsky, N. M., 1997, ''Hot Electron and Quasiballistic Transport of Nonequilibrium Electrons in Diamond Thin Films,'' J. Vac. Sci. Technol. B, **15**, pp. 398–400.

[32] Lerner, P., Cutler, P. H., and Miskovsky, N. M., 1997, ''Theoretical Analysis of Field Emission from a Metal Diamond Cold Cathode Emitter,'' J. Vac. Sci. Technol. B, **15**, pp. 337–342.

[33] Lerner, P., Miskovsky, N. M., and Cutler, P. H., 1998, ''Model Calculations of Internal Field Emission and J-V Characteristics of a Composite n-Si and N-Diamond Cold Cathode Source,'' J. Vac. Sci. Technol. B, **16**, pp. 900–905.

[34] Cutler, P. H., Miskovsky, N. M., Lerner, P. B., and Chung, M. S., 1999, ''The Use of Internal Field Emission to Inject Electronic Charge Carriers into the Conduction Band of Diamond Films: A Review,'' Appl. Surf. Sci., **146**, pp. 126–133.

[35] Everhart, T. E., 1967, ''Simplified Analysis of Point-Cathode Electron Sources,'' J. Appl. Phys., **38**, pp. 4944–4957.

[36] Robinett, R. W., 1997, *Quantum Mechanics: Classical Results, Modern Systems, and Visualized Examples*, Oxford University Press, New York, pp. 263–264.

[37] Jensen, K. L., Kodis, M. A., Murphy, R. A., and Zaidman, E. G., 1997, ''Space Charge Effects on the Current-Voltage Characteristics of Gated Field Emitter Arrays,'' J. Appl. Phys., **82**, pp. 845–854.

[38] Modinos, A., 1984, *Field, Thermionic and Secondary Electron Emission Spectroscopy*, Plenum Press, New York.

[39] Jensen, K. L., and Zaidman, E. G., 1993, ''Field Emission from an Elliptical Boss: Exact Versus Approximate Treatments,'' Appl. Phys. Lett., **63**, pp. 702–704.

[40] Jensen, K. L., 1999, ''Semianalytical Model of Electron Source Potential Barriers,'' J. Vac. Sci. Technol. B, **17**, pp. 515–519.

[41] Nazarov, Yu. V., 1989, ''Anomalous Current-Voltage Characteristics of Tunnel Junctions,'' Sov. Phys. J., **68**, pp. 561–566.

[42] Robinett, R. W., 1997, *Quantum Mechanics: Classical Results, Modern Systems, and Visualized Examples*, Oxford University Press, New York, pp. 229–233.

[43] Karabutov, A. V., Frolov, V. D., Pimenov, S. M., and Konov, V. I., 1999, ''Grain Boundary Field Electron Emission from CVD Diamond Films,'' Diamond Relat. Mater., **8**, pp. 763–767.

[44] Karabutov, A. V., Frolov, V. D., and Konov, V. I., 2001, ''Diamond/sp^2-Bonded Carbon Structures: Quantum Well Field Electron Emission,'' Diamond Relat. Mater., **10**, pp. 840–846.

[45] Dwight, H. B., 1961, *Tables of Integrals and Other Mathematical Data*, Macmillan Company, New York, p. 144.

[46] Collins, A. T., 1994, *Properties and Growth of Diamond*, G. Davies, ed., EMIS Datareviews Series No. 9, INSPEC, London.

[47] Koizumi, S., Kamo, M., Sato, Y., Mita, S., Sawabe, A., Reznik, A., Uzan-Saguy, C., and Kalish, R., 1998, ''Growth and Characterization of Phosphorus Doped *n*-type Diamond Thin Films,'' Diamond Relat. Mater., **7**, pp. 540–544.

[48] Sakaguci, I., Gamo, M. N., Kikuchi, Y., Yasu, E., and Haneda, H., 1999, ''Sulfur: A Donor Dopant for n-type Diamond Semiconductors,'' Phys. Rev. B, **60**, pp. R2139–R2141.

[49] Saada, D., Adler, J., and Kalish, R., 2000, ''Sulfur: A Potential Donor in Diamond,'' Appl. Phys. Lett., **77**, pp. 878–879.

[50] Geis, M. W., Twichell, J. W., and Lyszczarz, T. M., 1996, ''Diamond Emitters Fabrication and Theory,'' J. Vac. Sci. Technol. B, **14**, pp. 2060–2067.

[51] Koenigsfeld, N., Philosoph, B., and Kalish, R., 2000, ''Field Emission Controlled by the Substrate/CVD Diamond Interface,'' Diamond Relat. Mater., **9**, pp. 1218–1221.

[52] Silva, S. R. P., Amaratunga, G. A. J., and Okano, K., 1999, ''Modeling of the Electron Field Emission Process in Polycrystalline Diamond and Diamond-like Carbon Thin Films,'' J. Vac. Sci. Technol. B, **17**, pp. 557–561.

[53] Ristein, J., Stein, W., and Ley, L., 1998, ''Photoelectron Yield Spectroscopy on Negative Electron Affinity Diamond Surfaces: A Contactless Unipolar Transport Experiment,'' Diamond Relat. Mater., **7**, pp. 626–631.

[54] Baumann, P. K., and Nemanich, R. J., 1998, ''Surface Cleaning, Electronic States and Electron Affinity of Diamond (100), (111) and (110) Surfaces,'' Surf. Sci., **409**, pp. 320–355.

[55] Krainsky, I. L., and Asnin, V. M., 1998, ''Negative Electron Affinity Mechanism for Diamond Surfaces,'' Appl. Phys. Lett., **72**, pp. 2574–2576.

[56] Nemanich, R. J., Baumann, P. K., Benjamin, M. C., Nam, O.-H., Sowers, A. T., Ward, B. L., Ade, H., and Davis, R. F., 1998, ''Electron Emission Properties of Crystalline Diamond and III-Nitride Surfaces,'' Appl. Surf. Sci., **130**, pp. 694–703.

[57] Lui, W. W., and Fukuma, M., 1986, ''Exact Solution of the Schrödinger Equation Across an Arbitrary One-Dimensional Piecewise-Linear Potential Barrier,'' J. Appl. Phys., **60**, pp. 1555–1559.

[58] Fonseca, L. R. C., von Allmen, P., and Ramprasad, R., 2000, ''Numerical Simulation of the Tunneling Current and Ballistic Electron Effects in Field Emission Devices,'' J. Appl. Phys., **87**, pp. 2533–2541.

[59] Lang, N. D., 1985, ''Vacuum Tunneling Current from an Adsorbed Atom,'' Phys. Rev. Lett., **55**, pp. 230–233.

[60] Lang, N. D., 1986, ''Theory of Single-Atom Imaging in the Scanning Tunneling Microscope,'' Phys. Rev. Lett., **56**, pp. 1164–1167.

[61] Lang, N. D., 1986, ''Spectroscopy of Single Atoms in the Scanning Tunneling Microscope,'' Phys. Rev. B, **34**, pp. 5947–5950.

[62] Lucas, A. A., Morawitz, H., Henry, G. R., Vigneron, J.-P., Lambin, Ph., Cutler, P. H., and Feuchtwang, T. E., 1988, ''Scattering-Theoretic Approach to Elastic One-Electron Tunneling Through Localized Barriers: Application to Scanning Tunneling Microscopy,'' Phys. Rev. B, **37**, pp. 10 708–10 720.

[63] Lucas, A. A., Morawitz, H., Henry, G. R., Vigneron, J.-P., Lambin, Ph., Cutler, P. H., and Feuchtwang, T. E., 1988, ''Tunneling through Localized Barriers with Application to Scanning Tunneling Microscopy: New Scattering Theoretic Approach and Results,'' J. Vac. Sci. Technol. A, **6**, pp. 296–299.

[64] Huang, Z. H., Feuchtwang, T. E., Cutler, P. H., and Kazes, E., 1990, ''The Wentzel-Kramers-Brillouin Method in Multidimensional Tunneling: Application to Scanning Tunneling Microscopy,'' J. Vac. Sci. Technol. A, **8**, pp. 177–181.

[65] Miskovsky, N. M., and Cutler, P. H., 1999, ''Calculation of the Local Density of States for a Discrete Pyramidal Model of a Diamond Tip Surmounted by a Single Atom,'' Surf. Sci., **439**, pp. 173–180.

[66] Miskovsky, N. M., Park, S. H., He, J., and Cutler, P. H., 1993, ''Energy Exchange Processes in Field Emission from Atomically Sharp Metallic Emitters,'' J. Vac. Sci. Technol. B, **11**, pp. 366–370.

[67] Fursey, G. N., and Glazanov, D. V., 1998, ''Deviations from the Fowler-Nordheim Theory and Peculiarities of Field Electron Emission from Small-Scale Objects,'' J. Vac. Sci. Technol. B, **16**, pp. 910–915.

[68] He, J., Cutler, P. H., Miskovsky, N. M., and Feuchtwang, T. E., 1991, ''Derivation of the Image Interaction for Non-Planar Pointed Emitter Geometries: Application to Field Emission I-V Characteristics,'' Surf. Sci., **246**, pp. 348–364.

[69] He, J., Cutler, P. H., and Miskovsky, N. M., 1991, ''Generalization of Fowler-Nordheim Field Emission Theory for Nonplanar Metal Emitters,'' Appl. Phys. Lett., **59**, pp. 1644–1646.

[70] Cutler, P. H., He, J., and Miskovsky, N. M., 1993, ''Theory of Electron Emission in High Fields from Atomically Sharp Emitters: Validity of the Fowler-Nordheim Equation,'' J. Vac. Sci. Technol. B, **11**, pp. 387–391.

[71] Cutler, P. H., He, J., Miller, J., Miskovsky, N. M., Weiss, B., and Sullivan, T. E., 1993, ''Theory of Electron Emission in High Fields from Atomically Sharp Emitters: Validity of the Fowler-Nordheim Equation,'' Prog. Surf. Sci., **42**, pp. 169–185.

[72] Jensen, K. L., Mukhopadhyay-Phillips, P., Zaidman, E. G., Nguyen, K., Kodis, M. A., Malsawma, L., and Hor, C., 1997, ''Electron Emission from a Single Spindt-Type Filed Emitter: Comparison of Theory with Experiment,'' Appl. Surf. Sci., **111**, pp. 204–212.

[73] Gadzuk, J. W., and Plummer, E. W., 1973, ''Field-Emission Energy-Distribution (FEED),'' Rev. Mod. Phys., **45**, pp. 487–548.

[74] Kuyatt, C. E., and Simpson, J. A., 1967, ''Electron Monochromator Design,'' Rev. Sci. Instrum., **38**, pp. 103–111.

[75] Wysocki, J. K., 1982, ''Testing of a Field Electron Energy Analyser,'' Journal of Physics E-Scientific Instruments, **15**, pp. 1376–1385.

[76] Oshima, C., 1997, ''An Apparatus for High Resolution Field Emission Spectroscopy,'' Adv. Colloid Interface Sci., **71**, pp. 353–369.

[77] Bernhard, J. M., Rouse, A. A., Sosa, E. D., Gnade, B. E., Golden, D. E., and Chalamala, B. R., 1999, ''A Compact Electron Energy Analyzer for Measuring Field Emission Energy Distributions,'' Rev. Sci. Instrum., **70**, pp. 3299–3302.

[78] Grant, P., Py, C., Möbner, C., Blais, A., Tran, H., and Gao, M., 2000, ''Electron Field Emission From Diamond-like Carbon, a Correlation with Surface Modifications,'' J. Appl. Phys., **87**, pp. 1356–1360.

[79] Ehrich, F. F., 1954, ''Differentiation of Experimental Data Using Least Squares Fitting,'' J. Aeronaut. Sci., **22**, pp. 133–134.

[80] Jensen, K. L., Yater, J. E., Zaidman, E. G., Kodis, M. A., and Shih, A., 1998, ''Advanced Emitters for Next Generation RF Amplifiers,'' J. Vac. Sci. Technol. B, **16**, pp. 2038–2048.

[81] Beck, J. V., and Arnold, K. J., 1977, *Parameter Estimation in Engineering and Science*, Wiley, New York.

[82] Haftka, R. T., Scott, E. P., and Cruz, J. R., 1998, ''Optimization and Experiments: A Survey,'' Appl. Mech. Rev., **51**, pp. 435–448.

[83] Wisitsora-at, A., Kang, W. P., Davidson, J. L., Li, Q., Xu, J. F., and Kerns, D. V., 1999, ''Efficient Electron Emitter Utilizing Boron-Doped Diamond Tips with sp(2) Content,'' Appl. Surf. Sci., **146**, pp. 280–287.

[84] Gotoh, Y., Inoue, K., Ohtake, T., Ueda, H., Hishida, Y., Tsuji, H., and Ishikawa, J., 1994, ''Application of Focused Ion Beam Techniques to the Fabrication of Lateral-Type Thin-Film Edge Field Emitters,'' Japanese Journal of Applied Physics Part 2–Letters, **33**, pp. L63–L70.

[85] Tamtair, F. G., Chen, L. C., Wer, S. L., Hong, W. K., Chen, K. H., and Cheng, H. C., 2000, ''High Current Density Field Emission from Arrays of Carbon Nanotubes and Diamond-Clad Si Tips,'' J. Vac. Sci. Technol. B, **18**, pp. 1207–1213.

[86] Hatsopoulos, G. N., and Gyftopoulos, E. P., 1973, *Thermionic Energy Conversion*, Vol. I, MIT Press, Cambridge, MA, ch. 2.

Interface and Strain Effects on the Thermal Conductivity of Heterostructures: A Molecular Dynamics Study

Alexis R. Abramson

Chang-Lin Tien

Arun Majumdar
e-mail: majumdar@me.berkeley.edu

Department of Mechanical Engineering,
University of California,
Berkeley, CA 94720-1740

Molecular dynamics simulations are used to examine how thermal transport is affected by the presence of one or more interfaces. Parameters such as film thickness, the ratio of respective material composition, the number of interfaces per unit length, and lattice strain are considered. Results indicate that for simple nanoscale strained heterostructures containing a single interface, the effective thermal conductivity may be less than half the value of an average of the thermal conductivities of the respective unstrained thin films. Increasing the number of interfaces per unit length, however, does not necessarily result in a corresponding decrease in the effective thermal conductivity of the superlattice. [DOI: 10.1115/1.1495516]

Keywords: Conduction, Heat Transfer, Microscale, Molecular Dynamics, Nanoscale, Thin Films

Introduction

As the demand for miniaturization of microelectronics devices increases, superior thermal control becomes even more important to the future success of the microelectronics and other industries. Reduced feature sizes lead to an increase in power dissipation per unit area, and therefore thermal management is a major concern. However, research in this area has shown that thermal behavior in micro/nano-sized devices often cannot be predicted by conventional macroscopic theory. Nonetheless, the discovery of unique micro/nanoscale thermal phenomena has led to an interest in new devices and applications that take advantage of the unusual physics, and in particular has stimulated new research in the area of thermoelectrics [1,2]. An efficient thermoelectric device must maximize the ratio of electrical to thermal conductivity in addition to providing a high Seebeck coefficient. Hence, engineering a material with a low thermal conductivity is one manner in which to improve the functionality of the device. The ability to predict, control and manipulate the thermal transport in micro/nanostructures will most likely result in future progress in the area of thermoelectrics.

One of the first observations of unusual thermal characteristics of micro/nanostructures involved the appearance of a reduced thermal conductivity in superlattices [3,4], which are two-dimensional structures of alternating thin films. Capinski et al. [5,6] demonstrated that the thermal conductivity of GaAs/AlAs superlattices can be less than that of an alloy of the two materials. Lee et al. [7] also reported a reduced thermal conductivity associated with Si/Ge superlattices. They showed there is an increase in thermal conductivity with period thickness, resulting in a peak at ~200 Å, followed by a significant downward trend. In contrast, Yamasaki et al. [8] and Venkatasubramanian et al. [9] discovered the opposite trend in Bi_2Te_3/Sb_2Te_3 superlattices; for periods shorter than 60 Å, the thermal conductivity of these heterostructures actually *decreases* with increasing period thickness, followed by a trend of *increasingly* higher values. Moreover, Huxtable et al. studied $Si/Si_{0.7}Ge_{0.3}$ superlattices and uncovered no peak in thermal conductivity; rather, they revealed a non-linear decrease with decreasing period thickness from 300 Å to 45 Å [10]. Some investigations suggest that interface quality may also significantly affect the thermal conductivity of superlattices [11,12]. However, researchers have reported seemingly contradictory experimental results regarding the effect of interface roughness. In InSb/AlSb superlattices, thermal conductivity decreases as interfacial roughness becomes more pronounced [13], but the trend may be opposite for Si/Ge superlattices [14]. Although the effect of lattice strain on electronic properties in superlattices has been studied extensively over the past decade [15,16], there has been little or no research investigating how lattice strain may affect thermal conductivity in heterostructures. Theoretical studies [17–19] have demonstrated that phonon spectra are altered by strain in superlattices, but there is conflicting evidence describing the extent of the effect. Presently, questions regarding the cause of the unusual and somewhat perplexing thermal behavior in superlattices have remained unanswered. A variety of mechanisms such as acoustic impedance [20] and phonon spectra mismatch [21], mini-band formation and a corresponding phonon group velocity reduction [22–25], phonon tunneling [26], and interface scattering due to roughness, defects or dislocations [11,27] have been proposed as contributors. This work further suggests that lattice strain, commonly exhibited by symmetrically and asymmetrically strained superlattices, may also play a significant role in affecting thermal transport. There is limited understanding of these phonon heat conduction mechanisms and their relation to material properties, individual film thickness, the ratio of respective material composition, and superlattice configuration and quality. A goal of this research is to further reflect the complexity of the situation by using computer simulations to reveal interesting thermal characteristics of heterostructures.

A variety of distinctly different theoretical and computational approaches have been used to determine the effective thermal conductivity of a superlattice structure. Many studies have employed modified bulk formulas for the lattice thermal conductivity, using an appropriately adapted acoustic phonon dispersion relation for the structure [22,28]. Other investigators have applied the Boltzmann transport equation (BTE) for phonons [29,30] or Monte Carlo simulations [31,32]. Often, experimentally fitted values for the phonon relaxation time and acoustic phonon dispersion of bulk media are still employed for these methods. By including a specularity parameter in the solution of the BTE, researchers have

---

Contributed by the Heat Transfer Division for publication in the JOURNAL OF HEAT TRANSFER. Manuscript received by the Heat Transfer Division September 24, 2001; revision received May 13, 2002. Associate Editor: C. T. Avedisian.

been able to capture the effect of a partially diffuse interface [11,30]. This study, however, takes a different approach by using classical nonequilibrium molecular dynamics (MD) simulations to investigate the effective thermal conductivity of bi-material structures including simple representations of superlattices. Due to its classical nature, this technique cannot capture effects related to vibrational energy quantization that control heat capacity at temperatures much below the Debye temperature. However, phonon characteristics such as dispersion, interface reflection, confinement and tunneling are accurately captured without assuming empirically derived physical values, provided the interatomic potential is well known. Employing MD for this type of analysis is a less common approach, but previous research on two [33] and three-dimensional [34] superlattices using non-equilibrium and equilibrium MD techniques, respectively, have uncovered some interesting observations regarding thermal transport in superlattices.

There are various factors that may potentially influence the effective thermal conductivity of a heterostructure, including thin film thickness and the ratio of the respective material composition, numbers of interfaces, period thickness, and strain throughout the structure. This study offers a systematic examination of how these factors might influence the effective thermal conductivity and may, therefore, help to predict how to better engineer these structures for use in thermoelectric devices or other related applications. Lennard-Jones materials are simulated, and although their applicability in real applications is limited, the results should be used as a benchmark from which further study of other material systems will benefit.

Computational Model

The computational model is based on the classical MD subroutines given by Allen and Tildesley [35] and on the non-equilibrium simulations of thin films performed by Lukes et al. [36]. However, essential modifications to account for more than a single solid material have been made. A schematic of the three-dimensional molecular dynamics computational structure is shown in Fig. 1. Boundary conditions consist of an applied heat flux in the *x*-direction and are periodic over eight planes in the other two dimensions (the *y* and *z*-directions). The periodic boundary conditions simulate an infinite film in these directions, although their use does remove the existence of long-wavelength fluctuations in the system. Nonetheless, certain repeated simulations with up to four times the number of planes in each direction demonstrated no significant deviation from the results presented here. Fixed walls are used at the ends of the structure in the *x*-direction to discourage evaporation of the constituent atoms to vacuum. The heat flux is simulated by adding energy to the four planes adjacent to the leftmost fixed walls (the hot bath) and removing the same amount of energy from the four planes adjacent to the rightmost fixed walls (the cold bath). The atoms between these two baths are referred to as ‘‘regular’’ atoms. The effective cross-plane thermal conductivity of a structure is simply determined by the quotient of the heat flux and the temperature difference across the regular atoms in the structure, multiplied by the total thickness over which the thermal gradient is imposed. The instantaneous temperature at a point x is calculated classically from the planar average of the kinetic energy of the atoms in each y-z plane such that

$$T_{x,\text{inst}} = \frac{m \Sigma_i^{N_x} v_i^2}{3 N_x k_B} \tag{1}$$

where m is the mass and v the speed of the atom, N_x is the total number of atoms in the specific y-z plane and k_B is the Boltzmann constant. After the simulation has reached steady state, this temperature is averaged over an adequate time period, and this time-averaged value is used in the calculation of effective thermal conductivity. An appropriate imposed heat flux is chosen for each structure to ensure that the same temperature difference (cold bath at ~60 K and hot bath at ~90 K) is maintained across all structures. Argon (Ar) and krypton (Kr) are chosen as the materials for the analysis whose Debye temperatures are approximately 92 K and 72 K and melting temperatures are approximately 84 K and 116 K, respectively. To avoid melting conditions, the Kr film, with the higher of the two melting temperatures, is always nearest the hot bath, and the simulation checks to ensure that melting does not occur. It is important to note that across this temperature range, molecular dynamics simulations have revealed that thermal conductivity is not a strong function of temperature [36], and therefore, a linear temperature profile is expected, provided the thickness of the film/structure is greater than the phonon mean free path. The actual heat flux across each plane is calculated from particle positions and velocities using the equations of Irving and Kirkwood [37]. At steady state, a time average of this calculated flux is then spatially averaged across the structure to provide an *effective* heat flux. This value can be compared with the imposed heat flux to assess the degree to which heat spreading may occur in the structure in the *y*- and *z*-directions. The total simulation time is determined by estimating the thermal diffusion time for each structure and using a run time approximately 5–20 times this characteristic time scale. Femtosecond time steps are used, and the total simulation time ranges from 1–30 nanoseconds. The probable errors of the planar temperature, the effective heat flux and the effective thermal conductivity are determined in the manner outlined in the appendix and in more detail by Lukes et al. [36]. For large structures ($\geqslant$24 unit cells in the *x*-direction), the calculated effective heat flux differed by 8–12 percent of the imposed heat flux, while for smaller structures, the value ranged between 3–8 percent. The errors in thermal conductivity reported throughout this work are associated with the convergence criteria of the simulation. For the sake of computational time, the increased accuracy of the calculation is sacrificed for large structures that may require unreasonably long simulation times. Hence, runs that are too short may be to blame for larger errors, approximately 15 percent in some cases, associated with simulating thick structures.

Utilizing a true representation of the intermolecular potential in these MD simulations is critical for ensuring that the physics underlying the micro/nanoscale thermal phenomena is accurate. Therefore, only Lennard-Jones (LJ) solids, for which the intermolecular potential is well established, are chosen. The LJ 12-6 potential is

$$\Phi(r_{ij}) = 4\varepsilon \left[\left(\frac{\sigma_{LJ}}{r_{ij}} \right)^{12} - \left(\frac{\sigma_{LJ}}{r_{ij}} \right)^{6} \right] \tag{2}$$

where r_{ij} is the distance between atoms i and j, ε is the well depth of the potential and σ_{LJ} is the equilibrium separation parameter. The force experienced by an atom due to the presence of another atom is simply the first derivative of Eq. (2). Using Newton's equations of motion, a relationship between force and acceleration can be established. Therefore, an indirect relation exists between the interatomic potential and the vibrational motion of the atoms in the system. Using a finite difference approach, or the com-

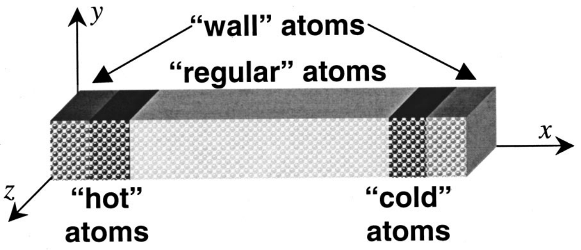

Fig. 1 Schematic of molecular dynamics simulation cell

monly employed velocity Verlet algorithm [38], the acceleration may be expressed in terms of velocity, position and time, and the solution then marches accordingly in time.

The phonon mean free path is generally less than ~2 nm in LJ materials [39] as compared to ~100 nm in ''real'' engineering materials such as semiconductors. Consequently, a much shorter simulation time is required to accurately capture the physics. To further reduce computation time, the common convention of using a cutoff radius outside of which atomic interactions are negligible is employed. Argon (Ar) and krypton (Kr) are chosen as the materials for the analysis because their interatomic potentials are well known. Both of these materials have a face-centered cubic unit cell (UC) structure, and therefore, one UC along the x-direction corresponds to two planes of atoms. Lorentz-Berthelot mixing rules [40] are used to account for interaction between Ar and Kr atoms. For simulations of bi-material films, the nondimensional units are based on the parameters for Kr. For some simulations, a structure with a coherent interface is desired. To achieve this, the equilibrium interatomic distance is chosen for both materials to be the same and that of Kr ($a=5.64$ Å). However, the equilibrium interatomic distance for Ar is actually slightly less ($a=5.31$ Å), thereby forcing the Ar film to be in tension. By varying parameters such as structure and individual film thicknesses, the ratio of the respective material composition, the number of interfaces, and lattice strain, the simulations performed here investigate the reduction in the effective thermal conductivity of various bi-material films and simplified superlattices. Computational power limits the capability of simulating complex superlattices, but simple structures with up to twelve periods are analyzed.

For all cases, the effective thermal conductivity of the entire structure is compared to an ''average'' thermal conductivity using a simple series resistance calculation involving the respective resistances of the individual Ar and Kr thin films in their natural lattice states such that

$$\begin{gathered} R_{\mathrm{ave}}=R_{\mathrm{Kr}}+R_{\mathrm{Ar}} \\ k_{\mathrm{ave}}=\frac{(t_{\mathrm{Kr}}+t_{\mathrm{Ar}})k_{\mathrm{Kr}}k_{\mathrm{Ar}}}{t_{\mathrm{Kr}}k_{\mathrm{Ar}}+t_{\mathrm{Ar}}k_{\mathrm{Kr}}} \end{gathered} \tag{3}$$

where R is the resistance, k is the thermal conductivity, and t is the individual film thickness. The subscript ave refers to the average property, while Kr and Ar describe the respective individual properties of each material. This equation represents the expected effective thermal conductivity if there were no interfacial thermal effects present to alter the property. Researchers often compare thermal conductivity of superlattices to an average of unstrained bulk values, assessing that the reduction in the thermal conductivity of the superlattice is due to a mechanism such as acoustic impedance mismatch. However, such a comparison may not be sufficient to further one's physical understanding of interfacial thermal effects since thin film and bulk properties may be markedly different. Therefore, this study utilizes an average of the *thin film* thermal conductivities at the appropriate corresponding temperatures for a more appropriate comparison to reveal that the interface can play a substantial role in altering thermal transport. Note that the average thermal conductivity is estimated using unstrained thermal conductivities of the individual films, which allows one to additionally compare the effect of strain in certain simulations.

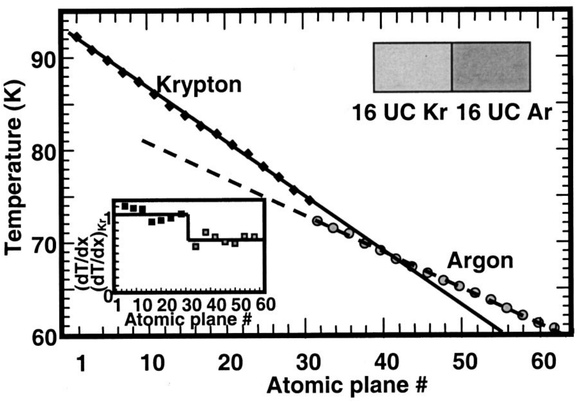

Fig. 2 One-dimensional temperature distribution from an MD simulation of a bi-material film composed of 16 unit cells Kr (solid diamond) adjacent to 16 unit cells Ar (solid circle). The temperature jump indicates the presence of interfacial thermal resistance. The inset illustrates the instantaneous and best-fit slopes of the lines corresponding to the two materials normalized using the best-fit slope of Kr.

Results and Discussion

Effect of Single Interface. An example of a temperature profile for a bi-material film (16 UC in the x-direction of Kr adjacent to 16 UC of Ar) is illustrated in Fig. 2. The temperature profiles for the simulations were reasonably linear for each individual film, and a temperature jump occurred at the interface between materials. Note that the x-axis corresponds to the atomic plane number, and plane number 1 corresponds to the first plane of regular atoms adjacent to the hot bath. The best-fit lines for both the Kr and Ar halves are shown, and the respective slopes are different because the thermal properties of the materials vary. From graphs such as this one, the effective cross-plane thermal conductivity is simply determined by the ratio of the effective heat flux and the temperature difference between the first and last plane of regular atoms (using values from the best fit lines as shown) multiplied by the total thickness of the regular atoms in the structure. Since the MD simulation of a single film calculates a nondimensional thermal conductivity for any Lennard-Jones solid, the dimensionalized values for individual films of Kr or Ar may be determined using the results from a single simulation and applying the respective transformation as given by Lukes et al. [36]. Comparing the two transformations, the dimensionalized thermal conductivity of a Kr film is theoretically about 70 percent that of Ar for any MD simulation. This is also evident from the simulations, and the normalized slopes of the two best-fit lines are illustrated on the inset to Fig. 2.

To initially assess the effect of a single interface on various thin film configurations, the thermal conductivities of lattice-strained bi-material films of differing overall thicknesses but with equal individual thicknesses of Kr and Ar are analyzed and shown in Fig. 3. The lattice strain is imposed by initially forcing the Ar

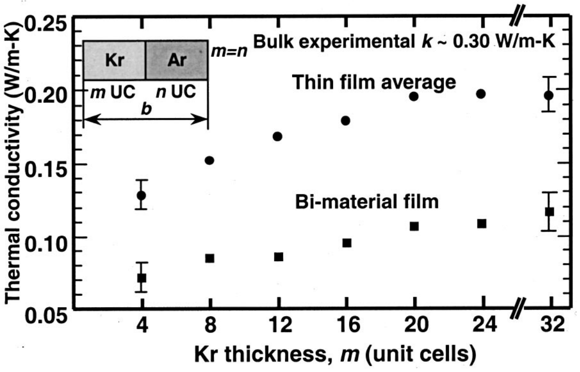

Fig. 3 Effective thermal conductivity of strained bi-material Kr/Ar films as a function of increasing thickness (solid square) and compared with thin film average (solid circle). Note $m=n$.

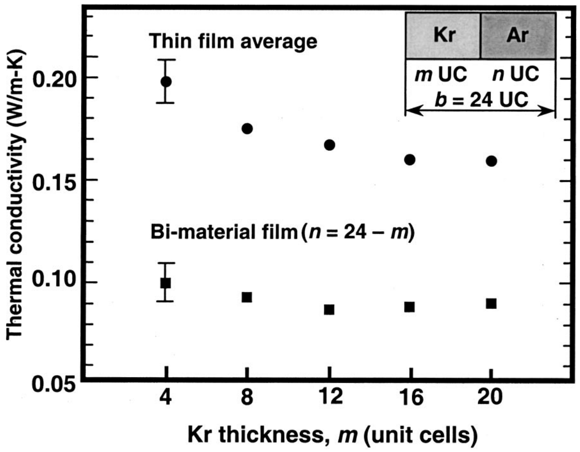

Fig. 4 Effective thermal conductivity of strained bi-material Kr/Ar films as a function of individual film thickness ratio, but the same overall thickness (solid square) and compared with thin film average (solid circle). Note $n=24-m$.

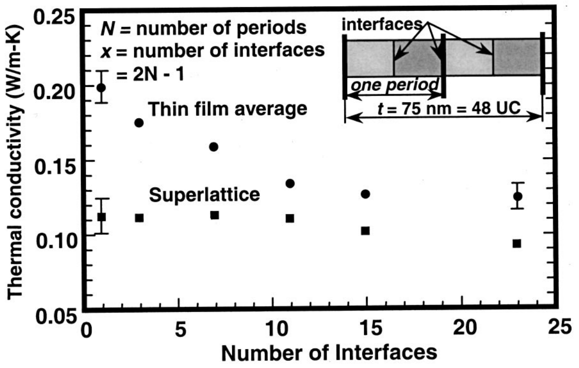

Fig. 5 Effective thermal conductivity of simple asymmetrically strained superlattices as a function of numbers of interfaces per unit thickness (solid square) and compared with thin film average (solid circle)

atoms to lattice spacings equal to that of the Kr atoms, imposing a coherent interface. Note that the structure consists of only two films and is not representative of a superlattice. The standard error analysis [36] for these simulations resulted in errors in the effective thermal conductivity between 8 and 15 percent of the calculated values. Error bars are shown for the first and last points only for clarity. The two different trends correspond to the MD simulation for the bi-material films (bottom trend) and the calculation of the "average" thermal conductivity (top trend). The latter assumes a simple series resistance analysis given by Eq. (3), using the MD calculated values for the individual film thermal conductivities at the appropriate corresponding temperatures. The first observation made from the data is that as individual thin film thickness increases from 4 UC to 32 UC, the effective thermal conductivity also appears to increase. The phonon mean free path of Ar is estimated to be approximately 2–3 UC [39] (and is assumed to be of the same order for Kr), and therefore boundary scattering is dominant for very thin films. Consequently, as film thickness increases, boundary effects become less pronounced, and thermal conductivity also increases. However, even for the thickest films, the thermal resistance due to interfacial effects and strain still cause a disparity between the thin film average and bi-material film values. Using the same series resistance formulation of previously reported experimental results for bulk Kr [41] and Ar [39,41], the effective thermal conductivity calculates to approximately 0.30 W/mK, which is comparable to the averaged MD results for the thicker films. Moreover, a comparison of the two trends illustrates that the presence of a single interface results in a reduction of the thermal conductivity by a factor of ~2. This discrepancy may be attributed to one or more of the thermal mechanisms responsible for interfacial thermal resistance except for the following: (i) interface scattering due to roughness, since the interface is atomically smooth, and (ii) mini-band formation, since there is no additional periodicity.

To assess the impact of the thickness ratio of the films, the effective thermal conductivities of lattice-strained bi-material films of the same overall thickness but varying thickness ratios are compared in Fig. 4. The standard error analysis for these simulations resulted in errors between 10 and 13 percent of the calculated values. For the series resistance calculation (top trend), as the amount of Ar is reduced in the structure, there is a corresponding reduction in the overall thermal conductivity since the thermal conductivity of Ar is approximately 1.4 times that of Kr. However, the decline flattens out for the 16 UC Kr/8 UC Ar and 20 UC Kr/4 UC Ar structures. It is important to recognize that there are two competing effects here: the fraction of Ar in the structure and the differences in thermal conductivities due to the disparity between film thicknesses. For example, in the 4 UC/20 UC averaged case, the structure is composed of 83 percent Ar, and the Ar film is "thick". Together, these effects result in a high thermal conductivity. However, for the 20 UC/4 UC averaged case, the structure is composed of only 17 percent Ar, but the thickness of the Kr film is large. Even though the thermal conductivity of Kr is theoretically 70 percent that of Ar, a 20 UC film of Kr has a thermal conductivity similar to that of a 4 UC film of Ar, and there is a flattening out of values rather than a continued decrease. There is, albeit questionably due to the relative magnitude of the results in Fig. 4, a corresponding trend for the case of the bi-material film (bottom). There is no conclusive evidence from this study that variation in the ratio of the constituent materials influences interfacial thermal effects. Nonetheless, it is important to consider this ratio in the design of engineering structures, by accounting not only for expected differences due to a disparity between thermal properties, but also for thin film boundary scattering effects if one or both of the films are of the order of or less than the phonon mean free path.

Effect of Multiple Interfaces. In engineering applications, structures consisting of multiple interfaces are often of great concern. However, there is limited understanding of how to best design a multilayer structure for superior control of thermal transport characteristics. Presently, a general rule of thumb relies on the hypothesis that increasing the number of interfaces per unit length will result in more phonons being reflected and therefore, a reduction in the effective thermal conductivity of the structure. However, some researchers have hypothesized that mini-band formation results in an overall decrease in the phonon group velocity, thereby causing a reduction in the thermal conductivity [22–25]. If this were true, increasing the numbers of interfaces per unit length would effectively decrease the period thickness, resulting in fewer locations along the dispersion relation where the group velocity approaches zero and a corresponding *increase* in thermal conductivity. Thus, if both mechanisms were significantly present, they would compete against each other to affect thermal transport. For this study, simple superlattices, all approximately 75 nm thick (48 UC), are used to assess the effect of systematically increasing the number of interfaces per unit length. The results for superlattice configurations consisting of a single interface and up to 23 interfaces (not including the boundaries) are shown in Fig. 5. This corresponds to structures comprised of one, two, four, six, eight and twelve periods but with the same overall thickness. The standard error analysis for these simulations resulted in errors in the effective thermal conductivity between 8 and 10 percent of the calculated values. The top trend in the figure, indicating the thin film average, demonstrates again that as the individual film thickness decreases (as it does with increasing number of periods/interfaces), the thermal conductivity decreases. However, the superlattice thermal conductivity (bottom trend) does not significantly change over the range investigated here. Nonetheless, there appears to be a larger disparity between the thin film average and the superlattice thermal conductivity for smaller numbers of periods. This may imply that for film thicknesses much greater than the dominant phonon wavelengths, a single interface and the effect of strain may be responsible for a considerable decrease in thermal conductivity. However, adding more interfaces while maintaining the same overall thickness will not necessarily result in a large decrease in thermal conductivity if the individual film thicknesses become very small. When the thin films are of the order of the dominant phonon wavelengths, phonon tunneling may counteract any additional interface reflection effects that would otherwise result with the addition of more interfaces. Furthermore, mini-band formation may emerge when multiple periods are present, acting to further counteract any increase in interface reflection. Interestingly, some analytical predictions indicate that the thermal conductivity in superlattices should decrease with increasing period thickness due to a corresponding decrease in phonon tunneling, and then approach a constant value at a critical thickness [21,42]. However, these analytical approaches cannot entirely capture competing interfacial thermal resistance effects. There is conflicting experimental evidence that affirms but also contradicts the finding that thermal conductivity decreases with increasing period thickness [7–9], but the superlattices in the referenced experiments are of markedly different materials, qualities and configurations. Certain factors such as phonon relaxation time variation, phonon coherence and interface scattering due to roughness may differ significantly among samples and are often too complicated to evaluate, making an accurate comparison of results difficult. Although MD inherently accounts for many of these factors, limits in computational power did not permit a simple analysis of superlattices with a greater number of interfaces. Future analysis of larger superlattices may reveal interesting characteristics. For many of the superlattices fabricated and proposed as potential thermoelectric components, the thin film thicknesses may approach the order of the dominant phonon wavelengths. Even though there are many complex factors to consider, improvements in the engineering design of these structures require that at the very least, the competing effects of phonon tunneling, mini-band formation and interfacial thermal resistance be considered.

Effect of Strain. It is well known that a lattice mismatch at the interface between conducting materials can influence charge transport due to the presence of defects or misfit dislocations, and due to strain-induced changes in the electronic band structure. The effects of interfacial strain on phonon transport and thermal conductivity are not well understood. For the aforementioned MD simulations, the lattice parameter of 5.64 Å (that of Kr) was imposed on both the Kr and Ar films to ensure a coherent interface. Similar to an asymmetrically strained superlattice, the Ar film was kept in tension while the Kr film was not strained. Allowing the natural lattice state of both materials to exist during the simulations resulted in an interesting reconfiguration of the lattice structure. Figure 6 illustrates the (*a*) initial and (*b*) final atomic lattice positions in a single $x-y$ plane of a 12 UC Kr/12 UC Ar structure (only the first 12 atomic planes on either side of the interface are shown for clarity). These snapshots were taken prior to imposing a heat flux. The natural lattice constants of the respective materials were initially set in this simulation and were purposely chosen to necessitate a large and unnatural degree of lattice mismatch. After an adequate time period (~2 ns), the atoms rearranged themselves to, presumably, their lowest energy state, and formed a semi-coherent or a relaxed interface to accommodate the disparity between lattice parameters. Even though periodic boundary conditions are imposed along the planes perpendicular to the interface to simulate an infinite film, the structure experiences the spatial constraints of the relatively small dimensions of the simulation. Consequently, it is favorable for the atomic spacing on either side of the interface to either slightly contract (Kr atoms) or expand (Ar atoms) to align with adjacent atoms, while the atoms farthest away from the interface maintain their respective lattice parameters. Since the structure exhibits a smooth transition from the Kr to Ar film, the interfacial strain is minimized and there is relatively no lattice strain in either film just a few atomic planes away from the interface. This behavior is similar to what one would expect at the interface between heterostructures of nanowires in which there are only a relatively small number of atoms along the interface as opposed to in an actual superlattice where an interface may consist of many millions of atoms.

The thermal conductivities of bi-material structures with relaxed interfaces and of differing overall thicknesses are compared with their strained counterparts and calculated average thermal conductivities in Fig. 7. The strained and average values for the thermal conductivity come directly from Fig. 3. The probable error of the effective thermal conductivity for the unstrained case is approximately 10 percent for all structures. The results demonstrate that for the MD simulations, allowing the two materials to exist in their natural lattice state rather than forcing a coherent interface results in an increase in thermal conductivity. In fact, the effective thermal conductivity of the strained structure is ~35 percent lower than when the entire structure is in a relaxed state. Using the thermal conductivity results from the strained and relaxed simulations along with the average calculation for the films given by Eq. (3), the boundary resistance (BR) for both the strained and relaxed cases can be determined and compared using a simple series resistance relationship, $R_{\mathrm{eff}}=R_{\mathrm{Kr}}+R_{\mathrm{Ar}}+R_{\mathrm{BR}}$. Consequently, the boundary resistance in the case of the strained structure is calculated to be more than three times that of the relaxed structure. Not only does strain throughout the Ar film

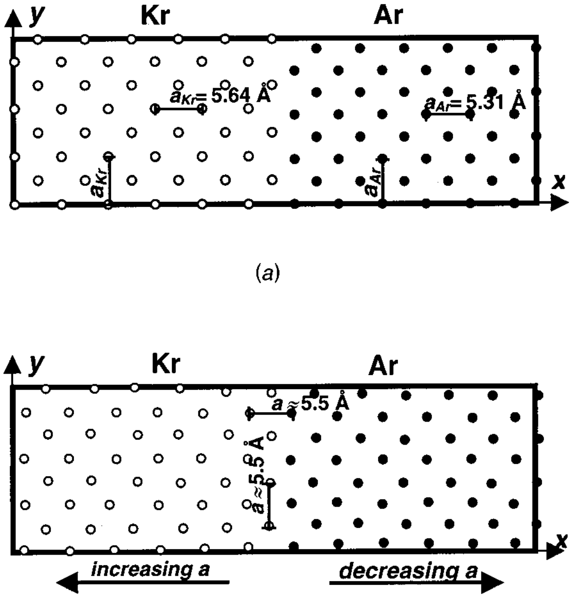

(*b*)

Fig. 6 (*a*) initial and (*b*) final positions of Kr (light circles) and Ar (dark circles) atoms for a molecular dynamics simulation of a bi-material film with a semi-coherent or relaxed interface. The initial conditions are set to the exact lattice parameters of Kr and Ar. After the simulation, the atoms rearranged themselves such that the lattice parameter at the interface is approximately the average of a_{Kr} and a_{Ar}. The interatomic distance grows smaller for the Ar atoms and larger for the Kr atoms away from the interface.

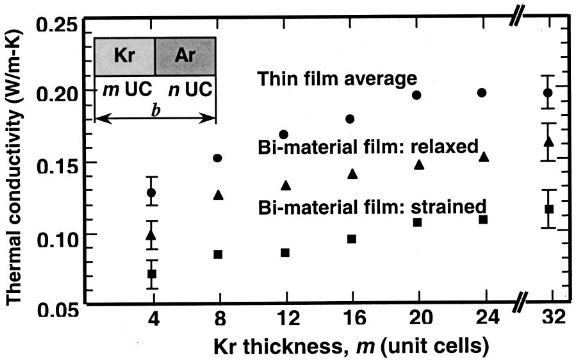

Fig. 7 Effective thermal conductivity of bi-material Kr/Ar films as a function of overall thickness (thickness ratio=1) for strained (solid square), relaxed (solid triangle) and thin film average (solid circle) cases. Note $m=n$.

result in a decrease in effective thermal conductivity, but the property mismatch that results from the strain also appears to contribute to a further reduction. Comparing the three trends in Fig. 7, it seems that the strain due to forcing a coherent interface may actually be a dominant contributor to the reduction in thermal conductivity. Reflection due to other mechanisms may only result in a reduction of ~20 percent of the average thermal conductivity value as compared to a reduction of ~50 percent for the strained heterostructures.

Performing a simple calculation to estimate the influence of lattice strain on the thermal conductivity provides elementary insight to the degree of its effect. Taking the second derivative of the interatomic potential [Eq. (2)] gives the spring stiffness, $g = d^2\Phi/dr_{ij}^2$ of the interatomic bond. Forcing the Ar film in tension to match the lattice constant of Kr, results in a strain, $\gamma=(a_s - a_0)/a_0 = 6.2$ percent experienced throughout the Ar film. For this calculation, a_s is the strained lattice constant, or in this case the lattice constant corresponding to Kr, and a_0 is the equilibrium lattice constant, or the natural lattice constant of Ar. The expression for the spring stiffness as a function of lattice strain is derived for the L-J potential to be

$$g = g_0\left[\frac{13}{6}\frac{1}{(1+\gamma)^{14}} - \frac{7}{6}\frac{1}{(1+\gamma)^{8}}\right] \tag{4}$$

where the spring stiffness at equilibrium, $g_0 = 72\varepsilon/2^{1/3}\sigma^2$. Because of anharmonicity in the interatomic potential, the spring stiffness of the strained lattice will be different from that of the relaxed state, and for $\gamma=6.2$ percent, $g/g_0 = 0.21$.

The change in spring stiffness fundamentally alters the phonon dispersion relation, which in turn modifies the phonon group velocity as well as the lifetime of phonon-phonon interaction, τ_{ph}. The effect of both these contributions to thermal conductivity can be significant. As a demonstration, consider only the effect of modifying the phonon group velocity and disregard a change in τ_{ph}. Then, applying kinetic theory and substituting the velocity, $v \approx r_{ij}\sqrt{g/m}$, into the expression for thermal conductivity,

$$k = \frac{1}{3} C r_{ij}^2 \frac{g}{m} \tau_{ph} \tag{5}$$

where C is heat capacity. Using the above expressions, the thermal conductivity of the relaxed Ar film is reduced by ~80 percent when a strain of 6.2 percent is imposed. However, molecular dynamics simulations of single Ar films in the strained and relaxed states revealed a reduction of only ~30 percent in thermal conductivity.

Conclusions

There is limited understanding of the many complex mechanisms affecting thermal transport in heterostructures with one or multiple interfaces. This study served to assess the feasibility of using molecular dynamics as a tool to further elucidate the effects of varying parameters in these types of structures such as overall thickness and the ratio of the respective material composition, the number of interfaces per unit length, and lattice strain. The results indicate that for simple asymmetrically strained bi-material films where a single interface is present, the thermal conductivity may be less than half the value of an average of two similar thin films. Moreover, one would expect that varying the ratio of the two materials in a simple bi-material film would also affect thermal transport, particularly if the thermal conductivities of the two materials are markedly different. However, when one or both of the films approach the phonon mean free path, the possible competing effects of thin film boundary scattering and the ratio of film composition must be considered. Nonetheless, there is no conclusive evidence from this study that variation in the ratio of the constituent materials significantly influences interfacial thermal effects. There are competing theories that suggest that increasing the number of interfaces per unit length will influence the thermal conductivity of the structure. However, this study demonstrated that a single interface results in a considerable decrease in thermal conductivity, but additional interfaces do not necessarily cause a further significant reduction in the property. Care must be taken to account for the competing increase in effective thermal conductivity due to phonon tunneling in superlattices with thin films of the order of or less than the dominant phonon wavelength, and it is important to also examine whether mini-band formation might be present to counteract phonon reflection at the interface. In one of the first investigations into the effect of lattice strain on thermal conductivity in heterostructures, this study revealed that the imposed tensile strain caused by forcing a coherent interface resulted in a significant decrease in the thermal conductivity. A more accurate theoretical analysis must quantify the effects of the imposed strain on the dispersion relation and phonon relaxation time before a thorough understanding of its effects on thermal conductivity can be fully appreciated. Nonetheless, results provide some insight into the mechanisms that may influence thermal transport, and should be carefully considered in the design of superlattices used for the purpose of manipulation of heat flow.

Acknowledgments

The authors gratefully acknowledge the financial support of the National Science Foundation and the Department of Energy.

Nomenclature

Ar = argon
C = specific heat (J/kg-K)
Kr = krypton
M = total number of planes
N_x = atomic plane number at location x
R = thermal resistance (K/W)
T_x = atomic plane temperature at location x
a = lattice constant (○)
b = slope
g = spring stiffness (N/m)
k = thermal conductivity (W/m-K)
k_B = Boltzmann's constant (1.38×10^{-23} J/K)
m = mass (kg)
q = heat flux (W/m^2)
r_{ij} = distance between atoms i and j
t = thickness (m)
v = velocity (m/s)

Greek Symbols

ε = well-depth parameter (J)

γ = strain
Φ = interatomic potential (J)
σ = probable error
σ_{sd} = probable error
$\sigma_{\langle\ \rangle}$ = standard error
σ_{LJ} = Lennard-Jones equilibrium separation parameter (○)
τ_{ph} = phonon relaxation time (s)
τ_{run} = run time (s)
τ_{corr} = autocorrelation time (s)

Subscript

0 = equilibrium
BR = boundary resistance
eff = effective
f = film
inst = instantaneous
s = strained
x = plane number

Appendix

The error analysis of the effective thermal conductivity involves a series of calculations that examine the statistical fluctuations of the simulation. Lukes et al. [36] provide additional details of the error analysis. The standard deviation of the planar temperature, $\sigma_{sd,Tx}$, is first used to determine the standard error of the planar temperature [35,43],

$$\sigma_{\langle Tx\rangle}=\sigma_{sd,Tx}\sqrt{2\,\tau_{\text{corr}}/\tau_{\text{run}}} \tag{6}$$

where τ_{run} is the run time of the simulation after reaching steady state, and τ_{corr} is the autocorrelation time of the instantaneous planar temperatures given approximately by the ratio of phonon mean free path [39] to the speed of sound [44]. For simulations involving bi-material structures, the average of the speeds of sound is used. The probable error associated with the slope of the best fit line of the temperature profile of the regular atoms is found using a weighted least squares method [45],

$$\sigma_{b_f}=\sqrt{\frac{\left(\sum_{x=1}^{M_f}\frac{1}{\sigma^2_{\langle Tx\rangle}}\right)}{\left(\sum_{x=1}^{M_f}\frac{1}{\sigma^2_{\langle Tx\rangle}}\right)\left(\sum_{x=1}^{M_f}\frac{x^2}{\sigma^2_{\langle Tx\rangle}}\right)-\left(\sum_{x=1}^{M_f}\frac{1}{\sigma^2_{\langle Tx\rangle}}\right)^2}} \tag{7}$$

where x is the plane number along the x-direction and M_f is the total number of planes in the film. For bi-material films, the slope, b_f, and its respective error, σ_{bf}, are calculated for each individual film. For example, a structure composed of four alternating layers of Kr and Ar will require the calculation of the four different slopes and their respective errors. Each individual film's thermal conductivity, k_f, is also calculated as the quotient of the effective heat flux, q_{eff}, and the respective slope, b_f, to be used in subsequent error calculations. There will also be a probable error associated with the effective heat flux, q_{eff} [45],

$$\sigma_{q_{\text{eff}}}=\sqrt{\left(\sum_{x=1}^{M}\sigma^2_{\langle q_x\rangle}\right)\frac{\partial q_{\text{eff}}}{\partial\langle q_x\rangle}} \tag{8}$$

where $\sigma_{\langle qx\rangle}$ is the standard error of the planar heat flux, q_x, calculated for each plane along the x-direction in the same manner as Eq. (7). Finally, the formulation for the total probable error of each film's thermal conductivity is

$$\sigma_{k_f}=\sqrt{\sigma^2_{q_{\text{eff}}}\left(\frac{\partial k_f}{\partial q_{\text{eff}}}\right)^2+\sigma^2_{b_f}\left(\frac{\partial k_f}{\partial b_f}\right)^2} \tag{9}$$

The largest value of σ_{kf} from those calculated for each film is used to represent the probable error of the effective thermal conductivity of the bi-material structure.

References

[1] Mahan, G., Sales, B., and Sharp, J., 1997, ‘‘Thermoelectric materials: New Approaches to an Old Problem,’’ Phys. Today, **50**, pp. 42–47.
[2] Dresselhaus, M. S., Dresselhaus, G., Sun, X., Zhang, Z., Cronin, S. B., Koga, T., Ying, J. Y., and Chen, G., 1999, ‘‘The Promise of Low-Dimensional Thermoelectric Materials,’’ Microscale Thermophys. Eng., **3**, pp. 89–100.
[3] Yao, T., 1987, ‘‘Thermal Properties of AlAs/GaAs Superlattices,’’ Appl. Phys. Lett., **51**, pp. 1798–1800.
[4] Weisbuch, C., and Vinter, B., 1991, *Quantum Semiconductor Structures*, Academic Press, Boston, MA.
[5] Capinski, W. S., and Maris, H. J., 1996, ‘‘Thermal Conductivity of GaAs/AlAs Superlattices,’’ Physica B, **220**, pp. 699–701.
[6] Capinski, W. S., Maris, H. J., Ruf, T., Cardona, M., Ploog, K., and Katzer, D. S., 1999, ‘‘Thermal Conductivity Measurements of GaAs/AlAs Superlattices Using a Picosecond Optical Pump-and-Probe Technique,’’ Phys. Rev. B, **59**, pp. 8105–8113.
[7] Lee, S. M., Cahill, D. G., and Venkatasubramanian, R., 1997, ‘‘Thermal Conductivity of Si-Ge Superlattices,’’ Appl. Phys. Lett., **70**, pp. 2957–2959.
[8] Yamasaki, I., Yamanaka, R., Mikami, M., Sonobe, H., Mori, Y., and Sasaki, T., 1998, ‘‘Thermoelectric Properties of Bi_2Te_3/Sb_2Te_3 Superlattice Structures,’’ *Proceedings 17th International Thermoelectrics Conference ICT ’98*, IEEE, CA, pp. 210–213.
[9] Venkatasubramanian, R., 2000, ‘‘Lattice Thermal Conductivity Reduction and Phonon Localization Like Behavior in Superlattice Structures,’’ Phys. Rev. B, **61**, pp. 3091–3097.
[10] Huxtable, S. T., Abramson, A. R., Majumdar, A., Tien, C. L., LaBounty, C., Fan, X., Zeng, G., Abraham, P., Bowers, J. E., Shakouri, A., and Croke, E. T., 2001, ‘‘Thermal Conductivity of Si/SiGe Superlattices,’’ *Proceedings IMECE ’01*, ASME, New York.
[11] Chen, G., and Neagu, M., 1997, ‘‘Thermal Conductivity and Heat Transfer in Superlattices,’’ Appl. Phys. Lett., **71**, pp. 2761–2763.
[12] Rosenblum, I., Adler, J., Brandon, S., and Hoffman, A., 2000, ‘‘Molecular-Dynamics Simulation of Thermal Stress at the (100) Diamond/Substrate Interface: Effect of Film Continuity,’’ Phys. Rev. B, **62**, pp. 2920–2936.
[13] Borca-Tasciuc, T., Achimov, D., Liu, W. L., Chen, G., Lin, C. H., Delaney, A., and Pei, S. S., 2001, ‘‘Thermal Conductivity of InAs/AlSb Superlattices,’’ *Proceedings International Conference on Heat Transfer and Transport Phenomena in Microscale*, Banff, Canada, Begell House, New York, pp. 369–371.
[14] Borca-Tasciuc, T., Liu, W. L., Liu, J. L., Zeng, Song, D. W., Moore, C. D., Chen, G., Wang, K. L., Goorsky, M. S., Radetic, T., Gronsky, R., Sun, X., and Dresselhaus, M. S., 1999, ‘‘Thermal Conductivity of Si/Ge Superlattices,’’ *Proceedings 18th International Conference on Thermoelectrics ICT ’99* IEEE, CA.
[15] Rieger, M. M., and Vogl, P., 1993, ‘‘Electronic-Band Parameters in Strained Si(1-x)Ge(x) Alloys on Si(1-y)Ge(y) Substrates,’’ Phys. Rev. B, **48**, pp. 14276–14287.
[16] Tserbak, C., Polataoglou, H. M., and Theodorou, G., 1993, ‘‘Unified Approach to the Electronic-Structure of Strained Si/Ge Superlattices,’’ Phys. Rev. B, **47**, pp. 7104–7124.
[17] Ghanbari, R. A., White, J. D., Fasol, G., Gibbings, C. J., and Tuppen, C. G., 1990, ‘‘Phonon Frequencies for Si-Ge Strained Layer Superlattices Calculated in a Three-Dimensional Model,’’ Phys. Rev. B, **42**, pp. 7033–7041.
[18] Qteish, A., and Molinari, E., 1990, ‘‘Interplanar Forces and Phonon Spectra of Strained Si and Ge: *Ab initio* Calculations and Applications to Si/Ge Superlattices,’’ Phys. Rev. B, **42**, pp. 7090–7096.
[19] Sui, Z., and Herman, I. P., 1993, ‘‘Effect of Strain on Phonons in Si, Ge, and Si/Ge Heterostructures,’’ Phys. Rev. B, **48**, pp. 17938–17953.
[20] Little, W. A., 1959, ‘‘The Transport of Heat Between Dissimilar Solids at Low Temperatures,’’ Can. J. Phys., **37**, pp. 334–349.
[21] Stoner, R. J., and Maris, H. J., 1993, ‘‘Kapitza Conductance and Heat Flow Between Solids at Temperatures From 50 to 300 K,’’ Phys. Rev. B, **48**, pp. 16373–16387.
[22] Tamura, S., Tanaka, Y., and Maris, H. J., 1999, ‘‘Phonon Group Velocity and Thermal Conduction in Superlattices,’’ Phys. Rev. B, **60**, pp. 2627–2630.
[23] Tamura, S., Hurley, D. C., and Wolfe, J. P., 1988, ‘‘Acoustic Phonon Propagation in Superlattices,’’ Phys. Rev. B, **38**, pp. 1427–1449.
[24] Simkin, M. V., and Mahan, G. D., 2000, ‘‘Minimum Thermal Conductivity of Superlattices,’’ Phys. Rev. Lett., **84**, pp. 927–930.
[25] Narayanamurti, V., Stormer, H. L., Chin, M. A., Gossard, A. C., and Wiegmann, W., 1979, ‘‘Selective Transmission of High-Frequency Phonons by a Superlattice: The ‘‘Dielectric’’ Phonon Filter,’’ Phys. Rev. Lett., **43**, pp. 2012–2016.
[26] Chen, G., 1999, ‘‘Phonon Wave Heat Conduction in Thin Films and Superlattices,’’ ASME J. Heat Transfer, **121**, pp. 945–953.
[27] Swartz, E. T., and Pohl, R. O., 1987, ‘‘Thermal Resistance at Interfaces,’’ Appl. Phys. Lett., **51**, pp. 2200–2202.
[28] Balandin, A., and Wang, K. L., 1998, ‘‘Significant Decrease of the Lattice Thermal Conductivity Due to Phonon Confinement in a Free-Standing Semiconductor Quantum Well,’’ Phys. Rev. B, **58**, pp. 1544–1549.
[29] Chen, G., 1997, ‘‘Size and Interface Effects on Thermal Conductivity of Superlattices and Periodic Thin-Film Structures,’’ ASME J. Heat Transfer, **119**, pp. 220–229.
[30] Chen, G., 1998, ‘‘Thermal Conductivity and Ballistic-Phonon Transport in the Cross-Plane Direction of Superlattices,’’ Phys. Rev. B, **57**, pp. 14958–14973.
[31] Peterson, R. B., 1994, ‘‘Direct Simulation of Phonon-Mediated Heat Transfer in a Debye Crystal,’’ ASME J. Heat Transfer, **116**, pp. 815–1994.

[32] Mazumdar, S., and Majumdar, A., 2001, ''Monte Carlo Study of Phonon Transport in Solid Thin Films Including Dispersion and Polarization,'' ASME J. Heat Transfer, **123**, pp. 749–759.

[33] Liang, X. G., and Shi, B., 2000, ''Two-Dimensional Molecular Dynamics Simulation of the Thermal Conductance of Superlattices,'' Mater. Sci. Eng., A, **292**, pp. 198–202.

[34] Volz, S., Saulnier, J. B., Chen, G., and Beauchamp, P., 2000, ''Molecular Dynamics of Heat Transfer in Si/Ge Superlattices,'' High Temp.-High Press., **32**, pp. 709–714.

[35] Allen, M. P., and Tildesley, D. J., 1987, *Computer Simulation of Liquids*, Clarendon Press, Oxford.

[36] Lukes, J. R., Li, D. Y., Liang, X. G., and Tien, C. L., ''Molecular Dynamics Study of Solid Thin-Film Thermal Conductivity,'' ASME J. Heat Transfer, **122**, pp. 536–543.

[37] Irving, J. H., and Kirkwood, J. G., 1950, ''The Statistical Mechanical Theory of Transport Processes A. The Equations of Hydrodynamics,'' J. Chem. Phys., **18**, pp. 817–829.

[38] Swope, W. C., Anderson, H. C., Berens, P. H., and Wilson, K. R., 1982, ''A Computer Simulation Method for the Calculation of Equilibrium Constants for the Formation of Physical Clusters of Molecules: Application to Small Water Clusters,'' J. Chem. Phys., **76**, pp. 637–649.

[39] Dobbs, E. R., and Jones, G. O., 1957, ''Theory and Properties of Solid Argon,'' Rep. Prog. Phys., **20**, pp. 516–564.

[40] Reid, R. C., Prausnitz, J. M., and Poling, B. E., 1987, *The Properties of Gases and Liquids*, Mc-Graw Hill, New York.

[41] White, G. K., and Woods, S. B., 1958, ''Thermal Conductivity of the Solidified Inert Gases: Argon, Neon and Krypton,'' Philos. Mag., **3**, pp. 785–797.

[42] Bao, Y., and Chen, G., 2000, ''Lattice Dynamics Study of Anisotropy of Heat Conduction in Superlattices,'' *Proceedings of MRS Spring Meeting, Symposium Z*, Materials Research Society, PA.

[43] Jacucci, G., and Rahman, A., 1984, ''Comparing the Efficiency of Metropolis Monte Carlo and Molecular Dynamics Methods for Configuration Space Sampling,'' Nuovo Cimento, **D4**, pp. 341–356.

[44] Weast, R. C., Astle, M. J., and Beyer, W. H., eds., 1996, *CRC Handbook of Chemistry and Physics*, CRC Press, Boca Raton.

[45] Press, W. H., Teukolsky, S. A., Vetterling, W. T., and Flannery, B. P., 1992, *Numerical Recipes in FORTRAN: The Art of Scientific Computing*, 2nd edition, Cambridge University Press, Cambridge.

Journal of Heat Transfer

Technical Notes

This section contains shorter technical papers. These shorter papers will be subjected to the same review process as that for full papers.

Wavelets and the Discrete Ordinate Method for Radiative Heat Transfer in a Two-Dimensional Rectangular Enclosure With a Nongray Medium

Ye Wang and Yildiz Bayazitoglu
Department of Mechanical Engineering and Materials Science, Rice University, Houston, TX 77005

Introduction

The mathematical model for describing a radiation field in a participating medium is the radiative transfer equation (RTE). The dependent variable in the RTE, the spectral radiative intensity, is a function of location, wavelength, and solid angle. This makes it very difficult to be solved, especially for multi-dimensional geometry. Therefore previously the gray medium assumption was usually used to simplify the problem [1–3], and combined conductive-radiative heat transfer in multi-dimensional geometry was also studied [4–6]. In order to incorporate the nongray effects, many approximate methods have been developed. One of them is to apply the picket fence model [7], where the band-distributed radiative properties are approximated by a box model. Another approach is the weighted-sum-of-gray-gases model [8], where the nongray gas is replaced by a number of gray gases. Other researchers [9–10] introduced the wavelet expansion to evaluate the spectral radiative intensity in their one-dimensional nongray analyses. This paper will extend the use of wavelets in the solution of nongray problems [10] to the two-dimensional geometries. The results of pure radiation without internal heat generation will be presented for nongray medium in a rectangular enclosure.

Numerical Analysis

In general, the governing equations for radiative heat transfer in the field of a participating medium are the radiative transfer equation and the energy conservation equation. By simultaneously solving these two-coupled equations, the temperature distribution and heat flux in the field can be obtained. For simplicity, the absorbing, emitting, and nonscattering medium in a two-dimensional rectangular enclosure is considered here, as shown in Fig. 1. The surfaces of the enclosure are assumed to be black and isothermal.

1 Radiative Transfer Equation. The RTE in a two-dimensional rectangular enclosure is

$$\mu\frac{\partial I'_\lambda}{\partial x}+\xi\frac{\partial I'_\lambda}{\partial y}+a_\lambda\cdot I'_\lambda=a_\lambda\cdot I'_{\lambda b}, \tag{1}$$

where $I'_\lambda=I'_\lambda(\lambda,x,y,\mu,\xi)$, $I'_{\lambda b}=I'_{\lambda b}(\lambda,x,y)$, $a_\lambda=a_\lambda(\lambda,x,y)$, and (μ,ξ) are the direction cosines.

The nondimensional form of the above equation is obtained

$$\mu\frac{\partial I'^*_\lambda}{\partial x^*}+r\cdot\xi\frac{\partial I'^*_\lambda}{\partial y^*}+\kappa_L\cdot I'^*_\lambda=\kappa_L\cdot I'^*_{\lambda b} \tag{2}$$

by introducing the following nondimensional parameters.

$$\begin{gathered}x^*=x/L,\quad y^*=y/H,\quad r=L/H\\ \kappa_L=a_\lambda\cdot L,\quad \kappa_H=\alpha_\lambda\cdot H\\ \lambda^*=(\lambda-\lambda_0)/\Delta\lambda\\ I'^*_\lambda=I'_\lambda\cdot\Delta\lambda/(\sigma T_1^4)\\ I'^*_{\lambda b}=I'_{\lambda b}\cdot\Delta\lambda/(\sigma T_1^4),\end{gathered} \tag{3}$$

where L and H are the width and height of the two-dimensional rectangular enclosure, κ_L and κ_H are the optical width and optical height, λ_0 and $\Delta\lambda$ are the starting wavelength and the wavelength width of the absorption band, respectively, and T_1 is the temperature of surface 1. Thus x^*, $y^*\in[0,1]$, $\lambda^*\in[0,1]$.

The nondimensional radiative intensity I'^*_λ in the RTE Eq. (2) is a function of the wavelength, location, and solid angle. Many successful methods to solve the location dependent problems (such as finite difference and finite element method) and the solid angle dependent problems (such as DOM and P-N approximation) already exist. Studies show that the absorption coefficients of most participating media are strongly dependent on wavelength. A similar behavior is expected for the radiative intensity. Since wavelet is relatively new and very useful tool for function approximation, the wavelet expansion in the wavelength domain is

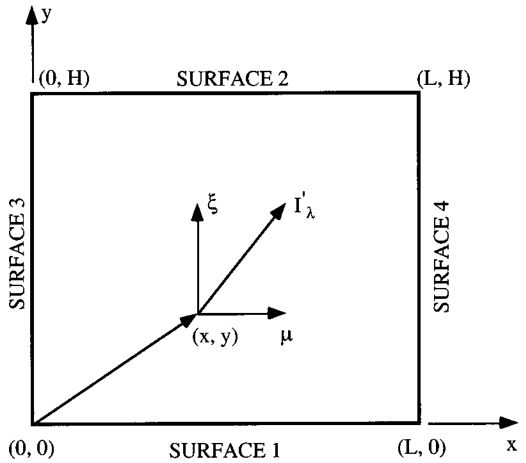

Fig. 1 Geometry and coordinate system of two-dimensional rectangular enclosure

---

8

Contributed by the Heat Transfer Division for publication in the JOURNAL OF HEAT TRANSFER. Manuscript received by the Heat Transfer Division February 5, 1999; revision received April 16, 2001. Associate Editor: P. Menguc.

introduced to evaluate the wavelength dependence of radiative intensity.

Applying the discrete wavelet transform method [11], the radiative intensity is first expanded in terms of the wrapped Daubechies wavelet W_i as,

$$I'^*_\lambda(\lambda^*,x^*,y^*,\mu,\xi)=\sum_{i=1}^{N} c_i(x^*,y^*,\mu,\xi)\cdot W_i\,, \tag{4}$$

where

$$W_1=1 \tag{5a}$$

$$W_i=2^{j/2}\cdot W(2^j\lambda^*-k) \qquad i=2,3,\ldots,N. \tag{5b}$$

Here j and k are integers and describe the scaling and dilation of the wavelets, respectively. Daubechies wavelets are a set of compact supported base functions. They constitute an orthonormal system, that is,

$$\int_0^1 W_i\cdot W_j\cdot d\lambda^*=\delta_{ij}\,, \tag{6}$$

where δ is Kronecker δ-function.

Now we substitute the expansion Eq. (4) back into the RTE Eq. (2) and apply the Galerkin method, considering the orthonormal property Eq. (6) of the wavelet functions. A set of equations about the expansion coefficients, $c_i(x^*,y^*,\mu,\xi)$, are created as

$$\mu\frac{dc_j}{dx^*}+r\cdot\xi\frac{dc_j}{dy^*}+\sum_{i=1}^{N} c_i\cdot\int_0^1\kappa_L\cdot W_i\cdot W_j\cdot d\lambda^*$$

$$=\int_0^1\kappa_L\cdot I'^*_{\lambda b}\cdot W_j\cdot d\lambda^*, \tag{7}$$

where $j=1,2,\ldots,N$.

In matrix form, it becomes

$$\mu\frac{dC}{dx^*}+r\cdot\xi\frac{dC}{dy^*}+A\cdot C=B \tag{8}$$

where

$$C=[c_1(x^*,y^*,\mu,\xi),\ldots,c_N(x^*,y^*,\mu,\xi)]^T \tag{9a}$$

$$A_{i,j}=\int_0^1\kappa_L\cdot W_i\cdot W_j\cdot d\lambda^*,\quad i,j=1,2,\ldots,N \tag{9b}$$

$$B=\left[\int_0^1\kappa_L\cdot I'^*_{\lambda b}\cdot W_1\cdot d\lambda^*,\ldots,\int_0^1\kappa_L\cdot I'^*_{\lambda b}\cdot W_N\cdot d\lambda^*\right]^T. \tag{9c}$$

The unknown vector C here is not dependent on the wavelength. It can be solved with any numerical method developed for gray media.

Among the numerical methods developed for solving gray medium radiative heat transfer, the DOM is considered to be a promising one with high accuracy and little computer time consumption. We use this method in this work to solve the set of equations about the expansion coefficients C, which are the functions of location and solid angle.

Applying the DOM, Eq. (8) is replaced by a set of equations of discrete ordinate directions,

$$\mu_m\frac{dC_m}{dx^*}+r\cdot\xi_m\frac{dC_m}{dy^*}+A\cdot C_m=B, \tag{10}$$

where $C_m=[c_{1,m}(x^*,y^*,\mu_m,\xi_m),\ldots,c_{N,m}(x^*,y^*,\mu_m,\xi_m)]^T$, with $m=1,2,\ldots,M$, A and B are as above in Eq. (9b,c). The selection of the ordinate directions (μ_m,ξ_m) and their quadrature weights w_m was given in [12]. Equation (10) is a set of differential equations about the coefficients $c_{i,m}$ and can be solved with numerical methods such as finite volume [13] when boundary conditions are given.

Boundary conditions for the DOM are generated by expressing the intensity leaving the surface along the ordinate direction m as the sum of emitted and reflected intensities. In a two-dimensional rectangular enclosure the boundary conditions are the following:

$$\text{at surface 1}\quad I'^*_{\lambda m}=\varepsilon I'^*_{\lambda b}+\frac{1-\varepsilon}{\pi}\sum_{\xi_{m'}<0} w_{m'}|\xi_{m'}|I'^*_{m'}\quad \xi_m>0 \tag{11a}$$

$$\text{at surface 2}\quad I'^*_{\lambda m}=\varepsilon I'^*_{\lambda b}+\frac{1-\varepsilon}{\pi}\sum_{\xi_{m'}>0} w_{m'}|\xi_{m'}|I'^*_{m'}\quad \xi_m<0 \tag{11b}$$

$$\text{at surface 3}\quad I'^*_{\lambda m}=\varepsilon I'^*_{\lambda b}+\frac{1-\varepsilon}{\pi}\sum_{\mu_{m'}<0} w_{m'}|\xi_{m'}|I'^*_{m'}$$

$$\mu_m>0 \tag{11c}$$

$$\text{at surface 4}\quad I'^*_{\lambda m}=\varepsilon I'^*_{\lambda b}+\frac{1-\varepsilon}{\pi}\sum_{\mu_{m'}>0} w_{m'}|\xi_{m'}|I'^*_{m'}$$

$$\mu_m<0 \tag{11d}$$

Since all the surfaces are assumed to be black, the boundary conditions come down to following:

$$I'^*_{\lambda m}=I'^*_{\lambda b,w}\,. \tag{12}$$

Now we apply Galerkin method to the boundary conditions by substituting the expansion Eq. (4) into Eq. (12), multiplying by the wavelet bases on both sides, and integrating over the wavelength domain. With the consideration of the orthonormal property of wavelet functions, a set of boundary conditions for Eq. (10) can be obtained as

$$c_{j,m}=\int_0^1 I'^*_{\lambda b,w}\cdot W_j\cdot d\lambda^*, \tag{13}$$

where $j=1,2,\ldots,N$.

The expansion coefficients in a particular direction, $c_{i,m}$, can be solved from Eq. (10) when the temperature distribution of the medium is given (since A and B in Eq. (9b,c) are functions of the temperature distribution). Once the expansion coefficients are determined, the radiative intensity and heat flux in the direction m can be calculated as follows:

$$I^*_m=\int_0^1 I'^*_{\lambda m}\cdot d\lambda^*=c_{1,m} \tag{14}$$

$$q^*_{r,x}=\sum_{m=1}^{M} w_m\cdot\mu_m\cdot I^*_m=\sum_{m=1}^{M} w_m\cdot\mu_m\cdot c_{1,m} \tag{15a}$$

$$q^*_{r,y}=\sum_{m=1}^{M} w_m\cdot\xi_m\cdot I^*_m=\sum_{m=1}^{M} w_m\cdot\xi_m\cdot c_{1,m} \tag{15b}$$

and the divergence of the radiative heat flux is

$$\nabla\cdot q^*_r=\frac{\partial q^*_{r,x}}{\partial x^*}+r\frac{\partial q^*_{r,y}}{\partial y^*}=\sum_{m=1}^{M} w_m\left(\mu_m\frac{\partial c_{1,m}}{\partial x^*}+r\cdot\xi_m\frac{\partial c_{1,m}}{\partial y^*}\right)$$

$$=\sum_{m=1}^{M} w_m\left(B_1-\sum_{i=1}^{N} A_{1i}\cdot c_{i,m}\right). \tag{16}$$

Note that these are values inside the absorption band. Outside the band, the radiative intensity and heat flux will not change throughout the medium since no absorption occurs there.

2 Energy Equation. For the case of pure radiation, the energy equation is

$$\nabla \cdot q_r = q'''. \tag{17}$$

Nondimensionalize the above equation as

$$\nabla \cdot q_r^* = 0 \quad \text{if } q''' = 0 \tag{18a}$$

$$\nabla \cdot q_r^* = 1 \quad \text{if } q''' \neq 0, \tag{18b}$$

and $r = L/H$ is the aspect ratio where L and H are width and height of two-dimensional enclosure, respectively. The dimensionless parameters are

$$\begin{aligned} q_r^* &= q_r/(\sigma T_1^4) \quad \text{if } q''' = 0 \\ q_r^* &= q_r/(q''' \cdot L) \quad \text{if } q''' \neq 0. \end{aligned} \tag{19}$$

Table 1 Convergence of nondimensional temperature distribution $(E-E_2)/(E_1-E_2)$ at centerline in two-dimensional square enclosure filled with nongray medium CO_2 (Case 1)

	$y^* = 0.0$	$y^* = 0.5$	$y^* = 1.0$	$\Delta_{\max}$
N=8	0.4682	0.1712	0.0618	
N=16	0.4866	0.1746	0.0612	0.0184
N=32	0.4961	0.1767	0.0608	0.0095
N=64	0.5009	0.1779	0.0606	0.0048

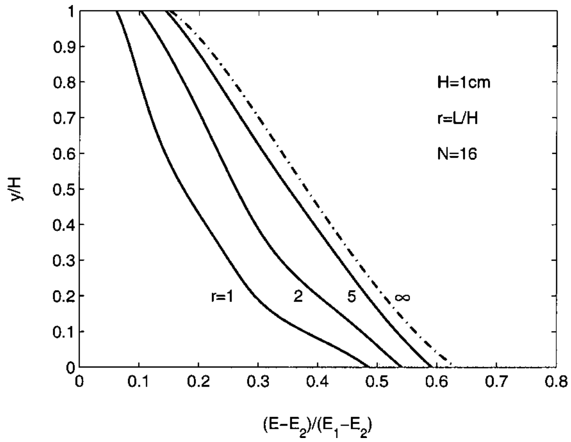

Fig. 2 Nondimensional temperature distribution at centerline in two-dimensional rectangular enclosure filled with nongray medium CO_2 for various aspect ratios (Case 1)

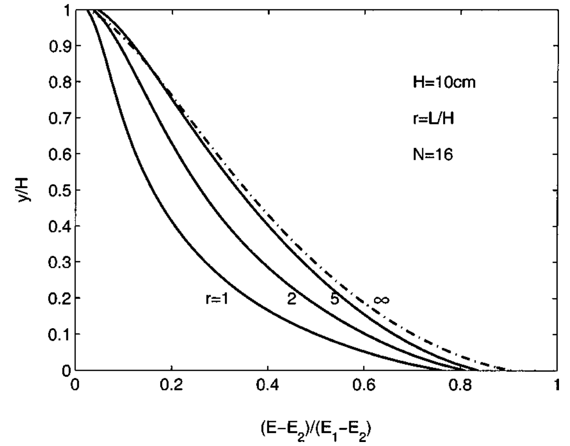

Fig. 3 Nondimensional temperature distribution at centerline in two-dimensional rectangular enclosure filled with nongray medium CO_2 for various aspect ratios (Case 2)

Table 2 Nondimensional surface heat fluxes $q_r/\sigma T_2^4$ in two-dimensional rectangular enclosures with nongray medium CO_2 for various aspect ratios (Case 1)

position	r=1.0	r=2.0	r=5.0
x^*		bottom (hot) wall	
0.1	195.709	195.587	195.315
0.2	195.752	195.489	195.145
0.3	195.731	195.409	195.068
0.4	195.712	195.362	195.033
0.5	195.705	195.346	195.023
transparent	196.754	196.754	196.754
y^*		side (cold) wall	
0.1	-59.852	-76.298	-88.309
0.2	-58.913	-76.308	-88.628
0.3	-57.785	-75.975	-88.639
0.4	-57.249	-75.340	-88.551
0.5	-57.041	-74.609	-88.420
0.6	-56.892	-74.011	-88.261
0.7	-56.709	-73.620	-88.063
0.8	-56.443	-73.379	-87.807
0.9	-56.078	-73.200	-87.487
transparent	-57.628	-75.153	-88.636
x^*		top (cold) wall	
0.1	-79.746	-119.729	-158.946
0.2	-80.371	-120.963	-159.938
0.3	-81.208	-121.190	-160.518
0.4	-81.550	-121.310	-160.597
0.5	-81.605	-121.387	-160.590
transparent	-81.498	-121.601	-161.300
		Total	
bottom wall	195.641	195.427	195.154
side wall	-57.446	-74.687	-88.117
top wall	-80.715	-120.623	-159.760
total	0.034	0.117	0.148
% error	0.017	0.060	0.076

Table 3 Nondimensional surface heat fluxes $q_r/\sigma T_2^4$ in two-dimensional rectangular enclosures with nongray medium CO_2 for various aspect ratios (Case 2)

position	r=1.0	r=2.0	r=5.0
x^*		bottom (hot) wall	
0.1	191.616	191.014	190.294
0.2	191.217	190.523	189.879
0.3	190.987	190.280	189.725
0.4	190.868	190.162	189.663
0.5	190.832	190.126	189.646
transparent	196.754	196.754	196.754
y^*		side (cold) wall	
0.1	-58.408	-74.803	-86.847
0.2	-57.446	-74.303	-86.638
0.3	-56.644	-73.840	-86.371
0.4	-56.175	-73.374	-86.117
0.5	-55.900	-72.934	-85.884
0.6	-55.693	-72.570	-85.670
0.7	-55.506	-72.292	-85.465
0.8	-55.307	-72.076	-85.262
0.9	-55.085	-71.894	-85.057
transparent	-57.628	-75.153	-88.636
x^*		top (cold) wall	
0.1	-78.052	116.765	-154.977
0.2	-78.366	117.366	-155.526
0.3	-78.742	117.531	-155.820
0.4	-78.894	117.630	-155.883
0.5	-78.920	117.679	-155.890
transparent	-81.498	121.601	-161.300
		total	
bottom wall	191.200	190.578	190.008
side wall	-56.309	-73.139	-85.897
top wall	-78.506	117.239	-155.426
total	0.077	0.200	0.223
% error	0.040	0.105	0.118

To solve the RTE and energy equation simultaneously, the modified quasi-linearization algorithm (MQA) [14] is applied by treating the energy equation as the constraint condition for the RTE.

In summary, the over-all solution procedure is as follows: (1) Assume the initial temperature distribution; (2) calculate the absorption coefficient a_λ; (3) calculate A and B according to expression (10*b*,*c*); (4) solve Eq. (10) for the coefficients $c_{i,m}$; (5) Calculate the radiative intensity and heat flux by expression (14) and (15); (6) if the energy equation (18) is satisfied, stop; otherwise, adjust the temperature distribution; and (7) repeat steps (2) to (6) until the energy equation is satisfied.

Results and Discussion

A square enclosure filled with a nongray medium is considered. It is assumed that surface 1 is hot at temperature T_1, the other three surfaces are cold at zero temperature. No heat generation takes place inside the medium, so Eq. (18*a*) is the energy equation where the nondimensional parameter is the emissive power of the hot wall. In this work, as an example, CO_2 is chosen and its 4.3 μm absorption band is studied. The absorption coefficient is evaluated by

$$a_\lambda=(\rho\cdot S/d)\,\frac{\sinh(2\pi\cdot\gamma/d)}{\cosh(2\pi\cdot\gamma/d)-1},\tag{20}$$

where ρ is density, S/d is mean-line-intensity-to-spacing ratio, and γ/d is line-width-to-spacing ratio for the considered narrow band. The parameters S/d and γ/d incorporate the effects of wavelength, temperature, and pressure and can be found in [15].

The examples considered are

$$\text{case 1:}\quad T_1=1500\ \text{K},\quad T_2=400\ \text{K},$$

$$P_{CO_2}=0.2\ \text{atm},\quad P_{N_2}=10\ \text{atm},\quad H=1\ \text{cm}$$

$$\text{case 2:}\quad T_1=1500\ \text{K},\quad T_2=400\ \text{K},$$

$$P_{CO_2}=1.0\ \text{atm},\quad P_{N_2}=0\ \text{atm},\quad H=10\ \text{cm}$$

These examples are chosen because there are one-dimensional results to compare with.

The convergence trend of the centerline temperature distribution for case 1 for an increasing number of wavelet expansion terms is presented in Table 1. Considering the current limit of computer capacity, all subsequent results for nongray medium are obtained with $N=16$. The temperature distributions at the centerline are shown in Figs. 2 and 3. The results for the limit $r\rightarrow\infty$ are taken from one-dimensional case [10]. The results follow the expected trend as the aspect ratio r increases. The nonsmoothness for optically thin medium in Fig. 2 is due to the ray effect that is inevitable while using discrete ordinate method. The surface heat fluxes are given in Tables 2 and 3. Compared to the case of transparent gas, the existence of the absorbing gas results in the decreases of surface heat flux.

The present work successfully solved the two-dimensional nongray radiation problem. The same method can be easily extended to three-dimensional problems. Conclusively, the introduction of wavelet functions makes it possible to study radiative transfer through a nongray medium with an arbitrary distribution of the absorption coefficient.

Acknowledgment

This work was in part supported by Texas Advanced Technology Program under Grant No. 003604-041.

Nomenclature

a_λ = spectral absorption coefficient
c_i = wavelet expansion coefficients of spectral radiative intensity I'_λ
d = spectral line spacing in Eq. (20)
E = emissive power $(=\sigma T^4)$
H = height of the two-dimensional rectangular enclosure
I = radiative intensity
I'_λ = spectral radiative intensity in a particular direction
$I'_{\lambda b}$ = spectral blackbody intensity in a particular direction
L = width of the two-dimensional rectangular enclosure
M = number of discrete ordinates in DOM
N = number of wavelet expansion terms of radiative intensity
q_r = radiative heat flux
q''' = internal heat generation rate
r = aspect ratio of two-dimensional rectangular enclosure $(=L/H)$
S = mean line intensity in Eq. (20)
T = temperature
T_i = temperature of surface $i(i=1-4)$
W_i = wrapped Daubechies wavelet functions
w_i = quadrature weight of discrete ordinate ω_i in DOM
x,y = coordinates

Greek Symbols

γ = line half width in Eq. (20)
δ_{ij} = Kronecker δ-function
ε = emissivity
κ_H = optical height for two-dimensional rectangular enclosure
κ_L = optical width for two-dimensional rectangular enclosure
λ = wavelength
λ_0 = start wavelength of the absorption band
$\Delta\lambda$ = wavelength width of the absorption band
μ,ξ,η = direction cosines
ρ = density
σ = Stefan-Boltzmann constant
ω = solid angle

Subscripts

H = height
L = width
m,m' = directions of the discrete ordinates
r = radiative
w = wall
λ = spectrally dependent

Superscripts

$*$ = nondimensional quantity

References

[1] Modest, M. F., 1975, "Radiative Equilibrium of a Gray Medium in a Rectangular Enclosure Bounded by Gray Walls," J. Quant. Spectrosc. Radiat. Transf., **15**, p. 445.
[2] Yuen, W. W., and Wong, L. W., 1984, "Analysis of Radiative Equilibrium in a Rectangular Enclosure With Gray Medium," ASME J. Heat Transfer, **106**, p. 433.
[3] Yuen, W. W., and Ho, C. F., 1985, "Analysis of Two-Dimensional Radiative Heat Transfer in a Gray Medium With Internal Heat Generation," Int. J. Heat Mass Transf., **28**, p. 17.
[4] Ratzel, A. G., 1981, "P-N Differential Approximation for Solution of One- and Two-Dimensional Radiation and Conduction Energy Transfer in Gray Participating Media," Ph.D. dissertation, Department of Mechanical Engineering, University of Texas, Austin.
[5] Yuen, W. W., and Takara, E. E., 1988, "Analysis of Combined Conductive-Radiative Heat Transfer in a Two-Dimensional Rectangular Enclosure With a Gray Medium," ASME J. Heat Transfer, **110**, p. 468.
[6] Kim, T. Y., and Baek, S. W., 1991, "Analysis of Combined Conductive and Radiative Heat Transfer in a Two-Dimensional Rectangular Enclosure Using the Discrete Ordinates Method," Int. J. Heat Mass Transf., **34**, pp. 2265.

[7] Modest, M. F., and Sikka, K. K., 1992, ‘‘The Stepwise Gray P-1 Approximation for Multi-Dimensional Radiative Transfer in Molecular- Gas-Particulate Mixtures,’’ J. Quant. Spectrosc. Radiat. Transf., **48**, pp. 159.
[8] Modest, M. F., 1991, ‘‘The Weighted-Sum-of-Gray-Gases Model for Arbitrary Solution Methods in Radiative Transfer,’’ ASME J. Heat Transfer, **113**, pp. 650.
[9] Bayazitoglu, Y., and Wang, B. Y., 1996, ‘‘Wavelets in the Solution of Nongray Radiative Heat Transfer Equation,’’ HTD-Vol. 332, *Proceeding of the ASME Heat Transfer Division*, **1**, pp. 129.
[10] Wang, Y., and Bayazitoglu, Y., 1998, ‘‘Wavelets and Discrete Ordinates Method in Solving One-Dimensional Nongray Radiation Problem,’’ Int. J. Heat Mass Transf., in press.
[11] Newland, D. E., 1993, *An Introduction to Random Vibrations, Spectral and Wavelet Analysis*, John Wiley & Sons Inc., New York.
[12] Truelove, J. S., 1987, ‘‘Discrete-Ordinate Solutions of the Radiation Transport Equation,’’ ASME J. Heat Transfer, **109**, p. 1048.
[13] Fiveland, W. A., 1984, ‘‘Discrete-Ordinates Solutions of the Radiative Transport Equation for Rectangular Enclosures,’’ ASME J. Heat Transfer, **106**, p. 699.
[14] Miele, A., and Iyer, R. R., 1970, ‘‘General Technique for Solving Nonlinear Two-Point Boundary-Value Problems via the Method of Particular Solutions,’’ Optimization Theory and Applications, **5**, p. 382.
[15] Edwards, D. K., 1976, ‘‘Molecular Gas Band Radiation,’’ *Advances in Heat Transfer*, **12**, Academic Press, New York p. 115.

Experimental Study on Forced Convection Heat Transfer Inside Horizontal Tubes in an Absorption/Compression Heat Pump

Li Yong and K. Sumathy
Department of Mechanical Engineering, University of Hong Kong, Hong Kong

Quasi-local absorption heat transfer coefficients and pressure drop inside a horizontal tube absorber have been investigated experimentally, with R-22/DMA as the working pair. The absorber is a counterflow coaxial tube-in-tube heat-exchanger with the working fluid flowing in the inner tube while the water moves through the annulus. A large temperature gliding has been experienced during the absorption process. Experimental results show that the heat transfer coefficient of the forced convective vapor absorption process is higher compared to the vertical falling film absorption. A qualitative study is made to analyze the effect of mass flux, vapor quality and solution concentration on pressure drop and heat transfer coefficients. On the basis of the experimental results, a new correlation is proposed whereby the two-phase heat transfer is taken as a product of the forced convection of the absorption and the combined effect of heat and mass transfer at the interface. The correlation is found to predict the experimental data almost within 30 percent. [DOI: 10.1115/1.1473142]

Keywords: Experimental, Forced Convection, Heat Transfer, Heat Pump

Introduction

Several large-scale absorption/compression heat pumps have been operated to identify the appropriate cycle components, but there is still considerable work to be done before the absorption/compression technology can be considered a viable alternative solution to the vapor-compression technology. Most of the experimental works reported have used the vertical or horizontal shell and tube heat-exchanger as absorber and desorber [1]. Torstensson and Nowacki [2] used coaxial tube-in-tube heat-exchangers to study its effect on the system performance, but the detailed analysis on heat transfer aspects was not carried out. Hence, an attempt has been made in the present study to improve the heat transfer coefficient in coaxial tube-in-tube heat-exchanger by incorporating certain modifications, which result in a forced convective vapor absorption process. Since the development of analytically based universal correlation for prediction of heat transfer is limited to the inherent complications of two-phase flow phenomena, use of semi-empirical correlation is widely accepted in practice by design engineers. This paper also presents a correlation for the forced convection heat transfer in horizontal tubes in an absorption/compression heat pump, with the obtained experimental results.

Test Facility and Procedure

The present experimental investigation is carried out on a test rig which has been designed and built for measurement of in-tube, two-phase-flow heat transfer coefficient of the absorption process. The schematic diagram of the test rig used in the present study is shown in Fig. 1. R-22/DMA is chosen as the working pair, in which R-22 serves as the refrigerant. The organic fluid DMA (N, N, dimethylacetamide) is used as an absorbent. The test facility consists of six main parts: a test section (absorber), an absorption/compression loop, a hot and cold water loop, a R-22 concentration regulating circuit, a cooling circuit of low capacity and a data acquisition system.

The Test-Section. A coaxial tube-in-tube heat-exchanger has been used as the absorber. The absorber tube has an OD of 19 mm and an ID of 16 mm and the annulus surrounding the absorber tube is also of the same length with an ID of 27 mm. The test section is of 24 m in length and is subdivided into four equal parts to detect the local heat transfer, which is transferred from the two-phase refrigerant mixture (R-22 vapor+weak solution) to water in the annulus. The exterior of the annulus is insulated with a thick layer of insulation to ensure adiabatic condition. The flow rates of the weak solution and R-22 vapor are controlled using a bypass valve V3 and compressor. Since the weak solution pump is very sensitive to cavitation, a cooling circuit of low capacity is used to cool the weak solution.

The R-22 Concentration Regulating Circuit. The circuit contains two valves and a R-22 accumulator with cooling water flowing through it. In order to test the effect of R-22 concentration on the heat transfer process, the R-22 concentration regulating circuit is used. Similarly, to increase the R-22 concentration, the system is halted temporarily such that the pressure in the recuperator as well as regenerator 1 reduces, and R-22 is added into the accumulator through valve V13. To reduce concentration, the pump circulating the weak solution is stopped, while the compressor continues to operate. Meanwhile, the R-22 in the accumulator gets cooled and condensed by the cooling water.

Experimental Procedure. A typical experimental run begins by first turning on the water pumps and fixing the mass flux and temperature at the desired level. Next, the compressor is turned on and valve V6 is opened for compressing the vapor into the absorber. The expansion valve V5 is also opened slightly for throttling the condensed liquid. On realizing the cooling effect in the cooling circuit, the weak solution pump is turned on and valve V1 is opened to circulate the weak solution in the system. Meanwhile, the expansion valve V5 and by-pass valve V3 are regulated to achieve desired pressure and flow rate. The system is then allowed to reach the steady-state condition before the data-acquisition process begins. Achieving ‘‘steady-state’’ conditions is defined by requiring less than 2 percent fluctuation in system pressure and temperatures within 10 minutes. Once the steady-state condition is reached, the data acquisition system records measurements of temperature, pressure, and mass flow rates at various points around the experimental loop. The experimental work were con-

---

Contributed by the Heat Transfer Division for publication in the JOURNAL OF HEAT TRANSFER. Manuscript received by the Heat Transfer Division July 13, 2001; revision received February 25, 2002. Associate Editor: B. T. F. Chung.

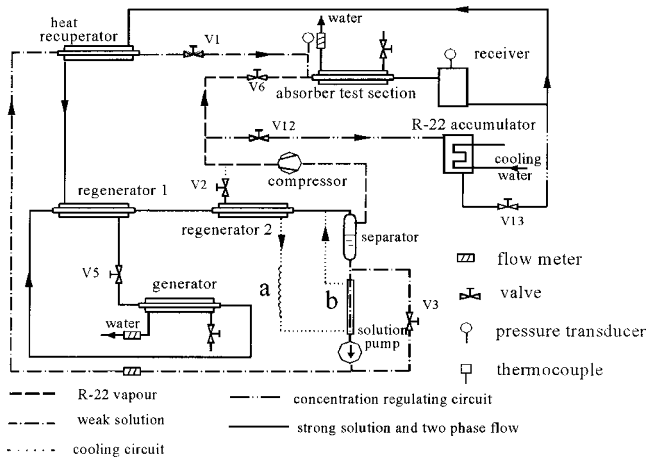

Fig. 1 Schematic diagram of the experimental setup

ducted under certain test conditions: (i) solution concentration—64 percent to 90 percent weight of R-22; (ii) weak solution mass flux—91 to 280 kg/(m^2 s); and (iii) absorption temperature—293 to 323 K.

Data Reduction

As mentioned earlier, since the absorber test section is very long (length$=$24 m), it is divided into four subsections, in order to detect the local parameters. Hence, the average heat transfer coefficient in each subsection is treated as quasi-local heat transfer coefficient, which in turn is determined from the overall heat transfer coefficient and the water-side heat transfer coefficient by using the procedures described below.

The water-side convective heat transfer coefficient (h_w) is calculated using the correlation of heat transfer in the annulus [3].

$$h_w=0.01032(\mathrm{Re}_w^{0.87}-280)\mathrm{Pr}_w^{0.4}(d_{oi}/d_{io})^{0.16}[\lambda_w/(d_{oi}-d_{io})] \tag{1}$$

where d_{io} and d_{oi} denote the inside diameter of the outer tube and outside diameter of the inner tube, respectively. The overall heat transfer coefficient (U) is found from the energy balance on the test sub-section.

$$U=\frac{Q}{A\cdot LMTD}. \tag{2}$$

The log mean temperature difference ($LMTD$) is determined from the water-side and absorption-side inlet and exit temperatures in each sub-section. The energy transferred (Q) in each sub-section is calculated from an energy balance on the water flowing in the annulus.

The quasi-local heat transfer coefficient (h_{tp}) of the two phase absorption process for each subsection of the absorber is determined as:

$$\frac{1}{h_{tp}}=\frac{d_{ii}}{d_{io}\cdot U}-\frac{d_{ii}}{d_{io}\cdot h_w}-\frac{d_{ii}}{2\lambda_c}\ln\frac{d_{io}}{d_{ii}} \tag{3}$$

where d_{ii} denotes the inside diameter of the inner tube. Physical properties of the working pairs are calculated using the database developed by Guo et al. [4].

The value of "Q" is checked by comparing the energy balance on the absorption side, Q_l, during single-phase flow experiments. The two energy balances—Q and Q_l agree within 2.2 percent for all runs. Temperatures of the fluid are measured by pairs of thermocouples at each location and have experimental uncertainties by about ±0.2 K. The pressures in test-section and pressure drop of each sub-section are measured respectively with strain-gauge-type pressure transducer and differential pressure transducer accurate to ±0.1 percent. The mass flow rates have uncertainties of ±0.5 percent and the water-side thermal resistance is about 22 percent~49 percent of the total thermal resistance and propagation-of-error [5] analyses provide the uncertainty as ±9.3 percent for h_{tp}.

Results

Experimental in-tube forced convective absorption heat transfer coefficient data and pressure drop results are reported for the working pair R-22/DMA in an absorption/compression heat pump. The results are compared to the conventional falling film situation. It is observed that the heat transfer coefficient is in the range of 800~2200 W/(m^2 K), higher than that of a falling film (200 ~900 W/(m^2 K), [6]). Also, a temperature gliding of about 25 K can be realized in the present experiments, which can be utilized to enhance the system COP.

Since the in-tube forced convective absorption was demonstrated to be more effective, experiments were also conducted to study the effect of various parameters that influence the heat and mass transfer coefficient as well as pressure drop of each sub-section, such as the mass flux and the solution concentration in the absorption section. Since the concentration could not be controlled directly, R-22 concentration is calculated based on conservation of species and energy. Hence, only certain range of R-22 concentration has been chosen to represent the quasi-constant concentration for the different mass flux (Fig. 2(*a*)). In the figures, the vapor quality (Y) represents the average quality of each sub-section.

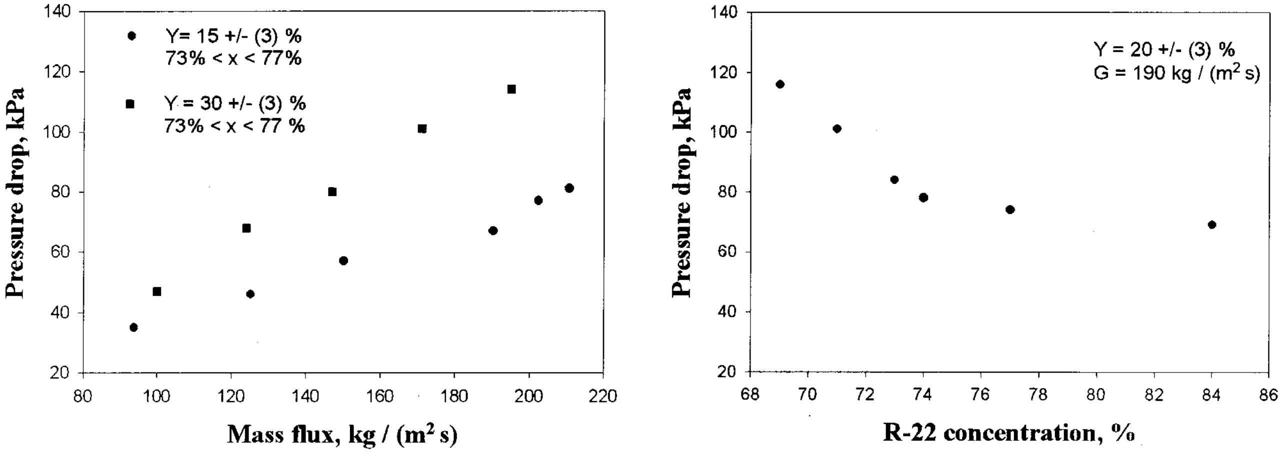

Fig. 2 Absorption pressure drop for DMA/R-22 mixture showing the effect of (*a*) mass flux, and (*b*) R-22 concentration

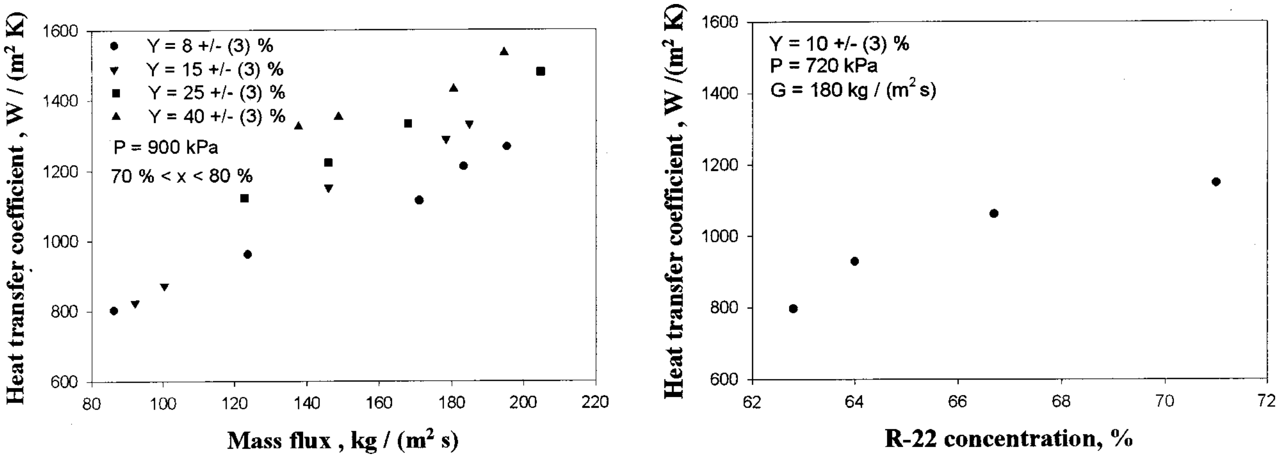

Fig. 3 Quasi-local heat transfer coefficient versus (*a*) mass flux, and (*b*) R-22 concentration

The absorption pressure drop of each sub-section for DMA/R-22 mixture is shown in Fig. 2. The data in the Fig. 2(*a*) corresponds to two average quality conditions corresponding to certain R-22 mass concentration within a range of 73 percent ~77 percent. It is seen that, the pressure drop increases with the increase in mass flux and also as expected, the pressure drop increases with the increase in the vapor quality, in the test section. Besides the influence from mass flux and vapor quality, another factor affecting the pressure drop might be the R-22 concentration. Hence, the influence of R-22 concentration on the pressure drop is plotted in Fig. 2(*b*). It is seen that, a higher pressure drop is experienced at lower R-22 concentrations. This is because of the fact that at any given temperature the viscosity of DMA (1.02×10^{-3} kg/(m s) at 298 K) is higher than R-22. Therefore, when R-22 concentration is lower, it implies that the fraction of DMA in the mixture is more which results in higher frictional losses, leading to a higher pressure drop in the test-section.

Figure 3 shows typical results of the effect of mass flux and R-22 concentration on the quasi-local absorption heat transfer for DMA/R-22 mixtures. It is found from the Fig. 3(*a*) that, other conditions remaining the same, high vapor-liquid mixture mass flux results in a higher absorption heat transfer coefficient. This is attributed to greater convection effects at higher mass fluxes. It is also apparent from the Fig. 3(*a*) that high average vapor quality produces higher coefficients, because the average film thickness is thinner. Thus, as absorption progresses, the rate of heat transfer decreases owing to the increase in the liquid film thickness and decrease in flow velocity. From Fig. 3(*b*), it can be seen that the heat transfer coefficient increases slightly with increase in average solution concentration. This is because the viscosity of the working pair decreases with the increase in R-22 concentration.

The Proposed Correlation

In the absorption process, the heat and mass transfer resistance mainly occurs in the liquid film. The absorption process of a mixture can exhibit significant differences from condensation of a single, pure component. The differences are related to the phase equilibrium effects which are referred to as mixture effects. The heat transfer is not only influenced by the physical properties of the mixture (such as thermal conductivity, viscosity, specific heat etc.), but also influenced by the phase equilibrium and mass diffusion resistance. With the heat and mass transfer coupled together, the mixture effects are determined by the combined effects of phase transition properties and mass transfer resistance.

Since there is a similarity between the in-tube forced convection absorption process and generation process, the model suggested by Guo et al. [7] for in-tube forced convection generation process has been used to include the mixture effects.

$$\frac{h_{tp}}{h_l}=C_1\left(\frac{1}{X_{tt}}\right)^{C_2}\frac{1}{1+P_E^{C_3}R_x\mathrm{Le}^{2/3}} \tag{4}$$

In the above equation, P_E is a new dimensionless parameter that represents the combined effect of heat mass transfer at the moving gas-liquid interface. The heat transfer coefficient with total mass flow rate as liquid (h_l), for each subsection of the absorber is determined using Dittus-Boelter equation [7].

The coefficients C_1, C_2, C_3 that appear in Eq. (4) are obtained from the experimental data by using a least-squares technique. Based on present experimental study the optimal values turn out to be 5.897, 0.149, and 1.016 respectively. The predicted heat transfer coefficients are then compared with the experimental values as shown in Fig. 4. It can be seen that the correlation (5) could predict the experimental data almost within 30 percent.

$$\frac{h_{tp}}{h_l}=5.897\left(\frac{1}{X_{tt}}\right)^{0.149}\frac{1}{1+P_E^{1.016}R_x\ \mathrm{Le}^{2/3}}. \tag{5}$$

Conclusion

In-tube forced convective absorption for working pair R-22/DMA has been studied experimentally in an absorption/

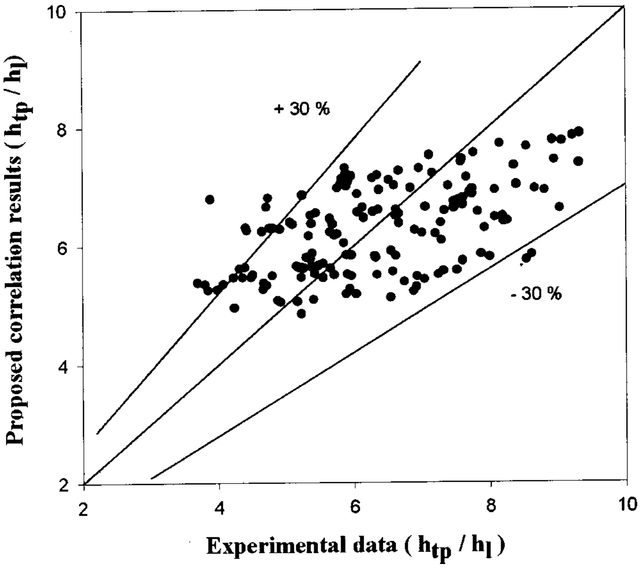

Fig. 4 Comparison of proposed correlation results with the experimental data

compression heat pump. The experimental data indicate that the coaxial tube-in-tube heat-exchanger can be used successfully in the absorption/compression heat pump and the heat transfer coefficient can be enhanced in the forced convection absorption process compared to the falling film absorption. Results demonstrate that the pressure drop in the test section increases with the mass flux, the quality and the R-22 concentration. It is also found that the heat transfer coefficient increases with the mass flux, the quality, the R-22 concentration. In the present study, an empirical correlation based on the model of in-tube generation process is also developed for the forced convective absorption process which agrees well with the experimental data in the given experimental range.

Nomenclature

A = heat transfer surface area, m^2
c_p = specific heat, kJ/(kg K)
COP = Coefficient of Performance
d = diameter, m
D = diffusion coefficient, m^2/s
h = heat transfer coefficient, W/(m^2 K)
h_{fg} = latent heat of condensation, J/kg
LMTD = log mean temperature difference
Q = heat transfer rate, W
R_x = the ratio of absorbent mass to the absorbate mass, $[(1-x)/x]$
T = temperature, K
U = overall heat transfer coefficient, W/(m^2 K)
x = average R-22 concentration
Y = average vapor quality

Subscripts

a = absorption
g = gas
i = inner
l = liquid
o = outer
s = solution
tp = two phase
w = water
wa = tube wall

Greek

α = thermal diffusivity, m^2/s
β = the slope of the curve in the phase equilibrium diagram for DMA/R-22, $-(dT/dx)$
μ = dynamic viscosity, kg/(m s)
ρ = density, kg/m^3
λ_c = thermal conductivity of the tube, W/(m K)
λ_l = thermal conductivity of the liquid solution, W/(m K)

Dimensionless Numbers

P_E = P_E number, $\beta c_p x/h_{fg}$
Pr = Prandtl number, $c_p\mu/\lambda$
Re = Reynolds number, $\rho u d/\mu$
Le = Lewis number, α/D
X_{tt} = Martinelli parameter, $(\mu_l/\mu_g)^{0.1}(\rho_g/\rho_l)^{0.5}[(1-Y)/Y]^{0.9}$

References

[1] Groll, E. A., 1997, "Current Status of Absorption/Compression Cycle Technology," ASHRAE Trans., **103**, Part 1, pp. 361–374.
[2] Torstensson, H., and Nowacki J. E., 1991, "A Sorption/Compression Heat Pump Using Exhaust Air a Heat Source," *Proceedings of Absorption Heat Pump Conference*, Tokyo, pp. 103–108.
[3] VDI-Warmeatlas1977, "*Berechnungsblatter fur den warmeubergang*," Siebte, erweiterte Auflage. VDI-Verlag (in German), ISBN 15063.3434.
[4] Guo, K. H., Chen, H. R. Mei, J. B., Shu, B. F. and Meng, Z. X., 1994, "Physical Properties Database of Absorption Working Pairs," project report, submitted to Chinese Academy of Sciences (in Chinese).
[5] Moffat, R. J., 1988, "Describing the Uncertainties in Experimental Results," Exp. Therm. Fluid Sci., **1**, pp. 3–17.
[6] Guo, K. H., Shu, B. F., and Chen, L. P., 1994, "Experimental and Theoretical Study on Falling Fil Absorption Process," Engineering Thermal Physics, **15**, pp. 160–170 (in Chinese), ISSN 0253-231X.
[7] Guo, K. H., Chen, Z., Shu, B. F., and Meng, Z. X., 1996, "Theoretical and Experimental Study on Forced Convection In-tube Generation Process," Engineering Thermal Physics, **17**, Suppl., pp. 187–190, (in Chinese), ISSN 0253-231X.

On the Accuracy of Beam-Averaged Interferometric Heat Transfer Measurements

D. Naylor
e-mail: dnaylor@ryerson.ca
Department of Mechanical, Aerospace and Industrial Engineering, Ryerson University, 350 Victoria Street, Toronto, Ontario, Canada, M5B 2K3

Laser interferometry can be used in a three-dimensional temperature field to measure the average fluid temperature and heat transfer rate, integrated over the length of an experimental model. However, such measurements are inherently approximate when the surface temperature varies in the direction of the test/object beam. In this study an analysis is performed to determine the accuracy of beam-averaged heat transfer rate measurements made in ideal gases. Two analysis methods are considered. The first method is based on extrapolation of the near-wall temperature field to obtain the surface gradient. In the second method, the temperature gradient at the surface is obtained directly from the gradient of the fringe field. The results show that the intrinsic error in the measurements depends strongly upon the form and magnitude of the temperature variation in the light beam direction. Although the error in the measured heat transfer rate is shown to be small for many commonly encountered conditions, it can be greater than ten percent in extreme cases.

[DOI: 10.1115/11482400]

Keywords: Convection, Heat Transfer, Interferometry, Measurement Techniques, Temperature

Introduction

A laser interferometer can be used in a three dimensional temperature field to measure the average fluid temperature, integrated over the length of the phase object. Such beam-averaged measurements have been made for a variety of three dimensional problems [1–5]. However, Frank [6] has shown that the average temperature measurements are inherently approximate when the temperature varies in the direction of the test/object beam. The error is caused by the nonlinear variation of refractive index with fluid temperature. In the present work, an analysis is performed to determine the accuracy of beam-averaged heat transfer measurements made in ideal gases. An improved understanding of intrinsic error associated with this technique, may promote its wider application to three-dimensional heat transfer problems.

Problem Definition

As shown in Fig. 1, consider a thermally developing flow of an ideal gas over a non-isothermal surface of length L. The surface temperature T_s varies in the direction of the light beam. The light

---

Contributed by the Heat Transfer Division for publication in the JOURNAL OF HEAT TRANSFER. Manuscript received by the Heat Transfer Division August 14, 2001; revision received March 20, 2002. Associate Editor: M. L. Hunt.

beam enters the test section at temperature T_∞ and exits at temperature T_h. This beam corresponds to the test beam of a Mach-Zehnder interferometer or the object beam of an holographic interferometer.

As mentioned previously, when there is a temperature variation in the direction of the light beam, the temperature that should be assigned to an interference fringe is not exactly the beam-averaged temperature. The effective fringe temperature can be derived as follows (Naylor and Machin [7]): Consider a ray of light in the test/object beam passing at a distance y above the surface shown in Fig. 1. Neglecting refraction effects, for an ideal gas the fringe shift order $\epsilon(y)$ is related to the refractive index field $N(x,y)$ as follows:

$$\epsilon(y)=\frac{1}{\lambda_0}\int_0^L (N(x,y)-N_{\text{ref}})dx=\frac{\text{PGL}}{R\lambda_0}\int_0^1\left(\frac{1}{T(x^*,y)}-\frac{1}{T_{\text{ref}}}\right)dx^* \tag{1}$$

where T_{ref} is the reference temperature, L is the length of the test model in the light beam direction, P is the gas pressure, R is the gas constant, G is the Gladstone-Dale constant, and λ_0 is the wavelength of the laser light source.

Now consider the hypothetical uniform temperature along the light ray, $\overline{T_f}$, that would produce same the fringe shift $\epsilon(y)$ as the non-uniform distribution, $T(x^*,y)$. With this uniform temperature, the fringe shift is

$$\epsilon(y)=\frac{\text{PGL}}{R\lambda_0}\left(\frac{1}{\overline{T_f}}-\frac{1}{T_{\text{ref}}}\right) \tag{2}$$

Equating Eqs. (1) and (2) and simplifying gives

$$\overline{T_f}=\left[\int_0^1\frac{1}{T(x^*,y)}dx^*\right]^{-1} \tag{3}$$

Equation (3) is the effective temperature that should be assigned to a fringe when the temperature varies in the test/object beam direction. But, in general, $T(x^*,y)$ is not known and cannot be determined from a single interferogram. The approach taken to overcome this difficulty in several previous studies has been to assume that $\overline{T_f}$ is equal to the arithmetic average fluid temperature, $\overline{T}$. With this approximation, it follows from Eq. (2) that

$$\overline{T}\simeq\overline{T_f}=\frac{T_{\text{ref}}}{1+\dfrac{\epsilon R\lambda_0 T_{\text{ref}}}{\text{PGL}}} \tag{4}$$

But, it is evident from Eq. (3) that the fringe temperature $\overline{T_f}$ is not the arithmetic average of $T(x^*,y)$. Recently, Naylor and Machin [7] have analyzed this source of error for a range of conditions that are used in interferometric heat transfer experiments. The study considered power function and periodic temperature variations in the beam direction, with water and ideal gases as the test fluids. The results show that the difference between $\overline{T_f}$ and $\overline{T}$ is less than two percent of the overall beam temperature difference (T_h-T_∞), even for the most adverse form of temperature distribution in the light beam direction. For many commonly encountered experimental conditions, the intrinsic error was less than one percent. From these results, one might be tempted to assume that the error in the beam-averaged heat transfer rate calculated from the approximate temperature measurements will also be small. It will be shown in the next section that this assumption is not always correct.

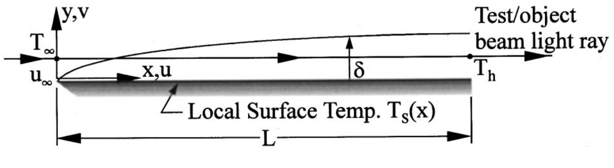

Fig. 1 Thermally developing flow over a surface with a temperature variation in the test/object beam direction

Analysis of Beam-Averaged Heat Transfer Rates

The heat transfer rate, averaged in the direction of the beam $(\overline{q})$ can be expressed in terms of gradient of the average fluid temperature $(\overline{T})$ as

$$\overline{q}=-k_s\left.\frac{\partial\overline{T}}{\partial y}\right|_{y=0} \quad \text{where} \quad \overline{T}=\int_0^1 T(x^*,y)dx^* \tag{5}$$

It is clear from Eq. (3) that, in general, the gradient of the effective fringe temperature $(\partial\overline{T_f}/\partial y|_{y=0})$ will not be exactly equal to the average fluid temperature gradient $(\partial\overline{T}/\partial y|_{y=0})$. To assess this source of error, two analysis methods for determining the heat flux from an interferogram have been considered. The first is the traditional approach of calculating the near-wall fluid temperature profile normal to the surface and using extrapolation to get the surface temperature gradient. The second approach is based on measuring the surface gradient of the fringe shift, $\partial\epsilon/\partial y|_{y=0}$.

Temperature Profile Extrapolation Method. To gain an understanding of the accuracy of the beam-averaged heat flux measurements, two dimensional laminar forced convection from a non-isothermal plate has been simulated. Fringe fields have been calculated using the temperature field from a similarity solution and the simulated measurements have been compared to the exact average heat transfer rates. Details of the similarity solution are given by Levy [8]. It will be outlined only briefly here.

The surface temperature of the plate was assumed to have a power function variation:

$$T_s=(T_L-T_\infty)(x^*)^n+T_\infty \tag{6}$$

where T_L is the surface temperature of the plate at $x^*=x/L=1$. The governing equations for constant property, incompressible, boundary layer flow over a zero incidence flat plate can be transformed into the following ordinary differential equations:

$$2f'''+ff''=0 \tag{7}$$

$$\theta''+n\text{Pr}f'(1-\theta)+\frac{\text{Pr}}{2}\theta' f=0 \tag{8}$$

where Pr is the Prandtl number and the following dimensionless parameters have been introduced:

$$\eta=\frac{y}{x}\sqrt{\text{Re}} \qquad f'=\frac{\partial f}{\partial\eta}=\frac{u}{u_\infty} \qquad \theta=\frac{T_s-T}{T_s-T_\infty} \tag{9}$$

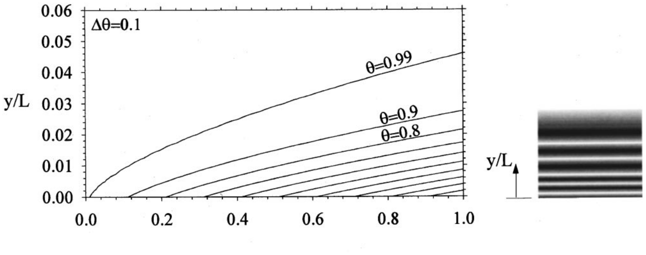

(*a*) (*b*)

Fig. 2 (*a*) Temperature contours of a forced convection boundary layer on a plate with a linear surface temperature variation ($n=1$) for $\text{Re}_L=10^4$, Pr=0.7, (*b*) Simulated beam-averaged infinite fringe interferogram ($T_L-T_\infty=20$ K, $P=100$ kPa, $G=2.256\times10^{-4}$ m³/kg, $\lambda_0=632.8$ nm, $L=0.4$ m, $R=287$ J/kgK, $T_\infty=300$ K).

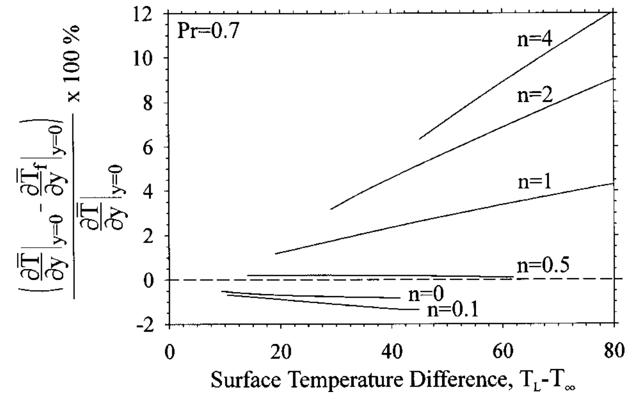

Fig. 3 Effect of surface temperature difference on the percentage error in the surface temperature gradient, calculated using the actual mean temperatures and the effective fringe temperatures ($PGL/R\lambda_0 = 4.97\times10^4$ K, $T_\infty = 300$ K)

In Eq. (9), u_∞ is the free stream velocity and Re is the Reynolds number based on the distance from the leading edge (x). The boundary conditions for Eqs. (7) and (8) are:

$$\begin{aligned} &\eta=0 \quad f=f'=0 \quad \theta=0 \\ &\eta\to\infty \quad f'\to 1 \quad \theta\to 1 \end{aligned} \tag{10}$$

Equations (7) and (8) have been solved subject to the above boundary conditions using the shooting method for temperature exponents in the range $0\leqslant n\leqslant 4$.

To illustrate the procedure used to calculate the fringe temperature gradient ($\partial \overline{T}_f/\partial y|_{y=0}$), Fig. 2($a$) shows the isotherms in the thermal boundary layer for a linear surface temperature distribution ($n=1.0$), obtained from the similarity solution. The beam-averaged fringe field was calculated from the temperature field using Eq. (1). This fringe field is shown as a simulated interferogram in Fig. 2(b). This interference pattern was calculated for the following set of conditions, which are typical for the application of interferometry: $G=2.256\times10^{-4}$ m^3/kg (air), $\lambda_o=632.8$ nm (He-Ne laser), $R=287$ J/kgK (air), $P=100$ kPa, $L=0.4$ m, $T_L-T_\infty=20$ K. These parameters correspond to $PGL/\lambda_o R=4.97\times10^4$ K.

Once the simulated fringe field was obtained, the surface temperature gradient was calculated using the two fringes closest to the plate surface. Effective fringe temperatures were calculated numerically at the y-locations corresponding to fringe shift orders of $\epsilon=1$ and $\epsilon=2$, using Eq. (3). In this calculation, the fringe shift order was taken to be zero at the surface. The surface gradient was then calculated using the effective fringe temperature at the first fringe $\overline{T}_f|_{\epsilon=1}$ and effective fringe temperature at the second fringe $\overline{T}_f|_{\epsilon=2}$, as follows

$$\frac{\partial \overline{T}_f}{\partial y}_{y=0} = (\overline{T}_f|_{\epsilon=2} - \overline{T}_f|_{\epsilon=1})/(y_2-y_1) \tag{11}$$

where y_1 and y_2 are the locations of the first and second fringes. This approximate gradient was compared to the actual gradient calculated in the same manner, using the actual average temperatures at the same y locations. In practice, higher order extrapolation schemes are sometimes used to determine the surface gradient from interferograms. But, since the same method of extrapolation has been applied in both cases, the difference between these gradients will give a meaningful indicator of the intrinsic error associated with the interferometric measurements.

Figure 3 shows the percentage difference in the surface gradient calculated using the actual mean temperatures and the effective fringe temperatures. Data are presented for various values of the surface temperature profile exponent, n. Note that the upper and lower limits of each curve correspond to a total fringe shift $5\leqslant\epsilon_{\max}\leqslant 20$. This is a typical range of total fringe shift for interferometric heat transfer measurements. It should be mentioned that smaller phase differences can be measured using modern optical methods [9,10]. But, when interference patterns are recorded on film, several fringes are usually needed to characterize the near-wall temperature profile.

It can be seen in Fig. 3 that the error in the gradient is less than two percent for $n=0$, 0.1, and 0.5, over the full range of surface temperature differences. In fact for $n=0.5$, which corresponds to a constant heat flux surface, the maximum error is only about 0.2 percent. But, for larger values of the exponent ($n=1,2,4$), the error increases rapidly with the overall surface temperature difference (T_L-T_∞) and can exceed ten percent in the most extreme conditions. So, for these exponents, beam-averaged interferometric measurements could significantly under predict the average heat flux. These results were found to be independent of Reynolds number and weakly dependent upon the parameter $PGL/\lambda_o R$, which affects the optical sensitivity.

In Fig. 3, results have been calculated up to a temperature difference of $T_L-T_\infty=80$ K. At this temperature difference, the nonlinear variation of refractive index with temperature can cause substantial measurement error. Whenever possible, the experimental model length (L) should be extended to decrease the temperature difference needed to produce the desired fringe shift. However, in many situations the model design requires a compromise between optical sensitivity and achieving the desired experimental conditions (Reynolds number, Rayleigh number, aspect ratio, etc.). As a result, it may be necessary to operate at higher temperature differences than are optimal based on strictly optical considerations.

It is interesting to note in Fig. 3 that for an isothermal surface ($n=0$) the inherent error in the beam-averaged gradient is not zero. The error is not zero because gradient was calculated using effective fringe temperatures ($\overline{T}_f$) that were calculated above the surface (at the locations of $\epsilon=1$ and $\epsilon=2$). At these y-locations there is a slight temperature variation along the light beam. So, $\overline{T}_f$ will not be exactly the average fluid temperature ($\overline{T}$). For an isothermal surface, $\overline{T}_f=\overline{T}$ in the limit as $y\to 0$. For this reason, the Fringe Gradient Method should be used on isothermal surfaces. This is discussed in the next section.

Fringe Gradient Method. The average heat flux can be determined using an alternate method, which makes direct use of the fringe gradient at the surface. This is done by differentiating Eq. (1) and evaluating the result at the surface, as follows

$$\left.\frac{\partial\epsilon}{\partial y}\right|_{y-0} = \frac{-PGL}{R\lambda_0}\int_0^1 \frac{1}{T_s^2}\left.\frac{\partial T}{\partial y}\right|_{y=0} dx^* \tag{12}$$

For an isothermal surface, the above equation can be rearranged to give the beam-averaged surface temperature gradient:

$$\left.\frac{\partial \overline{T}}{\partial y}\right|_{y=0} = \frac{-R\lambda_0 T_s^2}{PGL}\left.\frac{\partial\epsilon}{\partial y}\right|_{y=0} \tag{13}$$

Using the above equation, the beam-averaged heat flux on an isothermal surface can be calculated with no intrinsic beam-averaging error. This observation appears to have been first made by Papple and Tarasuk [4].

Equation (12) can also be used to get the exact beam-averaged heat transfer rate on an isoflux surface. For an isoflux surface Eq. (12) can be rearranged to give:

$$\left.\frac{\partial \overline{T}}{\partial y}\right|_{y=0} = \frac{-R\lambda_0}{PGL}\left.\frac{\partial\epsilon}{\partial y}\right|_{y=0}\left[\int_0^1 \frac{1}{T_s^2}dx^*\right]^{-1} \tag{14}$$

In applying Eq. (14), the integral of the surface temperature variation could be obtained from thermocouple measurements.

If the surface is neither isothermal nor isoflux, the average surface gradient ($\int \partial T/\partial y|_{y=0}dx^*$) cannot be isolated in Eq. (12) and the beam-averaged heat flux cannot be evaluated exactly. The remainder of this work will consider the use of the following approximation of Eq. (12):

$$\left[\left.\frac{\partial \overline{T}}{\partial y}\right|_{y=0}\right]_{\text{approx}} = \frac{-R\lambda_0 \overline{T}_s^2}{\text{PGL}}\left.\frac{\partial \epsilon}{\partial y}\right|_{y=0} \qquad \text{where} \qquad \overline{T}_s = \int_0^1 T_s(x^*)dx^* \tag{15}$$

In this case, $\overline{T}_s$ could be obtained from thermocouple measurements or from the optically measured beam-averaged surface temperature. The accuracy of this approximate method to obtain average heat transfer rates will now be considered.

Substituting Eq. (15) into Eq. (12), it can be seen that the approximate mean surface temperature gradient is related to the exact surface temperature gradient as follows:

$$\left[\left.\frac{\partial \overline{T}}{\partial y}\right|_{y=0}\right]_{\text{approx}} = \left(\int_0^1 T_s\,dx^*\right)^2 \int_0^1 \frac{1}{T_s^2}\left.\frac{\partial T}{\partial y}\right|_{y=0} dx^* \tag{16}$$

For forced convection over a flat plate with a power function temperature variation (Eq. (6)), the local surface temperature gradient is (Levy [8]):

$$\left.\frac{\partial T}{\partial y}\right|_{y=0} = (T_\infty - T_s)\left.\frac{\partial \theta}{\partial \eta}\right|_{\eta=0}\frac{\partial \eta}{\partial y} = C_1(x^*)^{n-1/2} \tag{17}$$

where C_1 is a constant for a fixed set of experimental conditions. The error in the beam-averaged surface temperature gradient can be calculated as:

$$\frac{\left[\left.\frac{\partial \overline{T}}{\partial y}\right|_{y=0}\right]_{\text{approx}} - \left[\left.\frac{\partial \overline{T}}{\partial y}\right|_{y=0}\right]_{\text{exact}}}{\left[\left.\frac{\partial \overline{T}}{\partial y}\right|_{y=0}\right]_{\text{exact}}} = \frac{\left(\int_0^1 T_s\,dx^*\right)^2 \int_0^1 T_s^{-2}\left.\frac{\partial T}{\partial y}\right|_{y=0} dx^* - \int_0^1 \left.\frac{\partial T}{\partial y}\right|_{y=0} dx^*}{\int_0^1 \left.\frac{\partial T}{\partial y}\right|_{y=0} dx^*} \tag{18}$$

where the local gradient at the surface ($\partial T/\partial y|_{y=0}$) and the surface temperature (T_s) vary as given in Eq. (17) and Eq. (6).

Equation (18) has been evaluated analytically using a commercial symbolic computation program for $n=0$ to 4. Calculations have been done for a surface temperature difference range of 0 $K \leq T_L - T_\infty \leq 80$ K. The results are given in Fig. 4(*a*). It can be seen that the results are very similar to those in Fig. 3, which were obtained using linear temperature profile extrapolation. As previously discussed, for this method the error is always zero for an isothermal surface ($n=0$), when the surface temperature gradient is calculated from the fringe gradient. As in the previous analysis, for the constant heat flux case ($n=0.5$) the error is very small over the complete range of surface temperature difference. But, comparing Fig. 4(*a*) to Fig. 3, it can be seen that the Fringe Gradient Method gives slightly higher level of error than the Temperature Profile Extrapolation Method for $n=4.0$. But, it would be unusual to encounter such an extreme surface temperature variation in a practical convection problem. For most applications, both methods will have a similar level of error. Note that the results in Fig. 4(*a*) are for forced convection, but are independent of Prandtl number, Reynolds number and the parameter that affects the optical sensitivity ($\text{PGL}/\lambda_o R$).

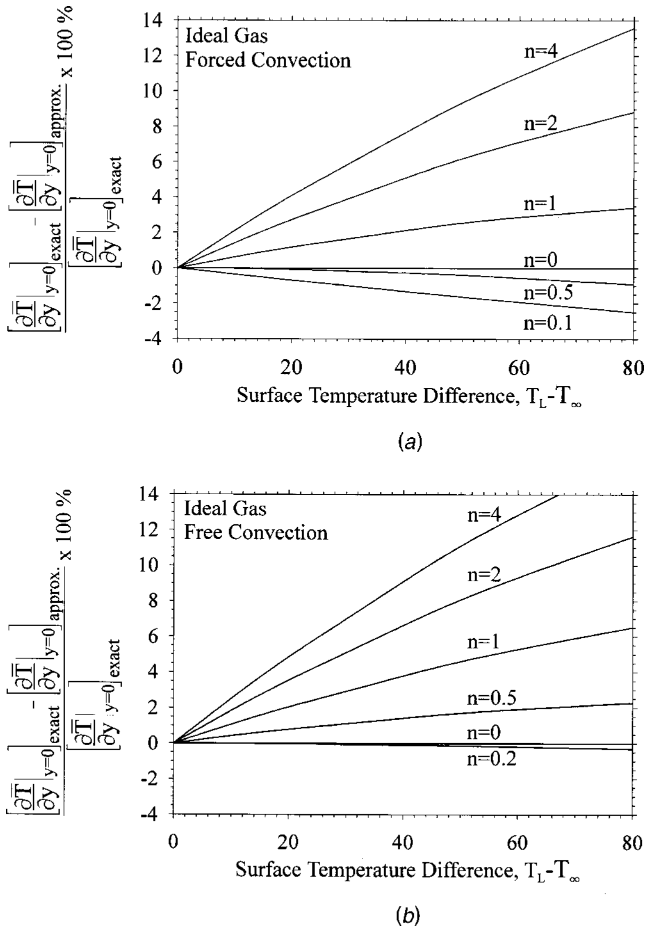

(*a*)

(*b*)

Fig. 4 Effect of the surface temperature difference on the percentage error in the surface temperature gradient, calculated using the fringe gradient for (*a*) forced convection and (*b*) free convection

This approximate "fringe gradient method" has also been applied for free convection from a vertical nonisothermal plate. In this case, if the surface temperature variation is a power function given by Eq. (6), the surface gradient varies with *x* as follows:

$$\left.\frac{\partial T}{\partial y}\right|_{y=0} = C_2(x^*)^{(5n-1)/4} \tag{19}$$

where C_2 is a constant for a fixed set of experimental conditions. The derivation of Eq. (19) can be found in the similarity solution of the boundary layer equations by Sparrow and Gregg [11].

Equation (18) has been evaluated analytically for the local surface temperature gradient and surface temperature variations given in Eq. (19) and Eq. (6). The results, which apply to free convection, are shown in Fig. 4(*b*). It can be seen that the results for free convection have a similar form the those for forced convection. Again, for an isoflux boundary condition ($n=0.2$), the error in the gradient is small over the full range of surface temperature difference. For larger values *n* ($n=0.5,1,2,4$), the error is greater than the forced convection case.

Concluding Remarks

The intrinsic error associated with beam-averaged measurements is often inadequately addressed or simply ignored in many previous interferometric studies. In the current work, an analysis has been performed to assess this measurement error, using solutions for two classical convective heat transfer problems. The results show that the measurement error in the beam-averaged surface temperature gradient will not always be small. For both methods considered, the error in beam-averaged temperature gradient was less than one percent, when measurements were made on an isothermal or isoflux surface. However, the error in the beam-averaged heat flux was found to be greater than ten percent, under some extreme conditions.

References

[1] Yousef, W. W., and Tarasuk, J. D., 1981, ''An Interferometric Study of Combined Free and Forced Convection in a Horizontal Isothermal Tube,'' ASME J. Heat Transfer, **103**, pp. 249–256.

[2] Kato, S., and Maruyama, N., 1989, ''Holographic Interferometric Measurements of the Three-Dimensional Temperature Field with Thermally Developing Flow in the Measuring-beam Direction,'' Exp. Therm. Fluid Sci., **2**, pp. 333–340.

[3] Li, J., and Tarasuk, J. D., 1992, ''Local Free Convection Around Inclined Cylinders in Air: an Interferometric Study, Experimental Thermal and Fluid Science,'' Exp. Therm. Fluid Sci., **5**, pp. 235–242.

[4] Papple, M. L. C., and Tarasuk, J. D., 1987, ''An Interferometric Study of Developing Natural Convective Flow in Inclined Isothermal Ducts,'' AIAA Paper 87-1589.

[5] Fehle, R., Klas, J., and Mayinger, F., 1995, ''Investigation of Local Heat Transfer in Compact Heat Exchangers by Holographic Interferometry,'' Exp. Therm. Fluid Sci., **10**, pp. 181–191.

[6] Frank, M. E., 1970, ''Interferometer Measurements in Free Convection on a Vertical Plate with Temperature Variation in the Light-beam Direction,'' *Fourth International Heat Transfer Conference*, Vol. 4, pp. 1–12.

[7] Naylor, D., and Machin, A. D., 2001, ''The Accuracy of Beam-Averaged Interferometric Temperature Measurements in a Three-Dimensional Field,'' Exp. Heat Transfer, **14**, pp. 217–228.

[8] Levy, S., 1952, ''Heat Transfer to Constant Property Laminar Boundary-Layer Flows with Power-Function Free-Stream and Wall-Temperature Variation,'' J. Aeronaut. Sci., **19**, pp. 341–348.

[9] Slepicka, J. S., and Cha, S. S., 1995, ''Stabilized Nonlinear Regression for Interferogram Analysis,'' Appl. Opt., **34**, pp. 5039–5044.

[10] Breuckmann, B., and Thieme, W., 1985, ''Computer-Aided Analysis of Holographic Interferograms Using the Phase-Shift Method,'' Appl. Opt., **24**, pp. 2145–2149.

[11] Sparrow, E. M., and Gregg, J. L., 1958, ''Similar Solutions for Free Convection From a Nonisothermal Vertical Plate,'' Trans. ASME, **80**, pp. 379–386.

Bulk Temperature Development in Transient Heat Transfer Measurements Using Heater Foils

Jens von Wolfersdorf
University of Stuttgart, Institute for Aerospace
Thermodynamics, Pfaffenwaldring 31, 70569 Stuttgart,
Germany
e-mail: Jens.Vonwolfersdorf@itlr.uni-stuttgart.de

The time and space development of the fluid bulk temperature in a transient heat transfer experiment for internal channel cooling investigations using heater foils is addressed. An analytical solution for uniform heat transfer coefficients is derived which shows the effect of wall heating on the bulk temperature during a transient test run. A simplified model is proposed for characterizing the bulk temperature development by introducing an upstream heat transfer parameter. With this, analytical solutions for the local wall temperature history can be derived. The presented solution can be used for data reduction of transient tests of this kind. [DOI: 10.1115/1.1482403]

Keywords: Heat Transfer, Measurement Techniques

1 Introduction

Transient heat transfer measurement techniques using Thermochromic Liquid Crystals (TLC) are nowadays one of the most popular techniques to obtain high resolution, full field heat transfer coefficient distributions for many applications. Especially for the investigation of internal cooling problems, for example in gas turbine blades, this technique has become a powerful experimental tool [1]. Thereby, the question of the correct choice and determination of the fluid reference temperature to be used for the calculation of the heat transfer coefficient has received increasing attention particularly for passages with large length-to-diameter ratios and significant heat exchange upstream of the position of interest. Some of the models and approaches developed are given in [2–4] and are reviewed by Ireland and Jones [1]. The above cited approaches are related to the transient techniques using hot (heated) fluid flow and cold model starting temperatures to establish a heat flux between the flow and the model surface. Another kind of transient heat transfer measurements uses electrically heated foils or coatings, where it can be assumed that an uniform heat flux is generated in the thin isothermal foil [5–8]. Consider a model of low conductivity which can be considered as semi-infinite during the test run and is covered by a heater foil. This model is initially at an uniform temperature equal to the flow temperature T_0 when the power to the heater foil is switched on and the model wall temperature rises. The response in wall temperature to this heating input q can be calculated by considering the wall of the model as a semi-infinite body:

$$h\,\frac{T_w-T_0}{q}=1-\exp\left(\frac{h^2t}{k_s}\right)\mathrm{erfc}\left(\frac{h\sqrt{t}}{\sqrt{k_s}}\right) \qquad (1)$$

In Eq. (1) h is the local heat transfer coefficient and $k_s=\lambda_s\rho_s c_{p_s}$. The local heat flux q, which is dissipated in the heater foil is divided into the convective heat flux at the wall q_w and the conduction flux q_s into the model (Fig. 1).

If this technique is applied to a long internal coolant channel, the heat input into the fluid will increase the fluid temperature and therefore the reference bulk temperature is a function of streamwise position and time. The use of Eq. (1) where the fluid temperature is taken as constant (equal T_0) with space and time will lead in this case to a wrong result for the heat transfer coefficient. It is the aim of the present paper to describe a simplified model for the fluid bulk temperature development during this kind of transient experiment similar to the one described in [4] for the case of heated flow. The first step is the derivation of an analytical solution in case of uniform heat transfer coefficient. Then the simplified model will be described leading to a simple expression for the bulk temperature space and time development. Using this expression in the boundary condition for the semi-infinite wall-conduction-convection problem, solutions for the local wall temperature history are obtained, which should be used in transient test analysis. The comparison between the analytical solution, numerical solutions and the simplified model is used to show the applicability of the approximations made in the simplified model's development.

2 Analytical Solution

The analytical solution for the conjugate convection problem will be determined for the case of an uniform heat transfer coefficient h. The fluid enters the channel (perimeter U, which is assumed to be constant) with a mass flow $\dot{m}$. The energy equation for the fluid can be written as:

$$\dot{m}c_p\frac{\partial T_f}{\partial x}=hU(T_w(x,t)-T_f(x,t)) \qquad (2)$$

where axial heat conduction effects have been neglected with the initial condition:

$$T_f(x,0)=T_0 \qquad (3)$$

and the boundary condition at the channel entrance:

$$T_f(0,t)=T_0 \qquad (4)$$

Contributed by the Heat Transfer Division for publication in the JOURNAL OF HEAT TRANSFER. Manuscript received by the Heat Transfer Division April 25, 2001; revision received March 22, 2002. Associate Editor: H. O. S. Lee.

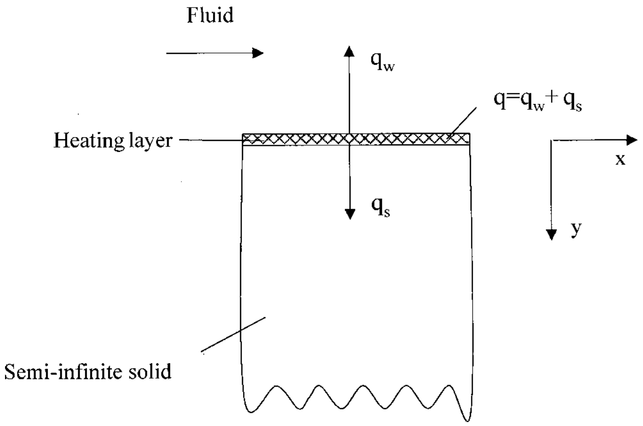

Fig. 1 Energy balance at the model surface

The solid wall will be considered as a semi-infinite body. Neglecting again axial heat conduction effects leads to:

$$\frac{\partial T_s}{\partial t}=a\frac{\partial^2 T_s}{\partial y^2} \quad \text{for } 0\leqslant y<\infty \tag{5}$$

with the initial condition:

$$T_s(x,y,0)=T_0 \tag{6}$$

and the boundary condition at the fluid-solid-interface:

$$-\lambda_s\frac{\partial T_s}{\partial y}\bigg|_{y=0}=q-h(T_s(y=0)-T_f)=h\left(\frac{q}{h}+T_f-T_w\right) \tag{7}$$

A small times solution to this system of equations can be derived using Laplace Transforms and power series expansions as described in [4] for the fluid and the solid wall temperatures. Since the main interest is the fluid temperature development, only this solution will be given here:

$$\begin{aligned}\Theta_f=\frac{T_f-T_0}{T_{\text{ref}}-T_0}&=\frac{2}{\sqrt{\pi}}\text{Bi}\,\sqrt{\text{Fo}}-\exp\left(-4St\frac{x}{d_h}\right)\text{Bi}\,\sqrt{\text{Fo}}\\&\times\left\{\frac{2}{\sqrt{\pi}}+\sum_{n=1}^{\infty}\frac{1}{n!}\left(4\text{St}\frac{x}{d_h}\right)^n(\text{Bi}\,\sqrt{\text{Fo}})^n\frac{1}{\Gamma\left(\frac{3}{2}+\frac{n}{2}\right)}\right.\\&+\sum_{j=2}^{\infty}\left\{\sum_{n=1}^{j-1}(-1)^{j-n}\frac{1}{(n-1)!n!(j-n)!}\left(4\text{St}\frac{x}{d_h}\right)^n\right\}\\&\left.\times(j-1)!\frac{1}{\Gamma\left(\frac{3}{2}+\frac{j}{2}\right)}(\text{Bi}\,\sqrt{\text{Fo}})^j\right\}\end{aligned} \tag{8}$$

where

$$\frac{q}{h}=T_{\text{ref}}-T_0, \quad \beta=\frac{h}{\lambda_s}, \quad b=\frac{hU}{\dot{m}c_p},$$

$$\text{Bi}^2\text{Fo}=\beta^2 at \quad \text{and} \quad 4\text{St}\frac{x}{d_h}=bx.$$

As mentioned, this equation is valid for sufficiently small $\beta^2 at$ as usually found in the transient experiments considered.

Numerical investigations of this equation have shown, that for $\text{Bi}^2\text{Fo}>6$ the solution starts to deviate, probably due to numerical accuracy in calculating the infinite sums (very large and small terms cancel out each other) as well as due to the validity of the small times approximation. In these investigations each summation was performed until the individual contributors were less than 1.*e*-10 leading to about 30 terms in the sums. Nevertheless for the range of parameters usually found in the transient experiments considered $(\text{Bi}^2\text{Fo}<6)$, the solution is suitable for comparison with the following simplified model.

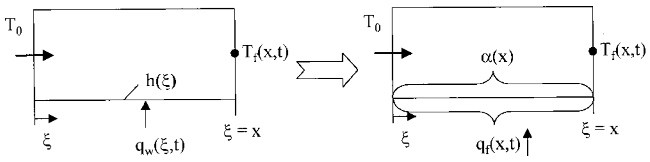

Fig. 2 Description of simplified model

3 Simplified Model

For the determination of the time variation of the fluid temperature at a given position x a simplified one-dimensional model similar to the one given in [4] is proposed. The fluid enters the channel at $x=0$ with a constant temperature T_0 and is heated up to the position x by the convective heat flux at the wall q_w. The total amount of heat transferred up to the position x is for a constant perimeter U:

$$Q(x,t)=U\int_0^x q_w(\xi,t)d\xi=U\int_0^x h(\xi)(T_w(\xi,t)-T_f(\xi,t))d\xi \tag{9}$$

This heat flux is described by a time dependent, space-averaged heat flux q_f and a single averaged heat transfer parameter $\alpha(x)$, both of which are characteristic for the measurement location x (see Fig. 2).

$$q_f(x,t)=\frac{1}{x}\int_0^x q_w(\xi,t)d\xi=\frac{\alpha(x)}{x}\int_0^x(T_w(\xi,t)-T_f(\xi,t))d\xi \tag{10}$$

where

$$\alpha(x)=\frac{\int_0^x h(\xi)(T_w(\xi,t)-T_f(\xi,t))d\xi}{\int_0^x(T_w(\xi,t)-T_f(\xi,t))d\xi}. \tag{11}$$

This definition implies that the fluid entering the channel experiences at any time t a constant heat flux boundary condition and a constant lumped heat transfer parameter up to the position of interest. Therefore one obtains from a simplified energy balance equation for the time history of the fluid temperature at the position x the simple expression.

$$T_f(x,t)=T_0+q_f(x,t)\frac{U}{\dot{m}c_p}x \tag{12}$$

From Eq. (1) one knows the wall temperature response to the heating based on the inlet temperature T_0. Using a heat transfer coefficient h_0 based on the inlet temperature and not on the local fluid temperature one obtains:

$$h_0\frac{T_w-T_0}{q}=1-\exp\left(\frac{h_0^2t}{k_s}\right)\text{erfc}\left(\frac{h_0\sqrt{t}}{\sqrt{k_s}}\right) \tag{13}$$

The left hand side of Eq. (13) is the ratio of the local convective heat flux into the fluid to the total heat dissipated in the heating layer per area. Therefore one can approximate the time history of the heat flux up to the position x in Eq. (12) by using a space-averaged heat transfer coefficient based on the inlet temperature.

$$\frac{q_f}{q}=1-\exp\left(\frac{\overline{h_0^2}t}{k_s}\right)\text{erfc}\left(\frac{\overline{h_0}\sqrt{t}}{\sqrt{k_s}}\right) \tag{14}$$

This average heat transfer coefficient is defined as:

$$\overline{h}_0=\frac{1}{x}\int_0^x h_0(\xi)d\xi \tag{15}$$

For the case of a constant heat flux and a constant $\alpha(x)$ up to the position x as implied by Eqs. (10) and (12), the relationship which exists between $h_0(\xi)$ and $\alpha(x)$ is given by:

$$h_0=\frac{\alpha}{1+\frac{\alpha U}{\dot{m}c_p}\xi} \tag{16}$$

Integrating Eq. (16) according to Eq. (15) one obtains:

$$\frac{\overline{h}_0}{\alpha}=\frac{\ln\left(1+\frac{\alpha U}{\dot{m}c_p}x\right)}{\frac{\alpha U}{\dot{m}c_p}x}=A \tag{17}$$

using the parameter A for brevity.

With this the simplified model of the fluid bulk temperature development is given from Eqs. (12), (14), and (17) by:

$$T_f-T_0=\frac{qU}{\dot{m}c_p}x\left\{1-\exp\left(\frac{\alpha^2 t}{k_s}A^2\right)\operatorname{erfc}\left(\frac{\alpha\sqrt{t}}{\sqrt{k_s}}A\right)\right\} \tag{18}$$

Now one can solve for the wall temperature history using Eq. (18) as the fluid temperature boundary condition. Solving Eqs. (5), (6), and (7) one obtains for the general case where $\alpha A\neq h$:

$$\begin{aligned}T_w-T_0=&\left(\frac{qU}{\dot{m}c_p}x+\frac{q}{h}\right)\left[1-\exp\left(\frac{h^2t}{k_s}\right)\operatorname{erfc}\left(\frac{h\sqrt{t}}{\sqrt{k_s}}\right)\right]\\&+\frac{qU}{\dot{m}c_p}x\left(\frac{1}{A\frac{\alpha}{h}-1}\right)\left\{\exp\left(\frac{\alpha^2t}{k_s}A^2\right)\operatorname{erfc}\left(\frac{\alpha\sqrt{t}}{\sqrt{k_s}}A\right)\right.\\&\left.-\exp\left(\frac{h^2t}{k_s}\right)\operatorname{erfc}\left(\frac{h\sqrt{t}}{\sqrt{k_s}}\right)\right\}\end{aligned} \tag{19}$$

For the special case $\alpha A=h$ the solution is given by:

$$\begin{aligned}T_w-T_0=&\left(\frac{qU}{\dot{m}c_p}x+\frac{q}{h}\right)\left[1-\exp\left(\frac{h^2t}{k_s}\right)\operatorname{erfc}\left(\frac{h\sqrt{t}}{\sqrt{k_s}}\right)\right]+\frac{qU}{\dot{m}c_p}x\\&\times\left\{\frac{2}{\sqrt{\pi}}\frac{h\sqrt{t}}{\sqrt{k_s}}-\frac{2h^2t}{k_s}\exp\left(\frac{h^2t}{k_s}\right)\operatorname{erfc}\left(\frac{h\sqrt{t}}{\sqrt{k_s}}\right)\right\}\end{aligned} \tag{20}$$

These equations should be used for data reduction purposes in the transient tests considered for the determination of the heat transfer coefficients. Therefore more than one local wall temperature indication using, e.g., liquid crystals is needed to determine the two unknowns h, the local heat transfer coefficients and α, the upstream heat transfer parameter.

4 Results and Discussion

The simplified model of the fluid bulk temperature development (Eq. (18)) will be compared to the analytical solution (Eq. (8)) for the case of uniform heat transfer coefficient and with numerical solutions using a one-dimensional method. In this method the one-dimensional thermal energy equation for an incompressible, constant property fluid as a function of space and time with convective heat transfer to a semi-infinite solid was numerically integrated taking into account the heat generating layer on the solid-fluid interface. The heat flux split according to Fig. 1 was determined using the prescribed local heat transfer coefficients and the calculated wall temperature from the analytical solution of transient heat conduction in a semi-infinite wall with the heat flux boundary condition Eq. (7) applying Duhamel's Theorem for the time dependency. From this, the heat input into the fluid was determined for a given mass flow rate assuming a constant area channel with constant perimeter and therefore hydraulic diameter.

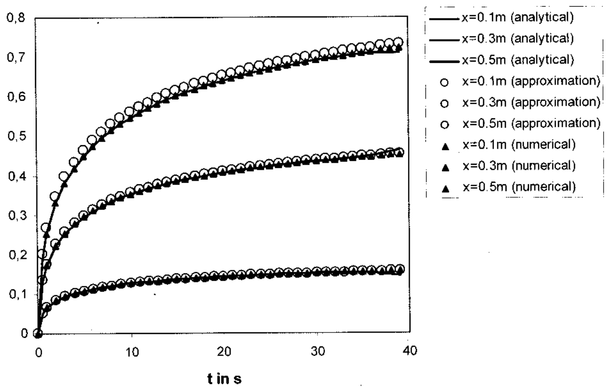

Fig. 3 Comparison of the simplified model with analytical and numerical solutions (uniform heat transfer coefficient distribution)

For this comparison the following data are used. A 500 mm long square cooling channel with a hydraulic diameter of 20 mm is considered. A mass flow rate of 0.01 kg/s with an inlet temperature of 293 K enters the channel. The wall material is assumed to be Perspex ($\sqrt{k_s}=569\ \mathrm{W}\sqrt{\mathrm{s}}/\mathrm{m}^2\mathrm{K}$) with an initial temperature equal to the fluid inlet temperature. For the heat transfer coefficient a value of $250\ \mathrm{W/m^2K}$ is used for both, the local heat transfer coefficient and the upstream heat transfer parameter. The heater foil is taken to dissipate an area-specific heat flux of $10\,000\ \mathrm{W/m^2}$ leading to $q/h=40\,\mathrm{K}$, which is typical for the transient experiments considered. Figure 3 shows the time development of the fluid bulk temperature at the stream-wise positions $x=0.1\,\mathrm{m}$, $x=0.3\,\mathrm{m}$, and $x=0.5\,\mathrm{m}$. The agreement between the analytical and the approximative solution is generally good with some small differences at the last station. The maximum difference between the solutions is within 5 percent.

As a second comparison a heat transfer coefficient distribution is randomly generated with values between 100 $\mathrm{W/m^2}K$ and 400 $\mathrm{W/m^2K}$. The simplified model is compared to the numerical solution in Fig. 4, where for the heat transfer parameter α at the respective positions the average heat transfer coefficients up to $x=0.1\,\mathrm{m}$, $x=0.3\,\mathrm{m}$, and $x=0.5\,\mathrm{m}$ from the random distribution have been used. Also in this case the agreement is very good, which shows the applicability of the assumptions made in the simplified model's development. The model (Eq. (18)) is therefore well suited for pre-test estimation of the importance of the fluid's

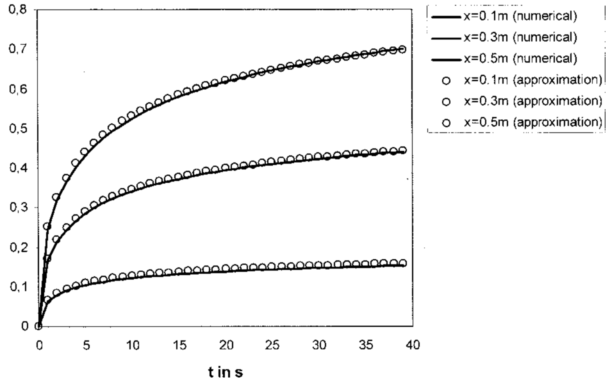

Fig. 4 Comparison of the simplified model with numerical solutions (random heat transfer coefficient distribution)

upstream heating as well as for the final data reduction using Eqs. (19) and (20).

5 Conclusions

A simplified model describing the time and space development of the fluid bulk temperature in a transient test with heater foils at the wall is derived for internal cooling channel applications. This model, which compares well to an analytical solution and numerical solutions is suited to estimate the heating effect on the measurement results. Using the model in a transient test, two unknowns (the local heat transfer coefficient and an upstream heat transfer parameter) have to be determined from wall temperature indications.

Nomenclature

Symbols

a = thermal diffusivity
A = parameter, Eq. (17)
Bi = Biot number
c_p = specific heat at constant pressure
d_h = hydraulic diameter
Fo = Fourier number
h = heat transfer coefficient
k = material parameter
$\dot{m}$ = mass flow rate
q = heat flux per area
Q = heat flux
St = Stanton number
t = time
T = temperature
U = perimeter
x = stream-wise position
y = vertical coordinate
α = heat transfer parameter
λ = thermal conductivity
ρ = density
ξ = axial coordinate
Θ = dimensionless temperature

Subscripts

0 = entrance or inlet
f = fluid
s = solid
w = wall

References

[1] Ireland, P. T., and Jones, T. V., 2000, ‘‘Liquid Crystal Measurements of Heat Transfer and Surface Shear Stress,’’ Meas. Sci. Technol., **11**, pp. 969–986.

[2] Chyu, M. K., Ding, H., Downs, J. P., Van Sutendael, A., and Soechting, F. O., 1998, ‘‘Determination of Local Heat Transfer Coefficient Based on Bulk Mean Temperature Using a Transient Liquid Crystals Technique,’’ Exp. Therm. Fluid Sci., **18**, pp. 142–149.

[3] Saabas, J., Arora, S. C., and Abdel Messeh, W., 1987, ‘‘Application of the Transient Test Technique to Measure Local Heat Transfer Coefficients Associated With Augmented Airfoil Cooling Passages,’’ ASME Paper 87-GT-212.

[4] von Wolfersdorf, J., Hoecker, R., and Hirsch, C., 1998, ‘‘A Data Reduction Procedure for Transient Heat Transfer Measurements in Long Internal Cooling Channels,’’ ASME J. Heat Transfer, **120**, pp. 314–321.

[5] von Wolfersdorf, J., Hoecker, R., and Sattelmayer, T., 1993, ‘‘A Hybrid Transient Step-Heating Heat Transfer Measurement Technique Using Heater Foils and Liquid-Crystal Thermography,’’ ASME J. Heat Transfer, **115**, pp. 319–324.

[6] Turnbull, W. N., and Oosthuizen, P. H., 1999, ‘‘A New Experimental Technique for Measuring Surface Heat Transfer Coefficients Using Uncalibrated Liquid Crystals,’’ *Proceedings of the ASME Heat Transfer Divison. HTD—Vol. 364-4*, pp. 121–126.

[7] Turnbull, W. N., and Oosthuizen, P. H., 1999, ‘‘Theoretical Evaluation of New Phase Delay Methods for Measuring Local Heat Transfer Coefficients,’’ Trans. Can. Soc. Mech. Eng., **23**(3 and 4), pp. 361–376.

[8] Farmer, J. P., Seager, D. J., and Liburdy, J. A., 1997, ‘‘The Effect of Shaping Inclined Slots on Film Cooling Effectiveness and Heat Transfer Coefficient,’’ ASME Paper 97-GT-339.

Solutions of Radiative Heat Transfer in Three-Dimensional Inhomogeneous, Scattering Media

L. M. Ruan
e-mail: ruanlm@hope.hit.edu.cn

H. P. Tan
School of Energy Science and Engineering,
Harbin Institute of Technology,
Harbin, PR China, 150001

In the present study, we use the Monte-Carlo (MC) method to simulate radiative heat transfer in three-dimensional inhomogeneous scattering unit cube with black or gray walls. The results show that the averaging method of non-uniform radiative properties in each medium element has influence on the results. One reasonable averaging method has been employed in our model. In mean while, several characters of exchange factor have been employed to estimate the performance of pseudo-random numbers generator and the numerical uncertainty of MC simulation. [DOI: 10.1115/1.1495519]

Keywords: Heat Transfer, Monte Carlo, Participating Media, Radiation, Scattering, Three-Dimensional

1 Introduction

Radiative heat transfer in three-dimensional inhomogeneous, scattering media has played an important role in engineering applications. Because of the non-uniform distribution of temperature and absorbing gaseous species, and scattering particles concentrations, the flame and combustion system should be treated as inhomogeneous media. Some researchers have studied this problem successfully by means of several methods, such as YIX method [1] and MC method [2]. Hsu et al. [3,4] developed a benchmark solution set using MC method and YIX method, while Guo and Maruyama [5,6] studied the same problem by REM method and scaling technique. The benchmarking results for radiative heat transfer in a unit cube with black walls were given in their papers.

In present study, firstly, we use MC method to simulate the same problem as that in the paper by Hsu and Farmer [4]. In numerical simulation, a piecewise constant interpolation of radiative properties should be used. However, analyzing the results of simulating cases in this paper, we find that the averaging method of non-uniform radiative properties in each element has influence on the results, especially for non-radiative equilibrium problem. The detailed conclusion needs study in the future. We think that some mean properties adopted by Hsu and Farmer [4] is not precise, though the influence is not obvious in some cases. Then the radiative heat transfer in a unit cube with gray walls is calculated, as well. In mean while, several characters of exchange factor have been employed to estimate the performance of pseudo-random numbers generator and the uncertainty of Monte-Carlo simulation.

Contributed by the Heat Transfer Division for publication in the JOURNAL OF HEAT TRANSFER. Manuscript received by the Heat Transfer Division September 14, 2001; revision received May 13, 2002. Associate Editor: K. S. Ball.

2 Analysis

2.1 Monte-Carlo Simulation for the Exchange Factor. The total radiative exchange factor (exchange factor) RD_{ij} is defined as: fraction of emissive power of element *i* which is absorbed by element *j*. The MC technique is employed to calculate this factor. Solving a thermal radiation problem by MC implies simulating a series of stochastic process. There are a great number of bundles emitting from each element, then the algorithm follows every bundle till it is absorbed by one element or goes out of the system. If total n_i bundles are emitted from element *i* in which n_{ij} bundles are absorbed by element *j*, so the exchange factor can be calculated as: $RD_{ij}=n_{ij}/n_i$.

Several textbooks (such as Modest [7] and Yang [8]) had described the MC simulation detailed. In general, the radiative properties have little relation with temperature, so RD_{ij} will be a constant for a certain sizing grid and radiative property profile in medium. Because exchange factor is directly related with the emitting power of element, we can calculate many radiative transfer properties of the medium, by means of the factor.

2.2 Energy Equation. In order to carry out numerical calculations, the enclosure should be divided into M1 finite surface-elements and M2 finite volume-elements, so the energy equation of element *i* at radiative equilibrium is expressed as follows:

$$Q_i=\sum_{j=1}^{M2} 4\kappa_{aj}V_jRD_{ji}E_b(T_j)+\sum_{k=1}^{M1} \varepsilon_kF_kRD_{ki}E_b(T_k) \qquad (1)$$

where Q_i is the emissive energy of element *i*. If element *i* is a sub-volume, then $Q_i=4\kappa_{ai}V_iE_b(T_i)$, and if element *i* is a sub-surface, $Q_i=\varepsilon_iF_iE_b(T_i)$. V_i and κ_{ai} are the volume and the absorption coefficient of volume element *i*; F_k and ε_k are the area and the emissivity of surface element *k*.

3 Results and Discussion

3.1 The Uncertainty Analysis. The exchange factor *RD* has some properties that are similar to the view factor. These can be used as benchmarks to estimate the performance of pseudo-random numbers generator, which is very important to MC program, and the uncertainty of MC simulation. For an enclosure consisting of *N* elements, the features are shown as follows:

1. Summation relationship: $\Sigma_{j=1}^{N}RD_{ij}=1$
2. Reciprocity relationship: $\varepsilon_iF_iRD_{ij}=\varepsilon_jF_jRD_{ji}$, for two surface element *i* and *j*; $\varepsilon_iF_iRD_{ij}=4\kappa_{aj}V_jRD_{ji}$, for surface element *i* and volume element *j*; and $4\kappa_{ai}V_iRD_{ij}=4\kappa_{aj}V_jRD_{ji}$, for two volume element *i* and *j*.
3. Conservation relationship: For an enclosure consisting of M1 surface elements and M2 volume elements: $\Sigma_{j=1}^{M1}\varepsilon_jF_jRD_{ji}+\Sigma_{k=1}^{M2}4\kappa_{ak}V_kRD_{ki}=\varepsilon_iF_i$, where *i* denotes the surface element or $\Sigma_{j=1}^{M1}\varepsilon_jF_jRD_{ji}+\Sigma_{k=1}^{M2}4\kappa_{ak}V_kRD_{ki}=4\kappa_{ai}V_i$, where *i* denotes the volume element.

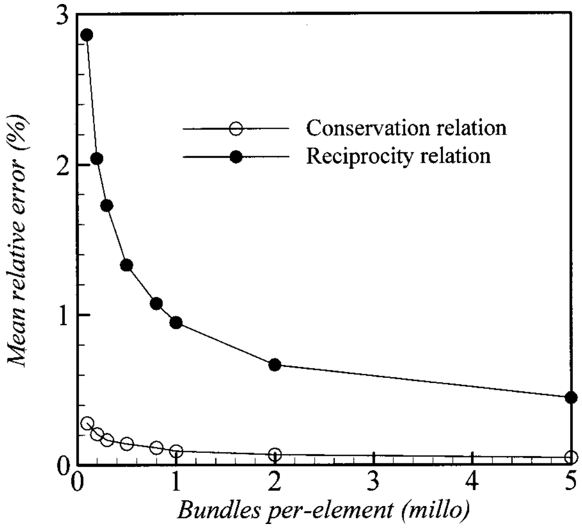

Fig. 1 The satisfaction with reciprocity and conservation relationship of RD

Table 1 Conditions of different cases

Case	Albedo ω	*B*	Constants in Eq. (3)	Boundary conditions
E2	0.9	0	a=0.9,b=0.1	6 cold black walls
E3	0.9	1	a=0.9,b=0.1	1 hot/5 cold black walls
E4	0.9	-1	a=0.9,b=0.1	1 hot/5 cold black walls
E7	0.9	1	a=5.0,b=5.0	1 hot/5 cold black walls
E13	0.9	1	a=0.9,b=0.1	1 hot/5 cold gray walls ($\varepsilon=0.5$)
E14	0.9	-1	a=0.9,b=0.1	1 hot/5 cold gray walls ($\varepsilon=0.5$)
E23	0.9	1	a=0.9,b=0.1	1 hot/5 cold gray walls ($\varepsilon=0.75$)
E24	0.9	-1	a=0.9,b=0.1	1 hot/5 cold gray walls ($\varepsilon=0.75$)

In general, the summation relationship can be guaranteed exactly, if the MC model has no theoretical errors. However, the other two relationships cannot be agreed exactly at any time, because of the inevitable statistical error of MC method. If a set of truly random numbers is used for the simulation, then the errors will decrease as the number of sample increase.

One homogeneous, absorbing and scattering square medium with optical thickness $\kappa L_x=\kappa L_y=1$ and bounded by gray boundaries is treated as an example. The scattering albedo ω=0.5 and linearly scattering phase function $\Phi(\theta)=1+\cos(\theta)$ is adopted. The emissivities of four boundaries are 0.5, 0.6, 0.7, and 0.8, respectively. The 5×5 square grid is used with side length of 0.2. Some results about reciprocity relationship and conservation relationship of *RD* are shown in Fig. 1. We can see that both mean errors of reciprocity and conservation relationship are decreased with the increase of samples emitted from every sub-element. Our MC code runs on Legend 2000 PIII/933. The total CPU time is 1364.51 (sec) for 5×10^6 bundles per sub-element. The CPU time for MC simulation is strongly relative with the optical thickness and scattering albedo of medium, the emissivity of boundaries and the simulated bundles. Except the characters mentioned above, the symmetry of *RD* in symmetric system is one other criterion of MC model.

Table 2 Relative difference between $\bar{\kappa}_1$ and $\bar{\kappa}_2$ (percent) ((a)=0.9, (b)=0.1, z=0)

	x=4/9	3/9	2/9	1/9	0
y=4/9	0.5611	1.4071	2.0266	2.4905	5.7082
3/9	1.4071	2.8595	3.5974	4.0453	8.8169
2/9	2.0266	3.5974	4.2583	4.6246	9.8921
1/9	2.4905	4.0453	4.6246	4.9235	10.439
0	5.7082	8.8169	9.8921	10.439	16.526

Table 3 Divergence of radiative heat fluxes at $y=z=0$ and surface heat fluxes at $x=-0.5$ and $y=0$ (Case E2)

x	MC	$\bar{\kappa}=\bar{\kappa}_2$	$\bar{\kappa}=\bar{\kappa}_1$	σ_{10}	Error %
	Divergence of radiative heat fluxes				
4/9	0.07974	0.07919	0.07490	0.000030	5.727
3/9	0.15866	0.15746	0.14479	0.000071	8.751
2/9	0.23673	0.23500	0.21399	0.000125	9.818
1/9	0.31433	0.31228	0.28305	0.000143	10.327
0	0.39192	0.38951	0.33472	0.000152	16.369
	Surface heat fluxes				
4/9	0.01219	0.01224	0.01194	0.000072	2.513
3/9	0.01564	0.01572	0.01528	0.000075	2.880
2/9	0.01892	0.01862	0.01822	0.000101	2.195
1/9	0.02103	0.02084	0.02019	0.000116	3.219
0	0.02202	0.02164	0.02104	0.000096	2.852

Table 4 Emissive power at $y=z=0$ (Case E3, E4 and E7)

x	E3			E4			E7		
	MC	Present	σ_{10}	MC	Present	σ_{10}	MC	Present	σ_{10}
-4/9	0.46100	0.45660	0.00221	0.47660	0.47455	0.00261	0.64420	0.64343	0.00126
-3/9	0.36640	0.36458	0.00198	0.37990	0.38453	0.00281	0.48220	0.48136	0.00168
-2/9	0.28420	0.28706	0.00180	0.29450	0.29947	0.00210	0.35100	0.35082	0.00163
-1/9	0.21830	0.21821	0.00126	0.22430	0.22471	0.00126	0.24700	0.24644	0.00072
0	0.16650	0.16687	0.00099	0.16640	0.16781	0.00123	0.16640	0.16622	0.00032
1/9	0.12580	0.12756	0.00098	0.12120	0.12162	0.00099	0.10760	0.10875	0.00037
2/9	0.09642	0.10168	0.00086	0.08987	0.09582	0.00084	0.06878	0.06982	0.00033
3/9	0.07516	0.07612	0.00058	0.06820	0.06751	0.00064	0.04310	0.04321	0.00030
4/9	0.05986	0.06206	0.00059	0.05326	0.05490	0.00078	0.02484	0.02526	0.00028

Table 5 Surface heat fluxes at $x=-0.5$ and $y=0$ (E3, E4 and E7)

z	E3			E4			E7		
	MC	Present	σ_{10}	MC	Present	σ_{10}	MC	Present	σ_{10}
-4/9	0.98490	0.98605	0.00012	0.96560	0.96723	0.00010	0.73260	0.73349	0.00041
-3/9	0.98010	0.98163	0.00016	0.95100	0.95275	0.00021	0.62550	0.62675	0.00036
-2/9	0.97620	0.97761	0.00019	0.93870	0.94071	0.00022	0.56670	0.56899	0.00044
-1/9	0.97310	0.97521	0.00017	0.92950	0.93208	0.00025	0.53450	0.53678	0.00060
0	0.97170	0.97379	0.00018	0.92530	0.92839	0.00016	0.52340	0.52485	0.00030

Table 6 Emissive power at $z=0$ (Case E3)

x	-4/9	-3/9	-2/9	-1/9	0	1/9	2/9	3/9	4/9
$\bar{\kappa}=\bar{\kappa}_1$									
y=4/9	0.3513	0.2426	0.1908	0.1542	0.1107	0.0930	0.0773	0.0614	0.0480
3/9	0.4350	0.3168	0.2353	0.1764	0.1346	0.1103	0.0874	0.0710	0.0576
2/9	0.4408	0.3477	0.2638	0.1963	0.1517	0.1220	0.0909	0.0735	0.0605
1/9	0.4581	0.3556	0.2799	0.2093	0.1673	0.1259	0.0965	0.0782	0.0602
0	0.4566	0.3645	0.2870	0.2182	0.1669	0.1275	0.1017	0.0761	0.0620
$\bar{\kappa}=\bar{\kappa}_2$									
y=4/9	0.3583	0.2410	0.1949	0.1534	0.1115	0.0916	0.0789	0.0589	0.0531
3/9	0.4351	0.3154	0.2366	0.1769	0.1364	0.1106	0.0902	0.0647	0.0550
2/9	0.4391	0.3492	0.2637	0.1956	0.1559	0.1169	0.0913	0.0732	0.0582
1/9	0.4583	0.3574	0.2815	0.2091	0.1674	0.1253	0.0963	0.0751	0.0638
0	0.4599	0.3645	0.2878	0.2196	0.1662	0.1257	0.0972	0.0718	0.0662
Homogeneous medium assumption ($\bar{\kappa}$=0.2125)									
y=4/9	0.3588	0.2438	0.1870	0.1466	0.1200	0.0985	0.0783	0.0659	0.0552
3/9	0.4239	0.3103	0.2302	0.1757	0.1403	0.1128	0.0901	0.0727	0.0599
2/9	0.4568	0.3413	0.2638	0.1983	0.1549	0.1217	0.0962	0.0792	0.0653
1/9	0.4587	0.3625	0.2782	0.2135	0.1638	0.1282	0.1015	0.0801	0.0659
0	0.4602	0.3674	0.2727	0.2092	0.1660	0.1343	0.1031	0.0834	0.0668

Table 7 Emissive power at $y=z=0$

x	E13	σ_{10}	E23	σ_{10}	E14	σ_{10}	E24	σ_{10}
-4/9	0.30662	0.00378	0.37164	0.00468	0.31964	0.00391	0.38520	0.00452
-3/9	0.27602	0.00254	0.31835	0.00265	0.28845	0.00183	0.33233	0.00261
-2/9	0.22659	0.00121	0.26186	0.00201	0.23505	0.00176	0.26789	0.00221
-1/9	0.19747	0.00122	0.20758	0.00115	0.19944	0.00099	0.21291	0.00119
0	0.16595	0.00099	0.16635	0.00123	0.16646	0.00123	0.16534	0.00105
1/9	0.14339	0.00105	0.13273	0.00065	0.14221	0.00086	0.13017	0.00083
2/9	0.12516	0.00131	0.11066	0.00050	0.12065	0.00133	0.10588	0.00110
3/9	0.11634	0.00113	0.09496	0.00079	0.10970	0.00105	0.08845	0.00071
4/9	0.10831	0.00134	0.08382	0.00073	0.10493	0.00168	0.07992	0.00088

One of the most straightforward ways of estimating the error associated with the sampling result $S(N)$ is to break up the result into a number of I sub-samples $S(N_i)$, then the variance or adjusted mean square deviation can be obtained as follows [7]:

$$\sigma_I^2=\frac{1}{I(I-1)}\sum_{i=1}^{I}\left[S(N_i)-S(N)\right]^2 \tag{2}$$

where $S(N)=1/I\Sigma_{i=1}^{I}S(N_i)$ is the mean value of I $S(N_i)$.

3.2 Inhomogeneous Media With Black Walls. The radiative heat transfer in a unit cube with black wall was calculated by YIX and MC methods in Hsu and Farmer's paper [4]. We simulate the same problem in this paper. The coordinate origin lies at the center of the cube and $-0.5\leqslant(x,y,z)\leqslant 0.5(m)$ is the domain of computation. The inhomogeneous extinction coefficient (m^{-1}) distribution is given by

Table 8 Surface heat fluxes at $x=-0.5$ and $y=0$

z	E13	σ_{10}	E23	σ_{10}	E14	σ_{10}	E24	σ_{10}
-4/9	0.43933	0.00016	0.69411	0.00019	0.43439	0.00021	0.68302	0.00016
-3/9	0.44502	0.00008	0.69872	0.00015	0.43783	0.00011	0.68244	0.00019
-2/9	0.44669	0.00011	0.69942	0.00012	0.43759	0.00016	0.67913	0.00018
-1/9	0.44723	0.00009	0.69928	0.00016	0.43701	0.00009	0.67557	0.00017
0	0.44744	0.00015	0.69905	0.00016	0.43667	0.00025	0.67402	0.00012

$$\kappa(x,y,z)=a\left(1-\frac{|x|}{0.5}\right)\left(1-\frac{|y|}{0.5}\right)\left(1-\frac{|z|}{0.5}\right)+b \tag{3}$$

The constants a and b for several cases are listed in Table 1. A linear anisotropic scattering phase function is employed: $\Phi(\theta)=1+B\cos(\theta)$, the constant B is listed in Table 1 as well. For case E2, unity blackbody emissive power in the medium is given. For case E3, E4, and E7, the radiative equilibrium is assumed and only one of the black walls $(x=-0.5)$ has unity emissive power.

The emissive power and surface flux, or radiative flux divergence and surface flux for several cases are calculated. In actual computation, 9×9×9 cubic grid with side length of 1/9 is used, the bundles that emitted from one sub-element are 10^6 for case2 and 10^7 for all other cases, so the total bundles are 1.215×10^9 for case2 and 1.215×10^{10} for other cases. Each element is assumed to be homogenous for numerical calculation, although the medium as whole is inhomogeneous. The mean extinction coefficient in each element must be calculated firstly. In Hsu and Farmer's paper [4], we cannot find the formula for the mean radiative properties. Comparing with the results of our calculation (see Table 3), we believe that the extinction coefficient $\overline{\kappa_{2i}}$ at center of each element i was treated as the mean value by Hsu and Farmer. However, we think that the average extinction coefficient should be calculated as follows:

$$\overline{\kappa_{1i}}=\int\int\int_{v_i}\kappa(x,y,z)dv\Big/\int\int\int_{v_i}dv \tag{4}$$

The extinction coefficients that calculated by two kinds of average methods are different. The relative difference between them are shown in Table 2, in which the coordinates at center of volume element are represented as this element. The maximum relative difference is appeared at the center of the cube. Certainly, this kind of deviation will be reduced as the grids increasing. For case E2, we calculated the divergence of radiative heat flux based on $\overline{\kappa_2}$ and $\overline{\kappa_1}$ respectively (see Table 3). The relative difference profile is also shown in Table 3, which is just close to the difference distribution between $\overline{\kappa_2}$ and $\overline{\kappa_1}$. In mean time, the surface heat flux was calculated based on $\overline{\kappa_2}$ and $\overline{\kappa_1}$ respectively, and relative differences between them are almost same and close to the difference between $\overline{\kappa_2}$ and $\overline{\kappa_1}$ in the medium-elements which are near the surfaces. For cases E3, E4, and E7, suppose $\overline{\kappa}=\overline{\kappa_1}$, the calculating values are shown in Table 4 and 5. In these tables, the "MC" indicates Hsu and Farmer's values [4], and σ_{10} is defined in Eq. (2) for $I=10$.

For case E2, the energy source is unity blackbody emissive power in medium and all six walls are blackbody and cold. The walls only absorb energy, which can be treated as heat sink, and have no reflection and emission. So this is a non-radiative-equilibrium problem. The extinction coefficient κ_i (or absorbing coefficient $\kappa_{ai}=\omega\kappa_i$) has influence on not only transferring and absorbing power in medium, but also emitting power $(4\kappa_{ai}V_iE_b)$ of each source element. There is different emissive power in different volume element due to the different absorbing coefficient. So the value of the average extinction coefficient has great influence on radiative heat transfer for case E2.

However, for case E3 and E4, the source is one of the black walls with unity emissive power and radiative equilibrium is assumed. The extinction coefficient has no influence on the source, no matter which mean extinction coefficient is adopted, there is little difference in results. Even when we simplify the inhomogeneous unit cube as homogeneous one, in which the mean extinction coefficient $\overline{\kappa}=0.2125$ is averaged by Eq. (3) in the whole cube, there is no obvious difference in emissive power of medium. The emissive power at $z=0$ of case E3 with different extinction coefficients by three average methods are shown in Table 6. For case E7, the optical thickness is large, how to calculate mean extinction coefficient has little influence on radiative transfer.

3.3 Inhomogeneous Media With Gray Walls. In present study, the radiative transfer in a unit cube with gray and diffuse wall is simulated. The conditions of different cases are listed in Table 1. The inhomogeneous extinction coefficient distribution is same as above. For case E13, E14, E23, and E24, the radiative equilibrium is assumed and one of the gray walls ($x=-0.5$) has unity blackbody emissive power. The results are shown in Tables 7 and 8. It can be seen that the decrease of wall emissivity will decrease the emissive power in the medium near hot surface and increase it near cold surface. For all our cases, a constant value of emissive power is kept as about 1/6 at $x=y=z=0$, which is just the exact solution. It proves the precision of our model once more.

4 Conclusions

In this paper, the Monte-Carlo method is used to simulate radiative heat transfer in three-dimensional inhomogeneous, anisotropically scattering media. In numerical simulation, a piecewise constant interpolation of radiative properties should be used. Basing upon our calculation, how to average the inhomogeneous radiative properties in one medium element will have influence on the results. Although both property evaluation methods are approximate, it can obtain more reasonable results to simulate by means of one suitable averaging property. The performance of pseudo-random numbers generator is very important to the precision of MC model. Several characters of exchange factor have been employed to estimate the performance of pseudo-random numbers generator and the numerical uncertainty of MC simulation. Finally, the radiative heat transfer in a unit cube with gray walls is simulated, and the results can be treated as a benchmark.

Acknowledgments

This research is supported by the National Natural Science Foundation of China (59806003).

References

[1] Hsu, P. F., Tan, Z., and Howell, J. R., 1993, "Radiative Transfer by YIX Method in Nonhomogeneous, Scattering and Non-Gray Media," AIAA Journal of Thermophysics and Heat Transfer, **7**(3), pp. 487–495.
[2] Farmer, J. T., and Howell, J. R., 1994, "Monte Carlo Prediction of Radiative Heat Transfer in Inhomogeneous, Anisotropic, Nongray Media," AIAA Journal of Thermophysics and Heat Transfer, **8**(1), pp. 133–139.
[3] Hsu, P. F., and Tan, Z., 1995, "Recent Benchmarks of Radiative Heat Transfer Within Nonhomogeneous Participating Media and the Improved Method," *Proceedings of the Int. Symp. On Radiation Transfer*, pp. 107–126.
[4] Hsu, P. F., and Farmer, J. T., 1997, "Benchmark Solution of Radiative Heat Transfer Within Nonhomogeneous Participating Media Using the Monte Carlo and YIX Method," ASME J. Heat Transfer, **119**(1), pp. 185–188.
[5] Guo, Z. X., and Maruyama, S., 1999, "Scaling Anisotropic Scattering in Radiative Transfer in Three Dimensional Nonhomogeneous Media," Int. Commun. Heat Mass Transfer, **26**(7), pp. 997–1007.
[6] Guo, Z. X., and Maruyama, S., 2000, "Radiative Heat Transfer in Inhomogeneous, Nongray, and Anisotropically Scattering Media," Int. J. Heat Mass Transf., **43**(13), pp. 2325–2336.
[7] Modest, M. F., 1993, *Radiative Heat Transfer*, McGraw-Hill, Singapore.
[8] Yang, W. J., Taniguchi, H., and Kudo, K., 1995, "Radiative Heat Transfer by the Monte Carlo Method," *Advances in Heat Transfer*, **27**, Academic Press, New York.

Electric Network Representation of the Unsteady Cooling of a Lumped Body by Nonlinear Heat Transfer Modes

Francisco Alhama
Dpto. de Física Aplicada, E.T.S. Ingenieros Industriales,
Universidad Politécnica de Cartagena,
30203 Cartagena, Murcia, Spain

Antonio Campo[1]
College of Engineering, Idaho State University,
Pocatello, ID 83209

Keywords: Analog Techniques, Cooling, Forced Convection, Natural Convection, Radiation

Introduction

The solution of the unsteady heat conduction equation in a solid body is difficult because of the dependence of the temperature on the space variable(s) and time. In most situations, the solution sought is approached by establishing a distributed model consisting of a partial differential equation, the boundary conditions and an initial condition.

In general, the rate of heat conduction in a solid body absent of internal heat generation is dependent upon two resistances: the internal resistance inside the body and the surface resistance between the body surface and the surrounding fluid. Within this ample framework, there are two limiting cases of importance, case (*a*) negligible internal resistance and case (*b*) negligible surface resistance. The former is associated with a small temperature variation inside the body and a large temperature difference between the body surface and the fluid. Putting this statement in perspective, the body can be considered as a "lump" with nearly uniform temperature at any instant of time. This simplified approach establishes the basic assumption in the lumped model.

From a physical standpoint, there is an electric analogy to the lumped model, owing to the mathematical equivalence of the lumped heat equation to the equation that governs the voltage in a resistance-capacitance electric circuit (the so-called RC circuit). However, it is important to stress that the electric analogy in question applies exclusively when the heat exchange between a solid body and a fluid occurs by a linear heat transfer mode, such as forced convection, where the forced convection coefficient remains constant during the entire cooling period.

The objective of this technical note is to establish for the first time the basis for the construction of advanced electric analogies to the lumped model embodying heat exchange at the solid-fluid interface by a nonlinear heat transfer mode, for instance natural convection or thermal radiation. Due to the intrinsic nonlinearity of these two modes, the natural convection coefficient and the equivalent radiation coefficient in the lumped heat equation are no longer constants, but vary with the instantaneous temperature of the body during the cooling period.

Mathematical Modeling

Fundamentally, when a solid body is immersed in a fluid at a different temperature, the heat exchange between the body surface and the fluid may occur by three distinct heat transfer modes: (1)

---

[1] Current address: Mechanical Engineering Dept., The University of Vermont, Burlington, VT 05405

Contributed by the Heat Transfer Division for publication in the JOURNAL OF HEAT TRANSFER. Manuscript received by the Heat Transfer Division August 21, 2001; revision received May 8, 2002. Associate Editor: M. L. Hunt.

forced convection, (2) natural convection, and (3) thermal radiation. Also, there is a possibility that two of these modes are combined.

For the sake of generality, the solid body in this work has been conceived as a small metallic sphere whose volume/surface area ratio V/A amounts to $D/6$, but the theory is equally applicable to plates and cylinders. For simplicity, the chosen coolant is air at standard atmospheric conditions. The thermal properties of both metal and air are taken as uniform and are evaluated at the proper film temperature $T_f=(T_i+T_\infty)/2$.

Forced Convection Cooling. The cooling of a lumped sphere by a forced flow of a single-phase viscous fluid is described by the lumped heat equation along with the initial condition

$$\rho_s c_s D \frac{dT}{dt} = -6\overline{h}(T-T_\infty), \quad T(0)=T_i \tag{1}$$

In this differential equation of first order, the forced convection coefficient, $\overline{h}$, is constant and its magnitude may be taken from the experimental-based correlation equation recommended by Whitaker [1]:

$$\overline{\mathrm{Nu}} = 2+(0.4\,\mathrm{Re}^{1/2}+0.06\,\mathrm{Re}^{2/3})\mathrm{Pr}^{0.4} \tag{2}$$

which is valid for gases and common liquids $(0.7<\mathrm{Pr}<380)$ operating within the range of $3.5<\mathrm{Re}<7.6\times10^4$. Other correlation equations for higher Re have been proposed by Ahmed and Yovanovich [2].

As the fluid velocity approaches zero, $u_\infty\rightarrow0$, $\mathrm{Re}\rightarrow0$ in Eq. (2), so that the fluid motion tends to disappear giving way to a no-flow condition. This limiting condition yields a constant Nusselt number $\mathrm{Nu}\rightarrow2$ (a diffusive limit). Since $\overline{h}\rightarrow2k_a/D$, the heat transfer mode switches from forced convection to conduction in a stationary infinite air medium around the sphere.

The forced convection coefficient, $\overline{h}$, may be isolated for air $(\mathrm{Pr}=0.7)$ in Eq. (2), leading to the function

$$\overline{h} = 2\frac{k_a}{D} + \frac{k_a}{D}\left[0.35\left(\frac{u_\infty D}{v_a}\right)^{1/2} + 0.05\left(\frac{u_\infty D}{v_a}\right)^{2/3}\right] \tag{3}$$

where the subscript "a" in the thermal properties k_a and v_a identifies the air. Once the air velocity u_∞ is assigned, $\overline{h}$ turns out to be a constant quantity in the temperature domain $[T_\infty, T_i]$.

Introducing Eq. (3) into Eq. (1) and separating variables supplies the exponential temperature distribution

$$\frac{T(t)-T_\infty}{T_i-T_\infty} = \exp\left(-\frac{6\overline{h}}{\rho_s c_s D}\cdot t\right) \tag{4}$$

which has been the trademark of the lumped model under the assumption that the forced convection coefficient, $\overline{h}$, is constant (Kreith and Bohn [3]). In Eq. (4), the quantity $\rho_s c_s D/6h$ may be viewed as the product of the capacitance and the resistance, i.e., the thermal time constant, t_c.

Natural Convection Cooling. The lumped heat equation for the sphere, along with the initial condition, is given again by Eq. (1). The natural convection mode implies that the cooling of the sphere is driven by a buoyant upflow of a single-phase viscous fluid. In this regard, the natural convection coefficient, $\overline{h}$, may be quantified by the experimental-based correlation equation credited to Churchill [4]:

$$\overline{\mathrm{Nu}} = \frac{\overline{h}D}{k_a} = 2+0.589\frac{(\mathrm{GrPr})^{1/4}}{f(\mathrm{Pr})} \tag{5a}$$

where $f(\mathrm{Pr})$ stands for a "universal" Prandtl number function

$$f(\mathrm{Pr}) = \left[1+\left(\frac{0.469}{\mathrm{Pr}}\right)^{9/16}\right]^{4/9} \tag{5b}$$

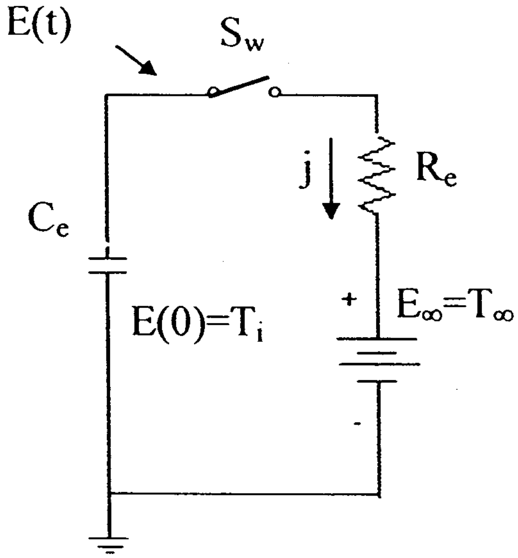

Fig. 1 Electric circuit for forced convection cooling of a metallic sphere

The validity of Eq. (5a) covers the interval $0<\mathrm{GrPr}<10^{11}$ and the spectrum of gases and common liquids with $\mathrm{Pr}\geqslant0.7$. An equally handy correlation equation for $\mathrm{GrPr}>10^{11}$ is found in [4].

As the instantaneous temperature T of the sphere approaches the air temperature T_∞, the fluid motion tends to disappear giving way to a no-flow condition equivalent to $\mathrm{Gr}\rightarrow0$. Similar to the case of forced convection, this limiting condition is characterized by a constant Nusselt number $\mathrm{Nu}\rightarrow2$ (a diffusive limit) in Eq. (5a) and the heat transfer mode switches from natural convection to conduction in a stationary infinite air medium around the sphere.

The natural convection coefficient, $\overline{h}$, for air $(\mathrm{Pr}=0.7)$ may be extracted from Eq. (5a) resulting in the function

$$\overline{h} = 2\frac{k_a}{D} + 0.413\frac{k_a}{D^{1/4}}\left(\frac{g\beta_a}{v_a^2}\right)^{1/4}(T-T_\infty)^{1/4} \tag{6}$$

where again the subscript "a" in the thermophysical properties k_a, v_a, and β_a are indicative of air. Contrary to the case of linear forced convection cooling emblematic of a constant $\overline{h}$ over the temperature domain $[T_\infty, T_i]$, now for natural convection Eq. (6) indicates that $\overline{h}$ is by no means a constant quantity over $[T_\infty, T_i]$. In actuality, since the diameter D and the air temperature T_∞ are fixed quantities, $\overline{h}$ is a derived quantity that varies with the instantaneous temperature, T. Specifically, for laminar natural convection of air, $\overline{h}$ is regulated by the nonlinear temperature function $\overline{h}(T)$ in Eq. (6)[1] whose range is $[\overline{h}_{\min}, \overline{h}_{\max}]$. Substituting Eq. (6) into Eq. (1) leads to

$$\rho_s c_s D\frac{dT}{dt} = -12\frac{k_a}{D}(T-T_\infty) - 2.478\frac{k_a}{D^{1/4}}\left(\frac{g\beta_a}{v_a^2}\right)^{1/4}(T-T_\infty)^{5/4} \tag{7}$$

In all likelihood, the nonlinear first-order differential equation (7) does not admit an analytic solution. Notwithstanding, adoption of the temperature transformation

$$\theta = T-T_\infty \tag{8}$$

converts Eq. (7) into Bernoulli equation (Polyanin and Zaitsev [5])

---

[1] When the buoyant air flow is turbulent, the temperature function is of the form $(T-T_\infty)^{1/3}$, but the solution procedure is unaffected.

$$\frac{d\theta}{dt}+a\,\theta=-b\,\theta^{5/4},\quad \theta(0)=T_i-T_\infty \tag{9}$$

where the coefficients “a” and “b” are computed from the ratios

$$a=\frac{12k_a}{\rho_s c_s}\cdot\frac{1}{D^2},\quad b=\frac{2.478k_a}{\rho_s c_s}\left(\frac{g\beta_a}{v_a^2}\right)^{1/4}\cdot\frac{1}{D^{5/4}} \tag{10}$$

Despite that the presence of $\theta^{5/4}$ prevents Eq. (9) from being linear, the equation does admit an analytic solution via a variable transformation. Letting $u=\theta^{-1/4}$, Eq. (9) is modified into a linear differential equation in the new variable u which is amenable to the method of separation of variables. In the end, the analytic temperature distribution may be written as

$$\frac{T(t)-T_\infty}{T_i-T_\infty}=\left[\frac{a}{(a+b)\exp\left(\dfrac{at}{4}\right)-b}\right]^4 \tag{11}$$

It should be noted that the structure of Eq. (11) deviates markedly from the structure of Eq. (4) for forced convection cooling. Natural convection cooling does not lead to an exponential solution, so a time constant as such does not exists.

Thermal Radiation Cooling. If a hot sphere is cooled by thermal radiation in air, the lumped heat equation, together with the initial condition is described by

$$\rho_s c_s D\,\frac{dT}{dt}=-6\epsilon_s\sigma(T^4-T_\infty^4),\quad T(0)=T_i \tag{12}$$

where T and T_∞ are absolute temperatures. For the thermal radiative analysis, the two key assumptions are: (1) the sphere surface is gray, and (2) the configuration factor between the sphere and the air space is one [3].

Although Eq. (12) is nonlinear, fortunately it does admit an analytic solution. Thus, separating variables and integrating from the initial condition $(T_i,0)$ to a given arbitrary condition (T,t), yields

$$\int_{T_i}^{T}\frac{dT}{T^4-T_\infty^4}=-e\int_0^t dt \tag{13}$$

where the coefficient “e” is computed from the ratio:

$$e=\frac{6\epsilon_s\sigma}{\rho_s c_s}\cdot\frac{1}{D} \tag{14}$$

The denominator of the integrand on the LHS of Eq. (13) may be broken into partial fractions. Subsequently, after evaluating the integrals and rearranging terms, the solution of Eq. (13), though in implicit form, delivers the analytic temperature distribution

$$\frac{1}{2}\ln\left|\frac{T-T_\infty}{T+T_\infty}\right|-\frac{1}{2}\ln\left|\frac{T_i-T_\infty}{T_i+T_\infty}\right|-\tan^{-1}\left(\frac{T}{T_\infty}\right)+\tan^{-1}\left(\frac{T_i}{T_\infty}\right)=-2et \tag{15}$$

In this equation, it is apparent that the numerical evaluation of t in terms of T is direct. Thermal radiation cooling does not lead to an exponential solution, so a time constant, as such does not exists.

Electric Circuits

Forced Convection Cooling. When the cooling occurs by forced convection (a linear heat transfer mode), the forced convection coefficient h is a constant quantity and the electric circuit analogous to the thermal system is shown in Fig. 1. In the thermal system, the thermal resistance is $R=1/h$, the thermal capacitance is $C=\rho_s c_s D/6$, the thermal potential is $T-T_\infty$ and the heat flow is Q. In the electric circuit, the electrical resistance is R_e, the electrical capacitance is C_e, the electrical potential is $E-E_\infty$, and the current is j. To construct an electric circuit that would behave exactly similar to the thermal system, $E(t)-E_\infty=T(t)-T_\infty$, the ratio $\rho_s c_s D/6h$ needs to be equal to the time constant $R_e C_e$, and the initial voltage of the capacitor is identical to the initial temperature T_i. In this way, the set of equivalences that surfaces up is: $R_e=1/h$, $C_e=\rho_s c_s D/6$, $E(0)=T_i$ and $E_\infty=T_\infty$.

When the switch S_w in the electric circuit of Fig. 1 is closed at $t=0$, the energy stored in the capacitor C_e is discharged through the resistance R_e. As a result, internal energy is stored in the thermal system, whereas electric charge is stored in the electric circuit.

Current textbooks on heat transfer (for instance [3]) report the RC electric circuit for forced convection cooling with a constant forced convection coefficient h that involves a capacitor and a resistor in parallel to the voltage source. Conversely, the old textbook by Giedt [6] presents a RC electric circuit containing a ca-

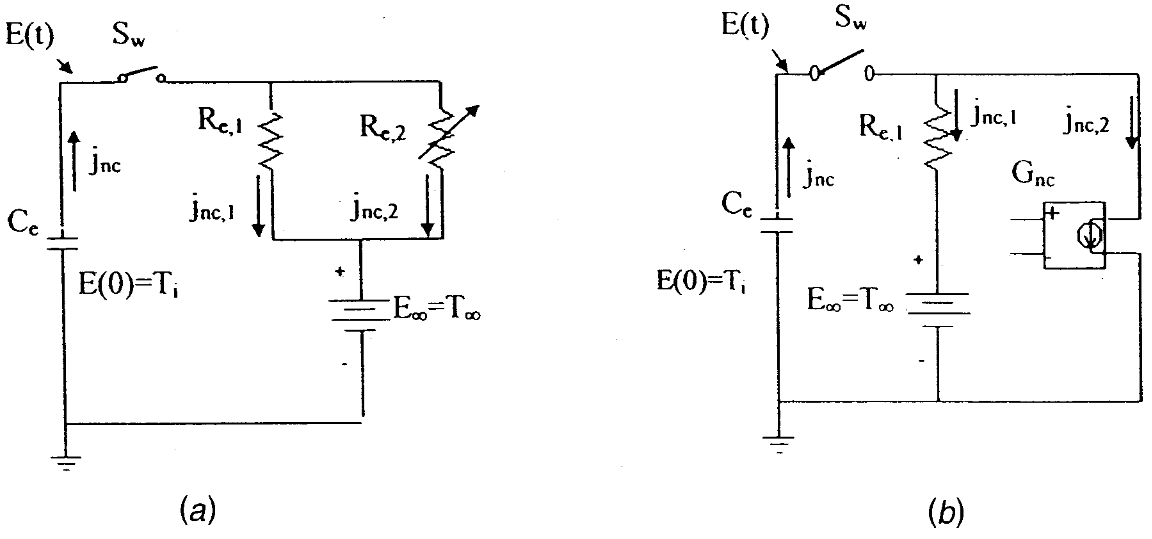

Fig. 2 Electric circuit for natural convection cooling of a metallic sphere

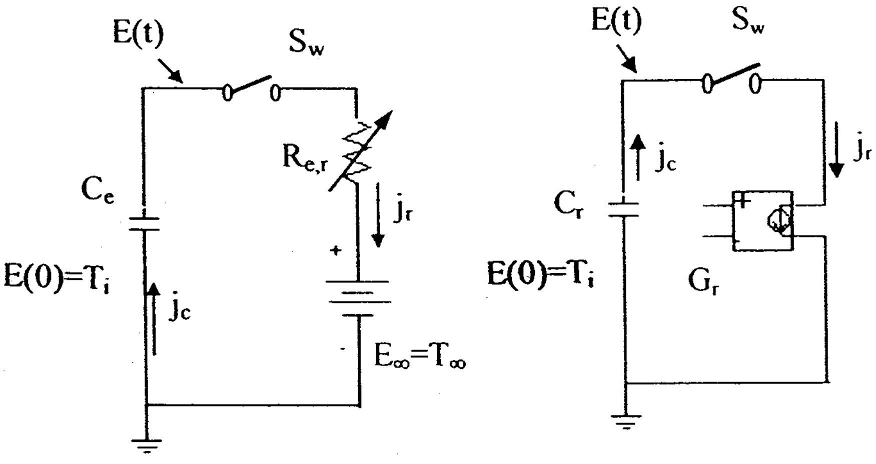

(*a*) (*b*)

Fig. 3 Electric circuit for thermal radiation cooling of a metallic sphere

pacitor and a resistor in series to the voltage source. We opted for the latter and the electric circuit sketched in Fig. 1 is identical to the one used in [6].

Natural Convection Cooling. For natural convection cooling (a nonlinear heat transfer mode), the natural convection coefficient $\bar{h}$ is no longer constant; that is, $\bar{h}$ depends on the instantaneous temperature T of the sphere. For the design of the electric circuit analogous to the thermal system cooled by natural convection a different avenue needs to be taken. The nonlinear, nonhomogeneous first-order ordinary differential equation (7) is rewritten in terms of the current j in the following form

$$j_{nc}-j_{nc,1}-j_{nc,2}=0 \tag{16}$$

where these elements are defined by

$$j_{nc}=\rho_s c_s D\,\frac{dT}{dt} \tag{17a}$$

$$j_{nc,1}=-12(k_a/D)(T-T_\infty) \tag{17b}$$

$$j_{nc,2}=-2.478(k_a/D^{1/4})(g\beta_a/\nu_a^2)^{1/4}(T-T_\infty)^{5/4} \tag{17c}$$

In the spirit of an electric analogy, Eq. (17*a*) is the current of a capacitor whose capacitance is $C_e=\rho_s c_s D$ and Eq. (17*b*) is the current of a resistor whose resistance is $R_{e,1}=D/(12k)$. The resistance ends are the voltage difference $T-T_\infty$. Meanwhile, Eq. (17*c*) is the current of a voltage-dependent resistor (VDR) whose resistance is $R_{e,2}=2.478(k_a/D^{1/4})(g\beta_a/\nu_a^2)^{1/4}(T-T_\infty)^{1/4}$. The initial voltage of the capacitor corresponds to the initial temperature T_i. Now, taking into account the signs of each of the currents according to Eq. (16), the analogous electric circuit is illustrated in Fig. 2(*a*).

When the switch S_w is closed at $t=0$ in the electric circuit of Fig. 2(*a*) the energy stored in the capacitor C_e is discharged through two resistors $R_{e,1}$ and $R_{e,2}$. As a result, internal energy is stored in the thermal system, whereas electric charge is stored in the electric circuit. The variable resistor in Fig. 2(*a*) is substituted by a VDR device which for short is denoted by the symbol G_{nc} in Fig. 2(*b*). In this device, the current $j_{nc,2}=2.478(k_a/D^{1/4})\times(g\beta_a/\nu_a^2)^{1/4}(T-T_\infty)^{5/4}$, turns out to be a function of the voltage (synonymous with the temperature) in the capacitor.

Thermal Radiation Cooling. Let us state Eq. (12) in the alternate form

$$\rho_s c_s D\,\frac{dT}{dt}=-6\epsilon_s\sigma h_r(T)(T-T_\infty), \quad T(0)=T_i \tag{18}$$

where the radiation coefficient $h_r(T)$ is given by the function

$$h_r(T)=\epsilon_s\sigma(T^2+T_\infty^2)(T+T_\infty) \tag{19}$$

since T and T_∞ are absolute temperatures.

The analogous electric circuit for the case of thermal radiation cooling is designed by way of a voltage dependent resistor (VDR) in series with a capacitor and a constant voltage source as pictured in Fig. 3(*a*). The respective values of the capacitance $C_e=\rho_s c_s D$ and the resistance $R_{e,r}=6\epsilon_s\sigma h_r(T)$ may be readily derived. The function for the VDR device is designated by G_r (see Fig. 3(*b*)). The current of the source $j_r=(T-T_\infty)/R_r=6\epsilon_s\sigma h_r(T)(T-T_\infty)$ is just the same current in the capacitor $j_c=\rho_s c_s D(dT/dt)$. The resistance ends are the voltage difference $T-T_\infty$. The initial temperature T_i provides the input for the initial voltage of the capacitor. The discharge of the capacitor is controlled by the source which in real time gives a current that depends on the voltage in the capacitor. The constant voltage source may be eliminated in the electric circuit of Fig. 3(*b*) since its influence in the solution is taken into account in the equation that specifies the current in the source G_r.

When the switch S_w in the electric circuit of Fig. 3 is closed at $t=0$, the energy stored in the capacitor C_e is discharged through the resistance $R_{e,r}$. As a result, internal energy is stored in the thermal system, whereas electric charge is stored in the electric circuit.

Computer Tools for Electric Circuit Analysis. Electric circuits containing linear elements, such as voltage sources, currents and resistances can be analyzed in straightforward mathematical way. Clearly, these three elements are associated with the forced convection mode. Important circuit elements, such as diodes, transistors, and voltage-dependent resistors (VDR) are nonlinear and computer tools for the analysis of circuits containing these elements are readily available in the market. One of these nonlinear elements, the voltage-dependent resistor may be connected to natural convection and thermal radiation modes. The best-known family of software tools for electric circuit analysis that include linear and nonlinear elements is named Simulation Program with Integrated Circuit Emphasis (SPICE) (Nagel [7]). In order to use SPICE, the analyst must first provide a complete description of the electric circuit. This step is done through a series of element statements, with one such statement for every element in the circuit. Second, these statements are followed by control statements, which instruct the program what needs to be calculated.

Conclusions

Under the premises of the powerful lumped model, the RC electric circuit that simulates forced convection cooling (linear heat transfer mode) with a constant convection coefficient has been a staple in the theory of heat conduction for many decades [3]. However, for the equally important situations of cooling by natural convection (nonlinear heat transfer mode) or thermal radiation (nonlinear heat transfer mode) the appropriate electric circuits do not exist in the heat transfer literature. These shortcomings were precisely the source of motivation for undertaking this study on advanced electro-thermal analogies.

When the cooling occurs by natural convection, the controlling natural convection coefficient is susceptible to the shape of the solid body and its orientation. Because of this, the Nu correlation equations may involve one, two or even three terms and the appropriate electric circuits may vary slightly from the one sketched in Fig. 2. In contrast, the electric circuit for thermal radiation cooling regardless of the body shape is given by Fig. 3.

Nomenclature

a,b = constants in Eq. (10)
C = thermal capacitance, J/K
C_e = electric capacitance, farads
e = constant in Eq. (14)
$E-E_\infty$ = electric potential, volts
h = forced or natural convection coefficient, W/m^2·K
$h_r(T)$ = radiation coefficient, W/m^2·K
j = current flow, amperes
Q = heat flow, W
R = thermal resistance, K/W
R_e = electric resistance, ohms
$T-T_\infty$ = thermal potential, K

Greek letters

θ = temperature transformation for natural convection, $T-T_\infty$, K

References

[1] Whitaker, S., 1972, ‘‘Forced Convection Heat Transfer Correlations for Flow Past Flat Plates, Single Cylinders and Single Spheres,’’ AIChE J., **18**, pp. 361–372.
[2] Ahmed, G. R., and Yovanovich, M. M., 1994, ‘‘Approximate Analytical Solution of Forced Convection Heat Transfer From Isothermal Spheres for all Prandtl Numbers,’’ ASME J. Heat Transfer, **116**, pp. 838–843.
[3] Kreith, F., and Bohn, M. S., 1993, *Principles of Heat Transfer*, Fifth Edition, West, New York, pp. 120–126.
[4] Churchill, S. W., 1990, ‘‘Free Convection Around Immersed Bodies,’’ in *Hemisphere Heat Exchanger Design Handbook*, G. F. Hewitt, ed., Section 2.5.7, Hemisphere, New York.
[5] Polyanin, A. D., and Zaitsev, V. F., 1995, *Handbook of Exact Solutions for Differential Equations*, CRC Press, Boca Raton, FL.
[6] Giedt, W. H., 1957, *Principles of Engineering Heat Transfer*, Van Nostrand, Princeton, NJ, pp. 283–286.
[7] Nagel, L. W., 1975, ‘‘SPICE2: A Computer Program to Simulate Semi-Conductor Circuits,’’ Memo No. UCB/ERL M520, Electronic Research Laboratory, University of California, Berkeley, CA.

Experimental Validation of a Combined Electromagnetic and Thermal Model for a Microwave Heating of Multi-Layered Materials Using a Rectangular Wave Guide

P. Rattanadecho
e-mail: phadu@blue.nagaokaut.ac.jp
Department of Mechanical Engineering,
Faculty of Engineering, Thammasat University
(Rangsit Campus), Prathumthani, 12121, Thailand

K. Aoki and M. Akahori
Department of Mechanical Engineering, Nagaoka
University of Technology, 1603-1, Kamitomioka,
Nagaoka, Niigata, 940-2188, Japan

The heating of multi-layered materials by microwave heating with rectangular wave guide has been investigated numerically and experimentally. The multi-layered materials, which consist of the layer of higher dielectric material (antireflection layer) and lower dielectric material (sample), have the convergent effect of the incident microwave in sample, and it can change the heating pattern in the sample with ease. In this study, the effect of an antireflection layer thickness on the heating process is clarified in detail, considering the interference between incidents and reflected waves in the dielectric materials. Based on a model combining the Maxwell and heat transport equations, the results showed that when a layer of lower dielectric material is attached in front of sample, the microwave energy absorbed and distribution of temperature within the sample are enhanced. The predicted results are in agreement with experimental results for microwave heating of multi-layered materials using a rectangular wave guide.

[DOI: 10.1115/1.1495521]

Keywords: Heat Transfer, Materials, Microwave, Modeling, Numerical Methods, Thermal

1 Introduction

The microwave heating of layered materials has been studied by many investigators, including Etternberg [1], Gori et al. [2], Nikawa et al. [3], Ayappa et al. [4] and Lin and Ghandhi [5]. Although most previous investigations are deplete with numerical simulations of simple model in one-dimensional form, there are only few papers have been reported on microwave heating of layered materials inside a rectangular wave guide, especially a full comparison of the space-time evolution of temperature between simulated results with experimental heating data. Part of the reason may be that analysis of microwave heating of layered materials is considerably more challenging due to the influence of dielectric properties in each layer, resulting to the complex interactions of microwave field with layered materials.

For microwave heating process, deep and localized heating technique for the dielectric material layer are sometimes demanded. When microwave fields are used, the depth of penetration is generally shallow and it is difficult to heat deep-lying layer and relatively large layered volumes without excessive surface heating. In order to overcome this difficulty, using the multi-layered material approach is one of the best means. The authors

---

Contributed by the Heat Transfer Division for publication in the JOURNAL OF HEAT TRANSFER. Manuscript received by the Heat Transfer Division October 10, 2001; revision received April 22, 2002. Associate Editor: P. S. Ayyaswamy.

suggest that the microwave energy absorbed and distribution of temperature within the sample are enhanced when a layer of lower dielectric material (called antireflection layer) is attached in front of sample (called higher dielectric material).

The characteristics of microwave heating of multi-layered materials studied here are potentially applicable to design of electromagnetic hyperthermia system for the treatment of cancer. The using of lower dielectric material as a mean of antireflection layer allowing more of the microwave energy can deposit deep inside the human tissues to keep them at the desired temperature elevation. Furthermore, the concept of microwave heating of multi-layered materials can be also useful for explaining the drying phenomenon in a fundamental level, particularly the complex interactions of microwave field with multi-layered materials. Considering microwave drying of porous materials (Ratanadecho et al. [6]), the drying layer takes place on a front retreating from the surface into the interior of the sample dividing it into two layers, dry and wet layers. Inside the drying front, the sample is wet, i.e., the voids contain liquid water and this layer acts as higher dielectric material. Outside the drying front, no liquid water exists, all water is in vapor state and the dry layer acts as the lower dielectric material. The changing of dry layer thickness (or lower dielectric material) would change the intensity of electric field, wavelength and location of maximum microwave energy absorbed with respect to drying times. This phenomenon explains why the understanding of interactions of microwave field with layered materials much be carefully performed.

Since the microwave heating of layered material is very complicated, consequently, the study in microwave heating of layered materials should be systematically studied. This work, the microwave heating of multi-layered material based on a two-dimensional model with experimental data, in which the microwave of TE_{10} mode operating at a frequency of 2.45 GHz, is completely presented in order to validate the possibility for using the multi-layered materials as a heating sample. The result presented here provides a basis for fundamental understanding of microwave heating of multi-layered materials.

2 Experimental Configuration

Figure 1 shows the experimental apparatus. The microwave system was a monochromatic wave of TE_{10} mode operating at a frequency of 2.45 GHz. Microwave energy was generated by magnetron (Micro Denshi Co., model UM-1500), it was transmitted along the z-direction of the rectangular wave guide with inside dimensions of 110 mm×54.61 mm toward a water load that was situated at the end of the wave guide. The water load (lower absorbing boundary) ensured that only a minimal amount of microwave was reflected back to the sample. The sample heated was a packed bed of 50 mm in thickness, which was composed of glass beads and water, called a higher dielectric material. The antireflection layer was also a packed bed ($d=1.0\,\mathrm{mm}$) which was composed of glass beads ($d=1.0\,\mathrm{mm}$) and air, called a lower dielectric material. The sample and the antireflection layer are arranged in series perpendicular to direction of irradiation via a rectangular wave guide. During the experiment, output of magnetron was adjusted at 1000 W. The powers of incident, reflected and transmitted waves were measured by a wattmeter using a directional coupler (Micro Denshi Co., model DR-5000). The temperature was measured with a Luxtron fluroptic thermometer model 790 (accurate to ±0.5°C).

3 Analysis of Microwave Heating Using a Rectangular Wave Guide

Physical Model. Figure 2 shows the physical model for the microwave heating of multi-layered materials using rectangular wave guide. Since microwave of TE_{10} mode which propagates in rectangular wave guide is uniformed in y-direction, the electromagnetic field can be considered in two-dimensional model on x-z plane. Corresponding to electromagnetic field, temperature fields also can be considered in two-dimensional model. The model proposed is based on the following assumptions:

1) The absorption of microwave by air in rectangular wave guide is negligible.
2) The walls of rectangular wave guide are perfect conductors.
3) All materials are non-magnetic.
4) The packed bed is an isotropic medium and thermal properties of packed bed are constant.
5) The liquid phase is incompressible fluid.
6) The effect of the sample container on the electromagnetic, velocity and temperature fields can be neglected.

Maxwell's Equation. Assuming the microwave of TE_{10} mode, the governing equations for the electromagnetic field can be written in term of the component notations of electric and magnetic field intensities (Ratanadecho et al. [6,7])

$$\frac{\partial E_y}{\partial z}=\mu\frac{\partial H_x}{\partial t} \tag{1}$$

$$\frac{\partial E_y}{\partial x}=-\mu\frac{\partial H_z}{\partial t} \tag{2}$$

$$-\left(\frac{\partial H_z}{\partial x}-\frac{\partial H_x}{\partial z}\right)=\sigma E_y+\varepsilon\frac{\partial E_y}{\partial t} \tag{3}$$

where, permittivity or dielectric constant ε, magnetic permeability μ and electric conductivity σ are given by

$$\varepsilon=\varepsilon_0\varepsilon_r,\quad \mu=\mu_0,\quad \sigma=2\pi f\varepsilon\tan\delta \tag{4}$$

The dielectric properties are assumed to vary with temperature during the heating process. To determine the functional dependence of the temperature [8], the theory of mixing formulas is used (Wang and Schmugge [9]). Further, all boundary conditions for solving Maxwell's equations have been already presented in previous work (Ratanadecho et al. [6]).

Heat Transport Equation. The temperature of the material exposed to incident wave is obtained by solving the conventional heat transport equation with the microwave power included as a local electromagnetic heat generation term:

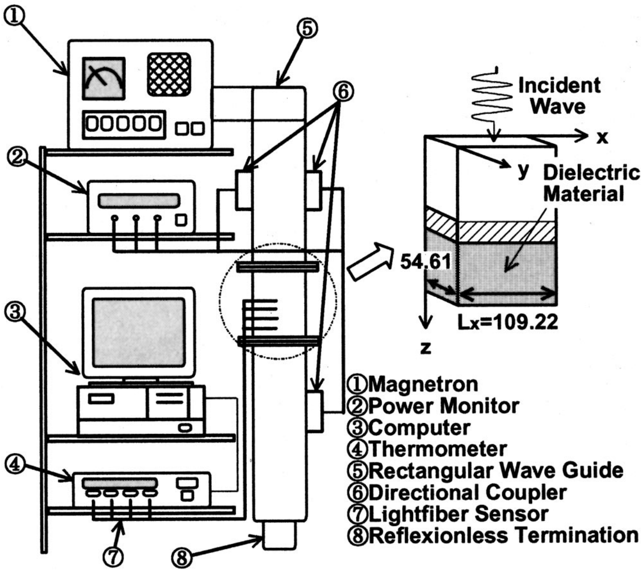

Fig. 1 Schematic of experimental facility

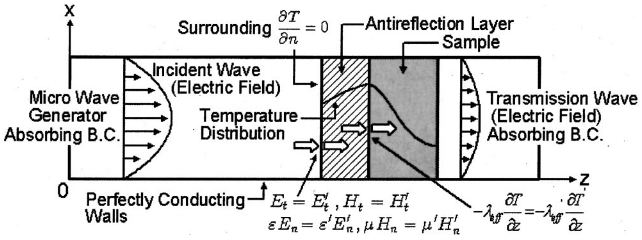

Fig. 2 Physical model

$$\frac{\partial T_j}{\partial t} = a_j\left(\frac{\partial^2 T_j}{\partial x^2} + \frac{\partial^2 T_j}{\partial z^2}\right) + \frac{Q_j}{\rho_j \cdot C_{pj}} \tag{5}$$

where, T is temperature, a is thermal diffusivity, ρ is density, c_p is heat capacity at constant pressure, and subscript j denotes lower or higher dielectric materials. The local electromagnetic heat generation term Q_j is directly depended upon the electric field distribution defined as:

$$Q_j = 2\pi \cdot f \cdot \varepsilon_0 \cdot \varepsilon_r (\tan\delta) E_y^2 \tag{6}$$

The boundary conditions for solving heat transport equation are shown in Fig. 2.

4 Results and Discussion

The experimental results for the microwave heating of multi-layered materials were compared with predictions from mathematical model. Some of the input data for electromagnetic and thermo-physical properties are given in Table 1.

In order to predict the electromagnetic and temperature fields, a finite difference time domain (FDTD) method is employed. The total 110×250 cells in computational domain are used in the numerical calculation. Since the propagating velocity of microwave is very fast compared with the rate of heat transfer, different time steps of $dt = 1$ [ps] and 1 [s] are used for the computation of the electromagnetic field and temperature profile and the spatial step size of $dx = dz = 1$ [mm] is selected.

4.1 The Variation of the Reflection Rate. Figure 3 shows the variation of the reflection rate versus the thickness of antireflection layer. It is found that the reflection rate strongly depends on the thickness of antireflection layer and displays a wavy behavior with respect to the thickness. The maximum and minimum reflection rates that occur in each thickness of antireflection can be clearly seen in that figure. This variation of the reflection rate is caused due to the interference between transmitted and reflected waves in an antireflection layer. The predicted results are in good agreement with the experimental results.

4.2 The Distribution of Electric Field. To understand the distribution of electrical field inside the rectangular wave guide and the multi-layered materials, the simulation analysis is required. For different heating sample configuration, the electric field pattern even with the same microwave power level. In Figs. 4–6, the simulation of the typical electric field of TE_{10} mode along the center axis ($x = 54.61$) of rectangular wave guide, for the cases of without and with antireflection layer, is presented. The vertical axis represents the intensity of the electric field E_y, which is normalized to the amplitude of the input electromagnetic wave, E_{yin}.

Table 1 The electromagnetic and thermo-physical properties used in computations

$\varepsilon_0 = 8.85419 \times 10^{-12}$[F/m],	$\mu_0 = 4.0\pi \times 10^{-7}$[H/m]	
$\varepsilon_{ra} = 1.0$,	$\varepsilon_{rp} = 5.1$	
$\mu_{ra} = 1.0$,	$\mu_{rp} = 1.0$,	$\mu_{rw} = 1.0$
$\tan\delta_a = 0.0$,	$\tan\delta_p = 0.01$	
$\rho_a = 1.205$[kg/m^3],	$\rho_p = 2500.0$[kg/m^3],	$\rho_w = 1000.0$[kg/m^3]
$C_{pa} = 1.007$[kJ/(kg·K)],	$C_{pp} = 0.80$[kJ/(kg·K)],	$C_{pw} = 4.186$[kJ/(kg·K)]
$\lambda_a = 0.0262$[W/(m·K)],	$\lambda_p = 1.0$[W/(m·K)],	$\lambda_w = 0.610$[W/(m·K)]

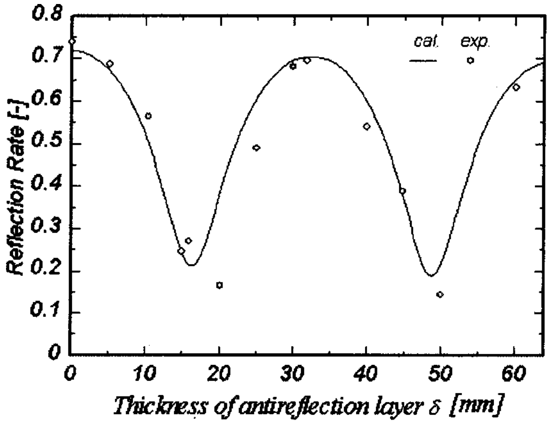

Fig. 3 Variation of the reflection rate versus thickness of antireflection layer

In Fig. 4, corresponding to that case without antireflection layer ($\delta = 0$ mm), since the microwave passing through cavity having low permittivity is directly irradiated to the sample having high permittivity, large part of microwaves are reflected from the surface of the sample (as referred to Fig. 3) and a stronger standing wave with larger amplitude is formed within the cavity by the superimposition of forward wave propagated from the wave input region and of the reflected wave from the surface of the sample.

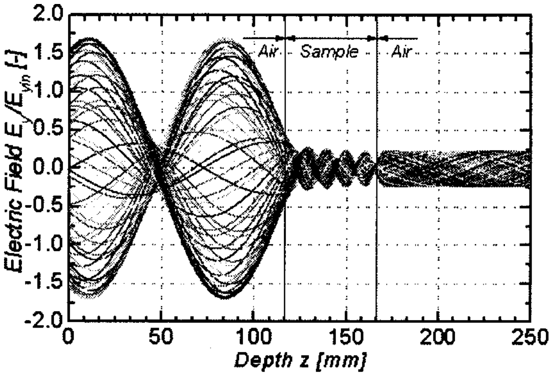

Fig. 4 Distribution of electric field in case without antireflection layer on the sample

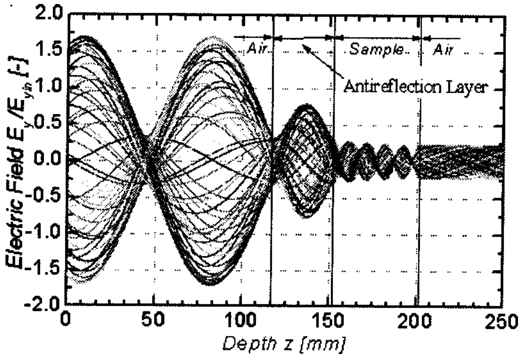

Fig. 5 Distribution of electric field in the case that antireflection layer is attached on the sample (δ=32 mm)

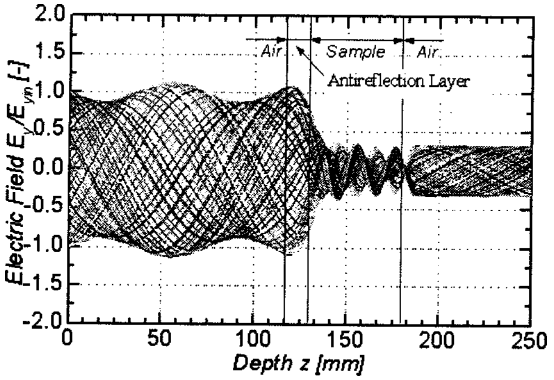

Fig. 6 Distribution of electric field in case that antireflection layer is attached on the sample (δ=16 mm)

However, the electric field within the sample is almost extinguished where the electric field attenuates owing to microwave energy absorbed, and thereafter the microwave energy absorbed is converted to the thermal energy.

Figure 5 shows the distribution of electric field for the case of antireflection layer with thickness of 32 mm is attached in front of sample. It can be seen that the distribution of electric field for this case is nearly the same as that without antireflection layer (Fig. 4). Therefore, the presence of antireflection layer at thickness of 32 mm slightly affects the distribution of electric field, due to the large part of microwaves are reflected from the surface (as referred to Fig. 3).

Figure 6 shows the distribution of electric field for the case of antireflection layer with thickness of 16 mm is attached in front of sample. With the presence of antireflection layer, the small part of microwave is reflected from the surface of the sample (as referred to Fig. 3). Since the large part of microwaves can further penetrate into the sample, the wave reflected from the sample-air interface at the lower surface has the same order as propagating wave. The propagating and reflected waves will contribute to the standing wave pattern with the larger amplitude and wavelength inside the sample, such pattern can lead to higher microwave energy absorbed in the interior in comparison with other cases.

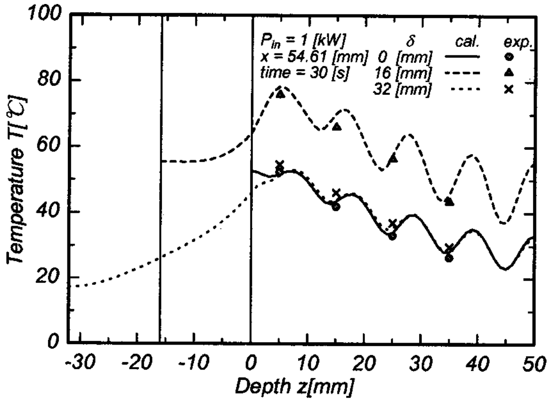

Fig. 7 Temperature distributions as a parameter of thickness of antireflection layer

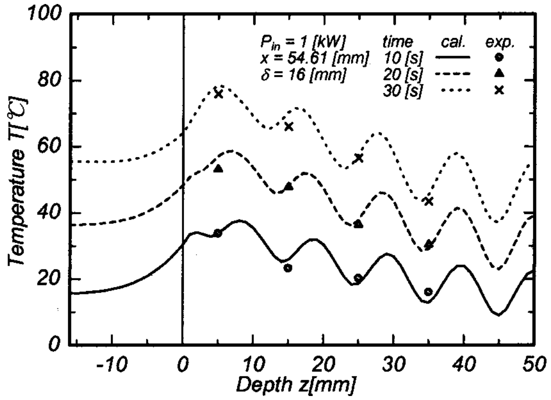

Fig. 8 Temperature distributions in case that antireflection layer (δ=16 mm) is attached on the sample

4.3 The Distribution of Temperature Field. The predictions from mathematical model are compared with experimental microwave heating data in Figs. 7 and 8, which corresponds to that of initial temperature of 0°C at heating times of 30 s, along with the center axis ($x = 54.61$ mm) of rectangular wave guide. It is clearly seen that the distribution of temperature in the sample is wavy behavior corresponding to that of electromagnetic field and the peaks of the temperature distribution decay slowly along the propagation direction. The distribution of temperature for case of antireflection layer with thickness of 32 mm is nearly the same as that without antireflection layer (Fig. 7), except at the surface part of the sample where the temperature drops due to the conduction of heat to the antireflection layer.

When the antireflection layer with thickness of 16 mm is attached in front of sample, the distribution of temperature is higher than those cases without antireflection layer and attaching the antireflection layer with thickness of 32 mm. This implies that with the presence of suitable antireflection thickness, a stronger standing wave with larger amplitude will be formed within the sample, consequently, a higher maximum temperature will be produced. Compared to the results for other cases (δ=0 mm and δ=32) at

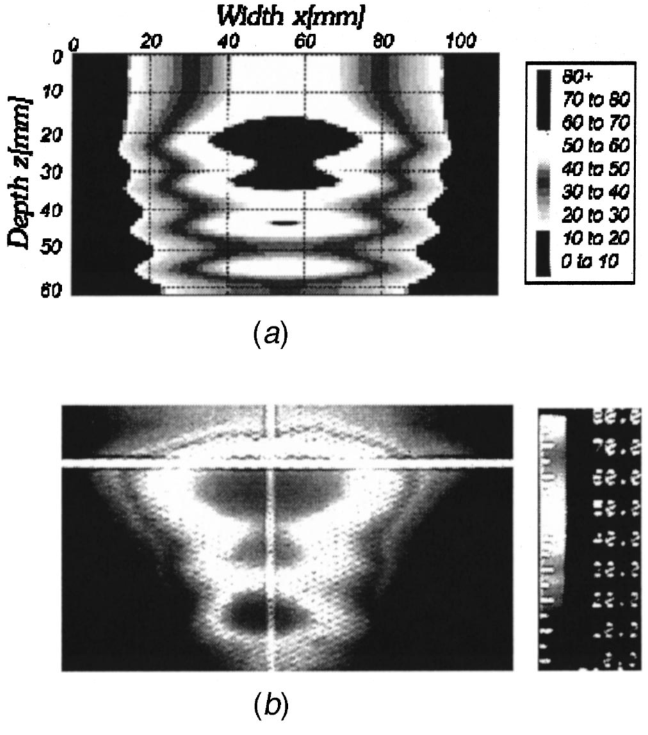

Fig. 9 Comparison between simulated results (a) and experimental results (b) for microwave heating in the case that antireflection layer is attached on the sample (δ=16 mm., t=30 s): (*a*) simulated temperature distributions (Units: °C); and (*b*) measured temperature distributions (Units: °C).

heating times of 30 s, the maximum temperature is about 78°C. For other cases (δ=0 mm and δ=32) with the same microwave power level at the same heating time, it is about 50°C, which is about 56 percent higher. The distribution of temperature with respect to times for the case of antireflection layer with thickness of 16 mm is also shown in Fig. 8. The wavy behavior of temperature distributions appear and rapidly raise with elapsed time because of a stronger standing wave with larger amplitude is formed in the sample and the antireflection layer protects the reflected wave from the surface. The predicted results are in agreement with experimental results for microwave heating of multi-layered materials using a rectangular wave guide.

Furthermore, the distribution of temperature within the multi-layered materials in the vertical plane (x-z) is shown in Fig. 9. The result shows the greatest temperature at the center of heating sample where the microwave energy absorbed is maximum. It can be seen that the agreement between the two heating patterns is good, particularly concerning the location of the hot region.

From this study, the result predicts the possibility of effective depth and localized heating in a dissipative medium such as dielectric material. It seems that a proper selection of the suitable antireflection layer thickness could lead to the increase in the penetration depth and the heat generation in the dielectric materials.

5 Conclusions

The experimental and numerical of two-dimensional model for microwave heating of multi-layered materials is presented in order to validate the possibility for using the multi-layered materials as a heating sample. In this study, the influence of the thickness of antireflection layer on the microwave energy absorbed and heating pattern that develop within multi-layered materials is clarified in detail. The results showed that the microwave energy absorbed as well as wavelength and distribution of temperature within the sample are enhanced when a suitable thickness of antireflection layer (lower dielectric material) is attached in front of sample (higher dielectric material). This is due to attaching the suitable thickness of antireflection layer decreases the reflected wave from the surface of sample (higher dielectric material), the latter arises from the fact that the large parts of microwaves can penetrate further into the sample. The propagating and reflected waves at each interface will contribute to the stronger standing wave with the larger amplitude and wavelength, resulting in a higher microwave energy absorbed in the interior in comparison with other cases. On the other hand, in other cases that the reflected wave is still higher resulting in a lower microwave energy absorbed in the interior. The predicted results are in agreement with experimental results for microwave heating of multi-layered materials using a rectangular wave guide.

Nomenclature

a = thermal diffusivity [m^2/s]
E = electric field intensity [V/m]
f = frequency of incident wave [Hz]
H = magnetic field intensity [A/m]
P = power [W]
Q = electromagnetic heat generation [W/m^3]
$\tan\delta$ = dielectric loss tangent coefficient
t = time [s]

Greek letters

δ = layer thickness [m]
ε = permittivity or dielectric constant [F/m]
ε_r = relative permittivity or relative dielectric constant
λ = thermal conductivity of materials [W/m^{2}K]
μ = magnetic permeability [H/m]
σ = electric conductivity [S/m]
ω = angular frequency [rad/s]

Subscripts

0 = free space
a = air
in = input
p = particle
r = relative
w = water
x,y,z = coordinates

Superscripts

$'$ = interfacial position

References

[1] Ettenberg, M., 1985, "Microwave Hypothermia and Radiometry: One-Dimensional Computer Models," RCA Rev., **46**, pp. 510–527.

[2] Gori, F., Gentili, G., and Matini, L., 1987, "Microwave Heating of Porous Media," ASME J. Heat Transfer, **109**, pp. 522–525.

[3] Nikawa, Y., Katsumata, T., Kikuchi, M., and Mori, S., 1986, "An Electric Field Converging Applicator with Heating Pattern Controller for Microwave Hyperthermia," IEEE Trans. Microwave Theory Tech., **34**(5), pp. 631–635.

[4] Ayappa, K. G., Davis, H. T., Davis, E. A., and Gordon, J., 1991, "Analysis of Microwave Heating of Materials with Temperature-Dependent Properties," AIChE J., **37**, pp. 313–322.

[5] Lin, J. C., and Gandhi, Om P., 1996, "Computer Methods for Predicting Field Intensity," *Handbook of Biological Effects of Electromagnetic Fields*, 2nd ed., Polk and Postow, eds., CRC Press, Boca Raton, FL.

[6] Ratanadecho, P., Aoki, K., and Akahori, M., 2002, "Influence of Irradiation Time, Particle Sizes and Initial Moisture Content During Microwave Drying of Multi-Layered Capillary Porous Materials," ASME J. Heat Transfer, **124**, pp. 151–161.

[7] Ratanadecho, P., Aoki, K., and Akahori, M., 2002, "The Characteristics of Microwave Melting of Frozen Packed Bed Using a Rectangular Wave Guide," IEEE Trans. Microwave Theory Tech., pp. 1487–1494.

[8] Von Hippel, A. R., 1954, *Dielectric Materials and Applications*, MIT Press, Boston.

[9] Wang, J., and Schmugge, T., 1980, "An Empirical Model for the Complex Dielectric Permittivity of Soil as a Function of Water Content," IEEE Trans. Geosci. Remote Sens., **GE-18**(4), pp. 288–295.